THESIS FOR THE DEGREE OF DOCTOR OF PHILOSOPHY

Crystallization of the superconducting phase in unconventional superconductors

PATRIC HOLMVALL

Department of Microtechnology and Nanoscience (MC2)
Applied Quantum Physics Laboratory
CHALMERS UNIVERSITY OF TECHNOLOGY

Göteborg, Sweden 2019

Crystallization of the superconducting phase in unconventional superconductors
PATRIC HOLMVALL
Göteborg, Sweden 2019
ISBN 978-91-7905-217-1

Doktorsavhandlingar vid Chalmers tekniska högskola
Ny serie Nr 4684
ISSN 0346-718X

Applied Quantum Physics Laboratory
Department of Microtechnology and Nanoscience (MC2)
Chalmers University of Technology
SE-412 96 Göteborg, Sweden
Telephone: +46 (0)31-772 1000

Cover
Periodic modulation of the superconducting phase (surface). Arrows indicate the corresponding superfluid momentum (top) and total charge current (bottom).

Printed by Chalmers Reproservice
Göteborg, Sweden 2019

Crystallization of the superconducting phase in unconventional superconductors

PATRIC HOLMVALL
Applied Quantum Physics Laboratory
Department of Microtechnology and Nanoscience (MC2)
Chalmers University of Technology

ABSTRACT

Superconductivity is a macroscopic quantum phenomenon, in the sense that a macroscopic number of electrons form a pair condensate, that occupies a single ground state. The electrons in this state are phase-coherent, breaking global $U(1)$-symmetry, and spatial variations of the phase imply superflows that usually cost kinetic energy, resulting in a uniform and rigid phase. It would therefore be surprising if a more ordered state with a non-uniform phase existed. This thesis proposes that such a ground state can occur in the absence of external perturbations, deep inside the superconducting state, where a periodic pattern is spontaneously imprinted on the superconducting phase, breaking continuous translational invariance. The resulting phase gradients break time-reversal symmetry, manifested through finite superflows and equilibrium charge currents with peculiar patterns. In analogy to crystallization in solids, the new order parameter is defined as a finite Fourier amplitude at the wavevector corresponding to the phase-periodicity. This ground state is hence referred to as a phase crystal.

The thesis employs the quasiclassical theory of superconductivity, combined with a non-local Ginzburg-Landau theory, to derive the inhomogeneous superfluid density tensor and the conditions under which phase crystallization can occur. It is shown how the phase can be realized at certain interfaces of unconventional superconductors, and in conventional superconductor-ferromagnet structures. The instability phase diagram is obtained, and the transition classified as second-order, surviving moderately strong external fields. The phase is tied to critical points in the superflow field, satisfying a generalized Poincaré-Hopf theorem. Geometric perturbations and disorder are studied, and characteristic signatures identified, in an attempt to aid experimental efforts in potential realization of the phase.

In conclusion, the model based on the non-local superfluid tensor provides a unified approach to studying surface phenomena, e.g. topological states and inhomogeneous superconductivity, and is used to both verify and explain several previous numerical observations. The model directly highlights the role of non-local correlations and phase variations as drivers in phase transitions, motivating a search for new non-local phenomena in various condensed matter systems.

Keywords: unconventional superconductivity, mesoscopic thin-films, quasiclassical theory, Andreev states, phase crystals, spontaneous symmetry breaking, pattern formation, non-local Ginzburg-Landau theory

ACKNOWLEDGEMENTS

I would not be where I am today, if it was not for all the wonderful people I met over the years. You are far too many to mention, but know that I am grateful for your presence in my life.

When I started my PhD, I knew close to nothing about condensed matter physics, let alone superconductivity. My supervisors, Tomas Löfwander and Mikael Fogelström, were brave indeed to take me under their wings. A great deal of patience and time has been sacrificed on their side, during countless hours of discussions and collaboration. What I know about superconductivity today, I owe mostly to their supervision. They have also taught me invaluable lessons about scientific research, especially to keep my feet on the ground and my mind on the task at hand, and how to become more independent as a researcher. Together with the other members at Applied Quantum Physics Laboratory at Chalmers, they have created an environment in which to thrive and grow as a researcher. I thank all the members of this group, present and past, for all the years spent together. Thank you for all the Swedish Fika and the many thought-provoking discussions. It has been quite a journey, perhaps not so much spatially, but certainly mentally. I would like to especially thank Mikael Håkansson for sharing his computational framework and helping me out during the start of my PhD. He and many others have helped me to better grasp superconductivity, including Niclas Wall Wennerdal, Oleksii Shevtsov, Daniel Persson, Kevin Marc Seja, Vitaly Shumeiko, Dag Winkler, Per Delsing, Alexei Kalaboukhov, Henrik Johannesson, James Sauls, William Halperin, Joshua Wiman and Matthias Eschrig. I also thank Matthias for being the discussion leader during my Licentiate defense. I thank Raffaella Negretti, Maciej Misiorny and Jens Schulenborg for continued assistance.

I spent a significant portion my PhD in the US, and in particular in Bozeman, Montana. I want to thank all the friendly people I met there for their warm reception, the fun activities, and for organizing all the seminars. I thank Anthony van Eysden for hosting me, and for all the great times spent together. Anthony has a brilliant mind, and it was a pleasure to discuss everything from neutron-star superfluidity to the history of the Roman empire, especially over American-sized brunch. Thank you for finally bringing the “crazy Swede and Russian” to hike up the M-trail during a blizzard. On a similar note, I am deeply grateful to Charles and Carol Kankelborg for their warm hospitality, for opening their home to me during my second visit to Bozeman, and for showing me what Super Bowl is all about (the commercials, of course). Many great discussions were shared on astronomy and rocket science, tricky integrals, and philosophy. Although not an official supervisor, Anton Vorontsov has sure filled the role as one. Our collaboration has been both fruitful and exciting. I am grateful for his invitation to Montana State University in Bozeman. Besides research, Anton took me on several adventures, some of which were very enjoyable, and others that were... interesting. The trip with Takeshi Mizushima to Santa Monica Beach definitely belongs to the former category, while the various trips in Montana were a good mix of the two. My idea of skiing a steep mountain has always been downhill on alpine skis. Antons idea is completely different however: uphill on cross-country skis. I now know that this is a terrific workout, especially on unwaxed skis. Unfortunately, our first attempt to reach Yellowstone Park did not succeed. Severe weather conditions had covered the entire interstate in black ice. After driving 10 mph for a few hours, without proper winter tires, we were caught in a blizzard white-out. When your driver tells you, with a Russian accent, that “this is completely dangerous”, you know you are in trouble. Luckily, we were successful on our second attempt, and I had made sure to bring properly waxed skis. The icy terrain made the ascents much easier this time around, and on our narrow path next to a ravine, we had many close encounters with the friendly locals - the buffalo bison. The problem with ascending a mountain on cross-country skis, however, is that you also have to descend a mountain on cross-country skis. For the unfamiliar, this is a truly terrifying experience, as you have little to no control of speed or direction. Having no chance to break or slow down on the ice, the descent turned into an adrenaline-fueled slalom between upset buffalo bison and the ravine, that I will never forget. After all the cross-country skiing with Anton, I am most grateful to Anne, Bennett, Carla and Jennifer for taking me alpine skiing in Bridger Bowl.

Between the trips to Bozeman and the APS conferences, I was also fortunate enough to visit Northwestern University, and the groups of James Sauls and William Halperin. The sheer amount of knowledge on superconductivity shared by this iconic duo is astounding, and having the opportunity to discuss and learn from them was both inspiring and motivating. I am thankful to their students for making my stay most enjoyable, and for their patience during hours of questions about their research. I thank William Halperin for inviting me to their group party at his home, and for teaching me how to make ice cream with liquid nitrogen.

A great part of my life has been spent at Chalmers University of Technology. There really is such a thing as the “Chalmers spirit”, and I am glad to have been a part of it. The subatomic physics group at Chalmers opened the door to academic research for me many years ago, by giving me the courage to pursue higher education and my own research. There, Christian Forssen showed me how I could combine physics with my interest in computer science, by throwing me into the world of high-performance computing. I have met few people who are as pedagogical as Christian. Thank you for being an outstanding mentor. I want to thank my collaborator at the time, Olof Ahlén, for encouraging me to do a summer internship at CERN, which led to one of the best times of my life. There, I met amazing and inspiring people from all over the world, who completely changed the course of my life. I thank Thomas Nilsson, who not only helped send me to CERN, but also to Institut Laue Langevin in Grenoble for my masters thesis work. There I met the eccentric Ulli Köster, who is one of a kind, to say the least. Our experiments were literally a blast. Thank you for giving me free reigns to do my own research, and "thank you" for the mountain climbing adventure in the alps. I am terribly afraid of heights, and promised myself I would never climb again after that experience. Now I do it every second day. I also got excellent supervision from the Chalmers side, by Andreas Heinz, Håkan Johansson and Thomas Nilsson. You have all been defining in my early development as a scientist, and you are all to thank for my pursuit of a PhD. Thank you Andreas for teaching me that "science is never done", otherwise you would probably still receive updated drafts of my Masters thesis. Before embarking on my PhD, I was fortunate to be able to take a detour to the Max-Planck Institute in Greifswald thanks to Tünde Fulöp. There, I had the excellent supervisors Gabriel Plunck and Per Helander, who shared their pure joy for theory and pen-and-paper calculations, steering me away from experiments to theoretical physics. I am grateful to everyone I met in Greifswald for making such a small town so full of friendship and activities.

Finally, my deepest gratitude goes to my friends, my family, and to Laura. Thank you all for patiently standing by my side while I pursue my dreams. If it was not for your continued support, I would never have made it as far as I did.

List of publications

This thesis presents an introduction, summary and extension to the following appended papers:

[I] P. Holmvall, M. Fogelström, T. Löfwander, and A. B. Vorontsov, "Phase Crystals", arXiv:1906.04793 (2019), submitted to Phys. Rev. X.

[II] P. Holmvall, A. Vorontsov, M. Fogelström, and T. Löfwander, "Broken translational symmetry at edges of high-temperature superconductors", Nat. Commun. **9**, 2190 (2018).

[III] P. Holmvall, A. B. Vorontsov, M. Fogelström, and T. Löfwander, "Spontaneous symmetry breaking at surfaces of *d*-wave superconductors: Influence of geometry and surface ruggedness", Phys. Rev. B **99**, 184511 (2019).

[IV] P. Holmvall, T. Löfwander, and M. Fogelström, "Spontaneous generation of fractional vortex-antivortex pairs at single edges of high-Tc superconductors", J. Phys.: Conf. Ser. **969**, 012037 (2018).

These publications are always referred to as paper I, II, III and IV, according to the labeling in the list above. Please note that the paper numbering does not correspond to chronological order of publication, but rather in order of relevance to the story of the thesis.

SPECIFICATION OF MY CONTRIBUTIONS TO THE APPENDED PAPERS

I The initial idea of an analytic approach to the phase crystal phenomenon was hatched during discussions with my supervisors. Later, during a visit from Anton Vorontsov, a first model and approach emerged during numerous discussions between all of the authors. These calculations, along with the numerics, were later carried out in tandem between Anton Vorontsov and myself. The analytics that ended up in the paper is mainly based on Antons calculations and notation, while the numeric results and figures are mainly based on mine. The manuscript was assembled by Anton Vorontsov, with substantial input from all the authors.

II My collaborators came up with the main idea behind this study. My contribution was to build upon this idea, carrying out the numerics, producing the figures, and writing the first draft of the manuscript. The analytic calculations were carried out together with Anton Vorontsov.

III My contribution consisted of coming up with the main ideas for this study, carrying out the numerical calculations, producing the figures, writing the first draft of the manuscript, and doing parts of the analytic calculations.

IV My collaborators came up with the initial idea behind this study, while my contribution consisted of carrying out the numerical calculations, producing the figures, and writing the first draft of the manuscript.

List of figures

NOMENCLATURE

ABS	Andreev bound states
BCS	Bardeen-Cooper-Schrieffer
DOS	Density of states
FS	Fermi surface
FFLO	Fulde-Ferrell-Larkin-Ovchinnikov state
GS	Ground state
LDOS	Local density of states
MED	Magnetic energy density
MGS	Midgap states
MS	Metastable state
N	Normal state
OP	Order parameter
S	Superconducting state
SC	Superconductor

Symbols

Δ	Superconducting order parameter
η	Pairing-symmetry basis-function of the order parameter
z	Complex energy
z_p	Complex energy shifted by superflow $z_p \equiv z - \boldsymbol{v}_\mathrm{F} \cdot \boldsymbol{p}_\mathrm{s}$
z^M	Matsubara energy $z^\mathrm{M} = i\varepsilon_n$
z^R	Retarded energy $z^\mathrm{R} = \varepsilon + i0^+$
ε_n	Matsubara energy $\varepsilon_n = \pi k_\mathrm{B} T(2n+1)$
$\boldsymbol{p}_\mathrm{s}$	Superfluid momentum; superflow

ϵ_{F}	Fermi energy
$\boldsymbol{p}_{\mathrm{F}}$	Fermi momentum
$\boldsymbol{v}_{\mathrm{F}}$	Fermi velocity on the Fermi surface at momentum $\boldsymbol{p}_{\mathrm{F}}$
θ_{F}	Angle relative to Fermi momentum direction
$\boldsymbol{K}$	Inhomogeneous superfluid density tensor
$\boldsymbol{\rho}$	Homogeneous bulk density tensor
ρ	Homogeneous bulk density tensor at zero temperature
f	Pair propagator
g	Quasiparticle propagator
γ	Coherence function, Riccati amplitude
T_{c}	Superconducting transition temperature
ξ_0	Zero-temperature coherence length
κ_0	Zero-temperature Ginzburg-Landau parameter
λ	Superconducting coupling constant
λ_L	London penetration depth
λ_0	Zero-temperature London penetration depth
h	Planck constant
e	Elementary charge ($e = -\lvert e\rvert$)
c	Speed of light
$\hbar$	Reduced Planck constant
k_{B}	Boltzmann constant
N	DOS
N_{F}	Normal-state DOS at the Fermi surface
$\delta\Omega$	Free-energy difference between normal and superconducting states
$\boldsymbol{j}$	Total current density
$\boldsymbol{H}$	Magnetic field

$\boldsymbol{B}$	Magnetic flux density
$\boldsymbol{B}_{\mathrm{ext}}$	External magnetic flux density applied to the system
$\boldsymbol{B}_{\mathrm{ind}}$	Magnetic flux density induced by currents in the system
$\boldsymbol{A}$	Magnetic vector potential
Φ_0	Magnetic flux quantum

Contents

1 Introduction

Nanoscience and nanotechnology are active areas in contemporary research, with bold promises of new technologies and quantum devices that will revolutionize the world as it is know [1–4]. Superconducting devices have proven to be indispensable tools in this line of research, due to the versatile and distinguished properties of superconductivity. Such superconducting devices often come in the form of thin-film hybrid structures or circuit elements that operate in the mesoscopic regime [5–8], referring to the intermediate realm between the macroscopic regime of bulk materials, and the microscopic quantum regime. Since the properties of superconductivity typically vary over the mesoscopic scale, finite-size and surface effects can cause pronounced inhomogeneities, especially in unconventional superconductors, leading to phenomena not present in bulk systems [9]. However, the basic understanding of many of these phenomena is far from complete. This is a topic of modern research, and the goal of this thesis is to study such properties. Of particular interest are systems which create an unfavorable environment for the superconducting order, due to boundary conditions and competing orders, where spontaneous symmetry breaking can counteract these unfavorable effects. The thesis and the appended papers use numeric simulations based on the quasiclassical theory of superconductivity to study these effects. To interpret these simulations and make new predictions, an analytic model is developed which combines quasiclassics with a non-local and inhomogeneous Ginzburg-Landau theory.

This chapter gives a very brief introduction to these concepts, with some in-depth explanations in the following chapters. For a more thorough introduction, see the Licentiate thesis (half-way thesis), from here on referred to as Lic. Th. [10], as well as standard literature on condensed matter physics [11–13], superconductivity [14–17], and the references in the introductions of the appended papers. Furthermore, it is noted that Lic. Th. [10] is completely devoted to the numeric simulations, while this PhD thesis focuses more on the analytic approach. At the end of this chapter, the research topic and scope of the PhD thesis are stated, with a detailed outline of the chapters and appendices to follow.

1.1 Phase transitions and order parameters: pattern formation in condensed matter

Structure and pattern formation is a ubiquitous phenomenon in nature, ranging from the realization of solids with both periodic and quasi-periodic crystal structures [18–21], stunning decorations in liquid crystals [22, 23], the growth and organization of cells and bacteria [24–28], microscopic patterns and structural coloration in plants and animals [29–33], to the assembly of topological defects in superconductors [34–36]. Although these phenomena span widely different fields and origins, with varying degrees of complexity, they all follow the same fundamental principles of energy minimization, phase transitions and ordering.

In physics, such principles are typically described in terms of Landau's theory of phase transitions [37], where the transition into a phase which lowers the entropy, and hence corresponds to a more ordered state (possibly with a lower symmetry), might be quantified by an order parameter Ψ. For example, in a typical liquid-solid transition, the system goes from being translationally invariant to being periodically ordered with the appearance of a crystalline lattice [18]. The more ordered solid state hence breaks continuous translational symmetry, and the order parameter may be defined as the finite Fourier amplitude corresponding to the periodicity [18–20]. The appropriate classification of the order parameter varies between different phases, systems and fields. In liquid crystals and biological systems, for example, the order parameter is typically defined as a unit vector $\hat{\boldsymbol{n}}$ corresponding to the local average orientation of the molecules that constitute these systems [22], and transitions might occur between phases with different preferred molecular orientations and patterns [23]. The preferred phase is the one that minimizes the energy of the system, and typically depends on the relevant interactions, parameters (e.g. temperature), and externally applied perturbations. In Ginzburg-Landau theory [38, 39], this is quantified in the form of a free-energy functional, given as an expansion in the order parameter close to the phase transition, with phenomenological coefficients and terms that depend on the parameters, interactions and perturbations. Symmetry arguments are typically invoked to determine which expansion terms are possible. Consider an example with a scalar order parameter $\Psi(R, T)$ depending on temperature T and position R, which in the absence of external perturbations have the following expansions

$$f = \alpha|\Psi|^2 + \frac{\beta}{2}|\Psi|^4 + K\left|\boldsymbol{\nabla}_R\Psi\right|^2, \tag{1.1}$$

$$F = \frac{1}{2}\int dR f(\boldsymbol{R}), \tag{1.2}$$

where f is the free-energy density, F the total energy, and $\int dR \equiv \mathcal{V}$ is the volume of the system. With phenomenological coefficients $\beta > 0$, $\alpha(T > T_c) > 0$

and $\alpha(T \leq T_\mathrm{c}) \leq 0$, there is an instability below a transition temperature T_c where the energy turns negative for a finite order parameter $|\Psi(T \leq T_\mathrm{c})| \geq 0$ with $|\Psi(T > T_\mathrm{c})| = 0$. Here, $K > 0$ implies that spatial variations cost energy, favoring a homogeneous ground state. For bulk systems, this is often the case, as will be seen in the next section on superconductivity. It is also commonly the case in nematic liquid crystals, where the free energy is explicitly defined as a positive distortion energy caused by a deviation from a uniform liquid crystal, with terms different than the ones in Eq. (1.1) corresponding to the possible deformation modes [22, 40]. However, a sign change $K < 0$ would signal an instability towards inhomogeneities and pattern formation. This might happen when the system exhibits an unfavorable environment that suppresses the order and increases the energy, either induced by externally applied perturbations, or spontaneously due to boundary conditions and competing orders. The gradient terms and resulting order-parameter inhomogeneities might then act as a mechanism to counteract the unfavorable effects, lowering the free energy again due to $K < 0$ [41–45]. It is noted that the inverse might also occur, where an already inhomogeneous order causes instead a perturbation in the environment [30, 46]. Many of the pattern formations mentioned in the beginning of the section are related to such scenarios. The case of superconductors will now be discussed briefly, where interestingly, gradients in the order parameter directly imply (super)currents and magnetic fields.

1.2 Conventional superconductivity

In conventional superconductors, a phonon-mediated net attractive interaction between conduction electrons leads to an instability in normal metals, where a macroscopic number of electrons pair up and condense into a coherent state, described by a wave function ψ [47–50]. This wave function can be chosen[1] as the (complex-valued) order parameter $\Delta = \psi$

$$\Delta = |\Delta| e^{i\chi}, \tag{1.3}$$

where $|\Delta|$ corresponds to the pair density and a temperature-dependent gap in the electronic excitation spectrum (studied further in Ch. 3), and with a coherent phase χ (hence spontaneously breaking $U(1)$ gauge symmetry). This phase-coherence is mediated over the coherence length, typically defined as $\xi = \hbar v_{\mathrm{F}}/\Delta(T)$, where v_{F} is the Fermi velocity on the Fermi surface. The pairing is symmetric in momentum space, and commonly referred to as s-wave pairing. The superconducting state exhibits perfect DC conductivity and perfect diamagnetism (the Meissner effect) [51], where the former implies that the superconducting condensate acts as a superfluid with zero resistance. Furthermore, the number of electrons participating in the condensation is typically on the order of Avogadro's number. Since the particle number and phase are canonically conjugate variables fulfilling Heisenberg's uncertainty relation, fixing the phase, implies an uncertainty in the number of particles. In bulk systems, however, this uncertainty is typically small compared to the total number of particles, and allows for a quite precise specification of the particle number and phase simultaneously. Hence, the superconducting state truly signifies a macroscopic quantum phenomenon. Still, spatial variations of the phase $\boldsymbol{\nabla}\chi(\boldsymbol{R}) \neq 0$ give rise to fluctuations in the particle number, and consequently a superflow $\boldsymbol{p}_{\mathrm{s}}$ (i.e. the superfluid momentum $\boldsymbol{p}_{\mathrm{s}} = m\boldsymbol{v}_{\mathrm{s}}$), as seen from the gauge-invariant definition

$$\boldsymbol{p}_{\mathrm{s}}(\boldsymbol{R}) = \frac{\hbar}{2}\boldsymbol{\nabla}\chi(\boldsymbol{R}) - \frac{e}{c}\boldsymbol{A}(\boldsymbol{R}), \tag{1.4}$$

where $\boldsymbol{A}$ is the electromagnetic gauge field.

In the absence of external perturbations, the lowest-order Ginzburg-Landau energy might be written [38, 39]

$$f = \alpha|\Delta|^2 + \frac{1}{2}\beta|\Delta|^4 + K\boldsymbol{\nabla}\left|\Delta\right|^2 + K|\Delta|^2\left|\boldsymbol{\nabla}\chi\right|^2, \tag{1.5}$$

where K is the superfluid density, and the gradient term $K|\Delta|^2\left|\boldsymbol{\nabla}\chi\right|^2$ is the kinetic energy of the superfluid. Here, $K > 0$ ensures a homogeneous ground state with

---

[1] The superconducting order-parameter will later on be defined as a mean-field expectation value of the pair propagator.

a rigid phase ($\chi = \text{const}$) and thus no spontaneous superflow. In the presence of external fields, additional terms are added to Eq. (1.5), and inhomogeneous ground states are known to exist for fields applied perpendicularly to the superconductor (coupling to the orbital part of the pairs) i.e. the Abrikosov-vortex state [16, 34, 36], parallel to the superconductor (coupling to the spins of the pairs) e.g. the Fulde-Ferrell-Larkin-Ovchinnikov states [52, 53], and a combination of the two [35]. In the absence of external fields, $\chi = \text{const}$ and $K > 0$ are often assumed *a priori*. For a proper treatment, however, K should be derived from the underlying microscopic theory to decide whether superflow is unfavorable or not. A main result of this thesis is the derivation of the superfluid density in an inhomogeneous environment, where it takes the form of a tensor $K_{ij}(\boldsymbol{R}, \boldsymbol{R}')$ that correlates different spatial coordinates due to the non-locality introduced by the superconducting coherence length. Equation (1.5) is then modified to

$$F_{\text{sf}} = \frac{1}{2}\int\int dRdR' \, [\boldsymbol{\nabla}\chi(\boldsymbol{R})]_i \, K_{ij}(\boldsymbol{R}, \boldsymbol{R}') \, [\boldsymbol{\nabla}\chi(\boldsymbol{R}')]_j \, . \tag{1.6}$$

This is done using the quasiclassical theory of superconductivity, introduced in Ch. 2. As mentioned in Sec. 1.1, it is well-known from a number of other fields, particularly condensed matter physics, how boundary conditions or competing orders can create an environment where the order is suppressed, and a sign-change $K < 0$ can occur to counteract these unfavorable effects. In superconductors, a suppression of the order parameter can for example occur due to scattering that breaks the superconducting pairs. In particular, this thesis studies certain interfaces of unconventional superconductors, where pairbreaking scattering leads to a spectral weight of quasiparticle states below the superconducting gap, known as Andreev bound states, and how this can fulfill $K < 0$. This scenario will now be briefly explained.

1.3 Unconventional superconductivity

While the mechanism responsible for conventional superconductors is known and well-described by the BCS theory [49, 50], the mechanism in unconventional superconductors is still unknown and a topic of intense research. Per definition, superconductors that break additional symmetries to $U(1)$ symmetry are known as unconventional superconductors. As an example of unconventional superconductors, and of particular interest for this work, are the *cuprates* with superconducting copper-dioxide ($\mathrm{CuO_2}$) planes. Superconductivity is typically suppressed between these planes. Conventional superconductors have an isotropic s-wave pairing symmetry in momentum space $\Delta(\boldsymbol{R},\boldsymbol{p}_\mathrm{F}) = |\Delta(\boldsymbol{R})|e^{i\chi(\boldsymbol{R})}$, while the cuprates exhibits e.g. an anisotropic $d_{x^2-y^2}$-wave pairing symmetry (from here on just written d-wave) with $\Delta(\boldsymbol{R},\boldsymbol{p}_\mathrm{F}) = |\Delta(\boldsymbol{R})|e^{i\chi(\boldsymbol{R})}\eta(\theta_\mathrm{F})$ [54–56]. Here, $\boldsymbol{p}_\mathrm{F}$ is the Fermi momentum, θ_F its angle relative to the crystal $\hat{\boldsymbol{a}}$-axis, and η the basis function defining the pairing symmetry. In $2D$, the latter is often represented in Cartesian and polar form as

$$\eta_d = \hat{p}_x^2 - \hat{p}_y^2 = \sqrt{2}\cos(2\theta_\mathrm{F}), \tag{1.7}$$

respectively. This implies that the d-wave order parameter has point nodes at which it is suppressed, as well as lobes of different signs, see Fig. 1.1. Note that for a strong suppression between the superconducting $\mathrm{CuO_2}$ planes, a cylindrical symmetry is often assumed, implying instead line nodes. The anisotropy in Eq. (1.7) effectively enables scattering processes that couple order parameters of different signs. Consider a specular [110] interface (an interface aligned with the d-wave nodes), as illustrated in Fig. 1.1 (b). An incoming and an outgoing scattering trajectory couples a positive and a negative lobe, inducing a sign change in the order parameter. This leads to resonant Andreev reflection (referring to multiple retro-reflections where a particle is converted into a hole or vice versa) [57,

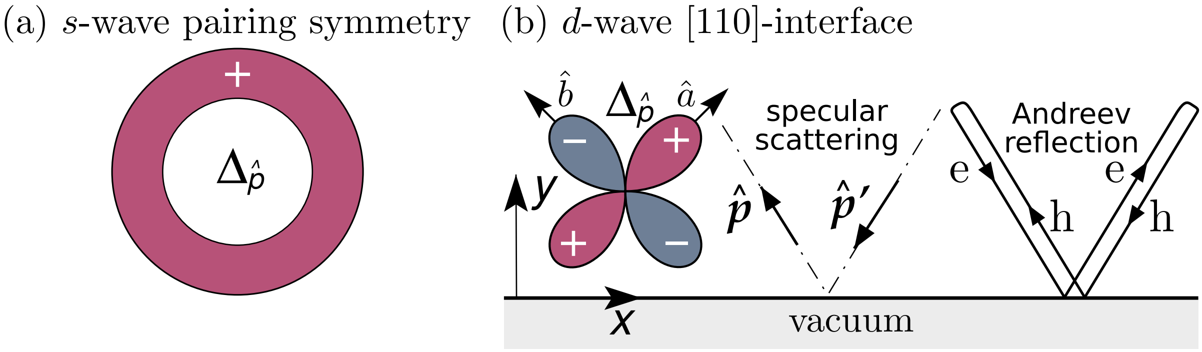

Figure 1.1: *Momentum-space representation of the order-parameter pairing-symmetry for (a) a conventional s-wave superconductor, and (b) an unconventional d-wave superconductor. Panel (b) shows the specular scattering between incoming and outgoing states with momenta $\boldsymbol{p}'$ and $\boldsymbol{p}$, as well as resonant Andreev-reflection.*

58], consequently inducing pairbreaking and a suppression of the order parameter on the coherence-length scale. The broken pairs are known as Andreev bound states, and for the sign-changing scattering, have a considerable spectral weight at zero-energy, i.e. at the Fermi surface [59–63]. These states come at a significant energy cost, since favorable condensation energy is lost in the pairbreaking (all of these properties are studied further in Ch. 4, where other situations leading to Andreev Bound states are briefly discussed).

Furthermore, while the conventional superconductors have a density of states which is fully gapped, the *d*-wave anisotropy gives rise to subgap quasiparticle states, with a linear density of states close to zero energy (studied in Ch. 3). This leads to modified thermodynamic and electrodynamic properties. In particular, while the superconducting condensate has a diamagnetic response to external fields (and superflow), the quasiparticle states have a paramagnetic response [64], where the latter reduces the kinetic energy. In the presence of a considerable weight of Andreev bound states, this ultimately leads to a negative kinetic energy (Ch. 4), favoring spontaneous superflow. The thesis derives a response theory where the superfluid kernel K_{ij} is obtained. This is used in the Ginzburg-Landau energy in Eq. (1.6) to derive the instability to spontaneous phase gradients and superflow announced in Sec. 1.2. Note that similar instabilities, e.g. with spontaneous superflow and currents that break time-reversal symmetry, have been proposed previously in the literature [65–67] (as discussed in Sec. 4.5). What is shown in this thesis, however, is that by minimizing the energy with respect to the shape of the superflow, it is favorable to also break continuous translational symmetry, in a ground state where χ oscillates in space, generating superflow and a current response with peculiar patterns. The conditions for this to occur are derived quite generally, and shown to be satisfied e.g. at the *d*-wave [110]-interfaces.

The research topic and scope of the thesis will now be presented.

1.4 Research topic and scope of the thesis

The overarching goal of the PhD project has been to study unconventional superconductivity, with an emphasis on thin films and mesoscopic grains. These systems might give rise to inhomogeneities that are unfavorable for the superconducting order, and caused for example by competing orders or boundary conditions. Of particular interest are Andreev bound states, arising at e.g. [110]-interfaces of d-wave superconductors. The main topic of the appended papers is to study how such environments can trigger spontaneous symmetry breaking, especially of continuous translational symmetry and time-reversal symmetry, as a means to heal a suppressed superconducting order. To study these systems and phenomena, two approaches are utilized. The first approach is based on a computational framework that implements the quasiclassical theory of superconductivity numerically, developed by Mikael Håkansson [68]. This framework was used extensively in papers II-IV. As mentioned in the beginning of the chapter, the numerics were mainly covered in Lic. Th. [10], while the PhD thesis focuses more on the second approach, the topic of paper I. This second approach is to develop a non-local response model based on Ginzburg-Landau theory, with terms derived from quasiclassics. In particular, the superfluid density tensor is derived in an inhomogeneous environment. The model provides direct analytic insight, and highlights the role of non-local correlations, inhomogeneities, and variations in the superconducting phase. This is used to verify and explain features of the numeric results in papers II-IV, as well as previous numerical observations in the literature. The model is also used to predict a class of inhomogeneous superconducting ground states, where the superconducting phase rather than the order-parameter magnitude is the main driving term.

The thesis considers clean spin-singlet superconductors in the weak-coupling limit and in equilibrium, that can be described in $2D$ with a cylindrical Fermi surface. Variations of the order parameter magnitude are typically neglected in the analytic calculations, but taken into account in the full numeric calculations. Interfaces are considered clean and specular. While the used scattering model is applicable to a variety of specular interfaces, analytic calculations mainly consider perfect reflection or transmission, with the same order parameter magnitude for incoming and outgoing scattering. Again, the latter assumptions are relaxed in the numerics. Effects of disorder or an extension to spin-triplet superconductivity are briefly discussed in paper III and in Lic. Th. [10].

The contents of the thesis will now be outlined in detail.

1.5 Outline of the thesis

Chapter 2 presents the theoretical framework known as the quasiclassical theory of superconductivity, which is the framework used to do the numerical and analytical calculations in this thesis. Chapter 3 proceeds to apply this framework to bulk superconductors in the presence of a homogeneous superflow (or inhomogeneous in the local response limit). A paradigm is established where the superflow is shown to be energetically unfavorable in a bulk system, due to a positive kinetic energy. In the presence of quasiparticles, however, for example due to thermal excitations or nodal structures in unconventional superconductors, the kinetic energy cost is shown to be reduced. This raises the question whether an environment exists where the superflow can actually be favorable.

Chapter 4 studies superconductivity at interfaces, and how these can give rise to surface Andreev bound states. It is shown how certain interfaces enforces an energetically unfavorable scenario, where superconducting pairs are broken into quasiparticles at zero-energy, at the expense of condensation energy. In this environment, a superflow is energetically favorable, as it Doppler shifts zero-energy states back to finite energies, effectively opening a gap in the spectrum. Since the superflow is unfavorable in the bulk, however, an inhomogeneous superflow with a spatial decay from the interface is proposed. This is discussed in relation to other Doppler-shifting mechanisms proposed previously in the literature.

Chapter 5 extends the surface model to account for inhomogeneous superflow, in a non-local linear response. The theory is described in terms of real-space correlators, and the inhomogeneous superfluid density tensor is derived. A mechanism for a spontaneous and inhomogeneous superflow is highlighted. Chapter 6 introduces a Ginzburg-Landau theory in terms of the inhomogeneous superfluid density. The conditions under which a spontaneous superflow can arise are derived, which are shown to be satisfied close to certain interfaces. With the microscopically derived superfluid density, the free energy is minimized with respect to the superflow, reproducing the same form and current response as in self-consistent numerics.

The appended papers are summarized in Ch. 7, and the thesis is concluded in Ch 8, with an outline of open questions and potential future research.

The appendices contain a number of technical details considered too lengthy for the main thesis. In App A, a gauge transformation is introduced which links the superconducting phase with the electromagnetic potential, and removes the explicit phase dependence of the order parameter in favor of an explicit superflow dependence in the equations of motion. In App. B, the Riccati equations are derived, which provide an approach for solving the quasiclassical equations of motion. These are solved analytically for both a homogeneous and a step-function order parameter. Appendices C–G contain derivations relevant for Chs. 3–6, respectively, on quasiclassics, bulk superconductivity, surface bound states, inhomogeneous superflow, and phase crystals.

2 The quasiclassical theory of superconductivity

The theory of Bardeen, Cooper and Schrieffer (BCS) is often hailed as one of the greatest theoretical achievements in condensed matter physics [49, 50]. It was the first theory to give a proper account of the microscopic origin of superconductivity, and could together with its extensions explain conventional superconductivity. Although unconventional superconductors have an unknown pairing mechanism, and are often significantly different from their conventional counterparts, the BCS theory can still be used to give surprisingly accurate predictions of their properties. The reason is that the BCS theory contains the most important ingredient for superconductivity, namely a net attractive interaction between electrons leading to a pairing. The precise nature of the attractive interaction is not crucial to describe many of the emergent properties, and the great success of the BCS theory in its application to even unconventional superconductors stems from the fact that the typical energies involved in superconductivity, such as the superconducting gap, are small in comparison to other relevant energy scales, like the Fermi energy. This enables a separation of scales [69–72], and the application of a quasiclassical approximation. The aim of this chapter is to introduce the quasiclassical theory of superconductivity and the Eilenberger equation [69, 73–75], which together with the superconducting gap equation forms the basis for the theoretical framework used in this thesis. As outlined in the introduction, the thesis is restricted to clean spin-singlet superconductivity in equilibrium. It is shown how to calculate various quantities and observables within this theoretical framework. In short, the framework is based on expressing the BCS theory in the powerful language of many-body Green functions [76–79], in particular the mean-field Green functions for quasiparticle- and pair-propagation. These propagators are known as the Gor'kov Green functions, and their equation of motion as the Gor'kov equation [80]. The quasiclassical equivalent is known as the Eilenberger equation [73, 74]. For a full derivation of the Gor'kov and Eilenberger equations, see for example Refs. [69, 75] and references therein, or the book by Kopnin [78]. For a more thorough treatment of BCS theory, see for example Schrieffer [81], de Gennes [15] and Tinkham [16].

2.1 The quasiclassical approximation and the Eilenberger equation

Most superconducting phenomena are described by low-lying excitations close to the Fermi surface, since the superconducting energy gap Δ is typically much smaller than the Fermi energy ϵ_{F}. Consequently, the length scale which describes spatial variations of Δ, the superconducting coherence length $\xi_0 \equiv \hbar v_{\mathrm{F}}/2\pi k_{\mathrm{B}} T_{\mathrm{c}}$, is usually much larger than the Fermi wavelength λ_{F} and the atomic scale a_0. Here, T_{c} is the superconducting transition temperature, and v_{F} is the Fermi velocity at Fermi momentum p_{F} on the Fermi surface. The quasiclassical approximation is thus based on separating the atomic and mesoscopic degrees of freedom, by expanding to leading order in the small parameters, e.g. $\hbar/p_{\mathrm{F}}\xi_0$, $\Delta/\epsilon_{\mathrm{F}}$, $k_{\mathrm{B}}T_{\mathrm{c}}/\epsilon_{\mathrm{F}}$, see for example Refs. [69–72, 82]. This is formally done by separating the microscopic mean-field Green-functions into high and low energy parts, where the high-energy part is either derived separately from full microscopic theories or taken phenomenologically from experiments,

$$\hat{G} = \hat{G}_{\mathrm{low}} + \hat{G}_{\mathrm{high}} \equiv \delta(\xi_{\boldsymbol{p}})\hat{g} + \hat{G}_{\mathrm{high}}. \tag{2.1}$$

Here, $\xi_{\boldsymbol{p}} = \boldsymbol{v}_F(\boldsymbol{p}_F)\cdot(\boldsymbol{p}-\boldsymbol{p}_F) - \mu$ is the single-particle energy at momentum $\boldsymbol{p}$, with $\boldsymbol{v}_F(\boldsymbol{p}_{\mathrm{F}}) = \boldsymbol{\nabla}_{\boldsymbol{p}}\xi_{\boldsymbol{p}}\big|_{\boldsymbol{p}=\boldsymbol{p}_{\mathrm{F}}}$. The "hat" symbol denotes Nambu × spin-space [83], sometimes referred to as Nambu-Gor'kov space, which is an extended 4×4 Hilbert space that captures both spin and particle-hole degrees-of-freedom. Integrating Eq. (2.1) over $\xi_{\boldsymbol{p}}$ and imposing a phenomenological energy-cutoff Ω_{c} yields the quasiclassical Green function $\hat{g}$

$$\hat{g}(\boldsymbol{p}_{\mathrm{F}}, \boldsymbol{R}; z) = \frac{1}{a}\int_{-\Omega_{\mathrm{c}}}^{\Omega_{\mathrm{c}}} d\xi_{\boldsymbol{p}} \hat{G}(\boldsymbol{p}, \boldsymbol{R}; z), \tag{2.2}$$

where a is a normalization factor, $k_{\mathrm{B}}T_{\mathrm{c}} \ll \Omega_{\mathrm{c}} \ll \epsilon_{\mathrm{F}}$ and $|\xi_{\boldsymbol{p}}| \leq \Omega_{\mathrm{c}}$, i.e. considering a thin shell around the Fermi surface. Here, $\boldsymbol{R}$ is the quasiparticle center-of-mass coordinate, and z the complex energy (the form of which depends on the type of propagator considered, see Sec. 2.2). Thus, Eq. (2.2) implies that the rapid oscillations of the Green function on the atomic scale are integrated out and replaced with the envelope, which varies on the coherence-length scale. As a consequence, certain information is lost, like quantum size effects. The quasiclassical approximation generally holds very well in conventional superconductors, where the small parameters are on the order of 10^{-3}, while they in the unconventional cuprate superconductors typically are 10^{-2}–10^{-1} [78]. The approximation breaks down when superconductivity varies on a much shorter length scale than ξ_0, e.g. at interfaces. To remedy this, boundary conditions are typically derived from microscopic theories and used as an input, see Refs. [69, 84–97] and references therein. Quasiclassical boundary conditions are briefly discussed in Sec. 2.5.

The equation of motion for the quasiclassical propagator $\hat{g}$ is known as the Eilenberger equation [73, 74]

$$i\hbar \boldsymbol{v}_{\mathrm{F}} \cdot \boldsymbol{\nabla}_R \hat{g}(\boldsymbol{p}_{\mathrm{F}}, \boldsymbol{R}; z) + \left[\left(z + \frac{e}{c} \boldsymbol{v}_{\mathrm{F}} \cdot \boldsymbol{A}(\boldsymbol{R}) \right) \hat{\tau}_3 - \hat{\Delta}(\boldsymbol{p}_{\mathrm{F}}, \boldsymbol{R}), \hat{g}(\boldsymbol{p}_{\mathrm{F}}, \boldsymbol{R}; z) \right] = 0, \quad (2.3)$$

accompanied with the normalization condition [73–75, 98–100]

$$\hat{g}^2(\boldsymbol{p}_{\mathrm{F}}, \boldsymbol{R}; z) = -\pi^2 \hat{1}. \quad (2.4)$$

Here, $\boldsymbol{A}$ is the electromagnetic gauge field, $\hat{\tau}_3$ the third Pauli-matrix in Nambu-spin space, and $\hat{\Delta}$ the mean-field order-parameter. The Eilenberger equation is a transport-like equation which describes quasiparticles moving along classical trajectories defined by the Fermi velocity $\boldsymbol{v}_{\mathrm{F}}(\boldsymbol{p}_{\mathrm{F}})$. Care needs to be taken when solving this equation, as it is unstable in certain integration directions and contains additional unphysical solutions. These issues are avoided by using the Riccati formalism, introduced in Sec. 2.4.

The Nambu × spin-space Green function $\hat{g}$ can be written in terms of spin-space Green functions as

$$\hat{g}(\boldsymbol{p}_{\mathrm{F}}, \boldsymbol{R}; z) = \begin{pmatrix} g(\boldsymbol{p}_{\mathrm{F}}, \boldsymbol{R}; z) & f(\boldsymbol{p}_{\mathrm{F}}, \boldsymbol{R}; z) \\ \tilde{f}(\boldsymbol{p}_{\mathrm{F}}, \boldsymbol{R}; z) & \tilde{g}(\boldsymbol{p}_{\mathrm{F}}, \boldsymbol{R}; z) \end{pmatrix}, \quad (2.5)$$

where the tilde operator denotes particle-hole conjugation

$$\tilde{\alpha}(\boldsymbol{p}_{\mathrm{F}}, \boldsymbol{R}; z, t) = \alpha^*(-\boldsymbol{p}_{\mathrm{F}}, \boldsymbol{R}; -z^*, t). \quad (2.6)$$

Here, g and f denote single-quasiparticle and pair propagators, respectively, which for a spin-singlet (s) system can be written with explicit spin-dependence

$$\begin{aligned} g(\boldsymbol{p}_{\mathrm{F}}, \boldsymbol{R}; z) &= [g_0(\boldsymbol{p}_{\mathrm{F}}, \boldsymbol{R}; z) + \boldsymbol{g}(\boldsymbol{p}_{\mathrm{F}}, \boldsymbol{R}; z) \cdot \boldsymbol{\sigma}]\, \sigma_0, && (2.7) \\ \tilde{g}(\boldsymbol{p}_{\mathrm{F}}, \boldsymbol{R}; z) &= \sigma_2 [\tilde{g}_0(\boldsymbol{p}_{\mathrm{F}}, \boldsymbol{R}; z) - \tilde{\boldsymbol{g}}(\boldsymbol{p}_{\mathrm{F}}, \boldsymbol{R}; z) \cdot \boldsymbol{\sigma}]\, \sigma_2, && (2.8) \\ f(\boldsymbol{p}_{\mathrm{F}}, \boldsymbol{R}; z) &= f_{\mathrm{s}}(\boldsymbol{p}_{\mathrm{F}}, \boldsymbol{R}; z) i\sigma_2, && (2.9) \\ \tilde{f}(\boldsymbol{p}_{\mathrm{F}}, \boldsymbol{R}; z) &= \tilde{f}_{\mathrm{s}}(\boldsymbol{p}_{\mathrm{F}}, \boldsymbol{R}; z) i\sigma_2, && (2.10) \end{aligned}$$

where the Pauli vector is $\boldsymbol{\sigma} \equiv \sigma_1 \hat{\boldsymbol{x}} + \sigma_2 \hat{\boldsymbol{y}} + \sigma_3 \hat{\boldsymbol{z}}$, with $\boldsymbol{\sigma}^* = -\sigma_2 \boldsymbol{\sigma} \sigma_2$. The mean-field order parameter is the off-diagonal self-energy

$$\begin{aligned} \hat{\Delta}(\boldsymbol{p}_{\mathrm{F}}, \boldsymbol{R}) &= \begin{pmatrix} 0 & \Delta(\boldsymbol{p}_{\mathrm{F}}, \boldsymbol{R}) \\ \tilde{\Delta}(\boldsymbol{p}_{\mathrm{F}}, \boldsymbol{R}) & 0 \end{pmatrix}, && (2.11) \\ \Delta(\boldsymbol{p}_{\mathrm{F}}, \boldsymbol{R}) &= \Delta_{\mathrm{s}}(\boldsymbol{p}_{\mathrm{F}}, \boldsymbol{R}) i\sigma_2, && (2.12) \\ \tilde{\Delta}(\boldsymbol{p}_{\mathrm{F}}, \boldsymbol{R}) &= \tilde{\Delta}_{\mathrm{s}}(\boldsymbol{p}_{\mathrm{F}}, \boldsymbol{R}) i\sigma_2. && (2.13) \end{aligned}$$

The order parameter is solved self-consistently through the superconducting gap equation, introduced in Sec. 2.3. The next section describes how observables are calculated in general, and introduces the various propagators that are commonly used.

2.2 Observables and propagators

An observable O can formally be obtained from the expression

$$O = \int_{-\Omega_c}^{\Omega_c} \frac{d\epsilon}{8\pi i} \left\langle \mathrm{Tr}\left[\hat{O}\hat{g}^{\mathrm{K}}(\boldsymbol{p}_{\mathrm{F}}, \boldsymbol{R}; z, t)\right]\right\rangle_{\theta_{\mathrm{F}}}, \tag{2.14}$$

with Fermi-surface average $\langle \ldots \rangle_{\theta_{\mathrm{F}}}$, where $\theta_{\mathrm{F}} \in [0, 2\pi]$ is the angle of the Fermi momentum $\boldsymbol{p}_{\mathrm{F}}$ relative to the crystal a-axis. This thesis only considers $2D$ superconductors with cylindrically symmetric Fermi surfaces, such that the average reduces to

$$\langle \circ \rangle_{\theta_{\mathrm{F}}} = \int_0^{2\pi} \frac{d\theta_{\mathrm{F}}}{2\pi} [\circ]. \tag{2.15}$$

In Eq. (2.14), Ω_c is a cutoff, $\hat{O}$ a diagonal matrix in Nambu-spin space, and g^{K} the non-equilibrium Keldysh propagator in Keldysh × Nambu × spin-space with energies $z^{\mathrm{K}} = \epsilon$ on the real axis [101]. This thesis is limited to equilibrium, in which case the time-dependence drops out and the Keldysh propagator is described in terms of the Retarded (R) and Advanced (A) propagators

$$\hat{g}^{\mathrm{K}}(\boldsymbol{p}_{\mathrm{F}}, \boldsymbol{R}; \epsilon) = \left[\hat{g}^{\mathrm{R}}(\boldsymbol{p}_{\mathrm{F}}, \boldsymbol{R}; z) - \hat{g}^{\mathrm{A}}(\boldsymbol{p}_{\mathrm{F}}, \boldsymbol{R}; z)\right] \tanh\frac{\beta\epsilon}{2}, \tag{2.16}$$

with $\beta \equiv 1/k_{\mathrm{B}}T$, and real energies $z^{\mathrm{R,A}} = \epsilon + i0^{\pm}$ with infinitesimal positive (negative) shift for R (A). The Keldysh propagator generally contains information about the dynamics of a system, while Retarded and Advanced propagators contain spectral information. The energy integral in Eq. (2.14) can be cumbersome to deal with numerically. The Matsubara technique offers a simplified alternative with faster convergence, and is a powerful tool to deal with equilibrium physics at finite temperatures in quantum field theory [76–79, 102]. The technique is based on performing a Wick rotation to imaginary times $\tau = it$, yielding the Matsubara Green functions $\hat{g}^{\mathrm{M}}$ which are periodic in τ and defined in the finite time interval $-\hbar/k_{\mathrm{B}}T < \tau < \hbar/k_{\mathrm{B}}T$. Fourier transforming from time to energy, the Matsubara propagators are only defined over a set of discrete and imaginary energies $z^{\mathrm{M}} = i\epsilon_n$, known as the Matsubara energies (or frequencies in natural units), which are poles on the imaginary axis $i\epsilon_n \equiv i\pi k_{\mathrm{B}}T(2n+1)$ with $n \in \mathbb{Z}$. The integral in Eq. (2.14) reduces to a sum over the Matsubara poles,

$$\sum_{|\varepsilon_n|<\Omega_c} \hat{g}^{\mathrm{M}}(\boldsymbol{p}_{\mathrm{F}}, \boldsymbol{R}; i\varepsilon_n) \longleftrightarrow \int_{-\Omega_c}^{\Omega_c} \frac{d\epsilon}{4\pi i} \left[\hat{g}^{\mathrm{R}}(\boldsymbol{p}_{\mathrm{F}}, \boldsymbol{R}; \epsilon) - \hat{g}^{\mathrm{A}}(\boldsymbol{p}_{\mathrm{F}}, \boldsymbol{R}; \epsilon)\right] \tanh\frac{\beta\epsilon}{2}, \tag{2.17}$$

$$O = \frac{1}{2} \sum_{|\varepsilon_n|<\Omega_c} \left\langle \mathrm{Tr}\left[\hat{O}\hat{g}^{\mathrm{M}}(\boldsymbol{p}_{\mathrm{F}}, \boldsymbol{R}; i\varepsilon_n)\right]\right\rangle_{\theta_{\mathrm{F}}}. \tag{2.18}$$

At low temperatures $T \to 0$, the Matsubara sum is replaced with an integral (e.g. as in [103])

$$\varepsilon_{n+1} - \varepsilon_n \xrightarrow[T\to 0]{} d\epsilon, \tag{2.19}$$

$$2\pi k_{\mathrm{B}} T \sum_{\varepsilon_n=0}^{\Omega_{\mathrm{c}}} \xrightarrow[T\to 0]{} \int_0^{\Omega_{\mathrm{c}}} d\epsilon. \tag{2.20}$$

Note that an even faster convergence is provided by the Ozaki technique [104], described in Sec. 3.5 of Lic. Th. [10]. The real-time Retarded (Advanced) propagator is directly related to the Matsubara propagator via analytic continuation over the positive (negative) imaginary axis. In this work, the Retarded propagator is used to obtain the spectral properties, namely the density of states and the spectral current. The Matsubara propagator is used to calculate the superconducting gap, the current density, the free energy, the entropy and the heat capacity. It will be shown how these quantities are calculated in detail in the following sections.

2.3 The superconducting gap equation

Consider a separable spin-singlet order-parameter with a single pairing channel

$$\Delta(\boldsymbol{p}_{\mathrm{F}},\boldsymbol{R}) = \Delta(\boldsymbol{R})\eta(\theta_{\mathrm{F}}) = |\Delta(\boldsymbol{R})|e^{i\chi(\boldsymbol{R})}\eta(\theta_{\mathrm{F}}), \tag{2.21}$$

where $\chi(\boldsymbol{R})$ is the superconducting phase, and $\eta(\theta_{\mathrm{F}})$ the basis function describing the pairing symmetry in momentum space. This thesis mainly considers s-wave and d-wave pairing symmetry, with the typical basis functions

$$\begin{aligned} \eta_s(\theta_{\mathrm{F}}) &= 1, & (2.22)\\ \eta_{d_{x^2-y^2}}(\theta_{\mathrm{F}}) &= \sqrt{2}\cos(2\theta_{\mathrm{F}}), & (2.23) \end{aligned}$$

where it is reminded that θ_{F} is the angle between Fermi momentum $\boldsymbol{p}_{\mathrm{F}}$ and the crystal a-axis. The gap equation gives the order parameter in terms of the pair-propagator f

$$\Delta(\boldsymbol{R}) = Vk_{\mathrm{B}}T\left\langle \eta^*(\theta_{\mathrm{F}})\sum_{|\varepsilon_n|\leq\Omega_{\mathrm{c}}} f(\boldsymbol{p}_{\mathrm{F}},\boldsymbol{R};z)\right\rangle_{\theta_{\mathrm{F}}}, \tag{2.24}$$

with Matsubara energies $z = i\varepsilon_n \equiv i\pi k_{\mathrm{B}}T(2n+1)$, energy cutoff Ω_{c}, and pairing interaction V. N_{F} is the normal-state density of states at the Fermi surface (per spin projection), which for the Fermi surface considered in this thesis is defined as

$$N_{\mathrm{F}} \equiv \int_0^{2\pi}\frac{d\theta_{\mathrm{F}}p_{\mathrm{F}}}{(2\pi\hbar)^2\,|\boldsymbol{v}_{\mathrm{F}}(\boldsymbol{p}_{\mathrm{F}})|} = \frac{m}{2\pi\hbar^2}, \tag{2.25}$$

since $p_{\mathrm{F}} \equiv mv_{\mathrm{F}}$. The gap equation can be converted into a sum over only positive Matsubara energies (following App. G of Lic. Th. [10])

$$\Delta_s(\boldsymbol{R}) = Vk_{\mathrm{B}}T\left\langle \eta^*(\theta_{\mathrm{F}})\sum_{\varepsilon_n>0}^{\Omega_{\mathrm{c}}}\Big(f(\boldsymbol{p}_{\mathrm{F}},\boldsymbol{R};i\varepsilon_n) + \tilde{f}^*(\boldsymbol{p}_{\mathrm{F}},\boldsymbol{R};i\varepsilon_n)\Big)\right\rangle_{\theta_{\mathrm{F}}}. \tag{2.26}$$

It is noted that the gap equation is a self-consistency equation, since the pair-propagator depends in turn on Δ, as seen in e.g. Sec. 2.4. Furthermore, the phenomenological cutoff Ω_{c} and pairing interaction V can be eliminated in favor of the transition temperature [103]. This is done in Apps. C.1 and D.1, where it is shown that

$$V^{-1} \equiv (-N_{\mathrm{F}}\lambda_{\mathrm{c}})^{-1} = \ln\frac{T}{T_{\mathrm{c}}} + \sum_{n\geq 0}^{n_{\mathrm{c}}-1}\frac{2}{2n+1}, \tag{2.27}$$

where $n_{\mathrm{c}} = \mathrm{int}\,(\Omega_{\mathrm{c}}/2\pi k_{\mathrm{B}}T_{\mathrm{c}} - 1/2)$, and λ_{c} is the coupling constant.

2.4 The Riccati formalism

The Riccati parametrization is an efficient and numerically stable method of solving the Eilenberger equation [90, 97, 105–109], in which the quasiclassical Green functions are rewritten in terms of the coherence functions $\gamma(\boldsymbol{p}_\mathrm{F}, \boldsymbol{R}; z)$ and $\tilde{\gamma}(\boldsymbol{p}_\mathrm{F}, \boldsymbol{R}; z)$. These objects correspond to the Andreev reflection probability amplitudes, i.e. electron-hole conversion and hole-electron conversion, respectively. Appendix B.3 derives the coherence functions and their relation to the Green functions as

$$\hat{g} = -i\pi\hat{\mathcal{N}} \begin{pmatrix} \sigma_0 + \gamma\tilde{\gamma} & 2\gamma \\ -2\tilde{\gamma} & -\sigma_0 - \tilde{\gamma}\gamma \end{pmatrix}, \tag{2.28}$$

where

$$\hat{\mathcal{N}} = \begin{pmatrix} (\sigma_0 - \gamma\tilde{\gamma})^{-1} & 0 \\ 0 & (\sigma_0 - \tilde{\gamma}\gamma)^{-1} \end{pmatrix}, \tag{2.29}$$

and σ_0 is the unit matrix in spin-space. The spin-singlet coherence functions in spin-space are written in terms of the scalars γ_s and $\tilde{\gamma}_\mathrm{s}$

$$\gamma(\boldsymbol{p}_\mathrm{F}, \boldsymbol{R}; z) = \gamma_\mathrm{s}(\boldsymbol{p}_\mathrm{F}, \boldsymbol{R}; z) i\sigma_2, \tag{2.30}$$

$$\tilde{\gamma}(\boldsymbol{p}_\mathrm{F}, \boldsymbol{R}; z) = \tilde{\gamma}_\mathrm{s}(\boldsymbol{p}_\mathrm{F}, \boldsymbol{R}; z) i\sigma_2. \tag{2.31}$$

The Riccati parametrization automatically encodes the normalization condition in Eq. (2.4) into the definition of $\hat{g}$, removes the spurious solutions, and recasts the Eilenberger equation into a set of coupled Riccati-type ordinary differential equations

$$\left[i\hbar\boldsymbol{v}_\mathrm{F}\cdot\boldsymbol{\nabla}_R + 2\left(z + \frac{e}{c}\boldsymbol{v}_\mathrm{F}\cdot\boldsymbol{A}\right)\right]\gamma = \gamma\tilde{\Delta}\gamma - \Delta, \tag{2.32}$$

$$\left[i\hbar\boldsymbol{v}_\mathrm{F}\cdot\boldsymbol{\nabla}_R - 2\left(z + \frac{e}{c}\boldsymbol{v}_\mathrm{F}\cdot\boldsymbol{A}\right)\right]\tilde{\gamma} = \tilde{\gamma}\Delta\tilde{\gamma} - \tilde{\Delta}, \tag{2.33}$$

where the arguments $(\boldsymbol{p}_\mathrm{F}, \boldsymbol{R}; z)$ have been dropped for brevity. These equations are solved by integration along straight (ballistic) quasiparticle trajectories $\boldsymbol{s}$ parametrized by the Fermi velocity according to $\boldsymbol{s} = \boldsymbol{s}_0 + s\hat{\boldsymbol{v}}_\mathrm{F}$, with opposite directions being stable for γ and $\tilde{\gamma}$, see Fig. 2.1 and for example Ref. [72]. Quantum coherence exists on the length-scale of the superconducting coherence length along these trajectories, but not between neighboring trajectories. The order-parameter dependence of the phase χ can be eliminated with the gauge transformation in App. A, rendering the order parameter real $\Delta^*(\boldsymbol{p}_\mathrm{F}, \boldsymbol{R}) = \Delta(\boldsymbol{p}_\mathrm{F}, \boldsymbol{R})$, and giving the Riccati equations explicit dependence on the gauge invariant superflow $\boldsymbol{p}_\mathrm{s}(\boldsymbol{R}) = \hbar\boldsymbol{\nabla}\chi(\boldsymbol{R})/2 - e\boldsymbol{A}(\boldsymbol{R})/c$

$$\left[i\hbar\boldsymbol{v}_\mathrm{F}\cdot\boldsymbol{\nabla}_R + 2\left(z - \boldsymbol{v}_\mathrm{F}\cdot\boldsymbol{p}_\mathrm{s}\right)\right]\gamma = \gamma\tilde{\Delta}\gamma - \Delta, \tag{2.34}$$

$$\left[i\hbar\boldsymbol{v}_\mathrm{F}\cdot\boldsymbol{\nabla}_R - 2\left(z - \boldsymbol{v}_\mathrm{F}\cdot\boldsymbol{p}_\mathrm{s}\right)\right]\tilde{\gamma} = \tilde{\gamma}\Delta\tilde{\gamma} - \tilde{\Delta}, \tag{2.35}$$

Comparing Eqs. (2.28)–(2.31) with Eqs. (2.5)–(2.10), the spin-singlet Green functions can be expressed explicitly in terms of the scalar coherence functions

$$\begin{aligned} g_0 &= -i\pi\frac{1-\gamma_\mathrm{s}\tilde{\gamma}_\mathrm{s}}{1+\gamma_\mathrm{s}\tilde{\gamma}_\mathrm{s}}, && (2.36)\\ \tilde{g}_0 &= i\pi\frac{1-\gamma_\mathrm{s}\tilde{\gamma}_\mathrm{s}}{1+\gamma_\mathrm{s}\tilde{\gamma}_\mathrm{s}}, && (2.37)\\ f_\mathrm{s} &= -2i\pi\frac{\gamma_\mathrm{s}}{1+\gamma_\mathrm{s}\tilde{\gamma}_\mathrm{s}}, && (2.38)\\ \tilde{f}_\mathrm{s} &= 2i\pi\frac{\tilde{\gamma}_\mathrm{s}}{1+\gamma_\mathrm{s}\tilde{\gamma}_\mathrm{s}}. && (2.39) \end{aligned}$$

Depending on the choice of propagator $\hat{g}^{\mathrm{R,A,M}}$ (as described in Sec. 2.2), the corresponding coherence functions $\gamma^{\mathrm{R,A,M}}$ and $\tilde{\gamma}^{\mathrm{R,A,M}}$ have to be chosen. Again, this thesis is limited to Retarded propagators for spectral properties, and Matsubara propagators otherwise.

2.4.1 Solutions to the Riccati equations: piecewise constant Δ

Appendix B.4 solves the Riccati equations analytically for a spin-singlet superconductor assuming spin-degeneracy, with the following homogeneous solutions in bulk

$$\begin{aligned} \gamma_\mathrm{h}(\boldsymbol{p}_\mathrm{F};z) &= \frac{-\Delta(\boldsymbol{p}_\mathrm{F})}{z_p+i\Omega}, && (2.40)\\ \tilde{\gamma}_\mathrm{h}(\boldsymbol{p}_\mathrm{F};z) &= \frac{\tilde{\Delta}(\boldsymbol{p}_\mathrm{F})}{z_p+i\Omega}, && (2.41)\\ \Omega &\equiv \sqrt{|\Delta|^2-z_p^2}, && (2.42)\\ z_p &\equiv z-\boldsymbol{v}_\mathrm{F}\cdot\boldsymbol{p}_\mathrm{s}. && (2.43) \end{aligned}$$

By approximating a spatially varying $\Delta(\boldsymbol{R})$ as a piecewise constant function, the solution γ_f in a region labeled f with order parameter Δ_f can be described in terms of the solutions in the previous region along the trajectory labeled i, with γ_i and Δ_i, see Fig. 2.1. Note that $\tilde{\gamma}_\mathrm{i}$ is given in terms of $\tilde{\gamma}_\mathrm{f}$, since it is integrated in the opposite direction. The full solutions to Eqs.(2.34) and (2.35) are derived in App. B.4, along the straight trajectory defined by $\boldsymbol{v}_\mathrm{F}(\boldsymbol{p}_\mathrm{F})$ with coordinate s

$$\begin{aligned} \gamma_\mathrm{f}(s,\boldsymbol{p}_\mathrm{F};z) &= \gamma_\mathrm{f,h}+\frac{2i\Omega_\mathrm{f}C\exp(-s/\xi_\mathrm{f})}{1-\tilde{\Delta}_\mathrm{f}C\exp(-s/\xi_\mathrm{f})}, && (2.44)\\ \tilde{\gamma}_\mathrm{i}(s,\boldsymbol{p}_\mathrm{F};z) &= \tilde{\gamma}_\mathrm{i,h}+\frac{2i\Omega_\mathrm{i}\tilde{C}\exp(+s/\xi_\mathrm{i})}{1+\Delta_\mathrm{i}\tilde{C}\exp(+s/\xi_\mathrm{i})}, && (2.45)\\ \xi &\equiv \frac{\hbar v_\mathrm{F}}{2\Omega}, && (2.46) \end{aligned}$$

where h denotes the corresponding homogeneous solutions in Eqs. (2.40) and (2.41), and the integration constants C and $\tilde{C}$ are obtained from the appropriate boundary condition at the boundary separating f and i (quasiclassical boundary conditions are discussed in Sec. 2.5). Let $s = 0$ be the coordinate at the boundary. A continuous boundary condition with perfect specular reflection implies $\gamma_\mathrm{i}(0^-) = \gamma_\mathrm{f}(0^+)$ and $\tilde{\gamma}_\mathrm{i}(0^-) = \tilde{\gamma}_\mathrm{f}(0^+)$, from which the integration constants are found to be

$$C = \frac{(\gamma_\mathrm{i}(0) - \gamma_\mathrm{f,h})}{2i\Omega_\mathrm{f} + \tilde{\Delta}_\mathrm{f}\,(\gamma_\mathrm{i}(0) - \gamma_\mathrm{f,h})}, \tag{2.47}$$

$$\tilde{C} = \frac{(\tilde{\gamma}_\mathrm{f}(0) - \tilde{\gamma}_\mathrm{i,h})}{2i\Omega_\mathrm{i} - \Delta_\mathrm{i}\,(\tilde{\gamma}_\mathrm{f}(0) - \tilde{\gamma}_\mathrm{i,h})}. \tag{2.48}$$

These equations mark the starting point for a numeric implementation, and explicitly show that there are nonlocal correlations on the coherence length scale (see below).

2.4.2 Numeric implementation: stepping method

With a given initial condition at the start of a trajectory, it is possible to obtain the coherence functions at every point along the trajectory by using the solutions given by Eqs. (2.44)–(2.48) iteratively for each step in $\Delta(\boldsymbol{p}_\mathrm{F}, \boldsymbol{R})$. The coherence functions can then be solved together with the propagators and the gap equation in a self-consistency loop, to obtain a self-consistent solution with full spatial dependence for any of the quantities and observables presented in this chapter. This is one possible approach to a numeric implementation, where Δ and other quantities are defined on a discrete lattice (i.e. piecewise constant). Most of the numerics in the appended papers are based on a numeric framework that implements such an approach, originally developed by Mikael Håkansson [68]. A majority of the work effort in this PhD has been spent on understanding, using and extending this framework. However, this PhD thesis will not elaborate on such implementations, since this was done in Lic. Th. [10] and Ref. [68].

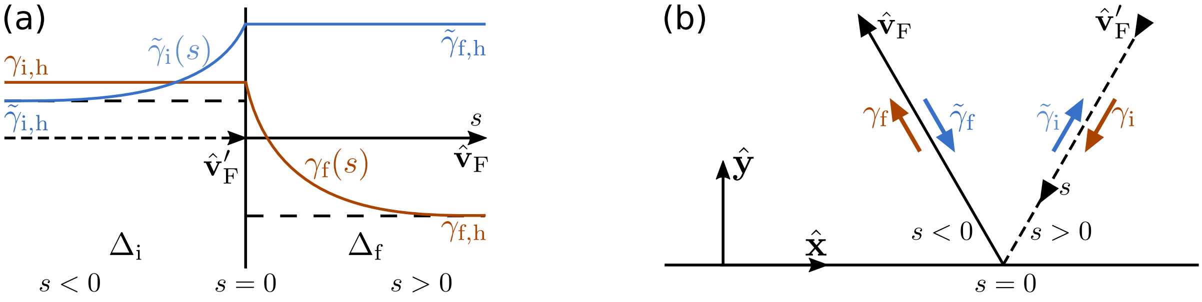

Figure 2.1: *(a) Inhomogeneous coherence functions due to a piecewise constant order-parameter, with continuous boundary conditions. (b) The trajectory need not be straight ($\hat{\boldsymbol{v}}_F \neq \hat{\boldsymbol{v}}'_F$), but might for example scatter specularly at an interface.*

2.4.3 Nonlocal correlations and the coherence length

The Eilenberger equation and the Riccati formalism makes it obvious that this is inherently a nonlocal theory, by virtue of the superconducting coherence length, which enters explicitly in the coherence functions in Eqs. (2.44)–(2.46). The coherence length defined in Eq. (2.46) depends on several parameters $\xi = \xi(\boldsymbol{p}_{\mathrm{F}}, \boldsymbol{R}; z, T, \boldsymbol{p}_{\mathrm{s}})$, not to be confused with the constant scale typically used $\xi_0 = \hbar v_{\mathrm{F}}/2\pi k_{\mathrm{B}} T_{\mathrm{c}}$ (or $\zeta_0 = \hbar v_{\mathrm{F}}/\Delta$ in other works). This non-locality may lead to non-trivial correlations where observables and various quantities are typically described by high-dimensional kernels (correlators) that couple all possible quasiparticle trajectories in a certain coherence volume. The coherence length is effectively the radius of this volume. Such correlators and kernels are derived in Chs. 5 and 6. Note that due to magnetic induction and screening, there are also non-localities due to the penetration depth length scale $\lambda_0 \equiv c/\sqrt{4\pi e^2 N_{\mathrm{F}} v_{\mathrm{F}}^2}$, but this work considers extreme type-II superconductors $\xi_0 \ll \lambda_0$ where such effects become very small. It will now be shown how to impose boundary conditions in quasiclassics, which is used in Ch. 4 to study interfaces.

2.5 Quasiclassical boundary conditions

Normal-state scattering at an interface is typically characterized in terms of reflection and transmission amplitudes. A scattered quasiparticle state is generally coupled to all incoming states at the interface, with individual weights set by the interface properties. If the interface is atomically clean, states scatter specularly and conserve the momentum parallel to the interface, with each scattered state being completely determined by a single reflected and transmitted state. Their reflection and transmission probabilities $\mathcal{R} = |r|^2$ and $\mathcal{D} = |t|^2$, respectively, fulfill the probability conservation law

$$\mathcal{R} + \mathcal{D} = 1. \tag{2.49}$$

Scattering in the superconducting state is less trivial due to the Andreev processes of retro-reflection (i.e. particle-hole conversion), which have to be taken into account when determining the scattered state. The so-called Zaitsev boundary conditions were derived for the quasiclassical Green functions [84–88], which due to quasiparticle interference take the form of nonlinear equations [88, 96]. These equations are plagued by numerical instabilities and unphysical solutions that have to be eliminated. These boundary conditions were eventually factorized thereby eliminating the unphysical solutions [89], and a representation was derived that is free from the spurious solutions and instabilities [90]. Generalizations and applications of these boundary conditions have been an active area of research for decades, resulting in a number of different representations and notations circulating in the literature. This section follows the notation of Refs. [90], where quasiclassical trajectories are separated into incoming coherence functions $\gamma_{1,2}$ and $\tilde{\gamma}_{1,2}$, and outgoing coherence functions $\Gamma_{1,2}$ and $\tilde{\Gamma}_{1,2}$. Here, 1 and 2 denote two regions separated by an interface, depicted in Fig. 2.2, where 1 will represent a superconducting system of interest. The goal is to find simplified expressions for the unknown scattered coherence functions Γ_1 and $\tilde{\Gamma}_1$ in terms of known incoming $\gamma_{1,2}$ and $\tilde{\gamma}_{1,2}$. The specular boundary conditions in equilibrium are [90]

$$\Gamma_1 = R_1\gamma_1 + D_1\gamma_2, \tag{2.50}$$
$$\tilde{\Gamma}_1 = \tilde{R}_1\tilde{\gamma}_1 + \tilde{D}_1\tilde{\gamma}_2, \tag{2.51}$$

with the generalized reflection and transmission coefficients

$$R_1 = \mathcal{R}\frac{1+\gamma_2\tilde{\gamma}_2}{1+\mathcal{R}\gamma_2\tilde{\gamma}_2+\mathcal{D}\gamma_1\tilde{\gamma}_2}, \tag{2.52}$$
$$D_1 = \mathcal{D}\frac{1+\gamma_1\tilde{\gamma}_2}{1+\mathcal{R}\gamma_2\tilde{\gamma}_2+\mathcal{D}\gamma_1\tilde{\gamma}_2}, \tag{2.53}$$
$$\tilde{R}_1 = \mathcal{R}\frac{1+\gamma_2\tilde{\gamma}_2}{1+\mathcal{R}\gamma_2\tilde{\gamma}_2+\mathcal{D}\tilde{\gamma}_1\gamma_2}, \tag{2.54}$$
$$\tilde{D}_1 = \mathcal{D}\frac{1+\tilde{\gamma}_1\gamma_2}{1+\mathcal{R}\gamma_2\tilde{\gamma}_2+\mathcal{D}\tilde{\gamma}_1\gamma_2}, \tag{2.55}$$

where $\mathcal{R}$ and $\mathcal{D}$ are the normal-state scattering coefficients. This form closely resembles the normal-state scattering relations, but with generalized coefficients R and D that depend on $\gamma_{1,2}$ and $\tilde{\gamma}_{1,2}$, hence incorporating the Andreev processes [57, 58, 61], and that still fulfill the conservation

$$
\begin{aligned}
R_1 + D_1 &= 1, && (2.56)\\
\tilde{R}_1 + \tilde{D}_1 &= 1. && (2.57)
\end{aligned}
$$

The scattering coefficients on side 2 are readily obtained by interchanging the subscripts 1 and 2. The coefficients above are applicable to either of the Retarded, Advanced and Matsubara propagators[90, 97]. It is noted that when $\gamma_2 = \tilde{\gamma}_2 = 0$ (e.g. at an S-N interface), these coefficients reduce to the normal-state coefficients $R_1 = \tilde{R}_1 = \mathcal{R}$, $D_1 = \tilde{D}_1 = \mathcal{D}$. This does generally not reduce the R_2 and D_2 coefficients to the normal-state coefficients, however, since there is still Andreev reflection (see Sec. 4.1). The above boundary conditions can be used to obtain general solutions for the inhomogeneous coherence functions Γ_1 and $\tilde{\Gamma}_1$. This is done at various interfaces in Ch. 4, under the assumption of an order parameter with constant amplitude $\Delta_1(\boldsymbol{R}, \boldsymbol{p}_\mathrm{F}) = \Delta_1(\boldsymbol{p}_\mathrm{F})$.

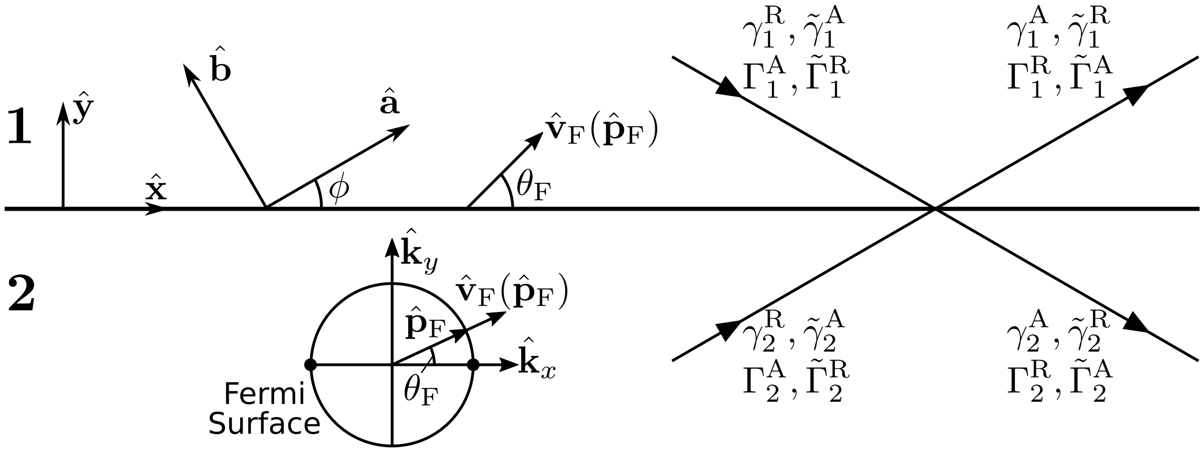

Figure 2.2: *Interface and scattering model, connecting two regions 1 and 2, where 1 will be a superconducting region of interest. The $\hat{\boldsymbol{x}}$-axis and $\hat{\boldsymbol{y}}$-axis denote directions parallel and perpendicular to the interface, respectively, while the crystal ab-axes are rotated ϕ relative to the interface. Therefore, it is understood that $\Delta(\boldsymbol{p}_F) = \Delta\eta(\theta_F - \phi)$ from here on, even if ϕ is dropped from the notation. The cases $\phi = 0$ and $\phi = \pi/4$ will be of special interest. Note that the angles are defined from the surface rather than the surface normal. The right part of the figure shows how the coherence functions are connected across the interface. Only the retarded quantities will be considered, and superscript R will therefore be dropped.*

2.6 Density of states and spectral current

In this section, an equation is provided for the local density of states (LDOS), from which the density of states (DOS) and spectral current are obtained. These expressions are used to get an equation for the total current density in Sec. 2.7. For a proper derivation of these expressions, see e.g. Refs. [10, 72, 78] and references therein.

The angle-resolved (i.e. momentum-resolved) LDOS is calculated with the imaginary part of the Retarded propagator from the expression

$$\begin{aligned} N(\boldsymbol{p}_{\mathrm{F}}, \boldsymbol{R}; \epsilon) &= -N_{\mathrm{F}} \frac{1}{2\pi} \operatorname{Im}\left[\operatorname{Tr}\left\{\hat{\tau}_3 \hat{g}^R(\boldsymbol{p}_{\mathrm{F}}, \boldsymbol{R}; \epsilon)\right\}\right] \\ &= -N_{\mathrm{F}} \frac{2}{\pi} \operatorname{Im}\left[g_0^R(\boldsymbol{p}_{\mathrm{F}}, \boldsymbol{R}; \epsilon)\right], \end{aligned} \tag{2.58}$$

where the trace is over 4×4 Nambu-spin space, $\boldsymbol{p}_{\mathrm{F}}$ is the Fermi momentum, $\boldsymbol{R}$ is the center-of-mass coordinate, $\hat{\tau}_3$ is the third Pauli matrix in Nambu-spin space, and the normal-state DOS (per spin-projection) N_{F} is defined in Eq. (2.25). The local and total DOS are

$$N(\boldsymbol{R}, \epsilon) = -N_{\mathrm{F}} \frac{2}{\pi} \left\langle \operatorname{Im}\left[g_0^R(\boldsymbol{p}_{\mathrm{F}}, \boldsymbol{R}; \epsilon)\right] \right\rangle_{\theta_{\mathrm{F}}}, \tag{2.59}$$

$$N(\epsilon) = -N_{\mathrm{F}} \frac{2}{\pi} \int d\boldsymbol{R} \left\langle \operatorname{Im}\left[g_0^R(\boldsymbol{p}_{\mathrm{F}}, \boldsymbol{R}; \epsilon)\right] \right\rangle_{\theta_{\mathrm{F}}}. \tag{2.60}$$

For a spin-degenerate singlet system, the LDOS can be expressed in terms of the scalar Riccati coherence functions using Eq. (2.36)

$$N(\boldsymbol{R}, \epsilon) = 2N_{\mathrm{F}} \operatorname{Re} \left\langle \frac{1 - \gamma\tilde{\gamma}}{1 + \gamma\tilde{\gamma}} \right\rangle_{\theta_{\mathrm{F}}}. \tag{2.61}$$

The spectral current is obtained by adding the contributions from comoving (+) and countermoving (−) excitations along the trajectory $\boldsymbol{p}_{\mathrm{F}}$

$$\boldsymbol{j}(\boldsymbol{p}_{\mathrm{F}}, \boldsymbol{R}; \epsilon) = e\boldsymbol{v}_{\mathrm{F}} \left[N(+\boldsymbol{p}_{\mathrm{F}}, \boldsymbol{R}; \epsilon) - N(-\boldsymbol{p}_{\mathrm{F}}, \boldsymbol{R}; \epsilon)\right] \tag{2.62}$$

where $\boldsymbol{v}_{\mathrm{F}} = \boldsymbol{v}_{\mathrm{F}}(\boldsymbol{p}_{\mathrm{F}})$ is the Fermi velocity on the Fermi surface at $\boldsymbol{p}_{\mathrm{F}}$. This expression is a measure of the contributions of quasiparticle states at position $\boldsymbol{R}$, energy ϵ and momentum $\boldsymbol{p}_{\mathrm{F}}$ to the current density. Thus, the total current density at $\boldsymbol{R}$ is obtained by multiplying the spectral current with the distribution function and integrating over energy and the Fermi momentum. In equilibrium, the distribution function is given in terms of the Fermi-Dirac distribution $f(\epsilon) = 1/\left[1 + \exp(\beta\epsilon)\right]$ with $\beta \equiv (k_{\mathrm{B}}T)^{-1}$

$$\boldsymbol{j}(\boldsymbol{R}) = \left\langle \int \frac{d\epsilon}{4\pi i} \left[2f(\epsilon) - 1\right] \boldsymbol{j}(\boldsymbol{p}_{\mathrm{F}}, \boldsymbol{R}; \epsilon) \right\rangle_{\theta_{\mathrm{F}}}. \tag{2.63}$$

2.7 Total current density

Using the Matsubara technique, the current density in Eq. (2.63) can be written as a sum

$$\boldsymbol{j}(\boldsymbol{R}) = \pi e N_{\mathrm{F}} \frac{1}{2} \left\langle \boldsymbol{v}_{\mathrm{F}} k_{\mathrm{B}} T \sum_{|\varepsilon_n|<\Omega_{\mathrm{c}}} \mathrm{Tr}\left\{\hat{\tau}_3 \hat{g}^{\mathrm{M}}(\boldsymbol{p}_{\mathrm{F}}, \boldsymbol{R}; z)\right\} \right\rangle_{\theta_{\mathrm{F}}} , \tag{2.64}$$

where Ω_{c} is a cutoff, $z = i\varepsilon_n \equiv i\pi k_{\mathrm{B}} T(2n+1)$ are the Matsubara energies, and $\hat{g}^{\mathrm{M}}$ is the Matsubara Green function. The trace reduces to

$$\mathrm{Tr}\left\{\hat{\tau}_3 \hat{g}^{\mathrm{M}}(\boldsymbol{p}_{\mathrm{F}}, \boldsymbol{R}; z)\right\} = 2g_0^{\mathrm{M}}(\boldsymbol{p}_{\mathrm{F}}, \boldsymbol{R}; z) - 2\tilde{g}_0^{\mathrm{M}}(\boldsymbol{p}_{\mathrm{F}}, \boldsymbol{R}; z) = 4g_0^{\mathrm{M}}(\boldsymbol{p}_{\mathrm{F}}, \boldsymbol{R}; z), \tag{2.65}$$

where subscript 0 denotes the scalar component, see Eq. (2.7). The sum can be converted to positive energies

$$\begin{aligned} \boldsymbol{j}(\boldsymbol{R}) &= 2k_{\mathrm{B}} T e N_{\mathrm{F}} v_{\mathrm{F}} \left\langle \sum_{\varepsilon_n>0}^{\Omega_{\mathrm{c}}} \hat{\boldsymbol{v}}_{\mathrm{F}} \left[g_0^{\mathrm{M}}(\boldsymbol{p}_{\mathrm{F}}, \boldsymbol{R}; z) + g_0^{\mathrm{M}}(\boldsymbol{p}_{\mathrm{F}}, \boldsymbol{R}; z)^* \right] \right\rangle_{\theta_{\mathrm{F}}} , \\ &= 4k_{\mathrm{B}} T e N_{\mathrm{F}} v_{\mathrm{F}} \left\langle \sum_{\varepsilon_n>0}^{\Omega_{\mathrm{c}}} \hat{\boldsymbol{v}}_{\mathrm{F}} \, \mathrm{Re}\left\{ g_0^{\mathrm{M}}(\boldsymbol{p}_{\mathrm{F}}, \boldsymbol{R}; z) \right\} \right\rangle_{\theta_{\mathrm{F}}} . \end{aligned} \tag{2.66}$$

Introducing the depairing current

$$j_{\mathrm{d}} \equiv 4\pi k_{\mathrm{B}} T_{\mathrm{c}} |e| N_{\mathrm{F}} v_{\mathrm{F}}, \tag{2.67}$$

the current density can be written as a dimensionless equation

$$\frac{\boldsymbol{j}(\boldsymbol{R})}{j_{\mathrm{d}}} = -\frac{T}{T_{\mathrm{c}}} \frac{1}{\pi} \left\langle \sum_{\varepsilon_n>0}^{\Omega_{\mathrm{c}}} \hat{\boldsymbol{v}}_{\mathrm{F}} \, \mathrm{Re}\left\{ g_0^{\mathrm{M}}(\boldsymbol{p}_{\mathrm{F}}, \boldsymbol{R}; z) \right\} \right\rangle_{\theta_{\mathrm{F}}} , \tag{2.68}$$

where the minus sign comes from the factor $e/|e| = -1$.

2.8 Thermodynamics

This thesis uses the Luttinger-Ward free-energy functional for analytic calculations, and the Eilenberger free-energy for numeric computations. They are both expressions of the free energy difference between the superconducting state and the normal state, in terms of quasiclassical Green functions and self energies. The entropy and heat capacity are used to calculate bulk properties in Apps. D.8 and D.9, and to study phase transitions in papers II–III.

2.8.1 Luttinger-Ward free energy

The Luttinger-Ward free-energy functional is given by [69, 109–112]

$$\delta\Omega(B,T) = \int d\boldsymbol{R}\left\{\frac{\boldsymbol{B}^2_{\mathrm{ind}}(\boldsymbol{R})}{8\pi} + N_{\mathrm{F}}k_{\mathrm{B}}T\frac{1}{2}\int_0^1 d\lambda \left\langle \sum_{\varepsilon_n} \mathrm{Tr}\left[\hat{\Delta}(\hat{g}_\lambda - \frac{1}{2}\hat{g})\right]\right\rangle_{\theta_{\mathrm{F}}}\right\}, \quad (2.69)$$

where $\hat{g}_\lambda$ is the solution to the Eilenberger equation with the substitution $\hat{\Delta} \to \hat{\Delta}\lambda$, with λ being a "dummy variable". The first term in Eq. (2.69) is the magnetic energy density (see e.g. Ch. 5.16 of Jackson [113]), which has the dimensionless expression

$$\frac{\boldsymbol{B}^2_{\mathrm{ind}}}{8\pi N_{\mathrm{F}}(k_{\mathrm{B}}T_{\mathrm{c}})^2} = \left(\frac{\boldsymbol{B}_{\mathrm{ind}}}{\Phi_0/\xi_0^2}\right)^2 2\pi^4\kappa_0^2, \quad (2.70)$$

where $\Phi_0 \equiv hc/2|e|$ is the flux quantum, and $\kappa_0 \equiv \lambda_0/\xi_0$ is the dimensionless Ginzburg-Landau parameter, with penetration depth $\lambda_0 \equiv c/\sqrt{4\pi e^2 N_{\mathrm{F}} v_{\mathrm{F}}^2}$ and coherence length $\xi_0 \equiv \hbar v_{\mathrm{F}}/2\pi k_{\mathrm{B}} T_{\mathrm{c}}$. Note that the induced field typically comes with a κ_0^{-2}-dependence (see e.g. Sec. 4.4 of Lic. Th. [10]), giving the whole magnetic energy density a κ_0^{-2}-dependence.

2.8.2 Eilenberger free energy

In the original paper introducing the Eilenberger equations [73], a simplified expression for the free-energy functional was guessed by Eilenberger. This expression was recently formally derived by [114]. In the literature, there exists several different notations and ways of expressing this Eilenberger free-energy functional. In this work, it is expressed in terms of the quasiclassical self-energies and Riccati coherence functions as

$$\begin{aligned}\delta\Omega(B,T) &= \int d\boldsymbol{R}\left\{\frac{\boldsymbol{B}^2_{\mathrm{ind}}(\boldsymbol{R})}{8\pi} + |\Delta(\boldsymbol{R})|^2 N_{\mathrm{F}} \ln\frac{T}{T_{\mathrm{c}}}\right. \\ &\qquad\left. + 2\pi N_{\mathrm{F}} k_{\mathrm{B}} T \sum_{\varepsilon_n>0}^{\Omega_{\mathrm{c}}}\left[\frac{|\Delta(\boldsymbol{R})|^2}{\varepsilon_n} + i\mathcal{I}(\boldsymbol{R};\varepsilon_n)\right]\right\}, && (2.71)\\ \mathcal{I}(\boldsymbol{R};\varepsilon_n) &= \left\langle\left[\tilde{\Delta}(\boldsymbol{p}_{\mathrm{F}},\boldsymbol{R})\gamma(\boldsymbol{p}_{\mathrm{F}},\boldsymbol{R};\varepsilon_n) - \Delta(\boldsymbol{p}_{\mathrm{F}},\boldsymbol{R})\tilde{\gamma}(\boldsymbol{p}_{\mathrm{F}},\boldsymbol{R};\varepsilon_n)\right]\right\rangle_{\theta_{\mathrm{F}}}. && (2.72)\end{aligned}$$

2.8.3 Entropy and heat capacity

Appendix C.3 introduces the entropy and derives an expression in terms of the free energy

$$S = -\left(\frac{\partial \Omega}{\partial T}\right)_W , \tag{2.73}$$

which holds under the assumption of no work done W. The appendix shows that for a bulk system, the entropy can alternatively be calculated from the typical statistical expression. Similarly, App. C.4 introduces the heat capacity, which also can be calculated using the statistical expression in a bulk system, or quite generally from the free energy

$$C = T\left(\frac{\partial S}{\partial T}\right)_W = -T\left(\frac{\partial^2 \Omega}{\partial T^2}\right)_W . \tag{2.74}$$

3 Bulk superconductivity with superflow: local response

Equipped with the quasiclassical theory presented in Ch. 2, this chapter sets out to study how various well-known properties of bulk superconductivity [15, 16, 78, 81] are modified in the presence of superflow [115, 116]. This superflow is assumed to be homogeneous, but some of the results hold also for inhomogeneous superflow in the case of local response, valid in the limit $\big|\boldsymbol{v}_{\mathrm{F}} \cdot \boldsymbol{\nabla}|\Delta|\big|/\pi T_{\mathrm{c}} \sim \xi/\lambda \ll 1$ [116]. Several of these bulk properties and results are used in the appended papers, as input to derive surface bound state properties in Ch. 4, and in the extension to a non-local response in Chs. 5–6. Like in the rest of the thesis, the chapter assumes a clean spin-singlet superconductor with spin-degeneracy, in equilibrium.

In particular, this chapter starts by presenting the solutions to the bulk Riccati equations, yielding a closed form expressions for the bulk coherence functions and quasiclassical propagators. These are used to obtain the bulk gap equation, density of states, current response and free energy. Results are derived for a conventional s-wave superconductor, highlighting the role of the superflow as a Doppler shift to the spectrum, and associated with a positive kinetic energy. At low temperatures, the response is linear and the superconducting order is unaffected up to a critical value, where a transition to the normal-state occurs. At finite temperatures, thermal quasiparticles lead to a non-linear response and an earlier breakdown of superconductivity. For an unconventional d-wave superconductor, there are subgap quasiparticle states even at low temperatures, leading to a much more complicated scenario.

In later chapters, it is shown that the situation can change drastically in an environment where the superconductor is already suppressed, e.g. in the presence of Andreev bound states, making the superflow energetically favorable as a mechanism to heal superconductivity.

3.1 Bulk propagators and coherence functions

In a spin-singlet bulk superconductor with a homogeneous order parameter, Eqs. (2.32) and (2.33) reduce to two spin-degenerate scalar equations (with an extra minus sign from factors $(i\sigma_2)^2 = -\sigma_0$)

$$\tilde{\Delta}_s(\boldsymbol{p}_\mathrm{F})\gamma_s^2(\boldsymbol{p}_\mathrm{F};z) + 2z_p\gamma_s(\boldsymbol{p}_\mathrm{F};z) + \Delta_s(\boldsymbol{p}_\mathrm{F}) = 0, \tag{3.1}$$

$$\Delta_s(\boldsymbol{p}_\mathrm{F})\tilde{\gamma}_s^2(\boldsymbol{p}_\mathrm{F};z) - 2z_p\tilde{\gamma}_s(\boldsymbol{p}_\mathrm{F};z) + \tilde{\Delta}_s(\boldsymbol{p}_\mathrm{F}) = 0. \tag{3.2}$$

The subscript s is dropped, and the same gauge as in App. A is chosen, where the order parameter is real and phase-independent $\tilde{\Delta}(\boldsymbol{p}_\mathrm{F}) = \Delta^*(\boldsymbol{p}_\mathrm{F}) = \Delta(\boldsymbol{p}_\mathrm{F}) = |\Delta|\eta(\theta_\mathrm{F})$, in favor of explicit superflow dependence $z_p \equiv z - \boldsymbol{v}_\mathrm{F}\cdot\boldsymbol{p}_\mathrm{s}$. Here, the superflow is now homogeneous, with angle ϕ relative to the crystal a-axis

$$\boldsymbol{p}_\mathrm{s} = \frac{\hbar}{2}\boldsymbol{\nabla}\chi - \frac{e}{c}\boldsymbol{A} = \mathrm{const}, \tag{3.3}$$

$$\boldsymbol{v}_\mathrm{F}\cdot\boldsymbol{p}_\mathrm{s} = v_\mathrm{F}p_\mathrm{s}\,(\cos\theta_\mathrm{F},\sin\theta_\mathrm{F})\cdot(\cos\phi,\sin\phi) = v_\mathrm{F}p_\mathrm{s}\cos(\theta_\mathrm{F}-\phi). \tag{3.4}$$

Inhomogeneous superflow $\boldsymbol{p}_\mathrm{s}(\boldsymbol{R})$ can however be treated in the same way in the local response limit $\big|\boldsymbol{v}_\mathrm{F}\cdot\boldsymbol{\nabla}|\Delta|\big|/\pi T_\mathrm{c} \sim \xi/\lambda \ll 1$ [116]. Appendix B.4 derives the homogeneous solutions

$$\gamma_\mathrm{bulk}(\boldsymbol{p}_\mathrm{F};z) = \frac{-\Delta(\boldsymbol{p}_\mathrm{F})}{z_p + i\Omega}, \tag{3.5}$$

$$\tilde{\gamma}_\mathrm{bulk}(\boldsymbol{p}_\mathrm{F};z) = \frac{\tilde{\Delta}(\boldsymbol{p}_\mathrm{F})}{z_p + i\Omega}, \tag{3.6}$$

$$\Omega \equiv \sqrt{|\Delta(\boldsymbol{p}_\mathrm{F})|^2 - z_p^2}. \tag{3.7}$$

Inserting these results into the Green functions in Eqs. (2.36)–(2.39), the bulk propagators are found to be

$$g_\mathrm{bulk}(\boldsymbol{p}_\mathrm{F};z) = -\pi\frac{z_p}{\Omega}, \tag{3.8}$$

$$\tilde{g}_\mathrm{bulk}(\boldsymbol{p}_\mathrm{F};z) = \pi\frac{z_p}{\Omega}, \tag{3.9}$$

$$f_\mathrm{bulk}(\boldsymbol{p}_\mathrm{F};z) = \pi\frac{\Delta(\boldsymbol{p}_\mathrm{F})}{\Omega}, \tag{3.10}$$

$$\tilde{f}_\mathrm{bulk}(\boldsymbol{p}_\mathrm{F};z) = \pi\frac{\tilde{\Delta}(\boldsymbol{p}_\mathrm{F})}{\Omega}. \tag{3.11}$$

As a sanity check, it is noted that in the limit $\Delta \to 0$ (or equivalently $T \to T_\mathrm{c}$) the quasiparticle propagators are non-zero $g \to -i\pi$ and $\tilde{g} \to i\pi$, while the pair propagators vanish $f \to 0$ and $\tilde{f} \to 0$. Hence, there are particle-correlations but no superconducting pair-correlations above the superconducting state.

These coherence functions and propagators are used to derive various bulk quantities and observables in App. D, which will now be used to study bulk superflow response, first in s-wave and then in d-wave superconductors.

3.2 Conventional s-wave superconductors

This section studies how the bulk properties of a conventional s-wave superconductor are modified by superflow, namely the gap, density of states, current response and energetics. These are calculated analytically at zero temperature. Effects of finite temperature are then discussed towards the end of the section.

Using the superflow gauge in App. A, the bulk s-wave order parameter is written $\Delta(\boldsymbol{p}_\mathrm{F}, \boldsymbol{R}; T) = |\Delta(T)|$. At zero temperature and in the absence of superflow, $\Delta_0 \equiv |\Delta(T=0)|$, the gap equation is solved in App. D.2

$$\frac{\Delta_0}{k_\mathrm{B}T_\mathrm{c}} = \pi e^{-\gamma_\mathrm{E}} \approx 1.76, \tag{3.12}$$

where $\gamma_\mathrm{E} \approx 0.58$ is the Euler-Mascheroni constant defined in Eq. (D.13). Condensation into the superconducting state leads to an energy gain, which at zero temperature is denoted $\delta\Omega_0^\mathrm{BCS}$, known as the BCS energy. In a homogeneous bulk superconductor, superflow usually leads to a positive kinetic energy $\delta\Omega_0^p$, and magnetic energy $\delta\Omega_0^B = \int dR \boldsymbol{B}_\mathrm{ind}^2/8\pi$, such that the total energy is

$$\delta\Omega_0 = \delta\Omega_0^\mathrm{BCS} + \delta\Omega_0^p + \delta\Omega_0^B. \tag{3.13}$$

Appendix D.4 uses the Luttinger-Ward free energy to derive

$$\frac{\delta\Omega_0^\mathrm{BCS}}{\mathcal{V}N_\mathrm{F}} = -\frac{\Delta_0^2}{2} \approx -1.55(k_\mathrm{B}T_\mathrm{c})^2, \tag{3.14}$$

$$\frac{\delta\Omega_0^p}{\mathcal{V}N_\mathrm{F}} = \frac{v_\mathrm{F}^2 p_\mathrm{s}^2}{2}, \tag{3.15}$$

where $\mathcal{V} \equiv \int dR$ is the volume of the superconductor. These equations define the critical field and superflow through $\delta\Omega_0 = 0$, i.e. when the energy cost of superflow and magnetic fields weigh up the gain of condensation. In the absence of superflow, the thermodynamical critical field is found,

$$B_\mathrm{c} = 2\sqrt{\pi N_\mathrm{F}}\Delta_0, \tag{3.16}$$

and for negligible fields, the critical superflow is

$$p_\mathrm{s,c} \equiv \frac{\Delta_0}{v_\mathrm{F}}. \tag{3.17}$$

Appendix D.3 shows that Eq. (3.12) holds for all superflow below $p_\mathrm{s,c}$, such that

$$\Delta_0(\boldsymbol{p}_\mathrm{s}) = \Delta_0 \qquad \forall p_\mathrm{s} < p_\mathrm{s,c}, \tag{3.18}$$

above which superconductivity breaks down rapidly to the normal-state, as seen in Fig. 3.1 (a). This is understood from the momentum-resolved density of states plotted in Fig. 3.1 (b), given by the integrand in the full bulk density of states,

$$\frac{N(\varepsilon)}{2N_\mathrm{F}} = \left\langle \Theta\left[(\varepsilon - \boldsymbol{v}_\mathrm{F}\cdot\boldsymbol{p}_\mathrm{s})^2 - |\Delta(T)|^2\right] \frac{|\varepsilon - \boldsymbol{v}_\mathrm{F}\cdot\boldsymbol{p}_\mathrm{s}|}{\sqrt{(\varepsilon - \boldsymbol{v}_\mathrm{F}\cdot\boldsymbol{p}_\mathrm{s})^2 - |\Delta(T)|^2}} \right\rangle_{\theta_\mathrm{F}}, \tag{3.19}$$

which is derived in App. D.6. In the absence of superflow, the angular average is trivial, and the DOS in Eq. (3.19) reduces to the integrand, which is zero for $|\varepsilon| < \Delta(T)$, a square-root singularity signifying the coherence peaks at $\varepsilon \to \Delta^+(T)$, and approaches the normal-state DOS $(2N_\mathrm{F})$ for $|\varepsilon| \gg \Delta(T)$. It is explicitly seen that the superfluid momentum directly acts as a Doppler shift to the energy, $\epsilon = \varepsilon - \boldsymbol{v}_\mathrm{F} \cdot \boldsymbol{p}_\mathrm{s}$, shifting the coherence peaks positively or negatively depending on the sign of $\boldsymbol{v}_\mathrm{F} \cdot \boldsymbol{p}_\mathrm{s}$. As $p_\mathrm{s} \to p_\mathrm{s,c}$, the shifted coherence peaks meet at $\varepsilon = 0$, closing the gap as evident in the momentum-averaged DOS in Fig. 3.1 (c). Note the similarity between the Doppler-shifted s-wave spectrum and a regular d-wave spectrum (solid line in panel (a) of Fig. 3.2), due to the trigonometric terms $\cos(\theta_\mathrm{F} - \phi)$ in $\boldsymbol{v}_\mathrm{F} \cdot \boldsymbol{p}_\mathrm{s}$ from Eq. (3.4). At zero temperature, the Fermi-distribution distribution function $f(\varepsilon, T)$ is given by a step function, implying full and zero occupation at negative and positive energies, respectively. Thus, for $p_\mathrm{s} > p_\mathrm{s,c}$, the negatively and positively shifted coherence peaks become populated and depopulated, respectively. This regime is generally beyond experiment, however, since superflow is typically generated by driving a current through the system. The critical depairing current is reached before this regime. Appendix D.5 derives the zero-temperature current response, which is found to be linear in the superflow,

$$\boldsymbol{j}_0 = e\rho\boldsymbol{p}_\mathrm{s} = N_\mathrm{F} v_\mathrm{F}^2 \boldsymbol{p}_\mathrm{s}, \tag{3.20}$$

where $\rho \equiv N_\mathrm{F} v_\mathrm{F}^2$ is the bulk superfluid density at zero temperature (App. D.5 relates ρ to the bulk density tensor $\boldsymbol{\rho}_s$). Inserting the critical superflow yields the critical depairing current

$$j_0^{s,\mathrm{c}} = |e| N_\mathrm{F} v_\mathrm{F} \Delta_0, \tag{3.21}$$

and the critical particle current $j_0^\mathrm{c} = \rho p_\mathrm{s}^\mathrm{c} = N_\mathrm{F} v_\mathrm{F} \Delta_0$. This can be used to make a consistency check of $\delta\Omega_0^p$, by comparing it to the kinetic energy $\delta\Omega_j = \frac{1}{2}\int d\boldsymbol{R}\,\{\boldsymbol{j} \cdot \boldsymbol{p}_\mathrm{s}\}$ (this form is derived in Sec. 6.1.1). Inserting the critical particle-current and superflow indeed reproduces $\delta\Omega_j/(\mathcal{V} N_\mathrm{F}) = (v_\mathrm{F} p_\mathrm{s})^2/2$.

Finite temperatures smear the distribution function, see Fig. 3.1 (b), with population and depopulation of positive and negative energies respectively, signifying thermally excited quasiparticles. In the absence of superflow, this leads to the usual temperature-dependent suppression seen in Fig. 3.1 (d), while finite superflow is pairbreaking. This pairbreaking further increases the suppression, with a monotonic reduction of $T_\mathrm{c}(p_\mathrm{s} \to p_\mathrm{s,c}) \to 0$, see Fig. 3.1 (a). This is because the excitations lead to a quasiparticle backflow, which grows with the superflow magnitude and is paramagnetic as opposed to the diamagnetic response of the condensate. These effects reduce the current in Eq. (3.20) through a non-linear response, with the following leading-order terms in the superflow [116]

$$\boldsymbol{j} \;=\; e\rho(T)\boldsymbol{p}_\mathrm{s}\left[1 - \alpha(T)\frac{p_\mathrm{s}^2}{p_\mathrm{s,c}^2(T)}\right], \tag{3.22}$$

$$\rho(T) \;=\; \rho - N_{\mathrm{F}} v_{\mathrm{F}}^2 \int_0^\infty \frac{d\varepsilon}{2k_{\mathrm{B}}T\cosh^2(\sqrt{\varepsilon^2 + |\Delta|^2})}, \tag{3.23}$$

where $p_{\mathrm{s,c}}(T) = \Delta(T)/v_{\mathrm{F}}$ is the temperature-dependent critical superflow, and the coefficient $\alpha(T) \geq 0$ is plotted in Fig. 3.1 (d). The temperature dependence of the current response is illustrated in Fig. 3.1 (a), based on self-consistent calculations.

The situation becomes significantly more complicated in the case of a nodal d-wave superconductor, with quasiparticle contributions already at $T = 0$, as discussed in Sec. 3.3.

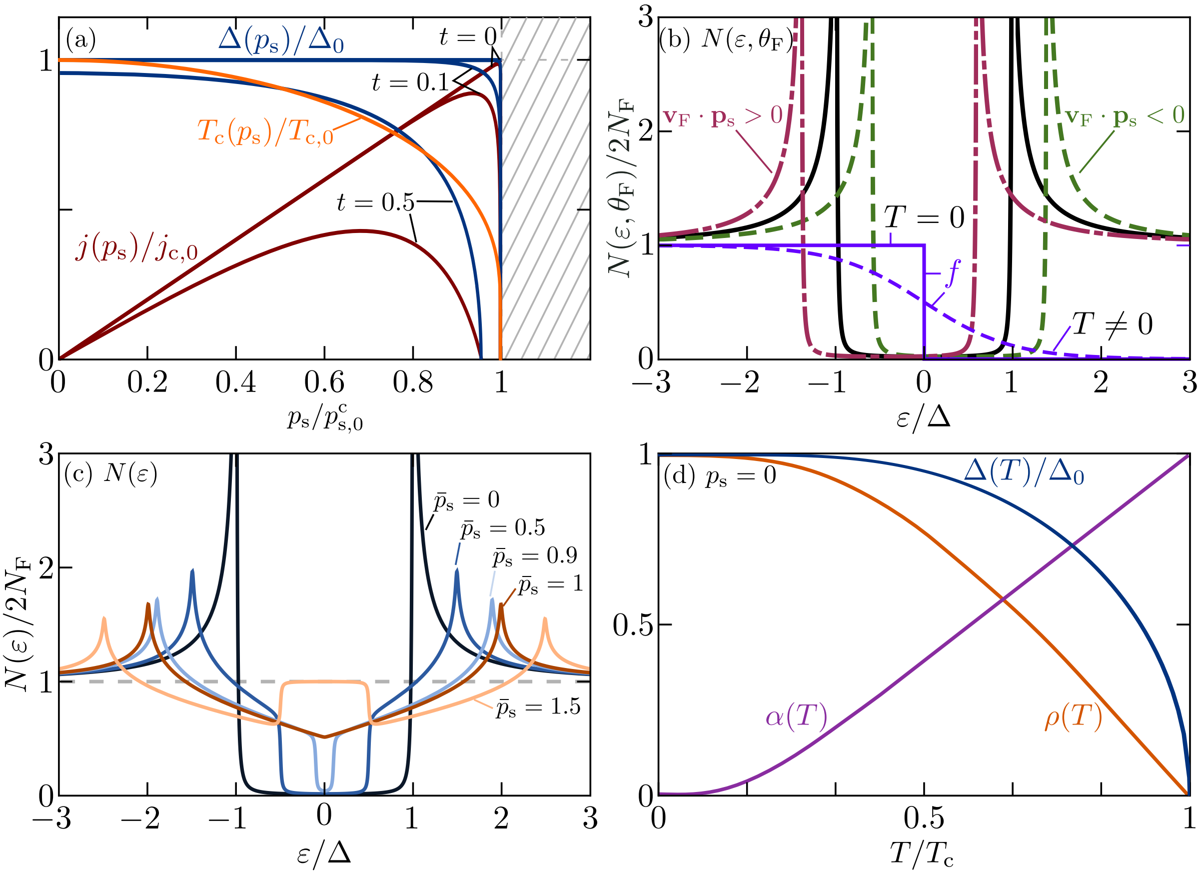

Figure 3.1: *Bulk s-wave response to homogeneous superflow. (a) Current response, gap suppression and transition temperature suppression, with* $t \equiv T/T_c$*. (b) Momentum-resolved density of states, showing a Doppler shift of coherence peaks depending on the sign of* $\boldsymbol{v}_F \cdot \boldsymbol{p}_s$*. Here,* $f(\varepsilon, T)$ *is the distribution function. (c) Momentum-averaged density of states, obtained with a smearing* $\delta = 0.01\Delta$ *in* $z^{\mathrm{R}} = \epsilon + i\delta$ *in the Retarded propagator, and where* $\bar{p}_s \equiv p_s v_F/\Delta(T)$*. (d) Temperature-dependence at zero superflow, where* $\alpha(T)$ *and* $\rho(T)$ *are approximately exponential at low temperatures, and linear at high temperatures.*

3.3 Unconventional d-wave superconductors

Consider a nodal d-wave superconductor, with $\Delta(\boldsymbol{p}_\mathrm{F},\boldsymbol{R};T) = |\Delta(T)|\eta(\theta_\mathrm{F})$, where $\eta(\theta_\mathrm{F}) = \sqrt{2}\cos(2\theta_\mathrm{F})$. Here, the nodes refer to the regions on the Fermi surface where the gap closes due to $\eta(\theta_\mathrm{F}) = 0$, e.g. at $\theta_\mathrm{F} = \pi/4$, see Fig. 3.2. This anisotropy leads to different results compared to the isotropic s-wave case. For example, the zero-temperature magnitude $\Delta_0 \equiv |\Delta(T)|$ (derived in App. D.2) is

$$\frac{\Delta_0}{k_\mathrm{B}T_\mathrm{c}} = \sqrt{2}\pi e^{-\gamma_\mathrm{E}-\frac{1}{2}} \approx 1.51, \tag{3.24}$$

with maximal gap $\Delta_0\sqrt{2} \approx 2.14 k_\mathrm{B}T_\mathrm{c}$ at the antinodes (e.g. $\theta_\mathrm{F} = 0$). The low-temperature condensation energy derived in App. D.4 is then given by

$$\frac{\delta\Omega_0^\mathrm{BCS}}{\mathcal{V}N_\mathrm{F}} = -\frac{\Delta_0^2}{2} \approx -1.14(k_\mathrm{B}T_\mathrm{c})^2. \tag{3.25}$$

The anisotropy gives rise to a completely different density of states (derived in App. D.7), which in the absence of superflow takes the form [117]

$$\frac{N_d(\varepsilon)}{2N_\mathrm{F}} = \frac{2}{\pi}\left[K\left(\frac{\Delta_d}{|\varepsilon|}\right)\Theta(\varepsilon^2-\Delta_d^2) + \frac{|\varepsilon|}{\Delta_d}K\left(\frac{|\varepsilon|}{\Delta_d}\right)\Theta(\Delta_d^2-\varepsilon^2)\right], \tag{3.26}$$

illustrated in Fig. 3.2 (a), where $\Delta_d = \sqrt{2}\Delta(T)$, and K is the complete elliptic integral of the first kind, defined in Eq. (D.51). Like the s-wave case, the d-wave DOS has divergent coherence peaks as $|\varepsilon| \to \Delta_d$, and converges to the normal-state DOS ($2N_\mathrm{F}$) as $|\varepsilon| \gg \Delta_d$, since $K(0) = \pi/2$. However, the spectrum is completely different for $|\varepsilon| \ll \Delta_d$, with linear dependence $N(\varepsilon) \approx |\varepsilon|/\Delta_d$. Hence, while the s-wave spectrum is fully gapped, the d-wave state is gapless. This leads to a modified current response, as understood from the momentum-resolved density of states, which in the presence of superflow is written

$$\frac{N(\varepsilon)}{2N_\mathrm{F}} = \left\langle \Theta\left[\epsilon^2 - |\Delta(\boldsymbol{p}_\mathrm{F})|^2\right] \frac{|\varepsilon - v_\mathrm{F}p_\mathrm{s}\cos(\theta_\mathrm{F}-\phi)|}{\sqrt{(\varepsilon - v_\mathrm{F}p_\mathrm{s}\cos(\theta_\mathrm{F}-\phi))^2 - \Delta_d^2\cos^2(2\theta_\mathrm{F})}}\right\rangle_{\theta_\mathrm{F}}, \tag{3.27}$$

where again, the superflow acts as a Doppler shift $\epsilon = \varepsilon - \boldsymbol{v}_\mathrm{F}\cdot\boldsymbol{p}_\mathrm{s}$. Figure 3.2 (a) and (b) shows the DOS for superflow along nodal and antinodal directions, respectively. Note that there are always directions close to the nodes where a finite superflow leads to $|\Delta(\boldsymbol{p}_\mathrm{F})|^2 + (\varepsilon - \boldsymbol{v}_\mathrm{F}\cdot\boldsymbol{p}_\mathrm{s})^2 < 0$, yielding a population and depopulation of negatively and positively shifted peaks respectively, even at $T = 0$. These quasiparticle excitations again give a paramagnetic response that reduce the current response, the latter which to leading order is [116]

$$\boldsymbol{j}_0 = e\rho\boldsymbol{p}_\mathrm{s}\left[1 - \beta(\phi)\frac{|\boldsymbol{p}_\mathrm{s}|}{p_\mathrm{s}^*}\right], \tag{3.28}$$

$$\beta(\phi) = \begin{cases} 1, & (\boldsymbol{p}_\mathrm{s} \parallel \text{node}), \\ \frac{1}{\sqrt{2}}, & (\boldsymbol{p}_\mathrm{s} \parallel \text{antinode}), \end{cases} \tag{3.29}$$

where it is reminded that $\rho = N_{\mathrm{F}} v_{\mathrm{F}}^2$, and where

$$p_{\mathrm{s}}^* \equiv \frac{\mu\Delta_0^d}{v_{\mathrm{F}}^*} > p_{\mathrm{s}}, \tag{3.30}$$

$$\mu \equiv \frac{1}{\Delta_0^d}\frac{d|\Delta(\boldsymbol{p}_{\mathrm{F}})|}{d\theta_{\mathrm{F}}}\Big|_{\theta_{\mathrm{F}}\to\mathrm{node}}, \tag{3.31}$$

with v_{F}^* and μ being the Fermi velocity and gap slope at the node. Due to Eq. (3.30), the current is still parallel with $\boldsymbol{p}_{\mathrm{s}}$, giving a diamagnetic response. Furthermore, the particle-current $j_p = j/e$ can be used to estimate the superflow kinetic energy from $\delta\Omega_0^p = \frac{1}{2}\int d\boldsymbol{R}\,\{\boldsymbol{j}_p \cdot \boldsymbol{p}_{\mathrm{s}}\}$ (again, this form is derived in Sec. 6.1.1), yielding

$$\frac{\delta\Omega_0^p}{\mathcal{V}N_{\mathrm{F}}} = \frac{v_{\mathrm{F}}^2 p_{\mathrm{s}}^2}{2}\left[1 - \frac{|\boldsymbol{p}_{\mathrm{s}}|}{p_{\mathrm{s}}^*}\right] > 0. \tag{3.32}$$

As in the s-wave case, a bulk superflow is hence positive and energetically unfavorable, and the critical superflow is $p_{\mathrm{s,c}} \approx \Delta_d/v_{\mathrm{F}}$ for $|\boldsymbol{p}_{\mathrm{s}}| \ll p_{\mathrm{s}}^*$. However, it is noted that the quasiparticles reduce the kinetic energy slightly, raising the question whether an environment exists where the superflow is favorable even favorable. This would occur when the paramagnetic response dominates, which since long was shown theoretically to occur at certain interfaces [64], and supported by early experiments [118, 119]. It is the topic of Ch. 4 to study this scenario.

Finite temperature lead to several complications that are considered beyond the scope of this chapter, see for example Refs. [116, 120].

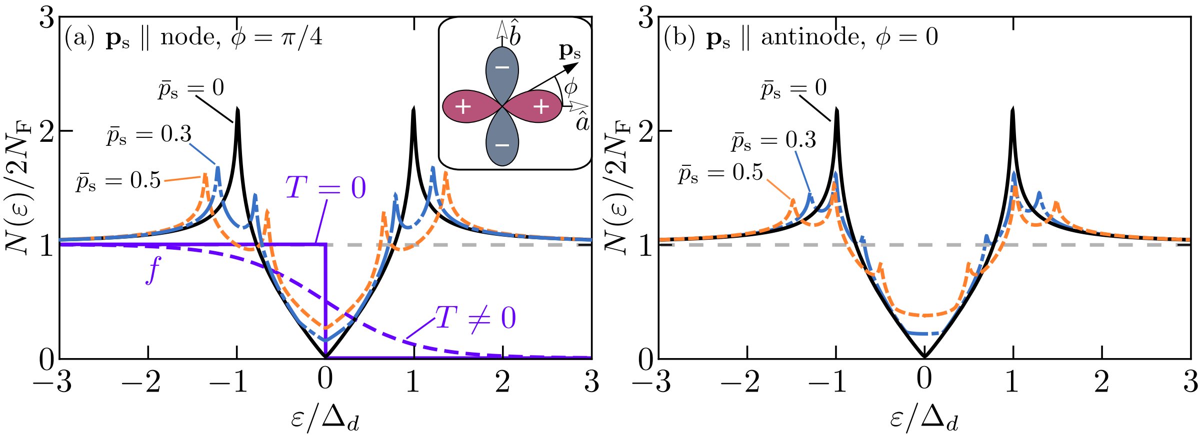

Figure 3.2: *Momentum-averaged density of states in a bulk d-wave superconductor with superflow parallel to the order parameter (a) nodes, and (b) antinodes. A smearing $\delta = 0.01\Delta_d$ was used in $z^{\mathrm{R}} = \epsilon + i\delta$ in the Retarded propagator. Here, $\bar{p}_s \equiv p_s v_F/\Delta_d(T)$. The d-wave basis function is sketched in the inset in (a).*

3.4 Chapter summary: favorable kinetic energy?

This chapter, and the related App. D, used the quasiclassical theory to study bulk superconductivity in the presence of a homogeneous superflow $\boldsymbol{p}_\mathrm{s}$ (or inhomogeneous superflow $\boldsymbol{p}_\mathrm{s}(\boldsymbol{R})$ in the local response limit). Several well-known results were produced, and it was shown that the main influence of a homogeneous superflow is in the form of a Doppler shift that moves the excitation spectrum up or down in energy depending on the projection of $\boldsymbol{p}_\mathrm{s}$ on $\boldsymbol{v}_\mathrm{F}$. The superflow leads to a cost in the free energy which scales mainly as $(v_\mathrm{F} p_\mathrm{s})^2/2$ at low temperatures, reducing the energy gain of condensation, and leading to a rapid breakdown of superconductivity above a critical value $p_\mathrm{s,c} = \Delta/v_\mathrm{F}$. For a conventional s-wave order parameter, the low-temperature response to the superflow was shown to be a diamagnetic condensate current $\boldsymbol{j} = e\rho\boldsymbol{p}_\mathrm{s}$, with superfluid density $\rho = N_\mathrm{F} v_\mathrm{F}^2$. Subgap quasiparticles, e.g. due to thermal excitations or the nodal structure of an unconventional d-wave order parameter, lead to a paramagnetic response which reduces both the gap and the current. This paramagnetic response also effectively reduces the superflow kinetic energy. While this might usually be negligible compared to the reduction of condensation energy, due to the pairbreaking superflow or thermal effects, the question still arises if a scenario exists where the superflow is ultimately energetically favorable. As counterintuitive as this might seem, Ch. 4 shows that this is indeed possible, namely when the environment suppresses the order parameter, for example at certain interfaces where the paramagnetic response is known to be dominant [64, 118, 119]. The superflow can then serves to heal superconductivity by removing the unfavorable low-energy states that are formed at those surfaces.

4 Andreev bound states at interfaces

Using the quasiclassical theory introduced in Ch. 2, this chapter studies how quasiparticle scattering at a clean and specular interface may lead to surface Andreev bound states [59–61]. These quasiparticles constitute broken pairs that lie below the superconducting gap, hence at the expense of favorable condensation energy. They can even have zero energy (i.e. on the Fermi surface), typically during scattering between order-parameters with opposite amplitudes [61–63]. Such a scenario is for example possible in reflection and tunneling processes at interfaces between two superconductors, or reflection at a superconductor interface to vacuum, a normal-metal, or a ferromagnetic insulator. In the latter case, the sign-change is induced by a spin-dependent phase shift caused by a finite magnetization, and may occur even in a conventional s-wave superconductor, as discussed in paper I. The rest of the sign-changing processes mentioned typically relies on unconventional nodal superconductors with lobes of different signs, with d-wave superconductors being of primary interest.

The chapter derives the coherence functions and surface propagators close to such interfaces, which are used to study the density of states and energetics of the midgap states. It is shown that the surface pairbreaking leads to an inhomogeneous and highly unfavorable environment for the superconducting order, which becomes more pronounced at low temperatures. The states are shown to have a Lorentzian spectrum, and an exponential decay from the interface over the coherence length. Chapter 3 showed that the quasiparticle states have a paramagnetic response in bulk, and speculated that if this paramagnetic response becomes dominant, superflow kinetic energy might turn negative and favorable. Indeed, the environment close to the interface fulfills this criterion [64], and the superflow Doppler shifts the quasiparticles states, effectively opening a new gap. Energy balancing leads to a length scale $\mathcal{L}_y \sim 4\xi_0$ from the surface where superflow is favorable. Note that this length scale is consistent with what is found in the self-consistent numerics in the appended papers. An inhomogeneous superflow is proposed ad-hoc that decays over this length scale, and discussed in light of other competing mechanisms also shifting quasiparticle states, previously proposed in the literature. To treat such an inhomogeneous superflow and find the responsible mechanism, however, the simple model has to be generalized, which is the topic of Chs. 5 and 6.

4.1 Andreev reflection and pairbreaking at interfaces

Section 2.5 introduced quasiclassical boundary conditions, which highlighted properties of superconductors that are not present in usual normal-state scattering, namely the Andreev processes [57, 58, 61]. As an example, consider an electron in a normal metal impinging on an interface to an insulator. If the electron has an energy below the insulating gap, there are no available states to tunnel into, and it will consequently normal reflect. Consider now a transparent normal-superconductor interface, and an electron impinging on the interface from the normal metal with an energy below the superconducting gap. Again, normal tunneling is prohibited as there are no available states, but it cannot be reflected either due to the perfect transmission. Instead, retro-reflection will occur, in which the incoming electron is converted into a hole with the opposite Fermi velocity, and a cooper pair is injected into the superconductor. This leads to the proximity effect [121, 122]. The conjugate process is also possible, in which a hole retro-reflects into an electron. Such particle-hole conversion processes, either inside or at the interfaces of a superconductor, are known as Andreev reflection. If multiple Andreev-reflections occur in a closed loop, as shown in Fig. 4.1 (a), then superconducting pairs are broken, forming Andreev bound states with energies inside the superconducting gap [59–63]. Furthermore, if the scattering occurs between order parameters of different sign, there are Andreev bound states at zero energy (as shown in Sec. 4.3), and consequently a suppression of the order parameter. Such scattering can occur for example at certain walls and tunneling-barriers of unconventional superconductors with a nodal structure (e.g. [110] interfaces of d-wave superconductors, or in polar p-wave systems [123–127]). It can even occur in conventional s-wave superconductors at spin-active interfaces (e.g. where the interface is described by a ferromagnetic insulator as discussed in paper I and at the end of App. E). See Figs. 4.1 (a)–(d) for illustrations of these cases. Similarly, at the interface to antiferromagnetic systems, the Andreev bound states are known to trigger inhomogeneous stripe instabilities [128–130]. Other examples leading to zero-energy states are scattering at impurities [131–133], and in vortex-cores [134–136]. This thesis mainly considers the cases in Figs. 4.1 (a) and (b).

To study these pairbreaking processes, it is convenient to use the coherence functions $\gamma(\boldsymbol{p}_\mathrm{F}, \boldsymbol{R}; z)$ and $\tilde{\gamma}(\boldsymbol{p}_\mathrm{F}, \boldsymbol{R}; z)$ introduced in Sec. 2.4, which give the probability amplitudes of electron-hole and hole-electron conversion respectively. The next section presents the coherence functions and propagators close to a specular interface with pairbreaking. In particular, the scenario with scattering between order parameters of opposite sign but the same magnitude is considered, here referred to as a maximally pairbreaking scenario (corresponding to e.g. the blue curve in Fig. 4.1 (d), compared to the other curves). Appendix E introduces a model with a more general approach, applicable to other scenarios. The propagators are used to derive the density of states in Sec. 4.3, highlighting the zero-energy states, and to study the energetics in Sec. 4.4.

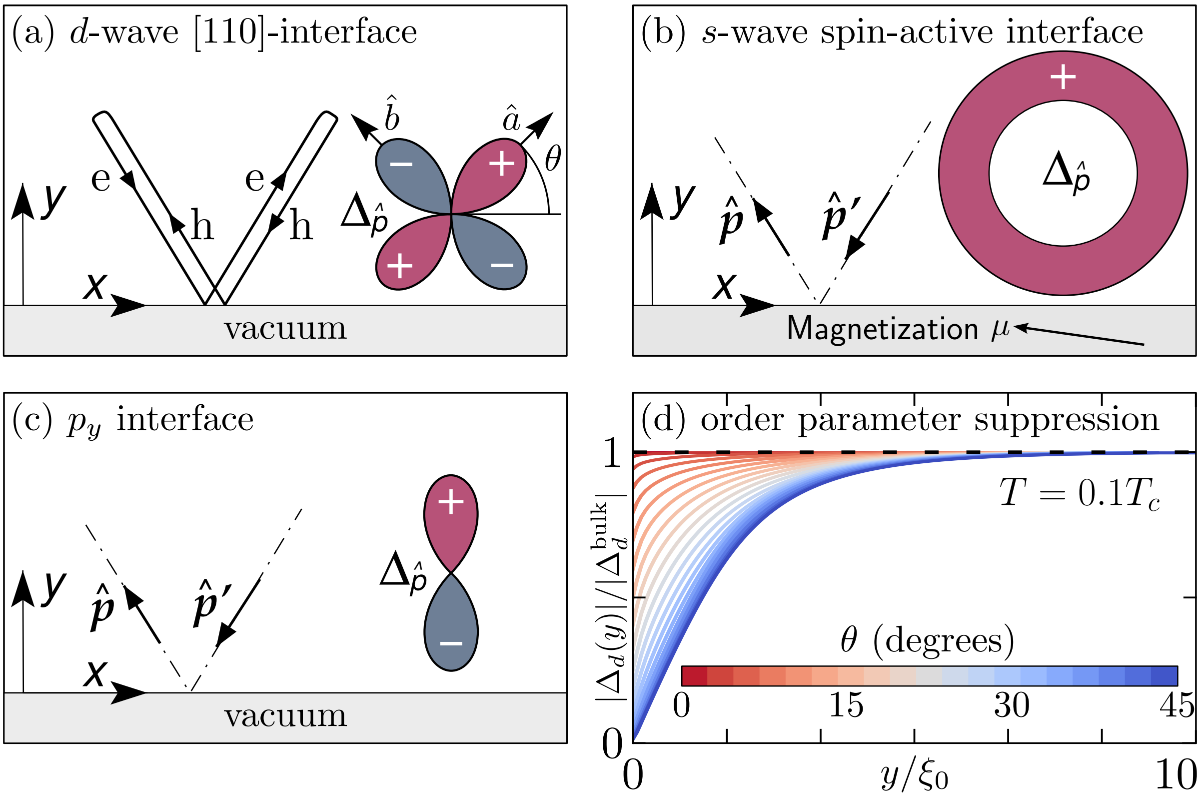

Figure 4.1: *Clean and specular interfaces with pairbreaking scattering between incoming and outgoing momenta* $\hat{\mathbf{p}}'$ *and* $\hat{\mathbf{p}}$ *respectively. Order parameter pairing symmetries in momentum space are illustrated by the cartoons. (a) A vacuum interface aligned with the nodes of a d-wave superconductor (i.e. a [110] interface), as illustrated by the graphics. The figure also shows the multiple Andreev-reflections leading to Andreev bound states. (b) A conventional s-wave superconductor, where a weak ferromagnetic insulator with finite magnetization* μ *acts as a spin-active interface, see paper I and the end off App. E for a description of the scattering process. (c) A vacuum-interface aligned with the nodes of a polar p-wave superconductor. Note that this corresponds to a spin-triplet superconductor (which is beyond the scope of this thesis). (d) Suppression of the order parameter due to pairbreaking scattering at the interface in panel (a), obtained from the self-consistent calculations in paper III.*

4.2 Surface propagators and coherence functions

The previous section introduced the notion of an interface where superconducting pairs are broken up into zero-energy states, due to coherence functions scattering between order parameters of opposite amplitudes. Such an interface is therefore referred to as pairbreaking. Appendix E.1 derives the following solutions to the Riccati equations at such an interface

$$\Gamma_1(\boldsymbol{p}_\mathrm{F}, y; z) = \gamma_{1,\mathrm{h}} \left[\frac{z_p - (z_p + i\Omega)e^{-y/\xi}}{z_p - (z_p - i\Omega)e^{-y/\xi}} \right], \tag{4.1}$$

$$\tilde{\Gamma}_1(\boldsymbol{p}_\mathrm{F}, y; z) = \tilde{\gamma}_{1,\mathrm{h}} \left[\frac{z_p - (z_p + i\Omega)e^{-y/\xi}}{z_p - (z_p - i\Omega)e^{-y/\xi}} \right], \tag{4.2}$$

which decay with distance y from the interface to the homogeneous solutions γ_h and $\tilde{\gamma}_\mathrm{h}$, over the coherence length $\xi = \hbar v_\mathrm{F}|\sin\theta_\mathrm{F}|/2\Omega$, where $z_p \equiv z - \boldsymbol{v}_\mathrm{F} \cdot \boldsymbol{p}_\mathrm{s}$ is the complex energy and $\Omega = \sqrt{|\Delta(\boldsymbol{p}_\mathrm{F})|^2 - z_p^2}$. The coherence functions are used in App. E.3 to derive the quasiparticle- and pair-propagators

$$g(\boldsymbol{p}_\mathrm{F}, y; z) = -\pi\frac{z_p}{\Omega}\left(1 - e^{-y/\xi}\right) + \pi\frac{\Omega}{z_p}e^{-y/\xi}, \tag{4.3}$$

$$\tilde{g}(\boldsymbol{p}_\mathrm{F}, y; z) = +\pi\frac{z_p}{\Omega}\left(1 - e^{-y/\xi}\right) - \pi\frac{\Omega}{z_p}e^{-y/\xi}, \tag{4.4}$$

$$f(\boldsymbol{p}_\mathrm{F}, y; z) = +\pi\frac{\Delta}{\Omega}\left(1 - e^{-y/\xi}\right) - i\pi\,\mathrm{sgn}(\hat{\boldsymbol{v}}_{\mathrm{F}y})\frac{\Delta}{z_p}e^{-y/\xi}, \tag{4.5}$$

$$\tilde{f}(\boldsymbol{p}_\mathrm{F}, y; z) = +\pi\frac{\tilde{\Delta}}{\Omega}\left(1 - e^{-y/\xi}\right) + i\pi\,\mathrm{sgn}(\hat{\boldsymbol{v}}_{\mathrm{F}y})\frac{\tilde{\Delta}}{z_p}e^{-y/\xi}. \tag{4.6}$$

The first terms are clearly the condensate terms, which heal to the bulk propagators in Eqs. (3.8)–(3.11) exponentially from the interface. The second terms are the bound state terms that instead decay exponentially from the interface, and where the Matsubara energy $z = i\varepsilon_n = i\pi k_\mathrm{B}T(2n+1)$ highlights a T^{-1}-dependence. This implies that the bound states might dominate the condensate at low temperatures and close to the surface. The pairbreaking interface would then create a highly unfavorable environment for the superconducting order, with a peculiar inhomogeneity and temperature-dependence.

Note that the above equations make it easy to separate the propagators into either pure condensate and bound-state terms, or bulk and surface terms. The surface propagators are used to study the density of states in Sec 4.3, and the energetics of the bound states in Sec. 4.4.

4.3 Density of states: zero-energy states and Tomasch-oscillations

This section presents the density of states in a superconductor with a tunneling barrier towards a normal metal, with transmission probability $\mathcal{D} = |t|^2$. A superconducting interface with maximal pairbreaking is assumed, i.e. when incoming and outgoing quasiparticles see an order parameter with the same magnitude but with different signs. Section 4.1 discussed how this occurs e.g. at a d-wave interface aligned with the nodes (a [110] surface), or at a spin-active interface of an s-wave superconductor. It is shown that this sign-change leads to zero-energy states, and to certain interference effects in the continuum.

Appendix E.4.1 derives the midgap part of the DOS, i.e. $\epsilon^2 < |\Delta(\boldsymbol{p}_{\mathrm{F}})|^2$, where $\epsilon \equiv \varepsilon - \boldsymbol{v}_{\mathrm{F}} \cdot \boldsymbol{p}_{\mathrm{s}}$ is the Doppler-shifted real energy. The sugbgap spectrum is found to be described by a Lorentzian centered at $\varepsilon_0 = \boldsymbol{v}_{\mathrm{F}} \cdot \boldsymbol{p}_{\mathrm{s}}$, and with width $\Gamma = \mathcal{D}|\Delta|/2\sqrt{1-\mathcal{D}}$

$$\frac{N(\boldsymbol{p}_{\mathrm{F}}, y; \epsilon < |\Delta(\boldsymbol{p}_{\mathrm{F}})|)}{2N_{\mathrm{F}}} = \frac{|\Delta|}{2} \frac{(2-\mathcal{D})}{\sqrt{1-\mathcal{D}}} \frac{\Gamma}{(\epsilon^2 + \Gamma^2)} e^{-y/\xi}, \tag{4.7}$$

$$\xi \equiv \frac{\hbar v_{\mathrm{F}} |\sin\theta_{\mathrm{F}}|}{2\sqrt{|\Delta(\boldsymbol{p}_{\mathrm{F}})|^2 - \epsilon^2}}, \tag{4.8}$$

which is truly a surface term as it decays exponentially with distance y from the interface. Note that App. E.4.1 showed that for complete transparency $\mathcal{D} \to 1$, the spectrum reduces to the normal-state DOS with a similar spatial decay, and for complete reflection $\mathcal{D} \to 0$, the density of states is described by a Dirac delta-distribution $N \propto \delta(\varepsilon - \boldsymbol{v}_{\mathrm{F}} \cdot \boldsymbol{p}_{\mathrm{s}})$. The momentum-resolved DOS in Eq. (4.7) is illustrated in Fig. 4.2 (a), where it is shown how finite transmission broadens the spectrum. In real systems, the distribution is typically broadened further by disorder or fluctuations, as briefly mentioned in paper IV.

Appendix E.4.2 derives the continuum-part of the spectrum, i.e. $\epsilon^2 > |\Delta(\boldsymbol{p}_{\mathrm{F}})|^2$,

$$\begin{aligned}\frac{N(\boldsymbol{p}_{\mathrm{F}}, y; \epsilon > |\Delta(\boldsymbol{p}_{\mathrm{F}})|)}{2N_{\mathrm{F}}} &= \frac{\epsilon}{\sqrt{\epsilon^2 - |\Delta(\boldsymbol{p}_{\mathrm{F}})|^2}} \qquad (4.9)\\ &\quad - \frac{(2-\mathcal{D})|\Delta(\boldsymbol{p}_{\mathrm{F}})|^2 \cos(y/\zeta)}{\sqrt{\epsilon^2 - |\Delta(\boldsymbol{p}_{\mathrm{F}})|^2}\left[(2-\mathcal{D})\epsilon + \mathcal{D}\sqrt{\epsilon^2 - |\Delta(\boldsymbol{p}_{\mathrm{F}})|^2}\right]},\end{aligned}$$

$$\zeta \equiv \frac{\hbar v_{\mathrm{F}} |\sin\theta_{\mathrm{F}}|}{2\sqrt{\epsilon^2 - |\Delta(\boldsymbol{p}_{\mathrm{F}})|^2}}, \tag{4.10}$$

which is the usual bulk DOS (the first term), modified by oscillations known as Tomasch-oscillations [137–143]. The latter correspond to quantized energies of degenerate states, generally arising due to the interference of quasiparticles that scatter at order-parameter inhomogeneities (in this case corresponding to the interface). These oscillations are illustrated in Fig. 4.2 (a).

In the absence of superflow, the Lorentzian is centered at zero energy, and the peak is populated even at zero temperature, leading to quasiparticle excitations with a paramagnetic response [64], as discussed in Ch. 3. Just as in the bulk case, the superflow directly acts as a Doppler shift that moves the peak up or down in energy depending on the sign of $\boldsymbol{v}_{\mathrm{F}} \cdot \boldsymbol{p}_{\mathrm{s}}$. The Doppler shift leads to a splitting of the peak in the momentum-averaged LDOS, see Fig. 4.2 (b). Figure 4.2 (c) shows the spatial dependence of this LDOS in the presence of a surface superflow (the latter which is inhomogeneous and of the form in paper II). Papers III–IV studies this complicated LDOS further. The energetics of the zero-energy states and the Doppler shift will now be studied in Sec. 4.4.

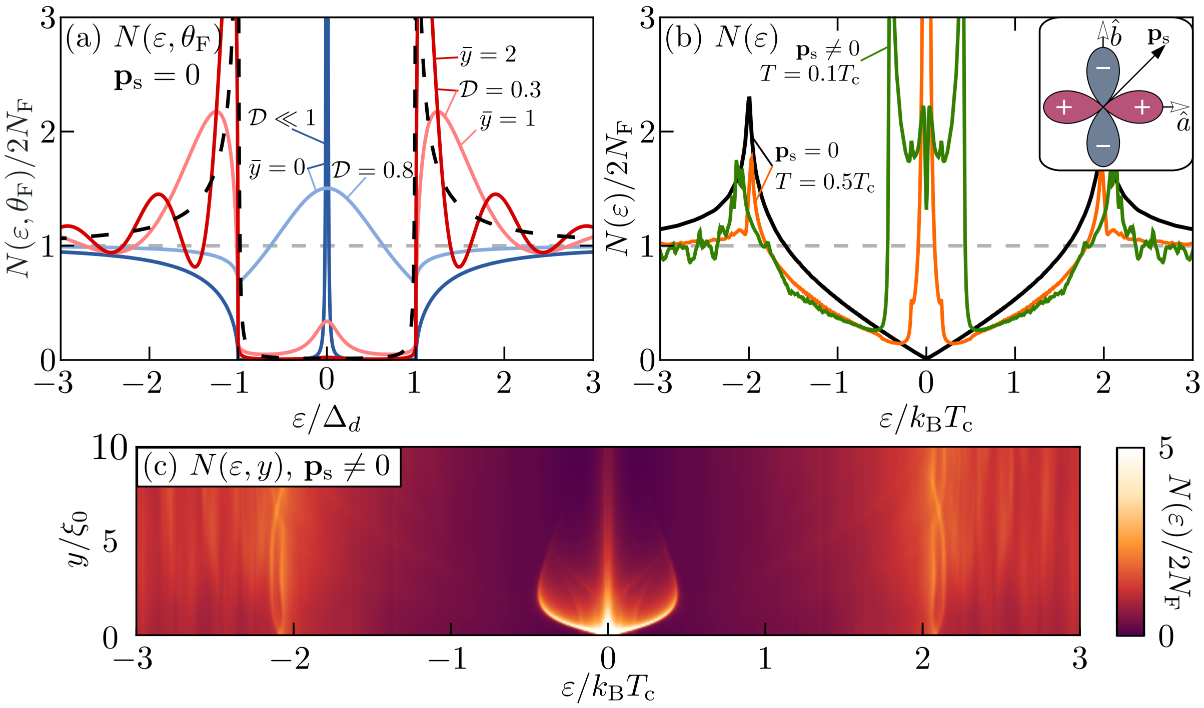

Figure 4.2: *(a) Momentum-resolved DOS at a pairbreaking interface, without superflow. The subgap part is given by the Lorentzian in Eq. (4.7), and the continuum part by Eq. (4.9). Blue curves compare high and low transparencies $\mathcal{D}$, at the surface $\bar{y} \equiv y/\zeta = 0$. Red curves compare the spectra at different coordinates $\bar{y}$ to highlight the Tomasch-oscillations, at transparency $\mathcal{D} = 0.3$. The bulk DOS from Ch. 3 is shown for reference (dashed line). (b) Momentum-averaged LDOS from self-consistent simulations as in papers II–IV, exactly at a vacuum-interface aligned with the nodes of a d-wave superconductor. Note the different energy scale with respect to panel (a). The split of the zero-energy peak is proportional to the magnitude of a superflow $|\boldsymbol{p}_s|$ that runs parallel to the interface. The spectra are relatively sharp since an infinitesimal smearing $\delta \ll \Delta_d$ was used in $z^{\mathrm{R}} = \epsilon + i\delta$ in the Retarded propagator. The spatial dependence (away from the surface) of the shifted LDOS is shown in panel (c).*

4.4 Surface energetics

This section studies the low-temperature free energy at an interface with maximally pairbreaking scattering (i.e. assuming a step-function order parameter with a sign change). Appendix E.4 showed that this leads to zero-energy midgap states, and that a superflow will Doppler shift these states to finite energies. This section presents the energy cost of these midgap states. Furthermore, the superflow gives rise to a magnetic field that costs energy, and the conditions under which the superflow and the Doppler shift are still energetically favorable are investigated.

Based on the Luttinger-Ward free energy $\delta\Omega$ in Eq. (2.69), App. E.5 uses the surface propagators to show that the surface free-energy, denoted $\delta\Omega_{\mathrm{surf}} \equiv \delta\Omega - \delta\Omega_{\mathrm{bulk}}$, can be written per interface sidelength $\mathcal{L}_x$ as

$$\frac{\delta\Omega_{\mathrm{surf}}}{\mathcal{L}_x N_{\mathrm{F}}} = 2\pi k_{\mathrm{B}} T \sum_{\varepsilon_n > 0}^{\Omega_{\mathrm{c}}} \left\langle \frac{\hbar |v_{\mathrm{F}y}|}{2} \left[\ln\left(\frac{|\Delta|^2 - z_p^2}{-z_p^2} \right) - \frac{|\Delta|^2}{|\Delta|^2 - z_p^2} \right] \right\rangle_{\theta_{\mathrm{F}}}, \tag{4.11}$$

which was shown to be real, with $v_{\mathrm{F}y} = v_{\mathrm{F}} \sin\theta_{\mathrm{F}}$ and $z_p = i\varepsilon_n - \boldsymbol{v}_{\mathrm{F}} \cdot \boldsymbol{p}_{\mathrm{s}}$. In the absence of superflow, Eq. (4.11) has a positive summand, giving the cost of midgap states $\delta\Omega^{\mathrm{MGS}} \equiv \delta\Omega^{\mathrm{surf}}(\boldsymbol{p}_{\mathrm{s}} = 0)$. Appendix E.5.2 shows that at zero temperature, this simplifies to

$$\begin{aligned} \frac{\delta\Omega_0^{\mathrm{MGS}}}{\mathcal{L}_x N_{\mathrm{F}}} &= \int_0^\infty d\varepsilon \left\langle \frac{\hbar |v_{\mathrm{F}y}|}{2} \left[\ln\left(\frac{|\Delta|^2 + \varepsilon^2}{\varepsilon^2} \right) - \frac{|\Delta|^2}{|\Delta|^2 + \varepsilon^2} \right] \right\rangle_{\theta_{\mathrm{F}}} && (4.12) \\ &= k_{\mathrm{B}} T_{\mathrm{c}} \xi_0 \frac{\pi^2}{2} \left\langle |\sin\theta_{\mathrm{F}}| \, |\Delta| \right\rangle_{\theta_{\mathrm{F}}}. && (4.13) \end{aligned}$$

In units of the condensation energy, this reduces to the same result for both the d-wave and s-wave superconductors (again, the latter is for a spin-active interface)

$$\frac{\delta\Omega_0^{\mathrm{MGS}}}{\left|\delta\Omega_0^{\mathrm{BCS}}\right|} \approx 4 \frac{\xi_0}{\mathcal{L}_y}, \tag{4.14}$$

where $\mathcal{V} \equiv \int dx \int dy = \mathcal{L}_x \mathcal{L}_y$ is the volume of the superconductor. Hence, at low temperatures, the energy of the surface states is positive and significantly larger than the condensation energy, suppressing superconductivity in a region $\mathcal{L}_y \sim 4\xi_0$ of the interface. For a mesoscopic grain, superconductivity might therefore be completely lost at low temperature due to pairbreaking scattering, which is investigated in paper III. At elevated temperatures, the bound state-contribution is suppressed as T^{-1} (App. E.3.2), and superconductivity is regained. The energy gain due to Doppler shifts by superflow is defined as $\delta\Omega_{\mathrm{Doppler}} \equiv \delta\Omega_{\mathrm{surf}} - \delta\Omega_{\mathrm{MGS}}$, and App. E.5.3 shows that at low temperatures, it becomes negative and linear in the superflow (as shown also in e.g. Ref. [144])

$$\frac{\delta\Omega_0^{\mathrm{Doppler}}}{\mathcal{L}_x N_{\mathrm{F}}} = -\pi k_{\mathrm{B}} T_{\mathrm{c}} \xi_0 v_{\mathrm{F}} p_{\mathrm{s}}. \tag{4.15}$$

4.4.1 Energy balancing

While the superflow kinetic energy is negative and favorable at the surface, the superflow also leads to a magnetic field with a magnetic energy density. To evaluate the full energetics and assess if the superflow is favorable, it is therefore necessary to calculate this energy cost. Since it was shown in Ch. 3 that the superflow is unfavorable in the bulk, the superflow (and hence the current) has to decay away from the surface. This problem was solved exactly analytically in Refs. [66, 67], leading to a phase transition with spontaneous superflow that is translationally invariant along the interface, screened by the magnetic induction over the penetration depth λ_0. The transition temperature was found to be of order $T^* \sim (\xi_0/\lambda_0)T_\mathrm{c}$, and therefore $T^* \ll T_\mathrm{c}$ for extreme type-II superconductors. Here, another scenario is proposed (ad-hoc) where the superflow decays on the length scale set by $\mathcal{L}_y \sim \xi_0$ from Eq. (4.14). In the absence of external fields, consider a current that is translationally invariant along the surface

$$\boldsymbol{j}(y) = j_0 e^{-y/a\xi_0}\hat{\boldsymbol{x}}, \tag{4.16}$$

where $j_0 = j(y=0)$ is determined by the superflow, and $a > 0$ is a constant. In the case of weak screening, the magnetic field due to the current is

$$\boldsymbol{B}(y) = a\xi_0 \frac{4\pi}{c} j_0 \left(e^{-y/a\xi_0} - 1\right), \tag{4.17}$$

(see App. E.5.4 for a derivation) with the magnetic energy

$$\frac{\delta\Omega_0^B}{\mathcal{L}_x\mathcal{L}_y N_\mathrm{F}(k_\mathrm{B}T_\mathrm{c})^2} = \frac{a^2}{2}\kappa_0^{-2}\frac{p_\mathrm{s}^2}{\tilde{p}_0^2}, \tag{4.18}$$

where $\tilde{p}_0 = k_\mathrm{B}T_\mathrm{c}/v_\mathrm{F}$ and $\kappa_0 = \lambda_0/\xi_0$. Hence, for extreme type-II superconductors, the magnetic energy should be negligible compared to the energy gain of Doppler shifts in Eq. (4.15). Combining the results, it appears favorable to have a backflow on a length $a\xi_0 \sim \mathcal{L}_y \ll \lambda_0$. The question arises if a mechanism exists to allow for such a superflow. The model developed in this chapter cannot account for inhomogeneous superflow, however. It is the task of Ch. 5 to provide a generalization with $\boldsymbol{p}_\mathrm{s} = \boldsymbol{p}_\mathrm{s}(\boldsymbol{R})$, such that a proper analysis of the energetics can be made. Using this extended model, Ch. 6 discusses a potential mechanism for a spontaneous superflow with a short decay length. There might be other competing mechanisms that also shift the zero-energy states, which will now be discussed.

4.5 Mechanisms for shifting zero-energy states

Section 4.4 showed that zero-energy states are energetically unfavorable, and that shifting the states to finite energies lowers the energy. Several origins of such a shift have been proposed in the literature over the years. One of the first mechanisms to be proposed is the appearance of an additional subdominant order parameter, e.g. s-wave, such that a new gap Δ_s opens in the peak of the zero-energy states below a finite transition temperature $T_s^* < T_\mathrm{c}$, splitting the states to $\pm\Delta_s$ [65, 145–148]. Another suggested mechanism is an induced ferromagnetic ordering below a transition temperature $T_\mathrm{fm}^* < T_\mathrm{c}$, which breaks the spin-degeneracy of the zero-energy states and splits them through the repulsive Coulomb interaction [149–151]. The spin-degeneracy was highlighted when the spinful Riccati equations were reduced to two identical equations Eq. (3.1) for γ, and two identical equations Eq. (3.2) for $\tilde{\gamma}$. Since this degeneracy was not lifted at any subsequent point, the spectrum derived for the zero-energy states is also spin-degenerate. Furthermore, for the translationally-invariant pairbreaking interfaces considered here, the states are also degenerate with respect to the direction of the surface-parallel momentum (i.e. the coherence trajectories are symmetric under reflection over the surface normal). In contrast to the proposed ferromagnetic ordering, the Doppler shift by a superflow breaks this momentum degeneracy. An instability to spontaneous and translationally invariant superflow has been suggested at infinite interfaces below $T^*/T_\mathrm{c} \sim (\xi_0/\lambda) \ll 1$ [64, 66, 67], or hybridized below $T^*/T_\mathrm{c} \sim (\xi_0/D) < 1$ by the presence of two such interfaces in a slab geometry of thickness D [127, 152–156]. Spontaneous superflow has also been proposed in finite mesoscopic grains of various shapes and for various pairing symmetries [123, 126, 157–160]. In contrast to the translational invariant superflow, the superflow that was first proposed in Ref. [157] and that is studied in this thesis (as well as in Lic. Th. [10]), breaks also translational symmetry, by forming a periodic configuration within a distance $\mathcal{L}_y$ of the interface. It is shown in papers I–II that this translational symmetry breaking is the main effect, in contrast to the time-reversal symmetry breaking that appears as a consequence (highlighted by the fact that the phase transition is derived also for a non-charged particle current). Reference [157] and paper II used self-consistent numeric calculations to show that the inhomogeneous superflow appear below a transition temperature $T^*/T_\mathrm{c} \approx 0.2 \sim (\xi_0/\mathcal{L}_y)$, which for type-II superconductors is much higher than the T^* of the translationally invariant superflow.

Out of all the mechanisms mentioned here, the one that would ultimately be the most favorable for realization in a real material, if any, would depend on the particular material properties. In general, there is a long-standing controversy regarding the experimental verification of spontaneous mechanisms that shift zero-energy states, with some experiments showing a positive signature [9, 161–167], while others report a negative result [168–172]. Ref. [157] and papers I-IV argues that the inhomogeneous superflow might provide a possible explanation of this issue, since it is realized in a peculiar way that in principle makes it difficult to detect, and at the same time seems very competitive due to its relatively high transition temperature. Indeed, it was shown to be very robust against a subdominant order parameter [157], and against various perturbations, e.g. geometric and external magnetic fields, as shown in papers II-IV. This motivates further studies. To treat such an inhomogeneous superflow, however, it is necessary to go beyond the local and translationally invariant model developed in this chapter. It is the topic of Chs. 5 and 6 to provide such a generalization.

4.6 Chapter summary: spontaneous superflow?

The previous chapter Ch. 3 used pure bulk arguments to hint at the possibility of negative and energetically favorable superflow kinetic energy, especially in an environment with a predominantly paramagnetic response. This chapter showed that such an environment exists, namely close to certain interfaces with strong pairbreaking scattering, where an effective sign-change in the order parameter for scattered quasiparticles leads to zero-energy states with a Lorentzian distribution centered at the Fermi energy. As examples, S-V and S-I-N interfaces of unconventional d-wave superconductors were considered (in particular with the interface aligned with the d-wave nodes, i.e. [110]-interfaces), or spin-active interfaces of conventional s-wave superconductors.

The zero-energy states were shown to be bound to the surface, with a T^{-1} temperature-dependent energy cost at low temperatures, several times larger than the condensation energy. The interface thus creates an inhomogeneous and highly unfavorable environment for the superconducting order. Furthermore, it was shown that the presence of a finite superflow Doppler shifts the bound states to finite energies, opening a new gap and lowering the free energy, thus confirming the suspicion presented in Ch. 3 for the bulk system. A mechanisms for translationally invariant superflow has been proposed previously [64, 66, 67], which decays over a distance λ_0 from the interface, resulting in a low transition temperature in type-II superconductors due to unfavorable superflow in the bulk. Another decay profile was proposed ad-hoc, decaying on the length scale $\mathcal{L}_y \sim 4\xi_0$ derived in this chapter, which would in principle have a much higher transition temperature. Such a superflow was indeed found based on self-consistent numeric calculations [157] (see also appended papers and Lic. Th. [10]), and it was discussed in relation to other competing mechanisms, in particular a subdominant order parameter and ferromagnetic ordering. It is the goal of Ch. 5 to develop a linear-response model which can properly take into account the inhomogeneous superflow $\boldsymbol{p}_\mathrm{s} = \boldsymbol{p}_\mathrm{s}(\boldsymbol{R})$ and explain features of the numeric observations. It is found that the model relies on a generalization to a non-local theory, with an inhomogeneous superfluid density tensor caused by the inhomogeneous environment close to the interface. Chapter 6 uses this tensor to minimize the free energy with respect to $\boldsymbol{p}_\mathrm{s}(\boldsymbol{R})$, obtaining the inhomogeneous superflow found numerically in [157], and furthermore, showing that a new class of inhomogeneous superconducting ground states might be possible.

5 Inhomogeneous superflow: non-local linear response

Chapter 4 showed that certain interfaces create an unfavorable environment for the superconducting order, by breaking superconducting pairs into surface bound states, removing favorable condensation energy. A spontaneous superflow that Doppler shifts these states and that decays into the bulk on the coherence-length scale was suggested, but without a proper motivation for a responsible mechanism. The aim of this chapter is to extend the interface-scattering model to properly account for inhomogeneous superflow $\boldsymbol{p}_{\mathrm{s}}(\boldsymbol{R})$ in a non-local but linear response, highlighting a possible mechanism for the superflow.

The chapter starts by introducing the linear-response Riccati equations, which are then symmetrized with respect to the Nambu-space coherence functions, by introducing the pair-propagator-like objects $\gamma_1/(1+\gamma_0\tilde{\gamma}_0)$ and $\tilde{\gamma}_1/(1+\gamma_0\tilde{\gamma}_0)$. The unperturbed solutions (0) are given in Ch. 4 (but with $\boldsymbol{p}_{\mathrm{s}} = 0$), and the first-order corrections (1) are derived. Assuming perfect reflection at the interface, the Riccati equations for these objects are solved, which are shown to depend on correlators $C(\boldsymbol{R}_{\mathrm{s}}, \boldsymbol{R}_{\mathrm{o}})$ that couple a perturbation at source point $\boldsymbol{R}_{\mathrm{s}}$ with an observation point $\boldsymbol{R}_{\mathrm{o}}$. The correlators decay exponentially over a length scale $\kappa^{-1} \propto \xi$, which is a modified coherence length due to the presence of inhomogeneities, in this case the exponential decay of surface bound states. The non-local particle-current response $\boldsymbol{j}(\boldsymbol{R}_{\mathrm{o}}) = \int dR_{\mathrm{s}} \boldsymbol{K}(\boldsymbol{R}_{\mathrm{o}}, \boldsymbol{R}_{\mathrm{s}}) \cdot \boldsymbol{p}_{\mathrm{s}}(\boldsymbol{R}_{\mathrm{s}})$ is derived, which is used in Ch. 6 to obtain the free energy $\Omega = \frac{1}{2} \int dR_{\mathrm{o}} \left[\boldsymbol{p}_{\mathrm{s}}(\boldsymbol{R}_{\mathrm{o}}) \cdot \boldsymbol{j}(\boldsymbol{R}_{\mathrm{o}})\right]$. Both the current and the free energy are given in terms of the non-local superfluid density tensor $\boldsymbol{K}(\boldsymbol{R}_{\mathrm{o}}, \boldsymbol{R}_{\mathrm{s}})$. Features of this complicated high-dimensional object are analyzed, and it is shown that it reduces to the well-known form in bulk. Chapter. 6 does an instability analysis by minimizing the energy with respect to $\boldsymbol{p}_{\mathrm{s}}(\boldsymbol{R})$.

It is noted that variations of the order-parameter amplitude are neglected, since the aim is to use the model for the low-temperature instability analysis. The numeric self-consistent calculations in the appended papers include these amplitude variations, and careful analysis of these results (not shown here) illustrate that the variations ($\delta\Delta/k_{\mathrm{B}}T_{\mathrm{c}} \sim 0.02$) are a percent effect compared to the spontaneous superflow at the instability. This is properly motivated by the fact that for small superflow, and at low temperatures, the current response to $\boldsymbol{p}_{\mathrm{s}}$ is given to leading order by the T^{-1} bound-state term in the propagator (App. E.3.2), and that the gap suppression gives only a small, higher-order, correction [116].

5.1 Linear response Riccati equations

Consider again the Riccati Eqs. (2.34)–(2.35) at the interface in Fig. 2.2, but with $\boldsymbol{p}_\mathrm{s} \to \boldsymbol{p}_\mathrm{s}(\boldsymbol{R})$. For a spin-singlet superconductor, the scalar equations are

$$\begin{aligned}
\left[i\hbar\boldsymbol{v}_\mathrm{F}\cdot\boldsymbol{\nabla}_R + 2\left(z - \boldsymbol{v}_\mathrm{F}\cdot\boldsymbol{p}_\mathrm{s}(\boldsymbol{R})\right)\right]\gamma &= -\gamma\tilde{\Delta}\gamma + \Delta, && (5.1)\\
\left[i\hbar\boldsymbol{v}_\mathrm{F}\cdot\boldsymbol{\nabla}_R - 2\left(z - \boldsymbol{v}_\mathrm{F}\cdot\boldsymbol{p}_\mathrm{s}(\boldsymbol{R})\right)\right]\tilde{\gamma} &= -\tilde{\gamma}\Delta\tilde{\gamma} + \tilde{\Delta}, && (5.2)
\end{aligned}$$

where it is reminded that $\tilde{\Delta}(\boldsymbol{p}_\mathrm{F}) = \Delta(\boldsymbol{p}_\mathrm{F})^* = \Delta(\boldsymbol{p}_\mathrm{F}) = |\Delta|\,\eta(\theta_\mathrm{F})$ in the present gauge (introduced in App. A). The Riccati equations are linearized in $\boldsymbol{p}_\mathrm{s}(\boldsymbol{R})$

$$\begin{aligned}
0 &= \left[i\hbar\boldsymbol{v}_\mathrm{F}\cdot\boldsymbol{\nabla}_R + 2z\right]\gamma_0 + \tilde{\Delta}\gamma_0^2 + \Delta, && (5.3)\\
0 &= \left[i\hbar\boldsymbol{v}_\mathrm{F}\cdot\boldsymbol{\nabla}_R - 2z\right]\tilde{\gamma}_0 + \Delta\tilde{\gamma}_0^2 + \tilde{\Delta}, && (5.4)\\
0 &= \left[i\hbar\boldsymbol{v}_\mathrm{F}\cdot\boldsymbol{\nabla}_R + 2\left(z + \gamma_0\tilde{\Delta}\right)\right]\gamma_1 - 2\boldsymbol{v}_\mathrm{F}\cdot\boldsymbol{p}_\mathrm{s}(\boldsymbol{R})\gamma_0, && (5.5)\\
0 &= \left[i\hbar\boldsymbol{v}_\mathrm{F}\cdot\boldsymbol{\nabla}_R - 2\left(z - \tilde{\gamma}_0\Delta\right)\right]\tilde{\gamma}_1 + 2\boldsymbol{v}_\mathrm{F}\cdot\boldsymbol{p}_\mathrm{s}(\boldsymbol{R})\tilde{\gamma}_0, && (5.6)
\end{aligned}$$

with the coherence functions

$$\begin{aligned}
\gamma &\approx \gamma_0 + \gamma_1, && (5.7)\\
\tilde{\gamma} &\approx \tilde{\gamma}_0 + \tilde{\gamma}_1. && (5.8)
\end{aligned}$$

Here, subscripts 0 refer to quantities unperturbed by $\boldsymbol{p}_\mathrm{s}$, with solutions given in Eqs. (E.14)–(E.15) for $\boldsymbol{p}_\mathrm{s} = 0$ (i.e. with $z_p \to z$), and subscripts 1 are the first-order corrections due to small $\boldsymbol{p}_\mathrm{s}(\boldsymbol{R})$. Similarly, the propagators are expanded as $g = g_0 + g_1$, $f = f_0 + f_1$, $\tilde{g} = \tilde{g}_0 + \tilde{g}_1$, and $\tilde{f} = \tilde{f}_0 + \tilde{f}_1$, where the zeroth-order propagators are given in App. E.3 (again with $\boldsymbol{p}_\mathrm{s} = 0$), and the first order corrections are derived in App. F.1

$$\begin{aligned}
g_1 &= +2i\pi\left(\frac{\gamma_1}{(1+\gamma_0\tilde{\gamma}_0)}\frac{\tilde{\gamma}_0}{(1+\gamma_0\tilde{\gamma}_0)} + \frac{\tilde{\gamma}_1}{(1+\gamma_0\tilde{\gamma}_0)}\frac{\gamma_0}{(1+\gamma_0\tilde{\gamma}_0)}\right), && (5.9)\\
\tilde{g}_1 &= -2i\pi\left(\frac{\gamma_1}{(1+\gamma_0\tilde{\gamma}_0)}\frac{\tilde{\gamma}_0}{(1+\gamma_0\tilde{\gamma}_0)} + \frac{\tilde{\gamma}_1}{(1+\gamma_0\tilde{\gamma}_0)}\frac{\gamma_0}{(1+\gamma_0\tilde{\gamma}_0)}\right), && (5.10)\\
f_1 &= -2i\pi\left(\frac{\gamma_1}{(1+\gamma_0\tilde{\gamma}_0)}\frac{(1+2\gamma_0\tilde{\gamma}_0)}{(1+\gamma_0\tilde{\gamma}_0)} + \frac{\tilde{\gamma}_1}{(1+\gamma_0\tilde{\gamma}_0)}\frac{\gamma_0^2}{(1+\gamma_0\tilde{\gamma}_0)}\right), && (5.11)\\
\tilde{f}_1 &= +2i\pi\left(\frac{\tilde{\gamma}_1}{(1+\gamma_0\tilde{\gamma}_0)}\frac{(1+2\gamma_0\tilde{\gamma}_0)}{(1+\gamma_0\tilde{\gamma}_0)} + \frac{\gamma_1}{(1+\gamma_0\tilde{\gamma}_0)}\frac{\tilde{\gamma}_0^2}{(1+\gamma_0\tilde{\gamma}_0)}\right). && (5.12)
\end{aligned}$$

These propagators will be used to derive the current response in Sec. 5.4. At this point, it would be rather straightforward to derive the solutions to γ_1 and $\tilde{\gamma}_1$ in Eqs. (5.5)-(5.6) (which is done in App. F.2). However, it is noted that the perturbed propagators are proportional to terms $\gamma_1/(1+\gamma_0\tilde{\gamma}_0)$ and $\tilde{\gamma}_1/(1+\gamma_0\tilde{\gamma}_0)$. These quantities look like pair propagators $f/(-2i\pi)$ and $\tilde{f}/(2i\pi)$, and it turns out that solving the Riccati equations for these quantities instead yield more symmetric solutions, which make subsequent calculations and analysis much simpler.

5.2 Symmetrization

Following App. F.3, the Riccati equations for $\gamma_1/(1+\gamma_0\tilde{\gamma}_0)$ and $\tilde{\gamma}_1/(1+\gamma_0\tilde{\gamma}_0)$ are

$$\begin{aligned}
(\boldsymbol{\nabla}_R+\kappa)\,\frac{\gamma_1}{1+\gamma_0\tilde{\gamma}_0}(\boldsymbol{p}_{\mathrm{F}},\boldsymbol{R}_{\mathrm{o}};z) &= -\frac{2i}{\hbar v_{\mathrm{F}}}\boldsymbol{v}_{\mathrm{F}}\cdot\boldsymbol{p}_{\mathrm{s}}\frac{\gamma_0}{1+\gamma_0\tilde{\gamma}_0}(\boldsymbol{p}_{\mathrm{F}},\boldsymbol{R}_{\mathrm{o}};z), \qquad (5.13)\\
(\boldsymbol{\nabla}_R-\kappa)\,\frac{\tilde{\gamma}_1}{1+\gamma_0\tilde{\gamma}_0}(\boldsymbol{p}_{\mathrm{F}},\boldsymbol{R}_{\mathrm{o}};z) &= +\frac{2i}{\hbar v_{\mathrm{F}}}\boldsymbol{v}_{\mathrm{F}}\cdot\boldsymbol{p}_{\mathrm{s}}\frac{\tilde{\gamma}_0}{1+\gamma_0\tilde{\gamma}_0}(\boldsymbol{p}_{\mathrm{F}},\boldsymbol{R}_{\mathrm{o}};z), \qquad (5.14)\\
\kappa(\boldsymbol{p}_{\mathrm{F}},\boldsymbol{R}_{\mathrm{o}};z) &\equiv \frac{i}{\hbar v_{\mathrm{F}}}\left(2z+\gamma_0\tilde{\Delta}(\boldsymbol{p}_{\mathrm{F}})-\tilde{\gamma}_0\Delta(\boldsymbol{p}_{\mathrm{F}})\right). \qquad (5.15)
\end{aligned}$$

As a side note, the term $(\gamma_0\tilde{\Delta}-\tilde{\gamma}_0\Delta)$ in κ is the momentum-resolved kernel $\mathcal{I}$ in Eq. (2.72), which captures the main inhomogeneous contribution to the Eilenberger free energy. In polar coordinates, let s be the coordinate along the trajectory defined by the Fermi momentum $\boldsymbol{p}_{\mathrm{F}}$, with $s=0$ denoting the interface between regions 1 and 2 in Fig. 2.2. Assuming perfect reflection at the interface, the solutions to Eqs. (5.13) and (5.14) are derived in App. F.4

$$\begin{aligned}
\frac{\gamma_1}{1+\gamma_0\tilde{\gamma}_0}(\boldsymbol{p}_{\mathrm{F}},s_{\mathrm{o}};z) &= -\frac{2i}{\hbar v_{\mathrm{F}}}\int_{-\infty}^{s_{\mathrm{o}}}ds\left[C(s,s_{\mathrm{o}})\boldsymbol{v}_{\mathrm{F}}\cdot\boldsymbol{p}_{\mathrm{s}}\frac{\gamma_0}{1+\gamma_0\tilde{\gamma}_0}\right](\boldsymbol{p}'_{\mathrm{F}},s;z), \qquad (5.16)\\
&= -\frac{2i}{\hbar v_{\mathrm{F}}}\int_{-\infty}^{s_{\mathrm{o}}}ds\left[C(s,s_{\mathrm{o}})\boldsymbol{v}_{\mathrm{F}}\cdot\boldsymbol{p}_{\mathrm{s}}\frac{f_0}{-2i\pi}\right](\boldsymbol{p}'_{\mathrm{F}},s;z), \qquad (5.17)\\
\frac{\tilde{\gamma}_1}{1+\gamma_0\tilde{\gamma}_0}(\boldsymbol{p}_{\mathrm{F}},s_{\mathrm{o}};z) &= -\frac{2i}{\hbar v_{\mathrm{F}}}\int_{s_{\mathrm{o}}}^{\infty}ds\left[C(s_{\mathrm{o}},s)\boldsymbol{v}_{\mathrm{F}}\cdot\boldsymbol{p}_{\mathrm{s}}\frac{\tilde{\gamma}_0}{1+\gamma_0\tilde{\gamma}_0}\right](\boldsymbol{p}'_{\mathrm{F}},s;z), \qquad (5.18)\\
&= -\frac{2i}{\hbar v_{\mathrm{F}}}\int_{s_{\mathrm{o}}}^{\infty}ds\left[C(s_{\mathrm{o}},s)\boldsymbol{v}_{\mathrm{F}}\cdot\boldsymbol{p}_{\mathrm{s}}\frac{\tilde{f}_0}{2i\pi}\right](\boldsymbol{p}'_{\mathrm{F}},s;z), \qquad (5.19)\\
C(s,s_{\mathrm{o}}) &\equiv \exp\left(-\int_{s}^{s_{\mathrm{o}}}d\rho\kappa(\rho)\right), \qquad (5.20)
\end{aligned}$$

where $\boldsymbol{p}'_{\mathrm{F}}$ defines the momentum direction in the source point s, and the ds-integrals sum up the contribution from all perturbations $\boldsymbol{p}_{\mathrm{s}}(s)$ along the trajectory, from $s=\mp\infty$ to the observation point s_{o} for normal and tilde coherence functions, respectively. The momentum direction $\boldsymbol{p}'_{\mathrm{F}}$ is therefore different for these trajectory integrals, with a specular momentum flip between $s<0$ and $s>0$, potentially leading to different values of $\Delta(\boldsymbol{p}'_{\mathrm{F}})$ (e.g. a sign change for the maximally pairbreaking interface). This is illustrated in Figs. 5.1 (a) and (b), for two opposite directions of $\boldsymbol{v}_{\mathrm{F}}$. The correlator $C(s,s_{\mathrm{o}})$ gives the weight of pair-correlations between s and s_{o}, with an exponential decay over the length-scale determined by κ^{-1}. This is described by the integral over the running point ρ from s to s_{o}. Appendix F.5 derives the following expression for κ

$$\kappa(\rho) \quad = \quad \xi^{-1}\frac{2i\Omega+(z-i\Omega)S}{2i\Omega+(z-i\Omega)S-(z-i\Omega)Se^{-|\rho|/\xi}}, \qquad (5.21)$$

$$\kappa^{-1} \xrightarrow[S\to 0]{} \xi \equiv \frac{\hbar v_{\mathrm{F}}}{2\Omega}, \tag{5.22}$$

$$\kappa^{-1} \xrightarrow[\rho\to\infty]{} \xi, \tag{5.23}$$

$$\kappa^{-1} \xrightarrow[\rho\to 0]{S\to 2} \zeta \equiv \frac{\hbar v_{\mathrm{F}}}{2\varepsilon_n}, \tag{5.24}$$

which gives κ^{-1} the interpretation of a coherence length modified by proximity to surface bound states, and where the boundary term S was analyzed in App. E.2. κ^{-1} reduces to the bulk coherence length far away from the interface ($S = 0$ or $\rho \to \infty$). At a pairbreaking interface ($S = 2$), the correlation length is determined by the bound states, with the Matsubara energy $\varepsilon_n \equiv \pi k_{\mathrm{B}} T(2n+1)$.

Explicit expressions for the correlators will now be presented, which will be used to obtain the current response.

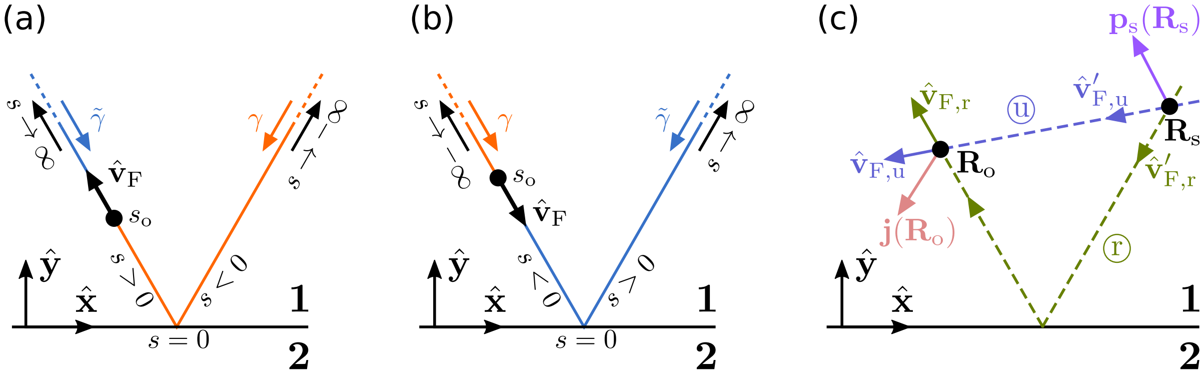

Figure 5.1: *(a), (b) The Fermi momentum determines the quasiclassical trajectories. The coordinate* s_o *is an observation point somewhere on the trajectory, and* s *denotes a source point along the trajectory with a perturbation* $\boldsymbol{p}_s(s)$*, with* $s = 0$ *at the interface. The correlator* $C(s, s_o)$ *gives the weight of pair-correlations between* s *and* s_o*, with an exponential decay over the length-scale given by* κ^{-1}*. (c) A superflow at point* $\boldsymbol{R}_s$ *give rise to a current response at observation point* $\boldsymbol{R}_o$*, due to non-local correlations along unreflected* ⓤ *and reflected* ⓡ *trajectories. The correlations are modified by the presence of surface bound states.*

5.3 Correlators

Since the trajectory between the source point s and the observation point s_o might reflect at the interface (see Figs. 5.1 or F.1), it is necessary to distinguish $d\rho$ integrals that cross or do not cross the interface, corresponding to unreflected ⓤ and reflected ⓡ trajectories. The trajectory that undergoes reflection is divided into an incoming trajectory from $\rho = s$ to $\rho = 0$ (at the interface) with momentum $\boldsymbol{p}'_\mathrm{F}$, and an outgoing trajectory from $\rho = 0$ to $\rho = s_\mathrm{o}$ with specularly reflected momentum $\underline{\boldsymbol{p}}'_\mathrm{F} = (p_{\mathrm{F},x}, -p_{\mathrm{F},y})$. Assuming perfect reflection, App. F.5 solves the $d\rho$-integrals in the correlator in Eq. (5.20) for these cases, yielding

$$
\begin{aligned}
C_{\textcircled{u}}(s_1, s_2) &= \frac{2i\Omega + (z - i\Omega)S - (z - i\Omega)Se^{-|s_<|/\xi}}{2i\Omega + (z - i\Omega)S - (z - i\Omega)Se^{-|s_>|/\xi}} e^{-|s_1 - s_2|/\xi}, \qquad (5.25)\\
C_{\textcircled{r}}(s_1, s_2) &= \frac{2i\Omega e^{-|s_1|/\xi}}{2i\Omega + (z - i\Omega)S - (z - i\Omega)Se^{-|s_1|/\xi}} (\boldsymbol{p}_{\mathrm{F},1}, s_1)\\
&\quad \times \frac{2i\Omega e^{-|s_2|/\xi}}{2i\Omega + (z - i\Omega)S - (z - i\Omega)Se^{-|s_2|/\xi}} (\boldsymbol{p}_{\mathrm{F},2}, s_2), \qquad (5.26)
\end{aligned}
$$

where $s_>$ and $s_<$ denote the coordinate closest and furthest from the interface along the trajectory, respectively,

$$
\begin{aligned}
s_< &= \min\left(|s_1|, |s_2|\right), \qquad (5.27)\\
s_> &= \max\left(|s_1|, |s_2|\right). \qquad (5.28)
\end{aligned}
$$

The correlator in Eq. (5.25) is the usual superconducting coherence factor in bulk, but modified by the presence of bound states. This is seen by letting both $s_{1,2}$ lie far from the interface (or $S \to 0$)

$$
C^{\mathrm{bulk}}(s_1, s_2) = e^{-|s_1 - s_2|/\xi}. \qquad (5.29)
$$

The correlator in Eq. (5.26) is a pure bound-state correlator, which decays exponentially when either of the two points are far from the interface. At a maximally pairbreaking interface ($S = 2$), the correlators can be re-written

$$
\begin{aligned}
C^{\mathrm{pb}}_{\textcircled{u}}(s_1, s_2) &= \frac{z - (z - i\Omega)e^{-|s_<|/\xi}}{z - (z - i\Omega)e^{-|s_>|/\xi}} e^{-|s_1 - s_2|/\xi}, \qquad (5.30)\\
C^{\mathrm{pb}}_{\textcircled{r}}(s_1, s_2) &= \left[\frac{i\Omega e^{-|s_1|/\xi}}{z - (z - i\Omega)e^{-|s_1|/\xi}}\right] (\boldsymbol{p}_{\mathrm{F},1}) \left[\frac{i\Omega e^{-|s_2|/\xi}}{z - (z - i\Omega)e^{-|s_2|/\xi}}\right] (\boldsymbol{p}_{\mathrm{F},2}) \qquad (5.31)
\end{aligned}
$$

The correlators will now be used to derive the current response.

5.4 Current response

Defining the particle-current density Eq. (2.66), i.e. without charge e, and expanding in $\boldsymbol{p}_\mathrm{s}$ yields

$$\begin{aligned} \boldsymbol{j}(\boldsymbol{R}_\mathrm{o}) - \boldsymbol{j}_0(\boldsymbol{R}_\mathrm{o}) &= \delta\boldsymbol{j}(\boldsymbol{R}_\mathrm{o}) = \boldsymbol{j}_1(\boldsymbol{R}_\mathrm{o}) + \mathcal{O}(\boldsymbol{p}_\mathrm{s}^2), && (5.32) \\ \boldsymbol{j}_1(\boldsymbol{R}_\mathrm{o}) &= 4k_\mathrm{B}TN_\mathrm{F}v_\mathrm{F}\left\langle \sum_{\varepsilon_n>0}^{\Omega_\mathrm{c}} \hat{\boldsymbol{v}}_\mathrm{F}\,\mathrm{Re}\left\{g_1(\boldsymbol{p}_\mathrm{F}, \boldsymbol{R}_\mathrm{o}; z)\right\}\right\rangle_{\theta_\mathrm{F}}, && (5.33) \end{aligned}$$

where the unperturbed current $\boldsymbol{j}_0 = 0$ due to there being no current-response without superflow (see e.g. App. D.5). Inserting g_1 from Eq. (5.9) and the coherence functions from Eqs. (5.16)–(5.20), the current response is

$$\begin{aligned} \boldsymbol{j}_1(\boldsymbol{R}_\mathrm{o}) &= 4k_\mathrm{B}TN_\mathrm{F}v_\mathrm{F}\sum_{\varepsilon_n>0}^{\Omega_\mathrm{c}}\mathrm{Re}\left\langle \hat{\boldsymbol{v}}_\mathrm{F}2i\pi\frac{-2i}{\hbar v_\mathrm{F}}\left[\int_{-\infty}^{s_\mathrm{o}} ds I_1 + \int_{s_\mathrm{o}}^{\infty} ds I_2\right]\boldsymbol{v}'_\mathrm{F}\cdot\boldsymbol{p}_\mathrm{s}(s)\right\rangle_{\theta_\mathrm{F}}, \\ &= 16\pi k_\mathrm{B}TN_\mathrm{F}\frac{v_\mathrm{F}}{\hbar}\sum_{\varepsilon_n>0}^{\Omega_\mathrm{c}}\mathrm{Re}\left\langle \hat{\boldsymbol{v}}_\mathrm{F}\left[\int_{-\infty}^{s_\mathrm{o}} ds I_1 + \int_{s_\mathrm{o}}^{\infty} ds I_2\right]\hat{\boldsymbol{v}}'_\mathrm{F}\cdot\boldsymbol{p}_\mathrm{s}(s)\right\rangle_{\theta_\mathrm{F}}, && (5.34) \\ I_1 &= \left(\frac{\tilde{\gamma}_0}{1+\gamma_0\tilde{\gamma}_0}(\boldsymbol{p}_\mathrm{F}, s_\mathrm{o})\right)C(s, s_\mathrm{o})\left(\frac{\gamma_0}{1+\gamma_0\tilde{\gamma}_0}(\boldsymbol{p}'_\mathrm{F}, s)\right), && (5.35) \\ &= \frac{\tilde{f}_0(\boldsymbol{p}_\mathrm{F}, s_\mathrm{o})}{2i\pi}C(s, s_\mathrm{o})\frac{f_0(\boldsymbol{p}'_\mathrm{F}, s)}{-2i\pi}, && (5.36) \\ I_2 &= \left(\frac{\gamma_0}{1+\gamma_0\tilde{\gamma}_0}(\boldsymbol{p}_\mathrm{F}, s_\mathrm{o})\right)C(s_\mathrm{o}, s)\left(\frac{\tilde{\gamma}_0}{1+\gamma_0\tilde{\gamma}_0}(\boldsymbol{p}'_\mathrm{F}, s)\right), && (5.37) \\ &= \frac{f_0(\boldsymbol{p}_\mathrm{F}, s_\mathrm{o})}{-2i\pi}C(s_\mathrm{o}, s)\frac{\tilde{f}_0(\boldsymbol{p}'_\mathrm{F}, s)}{2i\pi}. && (5.38) \end{aligned}$$

The unperturbed pair-propagators from Eqs. (E.51) and (E.52) can be re-written

$$\begin{aligned} \frac{f_0}{-2i\pi} &= -\left(\frac{\Delta}{2i\Omega}\right)\frac{2i\Omega + (z-i\Omega)S - (z+i\Omega\,\mathrm{sgn}\left[\hat{\boldsymbol{v}}_{\mathrm{F}y}(s)\right])\,Se^{-|s|/\xi}}{2i\Omega + (z-i\Omega)S} && (5.39) \\ &\xrightarrow[S\to 2]{} -\left(\frac{\Delta}{2i\Omega}\right)\frac{z - (z+i\Omega\,\mathrm{sgn}\left[\hat{\boldsymbol{v}}_{\mathrm{F}y}(s)\right])\,e^{-|s|/\xi}}{z}, && (5.40) \\ \frac{\tilde{f}_0}{2i\pi} &= +\left(\frac{\Delta}{2i\Omega}\right)\frac{2i\Omega + (z-i\Omega)S - (z-i\Omega\,\mathrm{sgn}\left[\hat{\boldsymbol{v}}_{\mathrm{F}y}(s)\right])\,Se^{-|s|/\xi}}{2i\Omega + (z-i\Omega)S} && (5.41) \\ &\xrightarrow[S\to 2]{} +\left(\frac{\Delta}{2i\Omega}\right)\frac{z - (z-i\Omega\,\mathrm{sgn}\left[\hat{\boldsymbol{v}}_{\mathrm{F}y}(s)\right])\,e^{-|s|/\xi}}{z}. && (5.42) \end{aligned}$$

Multiplying these propagators with the correlators give multiple cancellations of terms, reducing the integrands I_1 and I_2 to very simple continuum and bound-state forms, as will be seen below. It is noted that for a given direction $\hat{\boldsymbol{v}}_\mathrm{F}(\boldsymbol{p}_\mathrm{F})$, one of $I_{1,2}$ describes an integral over a reflected part of a trajectory, and the other over an unreflected part of a trajectory (compare panels (a) and (b) of Fig. 5.1). The ds-integrals are therefore split up just like the $d\rho$-integrals into trajectories where s_o and s lie on the same respectively the opposite sides of the interface (the point $s = 0$). The resulting integrals are recombined into continuum-like parts (the unreflected trajectories) and bound-state-like parts (the reflected trajectories). Below, ⓤ denotes ds-integrals where s_o and s lie on the same side, and ⓡ on the opposite sides, and with $A \equiv 16\pi k_\mathrm{B} T N_\mathrm{F} v_\mathrm{F}/\hbar$,

$$\begin{aligned}
\boldsymbol{j}_1(\boldsymbol{R}_\mathrm{o}) &= A \sum_{\varepsilon_n>0}^{\Omega_\mathrm{c}} \mathrm{Re} \int_0^\pi \frac{d\theta_\mathrm{F}}{2\pi} \hat{\boldsymbol{v}}_\mathrm{F} \left[\int_{-\infty}^{s_\mathrm{o}} ds I_1^{\textcircled{u}} + \int_{s_\mathrm{o}}^{0} ds I_2^{\textcircled{u}} + \int_0^\infty ds I_2^{\textcircled{r}} \right] \hat{\boldsymbol{v}}'_\mathrm{F} \cdot \boldsymbol{p}_\mathrm{s}(s) \\
& \quad A \sum_{\varepsilon_n>0}^{\Omega_\mathrm{c}} \mathrm{Re} \int_\pi^{2\pi} \frac{d\theta_\mathrm{F}}{2\pi} \hat{\boldsymbol{v}}_\mathrm{F} \left[\int_{-\infty}^{0} ds I_1^{\textcircled{r}} + \int_{0}^{s_\mathrm{o}} ds I_1^{\textcircled{u}} + \int_{s_\mathrm{o}}^\infty ds I_2^{\textcircled{u}} \right] \hat{\boldsymbol{v}}'_\mathrm{F} \cdot \boldsymbol{p}_\mathrm{s}(s) \\
&\propto 16\pi k_\mathrm{B} T N_\mathrm{F} \frac{v_\mathrm{F}}{\hbar} \sum_{\varepsilon_n>0}^{\Omega_\mathrm{c}} \mathrm{Re} \left\langle \hat{\boldsymbol{v}}_\mathrm{F} \int ds \left[I_{\textcircled{u}} + I_{\textcircled{r}} \right] \hat{\boldsymbol{v}}'_\mathrm{F} \cdot \boldsymbol{p}_\mathrm{s}(s) \right\rangle_{\theta_\mathrm{F}}, \qquad (5.43) \\
I_{\textcircled{u}} &= \left(\frac{\Delta}{2\Omega} \right)^2 e^{-|s_\mathrm{o}-s|/\xi} \left[1 - \frac{(z - i\Omega) S e^{-|s_<|/\xi}}{2i\Omega + (z - i\Omega)S} \right] \left[1 - \frac{(z + i\Omega) S e^{-|s_<|/\xi}}{2i\Omega + (z - i\Omega)S} \right] \qquad (5.44) \\
I_{\textcircled{u}}^{\mathrm{pb}} &= \left(\frac{\Delta}{2\Omega} \right)^2 e^{-|s_\mathrm{o}-s|/\xi} \left[1 - \left(1 - \frac{i\Omega}{z} \right) e^{-|s_<|/\xi} \right] \left[1 - \left(1 + \frac{i\Omega}{z} \right) e^{-|s_<|/\xi} \right] \qquad (5.45) \\
I_{\textcircled{r}} &= - \left[\frac{e^{-|s_\mathrm{o}|/\xi} \Delta}{2i\Omega + (z - i\Omega)S} \right] (\hat{\boldsymbol{v}}_\mathrm{F}, s_\mathrm{o}) \left[\frac{e^{-|s|/\xi} \Delta}{2i\Omega + (z - i\Omega)S} \right] (\hat{\boldsymbol{v}}'_\mathrm{F}, s) \qquad (5.46) \\
I_{\textcircled{r}}^{\mathrm{pb}} &= \left(\frac{\Delta}{2z} \right)^2 e^{-(|s_\mathrm{o}| + |s|)/\xi}, \qquad (5.47)
\end{aligned}$$

where (pb) means a pairbreaking interface ($S \to 2$). Here, the unreflected integrand $I_{\textcircled{u}}$ is the bulk coherence factor $(\Delta/2\Omega)^2 e^{-|s_\mathrm{o}-s|/\xi}$ multiplied by the pair-correlations that are modified by the surface bound states. The reflected integrand $I_{\textcircled{r}}$ is a pure bound-state term. The current can be written in terms of a response kernel, namely the non-local superfluid density tensor $\boldsymbol{K}$,

$$\begin{aligned}
\boldsymbol{j}(\boldsymbol{R}_\mathrm{o}) &= \int ds \boldsymbol{K}(\hat{\boldsymbol{v}}_\mathrm{F}, s_\mathrm{o}; \hat{\boldsymbol{v}}'_\mathrm{F}, s) \cdot \boldsymbol{p}_\mathrm{s}(s), \qquad (5.48) \\
\boldsymbol{K}(\hat{\boldsymbol{v}}_\mathrm{F}, s_\mathrm{o}; \hat{\boldsymbol{v}}'_\mathrm{F}, s) &\propto 16\pi k_\mathrm{B} T N_\mathrm{F} \frac{v_\mathrm{F}}{\hbar} \mathrm{Re} \sum_{\varepsilon_n>0}^{\Omega_\mathrm{c}} \left\langle \hat{\boldsymbol{v}}_\mathrm{F} \left[I_{\textcircled{u}} + I_{\textcircled{r}} \right] \hat{\boldsymbol{v}}'_\mathrm{F} \right\rangle_{\theta_\mathrm{F}}, \qquad (5.49)
\end{aligned}$$

where the dot product is with respect to the $\hat{\boldsymbol{v}}'_\mathrm{F}$ vector. To analyze the superfluid density tensor, it is convenient to introduce a coordinate transformation to cartesian coordinates $\langle \int ds \rangle_{\theta_\mathrm{F}} \to \int dR_\mathrm{s}$.

5.5 Cartesian coordinate transformation

In this section, a coordinate transformation to cartesian coordinates is introduced. In two dimensions, consider the infinitesimal variations ds and $d\theta_\mathrm{F} = |s_\mathrm{o} - s| dA$, which spans the Fermi surface element

$$\frac{d\theta_\mathrm{F}}{2\pi} ds = \frac{dx' dy'}{2\pi\,|s_\mathrm{o} - s|} = \frac{d^2 R_\mathrm{s}}{2\pi \Delta R}, \tag{5.50}$$

as illustrated in Fig. 5.2 (a), where ΔR is the distance between $\boldsymbol{R}_\mathrm{o}$ and $\boldsymbol{R}_\mathrm{s}$ along the trajectory, and the factor 2π is the normalization factor from the $2D$ Fermi-surface average $\langle \ldots \rangle_{\theta_\mathrm{F}} = \int [\ldots] d\theta_\mathrm{F}/2\pi$. It is noted that there are two possible ways to connect $\boldsymbol{R}_\mathrm{o}$ and $\boldsymbol{R}_\mathrm{s}$, namely through a reflected and an unreflected trajectory, see Fig. 5.2 (b). Table 5.1 summarizes the coordinate transformations between polar and cartesian coordinates, for the unreflected and reflected trajectories. Upon transforming to cartesian coordinates, both these trajectories have to be taken into account, which is done by splitting the integrand in $\boldsymbol{j}$ into unreflected ⓤ and reflected ⓡ parts. The i-component (e.g. $i \in \{x, y\}$) of the particle-current response $\boldsymbol{j}_1$ is written

$$j_i(\boldsymbol{R}_\mathrm{o}) = \int d^2 R_\mathrm{s} \hbar^{-2} K_{ij}(\boldsymbol{R}_\mathrm{o}, \boldsymbol{R}_\mathrm{s}) p_{\mathrm{s},j}(\boldsymbol{R}_\mathrm{s}), \tag{5.51}$$

$$\begin{aligned} K_{ij}(\boldsymbol{R}_\mathrm{o}, \boldsymbol{R}_\mathrm{s}) = {} & 16\pi k_\mathrm{B} T N_\mathrm{F} \hbar v_\mathrm{F} \,\mathrm{Re} \sum_{\epsilon_n > 0}^{\Omega_\mathrm{c}} \sum_{\textcircled{u},\textcircled{r}} \hat{k}_i \left[\frac{\tilde{f}_0(\boldsymbol{R}_\mathrm{o}, \hat{k})}{2i\pi} \frac{C(\boldsymbol{R}_\mathrm{s}, \boldsymbol{R}_\mathrm{o})}{2\pi\Delta R} \frac{f_0(\boldsymbol{R}_\mathrm{s}, \hat{k}')}{-2i\pi} \right. \\ & \left. + \frac{f_0(\boldsymbol{R}_\mathrm{o}, -\hat{k})}{-2i\pi} \frac{C(\boldsymbol{R}_\mathrm{o}, \boldsymbol{R}_\mathrm{s})}{2\pi\Delta R} \frac{\tilde{f}_0(\boldsymbol{R}_\mathrm{s}, -\hat{k}')}{2i\pi} \right] \hat{k}'_j, \end{aligned} \tag{5.52}$$

$$C(\boldsymbol{R}_\mathrm{s}, \boldsymbol{R}_\mathrm{o}) = \exp\left(- \int_{\boldsymbol{R}_\mathrm{s}}^{\boldsymbol{R}_\mathrm{o}} \kappa(\rho, \hat{\rho}) d\rho \right), \tag{5.53}$$

Note that the current density now has an integrable singularity as $\boldsymbol{R}_\mathrm{s} \to \boldsymbol{R}_\mathrm{o}$, i.e. in the local kernel $\boldsymbol{K}(\boldsymbol{R}_\mathrm{o}, \boldsymbol{R}_\mathrm{s} = \boldsymbol{R}_\mathrm{o}) \equiv \boldsymbol{K}(\boldsymbol{R}_\mathrm{o})$, due to the factor $1/\Delta R$ introduced by the coordinate change. This singularity is problematic in numerics, but can be formally treated, see App. F.6. Similar to the previous section, the kernel can be greatly simplified assuming the same order parameter structure for incoming and outgoing momenta.

The structure of this kernel is analyzed at a pairbreaking interface in Sec. 5.6. This is done analytically on a term-by-term basis, rather than plotting the spatial dependence, since the latter is non-trivial due to the high dimensionality of the kernel tensor, as well as the incommensurate correlations caused by the reflected and unreflected trajectories (referring to that they contribute to different momentum directions, and different points $s_>$ and $s_<$). Furthermore, even if this can be illustrated, the summation and integration in the current response might average out whatever features are read out from such plots. As discussed in Sec. 5.6, the most convenient way to illustrate the kernel contribution is by identifying the underlying symmetries and averaging over certain degrees of freedom, as done in Figs. 2 and 3 (b)–(d) in paper I. Still, a few visualizations of the kernel are found in App. G.

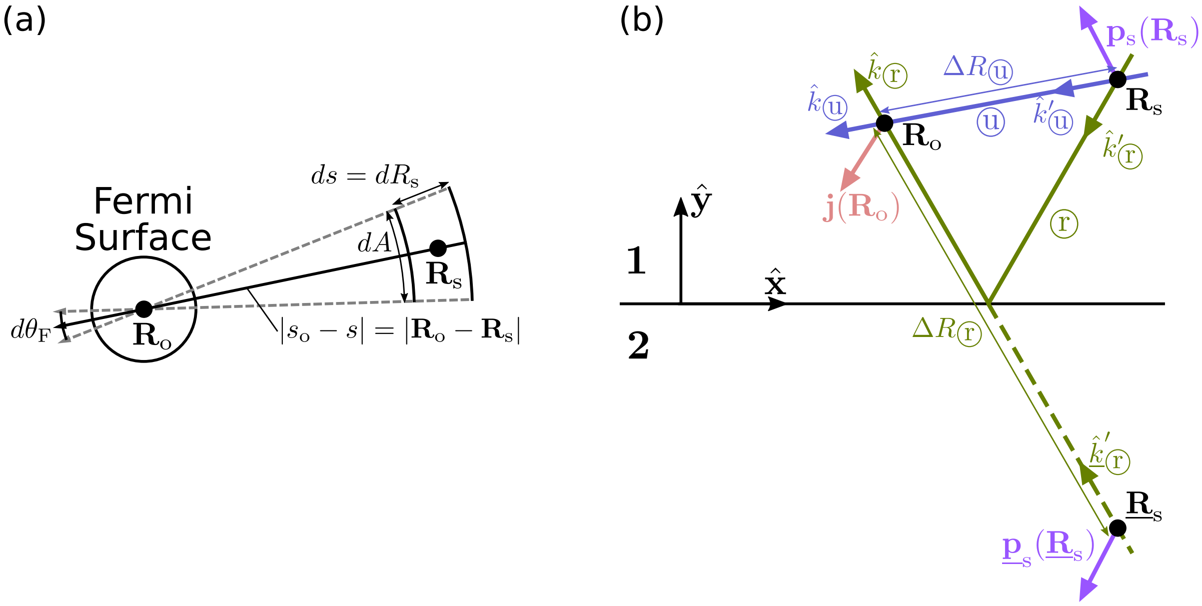

Figure 5.2: *(a) Relation between polar and cartesian Fermi-surface coordinates. (b) Coordinate relations close to a specular interface defined in Fig. 2.2.*

Table 5.1: *Coordinate transformations between polar coordinates (s_o, s, $\hat{k}$) and cartesian coordinates ($\boldsymbol{R}_o$ and $\boldsymbol{R}_s$), where $\boldsymbol{R}_o = (x_o, y_o)$ and $\boldsymbol{R}_s = (x_s, y_s)$. See Fig. 5.2 (b) for an illustration.*

	ⓤ	ⓡ
$\Delta R = \lvert s_\mathrm{o} - s \rvert$	$\sqrt{(x_\mathrm{o} - x_\mathrm{s})^2 + (y_\mathrm{o} - y_\mathrm{s})^2}$	$\sqrt{(x_\mathrm{o} - x_\mathrm{s})^2 + (y_\mathrm{o} + y_\mathrm{s})^2}$
k_x	$(x_\mathrm{o} - x_\mathrm{s})/\Delta R$	$(x_\mathrm{o} - x_\mathrm{s})/\Delta R$
k_y	$(y_\mathrm{o} - y_\mathrm{s})/\Delta R$	$(y_\mathrm{o} + y_\mathrm{s})/\Delta R$
s_o	y_o/k_y	y_o/k_y
s	y_s/k_y	$y_\mathrm{s}/\lvert\underline{k}_y = -y_\mathrm{s}/k_y$

5.6 Non-local superfluid density tensor

This section analyzes the structure of the superfluid density tensor in Eq. (5.52)

$$\boldsymbol{K}(\boldsymbol{R}_{\mathrm{o}},\boldsymbol{R}_{\mathrm{s}}) \;=\; \begin{pmatrix} K_{xx}(\boldsymbol{R}_{\mathrm{o}},\boldsymbol{R}_{\mathrm{s}}) & K_{xy}(\boldsymbol{R}_{\mathrm{o}},\boldsymbol{R}_{\mathrm{s}}) \\ K_{yx}(\boldsymbol{R}_{\mathrm{o}},\boldsymbol{R}_{\mathrm{s}}) & K_{yy}(\boldsymbol{R}_{\mathrm{o}},\boldsymbol{R}_{\mathrm{s}}) \end{pmatrix}. \tag{5.54}$$

At a maximally pairbreaking interface ($S=2$), the unreflected and reflected parts of the kernel take the forms (the reader is reminded that $\Delta = \Delta(\boldsymbol{p}_{\mathrm{F}})$ here)

$$K_{ij}^{\textcircled{r}} \;=\; 4k_{\mathrm{B}}TN_{\mathrm{F}}\hbar v_{\mathrm{F}}\left(\hat{k}_i\hat{\underline{k}}_j\right)\sum_{\varepsilon_n>0}^{\Omega_{\mathrm{c}}}\left(-\frac{\Delta^2}{\varepsilon_n^2}\right)\frac{e^{-(|s_{\mathrm{o}}|+|s|)/\xi}}{(|s_{\mathrm{o}}|+|s|)}, \tag{5.55}$$

$$\begin{aligned} K_{ij}^{\textcircled{u}} \;=\; & 4k_{\mathrm{B}}TN_{\mathrm{F}}\hbar v_{\mathrm{F}}\left(\hat{k}_i\hat{k}_j\right)\sum_{\varepsilon_n>0}^{\Omega_{\mathrm{c}}}\left(+\frac{\Delta^2}{\Omega^2}\right)\frac{e^{-|\boldsymbol{R}_{\mathrm{s}}-\boldsymbol{R}_{\mathrm{o}}|/\xi}}{|\boldsymbol{R}_{\mathrm{s}}-\boldsymbol{R}_{\mathrm{o}}|} \\ & \times\left[\left(1-e^{-|s_<|/\xi}\right)-\frac{\Omega}{\varepsilon_n}e^{-|s_<|/\xi}\right]\left[\left(1-e^{-|s_<|/\xi}\right)+\frac{\Omega}{\varepsilon_n}e^{-|s_<|/\xi}\right], \end{aligned} \tag{5.56}$$

where $\underline{\hat{k}} = (k_x, -k_y)$ from specularity. Note that combining and simplifying these terms is not trivial, since they contribute to different directions and coordinates ($s_<$ and $s_>$) in the current integrand, as illustrated in Fig. 5.2 (b), and in Tab. 5.1. This form of the kernel has the dimensions of energy density. Dividing by $N_{\mathrm{F}}(k_{\mathrm{B}}T_{\mathrm{c}})^2$ therefore gives a dimensionless expression. It is noted that the tensor couples the x and y degrees-of-freedom due to off-diagonal terms K_{xy} and K_{yx}, and that the spatial dependence is generally given by exponential decay from the surface and between source and observation points (both along the trajectory direction), with the decay length set by the coherence length $\xi = \hbar v_{\mathrm{F}}/2\Omega$. For a nodal superconductor, spatial dependence is more complicated, however, due to the basis function in $\Delta = |\Delta|\eta(\theta_{\mathrm{F}})$. The kernel is real and symmetric $K_{ij}(\boldsymbol{R}_1,\boldsymbol{R}_2) = K_{ji}(\boldsymbol{R}_2,\boldsymbol{R}_1)$, with translational invariance along x. The diagonal and off-diagonal components are symmetric and antisymmetric with respect to reflection symmetry $x \to -x$, respectively.

As will be seen in Ch. 6, a negative or positive sign of the kernel determines if the superflow is energetically favorable or not. It will now be shown that there are several terms competing for the overall sign.

Unreflected kernel: competition between continuum and bound-states

Starting with the unreflected kernel $K_{ij}^{\textcircled{u}}$, the term $\hat{k}_i\hat{k}_j$ comes from that $\hat{\boldsymbol{v}}_{\mathrm{F}}(s_0) = \hat{\boldsymbol{v}}'_{\mathrm{F}}(s)$ for this trajectory. It is again noted that the term $(\Delta/\Omega)^2 e^{-|\boldsymbol{R}_{\mathrm{s}}-\boldsymbol{R}_{\mathrm{o}}|/\xi}$ is the bulk coherence factor, but modified by the term $|\boldsymbol{R}_{\mathrm{s}}-\boldsymbol{R}_{\mathrm{o}}|^{-1}$ due to the change of coordinate system. The integrable singularity $\boldsymbol{R}_{\mathrm{s}} \to \boldsymbol{R}_{\mathrm{o}}$ in this term can be put in a local term and treated analytically by transforming back to polar coordinates (App. F.6). The whole expression decays if $\boldsymbol{R}_{\mathrm{s}}$ and $\boldsymbol{R}_{\mathrm{o}}$ are too far separated.

The terms in the brackets are the surface pair-correlators, with a continuum-part Δ/Ω and a bound-state part Δ/ε_n. The continuum term dominates at elevated temperatures and when both points lie far from the surface (when $s_<$ is large). At low temperatures and when one of the coordinates lies close to the surface, the bound-state term dominates. The relative sign-difference between the continuum and bound-state terms reflects that superflow is unfavorable in the bulk and favorable at the interface (diamagnetic versus paramagnetic response). The overall sign of the kernel fwill change depending on which of the two terms dominate.

Reflected kernel: competition between diagonal and off-diagonal terms

The reflected kernel $K_{ij}^{ⓡ}$ is a pure bound-state term proportional to $-\Delta^2/\varepsilon_n^2$, which is large at low temperatures and low energies, and where the minus sign comes from the sign-change in the order parameter between surface-incoming and outgoing trajectories. The kernel decays exponentially if either of the two points are far from the interface. The overall sign of the summand is negative, but the signs of the individual components might be different due to the specularity condition $\underline{\hat{k}}_y = -\hat{k}_y$ and $\underline{\hat{k}}_x = +\hat{k}_x$. For example, for both the reflected and unreflected kernels, the bound-state terms of K_{xx} are negative and add coherently, signifying a paramagnetic response. The continuum K_{xx} term, on the other hand, has a positive sign signifying a diamagnetic response. To determine the overall contribution to the current (and hence the energy), however, the kernel components have to be summed over spatial coordinates. This procedure can be simplified by identifying underlying symmetries and averaging over some spatial degrees of freedom, as illustrated in paper I, and as discussed in Ch. 6.

Local and bulk kernel

The local part of the superfluid density is derived in App. F.6, which gives the well-known bulk linear response in App. F.7 (see Eqs. (34)–(35) in Ref. [116])

$$j_i^{\mathrm{bulk}}(\boldsymbol{R}_{\mathrm{o}}) = K_{ij}^{\mathrm{bulk}}(\boldsymbol{R}_{\mathrm{o}}) p_{\mathrm{s},j}, \tag{5.57}$$

$$K_{ij}^{\mathrm{bulk}}(\boldsymbol{R}_{\mathrm{o}}) = 4\pi k_{\mathrm{B}} T N_{\mathrm{F}} v_{\mathrm{F}}^2 \left\langle (\hat{k}_i \hat{k}_j) \sum_{\varepsilon_n>0}^{\Omega_{\mathrm{c}}} \frac{|\Delta(\boldsymbol{p}_{\mathrm{F}})|^2}{\Omega^3} \right\rangle_{\theta_{\mathrm{F}}}. \tag{5.58}$$

At $T = 0$, the Matsubara sum is turned into an integral as in Eqs. (2.19)–(2.20)

$$\boldsymbol{j}_0^{\mathrm{bulk}}(\boldsymbol{R}_{\mathrm{o}}) = 2N_{\mathrm{F}} v_{\mathrm{F}}^2 \left\langle \int_0^\infty d\epsilon \frac{|\Delta(\boldsymbol{p}_{\mathrm{F}})|^2}{(|\Delta(\boldsymbol{p}_{\mathrm{F}})|^2 + \varepsilon_n^2)^{3/2}} \hat{\boldsymbol{v}}_{\mathrm{F}} \left[\hat{\boldsymbol{v}}_{\mathrm{F}} \cdot \boldsymbol{p}_{\mathrm{s}}\right] \right\rangle_{\theta_{\mathrm{F}}} \tag{5.59}$$

$$= 2N_{\mathrm{F}} v_{\mathrm{F}}^2 \left\langle \hat{\boldsymbol{v}}_{\mathrm{F}} \left[\hat{\boldsymbol{v}}_{\mathrm{F}} \cdot \boldsymbol{p}_{\mathrm{s}}\right] \right\rangle_{\theta_{\mathrm{F}}} \tag{5.60}$$

$$= N_{\mathrm{F}} v_{\mathrm{F}}^2 \boldsymbol{p}_{\mathrm{s}}, \tag{5.61}$$

with $K^{\mathrm{bulk}}(T = 0) = N_{\mathrm{F}} v_{\mathrm{F}}^2 \equiv \rho$, which reproduces the result in App. D.5.

5.7 Chapter summary: mechanism for spontaneous superflow?

This chapter linearized the Riccati equations with respect to an inhomogeneous superflow $\boldsymbol{p}_{\mathrm{s}}(\boldsymbol{R})$. The equations were solved in the non-local regime (still neglecting screening due to $\xi_0 \ll \lambda_0$), yielding a current response in terms of the non-local superfluid density tensor $K_{ij}\left(R_{\mathrm{o}}, \boldsymbol{v}_{\mathrm{F}}(R_{\mathrm{o}}); R_{\mathrm{s}}, \boldsymbol{v}'_{\mathrm{F}}(R_{\mathrm{s}}); T\right)$. This tensor couples the x and y degrees-of-freedom over distances set by the coherence length $\xi = \hbar v_{\mathrm{F}}/2\Omega$, where $\Omega \equiv \sqrt{|\Delta(\boldsymbol{p}_{\mathrm{F}})|^2 - z^2}$, and contains clearly distinguishable continuum and bound-state parts. As will be seen in Ch. 6, the free energy can be expressed as

$$\Omega = \frac{1}{2}\int dR_{\mathrm{o}}\left[\boldsymbol{p}_{\mathrm{s}}(\boldsymbol{R}_{\mathrm{o}}) \cdot \boldsymbol{j}(\boldsymbol{R}_{\mathrm{o}})\right] = \frac{1}{2}\int dR_{\mathrm{o}} \int dR_{\mathrm{s}}\left[\boldsymbol{p}_{\mathrm{s}}(\boldsymbol{R}_{\mathrm{o}}) \cdot \boldsymbol{K}(\boldsymbol{R}_{\mathrm{o}}, \boldsymbol{R}_{\mathrm{s}}) \cdot \boldsymbol{p}_{\mathrm{s}}(\boldsymbol{R}_{\mathrm{s}})\right]. \tag{5.62}$$

The sign of the kernel will thus define if the superflow is energetically favorable or not. It was shown that there is a competition for the overall sign of $\boldsymbol{K}$ between

1. the continuum and bound-state parts,
2. between the different components K_{xx}, K_{xy}, K_{yx}, K_{yy}.

Which terms dominate were shown to depend on temperature, the relative position of $\boldsymbol{R}_{\mathrm{o}}$ and $\boldsymbol{R}_{\mathrm{s}}$, and their distance from the interface. Lowering the temperature, it is predicted that the overall sign of the kernel switches from everywhere positive, to positive in the bulk and negative in a region $\sim \xi$ of the interface. This plants a seed for an instability towards a spontaneous and inhomogeneous superflow, with a much shorter screening than a translationally invariant superflow [66, 67], which would significantly reduce cost of bulk superflow. An inhomogeneous superflow was proposed in Ch. 4 based purely on energetics, and the present chapter has highlighted a possible mechanism to give rise to this superflow. Chapter 6 analyses the mechanism and the instability, by introducing a non-local Ginzburg-Landau theory in terms of $\boldsymbol{K}$, and minimizing the energy with respect to $\boldsymbol{p}_{\mathrm{s}}(\boldsymbol{R})$.

To conclude the chapter, the structure of the superfluid density makes it apparent that the introduction of a specular interface makes the geometry of the response theory incommensurate. While the propagators and coherence amplitudes are conveniently described and solved in polar coordinates defined by the Fermi surface, the superflow perturbation and the interface follows a cartesian symmetry defined by the interface. Hence, the specular interface breaks the symmetry between momentum space and coordinate space. As was shown, this leads to a coupling between surface-parallel and perpendicular degrees of freedom, such that an inhomogeneity perpendicular to the interface (like the bound-state decay) might translate into an inhomogeneity along the otherwise translationally invariant interface.

6 Phase crystallization

Chapter 5 extended a surface scattering model to take into account inhomogeneous superflow $\boldsymbol{p}_{\mathrm{s}}(\boldsymbol{R})$, in a non-local linear response. It was shown that the current response can be expressed in terms of an inhomogeneous response kernel $\boldsymbol{K}(\boldsymbol{R}_{\mathrm{o}}, \boldsymbol{R}_{\mathrm{s}})$, which is the superfluid density tensor. At a clean and specular interface with pairbreaking, it was shown that the components of this tensor change sign as a function of temperature and distance from a pairbreaking interface. In this chapter, an inhomogeneous Ginzburg-Landau model is introduced, where it is shown that the kernel $\boldsymbol{K}$ enters as the Ginzburg-Landau coefficient of the superflow kinetic energy. Due to the sign change in $\boldsymbol{K}$, it is found that the system is unstable towards a phase transition into an inhomogeneous superconducting ground state with spatial phase-oscillating $\chi(\boldsymbol{R}) \propto \cos(\boldsymbol{q} \cdot \boldsymbol{R})$, and as a result, periodic superflow and equilibrium currents with a peculiar pattern, reproducing the results of the self-consistent numerics in papers II–IV. These phase oscillations break continuous translational symmetry and time-reversal symmetry. Similar to the crystallization problem, the order parameter of the new phase is identified as a finite Fourier amplitude C_q at a finite wave vector q, defining the period of the phase oscillations. The ground state is therefore referred to as a phase crystal. The conditions for the appearance of the phase crystal are derived based on the Ginzburg-Landau theory. Using the microscopically derived response theory, it is shown explicitly how these conditions are satisfied close to the pairbreaking interface. The model calculation does not take into account variations of the order parameter amplitude, in contrast to the self-consistent numeric calculations. Since they essentially produce the same results, this highlights the fact that the phase sector of the order parameter can be a main driving term for phase transitions and the energetics. Furthermore, the take-home message is also that the superfluid density and the kinetic energy cannot *a priori* be assumed to be homogeneous and positive, respectively, but have to be treated with care by taking into account non-locality and inhomogeneities even on the coherence length scale. Doing so, new insight and interesting physics might become available. Note that the derivations in the chapter are based mainly on the particle current, and should therefore in principle also apply to uncharged superfluids (in particular ^{3}He) [144, 173, 174], but this is well beyond the scope of this thesis.

6.1 Phase crystallization due to non-locality

The goal of this section is to derive a relation between the free energy and the particle current, in terms of the superfluid density and superfluid momentum, using a non-local Ginzburg Landau theory. Following paper I, conditions are derived under which energy-minimization leads to spontaneous and inhomogeneous superflow.

6.1.1 Non-local Ginzburg-Landau theory

In a theory with a complex-valued order parameter $\Delta = |\Delta| e^{i\chi}$, the Ginzburg-Landau free-energy is typically given by the lowest-order $|\Delta|$ and gradient terms

$$\begin{aligned} f(\Delta) &= \alpha|\Delta|^2 + \frac{1}{2}\beta|\Delta|^4 + K|\boldsymbol{\nabla}\Delta|^2 && (6.1)\\ &= \alpha|\Delta|^2 + \frac{1}{2}\beta|\Delta|^4 + K\left[(\boldsymbol{\nabla}|\Delta|)^2 + |\Delta|^2(\boldsymbol{\nabla}\chi)^2\right], && (6.2)\end{aligned}$$

with parameters α, β and K determined by the underlying (microscopic) theory for a particular system. Here, $\alpha(T > T_\mathrm{c}) > 0$ and $\alpha(T \leq T_\mathrm{c}) \leq 0$ mark the onset of superconductivity at transition temperature T_c, with amplitude-regularizing term $\beta > 0$, favoring a finite order parameter. In the absence of magnetic fields and induction, variations in a superconducting phase lead to finite superflow

$$\boldsymbol{p}_\mathrm{s}(\boldsymbol{R}) = \frac{\hbar}{2}\boldsymbol{\nabla}\chi(\boldsymbol{R}), \tag{6.3}$$

with associated (local) free-energy density

$$f_\mathrm{sf}^\mathrm{loc}(\boldsymbol{R}) = K\,|\Delta(\boldsymbol{R})|^2\,(\boldsymbol{\nabla}\chi(\boldsymbol{R}))^2\,, \tag{6.4}$$

which gives the kinetic energy

$$F_\mathrm{sf}^\mathrm{loc} = \frac{1}{2}\int dR\, f_\mathrm{sf}(\boldsymbol{R}). \tag{6.5}$$

In the usual superconducting ground state, the superfluid density is positive $K > 0$, implying an energy cost of phase gradients, which ensures a rigid and uniform phase $\chi = \text{const}$. If K was to change sign below a transition temperature T^* somehow, however, there would be an instability towards a non-uniform phase $\chi(\boldsymbol{R}) \neq \text{const}$. Such an instability will now be considered on the level of Ginzburg-Landau phenomenology, and later microscopically by using the kernel K derived in Ch. 5. Generalizing to a non-local scenario,

$$F_\mathrm{sf} = \frac{1}{2}\int\int dRdR'\;[\boldsymbol{\nabla}\chi(\boldsymbol{R})]_i\,K_{ij}(\boldsymbol{R},\boldsymbol{R}')\,[\boldsymbol{\nabla}\chi(\boldsymbol{R}')]_j\,, \tag{6.6}$$

with summation over repeated indices. Here, K_{ij} is the non-local superfluid density kernel, which is real and symmetric

$$K_{ij}(\boldsymbol{R},\boldsymbol{R}') = K_{ji}(\boldsymbol{R}',\boldsymbol{R}). \tag{6.7}$$

Before discussing energy minimization, the relation between the current and the energy will be derived. Consider a small Galilean boost $\boldsymbol{u}$, such that $\boldsymbol{p}'_{\mathrm{s}} = \boldsymbol{p}_{\mathrm{s}} - m\boldsymbol{u}$, with mass m. Defining the superfluid velocity from $\boldsymbol{v}_{\mathrm{s}} = \boldsymbol{p}_{\mathrm{s}}/m$, Galilean invariance gives the free energy in the moving frame as

$$F_{\mathrm{sf}}[\boldsymbol{v}_{\mathrm{s}} - \boldsymbol{u}] = F_{\mathrm{sf}}[\boldsymbol{v}_{\mathrm{s}}] - m\boldsymbol{j}\cdot\boldsymbol{u}, \tag{6.8}$$

which defines the total particle current. Taylor expanding in $\boldsymbol{p}'_{\mathrm{s}}$, the particle current is

$$\begin{aligned} j_i(\boldsymbol{R}) &= \frac{\delta F_{\mathrm{sf}}[\boldsymbol{v}_{\mathrm{s}}]}{\delta p_{\mathrm{s},i}(\boldsymbol{R})} = \int dR'\, K_{ij}(\boldsymbol{R},\boldsymbol{R}')\,[\boldsymbol{\nabla}\chi(\boldsymbol{R}')]_j\,, \quad \Rightarrow & (6.9)\\ F_{\mathrm{sf}} &= \frac{1}{2}\int dR\,\boldsymbol{j}(\boldsymbol{R})\cdot\boldsymbol{p}_{\mathrm{s}}(\boldsymbol{R}), & (6.10)\end{aligned}$$

where Eq. (6.6) was used. Minimizing F_{sf} with respect to χ gives the continuity equation

$$0 = -\frac{\delta F_{\mathrm{sf}}[\boldsymbol{\nabla}\chi]}{\delta\chi(\boldsymbol{R})} = \boldsymbol{\nabla}\cdot\boldsymbol{j}(\boldsymbol{R}). \tag{6.11}$$

Current conservation is thus guaranteed at a minimum of the free energy. This is not always the case, as inserting any arbitrary superflow $\boldsymbol{p}_{\mathrm{s}}$ might lead to an unphysical scenario, where the conservation is violated, and the system is not in an energy minimum. Therefore, the superflow is only physical at a minimum of the energy, and if it corresponds to a phase χ as in Eq. (6.3). It is noted that if amplitude variations are negligible, e.g. deep inside the superconducting state where $|\Delta(T)| \sim |\Delta|$ and $F[\Delta T] \sim F_{\mathrm{sf}}[\Delta T]$, then the minimum of F_{sf} corresponds to the ground state. It is important to note that the instability analysis only considers the lowest-order gradient term $(\boldsymbol{\nabla}\chi)^2$. This of course leads to an unphysical scenario where $K < 0$ favors an infinite superflow magnitude $|\boldsymbol{p}_{\mathrm{s}}|$. To regularize the theory, higher-order terms have to be included, which will also determine the finite magnitude $|\boldsymbol{p}_{\mathrm{s}}|$ at the instability (possible higher-order terms are shown and discussed briefly in paper I). The goal is not to obtain this magnitude, however, but rather to show that the instability is in principle possible. Just like the superconducting phase transition, this occurs when the corresponding Ginzburg-Landau coefficient switches sign and the energy has a minimum $\min_{q_i} F[T = T^*] = 0$, with $\min_{q_i} F[T < T^*] < 0$. Here, q_i are variational parameters, for example temperature or external fields. Including only the second-order gradient term is therefore sufficient for this instability analysis, and to approximately determine the value of T^* and q_i at the transition.

6.1.2 Spontaneous pattern formation

It is convenient to Fourier transform the free-energy density, and express the energy minimization as a variational or an eigenvalue problem. For an infinite and translationally invariant system, the kernel depends only on the relative position $\boldsymbol{R}-\boldsymbol{R}'$, such that the Fourier transformed quantity can be described by a single momentum $\boldsymbol{q}$

$$F_{\mathrm{sf}}[\chi]=\frac{1}{2}\int\frac{d^nq}{(2\pi)^n}\chi(-\boldsymbol{q})\left[q_i^{\mathrm{T}}\hat{K}_{ij}(\boldsymbol{q})q_j\right]\chi(\boldsymbol{q}), \tag{6.12}$$

in n dimensions. The symmetry in Eq. (6.7) means that $\hat{K}(\boldsymbol{q})$ is a Hermitian matrix

$$\hat{K}^{\dagger}(\boldsymbol{q})=\hat{K}(\boldsymbol{q}), \tag{6.13}$$

with real eigenvalues λ_k and eigenvectors $\boldsymbol{e}_k$ that both depend on $\boldsymbol{q}$ and other parameters (e.g. temperature or external fields), and where $k\in\{0,1,\dots,n\}$. At the transition temperature T^*, the energy has a minimum that touches zero and turns negative below T^*. This might happen at a finite wavevector $\boldsymbol{q}_0$ with

$$0=\boldsymbol{q}_0^{\mathrm{T}}\hat{K}(\boldsymbol{q}_0)\boldsymbol{q}_0=\sum_{k=1}^{n}\lambda_k\left[\boldsymbol{e}_k\cdot\boldsymbol{q}_0\right]^2. \tag{6.14}$$

Consider the two-dimensional case ($n=2$) for simplicity, where a non-trivial solution ($\lambda_{1,2}\neq 0$) of Eq. (6.14) implies that $\lambda_1(T^*,\boldsymbol{q})=-\lambda_2(T^*,\boldsymbol{q})$. In linear response to $\chi(\boldsymbol{R})$, this leads to the relations

$$\begin{aligned}\boldsymbol{j}&=i\boldsymbol{j}_0\chi(\boldsymbol{q}_0), && (6.15)\\ \boldsymbol{j}_0&=\hat{K}(\boldsymbol{q}_0)\cdot\boldsymbol{q_0} && (6.16)\\ &=\lambda_1\boldsymbol{e}_1\left[\boldsymbol{e}_1\cdot\boldsymbol{q}_0\right]+\lambda_2\boldsymbol{e}_2\left[\boldsymbol{e}_2\cdot\boldsymbol{q}_0\right]. && (6.17)\end{aligned}$$

Current conservation at a finite wavevector implies orthogonality $\boldsymbol{q}_0\perp\boldsymbol{j}_0$ since

$$\boldsymbol{\nabla}\cdot\boldsymbol{j}\propto\boldsymbol{q}_0\cdot\boldsymbol{j}=0, \tag{6.18}$$

which is fulfilled when $\boldsymbol{q}_0\nparallel\boldsymbol{e}_{1,2}$. Hence, the symmetry between coordinate and momentum space has to be broken (e.g. at a pairbreaking interface as discussed in Sec. 5.7). This makes it possible to write

$$\begin{aligned}j_{0,x}q_{0,x}+j_{0,y}q_{0,y}&=0, && (6.19)\\ \frac{j_{0,x}}{j_{0,y}}&=\frac{-q_{0,x}}{q_{0,y}}. && (6.20)\end{aligned}$$

The symmetries of the system give constraints which determine the form of the eigenvectors, and therefore the instability. Two examples will now be shown.

Since $\chi(\boldsymbol{R})$ is real, inversion symmetry $\boldsymbol{R} \to -\boldsymbol{R}$ implies that Eqs. (6.19)–(6.20) must hold also for $-\boldsymbol{q}_0$. The two instability vectors $\boldsymbol{q}_0$ and $-\boldsymbol{q}_0$ lead to a spatially inhomogeneous and periodic phase, as well as stripe currents

$$\begin{aligned} \chi^{\text{stripe}}(\boldsymbol{R}) &= C\cos(\boldsymbol{q}_0 \cdot \boldsymbol{R}), && (6.21)\\ \boldsymbol{p}_{\text{s}}^{\text{stripe}}(\boldsymbol{R}) &= -\boldsymbol{q}_0 \frac{\hbar C}{2}\sin(\boldsymbol{q}_0 \cdot \boldsymbol{R}), && (6.22)\\ \boldsymbol{j}^{\text{stripe}}(\boldsymbol{R}) &= C\boldsymbol{j}_0 \sin(\boldsymbol{q}_0 \cdot \boldsymbol{R}) \perp \boldsymbol{q}_0, && (6.23) \end{aligned}$$

visualized in Fig. 6.1 (a), where $0 < C \leq \pi$ is a constant. Imposing reflection symmetry over $x \to -x$ gives another pair of instability vectors $\underline{\boldsymbol{q}}_0$ and $-\underline{\boldsymbol{q}}_0$ with $\underline{q}_{0,x} = -q_{0,x}$. The kernel is diagonalized at $\underline{\boldsymbol{q}}_0$, yielding the same eigenvalues $\lambda_{1,2}$ as for $\boldsymbol{q}_0$, but eigenvectors $\underline{\boldsymbol{e}}_{1,2} = [-(e_{1,2})_x, +(e_{1,2})_y]$ and the current $\underline{\boldsymbol{j}}_0 = \lambda_1 \underline{\boldsymbol{e}}_1 \left[\underline{\boldsymbol{e}}_1 \cdot \underline{\boldsymbol{q}}_0\right] + \lambda_2 \underline{\boldsymbol{e}}_2 \left[\underline{\boldsymbol{e}}_2 \cdot \underline{\boldsymbol{q}}_0\right]$. This leads to checkerboard-like patterns with loop currents

$$\begin{aligned} \chi^{\text{check}}(\boldsymbol{R}) &= C\cos(\boldsymbol{q}_0 \cdot \boldsymbol{R}) + \underline{C}\cos\big(\underline{\boldsymbol{q}}_0 \cdot \boldsymbol{R}\big), && (6.24)\\ \boldsymbol{p}_{\text{s}}^{\text{check}}(\boldsymbol{R}) &= -\boldsymbol{q}_0 \frac{\hbar C}{2}\sin(\boldsymbol{q}_0 \cdot \boldsymbol{R}) - \underline{\boldsymbol{q}}_0 \frac{\hbar \underline{C}}{2}\sin\big(\underline{\boldsymbol{q}}_0 \cdot \boldsymbol{R}\big), && (6.25)\\ \boldsymbol{j}^{\text{check}}(\boldsymbol{R}) &= C\boldsymbol{j}_0 \sin(\boldsymbol{q}_0 \cdot \boldsymbol{R}) + \underline{C}\underline{\boldsymbol{j}}_0 \sin\big(\underline{\boldsymbol{q}}_0 \cdot \boldsymbol{R}\big), && (6.26) \end{aligned}$$

illustrated in Fig. 6.1 (b).

To summarize, the realization of the non-uniform phase instability relies on the existence of a superfluid density tensor $\boldsymbol{K}(\boldsymbol{R}_{\text{o}}, \boldsymbol{R}_{\text{s}}; T)$ with

1. spatial anisotropy,
2. positive and negative eigenvalues $\lambda_{1,2}$ that depend on some parameter, e.g. temperature or external magnetic field,
3. eigenvectors $\boldsymbol{e}_{1,2} \not\parallel \boldsymbol{q}$, i.e. breaking the symmetry between $\boldsymbol{K}$ and momentum space quantities, in particular the Fermi surface and quasiparticle excitations.

As discussed in paper I, some of these conditions might be satisfied by a spin-population imbalance due to a Zeeman field (shown to give rise to inhomogeneous states at the normal-superconducting transition [52, 53, 175–178]), for non-circular Fermi surfaces, and multi-component order parameters (also shown to lead to inhomogeneous states [179, 180]). Paper I and Sec. 6.2 discusses how all of the conditions 1–3 can be satisfied at a pairbreaking interface, by using a Fourier representation of the microscopic response theory developed in Ch. 5. It is noted that the situation is much more complex in three dimensions, reflected by the fact that there are more ways to satisfy the energy minimum in Eq. (6.14), with a range of non-trivial solutions (as opposed to a single one in $2D$). This leads to a much more complicated analysis, as is typically the case for $3D$ pattern-forming instabilities, as exemplified by the plethora of competing phases in liquid crystals [22, 23, 45, 181].

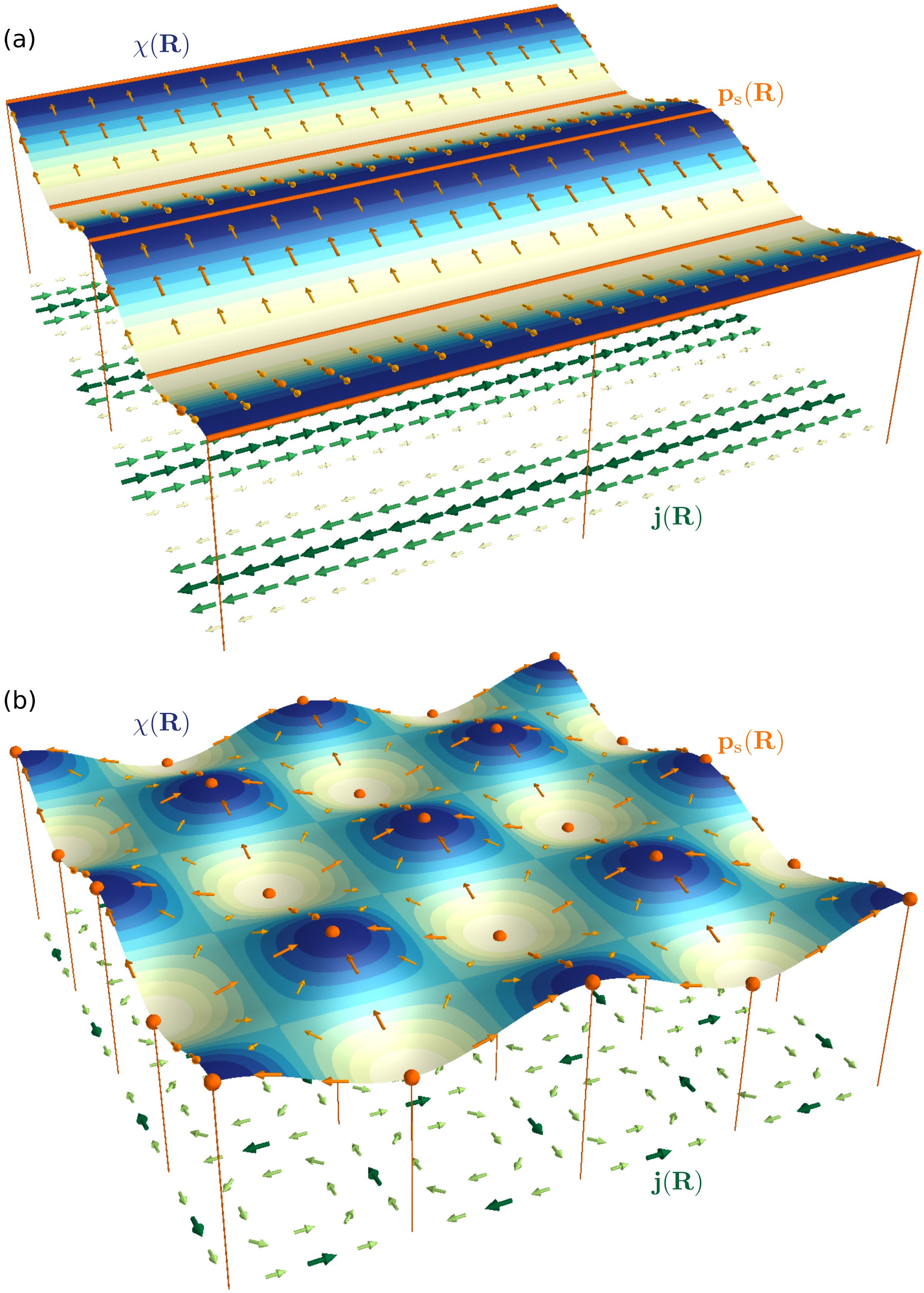

Figure 6.1: *Spatially periodic superconducting phase (surface), resulting in superflow (orange top arrows), and currents (green bottom arrows). These are described by (a) Eqs. (6.21)–(6.23), and (b) Eqs. (6.24)–(6.26). Orange tubes (spheres) show line (point) sources and sinks.*

6.1.3 Phase crystals

It was shown how the symmetries of the system can determine the patterns that in principle are possible. These patterns will have different energies, and therefore different transition temperatures. The pattern with the highest transition temperature, and consequently the lowest energy, will correspond to the ground state. As mentioned earlier, this transition occurs when the minimum of the free energy, with respect to the variational parameters, touches zero, corresponding to a physical superflow pattern and particle-current conservation. Going below the transition temperature T^*, the energy minimum is negative, signifying an energy gain. Furthermore, as will be shown in the next section, this corresponds to a finite Fourier amplitude C_{q_x} that develops at a single and finite wavenumber q_x^*. Paper I shows that this leads to a phase diagram with

$$T^*(q_x) = T^* - \beta(q_x - q_x^*)^2, \tag{6.27}$$

These properties are in direct analogy to the problem of weak crystallization [19], e.g. in a metallic alloy [20], where a periodic crystal structure appears at one or more finite wavenumbers q, and Eq. (6.27) is taken as an ansatz (rather than actually derived from microscopic theory as in paper I). It is therefore reasonable to refer to the instability with a periodic superconducting phase as a phase crystal.

An interesting point to note is that phase transitions usually rely on a competition between different terms in the Ginzburg-Landau functional. In this case, however, the competition is from the internal structure of $\boldsymbol{K}$ itself (e.g. diagonal versus off-diagonal terms, and continuum versus bound-state terms), which is highlighted by the non-local structure of $\boldsymbol{K}$. The stability of certain crystalline orders in solids also rely on non-local interactions [20]. The Abrikosov-Vortex state is another example of a highly non-local state due to an additional length-scale $\lambda_0 \gg \xi_0$, with a kind of crystalline ordering of topological defects, i.e. the vortex lattice. As a side note, this vortex lattice may under certain circumstances undergo various phase-transitions to e.g. a vortex-liquid, a vortex-glass, or clusters of vortex-molecules [35, 36]. It is important to point out that the phase crystallization described above is not related to flux quantization or Abrikosov vortices, at least not in the realization found here or in the appended papers. It is also distinctly different from the Fulde-Ferell-Larkin-Ovchinnikov state, as discussed in the introduction of paper I. The proposed phase crystal thus extends the existing paradigm of inhomogeneous superconducting ground states.

A particular realization of phase crystallization will now be discussed, namely at interfaces with Andreev bound states.

6.2 Surface phase crystals due to Andreev states

Chapter 5 used quasiclassical theory to derived the response kernel $K_{ij}(\boldsymbol{R}_{\mathrm{o}}, \boldsymbol{R}_{\mathrm{s}})$ to an inhomogeneous superflow $\boldsymbol{p}_{\mathrm{s}}(\boldsymbol{R}_{\mathrm{s}})$ close to a pairbreaking interface. Here, $\boldsymbol{R}_{\mathrm{o}}$ and $\boldsymbol{R}_{\mathrm{s}}$ are observation and source points respectively. The kernel satisfies conditions 1–3 presented at the end of Sec. 6.1.2. In particular, conditions 1–2 by the sign-change in the kernel as a function of both temperature and spatial coordinates, and condition 3 by the asymmetry close to the surface due to exponential decay of the Andreev bound states, with multiple $q_{0,y}$ components contributing at the instability. The latter will now be shown explicitly, by solving the energy-minimization problem in Fourier space as an eigenvalue problem, with the momentum-space kernel $K(q_x; q_{y_1}, q_{y_2})$. Later, the mixed representation $K(q_x; y_1, y_2)$ is used to solve energy minimization as a variational problem.

6.2.1 Momentum-space representation: optimal form of $\chi(R)$

The superfluid density $\boldsymbol{K}(\boldsymbol{R}_{\mathrm{s}}, \boldsymbol{R}_{\mathrm{o}})$ derived and analyzed in Sec. 5.6 is translationally invariant along the interface, and therefore only depends on the relative distance $\Delta x = x_{\mathrm{o}} - x_{\mathrm{s}}$ between observation and source points, $\boldsymbol{K}(\boldsymbol{R}_{\mathrm{s}}, \boldsymbol{R}_{\mathrm{o}}) \to \boldsymbol{K}(\Delta x, y_{\mathrm{o}}; 0, y_{\mathrm{s}})$. Fourier transforming, this leads to

$$\begin{aligned} K_{ij}(\boldsymbol{q}_1, \boldsymbol{q}_2) &= \int\!\!\int dR_1 dR_2\, e^{-i\boldsymbol{q}_1\cdot\boldsymbol{R}_1} e^{+i\boldsymbol{q}_2\cdot\boldsymbol{R}_2} K_{ij}(\boldsymbol{R}_1, \boldsymbol{R}_2) && (6.28)\\ &= 2\pi\delta\left(q_{x_1} - q_{x_2}\right) K_{ij}(q_x; q_{y_1}, q_{y_2}). && (6.29)\end{aligned}$$

Inserting this into the free-energy expression introduced in Sec. 6.1 yields

$$F_{\mathrm{sf}}[\chi] = \frac{1}{2}\int \frac{dq_x}{2\pi}\int \frac{dq_{y_1}}{2\pi}\int \frac{dq_{y_2}}{2\pi}\chi^*(q_x, q_{y_1})\chi(q_x, q_{y_2})\,\mathrm{Re}\left[\boldsymbol{q}_1^{\mathrm{T}} \circ \hat{K}(q_x; q_{y_1}, q_{y_2}) \circ \boldsymbol{q}_2\right], \tag{6.30}$$

where $\boldsymbol{q}_{1,2} = (q_x, q_{y_{1,2}})$, and $\circ$ implies vector-matrix multiplication. Here, the real phase has the Fourier transform

$$\chi(\boldsymbol{R}) = \int \frac{d^2q}{(2\pi)^2}\chi_{\boldsymbol{q}} e^{+i\boldsymbol{q}\cdot\boldsymbol{R}} = \int \frac{d^2q}{(2\pi)^2}\chi^*_{\boldsymbol{q}} e^{-i\boldsymbol{q}\cdot\boldsymbol{R}}. \tag{6.31}$$

The term in the bracket in Eq. (6.30) reduces to the scalar

$$k(q_x; q_{y_1}, q_{y_2}) = \boldsymbol{q}_1^{\mathrm{T}} \circ \hat{K}(q_x; q_{y_1}, q_{y_2}) \circ \boldsymbol{q}_2 = q_x^2 K_{xx} + q_x K_{xy} q_{y_2} + q_{y_1} K_{yx} q_x + q_{y_1} K_{yy} q_{y_2}. \tag{6.32}$$

The energy in Eq. (6.30) can be minimized with respect to $\chi(q_x, q_y)$ by solving the following eigenvalue problem for every temperature T

$$\begin{aligned} \lambda \boldsymbol{q}_1 \chi(q_x, q_{y_1}) &= \hat{K}(q_x; q_{y_1}, q_{y_2}) \circ \boldsymbol{q}_2 \chi(q_x, q_{y_2}), && (6.33)\\ \lambda &= \chi^*(q_x, q_{y_1})\boldsymbol{q}_1^{\mathrm{T}} \circ \hat{K}(q_x; q_{y_1}, q_{y_2}) \circ \boldsymbol{q}_2 \chi(q_x, q_{y_2}), && (6.34)\end{aligned}$$

with eigenvalues λ in the basis $\boldsymbol{q}\chi(q_x, q_y)$. Hence, the eigenvalue problem is solved by diagonalizing the matrix in Eq. (6.34). Above the transition temperature, the eigenvalues are positive definite. The temperature at which the smallest eigenvalue goes through zero marks the transition temperature. It turns out that the Fourier kernel becomes a narrow downward peak which becomes negative at the transition, such that only a single q_x contributes. The transition temperature can thus be written as $T^*(q_x)$, and the ground state is given by the q_x with the highest T^*. Diagonalizing the matrix, the lowest eigenvalue λ_0 has the corresponding eigenvector $\boldsymbol{q}_0$ which defines the Fourier spectrum $\chi(q_x, q_y)$. The real-space profile $\chi(q_x, y)$ can then be obtained through Eq. (6.31). Figure 6.2 shows that numerically solving the eigenvalue problem gives a spatial profile of $\chi(y)$ that matches the self-consistent calculations, where the latter are taken from paper II. The form of χ that minimizes the energy is well-described by the fit

$$\chi(x,y) \propto \left(1+\frac{y}{y_0}\right)e^{-y/y_0}\cos(q_x x), \qquad \Longrightarrow \tag{6.35}$$

$$\boldsymbol{p}_\mathrm{s}(x,y) \propto -\left[q_x\left(1+\frac{y}{y_0}\right)\sin(q_x x), \frac{y}{y_0^2}\cos(q_x x)\right]e^{-y/y_0}. \tag{6.36}$$

Figure 3 of paper I shows that this gives rise to the same superflow and current response as obtained numerically in papers II–IV.

The eigenvalue problem is relatively expensive to solve numerically. It will now be shown how the phase-diagram can be obtained using a variational approach.

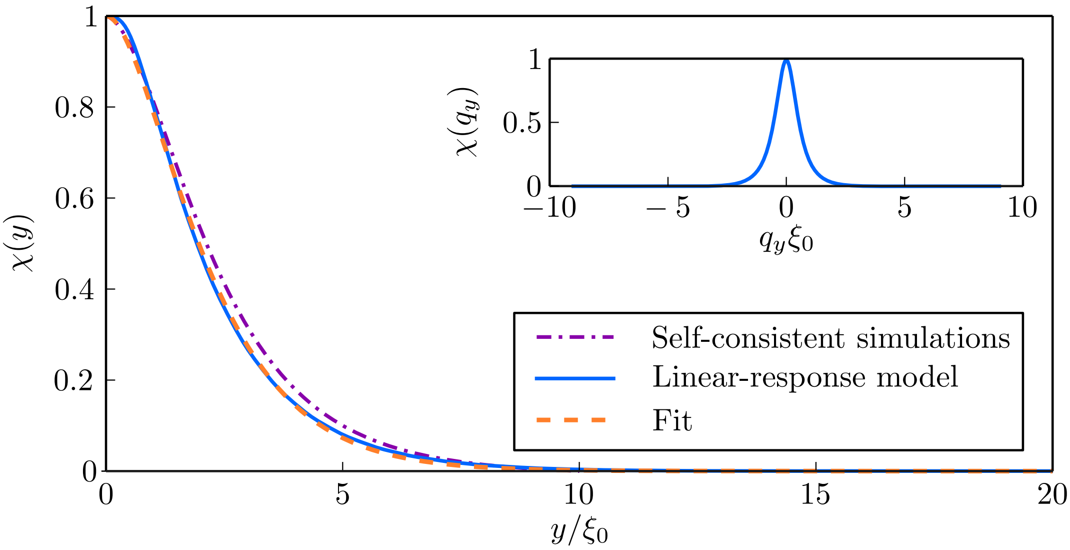

Figure 6.2: *Spatial profile of the superconducting phase obtained by the methods indicated by the legend, i.e. self-consistent numerics in paper II, the linear-response eigenvalue-problem in Eq. (6.34), and a fit to* $\chi(y) = [1+y/y_0]\,e^{-y/y_0}$. *The inset shows the Fourier-space representation of the eigenvalue-solution. Note that the amplitude has been normalized.*

6.2.2 Mixed representation: transition from variational analysis

In order to make both the kernel analysis and the numeric calculations easier, a mixed representation will now be derived. Fourier transforming with respect to only the x-coordinates and utilizing translational invariance as in Sec. 6.2.1, the free energy can be written

$$\begin{aligned} F_{\text{sf}}[\chi] &= \frac{1}{2}\int\frac{dq_x}{2\pi}\int_0^\infty dy_1\int_0^\infty dy_2\,[(-iq_x\hat{x}+\hat{y}\partial_{y_1})\chi^*(q_x,y_1)] \\ &\qquad \circ\hat{K}(q_x;y_1,y_2)\circ[(iq_x\hat{x}+\hat{y}\partial_{y_2})\chi(q_x,y_2)]\,. \end{aligned} \tag{6.37}$$

For a real phase $\chi^*(y)=\chi(y)$ with separable x and y-degrees of freedom, it is possible to write

$$\chi(x,y)=C_{q_x}\chi(y)e^{+iq_xx}, \tag{6.38}$$

where C_{q_x} is the Fourier-amplitude of the phase. Letting the prime symbol denote derivative with respect to the y-coordinate, the free energy is written

$$\begin{aligned} F_{\text{sf}}[\chi] &= \frac{1}{2}\int\frac{dq_x}{2\pi}|C_{q_x}|^2\int_0^\infty dy_1\int_0^\infty dy_2\Big[q_x^2K_{xx}\chi(y_1)\chi(y_2)+K_{yy}\chi'(y_1)\chi'(y_2) \\ &\qquad -iq_xK_{xy}\chi(y_1)\chi'(y_2)+iq_xK_{yx}\chi'(y_1)\chi(y_2)\Big]. \end{aligned} \tag{6.39}$$

Section 5.6 claimed that the diagonal and off-diagonal components are symmetric and antisymmetric with respect to reflection symmetry $x\to -x$, respectively. This means that the diagonal and off-diagonal Fourier components are purely real and imaginary, respectively since

$$K_{xx,yy}(q_x;y_1,y_2) = +K_{xx,yy}(-q_x;y_1,y_2), \tag{6.40}$$

$$K_{xy,yx}(q_x;y_1,y_2) = -K_{xy,yx}(-q_x;y_1,y_2), \tag{6.41}$$

such that the whole integrand in Eq. (6.39) is real. This is seen explicitly

$$K_{xx}(q_x;y_1,y_2) = +2\int_0^\infty dx\cos(q_xx)K_{xx}(x;y_1,y_2), \tag{6.42}$$

$$K_{yy}(q_x;y_1,y_2) = +2\int_0^\infty dx\cos(q_xx)K_{yy}(x;y_1,y_2), \tag{6.43}$$

$$K_{xy}(q_x;y_1,y_2) = -2i\int_0^\infty dx\sin(q_xx)K_{xy}(x;y_1,y_2), \tag{6.44}$$

$$K_{yx}(q_x;y_1,y_2) = -2i\int_0^\infty dx\sin(q_xx)K_{yx}(x;y_1,y_2). \tag{6.45}$$

The integrands can be obtained from Sec. 5.6, and Eq. (6.39) can then be minimized, for example using a variational approach for different functional forms $\chi(y)$ and variational parameters. For the form of χ given in Eq. (6.35), the variational parameters would be q_x and y_0, for each T. This is done in paper I to obtain the phase-diagram for the inhomogeneous superflow state, and discussed below.

6.3 Instability analysis: what sets T^* and q_x?

Paper I uses the variational method described in Sec. 6.2.2 to obtain the phase-diagram of the instability with $\chi(x, y)$ in Eq. (6.35), at a [110] vacuum-interface of a d-wave superconductor, and at a spin-active interface of a conventional s-wave superconductor. These phase diagrams (Figs. 3 and 4 of paper I) give the transition temperature T^*, wavenumber q_x (defining the period λ_x from $q_x\lambda_x = 2\pi$) and the decay length y_0. Table 6.1 compares these linear-response results with those obtained from the self-consistent numerics (papers II–IV).

System and methods comparison

The discrepancy between the two methods are due to the simplifying assumptions of the linear-response model. First and foremost, amplitude variations (both as a function space and temperature) are neglected in this model, while they are included in the self-consistency. As a test, self-consistent simulations were run with a constant order parameter magnitude, which gave $q_{x,d} \approx 1.59\xi_0^{-1}$, $y_0^d = 0.45$, $T_d^* \sim 0.39T_\mathrm{c}$. Second, the linear-response model neglects lowest-order response from the quasiparticle backflow in the subgap part of the spectrum, caused by thermal excitations (s-wave and d-wave) or gap nodes (d-wave), analyzed in Ch. 3. This could actually explain why the self-consistent numerics with constant order parameter provides an even higher transition temperature, since the additional quasiparticles are paramagnetic and seem to favor a superflow. Finally, the linear-response model is not a self-consistent solution. Given all these simplifying assumptions, it is quite remarkable that the linear response model can capture the essential features of the self-consistent numerics, most importantly the structure of the inhomogeneous superflow.

The difference between s-wave and d-wave results are to be expected, mainly due to gapped versus nodal order parameters, leading to e.g. different length scales (and responses, see Ch. 3). If this is indeed the case, then it is expected that a

Table 6.1: *Surface phase crystallization transition temperature T^* and length scales y_0, $\lambda_x = 2\pi/q_x$, from the linear-response model (paper I, developed in Ch. 5) and self-consistent numerics (papers II–IV). These are for a maximally pairbreaking d-wave superconductor-vacuum interface, and a spin-active s-wave interface.*

Method	$\frac{T_d^*}{T_\mathrm{c}}$	$\frac{T_s^*}{T_\mathrm{c}}$	$q_{x,d}\xi_0$	$q_{x,s}\xi_0$	$\frac{\lambda_{x,d}}{\xi_0}$	$\frac{\lambda_{x,s}}{\xi_0}$	$\frac{y_{0,d}}{\xi_0}$	$\frac{y_{0,s}}{\xi_0}$
Linear-response	0.32	0.17	1.0	0.5	2π	4π	0.73	1.3
Self-consistent	0.18	0.13	0.5	0.4	4π	5π	1.3	1.6

polar p_y-wave order parameter at a superconductor-vacuum interface should have intermediate values between the s-wave and d-wave results. As a side note, the existence of the phase in such a spin-triplet system was confirmed numerically.

What determines the scales?

The transition temperature, wavenumber and decay length are all closely related, and are determined by the temperature-dependence and the structure of the kernel $\boldsymbol{K}(\boldsymbol{R}_{\mathrm{o}}, \boldsymbol{R}_{\mathrm{s}}; T)$. At the present stage, it is uncertain if it is possible to obtain analytic closed forms of these quantities, due to the non-trivial averaging over the kernel structure. From the analysis in Sec. 5.6, however, it is certain that the transition temperature corresponds to the temperature where the T^{-1}-contribution from the bound-state terms overcome the competing contribution from the continuum terms. The finite q_x emerges from the competition between the different kernel components, in an attempt to minimize both the bulk superflow (with high-energy cost for low q_x) and the off-diagonal gradient terms (with high energy-cost for high q_x), see Fig. 2 of paper I. The scattering at the interface directly couples the x and y degrees of freedom, such that q_x and y_0 are related. Chapters 3–4, showed that finite superflow is unfavorable in bulk and favorable where there are Andreev bound states, respectively. The energy is therefore minimized when $y_0 \sim \xi_0$ corresponds to the decay length of Andreev bound states, as proposed in Ch. 4.

Periodic versus translational invariant superflow?

It is the correlations due to surface scattering and the non-local structure of $\boldsymbol{K}$ which ultimately provides the mechanism for the inhomogeneous superflow, and the self-screening length y_0 as opposed to the penetration depth screening λ_0 of a translationally invariant superflow [66, 67]. Hence, for an extreme type-II superconductor, the translationally invariant superflow leads to a huge cost of bulk superflow and a low transition temperature $T^* \sim T_{\mathrm{c}}(\xi_0/\lambda_0)$, while the inhomogeneous superflow has has little to no bulk superflow and a high transition temperature $T^* \sim T_{\mathrm{c}}(\xi_0/\mathcal{L}_y)$, where $y_0 \lesssim \mathcal{L}_y \ll \lambda_0$ is the region of superflow. If the Meissner screening was to be taken into account, the length-scale λ_0 would enter the model and modify the phase diagram, where for low $q_x \to 0$, the transition temperature would no longer go to zero but rather to $T^* \sim T_{\mathrm{c}}(\xi_0/\lambda_0)$ as in Refs. [66, 67]. When λ_0 becomes comparable with ξ_0, significant modifications are to be expected, and it is unclear what kind of transition would occur (if any).

It is noted that if the system would consist of two parallel pairbreaking interfaces separated by a distance D (as the annulus in Fig. 4 of paper I), then as $D \lesssim 2\pi/q_x$, there is a phase transition from the oscillating phase to translationally invariant phase gradients, i.e. from the phase crystal to the “Vorontsov phase” [152–156], as shown in Fig. 7.14 (p. 119) in Lic. Th. [10], and discussed in Ref. [144].

6.4 Chapter summary: outlook

Spontaneous pattern-forming instabilities can be notoriously difficult to study [19, 20, 23]. The phase crystallization phenomenon described in this chapter is no exception, characterized by a superfluid kernel tensor $\boldsymbol{K}(\boldsymbol{R}_{\mathrm{o}}, \boldsymbol{R}_{\mathrm{s}}; T)$ that correlates spatial coordinates and depend on a number of parameters. Even under several simplifying assumptions, it is currently uncertain if complete analytic solutions of the transition temperature and length scales are possible.

A non-local Ginzburg-Landau theory was introduced where $\boldsymbol{K}$ enters as the Ginzburg-Landau coefficient of the kinetic energy

$$F_{\mathrm{sf}} = \frac{1}{2}\int\int dR dR' \; [\boldsymbol{\nabla}\chi(\boldsymbol{R})]_i \, K_{ij}(\boldsymbol{R}, \boldsymbol{R}') \, [\boldsymbol{\nabla}\chi(\boldsymbol{R}')]_j \,. \tag{6.46}$$

Conditions were derived under which $\boldsymbol{K}$ changes sign below a temperature T^* (with $T^* \sim 0.2T_{\mathrm{c}}$ from self-consistent numerics), and where spatial inhomogeneities $\boldsymbol{\nabla}\chi(\boldsymbol{R})$ become energetically favorable. It was shown that an interface with Andreev bound states can satisfy these conditions, giving rise to an inhomogeneous superconducting phase of the form

$$\chi(x, y) = [1 + y/y_0]\, e^{-y/y_0} \cos(q_x x), \tag{6.47}$$

generating the superflow and circulating currents found numerically in papers II–IV, with $q_x \xi_0 \sim 1$, and $y_0 \sim \xi_0$ matching the decay length of Andreev bound states. The phase can be written in terms of the Fourier amplitude C_{q_x}

$$\chi(x, y) = C_{q_x} \chi(y) e^{+iq_x x}. \tag{6.48}$$

The sign-change in $\boldsymbol{K}$ is due to a competition between diagonal and off-diagonal components, as well as between continuum and bound-state terms, where it is ultimately the T^{-1}-contribution from the bound states that gives the negative sign at low temperatures. Exactly at the transition, there is a sharp downward peak in $\boldsymbol{K}$ that turns negative at a finite wavenumber q_x, such that only this q_x contributes. Above and below the transition, C_{q_x} is therefore zero and nonzero, respectively, and it is appropriate to define the Fourier amplitude C_{q_x} as the order parameter. As mentioned in Sec. 6.1.3, this is in direct analogy to certain crystallization transitions of solids [19, 20], and the ground state with periodic phase $\chi(\boldsymbol{R})$ is therefore referred to as a phase crystal. This phase is studied analytically in paper I, and numerically in papers II–IV and Lic. Th. [10].

These results raises several questions (see Sec. 8.1 for an outlook), mainly concerning potential experimental realization and detection of the phase, and the stability against other proposed competing phases. Furthermore, would it be possible to realize the phase in a bulk system, and would this be easier in full $3D$? What would be the excitations and propagating degrees of freedom of this phase, if any? How is the phase influenced when the model is extended to include various other interactions and perturbations?

7 Overview of the appended papers

This chapter presents a brief summary of each appended paper, including the main motivation, results and conclusions. Please note that the paper numbering does not correspond to chronological order of publication, but rather in order of relevance to the story of the thesis.

7.1 Paper I

Paper I proposes an extension to the existing paradigm of inhomogeneous superconducting states. So far, the best known examples of such inhomogeneous orderings are the Abrikosov vortex state [16, 34], and the FFLO state [35, 52, 53], which both occur at finite external magnetic fields, and are amplitude instabilities of the normal-state (i.e. below $T_\mathrm{c}(B)$, the normal state is unstable to the formation of a finite superconducting order $|\Delta(T)|$).

In the absence of external fields, the phase χ of the superconducting order parameter Δ is usually rigid, as any variations lead to finite superflow $\boldsymbol{p}_\mathrm{s} = \hbar\boldsymbol{\nabla}\chi/2$ associated with positive kinetic energy $f = K\,|\Delta|^2\,(\boldsymbol{\nabla}\chi)^2 > 0$ for $K > 0$. Using a non-local Ginzburg-Landau theory, the energy is re-written as $f = \int dR \int dR' \boldsymbol{\nabla}\chi(\boldsymbol{R}) \cdot \boldsymbol{K}(\boldsymbol{R}, \boldsymbol{R}') \cdot \boldsymbol{\nabla}\chi(\boldsymbol{R}')$. In Fourier space, the superfluid density is described by a Hermitian matrix $\hat{\boldsymbol{K}}(\boldsymbol{q}_1; \boldsymbol{q}_2; T)$, with real eigenvalues λ_k and eigenvectors $\boldsymbol{e}_k$. The conditions are derived under which $K < 0$ is possible, namely when $\hat{\boldsymbol{K}}$ has

1. spatial anisotropy,
2. positive and negative eigenvalues $\lambda_{1,2}$ that depend on some parameter, e.g. temperature or external magnetic field,
3. eigenvectors $\boldsymbol{e}_{1,2} \nparallel \boldsymbol{q}$, i.e. breaking the symmetry between the current response tensor and momentum space quantities, in particular the Fermi surface and quasiparticle excitations.

Paper I discusses how these conditions can be satisfied, e.g. in a superconductor with an anisotropic gap in the presence of a Zeeman field, or at a domain wall with a sign-change in the order parameter. Using quasiclassical theory, the superfluid density $\boldsymbol{K}$ is derived analytically, and it is shown that close to certain interfaces of unconventional superconductors or superconductor-ferromagnet structures that host Andreev bound states, all conditions 1–3 can be satisfied. The order parameter of the phase is identified to be the Fourier amplitude C_{q_x} of the phase $\chi(q)$, that develops at a single and finite wavenumber q_x^*, with corresponding phase diagram

$$T^*(q_x) = T^* - \beta(q_x - q_x^*)^2. \tag{7.1}$$

This is in direct analogy to the problem of weak crystallization [19, 20], where Eq. (7.1) is taken as an ansatz. The instability with a periodic superconducting phase is therefore referred to as a phase crystal. The results reproduce the superflow and current patterns obtained with self-consistent numeric calculations, e.g. in Ref. [157] and papers II–IV. A main take-home message of the paper is that the superfluid density tensor has to be treated in a proper non-local sense, especially in the presence of inhomogeneities. It is argued that this can lead to a deviation from the usual notion of a rigid and uniform phase, where the phase and its variations, rather than the order-parameter magnitude, can act as a driving term in phase transitions.

7.2 Paper II

It is the goal of paper II to characterize and classify the phase transition of surface phase crystallization, both with and without an external magnetic field. This was done by identifying the broken symmetry, its corresponding order parameter, and its defects. By studying the thermodynamics, it is shown that the phase transition is of second order, even in an external field, and occurs at temperature $T^* \sim 0.2T_\mathrm{c}$ at zero field. The magnetic field reduces the transition temperature, since it fills the same function as the spontaneous superflow, i.e. Doppler shifting the unfavorable Andreev bound states. The phase is robust against the fields in the whole Meissner state, and for several flux quanta, but eventually breaks down in the mixed state. The critical field where this occurs is highly dependent on sample geometry and size, as described in Lic. Th. [10]. The fundamental broken symmetry is continuous translational symmetry, due to the inhomogeneous and periodic superflow that appears. This paper was written before the development of the analytical model presented in the thesis and paper I, in which the order parameter is appropriately identified as the finite Fourier amplitude of the phase χ that generates the superfluid momentum. As of such, paper II identifies the order parameter as the superfluid momentum, which is essentially an analogous classification, due to the direct relation between the phase and the superfluid momentum $\boldsymbol{p}_\mathrm{s} = \hbar\boldsymbol{\nabla}\chi/2$. Breaking of time-reversal symmetry follows as a consequence of the phase gradients, since magnetic fields are induced in response to the superflow. In an external magnetic field, time-reversal symmetry is already broken explicitly. Together with the fact that the transition is found in paper I even for a neutral superfluid without generation of magnetic fields, this highlights that the main effect is translational-symmetry breaking. This viewpoint is in some contrast to how the situation of spontaneous superflow and currents has typically been portrayed previously in the literature

Paper II finds that the superconducting phase χ oscillates periodically along the surface with period $\sim 4\pi\xi_0$ independent of temperature. There is no phase winding or topological phase-defects as in the Abrikosov vortex phase. The emerging circulating current patterns are thus not related to Abrikosov vortices or flux quantization (neither full nor fractional, as opposed to how it is phrased in paper IV). The resulting superflow, however, is shown to form a periodic pattern with sources, sinks and saddle points along the surface. The "defects" are therefore present as critical points of the vector field $\mathbf{p}_\mathrm{s}$, rather than in the superconducting phase χ. It is shown that these critical points follow a generalized Poincaré-Hopf sum rule, relating the total winding number to the Euler characteristics of the system. It is shown in the supplementary material (appended after paper II), that by modifying the Euler characteristics, e.g. by making holes in the superconductor, the number and character of the critical points can be directly controlled, hinting at the possibility that they can be engineered [182–189].

7.3 Paper III

The initial studies of phase crystallization considered only scenarios and parameter regimes favorable for its realization, with perfect pairbreaking edges. Surfaces of real materials are rarely so ideal, but are rather influenced by surface disorder and other geometric perturbations. It was the goal of paper III to study the stability of the surface phase crystal against such perturbations, and to discuss experimental conditions where the phase can potentially be observed.

Paper III starts by studying effects that directly reduce the pairbreaking effect and the amount of zero-energy states. In this case, it was the angle between the interface and the d-wave crystal $\hat{\mathbf{a}}$ axis (thus controlling the amount of trajectories that end up being sign-changing), but it could analogously be other effects, e.g. an impurity potential or finite surface transmission. The resulting phase diagram illustrates that at appropriate temperatures, the phase survives down to very low angles, and that it might appear even in completely circular geometries. The system area is then varied, showing that it is truly a surface effect, since system-averaged quantities like total heat-capacity or total current magnitude scales as $1/\mathcal{L}$, where $\mathcal{L}$ is the side-length of the grain. This relation holds down to a critical side-length $\mathcal{L}_\mathrm{c}$, where finite-size effects kick in and the phase is suppressed by superconductivity itself being suppressed, with midgap states filling the whole grain. Area-averaged quantities therefore show a maximal observability for samples with $\mathcal{L} = \mathcal{L}_\mathrm{c}$. Finally, mesoscopic surface roughness is studied, and microscopic roughness is discussed, suggesting a stability of the phase as long as the disorder is within the limits quantified by the previously obtained phase diagrams. In conclusion, the results of paper III might serve as a helpful guideline for both sample fabrication and measurements of symmetry-breaking effects due to surface Andreev states.

7.4 Paper IV

Following the purely numeric study of the surface phase crystal by Håkansson et al. [157], questions were raised in the scientific community whether the phenomenon was a mesoscopic effect due to correlations between multiple pairbreaking interfaces, like Ref. [152]. It was the aim of paper IV to show that this is not the case, by stabilizing the phase at single pairbreaking interfaces, even when completely surrounded by bulk superconductivity. Furthermore, paper IV shows that the periodicity of the phase crystal does not depend on the side-length $\mathcal{L}$ of the pairbreaking interface, as long as $\mathcal{L} \gg \xi_0$, and that finite-size effects influence the periodicity for $\mathcal{L} \sim \xi_0$. Finally, the paper studies the surface density of states with a substantial smearing factor, showing a staggered pattern along the surface of broadened zero-energy peaks, and peaks split symmetrically around zero. These results are temperature-independent, consistent with certain tunneling conductance experiments [67].

8 Conclusions

The purpose of this thesis has been to study inhomogeneous and mesoscopic superconductivity, by using the quasiclassical theory of superconductivity introduced in Ch 2. Chapter 3 used this theoretical framework to study superflow response in bulk systems, where a paradigm was established in which the superflow mainly enters as a Doppler shift in the spectrum, suppressing the superconducting order and reducing the favorable condensation energy with a kinetic-energy cost. In the presence of quasiparticles, for example due to thermal excitations or nodal structures in unconventional superconductors, the results were shown to be modified by the paramagnetic response of the quasiparticles, in particular reducing the kinetic energy. This raised the question whether an environment exists where the superflow can actually be favorable. To answer this, Ch. 4 set out to study the physics of Andreev bound states in the presence of superflow, especially close to specular interfaces of unconventional superconductors, using an equilibrium scattering model. It was shown how scattering connecting order-parameter lobes of different signs leads to pairbreaking, and consequently midgap quasiparticle states with a Lorentzian density of states, centered at the Fermi energy. These states come with a significant cost in energy, but the presence of a superflow lowers the energy again by Doppler shifting the states back to finite energies. Thus, the superflow is in principle stable and energetically favorable at such a surface. Since it is unfavorable in the bulk however, a superflow with an exponentially decay into the bulk was proposed, and also argued to be favorable with an optimal decay length of $\mathcal{L}_y \sim \xi_0$.

To properly treat an inhomogeneous superflow $\boldsymbol{p}_{\mathrm{s}}(\boldsymbol{R})$, Ch. 5 introduced a non-local linear response model, with modified Riccati equations, and an explicit identification of the inhomogeneous superfluid density tensor $K_{ij}(\boldsymbol{R}, \boldsymbol{R}'; T)$. The structure of this tensor was analyzed, containing competing contributions from continuum and bound state terms, as well as from the diagonal and off-diagonal components. Hence, as function of temperature and coordinates, the overall sign of the tensor might change. Chapter 6 introduced a non-local Ginzburg-Landau theory, where the superfluid density directly enters as the coefficient of the kinetic energy

$$F_{\mathrm{sf}} = \frac{1}{2} \int \int dR dR' \; [\boldsymbol{\nabla}\chi(\boldsymbol{R})]_i \, K_{ij}(\boldsymbol{R}, \boldsymbol{R}') \, [\boldsymbol{\nabla}\chi(\boldsymbol{R}')]_j \, . \tag{8.1}$$

The sign of K_{ij} therefore determines if superflow is energetically favorable or not, and the conditions for such a sign change were derived. Minimizing this energy with respect to the phase $\chi(\boldsymbol{R})$, e.g. in a clean d-wave system with a specular [110]-interface, leads to a minimum for

$$\chi(x,y) \propto \left(1+\frac{y}{y_0}\right) e^{-y/y_0} \cos(q_x x), \qquad \Longrightarrow \tag{8.2}$$

$$\boldsymbol{p}_\mathrm{s}(x,y) \propto -\left[q_x \left(1+\frac{y}{y_0}\right) \sin(q_x x), \frac{y}{y_0^2} \cos(q_x x)\right] e^{-y/y_0}, \tag{8.3}$$

which reproduces the superflow and current response as in the self-consistent simulations. It is noted that Lic. Th. [10] does further numeric studies of the phase, as well as of more general properties of mesoscopic superconductivity.

In summary, the thesis proposes an inhomogeneous superconducting ground states, fundamentally different from the Abrikosov and FFLO states, in which the continuous translational symmetry of the superconducting phase χ is broken spontaneously at a finite transition temperature $T^*(\boldsymbol{q}) \approx 0.2T_\mathrm{c}$. The phase acquires a periodic pattern $\chi(\boldsymbol{R}) \propto \cos(\boldsymbol{q} \cdot \boldsymbol{R})$ at a finite wavevector $q_x \approx 0.5/\xi_0$, consequently breaking time-reversal symmetry due to finite superflow $\boldsymbol{p}_\mathrm{s}$ and equilibrium charge currents with peculiar patterns.

The thesis provides a toolbox for studying surface-related phenomena, in particular inhomogeneous superconductivity, topological states, superfluid response, and phase transitions. The derivation of the superfluid density tensor provides a unified approach to treat and explain several previous numerical observations. These results raises several questions, providing an interesting topic for further research both theoretically and experimentally. The following section goes through some of these open questions.

8.1 Open questions

For decades, both experimentalists and theoreticians have studied the physics of Andreev bound states at surfaces of unconventional superconductors. Still, there are many open questions about the realization and properties of these states, and how they influence mesoscopic superconductors. The midgap states come at a significant cost in the free energy, and theory has since long predicted the existence of phases characterized by spontaneous symmetry breaking, providing mechanisms which shift the states to finite energies. One such scenario is spontaneous surface currents and magnetic fields. Experimental verification of these symmetry-broken phases has been a controversial topic, however, as there are many experiments that show positive signatures [9, 161–167], while there are several that do not, and in particular, none that show direct imaging of the proposed spontaneous fields or currents [168–172]. The phase crystallization proposed in Ref. [157] and this thesis gives a possible explanation to the discrepancy, namely that the superflow exist only in a small region $\mathcal{L}_y \sim 2\pi\xi_0 \ll \lambda_0$ of the surface, which would make the spontaneous currents and fields extremely small in spatial extent. Furthermore, the oscillating nature of the phase leads to neighboring current loops with opposite circulation, implying zero net flow and magnetic flux over length scale considerably larger than $\mathcal{L}_y$. This means that the phase could easily have escaped previous observation. If such a phase truly exists, how can it be verified experimentally, and does it have any interesting effects in nanoscale superconducting devices? If on the other hand the phase does not exist, then why not? Is there a more ordered state, like the proposed ferromagnetic ordering [149–151], a subdominant order [65, 145–148], or perhaps a completely overlooked mechanism that is responsible for the positive signatures in experiment? It would certainly be interesting to see how a combination and competition of these effects play out.

While the thesis initially set out to study these issues, the theoretical model which emerged to describe the numeric calculations highlighted something much more fundamental. Namely, the role of spatial variations in the superconducting phase $\chi(\boldsymbol{R})$, as a means to minimize the energy and drive phase transitions, especially in an environment when the superconducting order is inhomogeneous and suppressed. The conditions derived for the instability were shown to be satisfied at an interface with surface bound states, but would it be possible to satisfy them in a bulk system? How are the conditions altered in a $3D$ system, and would they be easier to satisfy there? Furthermore, what are the fundamental excitations of such a phase, and are there any propagating degrees of freedom (e.g. density waves)? This would prove interesting questions, as the study of various density-waves is currently a very active area of research [190].

The appended papers and Lic. Th. [10] discussed other experimental signatures, mainly related to heat capacity measurements [191, 192], or direct imaging techniques [193–200]. Would such measurements provide a positive signature?

Furthermore, midgap states are known to modify the penetration-depth [118] and the first vortex entrance [201]. Perhaps the sudden Doppler shift of the midgap states below the transition temperature T^*, due to spontaneous superflow, could provide another signature? How would the transport characteristics be modified by the phase in narrow superconducting grains? To answer this question, the dynamics of the phase and its stability in non-equilibrium would have to be studied, e.g. thermal currents and electrodynamical currents. Does it couple to any dynamical modes [202]? Furthermore, paper III discussed the stability against atomic surface roughness, impurities and disorder, but how would the phase diagrams in the presence of these effects look? It is well-known that impurities have a strong suppressing effect on e.g. d-wave superconductivity [131, 132]. Could this perhaps create another unfavorable environment where the phase variations can again act to heal superconductivity, and if so even in a bulk system? It was proposed that other possibilities to satisfy the conditions for the phase are multicomponent order parameters, non-circular Fermi surfaces and spin-population imbalance due to a Zeeman field. How is the phase influenced by these effects, and is there an overlap with the FFLO phase diagram? To answer the latter question, amplitude variations would have to be taken into full consideration, as done in the self-consistent numerics.

A very easily accessible bulk system where there are plenty of states close to zero energy is the normal state. Hence, if the conditions for the sign change of the superfluid density were to be satisfied close to this transition in some way, e.g. by broken symmetries in an unconventional superconductor or external perturbations, then phase variations could play an important role in determining the ground state at the transition. Hence, in such systems, it would be crucial to take into account not just amplitude variations as is commonly the case, but also phase variations, necessitating a more general and non-local treatment similar to the method used in this thesis. Another question then arises, namely how the phase responds to phase fluctuations [203].

In closing, an analytic handle on the phase was possible due to an extension to a non-local Ginzburg-Landau theory with gradient terms of the form

$$f(R) = K(R)\,|\boldsymbol{\nabla}\Delta(\boldsymbol{R})|^2 \longrightarrow f(R,R') = \int dR'\,[\boldsymbol{\nabla}\Delta(\boldsymbol{R})]\cdot\boldsymbol{K}(\boldsymbol{R},\boldsymbol{R}')\cdot[\boldsymbol{\nabla}\Delta(\boldsymbol{R}')]\,. \tag{8.4}$$

The structure of the kernel directly highlights the role of phase variations and non-local correlations. Non-local interactions are known to play an important role in other fields that employ a phenomenological Ginzburg-Landau theory, like weak crystallization [20], liquid crystals [183, 204], and even in biological systems [205–207]. Could a similar extension provide new insight in such diverse fields?

Appendices

Appendix A

Gauge transformations

A gauge transformation will now be introduced, that removes the phase dependence from the order parameter and puts it explicitly in the Eilenberger equation. Consider the unitary operator $\hat{U}$ depending on the Nambu-space Pauli matrix $\hat{\tau}_3$

$$\hat{U} = e^{i\hat{\tau}_3\chi/2} = \begin{pmatrix} e^{i\chi/2} & 0 \\ 0 & e^{-i\chi/2} \end{pmatrix}, \tag{A.1}$$

$$\hat{U}^\dagger = e^{-i\hat{\tau}_3\chi/2} = \begin{pmatrix} e^{-i\chi/2} & 0 \\ 0 & e^{i\chi/2} \end{pmatrix}. \tag{A.2}$$

This operator removes the phase from the propagator and the order parameter

$$\hat{g} = \hat{U}\hat{g}_p\hat{U}^\dagger = \begin{pmatrix} g_p & f_p e^{i\chi} \\ \tilde{f}_p e^{-i\chi} & \tilde{g}_p \end{pmatrix}, \tag{A.3}$$

$$\hat{U}^\dagger\hat{\Delta}\hat{U} = \begin{pmatrix} 0 & \Delta e^{-i\chi} \\ \tilde{\Delta} e^{i\chi} & 0 \end{pmatrix} = \begin{pmatrix} 0 & \Delta_p \\ \tilde{\Delta}_p & 0 \end{pmatrix} = \hat{\Delta}_p, \tag{A.4}$$

where $\Delta_p(\boldsymbol{R}) = |\Delta(\boldsymbol{R})| = \tilde{\Delta}_p(\boldsymbol{R})$. It is noted that

$$\boldsymbol{\nabla}_R\hat{U} = \frac{i}{2}\left(\boldsymbol{\nabla}_R\chi\right)\hat{\tau}_3\hat{U}, \tag{A.5}$$

$$\boldsymbol{\nabla}_R\hat{U}^\dagger = -\frac{i}{2}\left(\boldsymbol{\nabla}_R\chi\right)\hat{\tau}_3\hat{U}^\dagger. \tag{A.6}$$

Substituting $\hat{g}$ into the Eilenberger equation and sandwiching by $\hat{U}^\dagger$ and $\hat{U}$ yields

$$0 = \hat{U}^\dagger\left[\left(z_A\hat{\tau}_3 - \hat{\Delta}\right), \hat{U}\hat{g}_p\hat{U}^\dagger\right]\hat{U} + \hat{U}^\dagger i\hbar\boldsymbol{v}_\mathrm{F}\cdot\boldsymbol{\nabla}_R\left(\hat{U}\hat{g}_p\hat{U}^\dagger\right)\hat{U} \tag{A.7}$$

$$= \left[\left(\left(z_A - \frac{\hbar}{2}\boldsymbol{\nabla}_R\chi\right)\hat{\tau}_3 - \hat{\Delta}_p\right), \hat{g}_p\right] + i\hbar\boldsymbol{v}_\mathrm{F}\cdot\boldsymbol{\nabla}_R\hat{g}_p. \tag{A.8}$$

Introducing the gauge invariant superflow $\boldsymbol{p}_\mathrm{s} = \hbar\boldsymbol{\nabla}\chi/2 - e\boldsymbol{A}/c$ and the energy

$$z_p \equiv z - \boldsymbol{v}_\mathrm{F}\cdot\boldsymbol{p}_\mathrm{s} = z - \left(\frac{\hbar}{2}\boldsymbol{\nabla}\chi - \frac{e}{c}\boldsymbol{A}\right), \tag{A.9}$$

leads to the gauge transformed Eilenberger equation

$$0 = \left[\left(z_p\hat{\tau}_3 - \hat{\Delta}_p\right), \hat{g}_p\right] + i\hbar\boldsymbol{v}_\mathrm{F}\cdot\boldsymbol{\nabla}_R\hat{g}_p. \tag{A.10}$$

Appendix B

The Riccati formalism

In this appendix, the quasiclassical Green function will be rewritten in terms of electron-hole coherence functions, through the use of the so-called Shelankov projectors [75, 90, 97]. The purpose of this is to automatically encode the normalization condition of the quasiclassical Green function into the equations, thus removing spurious solutions and ensuring numerical stability.

In the first section, the Shelankov projectors and the coherence functions are introduced, and it is proven that these projectors fulfill certain properties due to the normalization condition. In the second section, expressions for the spin-space Green functions are obtained. The projectors are substituted into the Eilenberger equation in the third section, recasting the latter into a set of coupled Riccati ordinary differential equations. The Riccati amplitudes to be solved for in these equations are the coherence functions γ and $\tilde{\gamma}$, to be defined in this appendix. In the fourth section, the Riccati equations are solved analytically under certain assumptions.

B.1 Projectors and coherence functions

A projector P is a linear transformation from a vector space V onto itself that fulfills idempotency, which means that having projected onto a state x, nothing changes upon applying the same projection operator again,

$$P^2 x = Px, \quad \forall x \in V. \tag{B.1}$$

Following the formalism of Ref. [90], the projection operators for retarded particle-like (+) and hole-like (−) excitations in Nambu space are introduced as

$$\hat{P}_+ = \frac{1}{2}\left(\hat{1} + \frac{\hat{g}}{-i\pi}\right) \tag{B.2}$$

$$\hat{P}_- = \frac{1}{2}\left(\hat{1} - \frac{\hat{g}}{-i\pi}\right), \tag{B.3}$$

respectively. It is straightforward to prove that $\hat{P}_\pm$ in Eqs. (B.2) and (B.3) are projection operators fulfilling idempotency

$$\begin{aligned}
\hat{P}_\pm^2 &= \frac{1}{4}\left(\hat{1} \pm \frac{\hat{g}}{-i\pi}\right)^2 \\
&= \frac{1}{4}\left(\hat{1} + \frac{\hat{g}^2}{-\pi^2} \pm 2\frac{\hat{g}}{-i\pi}\right) \\
&= \frac{1}{2}\left(\hat{1} \pm \frac{\hat{g}}{-i\pi}\right) = \hat{P}_\pm, \qquad \text{(B.4)}
\end{aligned}$$

where the normalization condition $\hat{g}^2 = -\pi^2\hat{1}$ was used in the last step. In addition, the projectors are complementary, since

$$\hat{P}_\pm + \hat{P}_\mp = \frac{1}{2}\left(\hat{1} \pm \frac{\hat{g}}{-i\pi}\right) + \frac{1}{2}\left(\hat{1} \mp \frac{\hat{g}}{-i\pi}\right) = \hat{1}. \qquad \text{(B.5)}$$

A set of operators which are both idempotent and complementary are also orthogonal

$$\begin{aligned}
\hat{P}_\pm\hat{P}_\mp &= \frac{1}{2}\left(\hat{1} \pm \frac{\hat{g}}{-i\pi}\right)\frac{1}{2}\left(\hat{1} \mp \frac{\hat{g}}{-i\pi}\right) \\
&= \frac{1}{4}\left(\hat{1} - \frac{\hat{g}^2}{-\pi^2}\right) \\
&= \frac{1}{4}\left(\hat{1} - \hat{1}\right) = \hat{0}, \qquad \text{(B.6)}
\end{aligned}$$

where the normalization condition was used again. An orthogonal projection operator P can be cast on a general form

$$P = A(A^TA)^{-1}A^T, \qquad \text{(B.7)}$$

where the middle term $(A^TA)^{-1}$ is a normalizing factor. The analogy of the transpose in Nambu space is particle-hole conjugation, denoted by the "tilde operator" $\tilde{A}(\boldsymbol{p}_F, \boldsymbol{R}; z, t) = A^*(-\boldsymbol{p}_F, \boldsymbol{R}; -z^*, t)$. The projection operators can then be decomposed into the retarded, complex, spin-matrices $\gamma(\mathbf{p}_F, \mathbf{R}; z)$ and $\tilde{\gamma}(\mathbf{p}_F, \mathbf{R}; z)$ as

$$\begin{aligned}
\hat{P}_+ &= \begin{pmatrix} 1 \\ -\tilde{\gamma} \end{pmatrix}(1 - \gamma\tilde{\gamma})^{-1}(1, \gamma) \qquad \text{(B.8)} \\
\hat{P}_- &= \begin{pmatrix} -\gamma \\ 1 \end{pmatrix}(1 - \tilde{\gamma}\gamma)^{-1}(\tilde{\gamma}, 1). \qquad \text{(B.9)}
\end{aligned}$$

Here, the matrix inversion is defined through $(1 + ab)^{-1}(1 + ab) = 1$. It will now be shown that this new form of $\hat{P}_\pm$ also satisfies idempotency, complementarity and orthogonality. Using the matrix inversion relation, idempotency is shown

$$\begin{aligned}\hat{P}_+^2 &= \begin{pmatrix} 1 \\ -\tilde{\gamma} \end{pmatrix}(1-\gamma\tilde{\gamma})^{-1}(1,\gamma)\begin{pmatrix} 1 \\ -\tilde{\gamma} \end{pmatrix}(1-\gamma\tilde{\gamma})^{-1}(1,\gamma) \\ &= \begin{pmatrix} 1 \\ -\tilde{\gamma} \end{pmatrix}(1-\gamma\tilde{\gamma})^{-1}(1-\gamma\tilde{\gamma})(1-\gamma\tilde{\gamma})^{-1}(1,\gamma) \\ &= \begin{pmatrix} 1 \\ -\tilde{\gamma} \end{pmatrix}(1-\gamma\tilde{\gamma})^{-1}(1,\gamma) = \hat{P}_+ \qquad \text{(B.10)} \\ \hat{P}_-^2 &= \begin{pmatrix} -\gamma \\ 1 \end{pmatrix}(1-\tilde{\gamma}\gamma)^{-1}(\tilde{\gamma},1)\begin{pmatrix} -\gamma \\ 1 \end{pmatrix}(1-\tilde{\gamma}\gamma)^{-1}(\tilde{\gamma},1) \\ &= \begin{pmatrix} -\gamma \\ 1 \end{pmatrix}(1-\tilde{\gamma}\gamma)^{-1}(1-\tilde{\gamma}\gamma)(1-\tilde{\gamma}\gamma)^{-1}(\tilde{\gamma},1) \\ &= \begin{pmatrix} -\gamma \\ 1 \end{pmatrix}(1-\tilde{\gamma}\gamma)^{-1}(\tilde{\gamma},1) = \hat{P}_-. \qquad \text{(B.11)}\end{aligned}$$

Using the relation $(1+ab)^{-1}a = a(1+ba)^{-1}$, complementarity is proven

$$\begin{aligned}\hat{P}_+ + \hat{P}_- &= \begin{pmatrix} 1 \\ -\tilde{\gamma} \end{pmatrix}(1-\gamma\tilde{\gamma})^{-1}(1,\gamma) + \begin{pmatrix} -\gamma \\ 1 \end{pmatrix}(1-\tilde{\gamma}\gamma)^{-1}(\tilde{\gamma},1) \\ &= \begin{pmatrix} (1-\gamma\tilde{\gamma})^{-1} & (1-\gamma\tilde{\gamma})^{-1}\gamma \\ -\tilde{\gamma}(1-\gamma\tilde{\gamma})^{-1} & -\tilde{\gamma}(1-\gamma\tilde{\gamma})^{-1}\gamma \end{pmatrix} \\ &\quad + \begin{pmatrix} -\gamma(1-\tilde{\gamma}\gamma)^{-1}\tilde{\gamma} & -\gamma(1-\tilde{\gamma}\gamma)^{-1} \\ (1-\tilde{\gamma}\gamma)^{-1}\tilde{\gamma} & (1-\tilde{\gamma}\gamma)^{-1} \end{pmatrix} \\ &= \begin{pmatrix} (1-\gamma\tilde{\gamma})^{-1} - \gamma\tilde{\gamma}(1-\gamma\tilde{\gamma})^{-1} & (1-\gamma\tilde{\gamma})^{-1}\gamma - (1-\gamma\tilde{\gamma})^{-1}\gamma \\ -\tilde{\gamma}(1-\gamma\tilde{\gamma})^{-1} + \tilde{\gamma}(1-\gamma\tilde{\gamma})^{-1} & -(1-\gamma\tilde{\gamma})^{-1}\tilde{\gamma}\gamma + (1-\gamma\tilde{\gamma})^{-1} \end{pmatrix} \\ &= \begin{pmatrix} 1 & 0 \\ 0 & 1 \end{pmatrix} = \hat{1}. \qquad \text{(B.12)}\end{aligned}$$

Orthogonality still holds

$$\begin{aligned}\hat{P}_+\hat{P}_- &= \begin{pmatrix} 1 \\ -\tilde{\gamma} \end{pmatrix}(1-\gamma\tilde{\gamma})^{-1}(1,\gamma)\begin{pmatrix} -\gamma \\ 1 \end{pmatrix}(1-\tilde{\gamma}\gamma)^{-1}(\tilde{\gamma},1) \\ &= \begin{pmatrix} 1 \\ -\tilde{\gamma} \end{pmatrix}(1-\gamma\tilde{\gamma})^{-1}(-\gamma+\gamma)(1-\tilde{\gamma}\gamma)^{-1}(\tilde{\gamma},1) \\ &= \hat{0} \qquad \text{(B.13)} \\ \hat{P}_-\hat{P}_+ &= \begin{pmatrix} -\gamma \\ 1 \end{pmatrix}(1-\tilde{\gamma}\gamma)^{-1}(\tilde{\gamma},1)\begin{pmatrix} 1 \\ -\tilde{\gamma} \end{pmatrix}(1-\gamma\tilde{\gamma})^{-1}(1,\gamma) \\ &= \begin{pmatrix} -\gamma \\ 1 \end{pmatrix}(1-\tilde{\gamma}\gamma)^{-1}(\tilde{\gamma}-\tilde{\gamma})(1-\gamma\tilde{\gamma})^{-1}(1,\gamma) \\ &= \hat{0}, \qquad \text{(B.14)}\end{aligned}$$

since a factors of $(-\gamma+\gamma)=(\tilde{\gamma}-\tilde{\gamma})=0$ appear in both expressions. Rewriting Eqs. (B.2)–(B.3), it is noted that

$$\begin{aligned}\hat{g} &= -i\pi(\hat{P}_+-\hat{P}_-) \quad &(B.15)\\ &= \mp i\pi(2\hat{P}_\pm-\hat{1}). \quad &(B.16)\end{aligned}$$

It is now possible to derive Eqs. (2.28)–(2.29), which expresses the quasiclassical Green function in terms of the coherence functions. This is done by inserting the projectors in Eqs. (B.8)–(B.9) into Eq. (B.15) to obtain

$$\hat{g} = -i\pi\hat{N}\otimes\begin{pmatrix}(\sigma_0+\gamma\otimes\tilde{\gamma}) & 2\gamma\\ -2\tilde{\gamma} & -(\sigma_0+\tilde{\gamma}\otimes\gamma)\end{pmatrix}, \quad (B.17)$$

$$\hat{N} = \begin{pmatrix}(\sigma_0-\gamma\otimes\tilde{\gamma})^{-1} & 0\\ 0 & (\sigma_0-\tilde{\gamma}\otimes\gamma)^{-1}\end{pmatrix}, \quad (B.18)$$

where the spin-dependence of the coherence functions is written explicitly as

$$\begin{aligned}\gamma &= (\gamma_s+\boldsymbol{\gamma}_t\cdot\boldsymbol{\sigma})\,i\sigma_2, \quad &(B.19)\\ \tilde{\gamma} &= i\sigma_2\,(\tilde{\gamma}_s-\tilde{\boldsymbol{\gamma}}_t\cdot\boldsymbol{\sigma}). \quad &(B.20)\end{aligned}$$

Comparing Eq. (B.17) with Eq. (2.5), it is seen that the coherence functions can be expressed in terms of the quasiparticle and pair propagators as $\gamma=-(i\pi-g)^{-1}f$ and $\tilde{\gamma}=(i\pi+\tilde{g})^{-1}\tilde{f}$. Noting that the inverse is nothing but a projector in spin-space, one can see that it is possible to interpret the coherence functions as the particle- and hole-like projections of the pair propagator in spin-space.

B.2 Scalar spin-singlet Green functions

For a unitary singlet system with $\gamma=\gamma_s i\sigma_2$ and $\tilde{\gamma}=i\sigma_2\tilde{\gamma}_s$, the Green function $\hat{g}$ in Nambu $\otimes$ spin-space is

$$\hat{g} = \begin{pmatrix}g_0\sigma_0+\boldsymbol{g}\cdot\boldsymbol{\sigma} & (f_s+\boldsymbol{f}_t\cdot\boldsymbol{\sigma})\,i\sigma_2\\ i\sigma_2\,(\tilde{f}_s-\tilde{\boldsymbol{f}}_t\cdot\boldsymbol{\sigma}) & \sigma_2\,(\tilde{g}_0-\tilde{\boldsymbol{g}}\cdot\boldsymbol{\sigma})\,\sigma_2\end{pmatrix} \overset{\text{singlet}}{=} \begin{pmatrix}g_0\sigma_0 & f_s i\sigma_2\\ i\sigma_2\tilde{f}_s & \tilde{g}_0\sigma_0\end{pmatrix} \quad (B.21)$$

Substituting the coherence functions into the Green function in Eq. (B.17) and comparing to Eq. (B.21), the scalar Green functions are found to be

$$\begin{aligned}g_0 &= -i\pi\frac{1-\gamma_s\tilde{\gamma}_s}{1+\gamma_s\tilde{\gamma}_s}, \quad &(B.22)\\ \tilde{g}_0 &= i\pi\frac{1-\gamma_s\tilde{\gamma}_s}{1+\gamma_s\tilde{\gamma}_s}, \quad &(B.23)\\ f_s &= -2i\pi\frac{\gamma_s}{1+\gamma_s\tilde{\gamma}_s}, \quad &(B.24)\\ \tilde{f}_s &= 2i\pi\frac{\tilde{\gamma}_s}{1+\gamma_s\tilde{\gamma}_s}. \quad &(B.25)\end{aligned}$$

B.3 Derivation of Riccati equations

The quasiclassical Green function $\hat{g} = \mp i\pi(2\hat{P}_\pm - \hat{1})$ in Eq. (B.16) will now be substituted into the Eilenberger equation in Eq. (2.3). It is noted that $\hat{1}$ commutes with every operator in Eq. (2.3), and that $\nabla_R \hat{1} = 0$. Substituting $\hat{g} = \mp i\pi(2\hat{P}_\pm - \hat{1})$ and re-scaling then yields equations of motion for the Shelankov projectors

$$i\hbar \boldsymbol{v}_F \cdot \boldsymbol{\nabla}_R \hat{P}_\pm + \left[z\hat{\tau}_3 - \hat{h}, \hat{P}_\pm\right] = \hat{0}, \tag{B.26}$$

where $z\hat{\tau}_3$ and $\hat{h}$ are the diagonal and off-diagonal self-energies, respectively. Choosing the $+$ branch and acting with $\hat{P}_-$ from the left or right yields

$$\begin{aligned} i\hbar \boldsymbol{v}_\mathrm{F} \cdot \hat{P}_- \boldsymbol{\nabla}_R \hat{P}_+ + \hat{P}_-(z\hat{\tau}_3 - \hat{h})\hat{P}_+ &= \hat{0} && \text{(B.27)} \\ i\hbar \boldsymbol{v}_\mathrm{F} \cdot (\boldsymbol{\nabla}_R \hat{P}_+)\hat{P}_- - \hat{P}_+(z\hat{\tau}_3 - \hat{h})\hat{P}_- &= \hat{0}, && \text{(B.28)} \end{aligned}$$

respectively, where orthogonality of the projectors have been used. The gradient term in Eq. (B.27) can be rewritten as

$$\begin{aligned} \hat{P}_- \boldsymbol{\nabla}_R \hat{P}_+ &= \hat{P}_- \begin{pmatrix} 0 \\ -\boldsymbol{\nabla}_R \tilde{\gamma} \end{pmatrix} (1-\gamma\tilde{\gamma})^{-1}(1,\gamma) \\ &\quad + \hat{P}_- \begin{pmatrix} 1 \\ -\tilde{\gamma} \end{pmatrix} \boldsymbol{\nabla}_R (1-\gamma\tilde{\gamma})^{-1}(1,\gamma) \\ &\quad + \hat{P}_- \begin{pmatrix} 1 \\ -\tilde{\gamma} \end{pmatrix} (1-\gamma\tilde{\gamma})^{-1}(0,\boldsymbol{\nabla}_R \gamma) \\ &= \hat{P}_- \begin{pmatrix} 0 \\ -\boldsymbol{\nabla}_R \tilde{\gamma} \end{pmatrix} (1-\gamma\tilde{\gamma})^{-1}(1,\gamma), \end{aligned} \tag{B.29}$$

due to orthogonality between the last factor in $\hat{P}_-$ and $\left(\begin{smallmatrix} 1 \\ -\tilde{\gamma} \end{smallmatrix}\right)$. Similarly,

$$(\boldsymbol{\nabla}_R \hat{P}_+)\hat{P}_- = \begin{pmatrix} 1 \\ -\tilde{\gamma} \end{pmatrix} (1-\gamma\tilde{\gamma})^{-1}(0,\boldsymbol{\nabla}_R \gamma)\hat{P}_-. \tag{B.30}$$

Equations (B.27) and (B.28) are written explicitly as

$$\begin{aligned} \hat{0} &= i\hbar \boldsymbol{v}_F \cdot \begin{pmatrix} -\gamma \\ 1 \end{pmatrix} (1-\tilde{\gamma}\gamma)^{-1}(\tilde{\gamma},1) \begin{pmatrix} 0 \\ -\boldsymbol{\nabla}_R \tilde{\gamma} \end{pmatrix} (1-\gamma\tilde{\gamma})^{-1}(1,\gamma) \\ &\quad + \begin{pmatrix} -\gamma \\ 1 \end{pmatrix} (1-\tilde{\gamma}\gamma)^{-1}(\tilde{\gamma},1)(z\hat{\tau}_3 - \hat{h}) \begin{pmatrix} 1 \\ -\tilde{\gamma} \end{pmatrix} (1-\gamma\tilde{\gamma})^{-1}(1,\gamma) && \text{(B.31)} \\ \hat{0} &= i\hbar \boldsymbol{v}_F \cdot \begin{pmatrix} 1 \\ -\tilde{\gamma} \end{pmatrix} (1-\gamma\tilde{\gamma})^{-1}(0,\boldsymbol{\nabla}_R \gamma) \begin{pmatrix} -\gamma \\ 1 \end{pmatrix} (1-\tilde{\gamma}\gamma)^{-1}(\tilde{\gamma},1) \\ &\quad + \begin{pmatrix} 1 \\ -\tilde{\gamma} \end{pmatrix} (1-\gamma\tilde{\gamma})^{-1}(1,\gamma)(z\hat{\tau}_3 - \hat{h}) \begin{pmatrix} -\gamma \\ 1 \end{pmatrix} (1-\tilde{\gamma}\gamma)^{-1}(\tilde{\gamma},1), && \text{(B.32)} \end{aligned}$$

respectivley. Equation (B.31) is simiplified by multiplying from the left with the inverse of $\left(\begin{smallmatrix}-\gamma\\1\end{smallmatrix}\right)(1-\tilde{\gamma}\gamma)^{-1}$, and from the right with the inverse of $(1-\gamma\tilde{\gamma})^{-1}(1,\gamma)$. Equation (B.32) is simiplified by multiplying from the left with the inverse of $\left(\begin{smallmatrix}1\\-\tilde{\gamma}\end{smallmatrix}\right)(1-\gamma\tilde{\gamma})^{-1}$, and from the right with the inverse of $(1-\tilde{\gamma}\gamma)^{-1}(\tilde{\gamma},1)$. This yields

$$i\hbar\boldsymbol{v}_F\cdot(\tilde{\gamma},1)\left(\begin{array}{c}0\\-\boldsymbol{\nabla}_R\tilde{\gamma}\end{array}\right)+(\tilde{\gamma},1)(z\hat{\tau}_3-\hat{h})\left(\begin{array}{c}1\\-\tilde{\gamma}\end{array}\right) = \hat{0} \tag{B.33}$$

$$i\hbar\boldsymbol{v}_F\cdot(0,\boldsymbol{\nabla}_R\gamma)\left(\begin{array}{c}-\gamma\\1\end{array}\right)-(1,\gamma)(z\hat{\tau}_3-\hat{h})\left(\begin{array}{c}-\gamma\\1\end{array}\right) = \hat{0}. \tag{B.34}$$

For the problems studied in this thesis, the self-energies are

$$z\hat{\tau}_3-\hat{h}=\left(\begin{array}{cc}z & \Delta\\-\tilde{\Delta} & -z\end{array}\right). \tag{B.35}$$

The Riccati equations (in spin-space) are

$$[i\hbar\boldsymbol{v}_\mathrm{F}\cdot\boldsymbol{\nabla}_R+2z]\,\gamma = \gamma\tilde{\Delta}\gamma-\Delta, \tag{B.36}$$

$$[i\hbar\boldsymbol{v}_\mathrm{F}\cdot\boldsymbol{\nabla}_R-2z]\,\tilde{\gamma} = \tilde{\gamma}\Delta\tilde{\gamma}-\tilde{\Delta}, \tag{B.37}$$

where in the presence of electromagnetic fields, $z\to z_A=z+e\boldsymbol{v}_\mathrm{F}\cdot\boldsymbol{A}/c$. In App. A, a gauge transformation was introduced that renders the order parameter real, and replaces $e\boldsymbol{A}/c\to-\boldsymbol{p}_\mathrm{s}$ in the Eilenberger equation, where $\boldsymbol{p}_\mathrm{s}=\hbar\boldsymbol{\nabla}\chi/2-e\boldsymbol{A}/c$ is the gauge invariant superfluid momentum. This superflow carries over trivially to the Riccati equations (in spin-space)

$$[i\hbar\boldsymbol{v}_\mathrm{F}\cdot\boldsymbol{\nabla}_R+2z_p]\,\gamma_p = \gamma_p\tilde{\Delta}_p\gamma_p-\Delta_p, \tag{B.38}$$

$$[i\hbar\boldsymbol{v}_\mathrm{F}\cdot\boldsymbol{\nabla}_R-2z_p]\,\tilde{\gamma}_p = \tilde{\gamma}_p\Delta_p\tilde{\gamma}_p-\tilde{\Delta}_p. \tag{B.39}$$

B.4 Analytic solutions

In this section, the Riccati equation in Eqs. (B.38)–(B.39) will be solved analytically for two different systems. The first system is a bulk superconductor with a homogeneous order parameter, and the second with a step function order parameter. An order parameter that can be discretized into a piecewise constant function (i.e. appropriate for numeric implementations) can be obtained from the step function solution. These equations can then be solved together with the gap equation to obtain a self-consistent solution.

Just like in the rest of the thesis, a clean superconductor in equilibrium and in the weak coupling regime is assumed, with spin-degeneracy, and a cylindrically symmetric Fermi surface. To make the notation and calculation simple, a spin-singlet order parameter is considered, in the same gauge as in App. A, i.e. with a real order parameter ($\tilde{\Delta} = \Delta^* = \Delta$) and with explicit dependence of the gauge invariant superflow. Starting from Eqs. (B.38)-(B.39), the Riccati equations in spin-space are reduced to degenerate scalar equations with extra signs from factors $(i\sigma_2)^2 = -\sigma_0$. The trajectory $\boldsymbol{s}(y) = \boldsymbol{s}_0 + y\hat{\boldsymbol{v}}_\mathrm{F}$ is considered, and the scalar equations are

$$\begin{aligned} \hbar v_\mathrm{F}\partial_y\gamma &= i\Delta + 2iz_p\gamma + i\tilde{\Delta}\gamma^2, && \text{(B.40)}\\ \hbar v_\mathrm{F}\partial_y\tilde{\gamma} &= i\tilde{\Delta} - 2iz_p\tilde{\gamma} + i\Delta\tilde{\gamma}^2, && \text{(B.41)} \end{aligned}$$

where it is reminded that $z_p = z - \boldsymbol{v}_\mathrm{F} \cdot \boldsymbol{p}_\mathrm{s}(\boldsymbol{R})$. These equations are first-order, non-linear, ODE:s known as Riccati equations, of the form

$$f'(y) = q_0(y) + q_1(y)f(y) + q_2(y)f^2(y), \tag{B.42}$$

with the solution

$$f(y) = f_\mathrm{h} + w^{-1}(y), \tag{B.43}$$

where f_h is the homogeneous solution, and $w(y)$ satisfies the linear ODE

$$w'(y) + \left[q_1(y) + 2q_2(y)f_\mathrm{h}\right] w(y) = -q_2(y). \tag{B.44}$$

Matching terms for the γ equation, it is found that

$$\begin{aligned} q_0(y) &= \frac{i\Delta}{\hbar v_\mathrm{F}}, && \text{(B.45)}\\ q_1(y) &= \frac{2iz_p}{\hbar v_\mathrm{F}}, && \text{(B.46)}\\ q_2(y) &= \frac{i\tilde{\Delta}}{\hbar v_\mathrm{F}}, && \text{(B.47)} \end{aligned}$$

and similar for the $\tilde{\gamma}$ equation. The homogeneous parts satisfy the equations

$$\begin{aligned} 0 &= \Delta + 2z_p f_\mathrm{h} + \tilde{\Delta} f_\mathrm{h}^2, && \text{(B.48)}\\ 0 &= \tilde{\Delta} - 2z_p \tilde{f}_\mathrm{h} + \Delta \tilde{f}_\mathrm{h}^2, && \text{(B.49)} \end{aligned}$$

with the solutions

$$\begin{aligned} f_\mathrm{h} &= \frac{-\Delta}{z_p \pm i\Omega}, && \text{(B.50)}\\ \tilde{f}_\mathrm{h} &= \frac{\tilde{\Delta}}{z_p \pm i\Omega}, && \text{(B.51)}\\ \Omega &\equiv \sqrt{|\Delta|^2 - z_p^2}. && \text{(B.52)} \end{aligned}$$

The correct choice of sign depends on which propagator is considered (e.g. Matsubara $z = i\varepsilon_n$, Retarded $z = \varepsilon + i0^+$, or Advanced $z = \varepsilon + i0^-$). To figure out which sign is correct, it is noted that the theory under consideration is in the low-energy, long-wavelength regime, where the results should not depend on high-energy contributions. This means that the homogeneous solutions should be bounded and vanish as $\varepsilon_n, \varepsilon \to \infty$. Hence, the upper sign $(+)$ is chosen for Matsubara and Retarded propagators, while the lower sign $(-)$ is chosen for Advanced propagators. This thesis works exclusively in equilibrium in terms of Matsubara and Retarded propagators, and the homogeneous parts are simply written

$$f_{\mathrm{h}} = \frac{-\Delta}{z_p + i\Omega}, \tag{B.53}$$

$$f_{\mathrm{h}} = \frac{\tilde{\Delta}}{z_p + i\Omega}. \tag{B.54}$$

It is noted that these solutions satisfy particle-hole symmetry (the "tilde-symmetry"), time-reversal symmetry, and that they are purely imaginary in the case of Matsubara propagators. This gives the linear ODEs

$$w'(y) + \frac{1}{\hbar v_{\mathrm{F}}}\left[2iz_p + 2i\tilde{\Delta}\frac{-\Delta}{z_p + i\Omega}\right] w(y) = \frac{-i\tilde{\Delta}}{\hbar v_{\mathrm{F}}}, \tag{B.55}$$

$$\tilde{w}'(y) + \frac{1}{\hbar v_{\mathrm{F}}}\left[-2iz_p + 2i\Delta\frac{\tilde{\Delta}}{z_p + i\Omega}\right] \tilde{w}(y) = \frac{-i\Delta}{\hbar v_{\mathrm{F}}}, \tag{B.56}$$

with the solutions

$$w^{-1}(y) = \frac{2i\Omega C \exp(-y/y_0)}{1 - \tilde{\Delta} C \exp(-y/y_0)}, \tag{B.57}$$

$$\tilde{w}^{-1}(y) = \frac{2i\Omega \tilde{C} \exp(+y/y_0)}{1 + \Delta \tilde{C} \exp(+y/y_0)}, \tag{B.58}$$

$$y_0 \equiv \frac{\hbar v_{\mathrm{F}}}{2\Omega} = \pi \left(\frac{\Omega}{k_{\mathrm{B}} T_{\mathrm{c}}}\right)^{-1} \xi_0, \tag{B.59}$$

$$\xi_0 \equiv \frac{\hbar v_{\mathrm{F}}}{2\pi k_{\mathrm{B}} T_{\mathrm{c}}}, \tag{B.60}$$

finally yielding the homogeneous and inhomogeneous coherence functions

$$\gamma_{\mathrm{h}} = \frac{-\Delta}{z_p + i\Omega}, \tag{B.61}$$

$$\tilde{\gamma}_{\mathrm{h}} = \frac{\tilde{\Delta}}{z_p + i\Omega}, \tag{B.62}$$

$$\gamma = \gamma_h + \frac{2i\Omega C \exp(-y/y_0)}{1 - \tilde{\Delta} C \exp(-y/y_0)}, \tag{B.63}$$

$$\tilde{\gamma} = \tilde{\gamma}_h + \frac{2i\Omega \tilde{C} \exp(+y/y_0)}{1 + \Delta \tilde{C} \exp(+y/y_0)}. \tag{B.64}$$

Here, C and $\tilde{C}$ are integration constants, and y_0 is the length scale over which the coherence functions decays from one value to another after encountering an inhomogeneity. It is explicitly seen that γ and $\tilde{\gamma}$ are stable in opposite integration directions. Different systems will now be considered, and analytically closed forms of the coherence functions will be found by determining the integration constants from continuous boundary conditions.

B.4.1 Bulk order parameter

For a bulk system with homogeneous order parameter $\Delta(\boldsymbol{R}) = \Delta$ and superflow $\boldsymbol{p}_\mathrm{s}(\boldsymbol{R}) = \boldsymbol{p}_\mathrm{s}$, there are no inhomogeneities, and the coherence functions are simply

$$\begin{aligned}\gamma_\mathrm{bulk} &= \gamma_\mathrm{h} = \frac{-\Delta}{z_p + i\Omega}, &\text{(B.65)}\\ \tilde{\gamma}_\mathrm{bulk} &= \tilde{\gamma}_\mathrm{h} = \frac{\tilde{\Delta}}{z_p + i\Omega}. &\text{(B.66)}\end{aligned}$$

A superfluid momentum (from either phase gradients or external flux) simply acts as a Doppler shift in the spectrum. The direction of $\boldsymbol{p}_\mathrm{s}$ with respect to the Fermi momentum direction determines the sign of the energy shift.

B.4.2 Step function order parameter

Consider an order parameter defined as a step function (as in Fig. 2.1)

$$\Delta(y) = \Theta(y)\Delta_1 + \Theta(-y)\Delta_2, \tag{B.67}$$

where Δ_1 and Δ_2 are two constant values, and Θ is the Heaviside step function. Coherence functions are thus homogeneous up to the interface, and inhomogeneous after it. Assuming that $\hat{\boldsymbol{y}} = +\hat{\boldsymbol{v}}_\mathrm{F}$, Eqs. (B.61)–(B.64) are used to get

$$\begin{aligned}\gamma(y<0) &= \frac{-\Delta_1}{z_p + i\Omega_1}, &\text{(B.68)}\\ \gamma(y>0) &= \frac{-\Delta_2}{z_p + i\Omega_2} + \frac{2i\Omega_2 C\exp(-y/y_0)}{1-\tilde{\Delta}_2 C\exp(-y/y_0)}, &\text{(B.69)}\\ \tilde{\gamma}(y<0) &= \frac{\tilde{\Delta}_1}{z_p + i\Omega_1} + \frac{2i\Omega_1 \tilde{C}\exp(+y/y_0)}{1+\Delta_1 \tilde{C}\exp(+y/y_0)}, &\text{(B.70)}\\ \tilde{\gamma}(y>0) &= \frac{\tilde{\Delta}_2}{z_p + i\Omega_2}, &\text{(B.71)}\end{aligned}$$

where it is seen that all solutions are numerically stable. Enforcing a continuous boundary condition at $y = 0$ yields the equations

$$\begin{aligned} \frac{-\Delta_1}{z_p + i\Omega_1} &= \frac{-\Delta_2}{z_p + i\Omega_2} + \frac{2i\Omega_2 C}{1 - \tilde{\Delta}_2 C}, && \text{(B.72)} \\ \frac{\tilde{\Delta}_1}{z_p + i\Omega_1} + \frac{2i\Omega_1 \tilde{C}}{1 + \Delta_1 \tilde{C}} &= \frac{\tilde{\Delta}_2}{z_p + i\Omega_2}, && \text{(B.73)} \end{aligned}$$

which uniquely determines the integration constants C and $\tilde{C}$. The full solutions are finally

$$\begin{aligned} \gamma &= \Theta(-y)\left[\frac{-\Delta_1}{z_p + i\Omega_1}\right] + \Theta(y)\left[\frac{-\Delta_2}{z_p + i\Omega_2} + \frac{2i\Omega_2 C \exp(-y/y_0)}{1 - \tilde{\Delta}_2 C \exp(-y/y_0)}\right], && \text{(B.74)} \\ \tilde{\gamma} &= \Theta(y)\left[\frac{\tilde{\Delta}_2}{z_p + i\Omega_2}\right] + \Theta(-y)\left[\frac{\tilde{\Delta}_1}{z_p + i\Omega_1} + \frac{2i\Omega_1 \tilde{C} \exp(y/y_0)}{1 + \Delta_1 \tilde{C} \exp(y/y_0)}\right], && \text{(B.75)} \\ C &= \frac{\gamma_{h,1} - \gamma_{h,2}}{2i\Omega_2 + \tilde{\Delta}_2 \left(\gamma_{h,1} - \gamma_{h,2}\right)}, && \text{(B.76)} \\ \tilde{C} &= \frac{\tilde{\gamma}_{h,2} - \tilde{\gamma}_{h,1}}{2i\Omega_1 - \Delta_2 \left(\tilde{\gamma}_{h,2} - \tilde{\gamma}_{h,1}\right)}, && \text{(B.77)} \end{aligned}$$

where $\gamma_{h,i} = -\Delta_i/(z_p{+}i\Omega_i)$ and $\tilde{\gamma}_{h,i} = \tilde{\Delta}_i/(z_p{+}i\Omega_i)$ are the homogeneous solutions in region i, and it is reminded again that $\hat{\boldsymbol{y}} = +\hat{\boldsymbol{v}}_{\mathrm{F}}$.

Bulk interface

For the special case $\Delta_2 = \Delta_1$ (no inhomogeneity), it is found that $C = \tilde{C} = 0$, with the coherence functions reducing to $\gamma = \gamma_h$ and $\tilde{\gamma} = \tilde{\gamma}_h$, which it should since it is again a bulk system.

Perfect pair-breaking interface

At a sign-changing interface with $\Delta_2 = -\Delta_1 \equiv \Delta$ (perfect pair-breaking)

$$\begin{aligned} C &= \frac{\Delta}{z_p(z_p + i\Omega)}, && \text{(B.78)} \\ \tilde{C} &= \frac{\tilde{\Delta}}{z_p(z_p + i\Omega)}, && \text{(B.79)} \end{aligned}$$

which yields the coherence functions

$$\begin{aligned} \gamma &= \gamma_h \left[\Theta(-y) + \Theta(y)\frac{z_p - (z_p + i\Omega)\exp(-y/y_0)}{z_p - (z_p - i\Omega)\exp(-y/y_0)}\right], && \text{(B.80)} \\ \tilde{\gamma} &= \tilde{\gamma}_h \left[\Theta(y) + \Theta(-y)\frac{z_p - (z_p + i\Omega)\exp(+y/y_0)}{z_p - (z_p - i\Omega)\exp(+y/y_0)}\right]. && \text{(B.81)} \end{aligned}$$

These coherence functions will lead to surface bound states, as is shown in Ch. 4, and it is reminded that they are only valid for a constant valued $\boldsymbol{p}_{\mathrm{s}}$. Thus, for a general spatially varying $\boldsymbol{p}_{\mathrm{s}}$, these solutions are the zeroth-order solutions in a linear expansion in $\boldsymbol{p}_{\mathrm{s}}$, which are used to derive the surface phase crystal instability in Ch. 6. Note that if $\boldsymbol{p}_{\mathrm{s}}$ cannot be expanded in a linear response, a more general solution has to be found to the Riccati Eqs. (B.40)–(B.41).

Appendix C

Technical details: quasiclassics

This appendix contains miscellaneous technical details and derivations, mainly for Ch. 2 on the quasiclassical theory.

C.1 Eliminating the coupling constant and energy cutoff

There is currently no ab-initio theory which can account for the superconducting transition temperature, or the pairing interaction in unconventional superconductors. There are thus a number of important parameters that are phenomenological and introduced ad-hoc, namely the unconventional coupling constant λ_Γ and energy cutoff Ω_c, as well as the transition temperature T_c. Since these are constants of the theory, they are not influenced by for example temperature, and it will now be shown how λ_Γ and Ω_c can be eliminated from the theory by expressing them in terms of T_c.

Consider the bulk gap equation for a singlet order parameter in Eq. (2.24) in the absence of superflow. As $T \to T_\mathrm{c}^-$, $|\Delta|/\varepsilon_n = |\Delta|/2\pi k_\mathrm{B}T(n+1/2)$ is small. Expanding in this small parameter, the gap equation is

$$\begin{aligned}
\Delta &= V_s \left\langle 2\pi k_\mathrm{B}T \sum_{\varepsilon_n>0}^{\Omega_\mathrm{c}} \left(\frac{\Delta}{|\varepsilon_n|}\right) \frac{|\eta(\theta_\mathrm{F})|^2}{\sqrt{\frac{|\Delta|^2}{\varepsilon_n^2}|\eta(\theta_\mathrm{F})|^2+1}} \right\rangle_{\theta_\mathrm{F}} && \text{(C.1)}\\
&\approx V_s \left\langle 2\pi k_\mathrm{B}T \sum_{\varepsilon_n>0}^{\Omega_\mathrm{c}} \left(\frac{\Delta}{|\varepsilon_n|}\right) |\eta(\theta_\mathrm{F})|^2 \right\rangle_{\theta_\mathrm{F}} && \text{(C.2)}\\
&= V_s\Delta \sum_{\varepsilon_n>0}^{\Omega_\mathrm{c}} \frac{1}{n+\frac{1}{2}}, && \text{(C.3)}
\end{aligned}$$

with a normalized basis function $\langle|\eta(\theta_\mathrm{F})|^2\rangle_{\theta_\mathrm{F}} = 1$, and where $V_s = -N_\mathrm{F}\lambda_s$ is the pair potential. Let $\Omega_\mathrm{c} = 2\pi k_\mathrm{B}T_\mathrm{c}(n_\mathrm{c}+1/2)$, such that

$$n_\mathrm{c} = \mathrm{int}\left(\frac{\Omega_\mathrm{c}}{2\pi k_\mathrm{B}T_\mathrm{c}} - \frac{1}{2}\right), \tag{C.4}$$

with $n \in [0, n_\mathrm{c} - 1]$. Dividing Eq. (C.3) with ΔV_s,

$$\begin{aligned} V_s^{-1} &= \sum_{n=0}^{n_\mathrm{c}-1} \frac{1}{n+\frac{1}{2}} && \text{(C.5)} \\ &= \psi\left(n_\mathrm{c} + \frac{1}{2}\right) - \psi\left(\frac{1}{2}\right), && \text{(C.6)} \\ \psi\left(\frac{1}{2}\right) &= -\gamma_\mathrm{E} - \ln(4), && \text{(C.7)} \\ \psi\left(n_\mathrm{c} + \frac{1}{2}\right) &= \ln\left(n_\mathrm{c} + \frac{1}{2}\right) + \mathcal{O}\left(\frac{1}{n_\mathrm{c}}\right), && \text{(C.8)} \end{aligned}$$

where $\psi(x)$ is the digamma function, which for large x has the expansion

$$\psi(x) = \ln(x) - \frac{1}{2x} + \mathcal{O}\left(\frac{1}{x^2}\right), \qquad \text{(C.9)}$$

and γ_E is the Euler-Mascheroni constant

$$\gamma_\mathrm{E} \equiv \lim_{n\to\infty} \left(\sum_{k=1}^{n} \frac{1}{k} - \ln n \right) \approx 0.577. \qquad \text{(C.10)}$$

Inserting Eqs. (C.7) and (C.4) into Eq. (C.6), it is found that

$$V_s^{-1} \equiv (-N_\mathrm{F}\lambda_s)^{-1} = \ln\left(4e^{\gamma_\mathrm{E}} \frac{\Omega_\mathrm{c}}{2\pi k_\mathrm{B} T_\mathrm{c}}\right). \qquad \text{(C.11)}$$

This expressions is used in the thesis to eliminate the dependence on the coupling constant λ_s and the cutoff Ω_c, in favor of T_c-dependence.

C.2 Luttinger-Ward trace

This appendix simplifies the trace in the Luttinger-Ward free-energy in Eq. (2.69). With the Nambu-space propagator and order parameter given in Eqs. (2.5) and (2.11), the matrix products entering the trace is

$$\hat{\Delta}\left(\hat{g}_\lambda - \frac{1}{2}\hat{g}\right) = \begin{pmatrix} \Delta\left(\tilde{f}_\lambda - \frac{1}{2}\tilde{f}\right) & \Delta\left(\tilde{g}_\lambda - \frac{1}{2}\tilde{g}\right) \\ \tilde{\Delta}\left(g_\lambda - \frac{1}{2}g\right) & \tilde{\Delta}\left(f_\lambda - \frac{1}{2}f\right) \end{pmatrix}, \tag{C.12}$$

where all terms are spin-space matrices given in Eqs. (2.7)–(2.13). The trace is

$$\mathrm{Tr}\left[\hat{\Delta}\left(\hat{g}_\lambda - \frac{1}{2}\hat{g}\right)\right] = \mathrm{Tr}\left[\Delta\left(\tilde{f}_\lambda - \frac{1}{2}\tilde{f}\right)\right] + \mathrm{Tr}\left[\tilde{\Delta}\left(f_\lambda - \frac{1}{2}f\right)\right], \tag{C.13}$$

where

$$\begin{aligned} \mathrm{Tr}\left[\Delta\left(\tilde{f}_\lambda - \frac{1}{2}\tilde{f}\right)\right] &= (\Delta_\mathrm{s} + \Delta_\mathrm{t})\left[\left(-\tilde{f}_{\mathrm{s}\lambda} + \tilde{f}_{\mathrm{t}\lambda}\right) - \frac{1}{2}\left(-\tilde{f}_\mathrm{s} + \tilde{f}_\mathrm{t}\right)\right] \\ &\quad + (-\Delta_\mathrm{s} + \Delta_\mathrm{t})\left[\left(\tilde{f}_{\mathrm{s}\lambda} + \tilde{f}_{\mathrm{t}\lambda}\right) - \frac{1}{2}\left(\tilde{f}_\mathrm{s} + \tilde{f}_\mathrm{t}\right)\right], \qquad \text{(C.14)} \\ \mathrm{Tr}\left[\tilde{\Delta}\left(f_\lambda - \frac{1}{2}f\right)\right] &= \left(\tilde{\Delta}_\mathrm{s} + \tilde{\Delta}_\mathrm{t}\right)\left[(-f_{\mathrm{s}\lambda} + f_{\mathrm{t}\lambda}) - \frac{1}{2}(-f_\mathrm{s} + f_\mathrm{t})\right] \\ &\quad + \left(-\tilde{\Delta}_\mathrm{s} + \tilde{\Delta}_\mathrm{t}\right)\left[(f_{\mathrm{s}\lambda} + f_{\mathrm{t}\lambda}) - \frac{1}{2}(f_\mathrm{s} + f_\mathrm{t})\right]. \qquad \text{(C.15)} \end{aligned}$$

Collecting the terms, the full trace can be separated into singlet and triplet parts

$$\begin{aligned} \mathrm{Tr}\left[\hat{\Delta}\left(\hat{g}_\lambda - \frac{1}{2}\hat{g}\right)\right] &= 2\Delta_\mathrm{s}\left(\frac{1}{2}\tilde{f}_\mathrm{s} - \tilde{f}_{\mathrm{s}\lambda}\right) + 2\tilde{\Delta}_\mathrm{s}\left(\frac{1}{2}f_\mathrm{s} - f_{\mathrm{s}\lambda}\right) \\ &\quad - 2\Delta_\mathrm{t}\left(\frac{1}{2}\tilde{f}_\mathrm{t} - \tilde{f}_{\mathrm{t}\lambda}\right) - 2\tilde{\Delta}_\mathrm{t}\left(\frac{1}{2}f_\mathrm{t} - f_{\mathrm{t}\lambda}\right), \qquad \text{(C.16)} \end{aligned}$$

with $\tilde{\Delta}_\mathrm{s} = \Delta_\mathrm{s}^*$ and $\tilde{\Delta}_\mathrm{t} = \Delta_\mathrm{t}^*$.

C.3 Entropy

This appendix introduces the entropy, which is mainly used to derive the heat capacity in App. C.4. Consider the thermodynamic potential

$$\Omega(\mu, \mathcal{V}, T) \equiv U - TS - \mu N, \tag{C.17}$$

with chemical potential μ, volume $\mathcal{V}$, internal energy U, temperature T, entropy S and particle-number N. A differential variation yields

$$d\Omega = dU - SdT - TdS - \mu dN. \tag{C.18}$$

The first and second laws of thermodynamics give

$$\begin{aligned} dU &= \delta Q - \delta W + \mu dN, & \text{(C.19)} \\ \delta Q &= TdS, & \text{(C.20)} \end{aligned}$$

where δQ is the infinitesimal heat flow into the system, and δW the infinitesimal work done by the system in terms of any extensive variables (e.g. volume and magnetic field). Substitution into Eq. (C.18) yields

$$d\Omega = -SdT - \delta W. \tag{C.21}$$

If no work is done, the entropy is obtained from the free energy

$$S = -\left(\frac{\partial \Omega}{\partial T}\right)_W. \tag{C.22}$$

Given the energy, this typically provides an inexpensive way to calculate the entropy in quasiclassics, as opposed to using the statistical expression. In a spin-degenerate bulk system, the latter is usually written

$$\begin{aligned} S &= -2k_\mathrm{B} \sum_{\boldsymbol{k}} \left[(1 - f_{\boldsymbol{k}}) \ln(1 - f_{\boldsymbol{k}}) + f_{\boldsymbol{k}} \ln f_{\boldsymbol{k}}\right] & \text{(C.23)} \\ &= -2\mathcal{V}k_\mathrm{B} \left\langle \int_{-\infty}^{\infty} d\xi N(E) \left[[1 - f(E)] \ln[1 - f(E)] + f(E) \ln f(E)\right] \right\rangle_{\theta_\mathrm{F}} & \text{(C.24)} \end{aligned}$$

where $\boldsymbol{k}$ denotes momentum, $\mathcal{V}$ volume, N the DOS, and $f_{\boldsymbol{k}} \equiv f(E_{\boldsymbol{k}})$ the Fermi-Dirac distribution

$$f(E_{\boldsymbol{k}}) \equiv \frac{1}{e^{\beta E_{\boldsymbol{k}}} + 1}, \tag{C.25}$$

with excitation spectrum $E_{\boldsymbol{k}} = \sqrt{\xi_{\boldsymbol{k}}^2 + |\Delta|^2}$, energy dispersion ξ relative to μ, and $\beta \equiv 1/k_\mathrm{B}T$.

C.4 Heat capacity

The heat capacity is typically measured with calorimetric methods, and can be used to infer a great number of properties, for example the transition temperature, the superconducting gap, the penetration depth, the coherence length, and the Fermi velocity [191]. In this thesis, the heat capacity is used to derive bulk properties in App. D.9. In paper II it is used to show that the phase crystallization is a second-order phase transition. This appendix starts by defining the heat capacity and relating it to the entropy. From this relation, it is shown that the heat capacity can either be calculated as a second-order temperature derivative from the free energy, or as an integral expression in terms of the quasiparticle excitation spectrum.

The heat capacity of a system is defined as the infinitesimal amount of heat δQ needed to raise the temperature of the system by an infinitesimal amount dT [208]

$$C \equiv \frac{\delta Q}{dT}. \tag{C.26}$$

The specific heat capacity (or specific heat in short) is defined as the heat capacity per unit substance, and this work exclusively considers the volumetric specific heat capacity, defined as the heat capacity per unit volume $C_{\mathcal{V}} \equiv C/\mathcal{V}$. The second law of thermodynamics states that if an infinitesimal amount of heat δQ is added to a system at temperature T in a reversible manner, then the entropy change is

$$dS = \frac{\delta Q}{T}, \tag{C.27}$$

which together with Eq. (C.26) yields

$$C = T\frac{dS}{dT}. \tag{C.28}$$

Considering the case of no work W done as in App. C.3, the heat capacity can be related to the free energy through

$$C = T\left(\frac{\partial S}{\partial T}\right)_W = -T\left(\frac{\partial^2 \Omega}{\partial T^2}\right)_W. \tag{C.29}$$

This is the expression that is used to do the numerics in the appended papers. It is noted that the first equality can be rewritten

$$C = T\frac{dS}{dT} = T\frac{dS}{d\beta}\frac{dT}{d\beta} = -\beta\frac{dS}{d\beta}. \tag{C.30}$$

Applying this to the entropy in Eq. (C.23) yields

$$\begin{aligned} C &= 2\beta k_{\mathrm{B}} \sum_{\boldsymbol{k}} \frac{d}{d\beta}\left[(1-f_{\boldsymbol{k}})\ln(1-f_{\boldsymbol{k}}) + f_{\boldsymbol{k}}\ln f_{\boldsymbol{k}}\right] \\ &= 2\beta k_{\mathrm{B}} \sum_{\boldsymbol{k}} \frac{df_{\boldsymbol{k}}}{d\beta}\ln\frac{f_{\boldsymbol{k}}}{1-f_{\boldsymbol{k}}}, \end{aligned} \tag{C.31}$$

where the total derivative is

$$\frac{df_{\boldsymbol{k}}}{d\beta} = \frac{\partial f_{\boldsymbol{k}}}{\partial \beta} + \frac{\partial f_{\boldsymbol{k}}}{\partial E_{\boldsymbol{k}}} \frac{dE_{\boldsymbol{k}}}{d\beta}. \tag{C.32}$$

Using the Fermi-Dirac distribution in Eq. (C.25) and assuming particle-hole symmetry close to the Fermi surface with $\mu \approx 0$ (which is quite generally a good approximation [81]), the above expressions are

$$\frac{\partial f_{\boldsymbol{k}}}{\partial \beta} = \frac{E_{\boldsymbol{k}}}{\beta} \frac{\partial f_{\boldsymbol{k}}}{\partial E_{\boldsymbol{k}}}, \tag{C.33}$$

$$\frac{\partial f_{\boldsymbol{k}}}{\partial E_{\boldsymbol{k}}} = -\beta f_{\boldsymbol{k}}(1 - f_{\boldsymbol{k}}), \tag{C.34}$$

$$\ln \frac{f_{\boldsymbol{k}}}{1 - f_{\boldsymbol{k}}} = -\beta E_{\boldsymbol{k}}. \tag{C.35}$$

With these expressions, the heat capacity can finally be written

$$C = 2\beta^2 k_{\mathrm{B}} \sum_{\boldsymbol{k}} f_{\boldsymbol{k}} (1 - f_{\boldsymbol{k}}) \left[E_{\boldsymbol{k}}^2 + \beta E_{\boldsymbol{k}} \frac{dE_{\boldsymbol{k}}}{d\beta} \right] \tag{C.36}$$

$$= 2\beta^2 k_{\mathrm{B}} \mathcal{V} \left\langle \int_{-\infty}^{\infty} d\xi N(\xi) f(\xi) \left[1 - f(\xi)\right] \left[E^2(\xi) + \beta E(\xi) \frac{dE}{d\beta} \right] \right\rangle_{\theta_{\mathrm{F}}}. \tag{C.37}$$

With the energy given by

$$E_{\boldsymbol{k}} = \sqrt{\xi^2 + |\Delta|^2}, \tag{C.38}$$

the heat capacity takes the form

$$C = 2\beta^2 k_{\mathrm{B}} \mathcal{V} \left\langle \int_{-\infty}^{\infty} d\xi N(\xi) f(\xi) \left[1 - f(\xi)\right] \left[E^2(\xi) + \frac{\beta}{2} \frac{d|\Delta|^2}{d\beta} \right] \right\rangle_{\theta_{\mathrm{F}}}. \tag{C.39}$$

Hence, like the entropy, the heat capacity takes on a form that is generally quite expensive to evaluate numerically, compared with e.g. Eq. (C.29).

Appendix D

Technical details: bulk calculations

This appendix contains technical details and derivations for Ch. 3 on bulk superconductivity in the presence of a homogeneous superflow.

D.1 Regularized gap equation

The bulk singlet gap equation is found by inserting the anomalous bulk propagators from Eqs. (3.10)–(3.11) into Eq. (2.26),

$$\Delta = V\left\langle 2\pi k_{\mathrm{B}}T\sum_{\varepsilon_n>0}^{\Omega_{\mathrm{c}}}\frac{\Delta|\eta(\theta_{\mathrm{F}})|^2}{\sqrt{|\Delta|^2|\eta(\theta_{\mathrm{F}})|^2-z_p^2}}\right\rangle_{\theta_{\mathrm{F}}}. \tag{D.1}$$

The sum is logarithmically divergent for large Ω_{c}, which is especially problematic numerically. This divergence is regularized by introducing factors $\Delta/|\varepsilon_n|-\Delta/|\varepsilon_n|$ in the summand

$$\Delta = V_s\left\langle 2\pi k_{\mathrm{B}}T\sum_{\varepsilon_n>0}^{\Omega_{\mathrm{c}}}\left[\frac{\Delta|\eta(\theta_{\mathrm{F}})|^2}{\sqrt{|\Delta|^2|\eta(\theta_{\mathrm{F}})|^2-z_p^2}}+\frac{\Delta}{|\varepsilon_n|}-\frac{\Delta}{|\varepsilon_n|}\right]\right\rangle_{\theta_{\mathrm{F}}}, \tag{D.2}$$

With V_s^{-1} given by the expression in Eq. (C.11) and $\varepsilon_n \equiv 2\pi k_{\mathrm{B}}T(n+1/2)$, it is possible to write the regularized gap equation as

$$\Delta\left(\frac{1}{V_s}-\sum_{\varepsilon_n>0}^{\Omega_{\mathrm{c}}}\frac{2\pi k_{\mathrm{B}}T}{|\varepsilon_n|}\right) = \left\langle 2\pi k_{\mathrm{B}}T\sum_{\varepsilon_n>0}^{\Omega_{\mathrm{c}}}\left[\frac{\Delta|\eta(\theta_{\mathrm{F}})|^2}{\sqrt{|\Delta|^2|\eta(\theta_{\mathrm{F}})|^2-z_p^2}}-\frac{\Delta}{|\varepsilon_n|}\right]\right\rangle_{\theta_{\mathrm{F}}} \tag{D.3}$$

$$\Delta\ln\left(\frac{T}{T_{\mathrm{c}}}\right) = \left\langle 2\pi k_{\mathrm{B}}T\sum_{\varepsilon_n>0}^{\Omega_{\mathrm{c}}}\left[\frac{\Delta|\eta(\theta_{\mathrm{F}})|^2}{\sqrt{|\Delta|^2|\eta(\theta_{\mathrm{F}})|^2-z_p^2}}-\frac{\Delta}{|\varepsilon_n|}\right]\right\rangle_{\theta_{\mathrm{F}}} \tag{D.4}$$

With $n_{\mathrm{c}} \equiv \Omega_{\mathrm{c}}/2\pi k_{\mathrm{B}}T_{\mathrm{c}}-1/2$, it is thus possible to write the pair potential as

$$\frac{1}{V_s} = \ln\left(\frac{T}{T_{\mathrm{c}}}\right)+\sum_{n=0}^{n_{\mathrm{c}}-1}\frac{1}{n+\frac{1}{2}}. \tag{D.5}$$

D.2 Low-temperature gap

At zero temperature, $\Delta(\boldsymbol{p}_\mathrm{F}, T=0) \equiv \Delta_0\eta(\theta_\mathrm{F})$, the Matsubara sum is replaced by an integral as in Eqs. (2.19)–(2.20), and the bulk gap Eq. (D.1) can be taken analytically

$$\begin{aligned}
\frac{1}{V} &= \left\langle \int_0^{\Omega_\mathrm{c}} \frac{|\eta(\theta_F)|^2 d\epsilon}{\sqrt{|\Delta\eta(\theta_F)|^2 + (\epsilon + i\boldsymbol{v}_\mathrm{F}\cdot\boldsymbol{p}_\mathrm{s})^2}} \right\rangle_{\theta_\mathrm{F}} && \text{(D.6)}\\
&= \left\langle |\eta(\theta_F)|^2 \left[\ln\left(\sqrt{|\Delta\eta(\theta_F)|^2 + (\epsilon + i\boldsymbol{v}_\mathrm{F}\cdot\boldsymbol{p}_\mathrm{s})^2} + (\epsilon + i\boldsymbol{v}_\mathrm{F}\cdot\boldsymbol{p}_\mathrm{s})\right)\right]_0^{\Omega_\mathrm{c}} \right\rangle_{\theta_\mathrm{F}} && \text{(D.7)}\\
&\approx \left\langle |\eta(\theta_F)|^2 \ln\left(\frac{2\Omega_\mathrm{c}}{\sqrt{|\Delta\eta(\theta_F)|^2 + (i\boldsymbol{v}_\mathrm{F}\cdot\boldsymbol{p}_\mathrm{s})^2} + i\boldsymbol{v}_\mathrm{F}\cdot\boldsymbol{p}_\mathrm{s}}\right) \right\rangle_{\theta_\mathrm{F}}, && \text{(D.8)}
\end{aligned}$$

for large Ω_c. Let the superflow angle relative to the crystal a-axis be ϕ, such that

$$\boldsymbol{v}_\mathrm{F}\cdot\boldsymbol{p}_\mathrm{s} = v_\mathrm{F} p_\mathrm{s}\,(\cos\theta_\mathrm{F}, \sin\theta_\mathrm{F})\cdot(\cos\phi, \sin\phi) = v_\mathrm{F} p_\mathrm{s}\cos(\theta_\mathrm{F} - \phi). \tag{D.9}$$

Introduce the notation $\bar{p}_\mathrm{s} = v_\mathrm{F} p_\mathrm{s}/\Delta_0 < 1$ (where the inequality follows from critical superflow derived in App. D.4), yielding

$$\frac{1}{V_s} = \ln\left(\frac{2\Omega_\mathrm{c}}{\Delta_0}\right) - \left\langle |\eta(\theta_F)|^2 \ln\left(\sqrt{|\eta(\theta_F)|^2 + (i\bar{p}_\mathrm{s})^2\cos^2(\theta_\mathrm{F} - \phi)} + i\bar{p}_\mathrm{s}\cos(\theta_\mathrm{F} - \phi)\right) \right\rangle_{\theta_\mathrm{F}}. \tag{D.10}$$

Eliminating the coupling constant and the cutoff in favor of T_c (as in App. C.1), the following expression is obtained for the order parameter

$$\begin{aligned}
\Delta_0 &= k_\mathrm{B} T_\mathrm{c} \pi e^{-\gamma_\mathrm{E}} e^{-\langle f(\theta_\mathrm{F},\phi)\rangle_{\theta_\mathrm{F}}}, && \text{(D.11)}\\
f(\theta, \phi) &\equiv |\eta(\theta_F)|^2 \ln\left[\sqrt{|\eta(\theta_F)|^2 + (i\bar{p}_\mathrm{s})^2\cos^2(\theta_\mathrm{F} - \phi)} + i\bar{p}_\mathrm{s}\cos(\theta_\mathrm{F} - \phi)\right], && \text{(D.12)}\\
\gamma_\mathrm{E} &\equiv \lim_{n\to\infty}\left(\sum_{k=1}^{n}\frac{1}{k} - \ln n\right) \approx 0.577. && \text{(D.13)}
\end{aligned}$$

where γ_E is the Euler-Mascheroni constant. At zero superflow, $\langle f\rangle_{\theta_\mathrm{F}} = 0$ for s-wave with $\eta(\theta_\mathrm{F}) = 1$, and $\langle f\rangle_{\theta_\mathrm{F}} = [1 - \ln(2)]/2$ for d-wave with $\eta(\theta_\mathrm{F}) = \sqrt{2}\cos(2\theta_\mathrm{F})$, such that

$$\begin{aligned}
\frac{\Delta_0^s}{k_\mathrm{B} T_\mathrm{c}} &= \pi e^{-\gamma_\mathrm{E}} \approx 1.76, && \text{(D.14)}\\
\frac{\Delta_0^d}{k_\mathrm{B} T_\mathrm{c}} &= \sqrt{2}\pi e^{-\gamma_\mathrm{E} - \frac{1}{2}} \approx 1.51. && \text{(D.15)}
\end{aligned}$$

Note that the maximal d-wave gap in the DOS is $\sqrt{2}\Delta_0^d \approx 2.14 k_\mathrm{B} T_\mathrm{c}$ [56]. Appendix D.3 shows that for s-wave, $\langle f(\theta, \phi)\rangle_{\theta_\mathrm{F}} = 0$ even for $p_\mathrm{s} \neq 0$, such that $\Delta_0^s(\boldsymbol{p}_\mathrm{s}) = \Delta_0^s$ until the critical superflow $p_\mathrm{s,c} = \Delta_0/v_\mathrm{F}$ (derived in App. D.4), where superconductivity is lost abruptly. The d-wave case with superflow is less trivial, since there are subgap states contributing even at zero temperature [116].

D.3 s-wave gap suppression by superflow: zero temperature

Following App. D.2, it is possible to choose $\phi = 0$ for an s-wave order parameter, yielding

$$\begin{aligned}
f_s(\theta,\phi) &= \ln\left[\sqrt{1-(\bar{p}_\mathrm{s})^2\cos^2(\theta_\mathrm{F})} + i\bar{p}_\mathrm{s}\cos(\theta_\mathrm{F})\right], && \text{(D.16)}\\
\langle f(\theta,\phi)\rangle_{\theta_\mathrm{F}} &= \int_0^{2\pi}\frac{d\theta_\mathrm{F}}{2\pi}f(\theta,\phi) && \text{(D.17)}\\
&= 2\int_0^{\pi}\frac{d\theta_\mathrm{F}}{2\pi}f(\theta,\phi) && \text{(D.18)}\\
&= \int_0^{\pi}\frac{d\theta_\mathrm{F}}{2\pi}\Bigg(\ln\left[\sqrt{1-(\bar{p}_\mathrm{s})^2\cos^2(\theta_\mathrm{F})} + i\bar{p}_\mathrm{s}\cos(\theta_\mathrm{F})\right]\\
&\qquad + \ln\left[\sqrt{1-(\bar{p}_\mathrm{s})^2\cos^2(\theta_\mathrm{F})} - i\bar{p}_\mathrm{s}\cos(\theta_\mathrm{F})\right]\Bigg) && \text{(D.19)}\\
&= \int_0^{\pi}\frac{d\theta_\mathrm{F}}{2\pi}\ln(1) && \text{(D.20)}\\
&= 0. && \text{(D.21)}
\end{aligned}$$

Hence,

$$\Delta_0^s(\boldsymbol{p}_\mathrm{s}) = \Delta_0^s = k_\mathrm{B}T_\mathrm{c}\pi e^{-\gamma_\mathrm{E}}, \tag{D.22}$$

which breaks down at a critical superflow $p_\mathrm{s} \to p_\mathrm{s,c} \equiv \Delta_0^s/v_\mathrm{F}$, derived in App. D.4.

D.4 Low-temperature energetics

The total free energy at zero temperature $\delta\Omega_0$ is split into

$$\delta\Omega_0 \;=\; \delta\Omega_0^{\rm BCS} + \delta\Omega_0^{p} + \delta\Omega_0^{B}, \tag{D.23}$$

with condensation energy $\delta\Omega_0^{\rm BCS} \equiv \delta\Omega_0(\boldsymbol{p}_{\rm s}=0) - \delta\Omega_0^{B}$, magnetic energy density $\delta\Omega_0^{B} \equiv \int d\boldsymbol{R}\boldsymbol{B}_{\rm ind}^2/8\pi$, and superflow kinetic energy $\delta\Omega_0^{p} \equiv \delta\Omega_0 - \delta\Omega_0(\boldsymbol{p}_{\rm s}=0)$. Here, $\delta\Omega$ is given by e.g. Luttinger-Ward in Eq. (2.69). With the bulk pair-propagators in Eqs. (3.10)–(3.11), the trace in Eq. (2.69) simplifies to (see App. C.2)

$$\mathrm{Tr}\left[\hat{\Delta}\left(\hat{g}_\lambda - \frac{1}{2}\hat{g}\right)\right] = 4\pi\,|\Delta(\boldsymbol{p}_{\rm F})|^2\left(\frac{1}{2\sqrt{|\Delta(\boldsymbol{p}_{\rm F})|^2 - z_p^2}} - \frac{\lambda}{\sqrt{|\Delta(\boldsymbol{p}_{\rm F})|^2\lambda^2 - z_p^2}}\right), \tag{D.24}$$

where $\Delta(\boldsymbol{p}_{\rm F}, T=0) = \Delta_0\eta(\theta_{\rm F})$, $z_p = z - \boldsymbol{v}_{\rm F}\cdot\boldsymbol{p}_{\rm s}$ with $z = i\varepsilon_n = i\pi k_B T(2n+1)$ for Matsubara. At zero temperature, the Matsubara sum is replaced by an integral as in Eqs. (2.19)–(2.20). Noting that $-(i\epsilon - \boldsymbol{v}_{\rm F}\cdot\boldsymbol{p}_{\rm s})^2 = (\epsilon + i\boldsymbol{v}_{\rm F}\cdot\boldsymbol{p}_{\rm s})^2$, the bulk free energy at zero temperature and zero field is found to be

$$\begin{aligned}
\frac{\delta\Omega_0^{\rm BCS} + \delta\Omega_0^{p}}{\mathcal{V}N_{\rm F}} &= \frac{1}{2}\int_0^1 d\lambda \frac{1}{2\pi} 2\int_0^\infty d\epsilon \Big\langle 4\pi|\Delta(\boldsymbol{p}_{\rm F})|^2 \Big(\frac{1}{2\sqrt{|\Delta(\boldsymbol{p}_{\rm F})|^2 + (\epsilon + i\boldsymbol{v}_{\rm F}\cdot\boldsymbol{p}_{\rm s})^2}} \\
&\qquad - \frac{\lambda}{\sqrt{|\Delta(\boldsymbol{p}_{\rm F})|^2\lambda^2 + (\epsilon + i\boldsymbol{v}_{\rm F}\cdot\boldsymbol{p}_{\rm s})^2}}\Big)\Big\rangle_{\theta_{\rm F}} \\
&= 2\int_0^\infty d\epsilon \Big\langle\Big(\frac{|\Delta(\boldsymbol{p}_{\rm F})|^2}{2\sqrt{|\Delta(\boldsymbol{p}_{\rm F})|^2 + (\epsilon + i\boldsymbol{v}_{\rm F}\cdot\boldsymbol{p}_{\rm s})^2}} + \sqrt{(\epsilon + i\boldsymbol{v}_{\rm F}\cdot\boldsymbol{p}_{\rm s})^2} \\
&\qquad - \sqrt{|\Delta(\boldsymbol{p}_{\rm F})|^2 + (\epsilon + i\boldsymbol{v}_{\rm F}\cdot\boldsymbol{p}_{\rm s})^2}\Big)\Big\rangle_{\theta_{\rm F}}.
\end{aligned} \tag{D.25}$$

For s-wave (or the continuum part of d-wave), Eq. (D.25) becomes

$$\begin{aligned}
\frac{\delta\Omega_0^{\rm BCS} + \delta\Omega_0^{p}}{\mathcal{V}N_{\rm F}} &= \left\langle\left[\left(\epsilon^2 + 2i\epsilon\boldsymbol{v}_{\rm F}\cdot\boldsymbol{p}_{\rm s}\right) - (\epsilon + i\boldsymbol{v}_{\rm F}\cdot\boldsymbol{p}_{\rm s})\sqrt{\Delta_0^2 + (\epsilon + i\boldsymbol{v}_{\rm F}\cdot\boldsymbol{p}_{\rm s})^2}\right]_0^\infty\right\rangle_{\theta_{\rm F}} \\
&= \frac{1}{2}\left\langle -\Delta_0^2 + 2(\boldsymbol{v}_{\rm F}\cdot\boldsymbol{p}_{\rm s})^2\right\rangle_{\theta_{\rm F}} \qquad \text{(D.26)} \\
&= \frac{-\Delta_0^2}{2} + \frac{v_{\rm F}^2 p_{\rm s}^2}{2}, \qquad \text{(D.27)}
\end{aligned}$$

where the angular average of the imaginary part was zero. Setting Eq. (D.27) to zero defines the critical superflow

$$p_{\rm s,c} \equiv \frac{\Delta_0}{v_{\rm F}}. \tag{D.28}$$

D.5 Low-temperature current response

The low-temperature current response to a uniform superflow $\boldsymbol{p}_{\mathrm{s}}$ will now be derived. Inserting the bulk Matsubara propagator from Eq. (3.8) into Eq. (2.66) yields the bulk-current response

$$\boldsymbol{j} = 4k_{\mathrm{B}}TeN_{\mathrm{F}}v_{\mathrm{F}}\left\langle \hat{\boldsymbol{v}}_{\mathrm{F}} \sum_{\varepsilon_n>0}^{\Omega_{\mathrm{c}}} \mathrm{Re}\left\{ -\pi \frac{i\varepsilon_n - \boldsymbol{v}_{\mathrm{F}}\cdot\boldsymbol{p}_{\mathrm{s}}}{\sqrt{|\Delta(\boldsymbol{p}_{\mathrm{F}})|^2 - (i\varepsilon_n - \boldsymbol{v}_{\mathrm{F}}\cdot\boldsymbol{p}_{\mathrm{s}})^2}} \right\} \right\rangle_{\theta_{\mathrm{F}}}. \tag{D.29}$$

It is immediately seen that if $\boldsymbol{v}_{\mathrm{F}}\cdot\boldsymbol{p}_{\mathrm{s}} = 0$, then $\mathrm{Re}\{g^{\mathrm{M}}\} = 0 \Rightarrow \boldsymbol{j} = 0$, and there are hence no spontaneous currents in a homogeneous bulk system (the energy cost of bulk superflow is derived in App. D.4). Consider non-zero superflow in the limits $T \to 0$ and $\Omega_{\mathrm{c}} \to \infty$ as in Eqs. (2.19)–(2.20), such that $\boldsymbol{j}_0 \equiv \boldsymbol{j}(T=0)$ takes the form

$$\boldsymbol{j}_0 = eN_{\mathrm{F}}v_{\mathrm{F}}\frac{2}{\pi}\left\langle \hat{\boldsymbol{v}}_{\mathrm{F}} \int_0^\infty d\epsilon\, \mathrm{Re}\left\{ (-i\pi) \frac{\epsilon + i\boldsymbol{v}_{\mathrm{F}}\cdot\boldsymbol{p}_{\mathrm{s}}}{\sqrt{|\Delta(\boldsymbol{p}_{\mathrm{F}})|^2 + (\epsilon + i\boldsymbol{v}_{\mathrm{F}}\cdot\boldsymbol{p}_{\mathrm{s}})^2}} \right\} \right\rangle_{\theta_{\mathrm{F}}}. \tag{D.30}$$

Care needs to be taken in the case of nodal superconductors, since there are momentum directions for which $|\Delta(\boldsymbol{p}_{\mathrm{F}})|^2 + (\epsilon + i\boldsymbol{v}_{\mathrm{F}}\cdot\boldsymbol{p}_{\mathrm{s}})^2 < 0$ due to the nodes. This leads to quasiparticle excitations with a backflow response $\boldsymbol{j}_0^{\mathrm{qp}} \neq 0$ that reduces the total current. The current is split into condensate ($|\Delta(\boldsymbol{p}_{\mathrm{F}})|^2 + (\epsilon + i\boldsymbol{v}_{\mathrm{F}}\cdot\boldsymbol{p}_{\mathrm{s}})^2 > 0$) and quasiparticle ($|\Delta(\boldsymbol{p}_{\mathrm{F}})|^2 + (\epsilon + i\boldsymbol{v}_{\mathrm{F}}\cdot\boldsymbol{p}_{\mathrm{s}})^2 < 0$) currents $\boldsymbol{j} = \boldsymbol{j}^{\mathrm{cond}} + \boldsymbol{j}^{\mathrm{qp}}$. For fully gapped superconductors, like s-wave, $\boldsymbol{j}_0^{\mathrm{qp}} = 0$ (for $p_{\mathrm{s}} < p_{\mathrm{s,c}}$). The primitive function is easily found for the condensate current, and with careful treatment of the complex square root, the bulk condensate response is

$$\begin{aligned}
\boldsymbol{j}_0^{\mathrm{cond}} &= 2eN_{\mathrm{F}}v_{\mathrm{F}}\left\langle \hat{\boldsymbol{v}}_{\mathrm{F}}\, \mathrm{Im}\left[\sqrt{|\Delta(\boldsymbol{p}_{\mathrm{F}})|^2 + (\epsilon + i\boldsymbol{v}_{\mathrm{F}}\cdot\boldsymbol{p}_{\mathrm{s}})^2} \right]_0^\infty \right\rangle_{\theta_{\mathrm{F}}} && \text{(D.31)}\\
&= 2eN_{\mathrm{F}}v_{\mathrm{F}}\left\langle \hat{\boldsymbol{v}}_{\mathrm{F}}\left(\boldsymbol{v}_{\mathrm{F}}\cdot\boldsymbol{p}_{\mathrm{s}}\right)\right\rangle_{\theta_{\mathrm{F}}} && \text{(D.32)}\\
&= eN_{\mathrm{F}}v_{\mathrm{F}}^2\boldsymbol{p}_{\mathrm{s}} && \text{(D.33)}\\
&= e\rho\boldsymbol{p}_{\mathrm{s}}, && \text{(D.34)}\\
\rho &\equiv N_{\mathrm{F}}v_{\mathrm{F}}^2, && \text{(D.35)}
\end{aligned}$$

where ρ is the bulk superfluid density at zero temperature. Note that this is consistent with the usual form of the bulk superfluid density tensor $\boldsymbol{\rho}_s$ (denoted $\boldsymbol{K}(\boldsymbol{R},\boldsymbol{R}')$ for the inhomogeneous non-local case in this thesis)

$$\begin{aligned}
(\boldsymbol{\rho}_s)_{ij} &= 4\pi k_{\mathrm{B}}TN_{\mathrm{F}}\left\langle \boldsymbol{v}_{\mathrm{F}i}\boldsymbol{v}_{\mathrm{F}j} \sum_{\varepsilon_n>0}^{\Omega_{\mathrm{c}}} \frac{|\Delta(\boldsymbol{p}_{\mathrm{F}})|^2}{\sqrt{|\Delta(\boldsymbol{p}_{\mathrm{F}})|^2 + \varepsilon_n^2}^{\,3}} \right\rangle_{\theta_{\mathrm{F}}} && \text{(D.36)}\\
&\xrightarrow[T\to 0]{\Omega_{\mathrm{c}}\to\infty} 2N_{\mathrm{F}}v_{\mathrm{F}}^2\left\langle \hat{\boldsymbol{v}}_{\mathrm{F}i}\hat{\boldsymbol{v}}_{\mathrm{F}j} \int_0^\infty d\varepsilon \frac{|\Delta(\boldsymbol{p}_{\mathrm{F}})|^2}{\sqrt{|\Delta(\boldsymbol{p}_{\mathrm{F}})|^2 + \varepsilon^2}^{\,3}} \right\rangle_{\theta_{\mathrm{F}}} && \text{(D.37)}\\
&= N_{\mathrm{F}}v_{\mathrm{F}}^2 \equiv \rho. && \text{(D.38)}
\end{aligned}$$

D.6 Density of states: s-wave

The density of states for a bulk s-wave superconductor will now be derived. Starting with the midgap case, the bulk propagator in Eq. (3.8) is expanded in δ

$$\begin{aligned} g^{\mathrm{R}}(|\epsilon| < |\Delta|) &= -\pi \frac{\varepsilon + i\delta - \boldsymbol{v}_{\mathrm{F}} \cdot \boldsymbol{p}_{\mathrm{s}}}{\sqrt{|\Delta|^2 - (\varepsilon + i\delta - \boldsymbol{v}_{\mathrm{F}} \cdot \boldsymbol{p}_{\mathrm{s}})^2}} && \text{(D.39)} \\ &= -\pi \frac{\epsilon + i\delta}{(|\Delta|^2 - \epsilon^2 + \delta^2) - 2i\delta\epsilon} && \text{(D.40)} \\ &\approx -\pi \frac{\epsilon + i\delta}{\sqrt{|\Delta|^2 - \epsilon^2 + \delta^2}} \left(1 + \frac{i\delta\epsilon}{|\Delta|^2 - \epsilon^2 + \delta^2} \right), && \text{(D.41)} \end{aligned}$$

where $\epsilon \equiv \varepsilon - \boldsymbol{v}_{\mathrm{F}} \cdot \boldsymbol{p}_{\mathrm{s}}$. Taking the imaginary part,

$$\operatorname{Im}\left[g^{\mathrm{R}}(|\epsilon| < |\Delta|) \right] \approx \frac{\delta |\Delta|^2}{\left(|\Delta|^2 - \epsilon^2\right)^{3/2}} \xrightarrow[\delta \to 0]{} 0, \tag{D.42}$$

and there is an energy gap of size Δ. Turning to the continuum case, the square root in the Retarded propagator is rewritten

$$\begin{aligned} g^{\mathrm{R}}(|\epsilon| > |\Delta|) &= -\pi \frac{\epsilon + i\delta}{i\sqrt{(\epsilon + i\delta)^2 - |\Delta|^2}} && \text{(D.43)} \\ &\approx i\pi \frac{\epsilon + i\delta}{\sqrt{\epsilon^2 - |\Delta|^2 - \delta^2}} \left(1 - \frac{i\delta\epsilon}{\epsilon^2 - |\Delta|^2 - \delta^2} \right). && \text{(D.44)} \end{aligned}$$

Taking the imaginary part and letting $\delta \to 0^+$,

$$\operatorname{Im}\left[g^{\mathrm{R}}\left(|\epsilon| > |\Delta|\right) \right] \approx \frac{\pi\epsilon}{\sqrt{\epsilon^2 - |\Delta|^2}}. \tag{D.45}$$

Combining the above, the s-wave DOS in the absence and presence of superflow are

$$\begin{aligned} N(\varepsilon) &= 2N_{\mathrm{F}} \Theta(\varepsilon^2 - |\Delta|^2) \frac{|\varepsilon|}{\sqrt{\varepsilon^2 - |\Delta|^2}}, && \text{(D.46)} \\ N(\varepsilon) &= 2N_{\mathrm{F}} \Theta(|\epsilon(\theta_{\mathrm{F}})|^2 - |\Delta|^2) \left\langle \frac{|\varepsilon - \boldsymbol{v}_{\mathrm{F}} \cdot \boldsymbol{p}_{\mathrm{s}}|}{\sqrt{(\varepsilon - \boldsymbol{v}_{\mathrm{F}} \cdot \boldsymbol{p}_{\mathrm{s}})^2 - |\Delta|^2}} \right\rangle_{\theta_{\mathrm{F}}}, && \text{(D.47)} \end{aligned}$$

with $\epsilon = \varepsilon - \boldsymbol{v}_{\mathrm{F}} \cdot \boldsymbol{p}_{\mathrm{s}}$. In the limit $\Delta \to |\epsilon|$, the DOS has a square-root divergence, signifying the coherence peaks. Furthermore, it is directly seen that the superflow $\boldsymbol{p}_{\mathrm{s}}$ acts as a Doppler shift, shifting states to positive or negative energies depending on the projection onto $\boldsymbol{v}_{\mathrm{F}}$. See Sec. 3.2 for further discussion and illustrations.

D.7 Density of states: d-wave

The density of states for a bulk d-wave superconductor will now be derived. Following the previous appendix, the Retarded Green function is written compactly as

$$g^{\mathrm{R}}(\boldsymbol{p}_{\mathrm{F}};\varepsilon) = \frac{-\pi}{\sqrt{\epsilon^2 - 2|\Delta|^2\cos^2(2\theta_{\mathrm{F}})}}\left(i|\epsilon| - \delta\left(1 + \frac{\epsilon}{\Delta^2(\theta_{\mathrm{F}}) - \epsilon^2}\right)\right) \tag{D.48}$$

where now $\Delta(\boldsymbol{p}_{\mathrm{F}}) = \sqrt{2}|\Delta|\cos(2\theta_{\mathrm{F}}) \equiv \Delta_d\cos(2\theta_{\mathrm{F}})$ and $\epsilon \equiv \varepsilon - \boldsymbol{v}_{\mathrm{F}}\cdot\boldsymbol{p}_{\mathrm{s}}$. As $\delta \to 0$,

$$N(\varepsilon) = 2N_{\mathrm{F}}\left\langle \frac{|\epsilon|}{\sqrt{\epsilon^2 - |\Delta_d|^2\cos^2(2\theta_{\mathrm{F}})}}\Theta(\epsilon^2 - |\Delta(\boldsymbol{p}_{\mathrm{F}})|^2)\right\rangle_{\theta_{\mathrm{F}}}. \tag{D.49}$$

In the absence of superflow, this reduces to the known d-wave DOS [117]

$$N(\varepsilon) = 2N_{\mathrm{F}}\frac{2}{\pi}\left[K\left(\frac{\Delta_d}{|\varepsilon|}\right)\theta(|\varepsilon| - \Delta_d) + \frac{|\varepsilon|}{\Delta_d}K\left(\frac{|\varepsilon|}{\Delta_d}\right)\theta(\Delta_d - |\varepsilon|)\right], \tag{D.50}$$

where K is the complete elliptic integral of the first kind

$$K(k) = \int_0^{\frac{\pi}{2}}\frac{d\theta}{1 - k^2\sin^2\theta}. \tag{D.51}$$

Studying Eq. (D.50), it is seen that as $|\varepsilon| \gg \Delta_d$, $K(\Delta_d/\varepsilon) \approx \pi/2$ and the DOS converges to the normal-state DOS, $2N_{\mathrm{F}}$. In the limit $\Delta_d \to |\varepsilon|$, the DOS diverges as $N \propto \Delta_d/0^+$, signifying the coherence peaks. Unique to the d-wave case in comparison to the s-wave case, is that for $|\varepsilon| \ll \Delta_0$, $K(|\varepsilon|/\Delta_d) \approx \pi/2$ and the DOS is linear $N(\varepsilon) \approx |\varepsilon|/\Delta_d$. This DOS is usually referred to as gapless, and stems from the nodal structure in the order parameter. See Sec. 3.3 for further discussion and illustrations.

D.8 Entropy

Considering a spin degenerate bulk system in the absence of magnetic fields, the entropy in Eq. (C.24) is

$$S = -2\mathcal{V}k_{\mathrm{B}} \left\langle \int_{-\infty}^{\infty} d\xi N(\xi) \left[[1 - f(E)] \ln[1 - f(E)] + f(E) \ln f(E) \right] \right\rangle_{\theta_{\mathrm{F}}}, \qquad \text{(D.52)}$$

where $E = \sqrt{\xi^2 + |\Delta|^2}$. At zero temperature, it is noted that

$$f(E) = \frac{1}{e^{\beta E} + 1} \xrightarrow[T \to 0]{} 0, \qquad \text{(D.53)}$$

$$[1 - f(E)] \ln [1 - f(E)] + f(E) \ln f(E) \xrightarrow[T \to 0]{} 0. \qquad \text{(D.54)}$$

Hence, the entropy vanishes

$$S \xrightarrow[T \to 0]{} 0, \qquad \text{(D.55)}$$

in accord with the third law of thermodynamics. On the other hand, in the limit $T \to T_{\mathrm{c}}$, then $\Delta \to 0$ and $E \to \xi$. The normal-state entropy S_{N} is then obtained

$$S \xrightarrow[T \to T_{\mathrm{c}}]{} S_{\mathrm{N}} \equiv -2\mathcal{V}k_{\mathrm{B}} \left\langle \int_{-\infty}^{\infty} d\xi N(\xi) \left[[1 - f(\xi)] \ln[1 - f(\xi)] + f(\xi) \ln f(\xi) \right] \right\rangle_{\theta_{\mathrm{F}}}. \qquad \text{(D.56)}$$

This means that, in the absence of magnetic fields, the entropy is continuous across the normal-superconducting phase-transition

$$\Delta S_{\mathrm{NS}} \equiv (S - S_{\mathrm{N}}) \Big|_{T_{\mathrm{c}}} = 0, \qquad \text{(D.57)}$$

and there is no latent heat. The phase transition can therefore not be of first order. In App. D.9, it is shown that the transition is of second order, with a discontinuous jump in the heat capacity. It is noted that for intermediate temperatures, ΔS_{NS} is negative, and the superconducting state is more ordered than the normal state.

D.9 Heat Capacity

This appendix sets out to show that at low temperatures, the heat capacity is exponentially suppressed in fully gapped superconductors (e.g. isotropic s-wave), while it follows a power law suppression in nodal superconductors (e.g. anisotropic $d_{x^2-y^2}$). It is then shown that in the absence of external fields, superconductivity is a second order phase-transition with a discontinuous jump in the heat capacity at the normal-superconducting phase transition. This jump is quantified in terms of the normal-state electronic heat capacity. The starting point is the heat capacity expression derived in Eq. (C.39),

$$C = 2\beta^2 k_{\mathrm{B}} \mathcal{V} \left\langle \int_{-\infty}^{\infty} d\xi N(\xi) f(E) \left[1 - f(E)\right] \left[E^2(\xi) + \frac{\beta}{2}\frac{d|\Delta|^2}{d\beta}\right] \right\rangle_{\theta_{\mathrm{F}}} . \tag{D.58}$$

It is noted that the function $f(1-f)$ describes a peak centered around μ (here set to zero) that drops off rapidly on an energy scale $k_{\mathrm{B}}T \ll \epsilon_{\mathrm{F}}$, where ϵ_{F} is the Fermi energy. Since the density of states $N(\xi)$ varies on the scale ϵ_{F}, it can be considered to be approximately constant $N(\xi) \approx N(0) \equiv N_{\mathrm{F}}$ in the region where $f(1-f)$ is non-zero, and therefore pulled out of the integral

$$C \approx 2\beta^2 k_{\mathrm{B}} \mathcal{V} N_{\mathrm{F}} \left\langle \int_{-\infty}^{\infty} d\xi f(E) \left[1 - f(E)\right] \left[E^2(\xi) + \frac{\beta}{2}\frac{d|\Delta|^2}{d\beta}\right] \right\rangle_{\theta_{\mathrm{F}}} . \tag{D.59}$$

Here, it is noted that the first term in the parenthesis is the electronic heat capacity for the normal state, denoted $C_{\mathrm{N}}^{\mathrm{el}}$ (i.e. obtained by letting $\Delta \to 0$ such that $E \to \xi$),

$$C_{\mathrm{N}}^{\mathrm{el}} \equiv 2\beta^2 k_{\mathrm{B}} \mathcal{V} N_{\mathrm{F}} \left\langle \int_{-\infty}^{\infty} d\xi f(\xi) \left[1 - f(\xi)\right] \xi^2 \right\rangle_{\theta_{\mathrm{F}}} . \tag{D.60}$$

D.9.1 Low-temperature heat capacity

Letting the temperature T tend to zero, it is noted that

$$\begin{aligned} \frac{\beta}{2}\frac{d|\Delta|^2}{d\beta} &= -k_{\mathrm{B}}T^2 \frac{d|\Delta|^2}{dT} \xrightarrow[T\to 0]{} 0, & \text{(D.61)} \\ f(E)\left[1 - f(E)\right] &= e^{-\beta E}\left(1 + e^{-\beta E}\right)^{-2} \approx e^{-\beta E}, & \text{(D.62)} \end{aligned}$$

yielding the low-temperature heat capacity

$$\begin{aligned} C &\approx 2\beta^2 k_{\mathrm{B}} \mathcal{V} N_{\mathrm{F}} \left\langle \int_{-\infty}^{\infty} d\xi e^{-\beta E} E^2 \right\rangle_{\theta_{\mathrm{F}}} & \text{(D.63)} \\ &= 2\beta^2 k_{\mathrm{B}} \mathcal{V} N_{\mathrm{F}} \left\langle \int_{-\infty}^{\infty} d\xi e^{-\beta\sqrt{\xi^2 + |\Delta|^2}} \left(\xi^2 + |\Delta|^2\right) \right\rangle_{\theta_{\mathrm{F}}} & \text{(D.64)} \\ &= 2\beta^2 k_{\mathrm{B}} \mathcal{V} N_{\mathrm{F}} \left\langle e^{-\beta|\Delta|} \left(\frac{\sqrt{\pi}}{2} \left(\frac{2|\Delta|}{\beta}\right)^{3/2} + |\Delta|^2 \sqrt{\frac{2\pi|\Delta|}{\beta}} \right) \right\rangle_{\theta_{\mathrm{F}}} . & \text{(D.65)} \end{aligned}$$

For a fully gapped superconductor, the angular average is expected to only produce a trivial pre-factor. Expanded to leading order in T for an isotropic s-wave superconductor yields an exponential suppression

$$\frac{C_s}{k_{\mathrm{B}}^2 T_{\mathrm{c}} \mathcal{V} N_{\mathrm{F}}} \approx \sqrt{8\pi} \left(\frac{\Delta_0^s}{k_{\mathrm{B}} T}\right)^{5/2} e^{-\Delta_0^s/k_{\mathrm{B}}T} \xrightarrow[T\to 0]{} 0. \tag{D.66}$$

For a nodal superconductor, on the other hand, the angular average has to be treated carefully. Consider a $d_{x^2-y^2}$ superconductor with $\Delta_d(\boldsymbol{p}_{\mathrm{F}}) = \Delta_0^d \cos(2\theta_{\mathrm{F}})$, where $\Delta_0^d \approx 2.14 k_{\mathrm{B}} T_{\mathrm{c}}$ at $T = 0$ in $2D$, such that $\langle \ldots \rangle_{\theta_{\mathrm{F}}} = \int [\ldots] d\theta_{\mathrm{F}}/2\pi$. Changing integration variable to $x \equiv E/\Delta_0^d = \sqrt{(\xi/\Delta_0^d)^2 + \cos^2(2\theta_{\mathrm{F}})}$, Eq. (D.63) becomes

$$\begin{aligned} C &= 2\beta^2 k_B \mathcal{V} N_F \Delta_0^3 \int_0^\infty dx e^{-\beta\Delta_0 x} x^2 \int_0^{2\pi} \frac{d\theta_{\mathrm{F}}}{2\pi} \frac{\Theta\left(|x| - |\cos(2\theta_{\mathrm{F}})|\right)}{\sqrt{1 - \frac{\cos^2(2\theta_{\mathrm{F}})}{x^2}}} \\ &= \frac{4}{\pi} \beta^2 k_B \mathcal{V} N_F \Delta_0^3 \int_0^\infty dx e^{-\beta\Delta_0 x} x^2 \Bigg[x K(x) \Theta(1-x) \\ &\qquad + K\left(\frac{1}{x}\right) \Theta(x-1) \Bigg], \end{aligned} \tag{D.67}$$

where Θ is the Heaviside step function and $K(x)$ the complete elliptic integral of the first kind, defined as

$$K(x) \equiv \int_0^{\pi/2} \frac{d\theta}{\sqrt{1 - x^2 \sin^2(\theta)}}. \tag{D.68}$$

Expanding to leading order in T, the heat capacity becomes

$$\begin{aligned} C &\approx \frac{4}{\pi} \beta^2 k_B \mathcal{V} N_F \Delta_0^3 \int_0^1 dx e^{-\beta\Delta_0 x} x^3 \frac{\pi}{2} \\ &= 12 k_B \mathcal{V} N_F \frac{(k_B T)^2}{\Delta_0}. \end{aligned} \tag{D.69}$$

Inserting Δ_0^d from Eq. (3.24) yields the low-temperature d-wave heat capacity

$$\frac{C_d}{k_B^2 T_c \mathcal{V} N_F} = \frac{6 e^{\gamma_{\mathrm{E}}}}{\pi\sqrt{e}} \left(\frac{T}{T_c}\right)^2 \approx 6 \left(\frac{T}{T_c}\right)^2, \tag{D.70}$$

which is the announced power law dependence. This behavior can be key in identifying gapped versus nodal superconductors in experiment.

D.9.2 Normal-superconducting phase transition

Going back to the heat capacity in Eq. (D.59), the heat-capacity difference at the normal-superconducting phase-transition is obtained in the limit $T \to T_\mathrm{c}$, with $\Delta \to 0$ and $E \to \xi$,

$$\Delta C_\mathrm{NS} \equiv \left(C_\mathrm{S} - C_\mathrm{N}^\mathrm{el}\right)\Big|_{T_c} = \frac{\mathcal{V} N_\mathrm{F}}{k_\mathrm{B}^2 T_\mathrm{c}^3} \left\langle \int_{-\infty}^{\infty} d\xi f(\xi)\left[1 - f(\xi)\right] \frac{d|\Delta|^2}{d\beta}\Big|_{T_c} \right\rangle_{\theta_\mathrm{F}}. \tag{D.71}$$

Here, the derivative can be shown to be (derived in App. D.6 of Lic. Th. [10])

$$\left\langle \frac{d|\Delta|^2}{d\beta}\Big|_{T_c} \right\rangle_{\theta_\mathrm{F}} = \alpha \tilde{\eta}^{-1} (k_B T_c)^3, \tag{D.72}$$

$$\tilde{\eta} \equiv \left\langle |\eta_\nu(\theta_\mathrm{F})|^4 \right\rangle_{\theta_\mathrm{F}} = \begin{cases} 1, & \nu = s, \\ \frac{3}{2}, & \nu = d_{x^2-y^2}, \end{cases} \tag{D.73}$$

$$\alpha \equiv \frac{8\pi^2}{7\zeta(3)} \approx 9.38, \tag{D.74}$$

where ζ is the Riemann-zeta function. With these results, the heat capacity jumps for s-wave and d-wave superconductors become

$$\frac{\Delta C_\mathrm{NS}^s}{k_\mathrm{B}^2 T_\mathrm{c} \mathcal{V} N_\mathrm{F}} = \alpha \approx 9.38, \tag{D.75}$$

$$\frac{\Delta C_\mathrm{NS}^d}{k_\mathrm{B}^2 T_\mathrm{c} \mathcal{V} N_\mathrm{F}} = \frac{2\alpha}{3} \approx 6.26. \tag{D.76}$$

The value in Eq. (D.76) is used as a scale for the heat capacity calculated numerically in papers II–III. In terms of the electronic heat capacity $C_\mathrm{N}^\mathrm{el}(T) = \gamma T$, where $\gamma \equiv 2\pi^2 k_\mathrm{B}^2 \mathcal{V} N_\mathrm{F}/3$, the jumps are

$$\frac{\Delta C_\mathrm{NS}^s}{C_\mathrm{N}^\mathrm{el}(T_\mathrm{c})} = \frac{12}{7\zeta(3)} \approx 1.43, \tag{D.77}$$

$$\frac{\Delta C_\mathrm{NS}^d}{C_\mathrm{N}^\mathrm{el}(T_\mathrm{c})} = \frac{2}{3}\frac{12}{7\zeta(3)} \approx 0.95, \tag{D.78}$$

which are well-known values for weak-coupling superconductors.

Appendix E

Technical details: surface states

This appendix contains technical details and derivations for Ch. 4 on surface bound state in the presence of a homogeneous superflow. The surface coherence functions are derived in App. E.1, in a convention where different boundary conditions and interfaces can be treated in a unified approach. Special cases are discussed in App. E.2, and the surface propagators are derived in App. E.3. Appendices E.4 and E.5 use these propagators to derive the density of states and energetics, respectively.

E.1 Coherence functions

Consider the interface in Fig. 2.2, and let s be the coordinate along the trajectory $\boldsymbol{v}_{\mathrm{F}}$, such that $\boldsymbol{s} = \boldsymbol{s}_0 + s\boldsymbol{v}_{\mathrm{F}}$, with $s = 0$ at the interface. Translational symmetry along the surface (i.e. along x) ensures that the derivative that enters the Riccati equations can be written

$$\boldsymbol{v}_{\mathrm{F}} \cdot \boldsymbol{\nabla} = v_{\mathrm{F}}\partial_s = v_{\mathrm{F}x}\partial_x + v_{\mathrm{F}y}\partial_y = v_{\mathrm{F}y}\partial_y, \tag{E.1}$$

with $v_{\mathrm{F}x} \equiv v_{\mathrm{F}} \cos\theta_{\mathrm{F}}$ and $v_{\mathrm{F}y} \equiv v_{\mathrm{F}} \sin\theta_{\mathrm{F}}$, and where θ_{F} is the angle between $\boldsymbol{v}_{\mathrm{F}}$ and the interface. Using the notation from Sec. 2.5, the coherence functions in region 1 are separated into the case of $\boldsymbol{v}_{\mathrm{F}}$ pointing away from the interface ($\theta_{\mathrm{F}} \in [0,\pi]$) and towards it ($\theta_{\mathrm{F}} \in [\pi, 2\pi]$)

$$\gamma(\boldsymbol{p}_{\mathrm{F}}, y \geq 0; z) = \begin{cases} \Gamma_1(\boldsymbol{p}_{\mathrm{F}}, y; z) & \forall\, \theta_{\mathrm{F}} \in [0,\pi] \\ \gamma_1(\boldsymbol{p}_{\mathrm{F}}, y; z) & \forall\, \theta_{\mathrm{F}} \in [\pi, 2\pi] \end{cases}, \tag{E.2}$$

$$\tilde{\gamma}(\boldsymbol{p}_{\mathrm{F}}, y \geq 0; z) = \begin{cases} \tilde{\gamma}_1(\boldsymbol{p}_{\mathrm{F}}, y; z) & \forall\, \theta_{\mathrm{F}} \in [0,\pi] \\ \tilde{\Gamma}_1(\boldsymbol{p}_{\mathrm{F}}, y; z) & \forall\, \theta_{\mathrm{F}} \in [\pi, 2\pi] \end{cases}. \tag{E.3}$$

The scattered coherence functions Γ and $\tilde{\Gamma}$ are obtained from the general inhomogeneous solutions derived in App. B.4 as

$$\Gamma_1(\boldsymbol{p}_\mathrm{F}, y; z) = \gamma_{1,\mathrm{h}} + \frac{2i\Omega C e^{-y/\xi}}{1 - \tilde{\Delta} C e^{-y/\xi}}, \tag{E.4}$$

$$\tilde{\Gamma}_1(\boldsymbol{p}_\mathrm{F}, y; z) = \tilde{\gamma}_{1,\mathrm{h}} + \frac{2i\Omega \tilde{C} e^{+y/(-\xi)}}{1 + \Delta \tilde{C} e^{+y/(-\xi)}}, \tag{E.5}$$

$$\gamma_{1,\mathrm{h}}(\boldsymbol{p}_\mathrm{F}, y; z) = \frac{-\Delta}{z_p + i\Omega}, \tag{E.6}$$

$$\gamma_{1,\mathrm{h}}(\boldsymbol{p}_\mathrm{F}, y; z) = \frac{\tilde{\Delta}}{z_p + i\Omega}, \tag{E.7}$$

$$\xi \equiv \frac{\hbar \left|v_{\mathrm{F}y}\right|}{2\Omega}, \tag{E.8}$$

where $z_p \equiv z - \boldsymbol{v}_\mathrm{F} \cdot \boldsymbol{p}_\mathrm{s}$ and $\Omega \equiv \sqrt{|\Delta|^2 - z_p^2}$. It is noted that both Γ and $\tilde{\Gamma}$ end up having the same sign in the exponentials, being stable for all $y \geq 0$. Applying the specular boundary conditions of Eqs. (2.50)–(2.55) at $y = 0$

$$\left[\gamma_{1,\mathrm{h}} + \frac{2i\Omega C}{1 - \tilde{\Delta} C}\right](\theta_\mathrm{F}, 0^+; z) = R_1 \gamma_1(\tilde{\theta}_\mathrm{F}, 0^+; z) + D_1 \gamma_2(\theta_\mathrm{F}, 0^-; z), \tag{E.9}$$

$$\left[\tilde{\gamma}_{1,\mathrm{h}} + \frac{2i\Omega \tilde{C}}{1 + \Delta \tilde{C}}\right](\theta_\mathrm{F}, 0^+; z) = \tilde{R}_1 \tilde{\gamma}_1(\tilde{\theta}_\mathrm{F}, 0^+; z) + \tilde{D}_1 \tilde{\gamma}_2(\theta_\mathrm{F}, 0^-; z), \tag{E.10}$$

$$\theta_\mathrm{F} + \tilde{\theta}_\mathrm{F} = 2\pi, \tag{E.11}$$

where θ_F and $\tilde{\theta}_\mathrm{F}$ are related by reflection of $\boldsymbol{v}_\mathrm{F}$ over the interface. Dropping the arguments, the integration constants have the solutions

$$C = \frac{\left(R_1 \gamma_1 + D_1 \gamma_2 - \gamma_{1,\mathrm{h}}\right)}{\left(2i\Omega + \tilde{\Delta}\right)\left(R_1 \gamma_1 + D_1 \gamma_2 - \gamma_{1,\mathrm{h}}\right)}, \tag{E.12}$$

$$\tilde{C} = \frac{\left(\tilde{R}_1 \tilde{\gamma}_1 + \tilde{D}_1 \tilde{\gamma}_2 - \tilde{\gamma}_{1,\mathrm{h}}\right)}{\left(2i\Omega - \Delta\right)\left(\tilde{R}_1 \tilde{\gamma}_1 + \tilde{D}_1 \tilde{\gamma}_2 - \tilde{\gamma}_{1,\mathrm{h}}\right)}. \tag{E.13}$$

Inserting these solutions into Eqs. (E.4)–(E.5) and rearranging, the scattered solutions can be written

$$\Gamma_1(\boldsymbol{p}_\mathrm{F}, y; z) = \gamma_{1,\mathrm{h}} \left[\frac{2i\Omega + (z_p - i\Omega) S_1 - (z_p + i\Omega) S_1 e^{-y/\xi}}{2i\Omega + (z_p - i\Omega) S_1 - (z_p - i\Omega) S_1 e^{-y/\xi}}\right], \tag{E.14}$$

$$\tilde{\Gamma}_1(\boldsymbol{p}_\mathrm{F}, y; z) = \tilde{\gamma}_{1,\mathrm{h}} \left[\frac{2i\Omega + (z_p - i\Omega) \tilde{S}_1 - (z_p + i\Omega) \tilde{S}_1 e^{-y/\xi}}{2i\Omega + (z_p - i\Omega) \tilde{S}_1 - (z_p - i\Omega) \tilde{S}_1 e^{-y/\xi}}\right], \tag{E.15}$$

where S_1 and $\tilde{S}_1$ are convenient algebraic constructions contain all terms related to the boundary condition

$$S_1(\boldsymbol{p}_\mathrm{F}, y; z) \equiv 1 - R_1 \frac{\gamma_1(\tilde{\theta}_\mathrm{F}, y = 0; z)}{\gamma_{1,\mathrm{h}}(\theta_\mathrm{F}, y = 0; z)} - D_1 \frac{\gamma_2(\theta_\mathrm{F}, y = 0; z)}{\gamma_{1,\mathrm{h}}(\theta_\mathrm{F}, y = 0; z)}, \tag{E.16}$$

$$\tilde{S}_1(\boldsymbol{p}_\mathrm{F}, y; z) \equiv 1 - \tilde{R}_1 \frac{\tilde{\gamma}_1(\tilde{\theta}_\mathrm{F}, y = 0; z)}{\tilde{\gamma}_{1,\mathrm{h}}(\theta_\mathrm{F}, y = 0; z)} - \tilde{D}_1 \frac{\tilde{\gamma}_2(\theta_\mathrm{F}, y = 0; z)}{\tilde{\gamma}_{1,\mathrm{h}}(\theta_\mathrm{F}, y = 0; z)}, \tag{E.17}$$

with $R_1, D_1, \tilde{R}_1, \tilde{D}_1$ given by Eqs. (2.52)–(2.55). It is seen that in the absence of inhomogeneities close to the interface, both Γ_1 and $\tilde{\Gamma}_1$ decay to their bulk solutions $\gamma_{1,\mathrm{h}}$ and $\tilde{\gamma}_{1,\mathrm{h}}$ exponentially from the interface, over a distance given by ξ. The above solutions are valid quite generally, even for inhomogeneous incoming coherence functions. However, when regions 1 and 2 are homogeneous (apart from the interface), the gauge that is used here $\tilde{\Delta} = \Delta^* = \Delta$ leads to

$$S_1 = \tilde{S}_1 \equiv S. \tag{E.18}$$

Furthermore, this thesis considers interfaces where the boundary term S reduces to a simple integer constant, greatly simplifying the solutions to the coherence functions. Appendix E.2 studies these simplifications, and shows that $S = 2$ at an interface with maximal pairbreaking, $S = 1$ at a transparent S-N interface, and $S = 0$ for angles where incoming and outgoing coherence functions sees the same order parameter amplitude (mimicking a bulk system). Appendix. E.3 uses the coherence functions and the simplifications to derive the surface propagators.

E.2 Scattering term S: important boundary cases

Although the notation with the scattering terms S_1 and $\tilde{S}_1$ introduced in App. E.1 might seem strange and foreboding, it is reminded that it is just a convenient algebraic construction that enables different interfaces and boundary conditions to be treated with a unified approach. The goal of this appendix is to show how these terms reduce to integer constants in important special cases. This simplifies the solutions of the inhomogeneous coherence functions, which are used in App. E.3 to derive surface propagators. It is also shown how scattering at various interfaces can lead to pairbreaking. It is reminded that $S_1 = \tilde{S}_1 \equiv S$ for homogeneous regions 1 and 2 (at least in the phase-less gauge). It is also noted that interface scattering and boundary conditions in general might be very complicated, much more so than presented here. What is described here is thus a very simplified model for clean and specular interfaces.

In general, the boundary terms S_1 and $\tilde{S}_1$ defined in Eqs. (E.16) and (E.17) are functions defined on the whole complex plane $S_1, \tilde{S}_1 \in \mathbb{C}$, due to the order parameters and and coherence functions being complex valued. They might even diverge due to the factors $\gamma_{1,\mathrm{h}}^{-1}$, e.g. when $\Delta(\theta_\mathrm{F}) = 0$ due to order-parameter suppression or along order-parameter nodes. In this case though, the scattered coherence functions are still bounded $\Gamma_1, \tilde{\Gamma}_1 \to 0$. With such a general scattering term, the physical intuition of any result is obscured, and certain calculations become difficult to carry out analytically. However, in the case when regions 1 and 2 are free of other inhomogeneities ($\gamma_1 = \gamma_{1,\mathrm{h}}$, $\gamma_2 = \gamma_{2,\mathrm{h}}$ and similar for tilde functions), the situation simplifies drastically. This is especially true when impinging coherence functions have the same order parameter structure as the scattered ones up to a sign, i.e. $\Delta_2/\Delta_1 = c_D \in \{0, \pm 1\}$ for transmitted coherence functions (with 0 for e.g. an S-N interface), and $\Delta_1(\tilde{\theta}_\mathrm{F})/\Delta_1(\theta_\mathrm{F}) = c_R = \pm 1$ for reflected quasiparticles. Using this together with $R_1 + D_1 = 1$ and $\tilde{R}_1 + \tilde{D}_1 = 1$ from Eqs. (2.56)–(2.57), reduces Eqs. (E.16)–(E.17) to

$$S_1 = 1 - c_1 R_1 - c_D D_1 = (1 - c_D) - R_1(c_R - c_D), \tag{E.19}$$

$$\tilde{S}_1 = 1 - c_R \tilde{R}_1 - c_D \tilde{D}_1 = (1 - c_D) - \tilde{R}_1(c_R - c_D), \tag{E.20}$$

With perfect reflection or transmission, there are three simple and important scenarios,

1. $S_1 = \tilde{S}_1 = 0$, (trivial case: no inhomogeneity at the interface),
2. $S_1 = \tilde{S}_1 = 1$, (e.g. transparent S-N interface),
3. $S_1 = \tilde{S}_1 = 2$, (e.g. maximally pairbreaking interface).

Scenario 1 arises when the impinging and scattered coherence functions see the same order parameter amplitude. This could either be for certain special angles, or in the trivial case for all angles. When it occurs for all angles, the entire system is essentially a bulk system, where the interface virtually does not exist. In any case, this gives the homogeneous coherence functions

$$S_1 = \tilde{S}_1 \quad \to \quad 0, \tag{E.21}$$

$$\Gamma_1(\boldsymbol{p}_{\mathrm{F}}; z) \quad = \quad \gamma_{1,\mathrm{h}}, \tag{E.22}$$

$$\tilde{\Gamma}_1(\boldsymbol{p}_{\mathrm{F}}; z) \quad = \quad \tilde{\gamma}_{1,\mathrm{h}}, \tag{E.23}$$

Scenario 2 occurs for example when there is perfect reflection and $\gamma_1(\tilde{\theta}_{\mathrm{F}}) = 0$, or when there is perfect transmission and $\gamma_2 = 0$. The coherence functions reduce to

$$S_1 = \tilde{S}_1 \quad \to \quad 1, \tag{E.24}$$

$$\Gamma_1(\boldsymbol{p}_{\mathrm{F}}, y; z) \quad = \quad (z_p + i\Omega)\,\gamma_{1,\mathrm{h}} \left[\frac{1 - e^{-y/\xi}}{(z_p + i\Omega) - (z_p - i\Omega)e^{-y/\xi}} \right], \tag{E.25}$$

$$\tilde{\Gamma}_1(\boldsymbol{p}_{\mathrm{F}}, y; z) \quad = \quad (z_p + i\Omega)\,\tilde{\gamma}_{1,\mathrm{h}} \left[\frac{1 - e^{-y/\xi}}{(z_p + i\Omega) - (z_p - i\Omega)e^{-y/\xi}} \right], \tag{E.26}$$

and the interface acts as a transparent S-N interface, where the order parameter and the incoming coherence functions are suppressed at the interface, and heals back to the bulk value in region 1 over the coherence length.

Scenario 3 occurs when the incoming and outgoing coherence functions see an order parameter with the same magnitude but with different signs. The solutions simplify to

$$S_1 = \tilde{S}_1 \quad \to \quad 2, \tag{E.27}$$

$$\Gamma_1(\boldsymbol{p}_{\mathrm{F}}, y; z) \quad = \quad \gamma_{1,\mathrm{h}} \left[\frac{z_p - (z_p + i\Omega)e^{-y/\xi}}{z_p - (z_p - i\Omega)e^{-y/\xi}} \right], \tag{E.28}$$

$$\tilde{\Gamma}_1(\boldsymbol{p}_{\mathrm{F}}, y; z) \quad = \quad \tilde{\gamma}_{1,\mathrm{h}} \left[\frac{z_p - (z_p + i\Omega)e^{-y/\xi}}{z_p - (z_p - i\Omega)e^{-y/\xi}} \right]. \tag{E.29}$$

This is a special topological scenario, where superconducting pairs are broken up into midgap quasiparticle states with a flat dispersion at zero energy, that are spin-degenerate and and degenerate over the parallel momentum $\boldsymbol{p}_{\parallel} \to -\boldsymbol{p}_{\parallel}$ [60, 61, 159, 160, 209]. These states lead to e.g. zero-bias conductance peaks [62, 63, 147, 210]. Superconductivity is again suppressed at the interface, and recovers exponentially over the coherence length into region 1. This so-called pairbreaking case is the main scenario considered in this thesis. In both the second and third scenarios, favorable condensation energy is lost due to lost superconductivity. The main difference is that at the pairbreaking interface, the bound states show a T^{-1} dependence in e.g. the propagator.

It will now be shown how the above cases might arise at particular interfaces.

A superconductor-vacuum interface

In a superconductor-vacuum interface, $D_1 = \tilde{D}_1 = 0$ and $\gamma_2 = \tilde{\gamma}_2 = 0$, with the scattering terms

$$S_1 = 1 - \frac{\gamma_1(\tilde{\theta}_\mathrm{F})}{\gamma_{1,\mathrm{h}}(\theta_\mathrm{F})}, \tag{E.30}$$

$$\tilde{S}_1 = 1 - \frac{\tilde{\gamma}_1(\tilde{\theta}_\mathrm{F})}{\tilde{\gamma}_{1,\mathrm{h}}(\theta_\mathrm{F})}. \tag{E.31}$$

In the case of a bulk superconductor with $\Delta(\tilde{\theta}_\mathrm{F}) = \pm\Delta(\theta_\mathrm{F})$,

$$S_1 = \tilde{S}_1 = 1 \mp 1 \in \{0, 2\}, \tag{E.32}$$

which reduces to the bulk ($S = 0$) or the pairbreaking case ($S = 2$) for equal or opposite order-parameter signs, respectively. This could for example be a [110]-interface of a d-wave superconductor (the interface is parallel to the nodes). Misaligning the interface with respect to the nodes slightly, there is still a sign-change (and hence zero-energy states), but the amplitude difference makes analytic calculations more difficult due to interference terms.

A tunneling barrier to a normal metal

At a tunneling barrier between a superconductor and a normal metal with $\gamma_2 = \tilde{\gamma}_2 = 0$, the reflection and transmission probability become the normal ones on the superconducting side $R_1 = \tilde{R}_1 = \mathcal{R}$, and the scattering terms take on the forms

$$S_1 = 1 - \mathcal{R}\frac{\gamma_1(\tilde{\theta}_\mathrm{F})}{\gamma_{1,\mathrm{h}}(\theta_\mathrm{F})}, \tag{E.33}$$

$$\tilde{S}_1 = 1 - \mathcal{R}\frac{\tilde{\gamma}_1(\tilde{\theta}_\mathrm{F})}{\tilde{\gamma}_{1,\mathrm{h}}(\theta_\mathrm{F})}. \tag{E.34}$$

For a bulk superconductor with $\Delta(\tilde{\theta}_\mathrm{F}) = \pm\Delta(\theta_\mathrm{F})$,

$$S_1 = \tilde{S}_1 = 1 \mp \mathcal{R} \in [0, 2], \tag{E.35}$$

and all of the three special scenarios discussed earlier are hence possible, depending on the order-parameter signs and the transmission at the interface.

A tunneling barrier to a superconductor

At a tunneling barrier between two superconductors, the scattering terms again take on the general forms given by Eqs. (E.16) and (E.17), where region 2 can have any complicated superconducting order. For two superconductors with $\Delta_1(\tilde{\theta}_\mathrm{F}) = \pm\Delta_1(\theta_\mathrm{F})$ and $\Delta_2 = \pm\Delta_1$, the scattering terms are again given by Eqs. (E.19) and (E.20). Table E.1 summarizes the possible values of S_1 and $\tilde{S}_1$, showing that the three special scenarios are possible.

A weak ferromagnet-superconductor interface

At a ferromagnet-superconductor interface, the interplay between the superconducting order and the magnetic order leads to interesting effects, like spin-polarization, spin singlet-triplet correlations, and surface Andreev states [88, 211–215]. Therefore, treating such a system is typically more complicated, as it involves full spin degrees of freedom. For simplicity, the ferromagnetic part is therefore treated as a ferromagnetic insulator with only reflection taken into account, as in Ref. [211]. A finite magnetization vector $\hat{m} = \hat{z}$ in the interface leads to modified boundary conditions [216, 217], with a spin-dependent phase shift for scattered coherence functions

$$\Gamma_1(\theta_\mathrm{F}) i\sigma_y = \mathcal{M}\gamma_1(\tilde{\theta}_\mathrm{F}) i\sigma_y \tilde{\mathcal{M}}, \tag{E.36}$$

$$\mathcal{M} \equiv e^{i\vartheta\hat{m}\cdot\boldsymbol{\sigma}/2}, \tag{E.37}$$

where ϑ is the spin-mixing angle and $\tilde{\mathcal{M}} = \mathcal{M}^*$, with a similar expression for tilde coherence functions. For general spin-mixing angles, interface scattering induces spin-triplet correlations, and Andreev bound states $\varepsilon_\mathrm{b} = \pm\Delta\cos(\vartheta/2)$. For the two special cases $\vartheta \in \{0, \pi\}$, however, the spin-triplet correlations vanish, and the scattered solution equals the incoming one up to a sign. Only these simplified cases are considered, where $\vartheta = \pi$ corresponds to the maximally pairbreaking interface with zero-energy states, and $\vartheta = 0$ essentially corresponds to an S-N interface. Since $\gamma_2 = \tilde{\gamma}_2 = 0$, $R_1 = \tilde{R}_1 = \mathcal{R}$, the boundary terms are

$$S_1 = 1 \mp \mathcal{R}\frac{\gamma_1(\tilde{\theta}_\mathrm{F})}{\gamma_{1,\mathrm{h}}(\theta_\mathrm{F})}, \tag{E.38}$$

$$\tilde{S}_1 = 1 \mp \mathcal{R}\frac{\tilde{\gamma}_1(\tilde{\theta}_\mathrm{F})}{\tilde{\gamma}_{1,\mathrm{h}}(\theta_\mathrm{F})}. \tag{E.39}$$

Table E.1: *Possible scattering term values at a simplified superconductor-superconductor tunneling barrier, with the same order parameter structure.*

$\frac{\Delta_1(\tilde{\theta}_\mathrm{F})}{\Delta_1(\theta_\mathrm{F})}$	$\frac{\Delta_2}{\Delta_1}$	S_1	$\tilde{S}_1$
$+1$	$+1$	0	0
$+1$	-1	$2(1-R_1)$	$2(1-\tilde{R}_1)$
-1	$+1$	$2R_1$	$2\tilde{R}_1$
-1	-1	2	2

For a bulk region with the same order parameter structures, the simple special case is again obtained

$$S_1 = \tilde{S}_1 = 1 \mp \mathcal{R} \in [0,2]. \tag{E.40}$$

E.3 Propagators

This appendix uses the coherence functions derived in App. E.1, to obtain the quasiclassical propagators when region 1 is a homogeneous system, i.e. when Δ_1 is homogeneous, resulting in $\gamma_1 = \gamma_{1,\mathrm{h}}$ and $\tilde{\gamma}_1 = \tilde{\gamma}_{1,\mathrm{h}}$. For a spin-singlet system, the scalar quasiparticle and pair propagators are given by Eqs. (2.36)–(2.39)

$$\begin{aligned}
g_0(\boldsymbol{p}_\mathrm{F}, \boldsymbol{R}; z) &= -i\pi \frac{1-\gamma\tilde{\gamma}}{1+\gamma\tilde{\gamma}}, && \text{(E.41)}\\
\tilde{g}_0(\boldsymbol{p}_\mathrm{F}, \boldsymbol{R}; z) &= +i\pi \frac{1-\gamma\tilde{\gamma}}{1+\gamma\tilde{\gamma}}, && \text{(E.42)}\\
f(\boldsymbol{p}_\mathrm{F}, \boldsymbol{R}; z) &= -2i\pi \frac{\gamma}{1+\gamma\tilde{\gamma}}, && \text{(E.43)}\\
\tilde{f}(\boldsymbol{p}_\mathrm{F}, \boldsymbol{R}; z) &= +2i\pi \frac{\tilde{\gamma}}{1+\gamma\tilde{\gamma}}. && \text{(E.44)}
\end{aligned}$$

Considering separately the cases of $\boldsymbol{v}_\mathrm{F}$ pointing towards and away from the surface,

$$\begin{aligned}
g_0(\boldsymbol{p}_\mathrm{F}, y; z) &= -i\pi \frac{1-\Gamma_1\tilde{\gamma}_1}{1+\Gamma_1\tilde{\gamma}_1}, \qquad \forall\, \theta_\mathrm{F} \in [0, \pi] && \text{(E.45)}\\
g_0(\boldsymbol{p}_\mathrm{F}, y; z) &= -i\pi \frac{1-\gamma_1\tilde{\Gamma}_1}{1+\gamma_1\tilde{\Gamma}_1}, \qquad \forall\, \theta_\mathrm{F} \in [\pi, 2\pi] && \text{(E.46)}
\end{aligned}$$

and similar for the other propagators. With the general solutions from Eqs. (E.14)–(E.15), the products take the form

$$\begin{aligned}
\Gamma_1\tilde{\gamma}_1 &= -\left(\frac{z_p - i\Omega}{z_p + i\Omega}\right) \frac{2i\Omega + (z_p - i\Omega)S_1 - (z + i\Omega)S_1 e^{-y/\xi}}{2i\Omega + (z_p - i\Omega)S_1 - (z - i\Omega)S_1 e^{-y/\xi}}, && \text{(E.47)}\\
\gamma_1\tilde{\Gamma}_1 &= -\left(\frac{z_p - i\Omega}{z_p + i\Omega}\right) \frac{2i\Omega + (z_p - i\Omega)\tilde{S}_1 - (z + i\Omega)\tilde{S}_1 e^{-y/\xi}}{2i\Omega + (z_p - i\Omega)\tilde{S}_1 - (z - i\Omega)\tilde{S}_1 e^{-y/\xi}}. && \text{(E.48)}
\end{aligned}$$

After some algebra, the propagators are found to be

$$\begin{aligned}
g_0(\boldsymbol{p}_\mathrm{F}, y; z) &= -\pi\frac{z_p}{\Omega}\left(1 - \frac{S z_p e^{-y/\xi}}{2i\Omega + (z_p - i\Omega)S}\right) + \pi\frac{S\Omega e^{-y/\xi}}{2i\Omega + (z_p - i\Omega)S}, && \text{(E.49)}\\
\tilde{g}_0(\boldsymbol{p}_\mathrm{F}, y; z) &= +\pi\frac{z_p}{\Omega}\left(1 - \frac{S z_p e^{-y/\xi}}{2i\Omega + (z_p - i\Omega)S}\right) - \pi\frac{S\Omega e^{-y/\xi}}{2i\Omega + (z_p - i\Omega)S}, && \text{(E.50)}\\
f(\boldsymbol{p}_\mathrm{F}, y; z) &= +\pi\frac{\Delta}{\Omega}\left(1 - \frac{S z_p e^{-y/\xi}}{2i\Omega + (z_p - i\Omega)S}\right) - i\pi\frac{\mathrm{sgn}(\hat{\boldsymbol{v}}_{\mathrm{F}y}) S\Delta e^{-y/\xi}}{2i\Omega + (z_p - i\Omega)S}, && \text{(E.51)}\\
\tilde{f}(\boldsymbol{p}_\mathrm{F}, y; z) &= +\pi\frac{\tilde{\Delta}}{\Omega}\left(1 - \frac{S z_p e^{-y/\xi}}{2i\Omega + (z_p - i\Omega)S}\right) + i\pi\frac{\mathrm{sgn}(\hat{\boldsymbol{v}}_{\mathrm{F}y}) S\tilde{\Delta} e^{-y/\xi}}{2i\Omega + (z_p - i\Omega)S}, && \text{(E.52)}\\
S(\boldsymbol{p}_\mathrm{F}, y; z) &= \begin{cases} S_1 & \forall\, \theta_\mathrm{F} \in [0, \pi] \\ \tilde{S}_1 & \forall\, \theta_\mathrm{F} \in [\pi, 2\pi] \end{cases}. && \text{(E.53)}
\end{aligned}$$

E.3.1 Surface propagators

Each propagator can conveniently be separated into a bulk and a surface part

$$
\begin{aligned}
g_0(\boldsymbol{p}_\mathrm{F}, y; z) &= g_0^\mathrm{bulk} + g_0^\mathrm{surf}, && \text{(E.54)}\\
g_0^\mathrm{bulk}(\boldsymbol{p}_\mathrm{F}; z) &= -\pi \frac{z_p}{\Omega}, && \text{(E.55)}\\
g_0^\mathrm{surf}(\boldsymbol{p}_\mathrm{F}, y; z) &= +\pi \frac{S|\Delta|^2}{\Omega\,[2i\Omega + (z_p - i\Omega)S]} e^{-y/\xi}, && \text{(E.56)}\\
f(\boldsymbol{p}_\mathrm{F}, y; z) &= f^\mathrm{bulk} + f^\mathrm{surf}, && \text{(E.57)}\\
f^\mathrm{bulk}(\boldsymbol{p}_\mathrm{F}; z) &= +\pi \frac{\Delta}{\Omega}, && \text{(E.58)}\\
f^\mathrm{surf}(\boldsymbol{p}_\mathrm{F}, y; z) &= -\pi S \left(\frac{\Delta}{\Omega}\right) \frac{z_p + i\,\mathrm{sgn}(\hat{\boldsymbol{v}}_{\mathrm{F}y})\Omega}{\Omega\,[2i\Omega + (z_p - i\Omega)S]} e^{-y/\xi}, && \text{(E.59)}
\end{aligned}
$$

or a condensate and midgap state part

$$
\begin{aligned}
g_0(\boldsymbol{p}_\mathrm{F}, y; z) &= g_0^\mathrm{cond} + g_0^\mathrm{MGS}, && \text{(E.60)}\\
g_0^\mathrm{cond}(\boldsymbol{p}_\mathrm{F}, y; z) &= -\pi \frac{z_p}{\Omega} \left(1 - \frac{S z_p e^{-y/\xi}}{2i\Omega + (z_p - i\Omega)S}\right), && \text{(E.61)}\\
g_0^\mathrm{MGS}(\boldsymbol{p}_\mathrm{F}, y; z) &= +\pi \frac{S\Omega e^{-y/\xi}}{2i\Omega + (z_p - i\Omega)S}, && \text{(E.62)}\\
f(\boldsymbol{p}_\mathrm{F}, y; z) &= f^\mathrm{cond} + f^\mathrm{MGS}, && \text{(E.63)}\\
f^\mathrm{cond}(\boldsymbol{p}_\mathrm{F}, y; z) &= +\pi \frac{\Delta}{\Omega} \left(1 - \frac{S z_p e^{-y/\xi}}{2i\Omega + (z_p - i\Omega)S}\right), && \text{(E.64)}\\
f^\mathrm{MGS}(\boldsymbol{p}_\mathrm{F}, y; z) &= -i\pi \frac{\mathrm{sgn}(\hat{\boldsymbol{v}}_{\mathrm{F}y}) S\Delta e^{-y/\xi}}{2i\Omega + (z_p - i\Omega)S}, && \text{(E.65)}
\end{aligned}
$$

with similar relations for tilde propagators. These separations make it convenient to calculate surface properties separately from the bulk properties (the latter which were computed in Ch. 3). In case of a complete bulk system, i.e. when $S = 0$ from Eq. (E.21), the propagators retain their respective bulk forms given by Eqs. (3.8)–(3.11).

E.3.2 Propagators at a pairbreaking interface

For a maximally pairbreaking interface with a sign-change in the order parameter, i.e. when $S = 2$ as in Eq. (E.27), the propagators are

$$
\begin{aligned}
g_0^{\mathrm{pb}}(\boldsymbol{p}_{\mathrm{F}}, y; z) &= -\pi \frac{z_p}{\Omega}\left(1 - e^{-y/\xi}\right) + \pi \frac{\Omega}{z_p} e^{-y/\xi}, && \text{(E.66)}\\
\tilde{g}_0^{\mathrm{pb}}(\boldsymbol{p}_{\mathrm{F}}, y; z) &= +\pi \frac{z_p}{\Omega}\left(1 - e^{-y/\xi}\right) - \pi \frac{\Omega}{z_p} e^{-y/\xi}, && \text{(E.67)}\\
f^{\mathrm{pb}}(\boldsymbol{p}_{\mathrm{F}}, y; z) &= +\pi \frac{\Delta}{\Omega}\left(1 - e^{-y/\xi}\right) - i\pi \operatorname{sgn}(\hat{\boldsymbol{v}}_{\mathrm{F}y}) \frac{\Delta}{z_p} e^{-y/\xi}, && \text{(E.68)}\\
\tilde{f}^{\mathrm{pb}}(\boldsymbol{p}_{\mathrm{F}}, y; z) &= +\pi \frac{\tilde{\Delta}}{\Omega}\left(1 - e^{-y/\xi}\right) + i\pi \operatorname{sgn}(\hat{\boldsymbol{v}}_{\mathrm{F}y}) \frac{\tilde{\Delta}}{z_p} e^{-y/\xi}. && \text{(E.69)}
\end{aligned}
$$

Here it is clearly seen that the condensate term is completely suppressed at the surface and heals to the bulk form exponentially from the interface, while the bound-state term is maximal at the interface and decays exponentially away from it, both over a distance given by ξ. Furthermore, in the absence of superflows, the bound-state term scales as $1/\varepsilon_n \sim 1/T$, which gives a completely different temperature scaling than the condensate term. The bound-state term might therefore dominate at low temperatures. These pairbreaking propagators are used to derive the surface bound state spectrum in Sec 4.3.

E.3.3 Propagators at a transparent S-N interface

For an interface where the order parameter goes from zero to a finite value (e.g. a step-function form at a transparent S-N interface), $S = 1$ from Eq. (E.27), and the propagators are

$$
\begin{aligned}
g_0^{\mathrm{SN}}(\boldsymbol{p}_{\mathrm{F}}, y; z) &= -\pi \frac{z_p}{\Omega}\left(1 - \frac{z_p e^{-y/\xi}}{z_p + i\Omega}\right) + \pi \frac{\Omega e^{-y/\xi}}{z_p + i\Omega}, && \text{(E.70)}\\
\tilde{g}_0^{\mathrm{SN}}(\boldsymbol{p}_{\mathrm{F}}, y; z) &= +\pi \frac{z_p}{\Omega}\left(1 - \frac{z_p e^{-y/\xi}}{z_p + i\Omega}\right) - \pi \frac{\Omega e^{-y/\xi}}{z_p + i\Omega}, && \text{(E.71)}\\
f^{\mathrm{SN}}(\boldsymbol{p}_{\mathrm{F}}, y; z) &= +\pi \frac{\Delta}{\Omega}\left(1 - \frac{z_p e^{-y/\xi}}{z_p + i\Omega}\right) - i\pi \frac{\operatorname{sgn}(\hat{\boldsymbol{v}}_{\mathrm{F}y}) \Delta e^{-y/\xi}}{z_p + i\Omega}, && \text{(E.72)}\\
\tilde{f}^{\mathrm{SN}}(\boldsymbol{p}_{\mathrm{F}}, y; z) &= +\pi \frac{\tilde{\Delta}}{\Omega}\left(1 - \frac{z_p e^{-y/\xi}}{z_p + i\Omega}\right) + i\pi \frac{\operatorname{sgn}(\hat{\boldsymbol{v}}_{\mathrm{F}y}) \tilde{\Delta} e^{-y/\xi}}{z_p + i\Omega}. && \text{(E.73)}
\end{aligned}
$$

E.4 Density of states

The goal of this appendix is to obtain a general expression for the momentum-resolved surface DOS, in terms of the boundary term S that was introduced towards the end of App. E.1 and analyzed in App. E.2. The LDOS is given by Eq. (2.59), with N_F being the normal-state DOS per spin

$$N(\boldsymbol{R},\varepsilon) = -N_\mathrm{F}\frac{2}{\pi}\left\langle \mathrm{Im}\left[g_0^R(\boldsymbol{p}_\mathrm{F},\boldsymbol{R};\varepsilon)\right]\right\rangle_{\theta_\mathrm{F}}, \tag{E.74}$$

which can be separated into a surface LDOS and a bulk LDOS (the latter derived in App. D.6 and D.7 for s and d-wave respectively), by separating the propagator into bulk and surface parts as in Eqs. (E.54)–(E.56). For the Retarded propagator,

$$z_p^\mathrm{R} = \varepsilon + i\delta - \boldsymbol{v}_\mathrm{F}\cdot\boldsymbol{p}_\mathrm{s} \equiv \epsilon + i\delta, \tag{E.75}$$

where $\delta = 0^+$ is infinitesimal, and $\epsilon = \varepsilon - \boldsymbol{v}_\mathrm{F}\cdot\boldsymbol{p}_\mathrm{s}$ is a Doppler-shifted real energy.

The subgap and continuum spectra are studied independently below, i.e. $\epsilon^2 < |\Delta(\boldsymbol{p}_\mathrm{F})|^2$ and $\epsilon^2 > |\Delta(\boldsymbol{p}_\mathrm{F})|^2$, respectively. Note that during the derivations, the arguments are typically dropped for brevity $\Delta(\boldsymbol{p}_\mathrm{F}) = \Delta$.

E.4.1 Subgap spectrum

Expanding the surface propagator in δ (i.e. the infinitesimal shift in the Retarded energy) and taking the imaginary part yields

$$\frac{\mathrm{Im}\left[g_\mathrm{surf}^\mathrm{R}(\boldsymbol{p}_\mathrm{F},y;z)\right]}{-\pi} = \frac{|\Delta|^2}{\Omega}Se^{-y/\xi}\frac{\Omega(2-S)+\delta\left[S-\frac{\epsilon^2}{\Omega^2}\left(1+\frac{y}{\xi}\right)\right]}{\left(S\epsilon+\delta(2-S)\frac{\epsilon}{\Omega}\right)^2+\left(\Omega(2-S)+S\delta\right)^2} + \mathcal{O}(\delta^2), \tag{E.76}$$

where $\xi \equiv \hbar\left|v_{\mathrm{F}y}\right|/2\Omega$, with $\Omega \equiv \sqrt{|\Delta|^2-\epsilon^2}$. Letting $\delta \to 0$, the momentum-resolved surface DOS is

$$N(\boldsymbol{p}_\mathrm{F},y;|\epsilon|<|\Delta|) = 2N_\mathrm{F}\frac{|\Delta|^2S(2-S)e^{-y/\xi}}{(S\epsilon)^2+(2-S)^2\Omega^2}. \tag{E.77}$$

This is obviously a surface term which decays over ξ into the bulk. As a consistency check, the DOS approaches the normal-state DOS ($2N_\mathrm{F}$) as $\Delta \to 0$, and there are no midgap states in the bulk system since $N(|\epsilon|<|\Delta|) = 0$ for $y \to \infty$ or $S = 0$ (recall that this is the momentum-resolved DOS, the momentum-averaged d-wave spectrum clearly has subgap states even in bulk, as evident in Sec. 3.3). It is noted that for a transparent S-N interface ($S = 1$), the spectrum is described by a normal-state DOS that decays from the surface

$$N(\boldsymbol{p}_\mathrm{F},y;|\epsilon|<|\Delta|) \xrightarrow[S\to 1]{} 2N_\mathrm{F}e^{-y/\xi}. \tag{E.78}$$

Re-arranging the terms in Eq. (E.77), it is found that the midgap state spectrum is given by a Lorentzian $L(\varepsilon;\varepsilon_0,\Gamma)$ with energy parameter ε, center ε_0 and full-width at half-maximum Γ

$$\frac{N(\boldsymbol{p}_{\mathrm{F}},y;|\epsilon|<|\Delta|)}{2N_{\mathrm{F}}} = \frac{S}{\sqrt{S-1}}\frac{\pi}{2}|\Delta|e^{-y/\xi}L(\varepsilon;\varepsilon_0,\Gamma), \tag{E.79}$$

$$L(\varepsilon;\varepsilon_0,\Gamma) = \frac{\frac{1}{\pi}\left(\frac{1}{2}\Gamma\right)}{(\varepsilon-\varepsilon_0)^2+\left(\frac{1}{2}\Gamma\right)^2}, \tag{E.80}$$

$$\epsilon_0 = \boldsymbol{v}_{\mathrm{F}}\cdot\boldsymbol{p}_{\mathrm{s}}, \tag{E.81}$$

$$\Gamma = \frac{2-S}{\sqrt{S-1}}|\Delta|. \tag{E.82}$$

The superflow term $\boldsymbol{v}_{\mathrm{F}}\cdot\boldsymbol{p}_{\mathrm{s}}$ explicitly acts as a Doppler-shift which moves the peak. As $S\to 2$, the width $\Gamma\to 0$ becomes infinitesimal, and the DOS is described by a delta-distribution $\delta(\epsilon)$. Note that e.g. at a tunneling barrier between a superconductor and normal system, the transmission probability $\mathcal{D}=|t|^2$ directly determines the shape of the Lorentzian, since then $S=1+\mathcal{R}=2-\mathcal{D}$ (see App. E.2). The energy cost of these zero-energy states are derived in App. E.5.2.

E.4.2 Continuum spectrum

As $\epsilon^2>|\Delta|^2$, the term Ω is rewritten $\Omega=-i\Omega'$, where $\Omega'\equiv\sqrt{\epsilon^2-|\Delta|^2}$. Taking the imaginary part of the full propagator and letting $\delta\to 0$, the momentum-resolved DOS is found to be

$$\frac{N(\boldsymbol{p}_{\mathrm{F}},y;|\epsilon|>|\Delta|)}{2N_{\mathrm{F}}} = \frac{\epsilon}{\Omega'} - \frac{S|\Delta|^2}{\Omega'\left[S\epsilon+(2-S)\Omega'\right]}\cos\!\left(\frac{2y\Omega'}{\hbar|v_{\mathrm{F}y}|}\right), \tag{E.83}$$

where the first term is the bulk DOS derived in Apps. D.6 and D.7, and the second term describes a modification due to interface interference. Again, the superflow in $\epsilon\equiv\varepsilon-\boldsymbol{v}_{\mathrm{F}}\cdot\boldsymbol{p}_{\mathrm{s}}$ acts as a Doppler shift to the real energy ε. In the normal-state ($\Delta\to 0$), or in the continuum limit ($|\varepsilon|\gg|\Delta|$), the normal-state DOS is retained $N\to 2N_{\mathrm{F}}$. For a pairbreaking system ($S=2$), or an S-N interface with perfect transmission ($S=1$), the LDOS simplifies to

$$\frac{N(\boldsymbol{p}_{\mathrm{F}},y;|\epsilon|>|\Delta|)}{2N_{\mathrm{F}}} \xrightarrow[S\to 2]{} \frac{\epsilon}{\Omega'} - \frac{|\Delta|^2}{\Omega'\epsilon}\cos\!\left(\frac{2y\Omega'}{\hbar|v_{\mathrm{F}y}|}\right), \tag{E.84}$$

$$\frac{N(\boldsymbol{p}_{\mathrm{F}},y;|\epsilon|>|\Delta|)}{2N_{\mathrm{F}}} \xrightarrow[S\to 1]{} \frac{\epsilon}{\Omega'} - \frac{|\Delta|^2}{\Omega'\left[\epsilon+\Omega'\right]}\cos\!\left(\frac{2y\Omega'}{\hbar|v_{\mathrm{F}y}|}\right). \tag{E.85}$$

Since the interference disappears whenever the amplitude is the same for an incoming and outgoing coherence functions ($S\to 0$), they are hence understood to come from scattering at inhomogeneities where $|\Delta|$ goes from one bulk value to another. This is in complete analogy with usual barrier scattering in quantum mechanics. The interference is maximal at

$$\frac{2y\Omega'}{\hbar|v_{\mathrm{F}y}|} = 2n\pi, \tag{E.86}$$

and minimal at

$$\frac{2y\Omega'}{\hbar|v_{\mathrm{F}y}|} = (2n+1)\pi, \tag{E.87}$$

where $n \in \mathbb{Z}$. As discussed in Sec. 4.3, these interference effects are known as Tomasch-oscillations [137–143], and have a tendency to occur close to inhomogeneities, like interface scattering that effectively connect different order parameter amplitudes.

E.5 Surface energetics

This appendix derives a simplified form of the Luttinger-Ward free energy close to an interface with maximally pairbreaking surface scattering. This is used to derive the energy cost of zero-energy midgap states derived in App. E.4, and the energy gain of Doppler shifting them with a superflow. The magnetic energy density due to the superflow is also estimated.

E.5.1 Surface free energy

The Luttinger-Ward free energy $\delta\Omega$ is defined in Eq. (2.69), and without the magnetic energy density it is

$$\delta\Omega = \int d\boldsymbol{R} \Bigg\{ N_{\mathrm{F}} k_{\mathrm{B}} T \frac{1}{2} \int_0^1 d\lambda \Bigg\langle \sum_{|\varepsilon_n|<\Omega_{\mathrm{c}}} \mathrm{Tr}\left[\hat{\Delta}(\hat{g}_\lambda - \frac{1}{2}\hat{g})\right] \Bigg\rangle_{\theta_{\mathrm{F}}} \Bigg\}, \tag{E.88}$$

where the trace for a spin-singlet system in the superflow gauge ($\tilde{\Delta} = \Delta^* = \Delta$) was simplified in App. C.2

$$\mathrm{Tr}\left[\hat{\Delta}\left(\hat{g}_\lambda - \frac{1}{2}\hat{g}\right)\right] = \Delta\left(f + \tilde{f}\right) - 2\Delta\left(f_\lambda + \tilde{f}_\lambda\right). \tag{E.89}$$

The propagators at a pairbreaking interface were derived in Eqs. (E.68)–(E.69),

$$\begin{aligned} f^{\mathrm{pb}}(\boldsymbol{p}_{\mathrm{F}}, y; z) &= \pi\frac{\Delta}{\Omega}\left(1 - e^{-y/\xi}\right) - i\pi\,\mathrm{sgn}(\hat{\boldsymbol{v}}_{\mathrm{F}y})\frac{\Delta}{z_p}e^{-y/\xi}, & \text{(E.90)} \\ \tilde{f}^{\mathrm{pb}}(\boldsymbol{p}_{\mathrm{F}}, y; z) &= \pi\frac{\tilde{\Delta}}{\Omega}\left(1 - e^{-y/\xi}\right) + i\pi\,\mathrm{sgn}(\hat{\boldsymbol{v}}_{\mathrm{F}y})\frac{\tilde{\Delta}}{z_p}e^{-y/\xi}, & \text{(E.91)} \end{aligned}$$

where $\xi = \hbar|v_{\mathrm{F}y}|/2\Omega$, $\Omega \equiv \sqrt{|\Delta|^2 - z_p^2}$ and $z_p \equiv z - i\boldsymbol{v}_{\mathrm{F}} \cdot \boldsymbol{p}_{\mathrm{s}}$. The following expressions are obtained

$$\begin{aligned} \Delta\left(f + \tilde{f}\right) &= 2\pi\frac{\Delta^2}{\sqrt{|\Delta^2| - z_p^2}}\left[1 - \exp\!\left(-\tilde{y}\sqrt{|\Delta|^2 - z_p^2}\right)\right], & \text{(E.92)} \\ 2\Delta\left(f_\lambda + \tilde{f}_\lambda\right) &= 4\pi\frac{\Delta^2\lambda}{\sqrt{|\Delta|^2\lambda^2 - z_p^2}}\left[1 - \exp\!\left(-\tilde{y}\sqrt{|\Delta|^2\lambda^2 - z_p^2}\right)\right], & \text{(E.93)} \end{aligned}$$

where $\tilde{y} \equiv 2y/\hbar|v_{\mathrm{F}y}|$. Taking the λ-integral,

$$-\int_0^1 2\Delta\left(f_\lambda + \tilde{f}_\lambda\right) d\lambda = 4\pi\left[\sqrt{-z_p^2} - \Omega + \frac{e^{-\tilde{y}\sqrt{-z_p^2}} - e^{-\tilde{y}\Omega}}{\tilde{y}}\right], \tag{E.94}$$

the free energy is

$$\frac{\delta\Omega}{N_{\mathrm{F}}} = 2\pi k_{\mathrm{B}}T \int d\boldsymbol{R} \sum_{|\varepsilon_n|<\Omega_{\mathrm{c}}} \left\langle \left[\frac{|\Delta|^2}{2\Omega} + \sqrt{-z_p^2} - \Omega\right] + \frac{e^{-\tilde{y}\sqrt{-z_p^2}} - e^{-\tilde{y}\Omega}}{\tilde{y}} - \frac{|\Delta|^2}{2\Omega} e^{-\tilde{y}\Omega} \right\rangle_{\theta_{\mathrm{F}}}, \tag{E.95}$$

where the first bracket constitutes the bulk free energy (derived for zero temperature in Sec. D.4). The surface free energy can thus be defined as

$$\delta\Omega_{\mathrm{surf}} \equiv \delta\Omega - \delta\Omega_{\mathrm{bulk}} = 2\pi k_{\mathrm{B}} T N_{\mathrm{F}} \int d\boldsymbol{R} \sum_{|\varepsilon_n|}^{\Omega_{\mathrm{c}}} \left\langle \frac{e^{-\tilde{y}\sqrt{-z_p^2}} - e^{-\tilde{y}\Omega}}{\tilde{y}} - \frac{|\Delta|^2}{2\Omega} e^{-\tilde{y}\Omega} \right\rangle_{\theta_{\mathrm{F}}}. \tag{E.96}$$

With $\int d\boldsymbol{R} = \int\int dx dy = \mathcal{L}_x \int dy$, the y-integral can be taken

$$\begin{aligned}
\frac{\delta\Omega_{\mathrm{surf}}}{\mathcal{L}_x N_{\mathrm{F}}} &= 2\pi k_{\mathrm{B}} T \int_0^\infty dy \sum_{|\varepsilon_n|<\Omega_{\mathrm{c}}} \left\langle \frac{\exp\left(-\tilde{y}\sqrt{-z_p^2}\right) - e^{-\tilde{y}\Omega}}{\tilde{y}} - \frac{|\Delta|^2}{2\Omega} e^{-\tilde{y}\Omega} \right\rangle_{\theta_{\mathrm{F}}} && \text{(E.97)} \\
&= 2\pi k_{\mathrm{B}} T \sum_{|\varepsilon_n|<\Omega_{\mathrm{c}}} \left\langle \frac{\hbar|v_{\mathrm{F}y}|}{2} \left[\ln\left(\frac{\Omega}{\sqrt{-z_p^2}}\right) - \frac{|\Delta|^2}{2\Omega^2}\right] \right\rangle_{\theta_{\mathrm{F}}} && \text{(E.98)} \\
&= 2\pi k_{\mathrm{B}} T \sum_{\varepsilon_n>0}^{\Omega_{\mathrm{c}}} \left\langle \frac{\hbar|v_{\mathrm{F}y}|}{2} \left[\ln\left(\frac{|\Delta|^2 - z_p^2}{-z_p^2}\right) - \frac{|\Delta|^2}{|\Delta|^2 - z_p^2}\right] \right\rangle_{\theta_{\mathrm{F}}}. && \text{(E.99)}
\end{aligned}$$

It is noted that in the absence of superflow, $-z_p^2 = \varepsilon_n^2$, and the summand is positive definite, signifying an energy cost. Furthermore, by splitting the angular integral into $\boldsymbol{v}_{\mathrm{F}} \cdot \boldsymbol{p}_{\mathrm{s}} > 0$ and $\boldsymbol{v}_{\mathrm{F}} \cdot \boldsymbol{p}_{\mathrm{s}} < 0$, and combining the results, it can be explicitly shown that the free energy is real

$$\frac{\delta\Omega_{\mathrm{surf}}}{\mathcal{L}_x N_{\mathrm{F}}} = 2\pi k_{\mathrm{B}} T \sum_{\varepsilon_n>0}^{\Omega_{\mathrm{c}}} \left\langle \frac{\hbar|v_{\mathrm{F}y}|}{2} \left[\ln\left[\frac{(\Omega\Omega^*)^2}{\left(z_p z_p^*\right)^2}\right] - \frac{|\Delta|^2\left(\Omega^2 + \left(\Omega^2\right)^*\right)}{(\Omega\Omega^*)^2}\right] \right\rangle_{\boldsymbol{v}_{\mathrm{F}}\cdot\boldsymbol{p}_{\mathrm{s}}>0} \tag{E.100}$$

where $\Omega^2 + \left(\Omega^2\right)^* = 2\,\mathrm{Re}\left[\Omega^2\right]$. At low temperatures $T \to 0$, the Matsubara sum is replaced with an integral, as in Eqs. (2.19)–(2.20), and Eq. (E.99) becomes

$$\frac{\delta\Omega_0^{\mathrm{surf}}}{\mathcal{L}_x N_{\mathrm{F}}} = \int_0^\infty d\varepsilon \left\langle \frac{\hbar|v_{\mathrm{F}y}|}{2} \left[\ln\left(\frac{|\Delta|^2 + (\varepsilon + i\boldsymbol{v}_{\mathrm{F}} \cdot \boldsymbol{p}_{\mathrm{s}})^2}{(\varepsilon + i\boldsymbol{v}_{\mathrm{F}} \cdot \boldsymbol{p}_{\mathrm{s}})^2}\right) - \frac{|\Delta|^2}{|\Delta|^2 + (\varepsilon + i\boldsymbol{v}_{\mathrm{F}} \cdot \boldsymbol{p}_{\mathrm{s}})^2}\right] \right\rangle_{\theta_{\mathrm{F}}}. \tag{E.101}$$

E.5.2 Midgap states: energy cost

In the absence of superflow, the low-temperature surface energy becomes

$$\frac{\delta\Omega_0^{\rm surf}(\boldsymbol{p}_{\rm s}=0)}{\mathcal{L}_x N_{\rm F}} = \int_0^\infty d\varepsilon \left\langle \frac{\hbar|v_{{\rm F}y}|}{2}\left[\ln\left(\frac{|\Delta|^2+\varepsilon^2}{\varepsilon^2}\right) - \frac{|\Delta|^2}{|\Delta|^2+\varepsilon^2}\right]\right\rangle_{\theta_{\rm F}}. \tag{E.102}$$

The integral can be taken analytically,

$$\begin{aligned}\frac{\delta\Omega_0^{\rm surf}(\boldsymbol{p}_{\rm s}=0)}{\mathcal{L}_x N_{\rm F}} &= \hbar v_{\rm F}\frac{\pi}{4}\langle|\sin\theta_{\rm F}|\,|\Delta|\rangle_{\theta_{\rm F}}, &\text{(E.103)}\\ &= k_{\rm B}T_{\rm c}\xi_0\frac{\pi^2}{2}\,\langle|\sin\theta_{\rm F}|\,|\Delta|\rangle_{\theta_{\rm F}}\,, &\text{(E.104)}\end{aligned}$$

where $\xi_0 \equiv \hbar v_{\rm F}/2\pi k_{\rm B}T_{\rm c}$. For a $2D$ system with cylindrically symmetric Fermi-surface, the angular average is $\langle\ldots\rangle_{\theta_{\rm F}} = \int_0^{2\pi}[\ldots]d\theta_{\rm F}/2\pi$. For a d-wave order parameter, $\Delta^d = \Delta_0^d\sqrt{2}\cos(2\theta_{\rm F})$, where the zero-temperature gap Δ_0^d was introduced in Eq. (D.15) in App. D.2. The angular average becomes

$$\begin{aligned}\frac{\delta\Omega_{\rm surf}^d(\boldsymbol{p}_{\rm s}=0)}{\mathcal{L}_x\xi_0 N_{\rm F}} &= k_{\rm B}T_{\rm c}\frac{\pi^2}{2}\left\langle|\sin\theta_{\rm F}|\,\Delta_0^d\sqrt{2}\,|\cos\left(2\theta_{\rm F}\right)|\right\rangle_{\theta_{\rm F}} &\text{(E.105)}\\ &= k_{\rm B}T_{\rm c}\pi\Delta_0^d\frac{(4-\sqrt{2})}{3}. &\text{(E.106)}\end{aligned}$$

In units of the condensation energy $\delta\Omega_0^{\rm BCS}/\mathcal{L}_x\mathcal{L}_y N_{\rm F} = -\Delta_0^2/2$ derived in Sec. D.4,

$$\begin{aligned}\frac{\delta\Omega_{\rm surf}^d(\boldsymbol{p}_{\rm s}=0)/\xi_0}{\left|\delta\Omega_{\rm BCS}^d/\mathcal{L}_y\right|} &= \frac{2\pi(4-\sqrt{2})}{3}\left(\frac{\Delta_0^d}{k_{\rm B}T_{\rm c}}\right)^{-1} &\text{(E.107)}\\ &= \frac{2(2\sqrt{2}-1)}{3}e^{\gamma_{\rm E}+\frac{1}{2}} &\text{(E.108)}\\ &\approx 3.6. &\text{(E.109)}\end{aligned}$$

Similarly, considering a spin-active s-wave interface with no transmission as in App. E.2, and using $\Delta^s = \Delta_0^s$ from Eq. (D.14), the angular average in Eq. (E.104) becomes

$$\begin{aligned}\frac{\delta\Omega_{\rm surf}^s(\boldsymbol{p}_{\rm s}=0)}{\mathcal{L}_x\xi_0 N_{\rm F}} &= k_{\rm B}T_{\rm c}\frac{\pi^2}{2}\,\langle|\sin\theta_{\rm F}|\,\Delta_0^s\rangle_{\theta_{\rm F}} &\text{(E.110)}\\ &= k_{\rm B}T_{\rm c}\pi\Delta_0^s, &\text{(E.111)}\\ \frac{\delta\Omega_{\rm surf}^s(\boldsymbol{p}_{\rm s}=0)/\xi_0}{|\delta\Omega_{\rm BCS}^s/\mathcal{L}_y|} &= 2\pi\left(\frac{\Delta_0^s}{k_{\rm B}T_{\rm c}}\right)^{-1} &\text{(E.112)}\\ &= 2e^{\gamma_{\rm E}} &\text{(E.113)}\\ &\approx 3.6. &\text{(E.114)}\end{aligned}$$

Hence, the cost of the midgap states, $\delta\Omega_{\rm MGS} \equiv \delta\Omega_{\rm surf}(\boldsymbol{p}_{\rm s}=0)$, is in both cases

$$\frac{\delta\Omega_0^{\rm MGS}}{\left|\delta\Omega_0^{\rm BCS}\right|} \approx 4\frac{\xi_0}{\mathcal{L}_y}. \tag{E.115}$$

E.5.3 Doppler shift: energy gain

The energy gain of Doppler shifting the midgap states will now be derived at low temperatures. Starting from Eq. (E.100) and letting $T \to 0$ as in Eqs. (2.19)–(2.20), the energy integral can be taken analytically

$$\begin{aligned}\frac{\delta\Omega_0^{\mathrm{surf}}}{\mathcal{L}_x N_{\mathrm{F}}} &= \Bigg\langle \frac{\hbar|v_{\mathrm{F}y}|}{2}\int_0^\infty d\varepsilon\Bigg[\ln\left(\frac{\left[|\Delta|^2+(\varepsilon+i\boldsymbol{v}_{\mathrm{F}}\cdot\boldsymbol{p}_{\mathrm{s}})^2\right]\left[|\Delta|^2+(\varepsilon-i\boldsymbol{v}_{\mathrm{F}}\cdot\boldsymbol{p}_{\mathrm{s}})^2\right]}{(\varepsilon+i\boldsymbol{v}_{\mathrm{F}}\cdot\boldsymbol{p}_{\mathrm{s}})^2(\varepsilon-i\boldsymbol{v}_{\mathrm{F}}\cdot\boldsymbol{p}_{\mathrm{s}})^2}\right) \\ &\quad -\frac{|\Delta|^2}{|\Delta|^2+(\varepsilon+i\boldsymbol{v}_{\mathrm{F}}\cdot\boldsymbol{p}_{\mathrm{s}})^2}-\frac{|\Delta|^2}{|\Delta|^2+(\varepsilon-i\boldsymbol{v}_{\mathrm{F}}\cdot\boldsymbol{p}_{\mathrm{s}})^2}\Bigg]\Bigg\rangle_{\boldsymbol{v}_{\mathrm{F}}\cdot\boldsymbol{p}_{\mathrm{s}}>0} \qquad \text{(E.116)} \\ &= \left\langle\frac{\hbar|v_{\mathrm{F}y}|}{2}\pi\left(|\Delta|-2\boldsymbol{v}_{\mathrm{F}}\cdot\boldsymbol{p}_{\mathrm{s}}\right)\right\rangle_{\boldsymbol{v}_{\mathrm{F}}\cdot\boldsymbol{p}_{\mathrm{s}}>0}. \qquad \text{(E.117)}\end{aligned}$$

Here, the first term is exactly the midgap-state derived in App. E.5.2

$$\begin{aligned}\left\langle\frac{\hbar v_{\mathrm{F}}|\sin\theta_{\mathrm{F}}|}{2}\pi|\Delta|\right\rangle_{\boldsymbol{v}_{\mathrm{F}}\cdot\boldsymbol{p}_{\mathrm{s}}>0} &= \hbar v_{\mathrm{F}}\frac{\pi}{4}\left\langle|\sin\theta_{\mathrm{F}}||\Delta|\right\rangle_{\theta_{\mathrm{F}}} \qquad \text{(E.118)} \\ &= \frac{\delta\Omega^d_{\mathrm{surf}}(\boldsymbol{p}_{\mathrm{s}}=0)}{\mathcal{L}_x N_{\mathrm{F}}}, \qquad \text{(E.119)}\end{aligned}$$

where the last equality comes from Eq. E.103. The second term of Eq. (E.117) is

$$-2\pi\left\langle\frac{\hbar|v_{\mathrm{F}y}|}{2}\boldsymbol{v}_{\mathrm{F}}\cdot\boldsymbol{p}_{\mathrm{s}}\right\rangle_{\boldsymbol{v}_{\mathrm{F}}\cdot\boldsymbol{p}_{\mathrm{s}}>0} = -\pi\frac{\hbar v_{\mathrm{F}}^2}{2\pi}p_{\mathrm{s}}. \qquad \text{(E.120)}$$

The energy gain of Doppler shifts, $\delta\Omega_{\mathrm{Doppler}} \equiv \delta\Omega_{\mathrm{surf}} - \delta\Omega_{\mathrm{surf}}(\boldsymbol{p}_{\mathrm{s}}=0)$, can finally be written on the following dimensionless form at low temperatures

$$\frac{\delta\Omega_0^{\mathrm{Doppler}}}{\mathcal{L}_x\xi_0 N_{\mathrm{F}}(k_{\mathrm{B}}T_{\mathrm{c}})^2} = -\pi\frac{v_{\mathrm{F}}p_{\mathrm{s}}}{k_{\mathrm{B}}T_{\mathrm{c}}}, \qquad \text{(E.121)}$$

where $\xi_0 \equiv \hbar v_{\mathrm{F}}/2\pi k_{\mathrm{B}}T_{\mathrm{c}}$ is the coherence length. Hence, in contrast to the bulk superflow cost in Eq. (D.27), which scales as $v_{\mathrm{F}}^2 p_{\mathrm{s}}^2$, the surface energy gain due to Doppler shifts is linear $v_{\mathrm{F}}p_{\mathrm{s}}$. Note that this result can be verified from the free energy $F = U - TS$, by setting the midgap states spectrum to be a Dirac delta-distribution $\delta(\varepsilon)$ (as in App. E.4.1 with $\mathcal{D} \to 0$, which this appendix is equivalent to), and inserting the latter into the internal energy $U = \int d\varepsilon f(\varepsilon)\varepsilon N(\varepsilon)$ and entropy S, where $f(\varepsilon)$ is the Fermi-Dirac distribution. Evaluating the energy $F(\boldsymbol{p}_{\mathrm{s}} \neq 0) - F(\boldsymbol{p}_{\mathrm{s}} = 0)$ indeed reproduces Eq. (E.121), as shown by Ref. [144]. Furthermore, paper III does a similar calculation to estimate the contribution from the midgap states spectrum for different orientations between the interface and the nodes of a d-wave order parameter.

E.5.4 Superflow magnetic energy density

Consider the surface current in Eq. (4.16) that decays exponentially into a bulk superconductor

$$\boldsymbol{j}(y) = j_0 e^{-y/a\xi_0}\hat{\boldsymbol{x}}, \tag{E.122}$$

where $j_0 = j(y=0)$ is determined by the superflow at the surface, and $a > 0$ is a constant. In the case that the magnetic screening can be neglected (i.e. when λ is much larger than other relevant scales), the magnetic field is given by Ampère's circuit law $\boldsymbol{\nabla} \times \boldsymbol{B} = 4\pi\boldsymbol{j}/c$. The field is oriented tangentially to the surface and perpendicular to the surface current. Solving this differential equation yields

$$B(y) = -\frac{4\pi}{c} j_0 \int e^{-y/a\xi_0} dy = a\xi_0 \frac{4\pi}{c} j_0 e^{-x/a\xi_0} + C, \tag{E.123}$$

where C is an integration constant. Requiring the field to vanish at the interface in the absence of external fields $B(0) = 0$, the constant is $C = -a\xi 4\pi j_0/c$, such that

$$\boldsymbol{B}(y) = a\xi_0 \frac{4\pi}{c} j_0 \left(e^{-x/a\xi_0} - 1\right). \tag{E.124}$$

The magnetic energy density is

$$\delta\Omega^B = \int d\boldsymbol{R} \frac{\boldsymbol{B}^2(y)}{8\pi}. \tag{E.125}$$

For a superconductor of thickness $\mathcal{L}_y$, where $\lambda \gg \mathcal{L}_y \gg a\xi_0$ and $\mathcal{L}_y\mathcal{A} = \mathcal{V} \equiv \int d\boldsymbol{R}$, it is noted that $1 = \int d\boldsymbol{R} \left(e^{-x/a\xi_0} - 1\right)^2 / \mathcal{V}$. Assuming that the current is still proportional to the superflow $\boldsymbol{j} = eN_\mathrm{F}v_\mathrm{F}^2\boldsymbol{p}_\mathrm{s}$ as derived in App. D.5, the magnetic energy density at zero temperature can be evaluated on the dimensionless form

$$\frac{\delta\Omega_0^B}{\mathcal{V}N_\mathrm{F}(k_\mathrm{B}T_\mathrm{c})^2} = \frac{a^2}{2}\kappa_0^{-2}\frac{p_\mathrm{s}^2}{\tilde{p}_0^2}, \tag{E.126}$$

where $\tilde{p}_0 = k_\mathrm{B}T_\mathrm{c}/v_\mathrm{F}$ and $\kappa_0 = \lambda_0/\xi_0$, with $\lambda_0 \equiv c/\sqrt{4\pi e^2 N_\mathrm{F} v_\mathrm{F}^2}$ and $\xi_0 \equiv \hbar v_\mathrm{F}/2\pi k_\mathrm{B}T_\mathrm{c}$.

Appendix F

Technical details: inhomogeneous superflow

This appendix contains technical details and derivations for Ch. 5 on non-local linear response to inhomogeneous superflow $\boldsymbol{p}_{\mathrm{s}}(\boldsymbol{R})$.

F.1 Propagators

The linear response propagators will now be derived, given the coherence functions $\gamma = \gamma_0 + \gamma_1$ and $\tilde{\gamma} = \tilde{\gamma}_0 + \tilde{\gamma}_1$. Inserting these into the spin-singlet quasiparticle propagator g defined in Eq. (2.36) and expanding in γ_1 and $\tilde{\gamma}_1$

$$\begin{aligned}
g &= -i\pi \frac{1-(\gamma_0+\gamma_1)(\tilde{\gamma}_0+\tilde{\gamma}_1)}{1+(\gamma_0+\gamma_1)(\tilde{\gamma}_0+\tilde{\gamma}_1)} && \text{(F.1)}\\
&= -i\pi \frac{(1-\gamma_0\tilde{\gamma}_0-\gamma_0\tilde{\gamma}_1-\tilde{\gamma}_0\gamma_1)}{(1+\gamma_0\tilde{\gamma}_0)} \frac{1}{1+(\gamma_0\tilde{\gamma}_1+\tilde{\gamma}_0\gamma_1)(1+\gamma_0\tilde{\gamma}_0)^{-1}} && \text{(F.2)}\\
&= -i\pi \frac{1-\gamma_0\tilde{\gamma}_0-\gamma_0\tilde{\gamma}_1-\tilde{\gamma}_0\gamma_1}{1+\gamma_0\tilde{\gamma}_0}\left(1+\frac{\gamma_0\tilde{\gamma}_1+\tilde{\gamma}_0\gamma_1}{1+\gamma_0\tilde{\gamma}_0}+\mathcal{O}\left(\gamma_1^2\right)\right) && \text{(F.3)}\\
&\approx g_0 + 2i\pi\frac{\gamma_0\tilde{\gamma}_1+\gamma_1\tilde{\gamma}_0}{(1+\gamma_0\tilde{\gamma}_0)^2}, \qquad \Longrightarrow && \text{(F.4)}\\
g_1 &= 2i\pi\frac{\gamma_0\tilde{\gamma}_1+\gamma_1\tilde{\gamma}_0}{(1+\gamma_0\tilde{\gamma}_0)^2}, && \text{(F.5)}\\
\tilde{g}_1 &= -2i\pi\frac{\gamma_0\tilde{\gamma}_1+\gamma_1\tilde{\gamma}_0}{(1+\gamma_0\tilde{\gamma}_0)^2}. && \text{(F.6)}
\end{aligned}$$

Similarly, expanding the spin-singlet pair propagator in Eq. (2.38),

$$\begin{aligned}
f &= -2i\pi\frac{(\gamma_0+\gamma_1)}{1+(\gamma_0+\gamma_1)(\tilde{\gamma}_0+\tilde{\gamma}_1)} && \text{(F.7)}\\
&= -2i\pi\frac{(\gamma_0+\gamma_1)}{(1+\gamma_0\tilde{\gamma}_0)}\frac{1}{1+(\gamma_0\tilde{\gamma}_1+\tilde{\gamma}_0\gamma_1)(1+\gamma_0\tilde{\gamma}_0)^{-1}} && \text{(F.8)}\\
&= -2i\pi\frac{\gamma_0+\gamma_1}{1+\gamma_0\tilde{\gamma}_0}\left(1+\frac{\gamma_0\tilde{\gamma}_1+\tilde{\gamma}_0\gamma_1}{1+\gamma_0\tilde{\gamma}_0}+\mathcal{O}\left(\gamma_1^2\right)\right) && \text{(F.9)}
\end{aligned}$$

$$
\begin{aligned}
&\approx && -2i\pi\left(\frac{\gamma_0}{1+\gamma_0\tilde{\gamma}_0}+\frac{\gamma_1}{1+\gamma_0\tilde{\gamma}_0}+\frac{(\gamma_0\tilde{\gamma}_1+\tilde{\gamma}_0\gamma_1)}{(1+\gamma_0\tilde{\gamma}_0)}\frac{\gamma_0}{(1+\gamma_0\tilde{\gamma}_0)}\right) && \text{(F.10)}\\
&\approx && f_0-2i\pi\frac{(1+2\gamma_0\tilde{\gamma}_0)\gamma_1+\gamma_0^2\tilde{\gamma}_1}{(1+\gamma_0\tilde{\gamma}_0)^2}, \qquad \Longrightarrow && \text{(F.11)}\\
f_1 &= && -2i\pi\frac{(1+2\gamma_0\tilde{\gamma}_0)\gamma_1+\gamma_0^2\tilde{\gamma}_1}{(1+\gamma_0\tilde{\gamma}_0)^2}, && \text{(F.12)}\\
\tilde{f}_1 &= && 2i\pi\frac{(1+2\gamma_0\tilde{\gamma}_0)\tilde{\gamma}_1+\tilde{\gamma}_0^2\gamma_1}{(1+\gamma_0\tilde{\gamma}_0)^2}. && \text{(F.13)}
\end{aligned}
$$

F.2 Solutions: unsymmetrized equations

This appendix solves the unsymmetrized linear Riccati Eqs. (5.5)–(5.6). Let s denote the coordinate along the trajectory defined by the Fermi momentum $\boldsymbol{p}_{\mathrm{F}}$, such that the Riccati equations become

$$
\begin{aligned}
\partial_s\gamma_1(s) &= -\kappa(s)\gamma_1(s)-R(s), && \text{(F.14)}\\
\partial_s\tilde{\gamma}_1(s) &= +\tilde{\kappa}(s)\tilde{\gamma}_1(s)+\tilde{R}(s), && \text{(F.15)}\\
\kappa(s) &\equiv -\frac{2i}{\hbar v_{\mathrm{F}}}\left(z+\gamma_0\tilde{\Delta}\right), && \text{(F.16)}\\
\tilde{\kappa}(s) &\equiv -\frac{2i}{\hbar v_{\mathrm{F}}}\left(z-\tilde{\gamma}_0\Delta\right), && \text{(F.17)}\\
R(s) &\equiv \frac{2i}{\hbar v_{\mathrm{F}}}\boldsymbol{v}_{\mathrm{F}}\cdot\boldsymbol{p}_{\mathrm{s}}(\boldsymbol{R})\gamma_0, && \text{(F.18)}\\
\tilde{R}(s) &\equiv \frac{2i}{\hbar v_{\mathrm{F}}}\boldsymbol{v}_{\mathrm{F}}\cdot\boldsymbol{p}_{\mathrm{s}}(\boldsymbol{R})\tilde{\gamma}_0. && \text{(F.19)}
\end{aligned}
$$

Introduce the substitutions

$$
\begin{aligned}
\gamma_1(s) &= \gamma_1'(s)\exp\left(-\int_{-\infty}^{s}d\rho\kappa(\rho)\right), && \text{(F.20)}\\
\tilde{\gamma}_1(s) &= \tilde{\gamma}_1'(s)\exp\left(+\int_{+\infty}^{s}d\rho\tilde{\kappa}(\rho)\right), && \text{(F.21)}
\end{aligned}
$$

such that Eqs. (F.14) and (F.15) become

$$
\begin{aligned}
\gamma_1'\partial_s\exp\left(-\int_{-\infty}^{s}d\rho\kappa(\rho)\right)+\exp\left(-\int_{-\infty}^{s}d\rho\kappa(\rho)\right)\left[\partial_s\gamma_1'+\kappa\gamma_1'\right] &= -R, && \text{(F.22)}\\
\tilde{\gamma}_1'\partial_s\exp\left(+\int_{+\infty}^{s}d\rho\tilde{\kappa}(\rho)\right)+\exp\left(+\int_{+\infty}^{s}d\rho\tilde{\kappa}(\rho)\right)\left[\partial_s\tilde{\gamma}_1'-\tilde{\kappa}\tilde{\gamma}_1'\right] &= -\tilde{R}. && \text{(F.23)}
\end{aligned}
$$

Using the fundamental theorem, Eqs. (F.22) and (F.23) simplify to

$$
\begin{aligned}
\partial_s\gamma_1'(s) &= -R(s)\exp\left(+\int_{-\infty}^{s}d\rho\kappa(\rho)\right), && \text{(F.24)}\\
\partial_s\tilde{\gamma}_1'(s) &= +\tilde{R}(s)\exp\left(-\int_{+\infty}^{s}d\rho\tilde{\kappa}(\rho)\right), && \text{(F.25)}
\end{aligned}
$$

with the solutions

$$\gamma_1'(s) = -\int_{-\infty}^{s} ds' R(s') \exp\left(+\int_{-\infty}^{s'} d\rho \kappa(\rho)\right), \tag{F.26}$$

$$\tilde{\gamma}_1'(s) = +\int_{+\infty}^{s} ds' \tilde{R}(s') \exp\left(-\int_{+\infty}^{s'} d\rho \tilde{\kappa}(\rho)\right). \tag{F.27}$$

Substituting back to γ_1 and $\tilde{\gamma}_1$

$$\gamma_1(s) = -\exp\left(-\int_{-\infty}^{s} d\rho \kappa(\rho)\right) \int_{-\infty}^{s} ds' R(s') \exp\left(+\int_{-\infty}^{s'} d\rho \kappa(\rho)\right), \tag{F.28}$$

$$= -\int_{-\infty}^{s} ds' R(s') \exp\left(+\int_{s}^{s'} d\rho \kappa(\rho)\right), \tag{F.29}$$

$$\tilde{\gamma}_1(s) = +\exp\left(+\int_{+\infty}^{s} d\rho \tilde{\kappa}(\rho)\right) \int_{+\infty}^{s} ds' \tilde{R}(s') \exp\left(-\int_{+\infty}^{s'} d\rho \tilde{\kappa}(\rho)\right), \tag{F.30}$$

$$= +\int_{+\infty}^{s} ds' \tilde{R}(s') \exp\left(\int_{s'}^{s} d\rho \tilde{\kappa}(\rho)\right). \tag{F.31}$$

Re-writing the indices $s \leftarrow s_\mathrm{o}$ and $s' \leftarrow s$, the solutions are finally found

$$\gamma_1(\boldsymbol{p}_\mathrm{F}, s_\mathrm{o}; z) = -\frac{2i}{\hbar v_\mathrm{F}} \int_{-\infty}^{s_\mathrm{o}} ds \exp\left(-\int_{s}^{s_\mathrm{o}} d\rho \kappa(\rho)\right) \left[\boldsymbol{v}_\mathrm{F} \cdot \boldsymbol{p}_\mathrm{s} \gamma_0\right](\boldsymbol{p}_\mathrm{F}, s; z), \tag{F.32}$$

$$\tilde{\gamma}_1(\boldsymbol{p}_\mathrm{F}, s_\mathrm{o}; z) = +\frac{2i}{\hbar v_\mathrm{F}} \int_{\infty}^{s_\mathrm{o}} ds \exp\left(+\int_{s}^{s_\mathrm{o}} d\rho \tilde{\kappa}(\rho)\right) \left[\boldsymbol{v}_\mathrm{F} \cdot \boldsymbol{p}_\mathrm{s} \tilde{\gamma}_0\right](\boldsymbol{p}_\mathrm{F}, s; z), \tag{F.33}$$

where s_o denotes the observation point, s the source point, and ρ the running point between s and s_o. The linearized Riccati equations will now be symmetrized, then solved in a similar manner.

F.3 Symmetrization

The Riccati equation will now be derived for the pair-propagator-like objects $\gamma_1/(1+\gamma_0\tilde{\gamma}_0)$ and $\tilde{\gamma}_1/(1+\gamma_0\tilde{\gamma}_0)$. Starting with the derivative term,

$$\boldsymbol{\nabla}\left(\frac{\gamma_1}{1+\gamma_0\tilde{\gamma}_0}\right) = \frac{(\boldsymbol{\nabla}\gamma_1)}{1+\gamma_0\tilde{\gamma}_0} - \frac{\gamma_1}{(1+\gamma_0\tilde{\gamma}_0)} \frac{(\gamma_0\boldsymbol{\nabla}\tilde{\gamma}_0 + \tilde{\gamma}_0\boldsymbol{\nabla}\gamma_0)}{(1+\gamma_0\tilde{\gamma}_0)}, \tag{F.34}$$

$$\boldsymbol{\nabla}\left(\frac{\tilde{\gamma}_1}{1+\gamma_0\tilde{\gamma}_0}\right) = \frac{(\boldsymbol{\nabla}\tilde{\gamma}_1)}{1+\gamma_0\tilde{\gamma}_0} - \frac{\tilde{\gamma}_1}{(1+\gamma_0\tilde{\gamma}_0)} \frac{(\gamma_0\boldsymbol{\nabla}\tilde{\gamma}_0 + \tilde{\gamma}_0\boldsymbol{\nabla}\gamma_0)}{(1+\gamma_0\tilde{\gamma}_0)}. \tag{F.35}$$

Inserting the expressions for $\boldsymbol{\nabla}\gamma_0$ and $\boldsymbol{\nabla}\tilde{\gamma}_0$, i.e. unperturbed Riccati Eqs. (5.3) and (5.4), and simplifying yields

$$\boldsymbol{\nabla}\left(\frac{\gamma_1}{1+\gamma_0\tilde{\gamma}_0}\right) = \frac{(\boldsymbol{\nabla}\gamma_1)}{1+\gamma_0\tilde{\gamma}_0} - \frac{i}{\hbar v_\mathrm{F}}\left(\gamma_0\tilde{\Delta} + \tilde{\gamma}_0\Delta\right), \tag{F.36}$$

$$\boldsymbol{\nabla}\left(\frac{\tilde{\gamma}_1}{1+\gamma_0\tilde{\gamma}_0}\right) = \frac{(\boldsymbol{\nabla}\tilde{\gamma}_1)}{1+\gamma_0\tilde{\gamma}_0} - \frac{i}{\hbar v_\mathrm{F}}\left(\gamma_0\tilde{\Delta} + \tilde{\gamma}_0\Delta\right). \tag{F.37}$$

Substituting the perturbed Riccati Eqs. (5.5) and (5.6) into the terms $\boldsymbol{\nabla}\gamma_1$ and $\boldsymbol{\nabla}\tilde{\gamma}_1$ and simplifying yields the symmetrized equations

$$\begin{aligned}
\boldsymbol{\nabla}\left(\frac{\gamma_1}{1+\gamma_0\tilde{\gamma}_0}\right) &= \frac{2i}{\hbar v_{\mathrm{F}}}\left(z+\gamma_0\tilde{\Delta}\right)\frac{\gamma_1}{1+\gamma_0\tilde{\gamma}_0} - \frac{2i}{\hbar v_{\mathrm{F}}}\boldsymbol{v}_{\mathrm{F}}\cdot\boldsymbol{p}_{\mathrm{s}}(\boldsymbol{R})\frac{\gamma_0}{1+\gamma_0\tilde{\gamma}_0} \\
&\quad -\frac{i}{\hbar v_{\mathrm{F}}}\left(\gamma_0\tilde{\Delta}+\tilde{\gamma}_0\Delta\right) && \text{(F.38)} \\
&= -\kappa\frac{\gamma_1}{1+\gamma_0\tilde{\gamma}_0} - \frac{2i}{\hbar v_{\mathrm{F}}}\boldsymbol{v}_{\mathrm{F}}\cdot\boldsymbol{p}_{\mathrm{s}}(\boldsymbol{R})\frac{\gamma_0}{1+\gamma_0\tilde{\gamma}_0}, && \text{(F.39)} \\
\boldsymbol{\nabla}\left(\frac{\tilde{\gamma}_1}{1+\gamma_0\tilde{\gamma}_0}\right) &= -\frac{2i}{\hbar v_{\mathrm{F}}}\left(z-\tilde{\gamma}_0\Delta\right)\frac{\tilde{\gamma}_1}{1+\gamma_0\tilde{\gamma}_0} + \frac{2i}{\hbar v_{\mathrm{F}}}\boldsymbol{v}_{\mathrm{F}}\cdot\boldsymbol{p}_{\mathrm{s}}(\boldsymbol{R})\frac{\tilde{\gamma}_0}{1+\gamma_0\tilde{\gamma}_0} \\
&\quad -\frac{i}{\hbar v_{\mathrm{F}}}\left(\gamma_0\tilde{\Delta}+\tilde{\gamma}_0\Delta\right) && \text{(F.40)} \\
&= \kappa\frac{\tilde{\gamma}_1}{1+\gamma_0\tilde{\gamma}_0} + \frac{2i}{\hbar v_{\mathrm{F}}}\boldsymbol{v}_{\mathrm{F}}\cdot\boldsymbol{p}_{\mathrm{s}}(\boldsymbol{R})\frac{\tilde{\gamma}_0}{1+\gamma_0\tilde{\gamma}_0}, && \text{(F.41)} \\
\kappa &\equiv \frac{i}{\hbar v_{\mathrm{F}}}\left(2z+\gamma_0\tilde{\Delta}-\tilde{\gamma}_0\Delta\right). && \text{(F.42)}
\end{aligned}$$

F.4 Solutions: symmetrized equations

Assuming perfect reflection, this appendix solves the symmetrized linear Riccati Eqs. (F.38)–(F.41) for the pair-propagator-like objects $\gamma_1/(1+\gamma_0\tilde{\gamma}_0)$ and $\tilde{\gamma}_1/(1+\gamma_0\tilde{\gamma}_0)$

$$\begin{aligned}
\partial_s\frac{\gamma_1}{1+\gamma_0\tilde{\gamma}_0}(s) &= -\kappa\frac{\gamma_1}{1+\gamma_0\tilde{\gamma}_0}(s) - R(s), && \text{(F.43)} \\
\partial_s\frac{\tilde{\gamma}_1}{1+\gamma_0\tilde{\gamma}_0}(s) &= +\kappa\frac{\tilde{\gamma}_1}{1+\gamma_0\tilde{\gamma}_0}(s) + \tilde{R}(s), && \text{(F.44)} \\
\kappa &\equiv \frac{i}{\hbar v_{\mathrm{F}}}\left(2z+\gamma_0\tilde{\Delta}-\tilde{\gamma}_0\Delta\right), && \text{(F.45)} \\
R(s) &\equiv \frac{2i}{\hbar v_{\mathrm{F}}}\boldsymbol{v}_{\mathrm{F}}\cdot\boldsymbol{p}_{\mathrm{s}}\frac{\gamma_0}{1+\gamma_0\tilde{\gamma}_0}(s), && \text{(F.46)} \\
\tilde{R}(s) &\equiv \frac{2i}{\hbar v_{\mathrm{F}}}\boldsymbol{v}_{\mathrm{F}}\cdot\boldsymbol{p}_{\mathrm{s}}\frac{\tilde{\gamma}_0}{1+\gamma_0\tilde{\gamma}_0}(s), && \text{(F.47)}
\end{aligned}$$

where again, s denotes the coordinate along the trajectory defined by the Fermi momentum $\boldsymbol{p}_{\mathrm{F}}$. Following the same method as in App. F.2, the solutions are found to be

$$\begin{aligned}
\frac{\gamma_1}{1+\gamma_0\tilde{\gamma}_0}(\boldsymbol{p}_{\mathrm{F}},s_{\mathrm{o}};z) &= -\frac{2i}{\hbar v_{\mathrm{F}}}\int_{-\infty}^{s_{\mathrm{o}}} ds C(s,s_{\mathrm{o}})\frac{\boldsymbol{v}_{\mathrm{F}}\cdot\boldsymbol{p}_{\mathrm{s}}\gamma_0}{1+\gamma_0\tilde{\gamma}_0}(\boldsymbol{p}_{\mathrm{F}},s;z), && \text{(F.48)} \\
\frac{\tilde{\gamma}_1}{1+\gamma_0\tilde{\gamma}_0}(\boldsymbol{p}_{\mathrm{F}},s_{\mathrm{o}};z) &= -\frac{2i}{\hbar v_{\mathrm{F}}}\int_{s_{\mathrm{o}}}^{\infty} ds C(s_{\mathrm{o}},s)\frac{\boldsymbol{v}_{\mathrm{F}}\cdot\boldsymbol{p}_{\mathrm{s}}\tilde{\gamma}_0}{1+\gamma_0\tilde{\gamma}_0}(\boldsymbol{p}_{\mathrm{F}},s;z), && \text{(F.49)} \\
C(s_1,s_2) &\equiv \exp\left(-\int_{s_1}^{s_2} d\rho\kappa(\rho)\right), && \text{(F.50)}
\end{aligned}$$

where $C(s, s_\mathrm{o})$ is a correlator that couples source point s and observation point s_o with correlation length κ^{-1}, and is solved in App. F.5. For further interpretation, see Sec. 5.2.

F.5 Correlators

In this appendix, an analytic expression for the correlator in Eq. (F.50) is derived, in particular at an interface with perfect reflection. Like in previous appendices, let s denote the coordinate along the trajectory, with $s = 0$ at the interface. The function $\kappa(s)$ is then written in terms of the unperturbed coherence functions, derived in App. E.1

$$\kappa(s > 0) = -\frac{2i}{\hbar v_\mathrm{F}}\left(z + \frac{\Gamma_0\tilde{\Delta} - \tilde{\gamma}_0\Delta}{2}\right) \tag{F.51}$$

$$\kappa(s < 0) = -\frac{2i}{\hbar v_\mathrm{F}}\left(z + \frac{\gamma_0\tilde{\Delta} - \tilde{\Gamma}_0\Delta}{2}\right). \tag{F.52}$$

These functions are the same but with $S_1 \leftrightarrow \tilde{S}_1$, where S_1 and $\tilde{S}_1$ are the boundary terms given by Eqs. (E.16) and (E.17). In the following, the index and the tilde will be dropped, and the boundary term will just be written as S. It is noted that when regions 1 and 2 are described by homogeneous regions, then in fact $S_1 = \tilde{S}_1 \equiv S$. Recalling that $\xi \equiv \hbar v_\mathrm{F}/2\Omega$ and inserting the coherence functions yield

$$\begin{aligned}
\frac{\Gamma_0\tilde{\Delta} - \tilde{\gamma}_0\Delta}{2} &= -\frac{1}{2}(z - i\Omega)\frac{2i\Omega + (z - i\Omega)S - (z + i\Omega)Se^{-s/\xi}}{2i\Omega + (z - i\Omega)S - (z - i\Omega)Se^{-s/\xi}} - \frac{1}{2}(z - i\Omega) \\
&= -(z - i\Omega)\frac{2i\Omega + (z - i\Omega)S - zSe^{-s/\xi}}{2i\Omega + (z - i\Omega)S - (z - i\Omega)Se^{-s/\xi}},
\end{aligned} \tag{F.53}$$

$$z + \frac{\Gamma_0\tilde{\Delta} - \tilde{\gamma}_0\Delta}{2} = i\Omega\frac{2i\Omega + (z - i\Omega)S}{2i\Omega + (z - i\Omega)S - (z - i\Omega)Se^{-s/\xi}}, \tag{F.54}$$

$$\kappa(\rho) = \left(\frac{2\Omega}{\hbar v_\mathrm{F}}\right)\frac{2i\Omega + (z - i\Omega)S}{2i\Omega + (z - i\Omega)S - (z - i\Omega)Se^{-\rho/\xi}} \tag{F.55}$$

$$= \xi^{-1}\frac{2i\Omega + (z - i\Omega)S}{2i\Omega + (z - i\Omega)S - (z - i\Omega)Se^{-\rho/\xi}}. \tag{F.56}$$

It is verified that κ^{-1} can indeed be interpreted as a coherence length modified by inhomogeneities at the interface, by studying a bulk system ($S = 0$), a maximally pairbreaking interface ($S = 2$), and a transmissive S-N interface ($S = 1$),

$$\kappa^{-1} \xrightarrow[\rho\to\infty]{} \xi \equiv \frac{\hbar v_\mathrm{F}}{2\Omega}, \tag{F.57}$$

$$\kappa^{-1} \xrightarrow[S\to 0]{} \xi, \tag{F.58}$$

$$\kappa^{-1}(\rho) \xrightarrow[S\to 2]{} \xi \frac{z - (z - i\Omega)e^{-\rho/\xi}}{z} \tag{F.59}$$

$$\xrightarrow{\rho\to 0} \frac{\hbar v_\mathrm{F}}{2\varepsilon_n}, \tag{F.60}$$

$$\kappa^{-1}(\rho) \xrightarrow[S\to 1]{} \xi \frac{z + i\Omega - (z - i\Omega)e^{-\rho/\xi}}{z + i\Omega} \tag{F.61}$$

$$\xrightarrow{\rho\to 0} \frac{\hbar v_\mathrm{F}}{\varepsilon_n + \Omega}. \tag{F.62}$$

Consider now the $d\rho$-integral entering Eqs. (F.48)–(F.49)

$$I = \int_{s_1}^{s_2} \kappa(\rho) d\rho \tag{F.63}$$

$$= \xi^{-1} \int_{s_1}^{s_2} \frac{2i\Omega + (z - i\Omega)S}{2i\Omega + (z - i\Omega)S - (z - i\Omega)Se^{-|\rho|/\xi}} \tag{F.64}$$

$$= \left[\left(\frac{1 - \mathrm{sgn}(\rho)}{2} \right) a(\rho) + \left(\frac{1 + \mathrm{sgn}(\rho)}{2} \right) b(\rho) \right]_{\rho = s_1}^{\rho = s_2}, \tag{F.65}$$

$$a(\rho) \equiv \frac{\rho}{\xi} - \ln\left(2i\Omega + (z - i\Omega)S - (z - i\Omega)Se^{-|\rho|/\xi} \right), \tag{F.66}$$

$$b(\rho) \equiv \ln \left(\frac{2i\Omega + (z - i\Omega)S - (z - i\Omega)Se^{-|\rho|/\xi}}{(2i\Omega)^2 e^{-|\rho|/\xi}} \right). \tag{F.67}$$

Hence, the solution depends on where the points s_1 and s_2 lie relative to the surface, as illustrated in Fig. F.1. Note that cases 1 and 2 correspond to an unreflected trajectory (u) between s_1 and s_2, while 3 and 4 correspond to a reflected trajectory (r). Due to different momentum directions (and possibly different order parameter values), the integrals in cases 3 and 4 are therefore split into an

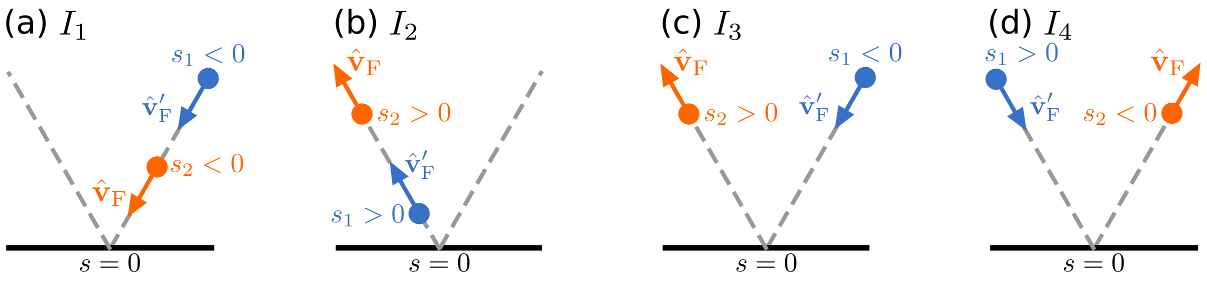

Figure F.1: *Correlations between s_1 and s_2, along the trajectory defined by $\boldsymbol{v}_F(\boldsymbol{p}_F)$.*

incoming part (from $\rho = s_1$ to $\rho = 0$) and an outgoing part (from $\rho = 0$ to $\rho = s_2$). Thus, for the four different cases, the integral can be written

1. $s_1 < 0$ and $s_2 < 0$, $\implies$ $I_1 = a(s_2) - a(s_1)$,
2. $s_1 > 0$ and $s_2 > 0$, $\implies$ $I_2 = b(s_2) - b(s_1)$,
3. $s_1 < 0$ and $s_2 > 0$, $\implies$ $I_3 = b(s_2) - b(0) + a(0) - a(s_1)$,
4. $s_1 > 0$ and $s_2 < 0$, $\implies$ $I_4 = a(s_2) - a(0) + b(0) - b(s_1)$,

Cases 1 and 2 simplify to

$$\begin{aligned} I_1 &= \frac{|s_1| - |s_2|}{\xi} + \ln\left(\frac{2i\Omega + (z - i\Omega)S - (z - i\Omega)Se^{-|s_1|/\xi}}{2i\Omega + (z - i\Omega)S - (z - i\Omega)Se^{-|s_2|/\xi}}\right), && \text{(F.68)} \\ I_2 &= \frac{|s_2| - |s_1|}{\xi} + \ln\left(\frac{2i\Omega + (z - i\Omega)S - (z - i\Omega)Se^{-|s_2|/\xi}}{2i\Omega + (z - i\Omega)S - (z - i\Omega)Se^{-|s_1|/\xi}}\right). && \text{(F.69)} \end{aligned}$$

By introducing the notation for the coordinate closest ($s_<$) and furthest ($s_>$) from the interface along the trajectory,

$$\begin{aligned} s_< &= \min\left(|s_1|, |s_2|\right), && \text{(F.70)} \\ s_> &= \max\left(|s_1|, |s_2|\right), && \text{(F.71)} \end{aligned}$$

integrals I_1 and I_2 can be combined to a single expressions

$$I_{ⓤ} = I_{1,2} = \frac{|s_> - s_<|}{\xi} + \ln\left(\frac{2i\Omega + (z - i\Omega)S - (z - i\Omega)Se^{-|s_>|/\xi}}{2i\Omega + (z - i\Omega)S - (z - i\Omega)Se^{-|s_<|/\xi}}\right). \quad \text{(F.72)}$$

Similarly, cases 3 and 4 can be massaged into the following expression

$$\begin{aligned} I_{ⓡ} = I_{3,4} &= +\frac{|s_1|}{\xi_1} + \ln\left(\frac{2i\Omega_1 + (z - i\Omega_1)S - (z - i\Omega_1)Se^{-|s_1|/\xi_1}}{2i\Omega_1}\right) \\ &\quad +\frac{|s_2|}{\xi_2} + \ln\left(\frac{2i\Omega_2 + (z - i\Omega_2)S - (z - i\Omega_2)Se^{-|s_2|/\xi_2}}{2i\Omega_2}\right), && \text{(F.73)} \end{aligned}$$

where all quantities that depend explicitly on Δ might be different at s_1 and s_2 due to the different momentum directions at these points. Finally using the definitions in Eqs. (F.50) and (F.63), the unreflected and reflected correlators can be written

$$\begin{aligned} C_{ⓤ}(s_1, s_2) &= \frac{2i\Omega + (z - i\Omega)S - (z - i\Omega)Se^{-|s_<|/\xi}}{2i\Omega + (z - i\Omega)S - (z - i\Omega)Se^{-|s_>|/\xi}} e^{-|s_> - s_<|/\xi}, && \text{(F.74)} \\ C_{ⓡ}(s_1, s_2) &= \frac{2i\Omega_1 e^{-|s_1|/\xi_1}}{2i\Omega_1 + (z - i\Omega_1)S - (z - i\Omega_1)Se^{-|s_1|/\xi_1}} \\ &\quad \times \frac{2i\Omega_2 e^{-|s_2|/\xi_2}}{2i\Omega_2 + (z - i\Omega_2)S - (z - i\Omega_2)Se^{-|s_2|/\xi_2}}. && \text{(F.75)} \end{aligned}$$

At a maximally pairbreaking interface, these reduce to

$$C_{\textcircled{u}}(s_1, s_2) \quad \xrightarrow[S\to 2]{} \quad \frac{z-(z-i\Omega)e^{-|s_<|/\xi}}{z(z-i\Omega)e^{-|s_>|/\xi}}e^{-|s_>-s_<|/\xi}, \tag{F.76}$$

$$C_{\textcircled{r}}(s_1, s_2) \quad \xrightarrow[S\to 2]{} \quad \frac{i\Omega_1 e^{-|s_1|/\xi_1}}{\left(z-(z-i\Omega_1)e^{-|s_1|/\xi_1}\right)}\frac{i\Omega_2 e^{-|s_2|/\xi_2}}{\left(z-(z-i\Omega_2)e^{-|s_2|/\xi_2}\right)}. \tag{F.77}$$

F.6 Local kernel: integrable singularity

The coordinate transformation from polar to cartesian coordinates in Sec. 5.5 introduced a term $(\Delta R)^{-1}$ in the kernel, which leads to an integrable singularity in the current at the point $\boldsymbol{R}_\mathrm{s} \to \boldsymbol{R}_\mathrm{o}$, i.e. corresponding to the local kernel $\boldsymbol{K}(\boldsymbol{R}_\mathrm{o}, \boldsymbol{R}_\mathrm{s} = \boldsymbol{R}_\mathrm{o}) \equiv \boldsymbol{K}(\boldsymbol{R}_\mathrm{o})$, which creates issues in numeric calculations. This appendix alleviates the issue by deriving an analytic expression that can be evaluated numerically. Assume that the kernel and the superflow are both piecewise constant in a small region of area $h \times h$, and that there are no reflections inside this region such that $\boldsymbol{v}'_\mathrm{F}(\boldsymbol{R}_\mathrm{s}) = \boldsymbol{v}_\mathrm{F}(\boldsymbol{R}_\mathrm{o})$ (the local kernel exactly at the interface therefore has to be treated separately). The current is split into two parts

$$j_i(\boldsymbol{R}_\mathrm{o}) \quad = \quad \delta j_i(\boldsymbol{R}_\mathrm{o}) + \int_{\boldsymbol{R}_\mathrm{o}\neq\boldsymbol{R}_\mathrm{s}} d^2R_\mathrm{s}\hbar^{-2}K_{ij}(\boldsymbol{R}_\mathrm{o}, \boldsymbol{R}_\mathrm{s})p_{\mathrm{s},j}(\boldsymbol{R}_\mathrm{s}), \tag{F.78}$$

where $\delta j_i(\boldsymbol{R}_\mathrm{o})$ gives the contribution from the local kernel. Choosing the coordinate system such that the observation point $s_\mathrm{o} = 0$ temporarily (again, not at the surface), and using the expression for the current in polar coordinates in Eq. (5.43),

$$\delta j_i(\boldsymbol{R}_\mathrm{o}) \quad = \quad 16\pi k_\mathrm{B}TN_\mathrm{F}\frac{v_\mathrm{F}}{\hbar}\sum_{\varepsilon_n>0}^{\Omega_\mathrm{c}}\mathrm{Re}\left\langle\left[\int_{-\delta s}^{0} dsI_1 + \int_{0}^{\delta s} dsI_2\right]\hat{k}_i\hat{k}_j p_{\mathrm{s},j}(\boldsymbol{R}_\mathrm{o})\right\rangle_{\theta_\mathrm{F}} \tag{F,79}$$

$$I_1 \quad = \quad \frac{\tilde{f}_0(\hat{k},0)}{2i\pi}C(s,0)\frac{f_0(\hat{k},s)}{-2i\pi}, \tag{F.80}$$

$$I_2 \quad = \quad \frac{f_0(\hat{k},0)}{-2i\pi}C(0,s)\frac{\tilde{f}_0(\hat{k},s)}{2i\pi}, \tag{F.81}$$

$$C(s_1, s_2) \quad \equiv \quad \exp\left(-\int_{s_1}^{s_2} d\rho\kappa(\rho,\hat{k})\right), \tag{F.82}$$

where δs is the distance to the boundary of the small region $h \times h$

$$\delta s = \begin{cases} \frac{h}{2k_x}, & k_x \geq k_y \\ \frac{h}{2k_y}, & k_x < k_y \end{cases}, \tag{F.83}$$

with $k_x = \cos(\theta_\mathrm{F})$ and $k_y = \sin(\theta_\mathrm{F})$. Neglecting variations of f, $\tilde{f}$ and κ inside the small region, the ds-integrals in Eq. (F.79) are found to be

$$\int_{-\delta s}^{0} dsI_1 = \frac{\tilde{f}_0(\hat{k},0)}{2i\pi}\frac{\left(1-\exp\left[-(\delta s)\kappa(0,\hat{k})\right]\right)}{\kappa(0,\hat{k})}\frac{f_0(\hat{k},0)}{-2i\pi}, \tag{F.84}$$

$$\int_{0}^{\delta s} dsI_2 = \frac{f_0(\hat{k},0)}{-2i\pi}\frac{\left(\exp\left[-(\delta s)\kappa(0,\hat{k})\right]-1\right)}{-\kappa(0,\hat{k})}\frac{\tilde{f}_0(\hat{k},0)}{2i\pi}. \tag{F.85}$$

Inserting the observation point coordinate again, the local current and kernel take the forms

$$\delta j_i(\boldsymbol{R}_\mathrm{o}) = K_{ij}(\boldsymbol{R}_\mathrm{o})p_{\mathrm{s},j}(\boldsymbol{R}_\mathrm{o}), \tag{F.86}$$

$$\begin{aligned} K_{ij}(\boldsymbol{R}_\mathrm{o}) = {} & 32\pi k_\mathrm{B}TN_\mathrm{F}\frac{v_\mathrm{F}}{\hbar}\Big\langle(\hat{k}_i\hat{k}_j)\,\mathrm{Re}\sum_{\varepsilon_n>0}^{\Omega_\mathrm{c}}\frac{\tilde{f}_0(\hat{k},\boldsymbol{R}_\mathrm{o})}{2i\pi} \\ & \times\frac{\left(1-\exp\left[-(\delta s)\kappa(\boldsymbol{R}_\mathrm{o},\hat{k})\right]\right)}{\kappa(\boldsymbol{R}_\mathrm{o},\hat{k})}\frac{f_0(\hat{k},\boldsymbol{R}_\mathrm{o})}{-2i\pi}\Big\rangle_{\theta_\mathrm{F}}. \end{aligned} \tag{F.87}$$

With the expressions for $\tilde{f}_0$ and f_0 in Eqs. (E.68) and (E.69) with $\boldsymbol{p}_\mathrm{s}=0$, and κ from Eq. (5.21) with $S=2$, then

$$\frac{\tilde{f}_0(\hat{k},s)}{2i\pi}\frac{f_0(\hat{k},s)}{-2i\pi} = \frac{\Delta^2}{(2\Omega)^2}\frac{\left[z-(z+i\Omega)e^{-|s|/\xi}\right]\left[z-(z-i\Omega)e^{-|s|/\xi}\right]}{z^2}, \tag{F.88}$$

$$\kappa^{-1}(s) = \frac{\hbar v_\mathrm{F}}{2\Omega}\frac{z-(z-i\Omega)e^{-|s|/\xi}}{z}. \tag{F.89}$$

The local kernel becomes

$$\begin{aligned} K_{ij}(\boldsymbol{R}_\mathrm{o}) = {} & 4\pi k_\mathrm{B}TN_\mathrm{F}v_\mathrm{F}^2\Big\langle(\hat{k}_i\hat{k}_j)\sum_{\varepsilon_n>0}^{\Omega_\mathrm{c}}\frac{\Delta^2}{\Omega^3}\left(1-\exp\left[-(\delta s)\kappa(\boldsymbol{R}_\mathrm{o},\hat{k})\right]\right) \\ & \times\left[1-\left(1+\frac{\Omega}{\varepsilon_n}\right)e^{-|s|/\xi}\right]\left[1-\left(1-\frac{\Omega}{\varepsilon_n}\right)e^{-|s|/\xi}\right]^2\Big\rangle_{\theta_\mathrm{F}}. \end{aligned} \tag{F.90}$$

F.7 Bulk superfluid density

Following App. F.6, the bulk linear response can be derived by letting $h\to\infty$ (i.e. $\delta s\to\infty$) and $|s|\to\infty$, such that

$$K_{ij}^\mathrm{bulk}(\boldsymbol{R}_\mathrm{o}) = 4\pi k_\mathrm{B}TN_\mathrm{F}v_\mathrm{F}^2\Big\langle(\hat{k}_i\hat{k}_j)\sum_{\varepsilon_n>0}^{\Omega_\mathrm{c}}\frac{\Delta^2}{\Omega^3}\Big\rangle_{\theta_\mathrm{F}}, \tag{F.91}$$

$$\boldsymbol{j}^\mathrm{bulk}(\boldsymbol{R}_\mathrm{o}) = 4\pi k_\mathrm{B}TN_\mathrm{F}v_\mathrm{F}^2\sum_{\varepsilon_n>0}^{\Omega_\mathrm{c}}\Big\langle\frac{\Delta^2}{\Omega^3}\hat{\boldsymbol{v}}_\mathrm{F}\left[\hat{\boldsymbol{v}}_\mathrm{F}\cdot\boldsymbol{p}_\mathrm{s}\right]\Big\rangle_{\theta_\mathrm{F}}, \tag{F.92}$$

which is to be compared with the bulk current response in Eq. (D.36) of App. D.5. This is the well-known form of the bulk superfluid density, usually denoted $\boldsymbol{\rho}_s$ in the literature, see Eqs. (34) and (35) in Ref. [116].

Appendix G

Technical details: phase crystallization

This appendix contains technical details for Ch. 6 on phase crystallization. In particular, attempts are made to visualize the kernel. Note however that while certain features can be identified, the kernel correlations are summed in a non-trivial manner to produce the current response and energetics in the end. The best analysis is therefore provided by instead studying the functional form of the kernel, e.g. as in Sec. 5.6, and averaging out relative coordinates as in paper I. At the present, the best visualizations of the kernel structure and its contribution are found in Fig. 2 (b) and Figs. 3 (b)–(d) of paper I.

Figure G.1 plots the diagonal and symmetric (with respect to $x \to -x$) components $K_{xx}(\Delta x; y_\mathrm{o}, y_\mathrm{s})$ and $K_{yy}(\Delta x; y_\mathrm{o}, y_\mathrm{s})$, while Fig. G.2 plots the off-diagonal and antisymmetric $K_{xy}(\Delta x; y_\mathrm{o}, y_\mathrm{s})$ and $K_{yx}(\Delta x; y_\mathrm{o}, y_\mathrm{s})$. These are plotted at low temperatures $T = 0.1T_\mathrm{c}$, with $\Delta x \equiv x_\mathrm{o} - x_\mathrm{s}$, and $K_0 \equiv 4\pi k_\mathrm{B} T_\mathrm{c} N_\mathrm{F} v_\mathrm{F}^2$. It is noted that all kernels change overall sign at a distance $\sim 2\xi_0$ from the interface, and that close to the surface, the sign of the diagonal components are mainly negative. This sign-change is not present at elevated temperatures, where the kernel is overall positive (not shown here). What is not visible in these figures are all the the rapid variations and detailed features of the kernel components close to $\boldsymbol{R}_\mathrm{s} = \boldsymbol{R}_\mathrm{o}$. The qualitative plots in Figs. G.3 and G.4 are similar plots that capture parts of these variations, by zooming in on the respective kernel components in a contour plot. Figures G.5–G.7 show the superfluid density tensor in a mixed representation $K_{ij}(q_x; y_1 = y_\mathrm{o}, y_2 = y_\mathrm{s})$ as introduced in Sec. 6.2.2, at $q_x = 0.6\xi_0^{-1}$ with temperatures $T = 0.1T_\mathrm{c}$, $T = 0.15T_\mathrm{c}$ and $T = 0.2T_\mathrm{c}$, respectively. Note the inverted color scheme in these and the following plots. The scale only goes between $\pm K_0$ to highlight overall features, but the maxima and minima are indicated in the figures. Cuts are taken in these figures at constant values of $y_{1,2}/\xi_0 = 0.4, 0.8.1.2, 1.6, 2.0$ and plotted in Figs. G.8–G.10, with y_1 and y_2 corresponding to solid and dashed lines, respectively. Here, $y = (y_1 - y_2)/2$ is the relative center-of-mass coordinate.

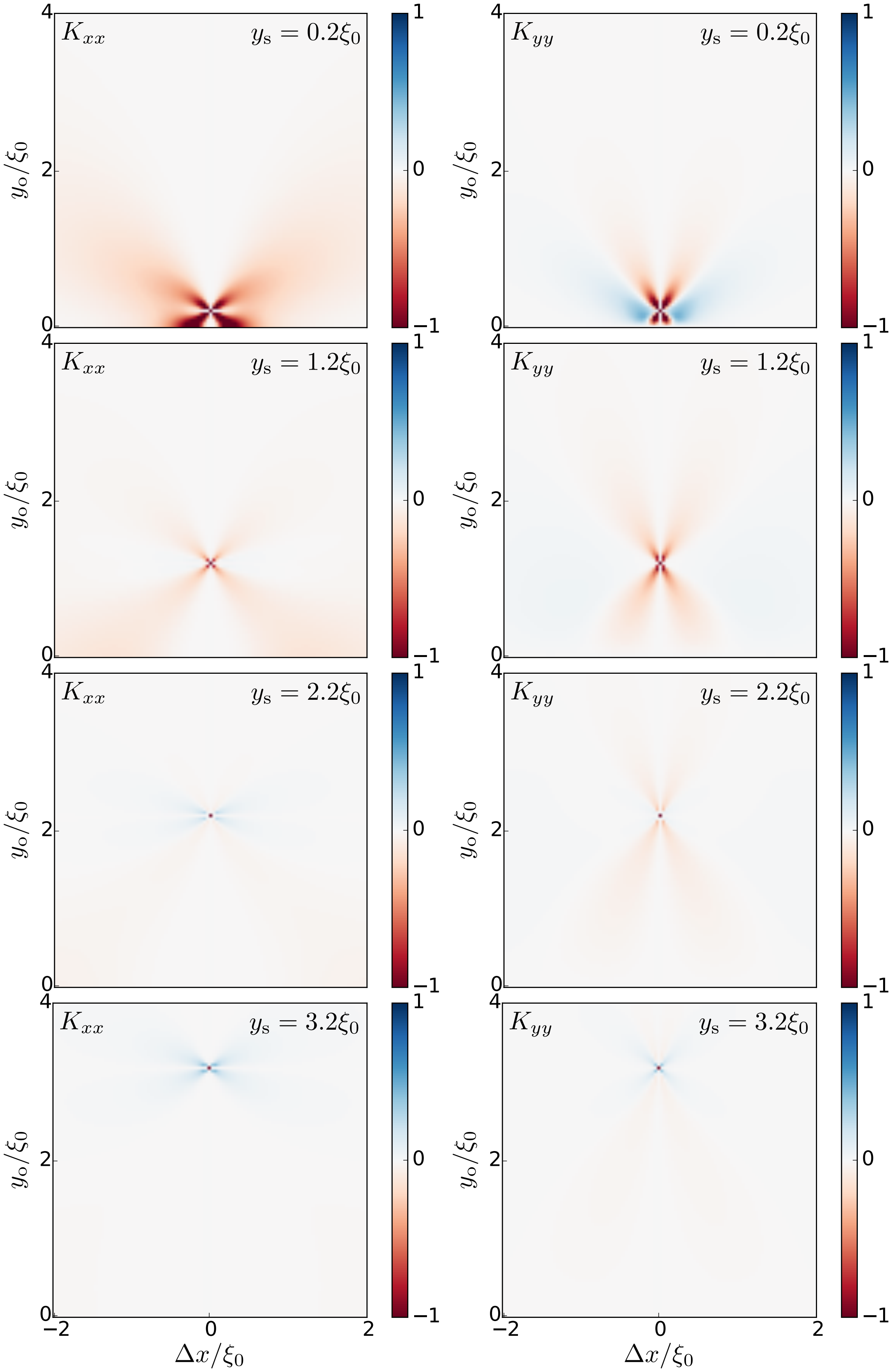

Figure G.1: *Diagonal components of the superfluid kernel at* $T = 0.1T_c$.

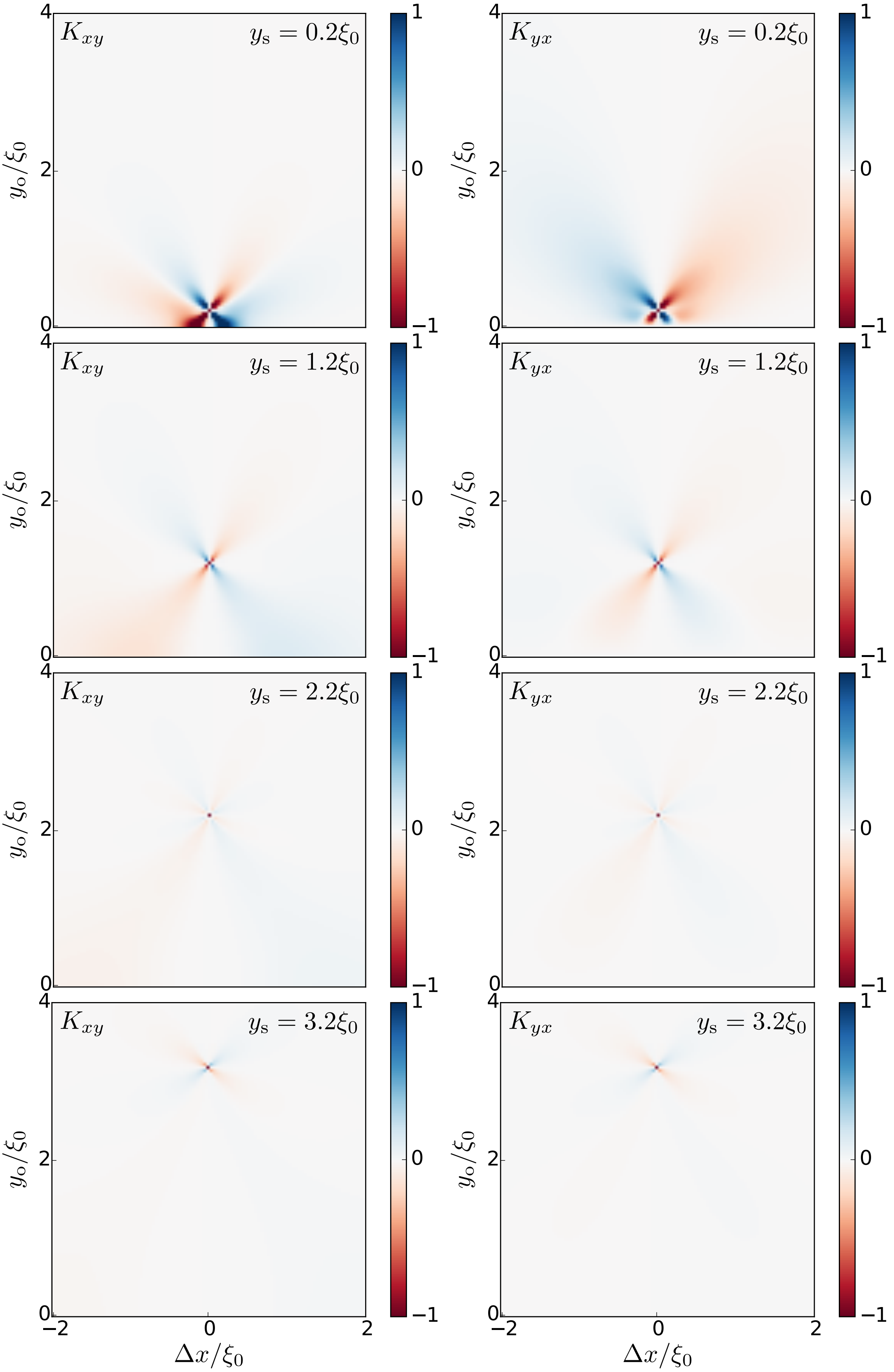

Figure G.2: *Off-diagonal components of the superfluid kernel at* $T = 0.1T_c$.

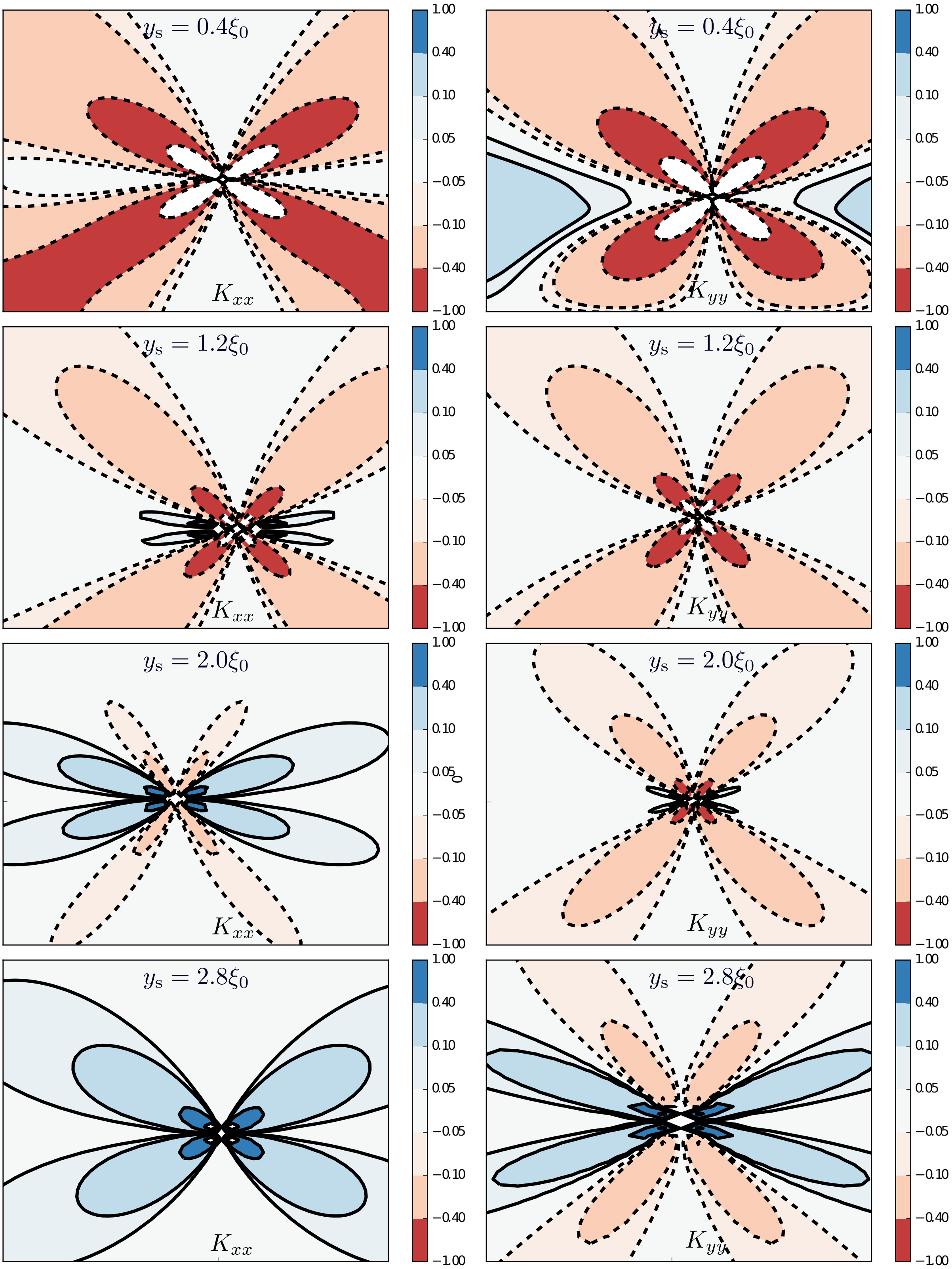

Figure G.3: *Diagonal components of the superfluid kernel at* $T = 0.1T_c$.

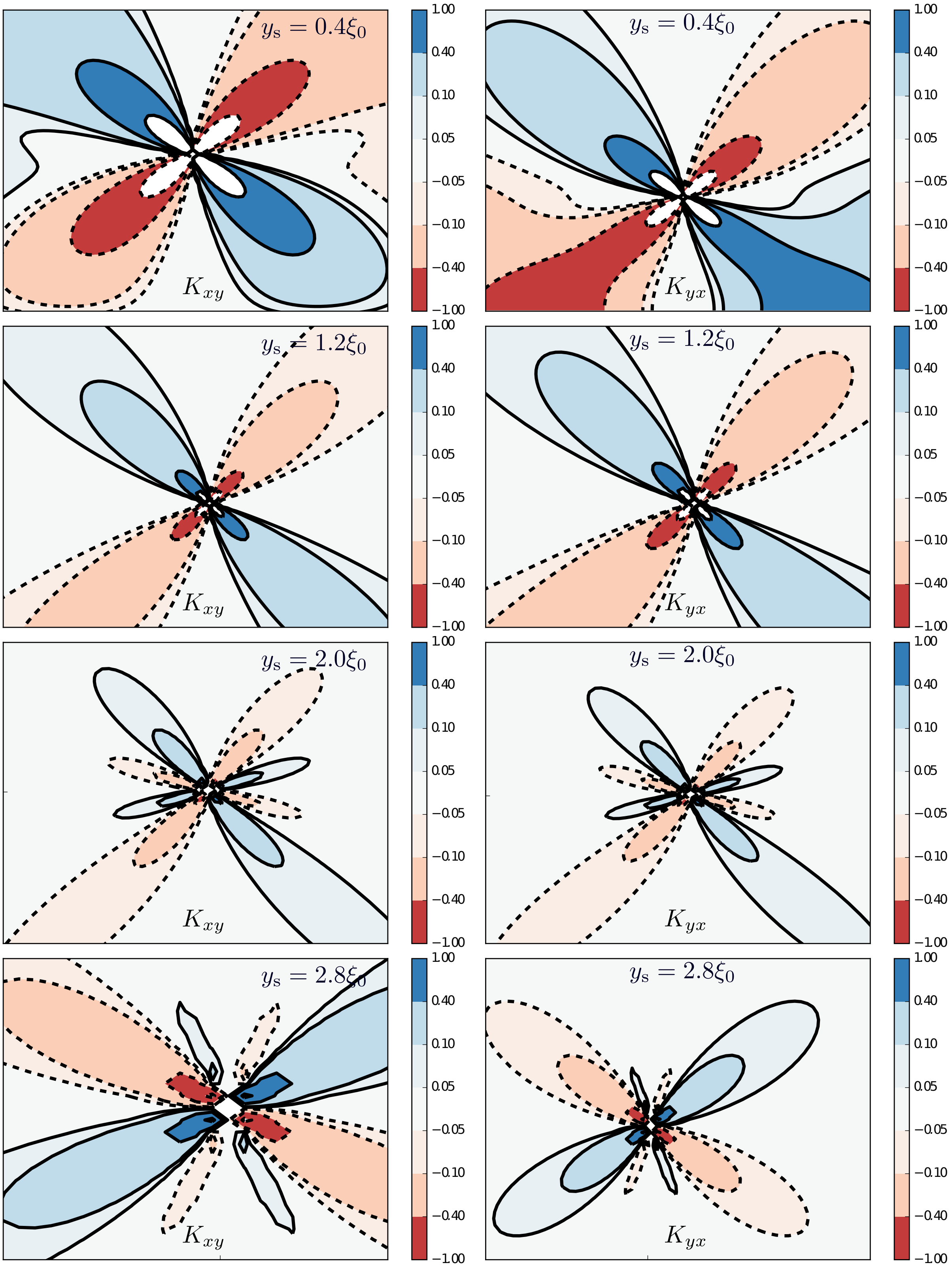

Figure G.4: *Off-diagonal components of the superfluid kernel at* $T = 0.1T_c$.

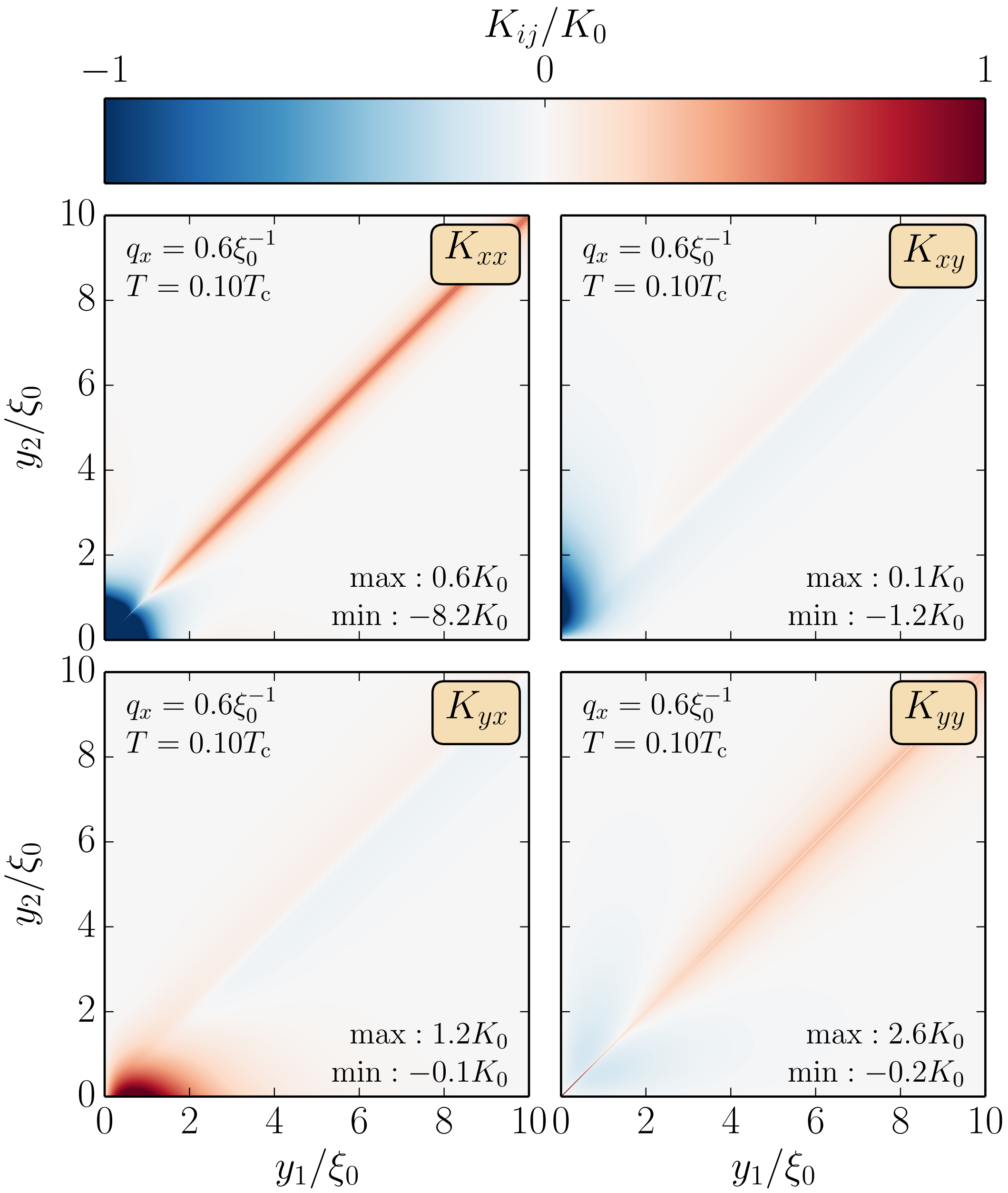

Figure G.5: *Superfluid kernel in mixed representation* $K_{ij}(q_x; y_1 = y_o, y_2 = y_s)$*, at* $T = 0.1T_c$*. Note the inverted color scheme from here on, compared to the previous plots.*

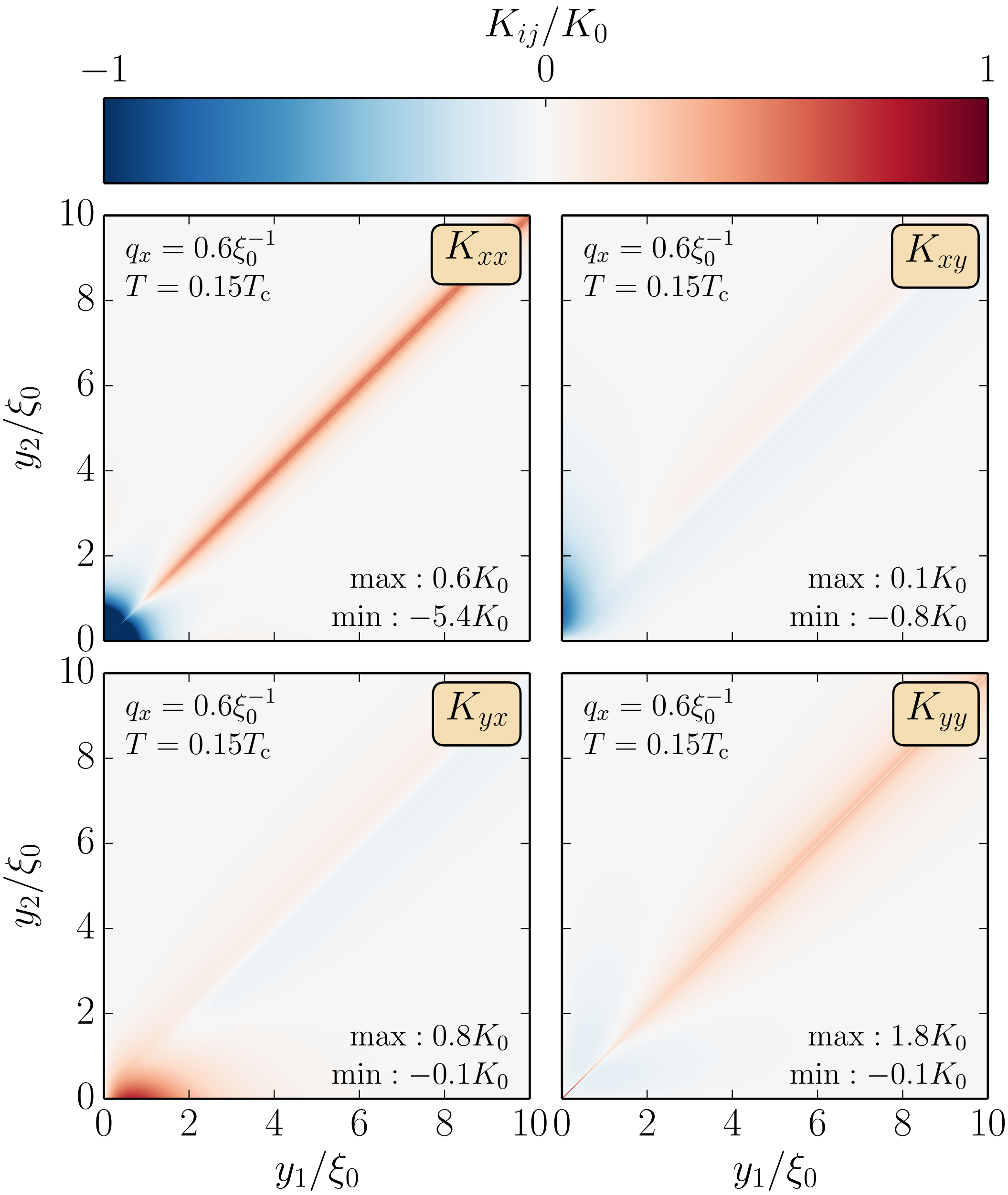

Figure G.6: *Superfluid kernel in mixed representation* $K_{ij}(q_x; y_1 = y_o, y_2 = y_s)$*, at* $T = 0.15T_c$*.*

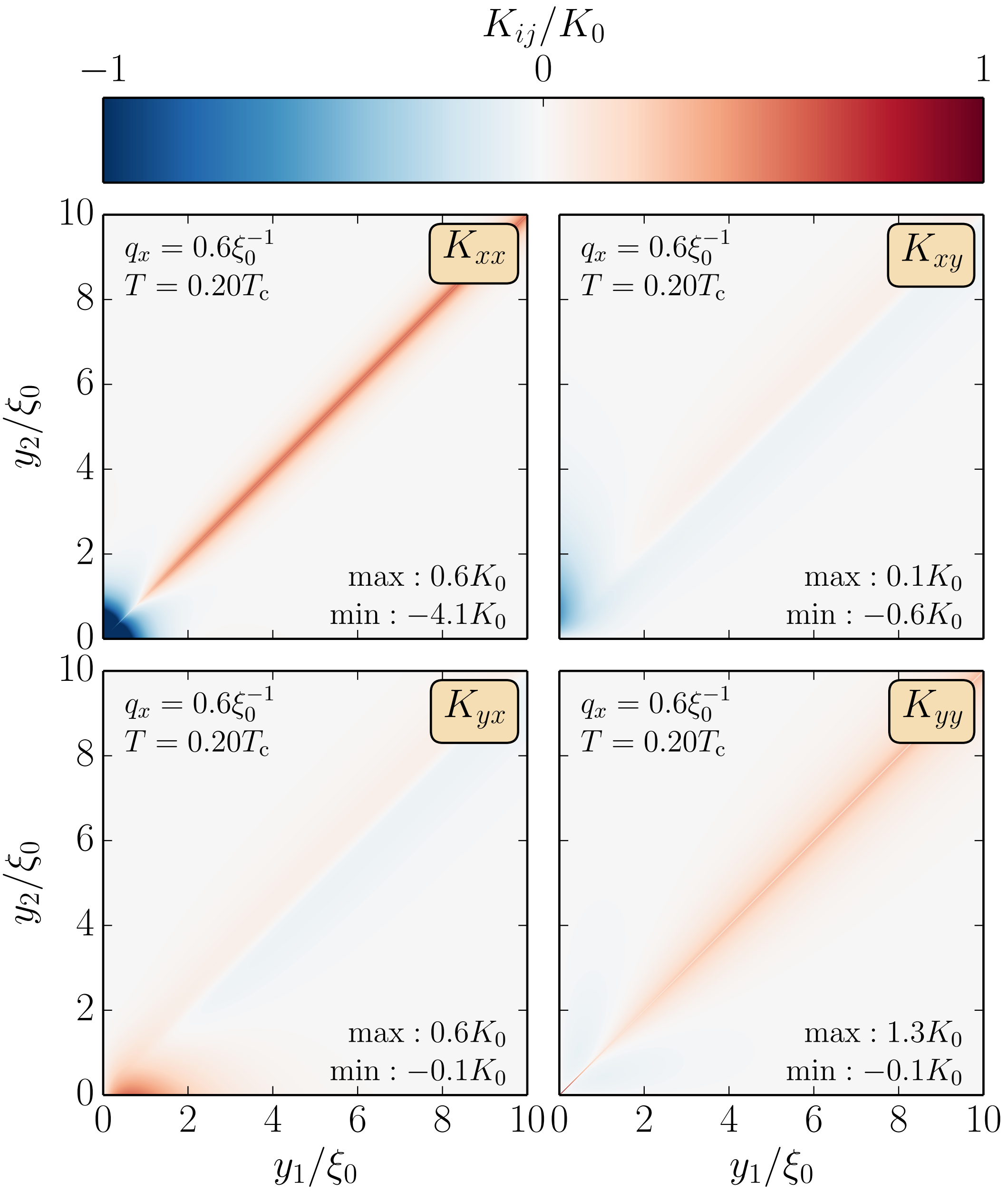

Figure G.7: *Superfluid kernel in mixed representation* $K_{ij}(q_x; y_1 = y_o, y_2 = y_s)$*, at* $T = 0.2T_c$.

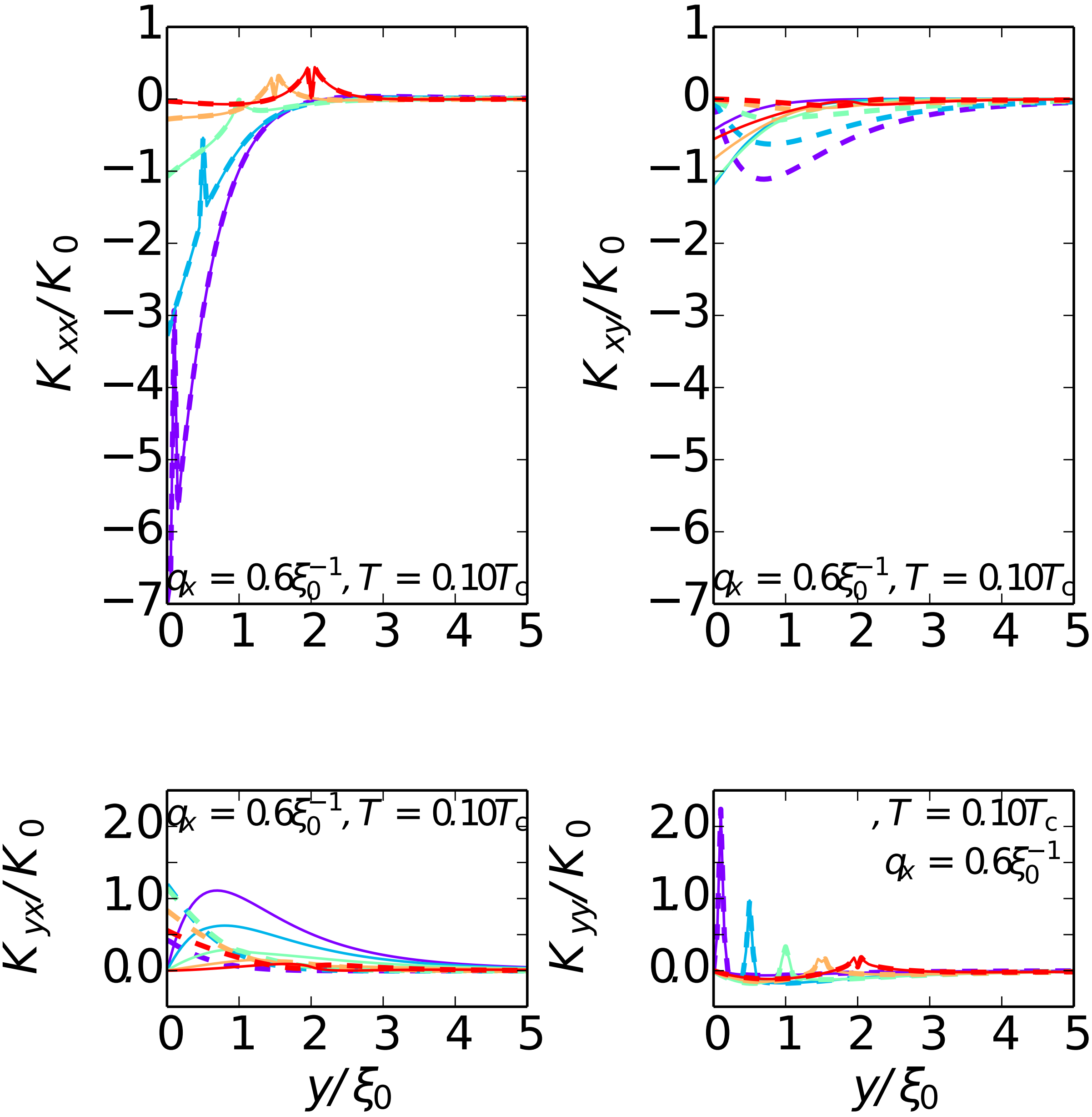

Figure G.8: *Superfluid kernel in mixed representation* $K_{ij}(q_x; y_1 = y_o, y_2 = y_s)$, *at* $T = 0.1T_c$ *at (solid lines)* $y_1/\xi_0 = const$ *and (dashed lines)* $y_2/\xi_0 = const$. *Here, the constant values are* $0.4, 0.8.1.2, 1.6, 2.0$ *(from purple to red).*

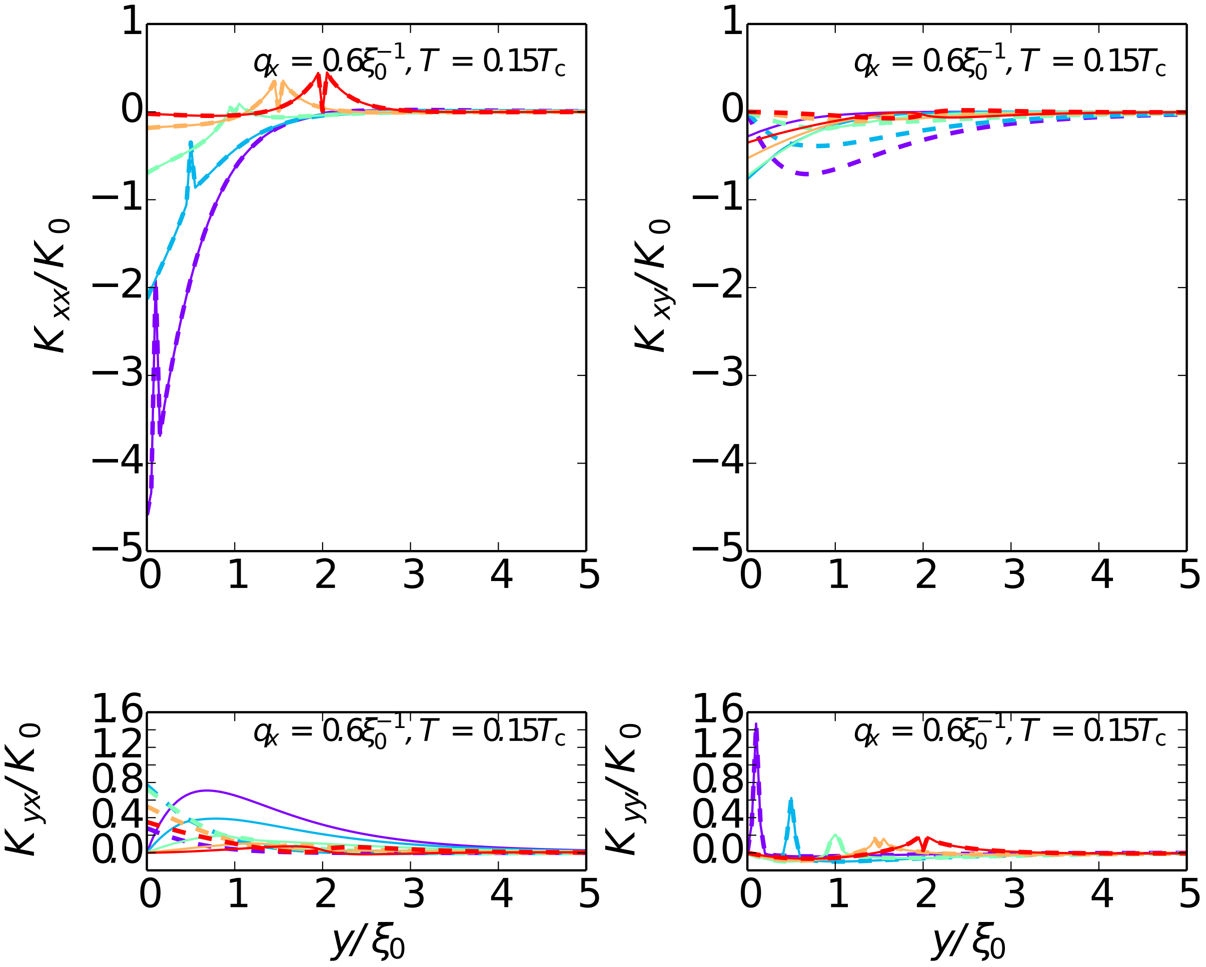

Figure G.9: *Superfluid kernel in mixed representation* $K_{ij}(q_x; y_1 = y_o, y_2 = y_s)$, *at* $T = 0.15T_c$ *at (solid lines)* $y_1/\xi_0 = const$ *and (dashed lines)* $y_2/\xi_0 = const$. *Here, the constant values are* $0.4, 0.8.1.2, 1.6, 2.0$ *(from purple to red).*

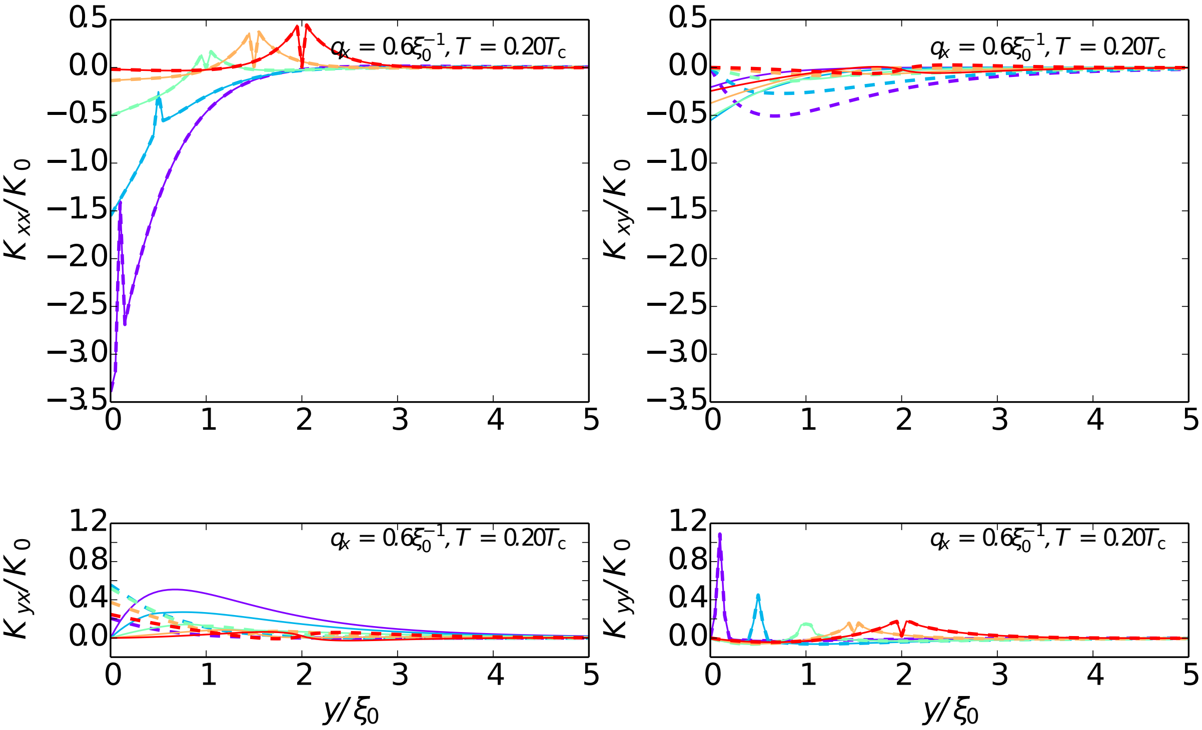

Figure G.10: *Superfluid kernel in mixed representation* $K_{ij}(q_x; y_1 = y_o, y_2 = y_s)$*, at* $T = 0.2T_c$ *at (solid lines)* $y_1/\xi_0 = const$ *and (dashed lines)* $y_2/\xi_0 = const$*. Here, the constant values are* $0.4, 0.8.1.2, 1.6, 2.0$ *(from purple to red).*

References

[1] R. P. Feynman, “Simulating physics with computers”, Int. J. Theor. Phys. **21**, 467–488 (1982) (cit. on p. 1).

[2] H. J. Kimble, “The quantum internet”, Nature **453**, 1023–1030 (2008), arXiv:`0806.4195 [quant-ph]` (cit. on p. 1).

[3] J. Preskill, *Quantum computing and the entanglement frontier*, 2012, arXiv:`1203.5813 [quant-ph]` (cit. on p. 1).

[4] F. Arute et al., “Quantum supremacy using a programmable superconducting processor”, Nature **574**, 505–510 (2019) (cit. on p. 1).

[5] G. N. Gol’tsman, O. Okunev, G. Chulkova, A. Lipatov, A. Semenov, K. Smirnov, B. Voronov, A. Dzardanov, C. Williams, and R. Sobolewski, “Picosecond superconducting single-photon optical detector”, Appl. Phys. Lett. **79**, 705, 705 (2001) (cit. on p. 1).

[6] S. de Franceschi, L. Kouwenhoven, C. Schönenberger, and W. Wernsdorfer, “Hybrid superconductor-quantum dot devices”, Nat. Nanotechnol. **5**, 703–711 (2010) (cit. on p. 1).

[7] U. Welp, K. Kadowaki, and R. Kleiner, “Superconducting emitters of THz radiation”, Nat. Photonics **7**, 702–710 (2013) (cit. on p. 1).

[8] A. Fornieri and F. Giazotto, “Towards phase-coherent caloritronics in superconducting circuits”, Nat. Nanotechnol. **12**, 944–952 (2017) (cit. on p. 1).

[9] D. Gustafsson, D. Golubev, M. Fogelström, T. Claeson, S. Kubatkin, T. Bauch, and F. Lombardi, “Fully gapped superconductivity in a nanometresize $YBa_2Cu_3O_{7-\delta}$ island enhanced by a magnetic field”, Nat. Nanotechnol. **8**, 25 (2013) (cit. on pp. 1, 43, 79).

[10] P. Holmvall, *Licentiate thesis: Modeling mesoscopic unconventional superconductors*, `https://research.chalmers.se/en/publication/253315` (Institutionen för mikroteknologi och nanovetenskap, Tillämpad kvantfysik, Chalmers tekniska högskola, 2017) (cit. on pp. 1, 8, 15, 16, 19, 23, 25, 43, 45, 70, 71, 74, 78, 79, 113).

[11] N. Ashcroft and N. Mermin, *Solid State Physics* (Brooks/Cole, 1976) (cit. on p. 1).

[12] P. Phillips, *Advanced Solid State Physics* (Cambridge University Press, 2012) (cit. on p. 1).

[13] M. Cohen and S. Louie, *Fundamentals of Condensed Matter Physics* (Cambridge University Press, 2016) (cit. on p. 1).

[14] J. Waldram, *Superconductivity of Metals and Cuprates* (Taylor & Francis, 1996) (cit. on p. 1).

[15] P.-G. de Gennes, *Superconductivity of Metals and Alloys*, Advanced book classics (Advanced Book Program, Perseus Books, 1999) (cit. on pp. 1, 11, 27).

[16] M. Tinkham, *Introduction to Superconductivity: Second Edition*, Dover Books on Physics (Dover Publications, 2004) (cit. on pp. 1, 5, 11, 27, 73).

[17] C. P. Poole, R. Prozorov, R. J. Creswick, and H. A. Farach, *Superconductivity.* Vol. 3rd ed (Elsevier, 2014) (cit. on p. 1).

[18] R. C. Powell, *Symmetry, Group Theory, and the Physical Properties of Crystals*, Vol. 824 (2010) (cit. on p. 2).

[19] E. Kats, V. Lebedev, and A. Muratov, "Weak crystallization theory", Phys. Rep. **228**, 1 –91 (1993) (cit. on pp. 2, 65, 71, 74).

[20] I. Martin, S. Gopalakrishnan, and E. A. Demler, "Weak crystallization theory of metallic alloys", Phys. Rev. B **93**, 235140 (2016) (cit. on pp. 2, 65, 71, 74, 80).

[21] R. Lifshitz, "Symmetry Breaking and Order in the Age of Quasicrystals", Isr. J. Chem. **51**, 1156–1167 (2011) (cit. on p. 2).

[22] P. de Gennes and J. Prost, *The Physics of Liquid Crystals*, International Series of Monogr (Clarendon Press, 1993) (cit. on pp. 2, 3, 63).

[23] W. Pesch and L. Kramer, "General Mathematical Description of Pattern-Forming Instabilities", in *Pattern Formation in Liquid Crystals*, edited by A. Buka and L. Kramer (Springer New York, New York, NY, 1996), pp. 69–90 (cit. on pp. 2, 63, 71).

[24] L. S. Hirst and G. Charras, "Biological physics: Liquid crystals in living tissue", Nature **544**, 164–165 (2017) (cit. on p. 2).

[25] K. Kawaguchi, R. Kageyama, and M. Sano, "Topological defects control collective dynamics in neural progenitor cell cultures", Nature **545**, 327–331 (2017) (cit. on p. 2).

[26] T. B. Saw, A. Doostmohammadi, V. Nier, L. Kocgozlu, S. Thampi, Y. Toyama, P. Marcq, C. T. Lim, J. M. Yeomans, and B. Ladoux, "Topological defects in epithelia govern cell death and extrusion", Nature **544**, 212–216 (2017) (cit. on p. 2).

[27] X. Trepat and E. Sahai, “Mesoscale physical principles of collective cell organization”, Nat. Phys. **14**, 671–682 (2018) (cit. on p. 2).

[28] H. Morales-Navarrete, H. Nonaka, A. Scholich, F. Segovia-Miranda, W. de Back, K. Meyer, R. L. Bogorad, V. Koteliansky, L. Brusch, Y. Kalaidzidis, F. Jülicher, B. M. Friedrich, and M. Zerial, “Liquid-crystal organization of liver tissue”, eLife **8**, edited by P. Sens, A. K. Chakraborty, and B. Ladoux, e44860 (2019) (cit. on p. 2).

[29] S. Vignolini, E. Moyroud, B. J. Glover, and U. Steiner, “Analysing photonic structures in plants”, J. Royal Soc. Interface **10**, 20130394 (2013) (cit. on p. 2).

[30] P. Rofouie, D. Pasini, and A. D. Rey, “Nano-scale surface wrinkling in chiral liquid crystals and plant-based plywoods”, Soft Matter **11**, 1127–1139 (2015) (cit. on pp. 2, 3).

[31] M. Mitov, “Cholesteric liquid crystals in living matter”, Soft Matter **13**, 4176–4209 (2017) (cit. on p. 2).

[32] S. L. Burg and A. J. Parnell, “Self-assembling structural colour in nature”, J. Phys. Condens. Matter **30**, 413001 (2018) (cit. on p. 2).

[33] Z. Wang, P. Rofouie, and A. D. Rey, “Surface Anchoring Effects on the Formation of Two-Wavelength Surface Patterns in Chiral Liquid Crystals”, Crystals **9** (2019) (cit. on p. 2).

[34] A. A. Abrikosov, “On the Magnetic properties of superconductors of the second group”, Zh. Eksp. Teor. Fiz. **32**, 1442 (1957), [Sov. Phys. JETP 5, 1174 (1957)] (cit. on pp. 2, 5, 73).

[35] U. Klein, D. Rainer, and H. Shimahara, “Interplay of Fulde–Ferrell–Larkin–Ovchinnikov and Vortex States in Two-Dimensional Superconductors”, J. Low Temp. Phys. **118**, 91–104 (2000) (cit. on pp. 2, 5, 65, 73).

[36] B. Rosenstein and D. Li, “Ginzburg-Landau theory of type II superconductors in magnetic field”, Rev. Mod. Phys. **82**, 109–168 (2010) (cit. on pp. 2, 5, 65).

[37] L. D. Landau, “Theory of phase transformations. I”, Zh. Eksp. Teor. Fiz. **7**, 19 (1937), [Sov. Phys. JETP 11, 26 (1937)] (cit. on p. 2).

[38] A. A. Abrikosov, “On the Magnetic properties of superconductors of the second group”, Zh. Eksp. Teor. Fiz. **20**, 1064 (1950) (cit. on pp. 2, 4).

[39] “On the theory of superconductivity”, in *Collected Papers of L.D. Landau*, edited by D. T. HAAR (Pergamon, 1965), pp. 546 –568 (cit. on pp. 2, 4).

[40] J. V. Selinger, “Interpretation of saddle-splay and the Oseen-Frank free energy in liquid crystals”, Liq. Cryst. Rev. **6**, 129–142 (2018) (cit. on p. 3).

[41] G. P. Crawford and S. Žumer, "SADDLE-SPLAY ELASTICITY IN NEMATIC LIQUID CRYTALS", Int. J. Mod. Phys. B **09**, 2469–2514 (1995) (cit. on p. 3).

[42] G. Barbero and V. M. Pergamenshchik, "Intermediate periodic "saddle-splay" nematic phase in the vicinity of a nematic–smectic-A transition", Phys. Rev. E **66**, 051706 (2002) (cit. on p. 3).

[43] V. M. Pergamenshchik, I. Lelidis, and V. A. Uzunova, "Stripe domains in a nearly homeotropic nematic liquid crystal: A bend escaped state at a nematic–smectic-A transition", Phys. Rev. E **77**, 041703 (2008) (cit. on p. 3).

[44] Ž. Kos and M. Ravnik, "Relevance of saddle-splay elasticity in complex nematic geometries", Soft Matter **12**, 1313–1323 (2016) (cit. on p. 3).

[45] M.-J. Gim, D. A. Beller, and D. K. Yoon, "Morphogenesis of liquid crystal topological defects during the nematic-smectic A phase transition", Nat. Commun. **8**, 15453 (2017) (cit. on pp. 3, 63).

[46] P. Rofouie, D. Pasini, and A. D. Rey, "Nanostructured free surfaces in plant-based plywoods driven by chiral capillarity", Colloids Interface Sci. Commun. **1**, 23 –26 (2014) (cit. on p. 3).

[47] H. Kamerlingh Onnes, "Further experiments with Liquid Helium. D. On the change of Electrical Resistance of Pure Metals at very low Temperatures, etc. V. The Disappearance of the resistance of mercury", Koninklijke Nederlandse Akademie van Wetenschappen Proceedings Series B Physical Sciences **14**, 113–115 (1911) (cit. on p. 4).

[48] L. N. Cooper, "Bound Electron Pairs in a Degenerate Fermi Gas", Phys. Rev. **104**, 1189–1190 (1956) (cit. on p. 4).

[49] J. Bardeen, L. N. Cooper, and J. R. Schrieffer, "Microscopic Theory of Superconductivity", Phys. Rev. **106**, 162–164 (1957) (cit. on pp. 4, 6, 11).

[50] J. Bardeen, L. N. Cooper, and J. R. Schrieffer, "Theory of Superconductivity", Phys. Rev. **108**, 1175–1204 (1957) (cit. on pp. 4, 6, 11).

[51] W. Meissner and R. Ochsenfeld, "Ein neuer Effekt bei Eintritt der Supraleitfähigkeit", Naturwissenschaften **21**, 787–788 (1933) (cit. on p. 4).

[52] P. Fulde and R. A. Ferrell, "Superconductivity in a Strong Spin-Exchange Field", Phys. Rev. **135**, A550–A563 (1964) (cit. on pp. 5, 63, 73).

[53] A. I. Larkin and I. U. N. Ovchinnikov, "Nonunifom state of superconductors", Zh. Eksp. Theor. Fiz **47**, 1136–1146 (1964), [Sov. Phys. JETP 20, 762 (1965)] (cit. on pp. 5, 63, 73).

[54] M. Sigrist and K. Ueda, "Phenomenological theory of unconventional superconductivity", Rev. Mod. Phys. **63**, 239 (1991) (cit. on p. 6).

[55] D. J. Van Harlingen, "Phase-sensitive tests of the symmetry of the pairing state in the high-temperature superconductors—Evidence for $d_{x^2-y^2}$ symmetry", Rev. Mod. Phys. **67**, 515–535 (1995) (cit. on p. 6).

[56] C. C. Tsuei and J. R. Kirtley, "Pairing symmetry in cuprate superconductors", Rev. Mod. Phys. **72**, 969 (2000) (cit. on pp. 6, 104).

[57] A. F. Andreev, "The Thermal Conductivity of the Intermediate State in Superconductors", Zh. Eksp. Teor. Fiz. **46**, 1823 (1964), [Sov. Phys. JETP 19, 1228 (1964)] (cit. on pp. 6, 22, 36).

[58] C. W. J. Beenakker, "Why Does a Metal—Superconductor Junction Have a Resistance?", in *Quantum Mesoscopic Phenomena and Mesoscopic Devices in Microelectronics*, edited by I. O. Kulik and R. Ellialtioğlu (Springer Netherlands, Dordrecht, 2000), pp. 51–60 (cit. on pp. 6, 22, 36).

[59] L. J. Buchholtz and G. Zwicknagl, "Identification of p-wave superconductors", Phys. Rev. B **23**, 5788–5796 (1981) (cit. on pp. 7, 35, 36).

[60] C.-R. Hu, "Midgap surface states as a novel signature for d^2_{xa}-x^2_b-wave superconductivity", Phys. Rev. Lett. **72**, 1526 (1994) (cit. on pp. 7, 35, 36, 119).

[61] T Löfwander, V. S. Shumeiko, and G Wendin, "Andreev bound states in high-T_c superconducting junctions", Supercond. Sci. Technol. **14**, R53 (2001) (cit. on pp. 7, 22, 35, 36, 119).

[62] S. Kashiwaya and Y. Tanaka, "Tunnelling effects on surface bound states in unconventional superconductors", Rep. Prog. Phys. **63**, 1641 (2000) (cit. on pp. 7, 35, 36, 119).

[63] J. A. Sauls, "Andreev bound states and their signatures", Philos. Trans. Royal Soc. A **376**, 20180140 (2018) (cit. on pp. 7, 35, 36, 119).

[64] S. Higashitani, "Mechanism of Paramagnetic Meissner Effect in High-Temperature Superconductors", J. Soc. Phys. Jpn. **66**, 2556 (1997) (cit. on pp. 7, 33–35, 40, 43, 45).

[65] M. Sigrist, "Time-reversal symmetry breaking states in high-temperature superconductors", Prog. Theor. Phys. **99**, 899–929 (1998) (cit. on pp. 7, 43, 79).

[66] Y. S. Barash, M. S. Kalenkov, and J. Kurkijärvi, "Low-temperature magnetic penetration depth in d-wave superconductors: Zero-energy bound state and impurity effects", Phys. Rev. B **62**, 6665 (2000) (cit. on pp. 7, 42, 43, 45, 58, 70).

[67] T. Löfwander, V. S. Shumeiko, and G. Wendin, "Time-reversal symmetry breaking at Josephson tunnel junctions of purely $\boldsymbol{d}$ -wave superconductors", Phys. Rev. B **62**, R14653 (2000) (cit. on pp. 7, 42, 43, 45, 58, 70, 76).

[68] M. Håkansson, *Mesoscopic thin film superconductors - A computational framework*, `https://research.chalmers.se/en/publication/211094` (Institutionen för mikroteknologi och nanovetenskap, Tillämpad kvantfysik, Chalmers tekniska högskola, 2015) (cit. on pp. 8, 19).

[69] J. Serene and D Rainer, "The quasiclassical approach to superfluid 3He", Phys. Rep. **101**, 221 –311 (1983) (cit. on pp. 11, 12, 25).

[70] M. Eschrig, J. Heym, and D. Rainer, "Corrections to Fermi-liquid theory of correlated metals", J. Low Temp. Phys. **95**, 323–327 (1994) (cit. on pp. 11, 12).

[71] M. Eschrig, D. Rainer, and J. A. Sauls, "Effects of strong magnetic fields on pairing fluctuations in high-temperature superconductors", Phys. Rev. B **59**, 12095–12113 (1999) (cit. on pp. 11, 12).

[72] J. A. Sauls and M Eschrig, "Vortices in chiral, spin-triplet superconductors and superfluids", New J. Phys. **11**, 075008 (2009) (cit. on pp. 11, 12, 17, 23).

[73] G. Eilenberger, "Transformation of Gorkov's equation for type II superconductors into transport-like equations", Z. Phys. A **214**, 195–213 (1968) (cit. on pp. 11, 13, 25).

[74] A. I. Larkin and Y. N. Ovchinnikov, "Quasiclassical Method in the Theory of Superconductivity", Zh. Eksp. Teor. Fiz. **55**, 2262 (1969), [Sov. Phys. JETP 28, 1200 (1969)] (cit. on pp. 11, 13).

[75] A. L. Shelankov, "On the derivation of quasiclassical equations for superconductors", English, J. Low Temp. Phys. **60**, 29–44 (1985) (cit. on pp. 11, 13, 85).

[76] H. Bruus and K. Flensberg, *Many-Body Quantum Theory in Condensed Matter Physics: An Introduction*, Oxford Graduate Texts (OUP Oxford, 2004) (cit. on pp. 11, 14).

[77] J. Rammer, *Quantum Field Theory of Non-equilibrium States* (Cambridge University Press, 2007) (cit. on pp. 11, 14).

[78] N. Kopnin, *Theory of Nonequilibrium Superconductivity*, International Series of Monographs on Physics (OUP Oxford, 2009) (cit. on pp. 11, 12, 14, 23, 27).

[79] G. Mahan, *Many-Particle Physics*, Physics of Solids and Liquids (Springer US, 2013) (cit. on pp. 11, 14).

[80] L. Gor'kov, " On the Energy Spectrum of Superconductors ", Zh. Eksp. Teor. Fiz. **34**, 735 (1958), [Sov. Phys. JETP 7, 505 (1958)] (cit. on p. 11).

[81] J. Schrieffer, *Theory Of Superconductivity*, Advanced Book Program Series (Avalon Publishing, 1983) (cit. on pp. 11, 27, 102).

[82] M. Eschrig and J. A. Sauls, “Charge dynamics of vortex cores in layered chiral triplet superconductors”, New. J. Phys. **11**, 075009 (2009) (cit. on p. 12).

[83] Y. Nambu, “Quasi-Particles and Gauge Invariance in the Theory of Superconductivity”, Phys. Rev. **117**, 648–663 (1960) (cit. on p. 12).

[84] A. V. Zaitsev, “Quasiclassical equations of the theory of superconductivity for contiguous metals and the properties of constricted microcontacts”, Zh. Eksp. Teor. Fiz. **86**, 1742 (1984), [Sov. Phys. JETP 59, 1015 (1984)] (cit. on pp. 12, 21).

[85] A. L. Shelankov, “Two-Particle Tunneling in a Normal Metal–Semiconductor Contact”, Fiz. Tverd. Tela **26**, 1615 (1984), [Sov. Phys. Solid State 26, 981 (1984)] (cit. on pp. 12, 21).

[86] B. Ashauer, G. Kieselmann, and D. Rainer, “On the proximity effect in unconventional superconductors”, J. Low Temp. Phys. **63**, 349–366 (1986) (cit. on pp. 12, 21).

[87] G. Kieselmann, “Self-consistent calculations of the pair potential and the tunneling density of states in proximity contacts”, Phys. Rev. B **35**, 6762–6770 (1987) (cit. on pp. 12, 21).

[88] A. Millis, D. Rainer, and J. A. Sauls, “Quasiclassical theory of superconductivity near magnetically active interfaces”, Phys. Rev. B **38**, 4504–4515 (1988) (cit. on pp. 12, 21, 121).

[89] S. K. Yip, “Josephson current between d-wave superconductors through an interface with finite transmission”, J. Low. Temp. Phys. **109**, 547–576 (1997) (cit. on pp. 12, 21).

[90] M. Eschrig, “Distribution functions in nonequilibrium theory of superconductivity and Andreev spectroscopy in unconventional superconductors”, Phys. Rev. B **61**, 9061–9076 (2000) (cit. on pp. 12, 17, 21, 22, 85).

[91] A. Shelankov and M. Ozana, “Quasiclassical theory of superconductivity: A multiple-interface geometry”, Phys. Rev. B **61**, 7077–7100 (2000) (cit. on p. 12).

[92] M. Ozana, “Mesoscopic Superconductivity: Quasiclassical Approach”, PhD thesis (Umeå University, 2001) (cit. on p. 12).

[93] M. Ozana and A. Shelankov, “Superconductivity in Multiple Interface Geometry: Applicability of Quasiclassical Theory”, J. Low Temp. Phys. **124**, 223–243 (2001) (cit. on p. 12).

[94] M. Ozana and A. Shelankov, “Quasiclassical theory of superconductivity: Interfering paths”, Phys. Rev. B **65**, 014510 (2001) (cit. on p. 12).

[95] M. Ozana, A. Shelankov, and J. Tobiska, “Bogoliubov–de Gennes versus quasiclassical description of Josephson layered structures”, Phys. Rev. B **66**, 054508 (2002) (cit. on p. 12).

[96] T. Löfwander, M. Fogelström, and J. A. Sauls, “Shot noise in normal metal–d-wave superconducting junctions”, Phys. Rev. B **68**, 054504 (2003) (cit. on pp. 12, 21).

[97] M. Eschrig, “Scattering problem in nonequilibrium quasiclassical theory of metals and superconductors: General boundary conditions and applications”, Phys. Rev. B **80**, 134511 (2009) (cit. on pp. 12, 17, 22, 85).

[98] G. M. Eliashberg, “Inelastic Electron Collisions and Nonequilibrium Stationary States in Superconductors”, Zh. Eksp. Teor. Fiz. **61**, 1254 (1972), [Sov. Phys. JETP 34, 668 (1972)] (cit. on p. 13).

[99] A. I. Larkin and Y. N. Ovchinnikov, “ Nonlinear conductivity of superconductors in the mixed state ”, Zh. Eksp. Teor. Fiz. **68**, 1915 (1975), [Sov. Phys. JETP 41, 960 (1975)] (cit. on p. 13).

[100] A. I. Larkin and Y. N. Ovchinnikov, “ Nonlinear effects during the motion of vortices in superconductors ”, Zh. Eksp. Teor. Fiz. **73**, 299 (1977), [Sov. Phys. JETP 46, 155 (1977)] (cit. on p. 13).

[101] L. V. Keldysh, “Diagram Technique for Nonequilibrium Processes”, Zh. Eksp. Teor. Fiz. **47**, 1515 (1964), [Sov. Phys. JETP 20, 1018 (1965)] (cit. on p. 14).

[102] T. Matsubara, “A New Approach to Quantum-Statistical Mechanics”, Prog. Theor. Phys. **14**, 351–378 (1955) (cit. on p. 14).

[103] R. Grein, T. Löfwander, and M. Eschrig, “Inverse proximity effect and influence of disorder on triplet supercurrents in strongly spin-polarized ferromagnets”, Phys. Rev. B **88**, 054502 (2013) (cit. on pp. 15, 16).

[104] T. Ozaki, “Continued fraction representation of the Fermi-Dirac function for large-scale electronic structure calculations”, Phys. Rev. B **75**, 035123 (2007) (cit. on p. 15).

[105] Y. Nagato, K. Nagai, and J. Hara, “Theory of the Andreev reflection and the density of states in proximity contact normal-superconducting infinite double-layer”, J. Low Temp. Phys. **93**, 33–56 (1993) (cit. on p. 17).

[106] N. Schopohl and K. Maki, “Quasiparticle spectrum around a vortex line in a d -wave superconductor”, Phys. Rev. B **52**, 490 (1995) (cit. on p. 17).

[107] N. Schopohl, “Transformation of the Eilenberger Equations of Superconductivity to a Scalar Riccati Equation”, (1998), eprint: `cond-mat/9804064` (cit. on p. 17).

[108] M. Eschrig, J. A. Sauls, and D. Rainer, “Electromagnetic response of a vortex in layered superconductors”, Phys. Rev. B **60**, 10447–10454 (1999) (cit. on p. 17).

[109] A. B. Vorontsov and J. A. Sauls, “Thermodynamic properties of thin films of superfluid $^3\mathrm{He}-A$”, Phys. Rev. B **68**, 064508 (2003) (cit. on pp. 17, 25).

[110] J. M. Luttinger and J. C. Ward, “Ground-State Energy of a Many-Fermion System. II”, Phys. Rev. **118**, 1417–1427 (1960) (cit. on p. 25).

[111] C. D. Dominicis and P. C. Martin, “Stationary Entropy Principle and Renormalization in Normal and Superfluid Systems. I. Algebraic Formulation”, J. Math. Phys. **5**, 14–30 (1964) (cit. on p. 25).

[112] C. D. Dominicis and P. C. Martin, “Stationary Entropy Principle and Renormalization in Normal and Superfluid Systems. II. Diagrammatic Formulation”, J. Math. Phys. **5**, 31–59 (1964) (cit. on p. 25).

[113] J. D. Jackson, *Classical electrodynamics*, 3rd ed. (Wiley, New York, NY, 1999) (cit. on p. 25).

[114] P. Virtanen, A. Vargunin, and M. Silaev, “Quasiclassical expressions for the free energy of superconducting systems”, (2019), `arXiv:1909.00992` (cit. on p. 25).

[115] J. Bardeen, “Critical Fields and Currents in Superconductors”, Rev. Mod. Phys. **34**, 667–681 (1962) (cit. on p. 27).

[116] D. Xu, S. K. Yip, and J. A. Sauls, “Nonlinear Meissner effect in unconventional superconductors”, Phys. Rev. B **51**, 16233–16253 (1995) (cit. on pp. 27, 28, 30, 32, 33, 47, 57, 104, 144).

[117] C. Zhou and H. J. Schulz, “Density of states and tunneling spectra in two-dimensional d-wave superconductors”, Phys. Rev. B **45**, 7397–7401 (1992) (cit. on pp. 32, 109).

[118] H. Walter, W. Prusseit, R. Semerad, H. Kinder, W. Assmann, H. Huber, H. Burkhardt, D. Rainer, and J. A. Sauls, “Low-Temperature Anomaly in the Penetration Depth of $\mathrm{YBa_2Cu_3}O_7$ Films: Evidence for Andreev Bound States at Surfaces”, Phys. Rev. Lett. **80**, 3598–3601 (1998) (cit. on pp. 33, 34, 80).

[119] A. Carrington, F. Manzano, R. Prozorov, R. W. Giannetta, N. Kameda, and T. Tamegai, “Evidence for Surface Andreev Bound States in Cuprate Superconductors from Penetration Depth Measurements”, Phys. Rev. Lett. **86**, 1074–1077 (2001) (cit. on pp. 33, 34).

[120] I. Kosztin and A. J. Leggett, “Nonlocal Effects on the Magnetic Penetration Depth in d-Wave Superconductors”, Phys. Rev. Lett. **79**, 135–138 (1997) (cit. on p. 33).

[121] P. D. Gennes and E. Guyon, "Superconductivity in "normal" metals", Phys. Lett. **3**, 168 –169 (1963) (cit. on p. 36).

[122] N. R. Werthamer, "Theory of the Superconducting Transition Temperature and Energy Gap Function of Superposed Metal Films", Phys. Rev. **132**, 2440–2445 (1963) (cit. on p. 36).

[123] S.-I. Suzuki and Y. Asano, "Paramagnetic instability of small topological superconductors", Phys. Rev. B **89**, 184508 (2014) (cit. on pp. 36, 43).

[124] V. V. Dmitriev, A. A. Senin, A. A. Soldatov, and A. N. Yudin, "Polar Phase of Superfluid ^{3}He in Anisotropic Aerogel", Phys. Rev. Lett. **115**, 165304 (2015) (cit. on p. 36).

[125] N. Zhelev, M. Reichl, T. S. Abhilash, E. N. Smith, K. X. Nguyen, E. J. Mueller, and J. M. Parpia, "Observation of a new superfluid phase for ^{3}He embedded in nematically ordered aerogel", Nat. Commun. **7**, 12975 (2016) (cit. on p. 36).

[126] S. B. Etter, A. Bouhon, and M. Sigrist, "Spontaneous surface flux pattern in chiral p-wave superconductors", Phys. Rev. B **97**, 064510 (2018) (cit. on pp. 36, 43).

[127] N. Miyawaki and S. Higashitani, "Influence of diffuse surface scattering on the stability of superconducting phases with spontaneous surface current generated by Andreev bound states", Phys. Rev. B **98**, 134516 (2018) (cit. on pp. 36, 43).

[128] B. M. Andersen and P. Hedegård, "Andreev bound states at the interface of antiferromagnets and d-wave superconductors", Phys. Rev. B **66**, 104515 (2002) (cit. on p. 36).

[129] B. M. Andersen, P. Hedegård, and H. Bruus, "Electronic Checkerboard Pattern in Striped Racetrack Domains: A Consistent Picture of Recent Neutron and STM Experiments", J. Low. Temp. Phys. **131**, 281–285 (2003) (cit. on p. 36).

[130] B. M. Andersen, I. V. Bobkova, P. J. Hirschfeld, and Y. S. Barash, "Bound states at the interface between antiferromagnets and superconductors", Phys. Rev. B **72**, 184510 (2005) (cit. on p. 36).

[131] A. V. Balatsky, I. Vekhter, and J.-X. Zhu, "Impurity-induced states in conventional and unconventional superconductors", Rev. Mod. Phys. **78**, 373–433 (2006) (cit. on pp. 36, 80).

[132] B. M. Andersen, A. Melikyan, T. S. Nunner, and P. J. Hirschfeld, "Andreev States near Short-Ranged Pairing Potential Impurities", Phys. Rev. Lett. **96**, 097004 (2006) (cit. on pp. 36, 80).

[133] M. Mashkoori, K. Björnson, and A. M. Black-Schaffer, "Impurity bound states in fully gapped d-wave superconductors with subdominant order parameters", Sci. Rep. **7**, 44107, 44107 (2017) (cit. on p. 36).

[134] C. Caroli, P. D. Gennes, and J. Matricon, "Bound Fermion states on a vortex line in a type II superconductor", Phys. Lett. **9**, 307 –309 (1964) (cit. on p. 36).

[135] H. F. Hess, R. B. Robinson, R. C. Dynes, J. M. Valles, and J. V. Waszczak, "Scanning-Tunneling-Microscope Observation of the Abrikosov Flux Lattice and the Density of States near and inside a Fluxoid", Phys. Rev. Lett. **62**, 214–216 (1989) (cit. on p. 36).

[136] C. Renner, A. D. Kent, P. Niedermann, O. Fischer, and F. Lévy, "Scanning tunneling spectroscopy of a vortex core from the clean to the dirty limit", Phys. Rev. Lett. **67**, 1650–1652 (1991) (cit. on p. 36).

[137] W. J. Tomasch, "Geometrical Resonance in the Tunneling Characteristics of Superconducting Pb", Phys. Rev. Lett. **15**, 672–675 (1965) (cit. on pp. 39, 128).

[138] W. J. Tomasch, "Geometrical Resonance and Boundary Effects in Tunneling from Superconducting In", Phys. Rev. Lett. **16**, 16–19 (1966) (cit. on pp. 39, 128).

[139] W. Tomasch, "Geometrical resonance effect in superconducting Sn", Phys. Lett. **23**, 204 –206 (1966) (cit. on pp. 39, 128).

[140] W. J. Tomasch and T. Wolfram, "Energy Spacing of Geometrical Resonance Structure in Very Thick Films of Superconducting In", Phys. Rev. Lett. **16**, 352–354 (1966) (cit. on pp. 39, 128).

[141] T. Wolfram and M. B. Einhorn, "Surface States and Additional Structure in the Mcmillan-Anderson Model for the Tomasch Effect", Phys. Rev. Lett. **17**, 966–968 (1966) (cit. on pp. 39, 128).

[142] W. L. McMillan and P. W. Anderson, "Theory of Geometrical Resonances in the Tunneling Characteristics of Thick Films of Superconductors", Phys. Rev. Lett. **16**, 85–87 (1966) (cit. on pp. 39, 128).

[143] T. Wolfram, "Tomasch Oscillations in the Density of States of Superconducting Films", Phys. Rev. **170**, 481–490 (1968) (cit. on pp. 39, 128).

[144] A. B. Vorontsov, "Andreev bound states in superconducting films and confined superfluid He-3", Philos. Trans. Royal Soc. A **376**, 201501444 (2018) (cit. on pp. 41, 59, 70, 132).

[145] M. Matsumoto and H. Shiba, "Coexistence of different symmetry order parameters near a surface in *d*-wave superconductors I", J. Phys. Soc. Jpn. **64**, 3384–3396 (1995) (cit. on pp. 43, 79).

[146] M. Matsumoto and H. Shiba, “Coexistence of different symmetry order parameters near a surface in d-wave superconductors II”, English, J. Phys. Soc. Jpn. **64**, 4867–4881 (1995) (cit. on pp. 43, 79).

[147] M. Fogelström, D. Rainer, and J. A. Sauls, “Tunneling into Current-Carrying Surface States of High- T_c Superconductors”, Phys. Rev. Lett. **79**, 281 (1997) (cit. on pp. 43, 79, 119).

[148] A. M. Black-Schaffer, D. S. Golubev, T. Bauch, F. Lombardi, and M. Fogelström, “Model Evidence of a Superconducting State with a Full Energy Gap in Small Cuprate Islands”, Phys. Rev. Lett. **110**, 197001 (2013) (cit. on pp. 43, 79).

[149] C. Honerkamp, K. Wakabayashi, and M. Sigrist, “Instabilities at [110] surfaces of $d_{x^2-y^2}$ superconductors”, Europhys. Lett. **50**, 368–374 (2007) (cit. on pp. 43, 79).

[150] A. C. Potter and P. A. Lee, “Edge ferromagnetism from Majorana flat bands: application to split tunneling-conductance peaks in high-T_c cuprate superconductors”, Phys. Rev. Lett. **112**, 117002 (2014) (cit. on pp. 43, 79).

[151] S. Matsubara and H. Kontani, “Emergence of strongly correlated electronic states driven by the Andreev bound state in d-wave superconductors”, (2019), arXiv:`1910.08727` (cit. on pp. 43, 79).

[152] A. B. Vorontsov, “Broken Translational and Time-Reversal Symmetry in Unconventional Superconducting Films”, Phys. Rev. Lett. **102**, 177001 (2009) (cit. on pp. 43, 70, 76).

[153] M. Hachiya, K. Aoyama, and R. Ikeda, “Field-induced reentrant superconductivity in thin films of nodal superconductors”, Phys. Rev. B **88**, 064519 (2013) (cit. on pp. 43, 70).

[154] S. Higashitani and N. Miyawaki, “Phase Transition to a Time-Reversal Symmetry-Breaking State in d-Wave Superconducting Films with Rough Surfaces”, J. Soc. Phys. Jpn. **84**, 033708 (2015) (cit. on pp. 43, 70).

[155] N. Miyawaki and S. Higashitani, “Fermi surface effect on spontaneous breaking of time-reversal symmetry in unconventional superconducting films”, Phys. Rev. B **91**, 094511 (2015) (cit. on pp. 43, 70).

[156] N. Miyawaki and S. Higashitani, “Temperature Dependence of the Critical Thickness of d-Wave Superconducting Films”, Phys. Proc. **65**, 25 (2015) (cit. on pp. 43, 70).

[157] M. Håkansson, T. Löfwander, and M. Fogelström, “Spontaneously broken time-reversal symmetry in high-temperature superconductors”, Nat. Phys. **11**, 755 (2015) (cit. on pp. 43–45, 74, 76, 79).

[158] S.-I. Suzuki and Y. Asano, “Spontaneous edge current in a small chiral superconductor with a rough surface”, Phys. Rev. B **94**, 155302 (2016) (cit. on p. 43).

[159] Y. Nagai, Y. Ota, and K. Tanaka, “Time-reversal symmetry breaking and gapped surface states due to spontaneous emergence of new order in *d*-wave nanoislands”, Phys. Rev. B **96**, 060503 (2017) (cit. on pp. 43, 119).

[160] Y. Nagai, Y. Ota, and K. Tanaka, “Time-reversal symmetry breaking phase and gapped surface states in d-wave nanoscale superconductors”, J. Phys.: Conf. Ser. **969**, 012039 (2018) (cit. on pp. 43, 119).

[161] M. Covington, M. Aprili, E. Paraoanu, L. H. Greene, F. Xu, J. Zhu, and C. A. Mirkin, “Observation of Surface-Induced Broken Time-Reversal Symmetry in $\mathrm{YBa_2Cu_3}O_7$ Tunnel Junctions”, Phys. Rev. Lett. **79**, 277 (1997) (cit. on pp. 43, 79).

[162] K. Krishana, N. P. Ong, Q. Li, G. D. Gu, and N. Koshizuka, “Plateaus Observed in the Field Profile of Thermal Conductivity in the Superconductor Bi2Sr2CaCu2O8”, Science **277**, 83 (1997) (cit. on pp. 43, 79).

[163] Y. Dagan and G. Deutscher, “Doping and Magnetic Field Dependence of In-Plane Tunneling into $\mathrm{YBa_2Cu_3}O_{7-x}$: Possible Evidence for the Existence of a Quantum Critical Point”, Phys. Rev. Lett. **87**, 177004 (2001) (cit. on pp. 43, 79).

[164] R. Gonnelli, A. Calzolari, D. Daghero, L. Natale, G. Ummarino, V. Stepanov, and M. Ferretti, “Evidence for pseudogap and phase-coherence gap separation by Andreev reflection experiments in $\mathrm{Au/La_{2-x}Sr_xCuO_4}$ point-contact junctions”, Eur. Phys. J. B **22**, 411 (2001) (cit. on pp. 43, 79).

[165] G. Elhalel, R. Beck, G. Leibovitch, and G. Deutscher, “Transition from a Mixed to a Pure *d*-Wave Symmetry in Superconducting Optimally Doped $\mathrm{YBa_2Cu_3O}_{7-x}$ Thin Films Under Applied Fields”, Phys. Rev. Lett. **98**, 137002 (2007) (cit. on pp. 43, 79).

[166] T. Watashige, Y. Tsutsumi, T. Hanaguri, Y. Kohsaka, S. Kasahara, A. Furusaki, M. Sigrist, C. Meingast, T. Wolf, H. v. Löhneysen, T. Shibauchi, and Y. Matsuda, “Evidence for Time-Reversal Symmetry Breaking of the Superconducting State near Twin-Boundary Interfaces in FeSe Revealed by Scanning Tunneling Spectroscopy”, Phys. Rev. X **5**, 031022 (2015) (cit. on pp. 43, 79).

[167] A. Bhattacharyya, D. T. Adroja, N. Kase, A. D. Hillier, A. M. Strydom, and J. Akimitsu, “Unconventional superconductivity in the cage-type compound $\mathbf{Sc_5Rh_6Sn_{18}}$”, Phys. Rev. B **98**, 024511 (2018) (cit. on pp. 43, 79).

[168] D. F. He, X. H. Zeng, H.-J. Krause, H. Soltner, F. Rüders, and Y. Zhang, “Radio frequency SQUIDs operating at 77 K with 1 GHz lumped-element tank circuits”, Appl. Phys. Lett. **72**, 969–971 (1998) (cit. on pp. 43, 79).

[169] R. Carmi, E. Polturak, G. Koren, and A. Auerbach, "Spontaneous macroscopic magnetization at the superconducting transition", Nature **404**, 853–855 (2000) (cit. on pp. 43, 79).

[170] J. Kirtley, C. Tsuei, A. Ariando, C. Verwijs, S. Harkema, and H. Hilgenkamp, "Angle-resolved phase-sensitive determination of the in-plane gap symmetry in $YBa_2Cu_3O_{7-\delta}$", Nat. Phys. **2**, 190–194 (2006) (cit. on pp. 43, 79).

[171] H. Saadaoui, G. D. Morris, Z. Salman, Q. Song, K. H. Chow, M. D. Hossain, C. D. P. Levy, T. J. Parolin, M. R. Pearson, M. Smadella, D. Wang, L. H. Greene, P. J. Hentges, R. F. Kiefl, and W. A. MacFarlane, "Search for broken time-reversal symmetry near the surface of superconducting $YBa_2Cu_3O_{7-\delta}$ films using β-detected nuclear magnetic resonance", Phys. Rev. B **83**, 054504 (2011) (cit. on pp. 43, 79).

[172] H. Saadaoui, Z. Salman, T. Prokscha, A. Suter, H. Huhtinen, P. Paturi, and E. Morenzoni, "Absence of spontaneous magnetism associated with a possible time-reversal symmetry breaking state beneath the surface of (110)-oriented $YBa_2Cu_3O_{7-\delta}$ superconducting films", Phys. Rev. B **88**, 180501 (2013) (cit. on pp. 43, 79).

[173] M. A. Silaev and G. E. Volovik, "Andreev-Majorana bound states in superfluids", J. Exp. Theor. Phys. **119**, 1042–1057 (2014) (cit. on p. 59).

[174] T. Mizushima, Y. Tsutsumi, T. Kawakami, M. Sato, M. Ichioka, and K. Machida, "Symmetry-Protected Topological Superfluids and Superconductors - From the Basics to 3He", J. Soc. Phys. Jpn. **85**, 022001 (2016) (cit. on p. 59).

[175] J. Wårdh and M. Granath, "Effective model for a supercurrent in a pair-density wave", Phys. Rev. B **96**, 224503 (2017) (cit. on p. 63).

[176] J. Wårdh, B. M. Andersen, and M. Granath, "Suppression of superfluid stiffness near a Lifshitz-point instability to finite-momentum superconductivity", Phys. Rev. B **98**, 224501 (2018) (cit. on p. 63).

[177] M. Barkman, A. Samoilenka, and E. Babaev, "Surface Pair-Density-Wave Superconducting and Superfluid States", Phys. Rev. Lett. **122**, 165302 (2019) (cit. on p. 63).

[178] A. Samoilenka, M. Barkman, A. Benfenati, and E. Babaev, "Superconductivity of surfaces, edges and vertices in systems with imbalanced fermions", (2019), arXiv:`1905.03774` (cit. on p. 63).

[179] M. Barkman, A. A. Zyuzin, and E. Babaev, "Antichiral and nematicity-wave superconductivity", Phys. Rev. B **99**, 220508 (2019) (cit. on p. 63).

[180] A. Benfenati, M. Barkman, T. Winyard, A. Wormald, M. Speight, and E. Babaev, “Magnetic signatures of domain walls in $s+is$ and $s+id$ superconductors: observability and what that can tell us about the superconducting order parameter”, (2019), arXiv:`1908.07969` (cit. on p. 63).

[181] T. N. Shendruk, K. Thijssen, J. M. Yeomans, and A. Doostmohammadi, “Twist-induced crossover from two-dimensional to three-dimensional turbulence in active nematics”, Phys. Rev. E **98**, 010601 (2018) (cit. on p. 63).

[182] D. S. Kim, S. Čopar, U. Tkalec, and D. K. Yoon, “Mosaics of topological defects in micropatterned liquid crystal textures”, Sci. Adv. **4** (2018) `10.1126/sciadv.aau8064` (cit. on p. 75).

[183] G. Babakhanova, T. Turiv, Y. Guo, M. Hendrikx, Q. Wei, A. P. Schenning, D. J. Broer, and O. D. Lavrentovich, “Liquid crystal elastomer coatings with programmed response of surface profile”, Nat. Commun. **9**, 456 (2018) (cit. on pp. 75, 80).

[184] P. Salamon, N. Éber, Y. Sasaki, H. Orihara, A. Buka, and F. Araoka, “Tunable Optical Vortices Generated by Self-Assembled Defect Structures in Nematics”, Phys. Rev. Applied **10**, 044008 (2018) (cit. on p. 75).

[185] L. K. Migara, H. Lee, C.-M. Lee, K. Kwak, D. Lee, and J.-K. Song, “External pressure induced liquid crystal defects for optical vortex generation”, AIP Adv. **8**, 065219 (2018) (cit. on p. 75).

[186] L. Migara, C.-M. Lee, K. Kwak, H. Lee, and J.-K. Song, “Tunable optical vortex arrays using spontaneous periodic pattern formation in nematic liquid crystal cells”, Curr. Appl. Phys. **18**, 819 –823 (2018) (cit. on p. 75).

[187] L. K. Migara and J.-K. Song, “Standing wave-mediated molecular reorientation and spontaneous formation of tunable, concentric defect arrays in liquid crystal cells”, NPG Asia Mater. **10** (2018) (cit. on p. 75).

[188] R. Amano, P. Salamon, S. Yokokawa, F. Kobayashi, Y. Sasaki, S. Fujii, Á. Buka, F. Araoka, and H. Orihara, “Tunable two-dimensional polarization grating using a self-organized micropixelated liquid crystal structure”, RSC Adv. **8**, 41472–41479 (2018) (cit. on p. 75).

[189] R. You, Y.-S. Choi, M. J. Shin, M.-K. Seo, and D. K. Yoon, “Reconfigurable Periodic Liquid Crystal Defect Array via Modulation of Electric Field”, Adv. Mater. Technol. **0**, 1900454 (2019) (cit. on p. 75).

[190] D. F. Agterberg, J. C. S. Davis, S. D. Edkins, E. Fradkin, D. J. V. Harlingen, S. A. Kivelson, P. A. Lee, L. Radzihovsky, J. M. Tranquada, and Y. Wang, *The Physics of Pair Density Waves*, 2019, arXiv:`1904.09687 [cond-mat.supr-con]` (cit. on p. 79).

[191] Z. Diao, D. Campanini, L. Fang, W.-K. Kwok, U. Welp, and A. Rydh, "Microscopic parameters from high-resolution specific heat measurements on superoptimally substituted $BaFe_2(As_{1-x}P_x)_2$ single crystals", Phys. Rev. B **93**, 014509 (2016) (cit. on pp. 79, 101).

[192] K. Willa, Z. Diao, D. Campanini, U. Welp, R. Divan, M. Hudl, Z. Islam, W.-K. Kwok, and A. Rydh, "Nanocalorimeter platform for in situ specific heat measurements and x-ray diffraction at low temperature", Rev. Sci. Instrum. **88**, 125108 (2017) (cit. on p. 79).

[193] D. Rugar, R. Budakian, H. Mamin, and B. Chui, "Single spin detection by magnetic resonance force microscopy", Nature **430**, 329–332 (2004) (cit. on p. 79).

[194] T. Nishio, T. An, A. Nomura, K. Miyachi, T. Eguchi, H. Sakata, S. Lin, N. Hayashi, N. Nakai, M. Machida, and Y. Hasegawa, "Superconducting Pb Island Nanostructures Studied by Scanning Tunneling Microscopy and Spectroscopy", Phys. Rev. Lett. **101**, 167001 (2008) (cit. on p. 79).

[195] T. Cren, L. Serrier-Garcia, F. Debontridder, and D. Roditchev, "Vortex Fusion and Giant Vortex States in Confined Superconducting Condensates", Phys. Rev. Lett. **107**, 097202 (2011) (cit. on p. 79).

[196] D. Vasyukov, Y. Anahory, L. Embon, D. Halbertal, J. Cuppens, L. Neeman, A. Finkler, Y. Segev, Y. Myasoedov, M. L. Rappaport, M. E. Huber, and E. Zeldov, "A scanning superconducting quantum interference device with single electron spin sensitivity", Nat. Nanotechnol. **8**, 639–644 (2013) (cit. on p. 79).

[197] G. Széchenyi and A. Pályi, "Coulomb-blockade and Pauli-blockade magnetometry", Phys. Rev. B **95**, 035431 (2017) (cit. on p. 79).

[198] M. Pelliccione, A. Jenkins, P. Ovartchaiyapong, C. Reetz, E. Emmanouilidou, N. Ni, and A. C. Bleszynski Jayich, "Scanned probe imaging of nanoscale magnetism at cryogenic temperatures with a single-spin quantum sensor", Nat. Nanotechnol. **11**, 700–705 (2016) (cit. on p. 79).

[199] A. Ariyaratne, D. Bluvstein, B. A. Myers, and A. C. Jayich, "Nanoscale electrical conductivity imaging using a nitrogen-vacancy center in diamond", Nat. Commun. **9**, 2406 (2018) (cit. on p. 79).

[200] F. Casola, T. van der Sar, and A. Yacoby, "Probing condensed matter physics with magnetometry based on nitrogen-vacancy centres in diamond", Nat. Rev. Mater. **3**, 17088 (2018) (cit. on p. 79).

[201] M. I. Dolz, N. R. C. Bolecek, J. Puig, H. Pastoriza, G. Nieva, J. Guimpel, C. J. van der Beek, M. Konczykowski, and Y. Fasano, "Enhancement of penetration field in vortex matter in mesoscopic superconductors due to Andreev bound states", Phys. Rev. B **100**, 064508 (2019) (cit. on p. 80).

[202] R. Matsunaga, Y. I. Hamada, K. Makise, Y. Uzawa, H. Terai, Z. Wang, and R. Shimano, “Higgs Amplitude Mode in the BCS Superconductors $\mathrm{Nb}_{1-x}\mathrm{Ti}_x\mathbf{N}$ Induced by Terahertz Pulse Excitation”, Phys. Rev. Lett. **111**, 057002 (2013) (cit. on p. 80).

[203] V. J. Emery and S. A. Kivelson, “Importance of phase fluctuations in superconductors with small superfluid density”, Nature **374**, 434–437 (1995) (cit. on p. 80).

[204] M. Warner and E. M. Terentjev, *Liquid Crystal Elastomers* (Oxford University Press, 2003) (cit. on p. 80).

[205] D. Tanaka and Y. Kuramoto, “Complex Ginzburg-Landau equation with nonlocal coupling”, Phys. Rev. E **68**, 026219 (2003) (cit. on p. 80).

[206] P. C. Bressloff and Z. P. Kilpatrick, “Nonlocal Ginzburg-Landau equation for cortical pattern formation”, Phys. Rev. E **78**, 041916 (2008) (cit. on p. 80).

[207] V. García-Morales and K. Krischer, “Nonlocal Complex Ginzburg-Landau Equation for Electrochemical Systems”, Phys. Rev. Lett. **100**, 054101 (2008) (cit. on p. 80).

[208] D. Schroeder, *An Introduction to Thermal Physics* (Addison Wesley Longman, 2000) (cit. on p. 101).

[209] M. Sato, Y. Tanaka, K. Yada, and T. Yokoyama, “Topology of Andreev bound states with flat dispersion”, Phys. Rev. B **83**, 224511 (2011) (cit. on p. 119).

[210] Y. Tanaka and S. Kashiwaya, “Theory of Tunneling Spectroscopy of d-Wave Superconductors”, Phys. Rev. Lett. **74**, 3451 (1995) (cit. on p. 119).

[211] T. Tokuyasu, J. A. Sauls, and D. Rainer, “Proximity effect of a ferromagnetic insulator in contact with a superconductor”, Phys. Rev. B **38**, 8823–8833 (1988) (cit. on p. 121).

[212] M. Eschrig, T. Löfwander, T. Champel, J. C. Cuevas, J. Kopu, and G. Schön, “Symmetries of Pairing Correlations in Superconductor–Ferromagnet Nanostructures”, J. Low Temp. Phys. **147**, 457–476 (2007) (cit. on p. 121).

[213] M. Eschrig and T. Löfwander, “Triplet supercurrents in clean and disordered half-metallic ferromagnets”, Nat. Phys. **4**, 138–143 (2008), arXiv:`cond-mat/0612533 [cond-mat.supr-con]` (cit. on p. 121).

[214] M. Eschrig, “Spin-polarized supercurrents for spintronics”, Phys. Today **64**, 43 (2011) (cit. on p. 121).

[215] M. Eschrig, “Theory of Andreev bound states in S-F-S junctions and S-F proximity devices”, Philos. Trans. Royal Soc. A **376**, 20150149 (2018) (cit. on p. 121).

[216] M. Fogelström, “Josephson currents through spin-active interfaces”, Phys. Rev. B **62**, 11812–11819 (2000) (cit. on p. 121).

[217] E. Zhao, T. Löfwander, and J. A. Sauls, “Nonequilibrium superconductivity near spin-active interfaces”, Phys. Rev. B **70**, 134510 (2004) (cit. on p. 121).

Appended Papers

Paper I

Phase Crystals

P. Holmvall, M. Fogelström, and T. Löfwander
Department of Microtechnology and Nanoscience - MC2,
Chalmers University of Technology, SE-41296 Göteborg, Sweden

A. B. Vorontsov*
Department of Physics, Montana State University, Montana 59717, USA

(Dated: November 5, 2019)

Superconductivity owes its properties to the phase of the electron pair condensate that breaks the $U(1)$ symmetry. In the most traditional ground state, the phase is uniform and rigid. The normal state can be unstable towards special inhomogeneous superconducting states: the Abrikosov vortex state, and the Fulde-Ferrell-Larkin-Ovchinnikov state. Here we show that the phase-uniform superconducting state can go into a fundamentally different and more ordered non-uniform ground state, that we denote as a phase crystal. The new state breaks translational invariance through formation of a spatially periodic modulation of the phase, manifested by unusual superflow patterns and circulating currents, that also break time-reversal symmetry. We list the general conditions needed for realization of phase crystals. Using microscopic theory we then derive an analytic expression for the superfluid density tensor for the case of a non-uniform environment in a semi-infinite superconductor. We demonstrate how the surface quasiparticle states enter the superfluid density and identify phase crystallization as the main player in several previous numerical observations in unconventional superconductors, and predict existence of a similar phenomenon in superconductor-ferromagnetic structures. This analytic approach provides a new unifying aspect for the exploration of boundary-induced quasiparticles and collective excitations in superconductors. More generally, we trace the origin of phase crystallization to non-local properties of the gradient energy, which implies existence of similar pattern-forming instabilities in many other contexts.

I. INTRODUCTION

The defining characteristic of superfluidity and superconductivity is spontaneous symmetry breaking of the global $U(1)$ phase χ, associated with the order parameter $\Delta = |\Delta| \exp(i\chi)$. The phase, and its spatial variations, give rise to phenomena of importance for technological applications, such as type II superconductivity where Abrikosov vortices are formed in an external magnetic field, and in Josephson junctions.[1] Within the BCS paradigm,[2] a uniform fixed value of the phase is directly tied to the finite amplitude $|\Delta|$ of the macroscopic Cooper-pair wavefunction. If the phase is non-uniform, by Galilean invariance it results in superflow with superfluid velocity and momentum $m\mathbf{v}_s = \mathbf{p}_s(\mathbf{R}) = (\hbar/2)\boldsymbol{\nabla}\chi(\mathbf{R})$, where m is the electron mass and $\hbar$ is the reduced Planck constant. Such phase variations and the associated condensate currents cost gradient energy

$$F_{\mathrm{sf}} = \frac{1}{2}\int d\mathbf{R}\, k|\Delta|^2\, |\boldsymbol{\nabla}\chi(\mathbf{R})|^2\,, \qquad (1)$$

where the gradient energy coefficient $k > 0$ should be computed from microscopic theory. A physical picture emerges where the phase is rigid, coherent over macroscopic distances, and the superconducting state is stable. Thus, it would be surprising if there existed a more ordered state with a softer phase and spontaneous superflow with energy gain $F_{\mathrm{sf}} < 0$.

Here, we propose that under certain conditions there exists a low-temperature superconducting state where the rigid phase acquires structure by breaking translational invariance. In this state, that we denote a phase crystalline state, a periodic pattern with wavevector $\mathbf{q}$ is formed

$$\chi(\mathbf{R}) = C_{\mathbf{q}}\, A_{\mathbf{q}}(\mathbf{R}_\perp)\, \cos(\mathbf{q}\cdot\mathbf{R}), \qquad (2)$$

where $A_{\mathbf{q}}(\mathbf{R}_\perp)$ is a function of coordinates orthogonal to $\mathbf{q}$. The additional order parameter in the phase crystal is the finite Fourier amplitude $C_{\mathbf{q}}$. The superconducting ground state with spatially oscillating phase also breaks time-reversal symmetry and sustains a non-trivial periodic superflow pattern and circulating currents $\mathbf{j}(\mathbf{R})$, as illustrated in Fig. 1**a**. Similar current patterns have been found in numerical work on mesoscopic grains of d-wave superconductors,[3] and the unusual superflow field $\mathbf{p}_s(\mathbf{R})$ was recently analyzed.[4] Here we establish that the physical origin of this surface state is phase crystallization.

Breaking of continuous translational symmetry is particularly striking. Its reduction to discrete translations gives a multitude of crystals[5] and ultimately quasicrystals where translational symmetry is absent.[6–8] Crystal analogues in the time dimension[9,10] have been recently observed.[11,12] Emergent multi-particle crystalline structures are predicted to appear in frustrated magnetic materials,[13] and have been engineered in ultracold atoms interacting with light.[14] Superconducting states with periodically modulated amplitude $\Delta(\mathbf{R}) \propto \Delta_{\mathbf{q}}\cos(\mathbf{q}\cdot\mathbf{R})$ were first proposed to exist in ferromagnetic metals,[15] and are currently investigated in a variety of systems ranging from cold Fermi-gases with spin imbalance[16,17] to color superconductivity.[18]

Several features make the phase crystal a distinctly different ground state from other non-uniform superconducting states. The amplitude-modulated state and its

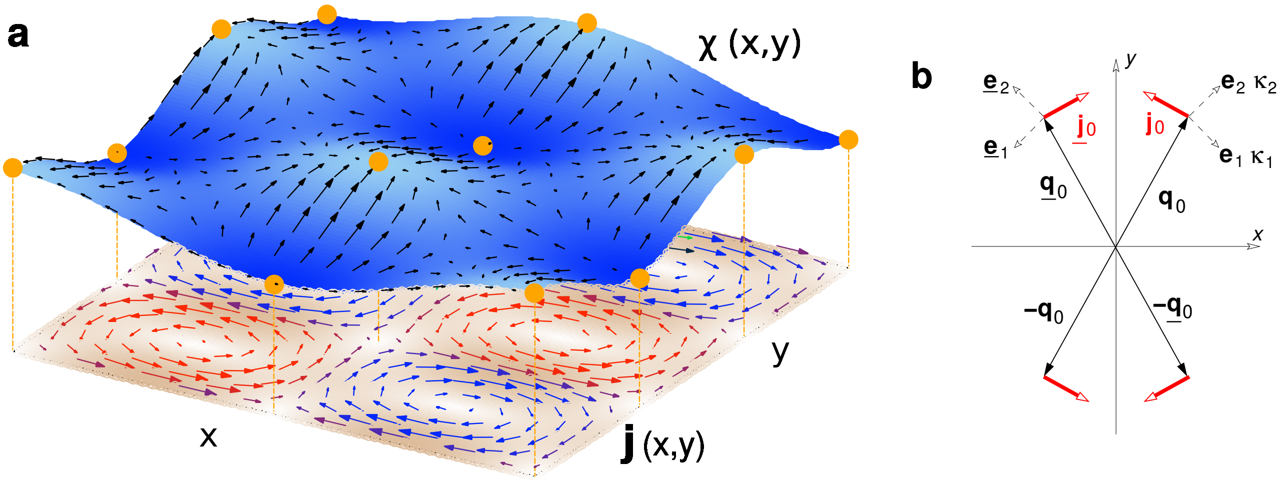

FIG. 1. **a**, The phase crystal has a periodic modulation of the superconducting phase $\chi(\mathbf{R})$ and a superflow $\mathbf{p}_s(\mathbf{R})$ that forms a special vector field with a lattice of sources and sinks (filled circles), while the particle-conserving current $\mathbf{j}(\mathbf{R})$ forms a checkerboard pattern with opposite circulation flow. **b**, This phase modulation is a result of four degenerate instability vectors $\{\pm\mathbf{q}_0, \pm\underline{\mathbf{q}}_0\}$ with non-zero currents orthogonal to them, see Eq. (6).

single-mode[19] counterpart $\Delta(\mathbf{R}) \propto \Delta_{\mathbf{q}} e^{i\mathbf{q}\cdot\mathbf{R}}$, are both *amplitude* instabilities of the normal metal occurring at finite $\mathbf{q}$, and they do not carry currents. The phase crystal, on the other hand, is associated with a modification of the symmetry variable χ describing the degeneracy manifold of the superconducting state, and can occur even when the order parameter amplitude $|\Delta|$ is large, i.e. deep inside the superconducting state far from the normal to superconductor transition; the phase crystal does maintain non-trivial particle currents. Moreover, it is also different from the textures appearing in systems with multi-component order parameters and a more complex degeneracy space, such as ^{3}He and liquid crystals.[20–22] In those systems the long-wavelength textures are a result of a competition between condensation and gradient terms involving different combinations of the order parameter components. The phase crystal is a result of a highly non-local superfluid response when sample surfaces, geometry, or other external influences, impose a certain structure on the superfluid kernel itself. The patterns are formed on the much shorter coherence length scale $\xi_0 = \hbar v_{\rm F}/2\pi k_{\rm B} T_{\rm c}$, where $v_{\rm F}$ is the Fermi velocity, $T_{\rm c}$ is the superconducting transition temperature and $k_{\rm B}$ is the Boltzmann constant ($\hbar = k_{\rm B} = 1$ in the following). To describe this physics we ignore the amplitude gradient terms in the free energy and generalize the kinetic superflow energy in the limit of small $\mathbf{p}_s$ as

$$F_{\rm sf}[\boldsymbol{\nabla}\chi] = \frac{1}{2}\iint d\mathbf{R}d\mathbf{R}'\ \nabla_i\chi(\mathbf{R})K_{ij}(\mathbf{R},\mathbf{R}')\nabla_j\chi(\mathbf{R}')\,, \tag{3}$$

where we introduce a non-local superfluid density kernel $K_{ij}(\mathbf{R},\mathbf{R}') = K_{ji}(\mathbf{R}',\mathbf{R})$. Summation over repeating spatial indices is assumed. Higher order gradient terms in $F_{\rm sf}$ would determine the magnitude of spontaneous currents at temperatures below the transition temperature. Here we neglect those and focus on the instability analysis.[23] The energy change due to a small Galilean boost $\mathbf{u}$, $F_{\rm sf}[\mathbf{v}_s - \mathbf{u}] = F_{\rm sf}[\mathbf{v}_s] - m\mathbf{j}\cdot\mathbf{u}$, defines the particle current

$$j_i(\mathbf{R}) = \frac{\delta F_{\rm sf}[\mathbf{v}_s]}{\delta p_{s,i}(\mathbf{R})} = \int d\mathbf{R}' K_{ij}(\mathbf{R},\mathbf{R}')\nabla_j\chi(\mathbf{R}')\,. \tag{4}$$

The physical χ and $\mathbf{j}$ are obtained by variational minimization of the free energy with respect to the phase. It gives the continuity equation, $-\delta F_{\rm sf}[\boldsymbol{\nabla}\chi]/\delta\chi(\mathbf{R}) = \boldsymbol{\nabla}\cdot\mathbf{j}(\mathbf{R}) = 0$.

II. PHASE INSTABILITY IN THE BULK

By using the non-local Ginzburg-Landau expression in Eq. (3) one can specify the general criteria when a non-trivial pattern of currents can emerge from the state with homogeneous phase $\chi_0 = 0$. In a translationally-invariant infinite system the superfluid free energy with kernel $\hat{K}(\mathbf{R}-\mathbf{R}')$ has the following form in Fourier space

$$F_{\rm sf} = \frac{1}{2}\int \frac{d^2q}{(2\pi)^2}\,\chi(-\mathbf{q})\,\left[\mathbf{q}^T\hat{K}(\mathbf{q})\,\mathbf{q}\right]\,\chi(\mathbf{q})\,. \tag{5}$$

For the two-dimensional case, the kernel is a two-by-two Hermitian matrix $\hat{K}(\mathbf{q}) = \hat{K}^\dagger(\mathbf{q})$ with real eigenvalues $\kappa_{1,2}$ and corresponding eigenvectors $\mathbf{e}_{1,2}$. Their values depend on temperature and $\mathbf{q}$. The instability at a particular wavevector $\mathbf{q}_0$ can happen when $\mathbf{q}_0^T\hat{K}(\mathbf{q}_0)\mathbf{q}_0 = \kappa_1[\mathbf{e}_1\cdot\mathbf{q}_0]^2 + \kappa_2[\mathbf{e}_2\cdot\mathbf{q}_0]^2 = 0$. This equality can be satisfied if the eigenvalues have opposite signs and are tunable by temperature, or more generally by some other parameter. To linear order in $\chi(\mathbf{q})$, the Fourier component of the current is $\mathbf{j} = \mathbf{j}_0\, i\,\chi(\mathbf{q}_0)$, where $i = \sqrt{-1}$ and

$\mathbf{j}_0 = \hat{K}(\mathbf{q}_0)\mathbf{q}_0 = \mathbf{e}_1\kappa_1[\mathbf{e}_1\cdot\mathbf{q}_0]+\mathbf{e}_2\kappa_2[\mathbf{e}_2\cdot\mathbf{q}_0]$. For a non-zero current to appear at the $\mathbf{q}_0 \neq 0$ transition, it must also satisfy the conservation law $\boldsymbol{\nabla}\cdot\mathbf{j} \propto \mathbf{q}_0\cdot\mathbf{j} = 0$. This implies an orthogonality constraint $\mathbf{q}_0 \perp \mathbf{j}_0$, which is possible to fulfill if the eigenvectors $\mathbf{e}_{1,2}$ are not collinear with $\mathbf{q}_0$, see Fig. 1**b**. In this case we can write $\mathbf{j}_0 = \hat{\mathbf{x}}j_{0x} + \hat{\mathbf{y}}j_{0y}$ with $j_{0x}/j_{0y} = -q_{0y}/q_{0x}$. Since the phase $\chi(\mathbf{R})$ is real, the same conditions must be satisfied for $-\mathbf{q}_0$, which requires inversion symmetry. With two instability vectors $\mathbf{q}_0$ and $-\mathbf{q}_0$ we get an emerging phase $\chi(\mathbf{R}) = C\cos(\mathbf{q}_0\cdot\mathbf{R})$ with stripes of current $\mathbf{j}(\mathbf{R}) = C\mathbf{j}_0\sin(\mathbf{q}_0\cdot\mathbf{R})$ running perpendicular to $\mathbf{q}_0$. Additional symmetries allow for other instability vectors. For example, reflection symmetry $x \to -x$ guarantees another pair of instability vectors, $\underline{\mathbf{q}}_0$ and $-\underline{\mathbf{q}}_0$, with $\underline{q}_{0x} = -q_{0x}$. Diagonalization of the kernel at $\underline{\mathbf{q}}_0$ gives the same eigenvalues $\kappa_{1,2}$ as those at $\mathbf{q}_0$, while the eigenvectors $\underline{\mathbf{e}}_{1,2}$ are obtained from $\mathbf{e}_{1,2}$ by flipping the x-components, and the current amplitude is $\underline{\mathbf{j}}_0 = \underline{\mathbf{e}}_1\kappa_1[\underline{\mathbf{e}}_1\cdot\underline{\mathbf{q}}_0]+\underline{\mathbf{e}}_2\kappa_2[\underline{\mathbf{e}}_2\cdot\underline{\mathbf{q}}_0]$. In the four-harmonics state the phase and current are given by

$$\begin{aligned}\chi(\mathbf{R}) &= \cos(\mathbf{q}_0\cdot\mathbf{R}) + \cos(\underline{\mathbf{q}}_0\cdot\mathbf{R}) \propto \cos(q_{0x}x)\cos(q_{0y}y),\\ \mathbf{j}(\mathbf{R}) &= \mathbf{j}_0\sin(\mathbf{q}_0\cdot\mathbf{R}) + \underline{\mathbf{j}}_0\sin(\underline{\mathbf{q}}_0\cdot\mathbf{R})\\ &\propto \begin{pmatrix} j_{x0}\sin(q_{0x}x)\cos(q_{0y}y)\\ j_{0y}\cos(q_{0x}x)\sin(q_{0y}y)\end{pmatrix},\end{aligned} \tag{6}$$

as plotted in Fig.1**a**. Higher order terms $\mathcal{O}[(\boldsymbol{\nabla}\chi)^4]$ must be included to determine the energetics between two- and four-harmonics states. One notices that the loop currents in the phase crystal appear without phase winding and are not associated with topological defects. We conclude that realization of spontaneous periodic loop-currents requires a superfluid density tensor with

(i) spatial anisotropy,
(ii) positive and negative eigenvalues that can be tuned by some parameter,
(iii) eigenvectors $\mathbf{e}_{1,2} \nparallel \mathbf{q}_0$.

Conditions (i) and (ii) can be satisfied simultaneously for example in an anisotropic-gap superconductor with an applied Zeeman field. Condition (iii) requires a mismatch between the symmetry of the Fermi surface and the quasiparticle excitations in momentum space, and the symmetry of the current response tensor. To satisfy this last geometric condition, one would generally require a system with as lower spatial symmetry as possible. To formalize the analysis we can write a general Ginzburg-Landau expansion of the tensor $\hat{K}(\mathbf{q})$ in the superconducting state with orthorhombic symmetry C_{2v}. This symmetry is also required by condition (i) to have two eigenvectors of the kernel of different sign. The general form of the tensor is

$$\begin{aligned}K_{ij}(q_x,q_y) &= K^{(0)}_{ij} + K^{(2)}_{ijlm}q_lq_m + \cdots =\\ &= \begin{pmatrix} a_0 + a_2q_x^2 + c_2q_y^2 & 2c_2q_xq_y\\ 2c_2q_xq_y & b_0 + b_2q_y^2 + c_2q_x^2\end{pmatrix}\end{aligned} \tag{7}$$

where finite components are $a_0 = K^{(0)}_{xx} \neq K^{(0)}_{yy} = b_0$, $K^{(2)}_{xxxx} = a_2$, $K^{(2)}_{yyyy} = b_2$, $K^{(2)}_{xxyy} = c_2$, and all permutation of indices allowed. The configuration space of these five coefficients is large enough to allow for a set of instability wavevector (q_x, q_y) that do not lie along the high symmetry directions, and thus do not coincide with direction of the current (j_x, j_y). Such configuration would not be possible in a state with square symmetry that has only three independent coefficients $a_0 = b_0$, $a_2 = b_2$ and c_2. The superfluid tensor will possess the C_{2v} symmetry in orthorhombic crystals, in nematically ordered systems, or in superconducting states with gap structure different along two principal axes, such as polar or planar states. The complete analysis of a crystallization transition with a short-wavelength modulations is quite complex, and has to include higher order $\mathbf{q}$-terms. We leave this for future studies. We note that in typical weak crystallization theories the instability vectors are only given at phenomenological level.[7,8] In the following we write down the microscopic theory for $\hat{K}$ near pair-breaking surfaces and show how all these conditions are naturally satisfied and why a preferred ordering vector emerges.

III. SURFACE PHASE CRYSTAL

Using microscopic quasiclassical theory, we derive the general expression for the superfluid density kernel. The technical details of the calculation are moved to Appendix A. We apply it first to the d-wave case and consider the s-wave case at the end of this section. The d-wave superconductor has an order parameter $\Delta(\mathbf{R},\mathbf{p}_{\mathrm{F}}) = \Delta_0(\mathbf{R})\,[2\hat{p}_x\hat{p}_y] \equiv \Delta_{\hat{p}}$, oriented as shown in Fig. 2**a**. The $\hat{p} = \mathbf{p}_{\mathrm{F}}/|\mathbf{p}_{\mathrm{F}}|$ is the unit vector pointing in the direction of momentum $\mathbf{p}_{\mathrm{F}}$ on the Fermi surface. The kernel between two points $\mathbf{R}$ and $\mathbf{R}'$ in a semi-infinite system has two contributions, $\hat{K}(\mathbf{R},\mathbf{R}') = \hat{K}^{\textcircled{1}}(\mathbf{R},\mathbf{R}') + \hat{K}^{\textcircled{2}}(\mathbf{R},\mathbf{R}')$, that correspond to propagation of quasiparticles along the direct path or with a reflection at the surface. We set a uniform amplitude $\Delta_0(\mathbf{R}) = \Delta_0$, which allows for analytic expressions, Appendix B. This assumption also demonstrates that the phase crystal is not caused by the suppression of the order parameter per se, but rather by the contribution from the symmetry-related surface Andreev bound states. The coordinate along a quasiparticle trajectory is denoted by s, with $s = 0$ at the reflection point. The kernel components are calculated in Appendix C, and for the direct path ($\hat{p}' = \hat{p}$) they are

$$\begin{aligned}K^{\textcircled{1}}_{ij}(\mathbf{R},\mathbf{R}') &= [\hat{p}_i\hat{p}_j]\; v_{\mathrm{F}}^2N_{\mathrm{F}}\; 4\pi T\sum_{\varepsilon_m>0}\frac{\Delta^2_{\hat{p}}}{\Omega^2}\frac{2}{v_{\mathrm{F}}}\,\frac{e^{-\kappa_u|\Delta s|}}{2\pi|\Delta s|}\\ &\times\left[\left(1-e^{-\kappa_u|s_<|}\right)^2 - \frac{\Omega^2}{\varepsilon_m^2}e^{-2\kappa_u|s_<|}\right],\end{aligned} \tag{8}$$

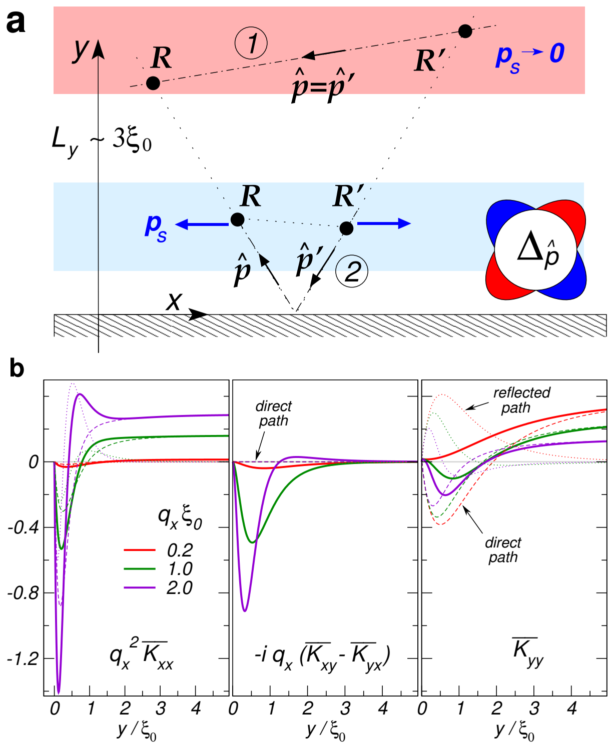

FIG. 2. **a**, Microscopic model of the superfluid density tensor near a pairbreaking surface of a d_{xy} superconductor. **b**, The averaged 'local' components, Eq. (11), as a function of distance to the surface y and the modulation vector q_x. The thinner dashed lines show direct path's contribution, dotted - reflected path. The superfluid density far from the surface is determined by correlations between two points, $\mathbf{R}$ and $\mathbf{R}'$, through the direct path. This leads to positive superflow energy from diagonal components, favoring a uniform phase $\mathbf{p}_s \propto \boldsymbol{\nabla}\chi_0 = 0$. Near the surface the superflow energy is lowered by negative contributions of K_{xx} and K_{yy} coming from Andreev bound states, favoring the non-uniform phase crystal $\boldsymbol{\nabla}\chi \neq 0$.

where $\varepsilon_m = \pi T(2m+1)$ are the Matsubara energies, $\kappa_u = 2\Omega/v_{\mathrm{F}}$ and $\Omega = \sqrt{\varepsilon_m^2 + \Delta_{\hat{p}}^2}$; also $\Delta s = s_{\mathbf{R}} - s_{\mathbf{R}'}$ is the trajectory distance between the two points, and $s_< = \min(y, y')/|\hat{p}_y|$ is the trajectory coordinate of the point, $\mathbf{R}$ or $\mathbf{R}'$, closest to the surface. For the reflection path $(\hat{p}' = \underline{\hat{p}} = \hat{p} - 2\hat{y}(\hat{y}\cdot\hat{p}))$

$$K_{ij}^{\textcircled{2}}(\mathbf{R},\mathbf{R}') = -\left[\hat{p}_i \underline{\hat{p}}_j\right] v_{\mathrm{F}}^2 N_{\mathrm{F}}\, 4\pi T \sum_{\varepsilon_m>0} \frac{\Delta_{\hat{p}}^2}{\varepsilon_m^2}\, \frac{2}{v_{\mathrm{F}}}\, \frac{e^{-\kappa_u|\Delta s|}}{2\pi|\Delta s|}, \tag{9}$$

where the overall minus sign is due to the fact that at the integration and observation points the order parameter has opposite signs $\Delta_{\underline{\hat{p}}} = -\Delta_{\hat{p}}$. This reflection involving the sign-change of the order parameter also leads to the zero-energy Andreev surface states.[24] The characteristic bound states term, proportional to $\Delta_{\hat{p}}^2/\varepsilon_m^2$, gives an overall $1/T$ temperature dependence of the kernel. The direct kernel in Eq. (8) may also show this $1/T$ dependence near the surface when the second term inside the square brackets dominates.

Pattern-forming instabilities are notorious for being technically challenging to analyze even at the level of linearised equations.[25] In what follows we work directly with the integral representation of the non-local physics. Since the unperturbed superconducting state is translationally invariant along the surface, we have $\hat{K}(\mathbf{R},\mathbf{R}') = \hat{K}(x_1 - x_2, y_1, 0, y_2)$, and we may write the superflow free energy in terms of Fourier components of the phase, $\chi(x,y) = C_{q_x}\chi(y)e^{+iq_x x}$, assuming the $\chi(y)$-profile to be real. We get

$$\begin{aligned} F_{\mathrm{sf}} =& \frac{1}{2}\int \frac{dq_x}{(2\pi)}|C_{q_x}|^2 \int_0^\infty dy_1 \int_0^\infty dy_2 \times \\ & \Big[q_x^2 K_{xx}\, \chi(y_1)\chi(y_2) + K_{yy}\, \chi'(y_1)\, \chi'(y_2) \\ & - iq_x K_{xy}\, \chi(y_1)\, \chi'(y_2) + iq_x K_{yx}\, \chi'(y_1)\, \chi(y_2) \Big], \end{aligned} \tag{10}$$

where the prime denotes a derivative with respect to the y-coordinate. The kernel is a complicated function of several variables $K_{ij} = K_{ij}(q_x, y_1, y_2; T)$. To describe its most important features we use a center coordinate representation $y = (y_1 + y_2)/2$, and integrate over the relative coordinate $\bar{y} = y_1 - y_2$,

$$\overline{K}_{ij}(q_x, y; T) = \int_{-2y}^{2y} d\bar{y}\, K_{ij}\left(q_x, y + \frac{1}{2}\bar{y}, y - \frac{1}{2}\bar{y}; T\right). \tag{11}$$

This averaged response is shown in Fig. 2**b** as function of distance from the surface y, where we also include the q_x multiplication factors to directly relate the kernel to the free energy. For $y \gtrsim L_y \approx 3 \div 5\xi_0$, the response is dominated by the direct path. The off-diagonal components are zero and K_{xx} and K_{yy} are positive. Near the surface the diagonal components become negative, causing the instability, and large off-diagonal components appear. All components have the $1/T$ low-temperature dependence near the surface. The sign-changing nature of K_{ij}, and its T-dependence, lead to fulfilment of conditions (i) and (ii) for the phase crystal near the surface. Moreover, exponential decay of the bound states into the bulk creates an asymmetric environment at the surface with multiple q_{0y} components contributing to the instability. Condition (iii) is thereby also satisfied.

We perform a variational analysis of Eq. (10) with an ansatz for the y-dependence of the phase decaying into the bulk on the scale of y_0,

$$\chi(y) = \left(1 + \frac{y}{y_0}\right) e^{-\frac{y}{y_0}}, \quad \chi'(y) = -\frac{y}{y_0^2} e^{-\frac{y}{y_0}}. \tag{12}$$

This choice is guided by considerations that there should be no currents deep in the sample, and we look for a

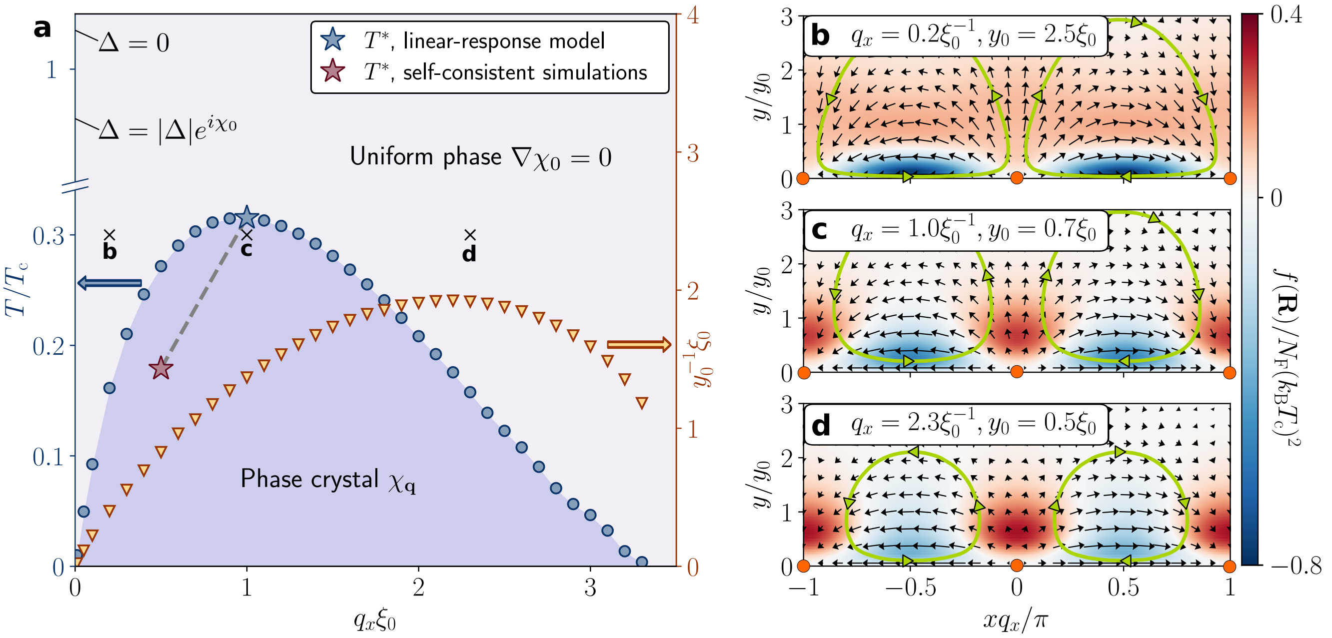

FIG. 3. **a**, The $U(1)$ phase of the superconducting order parameter acquires periodic modulation below $T^*(q_x)$ simultaneously breaking translational and time-reversal invariance of the d-wave superconducting state. The highest-T^* instability occurs at finite q_x, marked by the blue star. The red star denotes the transition observed in a numerical self-consistent calculation:[3] the lower T^* is a result of the reduced spectral weight of zero-energy states due to order parameter suppression. In **b**-**d** we show the geometrical structure of the superflow $\mathbf{p}_\mathrm{s}$ (black vector field) and current streamlines (green loops) corresponding to physical solutions. The background colors indicate distribution of gradient energy gain and loss in the system. At the optimal transition **c** the overall energy is close to zero. Increasing the pattern period, as in **b**, leads to larger y_0 and deeper extension of currents into the bulk with bigger contributions from costly bulk gradient energies. Making the pattern more compact, as in **d**, increases the energy close to the surface. In both **b** and **d** cases the loss in energy can only be compensated by lowering the temperature and thereby enhancing the negative bound states contribution through their $1/T$ dependence.

state with no superflow in the y-direction at the surface. The latter condition is not a strict requirement, since the physical condition of no current across the boundary $j_y(y=0)=0$ is fulfilled automatically by the form of the total kernel $\hat{K}(\mathbf{R},\mathbf{R}')$. This guess gives a good semi-quantitative result, but we note that to get the exact profile of $\chi(y)$ one has to perform a more sophisticated eigenvector analysis of the free energy Eq. (10). For each wave vector q_x and temperature T we scan the variational parameter y_0 and find the minimum of the free energy. This minimum corresponds to the physical solution with currents satisfying $\boldsymbol{\nabla}\cdot\mathbf{j}=0$. The instability into the modulated-phase state with a non-zero C_{q_x} occurs at a temperature where the minimum of F_sf crosses into negative values. The transition temperature $T^*(q_x)$ and the corresponding $y_0(q_x)$ are shown in Fig. 3**a**, for the d-wave case. The highest transition temperature $T^*\sim 0.3T_c$ occurs at finite modulation $q_x^*\approx\xi_0^{-1}$. By $x\to -x$ reflection symmetry there is degeneracy $(q_x,-q_x)$ that in the emerging state gives a real-valued phase and superflow

$$\chi(x,y)\propto -\left(1+\frac{y}{y_0}\right)e^{-y/y_0}\,\cos q_x x\,,$$
$$\mathbf{p}_s(x,y)\propto\left[q_x\left(1+\frac{y}{y_0}\right)\sin q_x x,\ \frac{y}{y_0^2}\cos q_x x\right]e^{-y/y_0},\tag{13}$$

with the superflow exhibiting critical points $\mathbf{p}_s=0$ at the surface, as marked in Figs. 3**b**-**d** by filled orange circles.

In the vicinity of the optimal transition, the instability temperature behaves as

$$T^*(q_x)=T^*-\beta(q_x-q_x^*)^2\,.\tag{14}$$

Such dependence is a characteristic ansatz in theories of weak crystallization,[7] where all the parameters are taken as phenomenological. We find $T^*\approx 0.3T_c$, $q_x^*\approx 1.0/\xi_0$ and $\beta\approx 0.15T_c\xi_0^2$. Here the appearance of a preferred finite phase modulation vector q_x^* is the result of an interplay between terms in the free energy Eq. (10) that in general have different dependence on the y-coordinates, T and q_x. This physics can be crudely visualized by considering the superfluid free energy density, as shown in Fig. 3**b**-**d**.[27] The key element is the dependence of the

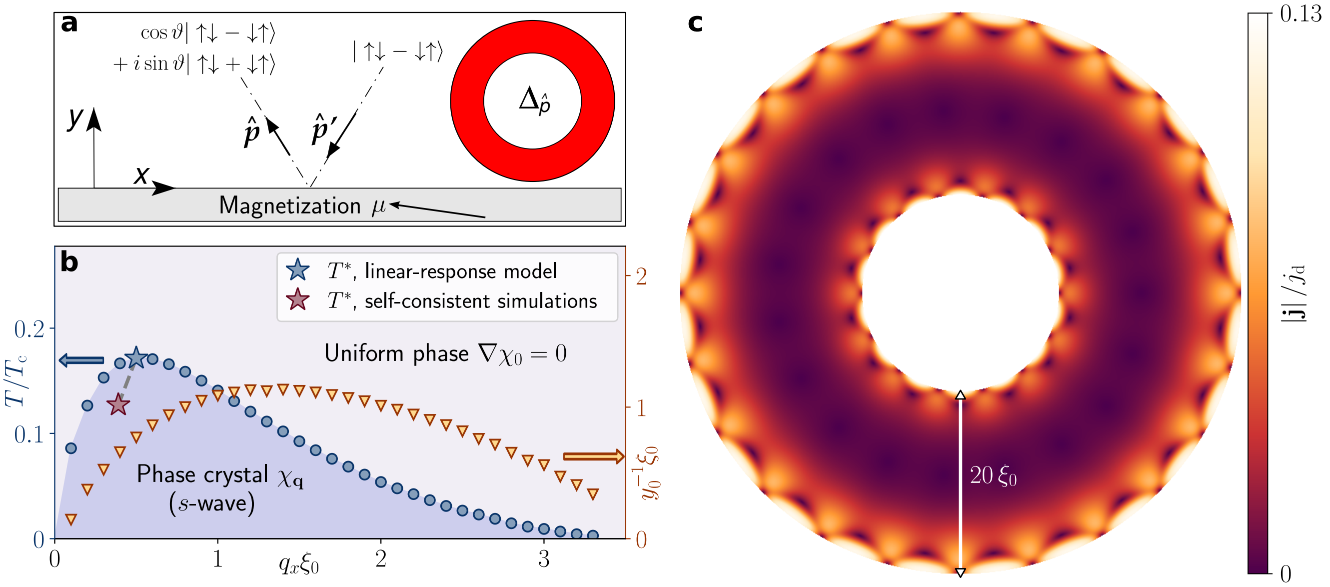

FIG. 4. **a**, The phase crystallization can happen in conventional s-wave superconductors with magnetically-active surfaces that mix singlet and triplet correlations.[26] The zero-energy bound states are a result of spin mixing scattering processes with spin-mixing angle $\vartheta = \pi$. **b**, The general form of the surface superfluid kernel remains the same as in the d-wave case, and as a result the phase diagram looks similar. **c**, The fully self-consistent numerical result for the currents. For magnetic scattering the orientation of the surface is not important, and spontaneous currents can appear in any geometry. For the 2D annulus shown here, the transition temperature is $T^*/T_c \approx 0.13$. Reduction of T^* compared with the d-wave case is traced to angular dependence of the order parameter.

phase decay length y_0 on q_x, see Fig. 3**a** where we plot the inverse $y_0^{-1}(q_x)$. The superfluid response amplitudes grow with increasing q_x. At the same time, the peaks in $q_x^2 K_{xx}$ and $q_x K_{xy,yx}$ move to smaller y, see Fig. 2**b**. This requires a smaller y_0 to control the current components to satisfy $\boldsymbol{\nabla}\cdot\mathbf{j} = 0$. Deviation of q_x from its optimal value to smaller q_x, compare Fig. 3**b** with Fig. 3**c**, leads to a longer extent away from the surface of the phase oscillations which increases the bulk energy cost from K_{xx} and K_{yy}. On the other hand, a deviation to larger q_x gives a small y_0 which results in a large cost due to off-diagonal $K_{xy,yx}$ components, compare Fig. 3**d** with Fig. 3**c**. The instability for non-optimal q_x occurs at a lower temperature, where the K_{xx}-component becomes more negative near the surface by virtue of its $1/T$ dependence, which compensates for the energy increase in the other terms.

From this analysis we may conclude that the non-local multi-component kernel leads to an intricate energy balance of the phase gradient terms in the free energy. Because of the kernel structure, that fulfills the criteria (i)-(iii), a non-trivial phase crystallization occurs at a particular $q_x^* \sim 1/\xi_0$. To this broad class of phase instabilities belong several previously described surface states with paramagnetic surface currents caused by spectral displacement of Andreev states.[28,29] That work assumed translational invariance of the superflow and currents along the surface, which guaranteed particle conservation $\boldsymbol{\nabla}\cdot\mathbf{j}(\mathbf{R}) = 0$, but as a result required additional mechanisms of reducing superflow in the bulk. In semi-infinite systems one relies on the Meissner effect to screen the bulk superflow on the penetration depth length scale λ, which leads to $T^* \sim (\xi_0/\lambda)T_c$.[30,31] In slabs of width $D < \lambda$ the bulk contribution is obviously limited, resulting in spontaneous superflow below $T^* \sim (\xi_0/D)T_c$.[32] In a similar fashion, we can interpret the phase crystal as self-screening of the loop currents over the surface region L_y leading to $T^* \sim (\xi_0/L_y)T_c$.

A similar transition can appear in other anisotropic superconductors with reduced point group symmetry of the order parameter, such as polar p-wave which may also host a flat band of zero-energy surface fermions. Interestingly, phase crystallization can happen in conventional s-wave superconductors, where orbital pairbreaking scattering is absent. In this case, magnetically active interfaces can provide the proper environment for the phase instability, for example in superconductor-ferromagnetic structures. Such systems are being considered as important building blocks for spintronics applications, where non-locality and quantum coherence will play important roles.[33] As described in Appendix C, a similar form of the superfluid density tensor appear for $\vartheta = \pi$ spin mixing angle. The phase diagram and the result of a self-consistent calculation are shown in Fig. 4.

The observable consequence of the spontaneous charge currents are magnetic fluxes near the surface. The associated reconstruction of the edge ground state is important from another perspective, since it can prevent realization of topological surface channels, as happens in topological insulators.[34,35] Moreover, softening of the surface superfluid density at some finite wavevector can result in special features of surface transport, even without a fully developed instability. This may be particularly relevant to transport in confined geometries.

Universal features of the pattern-formation phenomena in very different systems are manifested in the similarity of the phase diagram and the current patterns in Fig. 3 with those of the Rayleigh-Bénard convection instability, which is also a result of geometrical constraints and conservation laws. There, the control parameter, instead of T, is the inverse Rayleigh ratio of buoyancy force to dissipative forces.[36] We note that the convection roll currents in that case is due to an instability in a non-equilibrium driven system, while the phase crystal is a second-order phase transition into a new ground state.

IV. CONCLUSIONS

We have described a superconducting state where the global $U(1)$ phase spontaneously forms a modulation in space, breaking continuous translational invariance. The phase modulation results in a pattern of loop-currents and breaking of time-reversal symmetry. We have identified the general criteria (i)-(iii) that have to be met in order to get a non-local superfluid density tensor that favors phase crystallization. Using microscopic theory, we showed that the circulating currents can appear at pair breaking surfaces of d-wave superconductors. In that case, quasiparticle reflections off the surface play a double role: (a) they lead to a flat band of zero-energy Andreev bound states controlling signs of the superfluid components; and (b) they connect the y and x degrees of freedom at the level of the superfluid response resulting in preferred finite q_x-modulation of the superflow. From previous numerical studies we know that this state remains stable in external magnetic fields[4] and survives significant reduction of spectral weight of bound states.[37] Thus, one should expect that similar phenomena will arise in other condensates with zero-energy surface states. To demonstrate this, we have stabilized the phase crystal in a conventional s-wave superconductor in contact with a magnetically-active material, as can happen in hybrid superconductor-ferromagnet devices. One particularly interesting scenario, for the future, would be to generate this phase in a bulk system. The phase crystal presents an alternative vision of 'supersolids' where phase-coherent states also spontaneously break translational symmetry, only in the amplitude of the order parameter.[38–41] More generally, our results indicate that non-local effects in broken-symmetry states, especially with multi-component order parameters or competing orders, can lead to new states of matter. Such prospects are supported by early[42] and more recent[43] investigations of non-local physics in superconductors, as well as research into pattern formation due to long-range non-locality in biological systems.[44–46]

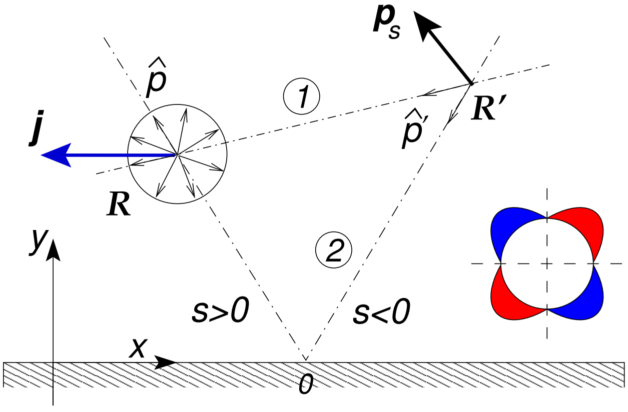

FIG. 5. The current at point $\mathbf{R}$ is determined by quasiparticles carrying information about the superflow field $\mathbf{p}_s$ in the entire space. Near the surface, quasiparticles from point $\mathbf{R}'$ can take two routes to get to point $\mathbf{R}$: directly ①, and through a reflection off the interface ②.

V. ACKNOWLEDGEMENTS

The computations were performed on resources at Chalmers Centre for Computational Science and Engineering (C3SE) provided by the Swedish National Infrastructure for Computing (SNIC). We thank the Swedish Research Council for financial support. P.H. acknowledges Chalmersska forskningsfonden for travel support.

Appendix A: Superfluid density near a surface

To find the superfluid response tensor we use a microscopic approach based on quasiclassical theory.[47] Our starting point is the Eilenberger equation for the quasiclassical propagator $\hat{g}$

$$[(i\varepsilon_m - \mathbf{v}_f\cdot\mathbf{p}_s)\hat{\tau}_3 - \hat{\Delta}(\mathbf{R},\mathbf{p}_{\mathrm{F}})\,,\,\hat{g}] + i\mathbf{v}_f\cdot\boldsymbol{\nabla}\hat{g} = 0 \tag{A1}$$

In this equation a spatially varying phase χ of the order parameter $\Delta = |\Delta|e^{i\chi(\mathbf{R})}$, was eliminated in favor of the superflow field $\mathbf{p}_s = \frac{1}{2}\boldsymbol{\nabla}\chi$. This can always be done, if needed, by a gauge transformation $\hat{g}\rightarrow\hat{U}\hat{g}\hat{U}^\dagger$ with $\hat{U} = e^{i\hat{\tau}_3\chi/2}$. The superflow is a function of position $\mathbf{p}_s = \mathbf{p}_s(\mathbf{R})$, and we consider a singlet mean-field order parameter $\Delta = \Delta(\mathbf{R},\mathbf{p}_{\mathrm{F}})$. The commutator-based Eilenberger equation is transformed into the Riccati-type equations for the coherence amplitudes[48]

$$\begin{aligned} i\mathbf{v}_{\mathrm{F}}\cdot\boldsymbol{\nabla}\gamma + 2[i\varepsilon_m - \mathbf{v}_{\mathrm{F}}\cdot\mathbf{p}_s]\gamma + \gamma\tilde{\Delta}\gamma + \Delta = 0, \\ i\mathbf{v}_{\mathrm{F}}\cdot\boldsymbol{\nabla}\tilde{\gamma} - 2[i\varepsilon_m - \mathbf{v}_{\mathrm{F}}\cdot\mathbf{p}_s]\tilde{\gamma} + \tilde{\gamma}\Delta\tilde{\gamma} + \tilde{\Delta} = 0. \end{aligned} \tag{A2}$$

These amplitudes conveniently parametrize the quasiclassical propagator,[49] and are functions of position, momentum, and energy, $\gamma = \gamma(\mathbf{R},\mathbf{p}_{\mathrm{F}};\varepsilon_m)$. The two coherence amplitudes are related by symmetry,

$$\tilde{\gamma}(\mathbf{R},\mathbf{p}_{\mathrm{F}};\varepsilon_m) = \gamma(\mathbf{R},-\mathbf{p}_{\mathrm{F}};\varepsilon_m)^*\,, \tag{A3}$$

that also applies to other tilde-related functions. For the singlet real order parameter $\tilde{\Delta}(\mathbf{R},\mathbf{p}_{\rm F}) \equiv \Delta^*(\mathbf{R},-\mathbf{p}_{\rm F}) = \Delta(\mathbf{R},\mathbf{p}_{\rm F})$. We look at the current response due to a small but arbitrary superflow field $\mathbf{p}_s = \mathbf{p}_s(\mathbf{R})$, starting from a current-less background state $\Delta_0(\mathbf{R},\mathbf{p}_{\rm F})$ and the corresponding coherence amplitudes $\gamma_0(\mathbf{R},\mathbf{p}_{\rm F};\varepsilon_m)$. The following linear response calculation is valid for any spatial profile of $\gamma_0(\mathbf{R},\mathbf{p}_{\rm F};\varepsilon_m)$, and we specify in the end its particular form. The current at a point $\mathbf{R}$ near the surface is calculated from the correction to the diagonal propagator δg, with $g = -i\pi{\rm sgn}(\varepsilon_m)\frac{1-\gamma\tilde{\gamma}}{1+\gamma\tilde{\gamma}}$, as

$$\mathbf{j}(\mathbf{R}) = 2T\sum_{\varepsilon_m>0} 2N_{\rm F}\,{\rm Re}\,\langle v_{\rm F}\hat{p}\;\delta g(\mathbf{R},\mathbf{p}_{\rm F};\varepsilon_m)\rangle_{\hat{p}}\,, \qquad \text{(A4)}$$

where $N_{\rm F}$ is density of states at the Fermi level per spin projection, and $\langle\ldots\rangle_{\hat{p}} = \int d\hat{p}/2\pi\,\ldots$ denotes a cylindrical Fermi surface average, Fig. 5. In terms of linearised coherence amplitudes $\gamma = \gamma_0 + \gamma_1$ the propagator change due to small superflow is

$$\delta g(\mathbf{R},\mathbf{p}_{\rm F};\varepsilon_m) = 2i\pi{\rm sgn}(\varepsilon_m)\frac{\gamma_1\tilde{\gamma}_0 + \gamma_0\tilde{\gamma}_1}{(1+\gamma_0\tilde{\gamma}_0)^2}. \qquad \text{(A5)}$$

We first neglect the effect of the superflow on the amplitude of the order parameter, assuming that $\Delta(\mathbf{R}) = \Delta_0(\mathbf{R})$ even in the current-carrying state, and linearise Eqs. (A2) to find transport equations for the function $\gamma_1/(1+\gamma_0\tilde{\gamma}_0)$,

$$\hat{p}\cdot\boldsymbol{\nabla}\frac{\gamma_1}{1+\gamma_0\tilde{\gamma}_0} + \kappa\frac{\gamma_1}{1+\gamma_0\tilde{\gamma}_0} = -2i\,\hat{p}\cdot\mathbf{p}_s\;\frac{\gamma_0}{1+\gamma_0\tilde{\gamma}_0}. \qquad \text{(A6)}$$

We get a similar equation for the tilde-analogue. The parameter

$$\kappa(\mathbf{R},\hat{p};\varepsilon_m) \equiv \frac{2}{v_{\rm F}}\left[\varepsilon_m + \frac{\gamma_0\tilde{\Delta}_0 - \tilde{\gamma}_0\Delta_0}{2i}\right] = \tilde{\kappa}\,, \qquad \text{(A7)}$$

determines the correlation length of the response. In a uniform state it reduces to $\kappa = 2v_{\rm F}^{-1}\sqrt{\Delta_{\hat{p}}^2 + \varepsilon_m^2} \sim 1/\xi_0$.

The solution of Eq. (A6) along a quasiclassical trajectory s is found, for positive ε_m, by integration forward along the trajectory starting from zero value in the bulk $\gamma_1(s=-\infty) = 0$, where there is no superflow. We get

$$\frac{\gamma_1}{1+\gamma_0\tilde{\gamma}_0}(\mathbf{R},\hat{p};\varepsilon_m) = -2i\int_{-\infty}^{s_{\mathbf{R}}} ds\;\exp\left(-\int_s^{s_{\mathbf{R}}}\kappa(\rho)d\rho\right) \times\,\hat{p}(s)\cdot\mathbf{p}_s(\mathbf{R}'(s))\;\frac{\gamma_0}{1+\gamma_0\tilde{\gamma}_0}(s). \qquad \text{(A8)}$$

To write the current at the observation point $\mathbf{R}$ we need to integrate over all trajectories coming into point $\mathbf{R}$. By introducing a correlation function connecting two points, $\mathbf{R}_1$ and $\mathbf{R}_2$, by a quasiclassical trajectory $\hat{\rho} = (\mathbf{R}_2 - \mathbf{R}_1)/|\mathbf{R}_2 - \mathbf{R}_1|$,

$$C(\mathbf{R}_2,\mathbf{R}_1) = \frac{1}{2\pi|\mathbf{R}_2 - \mathbf{R}_1|}\,\frac{2\varepsilon_m}{v_{\rm F}}\exp\left(-\int_{\mathbf{R}_1}^{\mathbf{R}_2}\kappa(\rho,\hat{\rho})d\rho\right), \qquad \text{(A9)}$$

one can combine the Fermi surface average at the observation point and integration along trajectories into integration over all space $\mathbf{R}'$, see Fig. 6, and write the current response as

$$j_i(\mathbf{R}) = \int d^2R'\;K_{ij}(\mathbf{R},\mathbf{R}')p_{s,j}(\mathbf{R}'). \qquad \text{(A10)}$$

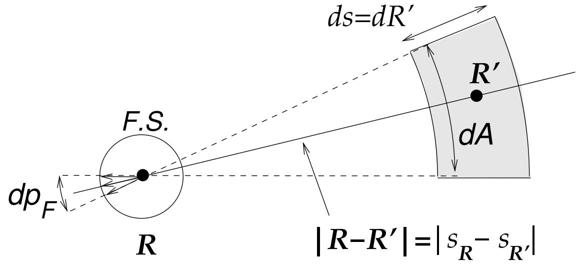

FIG. 6. The connection between spatial integral and the trajectory - Fermi surface integral. A volume element d^2R' in space can be written in cylindrical coordinates as $d^2R' = dA\,ds = |s_{\mathbf{R}} - s_{\mathbf{R}'}|d\mathbf{p}_{\rm F}\,ds$, where $|s_{\mathbf{R}} - s_{\mathbf{R}'}|$ is the distance between points $\mathbf{R}$ and $\mathbf{R}'$ along a trajectory, $d\mathbf{p}_{\rm F}$ is the angular integration over the Fermi surface.

Inserting (A8) into (A5) and using definition (A9), the superfluid kernel is then given by

$$\begin{aligned} K_{ij}(\mathbf{R},\mathbf{R}') = v_{\rm F}^2 N_{\rm F}\;8\pi T\sum_{\varepsilon_m>0}\sum_{\textcircled{1},\textcircled{2}}\frac{1}{4\pi^2\varepsilon_m}\times \\ \times{\rm Re}\Big[\hat{p}_i\tilde{f}_0(\mathbf{R},\hat{p})C(\mathbf{R},\mathbf{R}')f_0(\mathbf{R}',\hat{p}')\hat{p}'_j + \\ +\,\hat{p}'_j\tilde{f}_0(\mathbf{R}',-\hat{p}')C(\mathbf{R}',\mathbf{R})f_0(\mathbf{R},-\hat{p})\hat{p}_i\Big]\,, \end{aligned} \qquad \text{(A11)}$$

where f_0 and $\tilde{f}_0$ are off-diagonal propagators in the unperturbed state. In terms of coherence amplitudes $f_0 = -2i\pi\,{\rm sgn}(\varepsilon_m)\frac{\gamma_0}{1+\gamma_0\tilde{\gamma}_0}$. This kernel connects the observation point $\mathbf{R}$ to the integration point $\mathbf{R}'$. For each pair of points there are two paths, one direct ① and one involving reflection at the surface ②, where we assumed mirror-like reflection, see Fig. 5. The momentum direction $\hat{p}$ at the observation point is given by the trajectory direction $\mathbf{R}' \to \mathbf{R}$, and similarly for momentum at the integration point $\hat{p}'$ (Fig. 5). These directions are different for the direct and reflected paths.

Appendix B: Coherence amplitudes and propagators with a step-like order parameter

Neglecting the suppression of the order parameter at the surface allows us to proceed further analytically. The

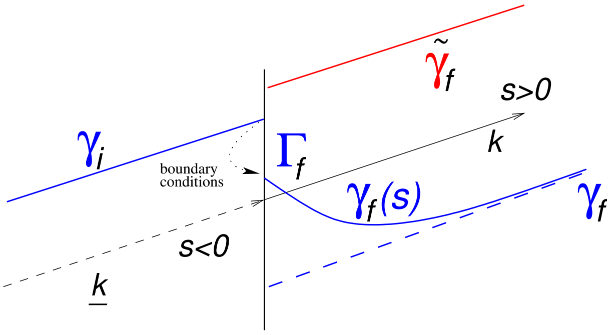

FIG. 7. The coherence amplitudes can be found analytically if we ignore suppression of the order parameter at the interface. For each trajectory the order parameter sharply changes between Δ_i and Δ_f at $s = 0$. In this case, γ_i on incoming trajectory is a constant, then a boundary condition $\gamma_i \to \Gamma_f$ gives initial value that evolves to γ_f on the outgoing part of trajectory. For typical non-magnetic specular scattering $\Gamma_f = \gamma_i$.

bulk uniform coherence amplitude is

$$\begin{aligned} \gamma &= i\frac{\Delta}{|\varepsilon_m| + \sqrt{\Delta^2 + \varepsilon_m^2}}\mathrm{sgn}(\varepsilon_m)\,, \\ \varepsilon_m - i\gamma\Delta &= \mathrm{sgn}(\varepsilon_m)\sqrt{\varepsilon_m^2 + \Delta^2} \end{aligned} \tag{B1}$$

Now consider, Fig. 7, a (straightened) trajectory that for $s < 0$ is in a region with the order parameter $\Delta_{\underline{k}} = \Delta_i$, and for $s > 0$ is in the region with $\Delta_k = \Delta_f$ (e.g. for the most pairbreaking surface $\Delta_i = -\Delta_f$). Denote

$$\begin{aligned} \Omega_i &= \sqrt{\Delta_i^2 + \varepsilon_m^2}\,, \quad \kappa_{u,i} = \frac{2}{v_f}\sqrt{\Delta_i^2 + \varepsilon_m^2}\,, \\ \Omega_f &= \sqrt{\Delta_f^2 + \varepsilon_m^2}\,, \quad \kappa_{u,f} = \frac{2}{v_f}\sqrt{\Delta_f^2 + \varepsilon_m^2}\,. \end{aligned} \tag{B2}$$

Far away from the interface, the coherence amplitudes have their uniform bulk values (we assume $\varepsilon_m > 0$, otherwise understand $\varepsilon_m = |\varepsilon_m|$ and add $\mathrm{sgn}(\varepsilon_m)$ in front)

$$\begin{aligned} \gamma_i &= i\frac{\Delta_i}{\varepsilon_m + \Omega_i}\,, \qquad \gamma_f = i\frac{\Delta_f}{\varepsilon_m + \Omega_f}\,, \\ \tilde{\gamma}_i &= -i\frac{\tilde{\Delta}_i}{\varepsilon_m + \Omega_i}\,, \qquad \tilde{\gamma}_f = -i\frac{\tilde{\Delta}_f}{\varepsilon_m + \Omega_f} \end{aligned} \tag{B3}$$

For a sudden-step order parameter the amplitudes $\gamma_0, \tilde{\gamma}_0(s)$ can be found analytically, integrating Riccati equations (A2) in forward or backward direction, correspondingly. Including the sudden jump of the amplitudes at the surface according to the boundary condition, we get

$$\begin{aligned} &\gamma_0(s<0) = \gamma_i \quad \to \quad \gamma_0(s=+0) = \Gamma_f \qquad \longrightarrow \\ &\gamma_0(s>0) = \gamma_f + \frac{(1+\gamma_f\tilde{\gamma}_f)(\Gamma_f - \gamma_f)e^{-\kappa_{u,f}s}}{1 + \gamma_f\tilde{\gamma}_f + (\Gamma_f - \gamma_f)\tilde{\gamma}_f(1 - e^{-\kappa_{u,f}s})} \end{aligned} \tag{B4}$$

and for tilde-function integrating backward:

$$\begin{aligned} &\tilde{\gamma}_0(s>0) = \tilde{\gamma}_f \quad \to \quad \tilde{\gamma}_0(s=-0) = \tilde{\Gamma}_i \qquad \longrightarrow \\ &\tilde{\gamma}_0(s<0) = \tilde{\gamma}_i + \frac{(1+\gamma_i\tilde{\gamma}_i)(\tilde{\Gamma}_i - \tilde{\gamma}_i)e^{\kappa_{u,i}s}}{1 + \gamma_i\tilde{\gamma}_i + \gamma_i(\tilde{\Gamma}_i - \tilde{\gamma}_i)(1 - e^{\kappa_{u,i}s})} \end{aligned} \tag{B5}$$

The propagators on the trajectory are (e.g. for $s > 0$)

$$g_0(s>0) = -i\pi\frac{1 - \gamma_f(s)\tilde{\gamma}_f}{1 + \gamma_f(s)\tilde{\gamma}_f} = -i\pi\left[\frac{1 - \gamma_f\tilde{\gamma}_f}{1 + \gamma_f\tilde{\gamma}_f}\left(1 - e^{-\kappa_{u,f}s}\right) + \frac{1 - \Gamma_f\tilde{\gamma}_f}{1 + \Gamma_f\tilde{\gamma}_f}e^{-\kappa_{u,f}s}\right] \tag{B6}$$

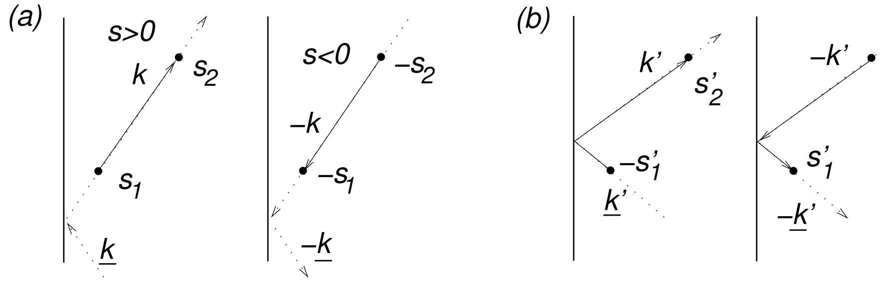

FIG. 8. The correlation functions that connect the integration point and the observation point along trajectories of type ① (a) and type ② (b).

and the off-diagonal component that enters the expression for the current response is

$$\begin{aligned}
\frac{f_0(s>0)}{-2i\pi} &= \frac{\gamma_f(s)}{1+\gamma_f(s)\tilde{\gamma}_f} = \frac{\gamma_f}{1+\gamma_f\tilde{\gamma}_f}\left(1-e^{-\kappa_{u,f}s}\right) + \frac{\Gamma_f}{1+\Gamma_f\tilde{\gamma}_f}e^{-\kappa_{u,f}s} \\
\frac{\tilde{f}_0(s>0)}{2i\pi} &= \frac{\tilde{\gamma}_f}{1+\gamma_f(s)\tilde{\gamma}_f} = \frac{\tilde{\gamma}_f}{1+\gamma_f\tilde{\gamma}_f}\left(1-e^{-\kappa_{u,f}s}\right) + \frac{\tilde{\gamma}_f}{1+\Gamma_f\tilde{\gamma}_f}e^{-\kappa_{u,f}s} \\
&= \frac{\tilde{\gamma}_f[1+\Gamma_f\tilde{\gamma}_f-(\Gamma_f-\gamma_f)\tilde{\gamma}_f e^{-\kappa_{u,f}s}]}{(1+\gamma_f\tilde{\gamma}_f)(1+\Gamma_f\tilde{\gamma}_f)} \\
\frac{f_0(s<0)}{-2i\pi} &= \frac{\gamma_i}{1+\gamma_i\tilde{\gamma}_i}\left(1-e^{-\kappa_{u,i}|s|}\right) + \frac{\gamma_i}{1+\gamma_i\tilde{\Gamma}_i}e^{-\kappa_{u,i}|s|} \\
&= \frac{\gamma_i[1+\gamma_i\tilde{\Gamma}_i-\gamma_i(\tilde{\Gamma}_i-\tilde{\gamma}_i)e^{-\kappa_{u,i}|s|}]}{(1+\gamma_i\tilde{\gamma}_i)(1+\gamma_i\tilde{\Gamma}_i)} \\
\frac{\tilde{f}_0(s<0)}{2i\pi} &= \frac{\tilde{\gamma}_i}{1+\gamma_i\tilde{\gamma}_i}\left(1-e^{-\kappa_{u,i}|s|}\right) + \frac{\tilde{\Gamma}_i}{1+\gamma_i\tilde{\Gamma}_i}e^{-\kappa_{u,i}|s|}
\end{aligned} \tag{B7}$$

where we wrote the functions in several different ways, to cancel some terms later on.

Notice the physical interpretation of the propagator form. For example, for $f_0(s>0)$ we have the same $\tilde{\gamma}_f$ in both terms since it is coming from $s=+\infty$, but the γ-amplitude can be either γ_f far from the reflection point or $\Gamma_f \leftarrow \gamma_i$ close to reflection points and they give rise to the two different terms in f_0. All other expressions for f-functions follow the same pattern. The second term, that mixes Γ_f and $\tilde{\gamma}_f$ in denominator, is the one that mainly determines bound states effects. In both diagonal and off-diagonal items the continuum and the bound states contribution are nicely separated.

Appendix C: Current kernel without the order parameter suppression

We use the results of Appendix B to calculate the current response kernel. First, we find κ that determines the correlations extent in the current response:

$$\kappa(s) = \frac{2}{v_f}\left[\varepsilon_m + \frac{\gamma_0\tilde{\Delta}_0-\tilde{\gamma}_0\Delta_0}{2i}\right] = \kappa_u \times \begin{cases} 1+\dfrac{(\Gamma_f-\gamma_f)\tilde{\gamma}_f e^{-\kappa_u s}}{1+\Gamma_f\tilde{\gamma}_f-(\Gamma_f-\gamma_f)\tilde{\gamma}_f e^{-\kappa_u s}}, & s>0 \\ 1+\dfrac{\gamma_i(\tilde{\Gamma}_i-\tilde{\gamma}_i)e^{\kappa_u s}}{1+\gamma_i\tilde{\Gamma}_i-\gamma_i(\tilde{\Gamma}_i-\tilde{\gamma}_i)e^{\kappa_u s}}, & s<0 \end{cases} \tag{C1}$$

Here we consider an order parameter orientation such that the amplitudes on the incoming and reflected parts of the trajectory are the same, so $\kappa_{u,i}=\kappa_{u,f}=\kappa_u$. The generalization for different amplitudes can be easily carried out retaining indices $\Omega_{i,f}$, $\kappa_{u;i,f}$ etc. This expression for $\kappa(s)$ is quite general and easy to integrate along trajectories, as required for correlation functions $C(\mathbf{R},\mathbf{R}')$ and $C(\mathbf{R}',\mathbf{R})$. In both these functions integration goes from initial to final point as determined by the momentum direction, and is shown in Fig. 8.

For the case (a) both s_1 and s_2 are on the same side of the interface and s_2 is further away from the interface than

s_1, we have

$$s-out: \qquad C_{①}\left(\frac{1}{2\pi|s_2-s_1|}\frac{2\varepsilon_m}{v_f}\right)^{-1} = \exp\left[-\int_{s_1}^{s_2}\kappa(\rho)d\rho\right] = \frac{1+\Gamma_f\tilde{\gamma}_f-(\Gamma_f-\gamma_f)\tilde{\gamma}_f e^{-\kappa_u s_1}}{1+\Gamma_f\tilde{\gamma}_f-(\Gamma_f-\gamma_f)\tilde{\gamma}_f e^{-\kappa_u s_2}} e^{-\kappa_u|s_2-s_1|} \tag{C2}$$

If we reverse the trajectory the signs of s change (so that s_1 and s_2 determine absolute distance to the surface)

$$s-in: \qquad C_{①}\left(\frac{1}{2\pi|s_2-s_1|}\frac{2\varepsilon_m}{v_f}\right)^{-1} = \exp\left[-\int_{-s_2}^{-s_1}\kappa(\rho)d\rho\right] = \frac{1+\gamma_i\tilde{\Gamma}_i-\gamma_i(\tilde{\Gamma}_i-\tilde{\gamma}_i)e^{-\kappa_u s_1}}{1+\gamma_i\tilde{\Gamma}_i-\gamma_i(\tilde{\Gamma}_i-\tilde{\gamma}_i)e^{-\kappa_u s_2}} e^{-\kappa_u|s_2-s_1|} \tag{C3}$$

For the (c) case we break the integral into two parts for in and out $s-in-out$:

$$C_{②}\left(\frac{1}{2\pi|s'_2+s'_1|}\frac{2\varepsilon_m}{v_f}\right)^{-1} = \exp\left[-\int_{-s'_1}^{s'_2}\kappa(\rho)d\rho\right] = \frac{1+\gamma_f\tilde{\gamma}_f}{1+\Gamma_f\tilde{\gamma}_f-(\Gamma_f-\gamma_f)\tilde{\gamma}_f e^{-\kappa_u s'_2}}\frac{1+\gamma_i\tilde{\gamma}_i}{1+\gamma_i\tilde{\Gamma}_i-\gamma_i(\tilde{\Gamma}_i-\tilde{\gamma}_i)e^{-\kappa_u s'_1}} e^{-\kappa_u(s'_2+s'_1)} \tag{C4}$$

The denominators in (C2-C4) will cancel numerators in some of the f-functions (B7) when combined in the kernel expression (A11). The numerators in (C2-C3) can be written as

$$\begin{aligned} 1+\Gamma_f\tilde{\gamma}_f-(\Gamma_f-\gamma_f)\tilde{\gamma}_f e^{-\kappa_u s} &= (1+\Gamma_f\tilde{\gamma}_f)(1-e^{-\kappa_u s})+(1+\gamma_f\tilde{\gamma}_f)e^{-\kappa_u s} \\ 1+\gamma_i\tilde{\Gamma}_i-\gamma_i(\tilde{\Gamma}_i-\tilde{\gamma}_i)e^{-\kappa_u|s|} &= (1+\gamma_i\tilde{\Gamma}_i)(1-e^{-\kappa_u|s|})+(1+\gamma_i\tilde{\gamma}_i)e^{-\kappa_u|s|} \end{aligned} \tag{C5}$$

For any given points $\mathbf{R}$ and $\mathbf{R}'$ we define two paths, direct and reflected, and each will have $\mathbf{R}\to\mathbf{R}'$ and $\mathbf{R}'\to\mathbf{R}$ contributions, $\tilde{f}(\hat{p},\mathbf{R})C(\mathbf{R},\mathbf{R}')f(\hat{p},\mathbf{R}')+\tilde{f}(-\hat{p},\mathbf{R})C(\mathbf{R}',\mathbf{R})f(-\hat{p},\mathbf{R})$. Let's denote by $\hat{k}$ momentum away from the surface, and in this case we identify indices $f=\hat{k}$, $i=\underline{\hat{k}}$. The trajectory we are integrating γ-function goes from $s_1=s_<$ (point closest to the interface) to $s_2=s_>$ (point farthest from interface). For reverse trajectory we have $f=-\underline{\hat{k}}$, $i=-\hat{k}$ and integration happens from $-s_2$ to $-s_1$.

The two terms give, after mentioned cancellations, for direct path

$$\begin{aligned} &\frac{\tilde{\gamma}_0}{1+\gamma_0\tilde{\gamma}_0}C(\mathbf{R}\leftarrow\mathbf{R}')\frac{\gamma_0}{1+\gamma_0\tilde{\gamma}_0}+\frac{\tilde{\gamma}_0}{1+\gamma_0\tilde{\gamma}_0}C(\mathbf{R}'\leftarrow\mathbf{R})\frac{\gamma_0}{1+\gamma_0\tilde{\gamma}_0} = \frac{1}{2\pi|s_>-s_<|}\frac{2\varepsilon_m}{v_f} \times \Bigg\{ \\ &\left[\frac{\tilde{\gamma}_{\hat{k}}}{1+\gamma_{\hat{k}}\tilde{\gamma}_{\hat{k}}}(1-e^{-\kappa_u s_<})+\frac{\tilde{\gamma}_{\hat{k}}}{1+\Gamma_{\hat{k}}\tilde{\gamma}_{\hat{k}}}e^{-\kappa_u s_<}\right] e^{-\kappa_u|s_>-s_<|} \left[\frac{\gamma_{\hat{k}}}{1+\gamma_{\hat{k}}\tilde{\gamma}_{\hat{k}}}(1-e^{-\kappa_u s_<})+\frac{\Gamma_{\hat{k}}}{1+\Gamma_{\hat{k}}\tilde{\gamma}_{\hat{k}}}e^{-\kappa_u s_<}\right]+ \\ &\left[\frac{\tilde{\gamma}_{-\hat{k}}}{1+\gamma_{-\hat{k}}\tilde{\gamma}_{-\hat{k}}}(1-e^{-\kappa_u s_<})+\frac{\tilde{\Gamma}_{-\hat{k}}}{1+\gamma_{-\hat{k}}\tilde{\Gamma}_{-\hat{k}}}e^{-\kappa_u s_<}\right] e^{-\kappa_u|s_>-s_<|} \left[\frac{\gamma_{-\hat{k}}}{1+\gamma_{-\hat{k}}\tilde{\gamma}_{-\hat{k}}}(1-e^{-\kappa_u s_<})+\frac{\gamma_{-\hat{k}}}{1+\gamma_{-\hat{k}}\tilde{\Gamma}_{-\hat{k}}}e^{-\kappa_u s_<}\right]\Bigg\} \end{aligned} \tag{C6}$$

For the reflected path this sum has a more compact form that directly reflects the bound states factors

$$\begin{aligned} &\frac{\tilde{\gamma}_0}{1+\gamma_0\tilde{\gamma}_0}C(\mathbf{R}\leftarrow\mathbf{R}')\frac{\gamma_0}{1+\gamma_0\tilde{\gamma}_0}+\frac{\tilde{\gamma}_0}{1+\gamma_0\tilde{\gamma}_0}C(\mathbf{R}'\leftarrow\mathbf{R})\frac{\gamma_0}{1+\gamma_0\tilde{\gamma}_0} = \\ &= \frac{1}{2\pi|s'_>+s'_<|}\frac{2\varepsilon_m}{v_f} \times \left\{\frac{\tilde{\gamma}_{\hat{k}'}\gamma_{\underline{\hat{k}}'}}{(1+\Gamma_{\hat{k}'}\tilde{\gamma}_{\hat{k}'})(1+\gamma_{\underline{\hat{k}}'}\tilde{\Gamma}_{\underline{\hat{k}}'})}e^{-\kappa_u|s'_>+s'_<|}+\frac{\tilde{\gamma}_{-\underline{\hat{k}}'}\gamma_{-\hat{k}'}}{(1+\gamma_{-\hat{k}'}\tilde{\Gamma}_{-\hat{k}'})(1+\Gamma_{-\underline{\hat{k}}'}\tilde{\gamma}_{-\underline{\hat{k}}'})}e^{-\kappa_u|s'_>+s'_<|}\right\} \end{aligned} \tag{C7}$$

Note, that to generalize for inequivalent gap size on in-out trajectories we need to use appropriate κ_u along given directions, e.g. $\kappa_u|s'_>+s'_<|\to\kappa_{u,\hat{k}'}s'_>+\kappa_{u,\underline{\hat{k}}'}s'_<$ for trajectory $\underline{\hat{k}}'\to\hat{k}'$ with reflection. These are completely general expressions for the one-component order parameters, where we neglect suppression of OP amplitude near the surface, and assume specular scattering.

We apply the developed formalism and approximations to a d-wave superconductor with maximally pairbreaking surface. In this case we have $\Delta_{\hat{k}}=-\Delta_{\underline{\hat{k}}}$ for all incident trajectories, and $\gamma_{-\hat{k}}=\gamma_{\hat{k}}=-\gamma_{\underline{\hat{k}}}$, $\tilde{\gamma}_{-\hat{k}}=\tilde{\gamma}_{\hat{k}}=\tilde{\gamma}_{\underline{\hat{k}}}$, $\Gamma_{\hat{k}}=\gamma_{\underline{\hat{k}}}=-\gamma_{\hat{k}}$, and two important combinations of the coherence amplitudes are

$$\frac{1}{1+\gamma_{\hat{k}}\tilde{\gamma}_{\hat{k}}}=\frac{\varepsilon_m+\Omega}{2\Omega}\,, \qquad \frac{1}{1+\Gamma_{\hat{k}}\tilde{\gamma}_{\hat{k}}}=\frac{\varepsilon_m+\Omega}{2\varepsilon_m} \tag{C8}$$

The correlation coefficient Eq. (C1) along a trajectory

s is

$$\kappa(s) = \kappa_u \left[\left(1 - e^{-\kappa_u |s|} \right) + \frac{\Omega}{\varepsilon_m} e^{-\kappa_u |s|} \right]^{-1}, \qquad \text{(C9)}$$

where $\kappa_u = 2\Omega / v_{\text{F}}$ and $\Omega = \sqrt{\varepsilon_m^2 + \Delta_{\hat{k}}^2}$. The distance along a trajectory, measured from the surface, is $s = y/\hat{k}_y$. One uses these relations for coherence amplitudes in combinations (C6) and (C7) to find the kernel (A11) components, as given in the main text, for the direct path, Eq. (8), and the reflection path, Eq. (9), correspondingly.

Similar expressions for the superfluid density are valid for an s-wave superconductor with scattering at a specular magnetically-active surface. We use the boundary conditions for coherence amplitudes[50]

$$\Gamma_{\hat{k}}\, i\sigma_2 = \mathcal{M} \gamma_{\underline{k}}\, i\sigma_2 \tilde{\mathcal{M}}$$

with $\mathcal{M} = e^{i\vartheta \hat{m}\cdot\sigma/2}$ and $\tilde{\mathcal{M}} = \mathcal{M}^*$. Magnetic spin mixing leads to the bound states $\varepsilon_b = \pm\Delta \cos(\vartheta/2)$, that result in zero energy states for $\vartheta = \pi$ and the boundary condition for coherence amplitudes $\Gamma_{\hat{k}} = -\gamma_{\underline{\hat{k}}}$.

---

[*] anton.vorontsov@montana.edu

[1] M. Tinkham, *Introduction to Superconductivity* (Robert E. Krieger Publishing Co. Malabar, Florida, 1985).

[2] J. Bardeen, L. Cooper, and R. Schrieffer, Physical Review **108**, 1175 (1957).

[3] M. Håkansson, T. Löfwander, and M. Fogelström, Nature Physics **11**, 755 (2015).

[4] P. Holmvall, A. B. Vorontsov, M. Fogelström, and T. Löfwander, Nature Communications **9**, 2190 (2018).

[5] R. C. Powell, *Symmetry, Group Theory, and the Physical Properties of Crystals* (Springer, Lecture Notes in Physics, 2010).

[6] M. Senechal, *Quasicrystals and Geometry* (Cambridge, 1995); R. Lifshitz, Israel Journal of Chemistry **51**, 1156 (2011).

[7] E. Kats, V. Lebedev, and A. Muratov, Physics Reports **228**, 1 (1993).

[8] I. Martin, S. Gopalakrishnan, and E. A. Demler, Phys. Rev. B **93**, 235140 (2016).

[9] F. Wilczek, Phys. Rev. Lett. **109**, 160401 (2012).

[10] N. Y. Yao, A. C. Potter, I.-D. Potirniche, and A. Vishwanath, Phys. Rev. Lett. **118**, 030401 (2017).

[11] J. Zhang, P. W. Hess, A. Kyprianidis, P. Becker, A. Lee, J. Smith, G. Pagano, I. D. Potirniche, A. C. Potter, A. Vishwanath, N. Y. Yao, and C. Monroe, Nature **543**, 217 (2017).

[12] S. Choi, J. Choi, R. Landig, G. Kucsko, H. Zhou, J. Isoya, F. Jelezko, S. Onoda, H. Sumiya, V. Khemani, C. von Keyserlingk, N. Y. Yao, E. Demler, and M. D. Lukin, Nature **543**, 221 (2017).

[13] Y. Kamiya and C. D. Batista, Phys. Rev. X **4**, 011023 (2014).

[14] S. Ostermann, F. Piazza, and H. Ritsch, Phys. Rev. X **6**, 021026 (2016).

[15] A. I. Larkin and Y. N. Ovchinnikov, Zh Eksp Teor Fiz **47**, 1136 (1964); SOV PHYS JETP **20**, 762 (1965).

[16] J. J. Kinnunen, J. E. Baarsma, J.-P. Martikainen, and P. Törmä, Reports on Progress in Physics **81**, 046401 (2018).

[17] S. Dutta and E. J. Mueller, Phys. Rev. A **96**, 023612 (2017).

[18] R. Casalbuoni and G. Nardulli, Rev. Mod. Phys. **76**, 263 (2004).

[19] P. Fulde and R. A. Ferrell, Physical Review **135**, A550 (1964).

[20] D.Vollhardt and P.Wölfle, *The Superfluid Phases of Helium 3* (Taylor & Francis, 1990).

[21] P. M. Chaikin and T. C. Lubensky, *Principles of Condensed Matter* (Cambridge, 1995).

[22] P. G. de Gennes and J. Prost, *The Physics of Liquid Crystals*, 2nd ed. (Oxford University Press, 1995).

[23] We also drop corrections to the superflow due to the vector potential $\mathbf{A}(\mathbf{R})$ of the self-induced field $\boldsymbol{\nabla}\chi \to \boldsymbol{\nabla}\chi - \frac{2\pi}{\Phi_0}\mathbf{A}$. These corrections result in energy terms that are smaller than the phase-gradient terms by factor $(\xi_0/\lambda)^2$, which is small in type-II superconductors. See e.g. Refs. 4 and 30.

[24] C. R. Hu, Physical Review Letters **72**, 1526 (1994).

[25] W. Pesch and L. Kramer, in *Pattern Formation in Liquid Crystals*, edited by A. Buka and L. Kramer (Springer, 1996) Chap. 3, pp. 69–90.

[26] M. Eschrig, in *Andreev bound states*, edited by L. H. Greene and J. A. Sauls (Philosophical Transactions of the Royal Society A, 2018) Chap. *Theory of Andreev bound states in S-F-S junctions and S-F proximity devices*, p. 2015.0149.

[27] The superfluid free energy density cannot be uniquely defined in non-uniform, and especially non-local, systems. However, the two following definitions gave similar pictures: $f_1(\mathbf{R}) = \int d\mathbf{r}\ \mathbf{p}_s(\mathbf{R}_+)^T\, \hat{K}(\mathbf{R}_+, \mathbf{R}_-)\, \mathbf{p}_s(\mathbf{R}_-)$ with $\mathbf{R}_\pm = \mathbf{R} \pm \mathbf{r}/2$, and $f_2(\mathbf{R}) = \mathbf{p}_s(\mathbf{R}) \cdot \mathbf{j}(\mathbf{R}) = \mathbf{p}_s(\mathbf{R})^T \int d\mathbf{R}'\, \hat{K}(\mathbf{R}, \mathbf{R}')\, \mathbf{p}_s(\mathbf{R}')$.

[28] M. Fogelström, D. Rainer, and J. A. Sauls, Physical Review Letters **79**, 281 (1997).

[29] S. Higashitani, Journal of the Physical Society of Japan **66**, 2556 (1997).

[30] Y. S. Barash, M. S. Kalenkov, and J. Kurkijärvi, Physical Review B **62**, 6665 (2000).

[31] T. Löfwander, V. S. Shumeiko, and G. Wendin, Physical Review B **62**, R14653 (2000).

[32] A. B. Vorontsov, Physical Review Letters **102**, 177001 (2009).

[33] M. Eschrig, Physics Today **64**, 43 (2011).

[34] P. Novelli, F. Taddei, A. K. Geim, and M. Polini, Phys. Rev. Lett. **122**, 016601 (2019).

[35] J. Wang, Y. Meir, and Y. Gefen, Phys. Rev. Lett. **118**, 046801 (2017).

[36] M. C. Cross and P. C. Hohenberg, Rev. Mod. Phys. **65**, 851 (1993).

[37] P. Holmvall, A. B. Vorontsov, M. Fogelström, and T. Löfwander, Phys. Rev. B **99**, 184511 (2019).

[38] M. Boninsegni and N. V. Prokof'ev, Rev. Mod. Phys. **84**, 759 (2012).

[39] J. Léonard, A. Morales, P. Zupancic, T. Esslinger, and T. Donner, Nature **543**, 87 (2017).

[40] F. Böttcher, J.-N. Schmidt, M. Wenzel, J. Hertkorn,

M. Guo, T. Langen, and T. Pfau, Phys. Rev. X **9**, 011051 (2019).

[41] L. Chomaz, D. Petter, P. Ilzhöfer, G. Natale, A. Trautmann, C. Politi, G. Durastante, R. M. W. van Bijnen, A. Patscheider, M. Sohmen, M. J. Mark, and F. Ferlaino, Phys. Rev. X **9**, 021012 (2019).

[42] A. B. Pippard and W. L. Bragg, Proceedings of the Royal Society of London. Series A. Mathematical and Physical Sciences. **A216**, 547 (1953).

[43] T. Koyama and M. Machida, Physica C: Superconductivity **484**, 100 (2013), proceedings of the 24th International Symposium on Superconductivity (ISS2011).

[44] D. Tanaka and Y. Kuramoto, Phys. Rev. E **68**, 026219 (2003).

[45] P. C. Bressloff and Z. P. Kilpatrick, Phys. Rev. E **78**, 041916 (2008).

[46] V. García-Morales and K. Krischer, Phys. Rev. Lett. **100**, 054101 (2008).

[47] J. W. Serene and D. Rainer, Physics Reports **101**, 221 (1983).

[48] M. Eschrig, Physical Review B **61**, 9061 (2000).

[49] N. Schopohl and K. Maki, Phys. Rev. B **52**, 490 (1995); A. Shelankov and M. Ozana, Phys. Rev. B **61**, 7077 (2000).

[50] M. Eschrig, Physical Review B **80**, 134511 (2009).

Paper II

nature COMMUNICATIONS

ARTICLE

DOI: 10.1038/s41467-018-04531-y OPEN

Broken translational symmetry at edges of high-temperature superconductors

P. Holmvall [1], A.B. Vorontsov [2], M. Fogelström [1] & T. Löfwander [1]

Flat bands of zero-energy states at the edges of quantum materials have a topological origin. However, their presence is energetically unfavorable. If there is a mechanism to shift the band to finite energies, a phase transition can occur. Here we study high-temperature superconductors hosting flat bands of midgap Andreev surface states. In a second-order phase transition at roughly a fifth of the superconducting transition temperature, time-reversal symmetry and continuous translational symmetry along the edge are spontaneously broken. In an external magnetic field, only translational symmetry is broken. We identify the order parameter as the superfluid momentum $\mathbf{p}_s$, that forms a planar vector field with defects, including edge sources and sinks. The critical points of the vector field satisfy a generalized Poincaré-Hopf theorem, relating the sum of Poincaré indices to the Euler characteristic of the system.

---

[1] Department of Microtechnology and Nanoscience-MC2, Chalmers University of Technology, SE-41296 Göteborg, Sweden. [2] Department of Physics, Montana State University, Bozeman, MT 59717, USA. Correspondence and requests for materials should be addressed to T.Löf. (email: tomas.lofwander@chalmers.se)

Superconducting devices are often experimentally realized as thin-film circuits or hybrid structures operating in the mesoscopic regime[1–4]. At this length scale, where the size of the circuit elements becomes comparable with the superconducting coherence length, the nature of the superconducting state may be dictated by various finite-size or surface/interface effects[5]. This holds true in particular for unconventional superconductors, such as the high-temperature superconductors with an order parameter of $d_{x^2-y^2}$ symmetry that changes the sign around the Fermi surface. Scattering at surfaces, or defects, leads to substantial pair breaking and formation of Andreev states with energies within the superconducting gap[6,7]. Today, the material control of high-temperature superconducting films is sufficiently good that many advanced superconducting devices can work at elevated temperatures[8,9]. This raises the question how the specific surface physics of d-wave superconductors influences devices.

From a theory point of view, the physics at specular pair-breaking surfaces of d-wave superconductors is rich and interesting. The reason is the formation of zero-energy (midgap) Andreev states due to the sign change of the d-wave order parameter for quasiparticles scattered at the surface[6,7,10]. In modern terms, there is a flat band of spin-degenerate zero-energy surface states as a function of the parallel component of the momentum, $p_{||}$, which is a good quantum number for a specular surface. A topological invariant has been identified[11,12], that guarantees the flat band for a time-reversal symmetric superconducting order parameter and $p_{||}$ conserved. However, the large spectral weight of these states exactly at zero energy (i.e., at the Fermi energy) is energetically unfavorable. Different scenarios have been proposed, within which there is a low-temperature instability and a phase transition into a time-reversal symmetry-broken phase where the flat band is split to finite energies, thus lowering the free energy of the system. One scenario is the presence of a subdominant pairing interaction and appearance of another order parameter component $\pi/2$ out of phase with the dominant one[13–15], for instance a subdominant s-wave resulting in an order parameter combination $\Delta_{\rm d} + i\Delta_{\rm s}$. The phase transition is driven by a split of the flat band of Andreev states to $\pm\Delta_{\rm s}$. The split Andreev states carry current along the surface, which results in a magnetic field that is screened from the bulk. In a second scenario, exchange interactions drive a ferromagnetic transition at the edge where the flat Andreev band is instead spin split[16,17]. A third scenario involves spontaneous appearance of supercurrents[18–20] that Doppler shifts the Andreev states and thereby lowers the free energy. Here the electrons couple to the electromagnetic gauge field $\mathbf{A}(\mathbf{R})$, and this mechanism was first considered theoretically for a translationally invariant edge. In this case, the transition is a result of the interplay of weakly Doppler shifted surface bound states, decaying away from the surface on the scale of the superconducting coherence length ξ_0, and weak diamagnetic screening currents, decaying on the scale of the penetration depth λ. The resulting transition temperature is very low, of order $T^* \sim (\xi_0/\lambda)T_{\rm c}$, where $T_{\rm c}$ is the d-wave superconducting transition temperature. Later, the transition temperature was shown to be enhanced in a film geometry[21–25] where two parallel pair-breaking edges are separated by a distance of the order of a few coherence lengths. The suppression of the order parameter between the pair-breaking edges can be viewed as an effective Zeeman field that splits the Andreev states and enhances the transition temperature. The mechanism does not involve subdominant channels or coupling to magnetic field, but depends on film thickness D, and the transition temperature decays rapidly with increasing thickness as $T^* \sim (\xi_0/D)T_{\rm c}$.

In this paper, we consider a peculiar scenario[26,27] where spontaneous supercurrents also break translational symmetry along the edge. This scenario too does not rely on any additional interaction term in the Hamiltonian. Instead, as we will discuss below, it relies on the development of a texture in the gradient of the d-wave order parameter phase χ, or more precisely in the gauge invariant superfluid momentum

$$\mathbf{p}_{\rm s}(\mathbf{R}) = \frac{\hbar}{2}\nabla\chi(\mathbf{R}) - \frac{e}{c}\mathbf{A}(\mathbf{R}), \tag{1}$$

where $\hbar$ is Planck's constant, e the charge of the electron, and c the speed of light. This superfluid momentum spontaneously takes the form of a planar vector field with a chain of sources and sinks along the boundary and saddle points in the interior, see Fig. 1. The vector field is illustrated by arrows showing the local unit vectors $\hat{\mathbf{p}}_{\rm s}(\mathbf{R})$, while the color scale illustrates the magnitude $p_{\rm s}(\mathbf{R})$. An interior critical point at $\mathbf{R}_0$ is characterized by a Poincaré index defined as[28,29]

$$I = \frac{1}{2\pi}\oint_{\Gamma} {\rm d}\theta, \tag{2}$$

where $\theta = \arctan(p_{{\rm s}y}/p_{{\rm s}x})$ is the angle of $\hat{\mathbf{p}}_{\rm s}(\mathbf{R})$ on the Jordan curve Γ encircling $\mathbf{R}_0$. Internal sources and sinks have $I = +1$, while saddle points have $I = -1$. Although the special points on the boundary have to be treated with care, there is a sum rule (Eq. (3)) for the Poincaré indices, as we will discuss below. We identify the $\mathbf{p}_{\rm s}$ vector field as the order parameter of the symmetry-broken phase, motivated by the fact that the free energy is lowered by a large split of the flat band of Andreev states by a Doppler shift $\mathbf{v}_{\rm F} \cdot \mathbf{p}_{\rm s}$, where $\mathbf{v}_{\rm F}$ is the Fermi velocity. This free energy gain is maximized by maximizing the magnitude of $\mathbf{p}_{\rm s}$, which is achieved by the peculiar vector field in Fig. 1. The balance of the Doppler shift gain and the energy cost in setting up the vector field with critical points where[30] $\nabla \times \mathbf{p}_{\rm s} \neq 0$ and the splay patterns between them leads to a high $T^* \approx 0.18T_{\rm c}$. The inhomogeneous vector field induces a chain of loop-currents at the edge circulating clockwise and anti-clockwise. The induced magnetic fluxes of each loop are a fraction of the flux quantum and form a chain of fluxes with alternating signs along the edge. Here we clarify the structure of the order parameter of the symmetry-broken phase, i.e., $\mathbf{p}_{\rm s}$, and study the thermodynamics of this phase under the influence of an external magnetic field, explicitly breaking time-reversal symmetry.

Results

Translational symmetry breaking in a magnetic field. In Fig. 2, we show the influence of a rather weak external magnetic field, $B = 0.5B_{\rm g1}$, applied to the d-wave superconducting grain with pair-breaking edges for varying temperature near the phase transition temperature T^*. The scale $B_{\rm g1} = \Phi_0/\mathcal{A}$ corresponds to one flux quantum threading the grain area $\mathcal{A}$, see the Methods section. The left and right columns show the currents and the magnetic field densities, respectively, induced in response to the applied field. To be concrete, we discuss a few selected sets of model parameters, as listed in Table 1. First, for $T > T^*$ (parameter set I), the expected diamagnetic response of the condensate in the inner part of the grain is present, see Fig. 2a, e. On the other hand, midgap quasiparticle Andreev surface states respond paramagnetically. This situation is well established theoretically and experimentally through measurements of the competition between the diamagnetic and paramagnetic responses seen as a low-temperature up-turn in the penetration depth[18,31,32]. Upon lowering the temperature to $T \gtrsim T^*$ (parameter set II), see Fig. 2b, f, the paramagnetic response at the edge becomes locally suppressed and enhanced, forming a sequence of local minima and maxima in the induced currents and fields. The bulk response is, on the other hand, relatively unaffected. Finally, as $T < T^*$ (parameter set III), see Fig. 2c, g, the regions of minimum current

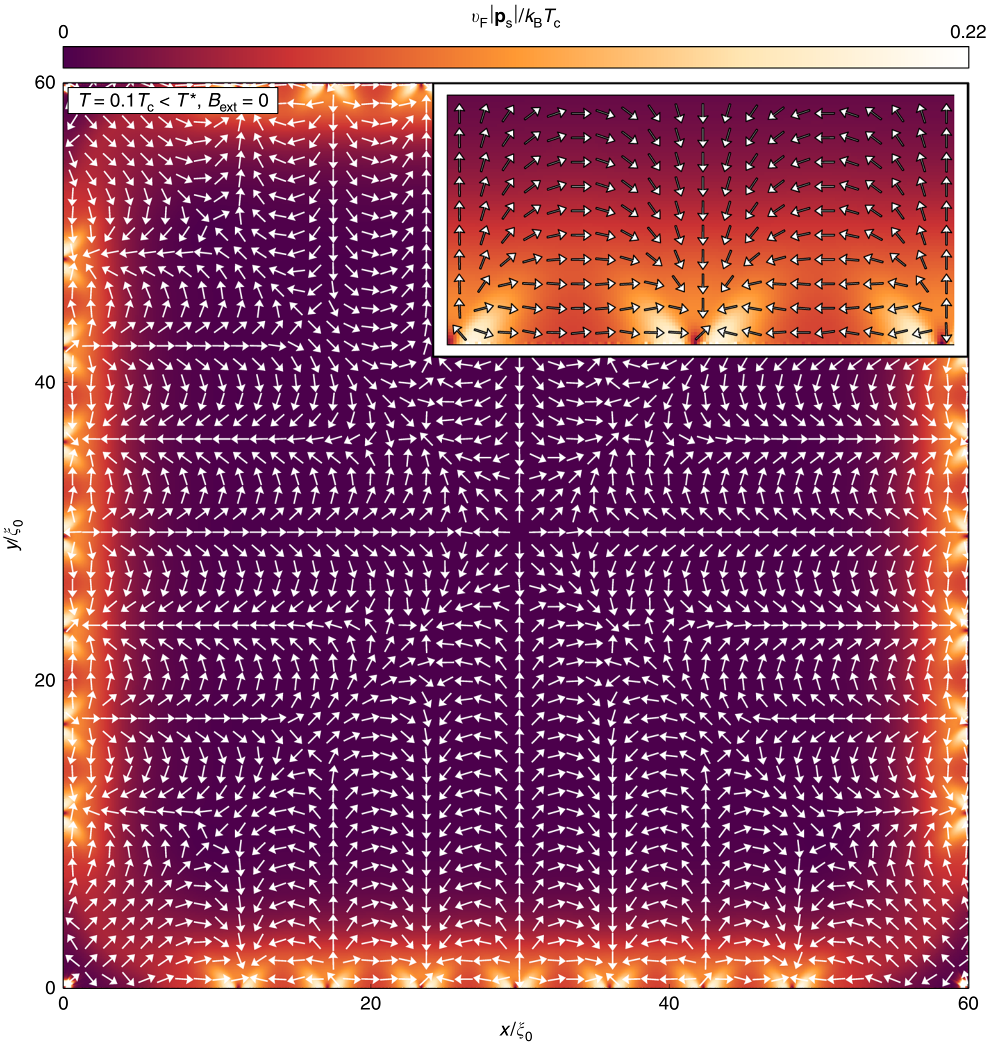

Fig. 1 Superfluid momentum as a vector field. The superfluid momentum $\mathbf{p}_s$ forms a non-trivial planar vector field with a regular chain of sources and sinks along the edge, thereby breaking local continuous translational symmetry along the edge. Several critical points, including saddle points, sources, and sinks, are formed in the interior. The Poincaré indices of the critical points add up to fulfill the generalized Poincaré-Hopf theorem in Eq. (3). The magnetic field is zero, $B_{ext} = 0$, while the temperature is $T = 0.1T_c$. Since T is well below T^*, the splay patterns are rather stiff, leading to triangular shapes near the edges. The stiffness is clear from the magnitude variation shown in color scale. The inset shows one period of the edge structure

turns into regions with reversed currents. The resulting loop currents with clock-wise and anti-clockwise circulations induce magnetic fluxes along the surface with opposite signs between neighboring fluxes. The situation for $T < T^*$ in an external magnetic field can be compared with the one in zero magnetic field[26] displayed in Fig. 2d, h. In the presence of the magnetic field, there is an imbalance between positive and negative fluxes, while in zero external magnetic field, the total induced flux integrated over the grain area is zero.

Topology of the superfluid momentum vector field. Let us quantify the symmetry-broken phase in a magnetic field by plotting the superfluid momentum defined in Eq. (1), see Fig. 3. For $T \gtrsim T^*$ (parameter set II), the amplitude of $\mathbf{p}_s$ varies along the edge (coordinate x), see Fig. 3a, reflecting the varying paramagnetic response in Fig. 2b, f. For $T < T^*$ (parameter set III), the sources and sinks have appeared pairwise together with a saddle point, see Fig. 3b. The left defects in the figure are not well developed because of the proximity to the corner. Finally, in Fig. 3c, we show the vector field at a lower temperature when the chain of sources, sinks, and saddle points are well established and the magnitude of $\mathbf{p}_s$ is large, much larger than in the interior part of the grain still experiencing diamagnetism. In a magnetic field, the vector field far from the surface has a preferred direction reflecting the diamagnetic response of the interior grain. This shifts the sources and sinks along the surface, as compared with the regular chain for zero field in Fig. 1, and moves the saddle points to the surface region.

The superflow pattern of sources, sinks, and saddle points satisfy a certain sum rule related to the topology of the sample. This relation also ties the special points of the $\mathbf{p}_s$ field on the edge of the sample with critical points in its bulk. The generalized Poincaré-Hopf theorem for manifolds with boundaries[33,34] connects the properties of a vector field v inside a manifold M, and on its boundary ∂M, with the Euler characteristic of the manifold $\chi(M)$. Using the formulation presented in ref. [34], we write

$$\mathrm{Ind}_M(v) + \frac{1}{2}\left[\mathrm{Ind}_{\partial_- M}(v_{||}) - \mathrm{Ind}_{\partial_+ M}(v_{||})\right] = \chi(M), \qquad (3)$$

where $\mathrm{Ind}_M(v)$ is the total Poincaré index of critical points of the field v internal to M, $\mathrm{Ind}_{\partial_\pm M}(v_{||})$ is the total Poincaré index of

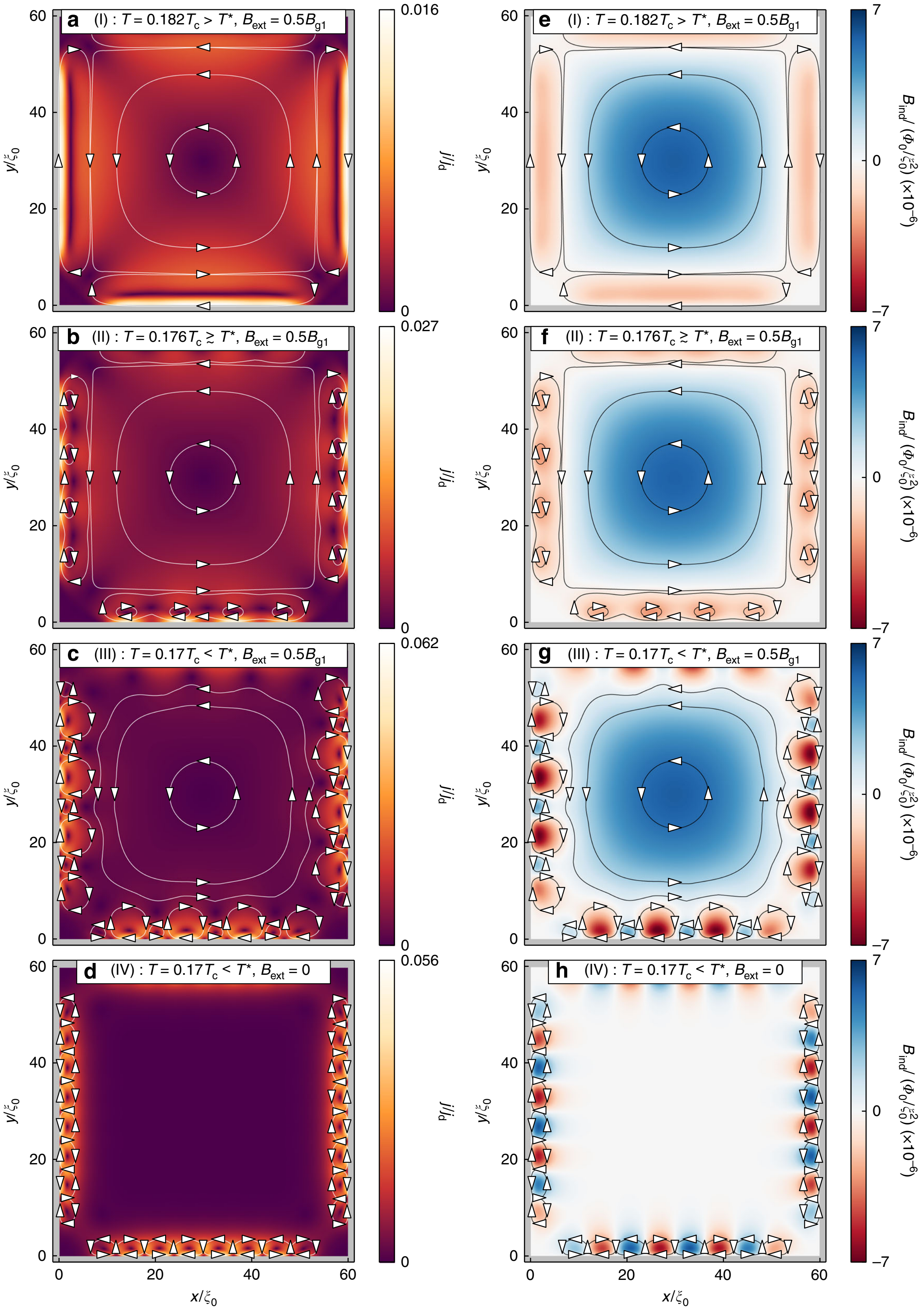

Fig. 2 Spontaneously formed currents and induced magnetic field. **a**-**d** Total current magnitude and **e**-**h** induced magnetic flux density for different temperatures and external fields (see annotations). Lines and arrows have been added to illustrate the flow of the currents

critical points of the tangent vector $v_{\parallel} \parallel \partial M$ on the boundary. The theorem applies when the boundary ∂M does not go through any critical points of v. Boundary indices where field points inside ($\partial_{-}M$) / outside ($\partial_{+}M$) of M, come with positive/negative signs. In Supplementary Note 1, we demonstrate in detail how the sum rule works for the vector field in Fig. 1, redrawn as a streamline plot in Supplementary Fig. 2. We also provide other examples of grain geometries in Supplementary Figs. 3–10. We utilize the sum rule as a tool to verify that the calculations are correct.

In a magnetic field, as in Fig. 3, a motif with one edge source, one edge sink, and one saddle point annihilate at T^*. In the same fashion, increasing the magnetic field strength, the motif gets smaller as the defects are forced toward each other to match the superflow in the bulk. However, the magnitude of $\mathbf{p}_s$ near the surface due to Meissner screening of the bulk is not large enough to force an annihilation of the motifs. The broken symmetry phase therefore survives the application of an external magnetic field within the whole Meissner state, $b \in [0, 1]$.

For higher fields, when Abrikosov vortices start to enter the grain, the problem quickly becomes complicated by the interplay of the Abrikosov vortex lattice formation and finite grain size effects. The free energy landscape is very flat and it is possible to find multiple metastable configurations. For a variety of grain sizes and magnetic field strengths, we have established coexistence of Abrikosov vortices and the spontaneously formed edge loop currents[35]. We therefore conclude that the edge loop-current phase established for $T < T^*$ should survive into the mixed state, but a complete investigation of the geometry-dependent phase diagram for large fields is beyond the scope of this paper.

Table 1 Sets of parameters used for presenting results

Set	Temperature	External magnetic field
(I)	$T = 0.182T_c > T^*$	$B_{\rm ext} = 0.5B_{\rm g1}$
(II)	$T = 0.176T_c \gtrsim T^*$	$B_{\rm ext} = 0.5B_{\rm g1}$
(III)	$T = 0.17T_c < T^*$	$B_{\rm ext} = 0.5B_{\rm g1}$
(IV)	$T = 0.17T_c < T^*$	$B_{\rm ext} = 0$

The field scale $B_{\rm g1} = \Phi_0/\mathcal{A}$ corresponds to an external magnetic flux through the grain area exactly equal to one flux quantum

Induced currents and magnetic fields. Let us investigate further how the currents and magnetic fields are induced at T^*. As we have seen, the paramagnetic response and the spontaneously appearing edge loop currents compete, as they both lead to shifts of midgap Andreev states. As the temperature is lowered, the strength of the paramagnetic response increases slowly and linearly, while the strength of the loop currents increases highly non-linearly. This is illustrated in Fig. 4, by plotting the area-averaged current magnitude

$$\bar{j} = \frac{1}{\mathcal{A}} \int {\rm d}^2 R\, |\mathbf{j}(\mathbf{R})|, \qquad (4)$$

as a function of temperature for the cases when $B_{\rm ext} = 0$ (solid line), $B_{\rm ext} = 0.5B_{\rm g1}$ (dashed line), and for comparison also for a system without pair-breaking edges having only a diamagnetic response at $B_{\rm ext} = 0.5B_{\rm g1}$ (dash-dotted line). The paramagnetic response is fully suppressed at low temperatures $T < T^*$. Such a sudden disappearance of the paramagnetic response at a temperature T^* should be experimentally measurable, for example in the penetration depth or by using nano-squids[36,37].

We show in Fig. 5a the total induced magnetic flux through the grain

$$\Phi_{\rm ind} = \int {\rm d}^2 R B_{\rm ind}(\mathbf{R}), \qquad (5)$$

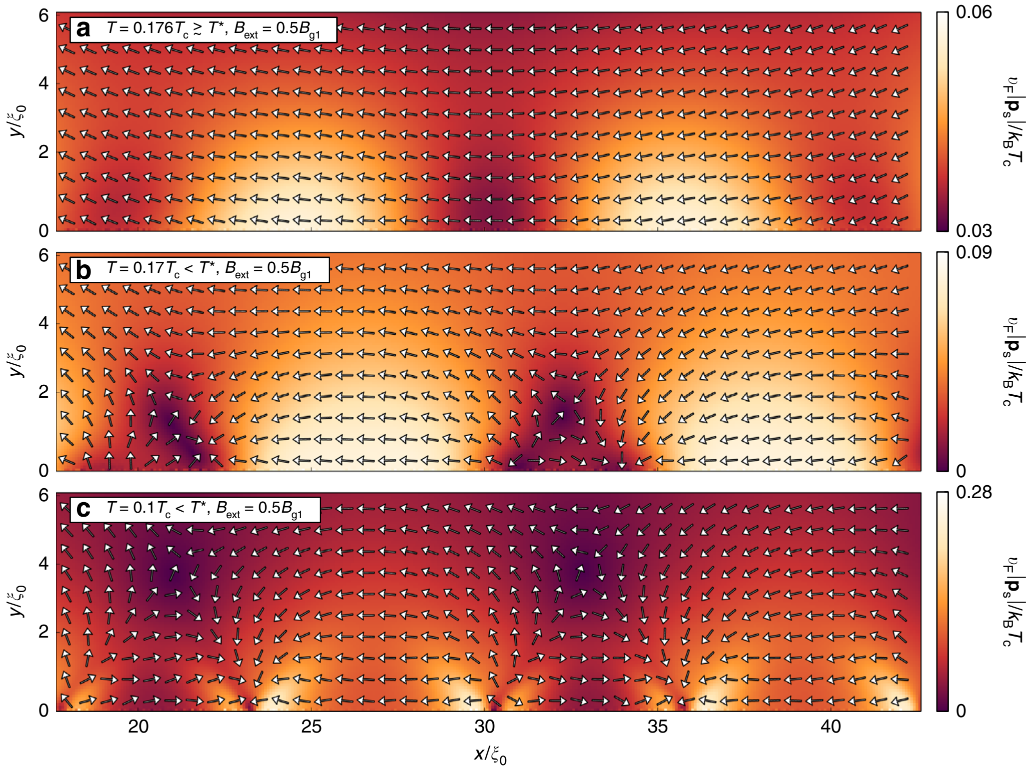

Fig. 3 Superfluid momentum for varying temperature. **a** The superfluid momentum induced in an external magnetic field of $B_{\rm ext} = 0.5B_{\rm g1}$ for a temperature slightly above the transition temperature T^* reflects the paramagnetic response. **b** At the phase transition, source–sink–saddle-point motifs appear and separate along the edge breaking translational invariance along the edge coordinate x. **c** For lower temperature, the magnitude $|\mathbf{p}_s|$ grows large. Note that different color scales are used in the subfigures in order to enhance visibility

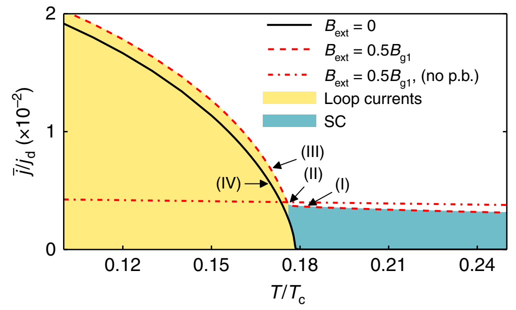

Fig. 4 Current as a function of temperature. The area-averaged current magnitude, defined in Eq. (4), is plotted for zero external magnetic field (solid line), with an external magnetic field of magnitude $B_\mathrm{ext} = 0.5B_\mathrm{g1}$ (dashed line), and for a system without pair-breaking edges at $B_\mathrm{ext} = 0.5B_\mathrm{g1}$ (dash-dotted line). In the latter case, the system only displays a diamagnetic response. Letters (I)–(IV) indicate the parameter values corresponding to the fields in Fig. 2, see Table 1

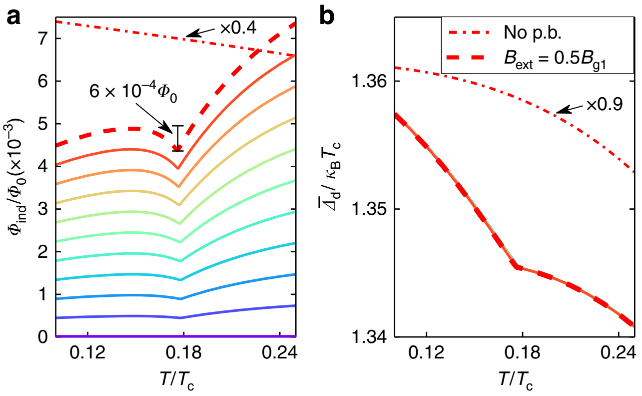

Fig. 5 Magnetic flux as a function of temperature. **a** Temperature dependence of the induced magnetic flux, defined in Eq. (5). The solid lines indicate, from bottom to top (colors purple to red), the external field magnitude from $B_\mathrm{ext} = 0$ to $B_\mathrm{ext} = 0.5B_\mathrm{g1}$ in steps of $0.05B_\mathrm{g1}$. The line corresponding to zero field lies exactly at zero since there is an equal amount of positive and negative fluxes induced in this case, see Fig. 2. Panel **b** shows the area-averaged order parameter magnitude defined in Eq. (6) versus temperature. Results are also shown for a system without pair-breaking edges (dash-dotted line) at $B_\mathrm{ext} = 0.5B_\mathrm{g1}$, but scaled with a factor 0.4 and 0.9 in **a** and **b**, respectively

and in Fig. 5b the area-averaged order parameter magnitude

$$\bar{\Delta}_\mathrm{d} = \frac{1}{\mathcal{A}}\int \mathrm{d}^2R|\Delta_\mathrm{d}(\mathbf{R})|, \tag{6}$$

both as functions of temperature for different values of B_ext. The figures also show results for a d-wave grain without pair-breaking edges at $B_\mathrm{ext} = 0.5B_\mathrm{g1}$ (dash-dotted line). For better visibility, the latter results have been scaled by a factor 0.4 and 0.9 in (a) and (b), respectively. Two different trends are distinguishable in the observables for $T < T^*$ and $T > T^*$, separated by a “kink”. The induced magnetic flux through the grain area decreases as T decreases down to T^* due to the increasing paramagnetic response that competes with the diamagnetic one. At T^*, the inhomogeneous edge state appear and starts competing with the paramagnetic response. Thus, the total magnetic flux increases again. At the same time, the order parameter is partially healed.

Phase transition and thermodynamics. The sudden changes with a discontinuity in the derivative as a function of temperature of the total induced current, the magnetic flux, as well as the order parameter (Figs. 4 and 5) indicate that there is a phase transition occurring at the temperature T^*. In zero external magnetic field, there is a second-order phase transition at T^*, where both time-reversal symmetry and continuous translational symmetry along the edge are spontaneously broken[26]. Let us now investigate the thermodynamics in an external magnetic field already explicitly breaking time-reversal symmetry.

In Fig. 6a, we plot the free energy difference between the superconducting and normal states $\Omega_\mathrm{S} - \Omega_\mathrm{N}$, defined in Eq. (29), for external field $B = 0.5B_\mathrm{g1}$ (red dashed line) and for zero field (solid black line). For comparison, we show the free energy difference for a purely real order parameter in zero field (gray fine line), i.e., without the symmetry breaking edge loop currents. For $T < T^*$, this solution is not the global minimum of the free energy, and we therefore refer to it as a metastable state. To enhance the visibility of the differences in free energy between the possible solutions, we show in Fig. 6b the free energy difference with respect to the metastable state, i.e., $\Omega_\mathrm{S} - \Omega_\mathrm{ms}$. The small slope in the red dashed line at $T > T^*$ in Fig. 6b is caused by the shift of midgap Andreev states due to the paramagnetic response, which increases as T decreases. The phase transition temperature T^* for the second-order phase transition can be identified with the “knee” in the entropy difference defined in Eq. (31), see Fig. 6c, d. Since time-reversal symmetry is already explicitly broken by the external magnetic field, the phase transition signals breaking of local continuous translational symmetry and establishment of the vector field $\mathbf{p}_\mathrm{s}$ with the chain of defects along the edge, as shown in Fig. 3. The magnitude of the order parameter follows the expected scaling law for second-order phase transitions, $p_\mathrm{s}(T) \propto (1 - T/T^*)^\beta$ with $\beta = 1/2$, as shown in the inset of Fig. 6d. However, the temperature range within which the scaling law holds is very limited and non-linear terms play an important role for lower temperatures $T < T^*$.

The knee in the entropy leads to a jump in the specific heat, as shown in Fig. 6e, f. The heat capacity is expressed in units of the heat capacity jump at the normal-superconducting phase transition at T_c for a bulk d-wave system

$$\Delta C_\mathrm{d} = \frac{2\alpha}{3}\mathcal{A}k_\mathrm{B}^2T_\mathrm{c}N_\mathrm{F}, \tag{7}$$

where $\alpha = 8\pi^2/[7\zeta(3)]$, with ζ being the Riemann-zeta function. The jump in heat capacity at the phase transition is an edge-to-area effect, and grows linearly as the sample becomes smaller. The jump is roughly 4.5% of ΔC_d for the mesoscopic $\mathcal{A} = 60\times60\xi_0^2$ grain considered here, and grows as the size of the grain is reduced. The phase transition temperature T^* is extracted as a function of B_ext as the midpoint temperature of the jump in the specific heat. Figure 7 shows a phase diagram where the T^*, extracted in this way from the specific heat, is plotted versus external field strength (crosses). We compare this with T^* extracted as the minimum (the “kink”, see Fig. 5a) in the induced flux. The small lowering of T^* with increased B_ext is caused by the competing paramagnetic response.

From the above, it is clear that the phase with edge loop currents shows extreme robustness against an external magnetic field in the whole Meissner region ($B_\mathrm{ext} \le B_\mathrm{g1}$). The magnitude of the spontaneously formed superfluid momentum $\mathbf{p}_\mathrm{s}$ at the edge grows non-linearly to be very large for $T < T^*$, fueled by the lowering of the free energy by Doppler shifts of the flat band of Andreev surface states. The corresponding correction to $\mathbf{p}_\mathrm{s}$, due to the process of screening of the external magnetic field, is in comparison small. Thereby, T^* is not dramatically shifted in a

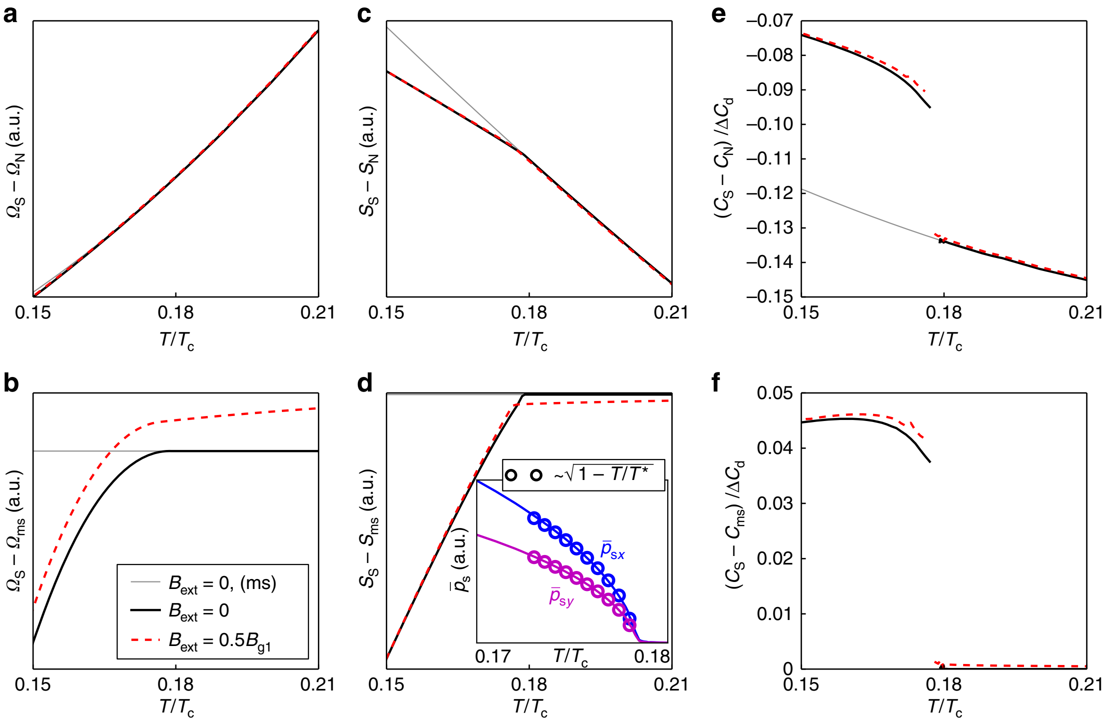

Fig. 6 Thermodynamics and phase transition. **a**, **b** free energy, **c**, **d** entropy, and **e**, **f** specific heat capacity, versus temperature. The lines correspond to a system with purely real order parameter without edge currents (gray fine line), a system with spontaneous edge currents in zero magnetic field (black solid line), and in a finite external field $B = 0.5B_{g1}$ (red dashed line). In the lower panels **b**, **d**, and **f**, the quantities have been subtracted by the corresponding values of the system with a purely real order parameter, the metastable (ms) state. The heat capacity is normalized by the heat capacity jump at the normal-superconducting phase transition for a bulk *d*-wave system, ΔC_d in Eq. (7). The inset in (**d**) shows the temperature dependence of the superfluid momentum near T^*, averaged over a few source-sink unit cells at one edge. It follows the expected temperature dependence for the order parameter at a mean-field second-order phase transition

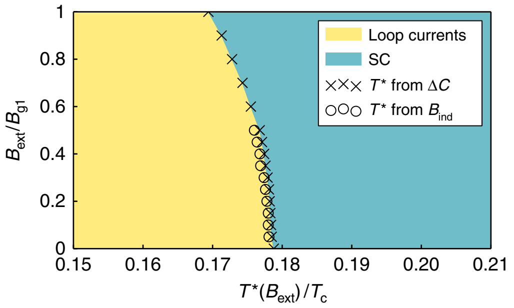

Fig. 7 Phase diagram. The transition temperature T^* to a state with spontaneously broken continuous translational symmetry is plotted as a function of the external magnetic flux density. The crosses show T^* extracted from the jump in the specific heat in Fig. 6e, while the open circles show T^* extracted from the minimum of the total induced magnetic flux in Fig. 5a

magnetic field and the symmetry-broken phase below T^* is robust.

Discussion

Which of the scenarios outlined in the introduction wins will ultimately depend on the material properties of a specific high-temperature superconducting sample, or the material properties of other candidate *d*-wave superconductors, e.g., FeSe[38]. In the scenario studied here, the resulting transition temperature is high, $T^* \sim 0.18T_c$. It means that the interaction terms in the Hamiltonian for the other scenarios would have to be sufficiently large in order to compete. It is even possible that one or another scenario wins in different parts of the material's phase diagram[16].

We note that the phase transition at T^* means that the initially topologically protected flat band of zero energy surface states is shifted away from the Fermi energy. Such fragility of topologically protected states has been studied recently e.g., for topological insulators[39] supporting the quantum spin-Hall state. In that case, an edge reconstruction due to Coulomb interactions leads to breaking of time-reversal symmetry. In the *d*-wave superconductor case, although the bulk Hamiltonian still maintains required symmetries, a local instability at the surface violates these symmetries spontaneously and moves the flat band of bound states to finite energies. The spontaneously broken translational symmetry allows for a larger shift from zero energy and a high T^*.

From an experimental point of view, the surface physics of *d*-wave superconductors is complicated by, for instance, surface roughness, inhomogeneous stoichiometry, and presence of impurities. The formation of a band of Andreev states centered at zero energy is well established by numerous tunneling experiments, in agreement with the expectation for *d*-wave symmetry of the order parameter, as reviewed in refs. [6,7]. One consistent experimental result is that the band is typically quite broad, with a width that saturates at low temperature. On the other hand, the establishment of a time-reversal symmetry breaking phase remains under discussion, see for instance refs. [40,41]. Several tunneling experiments on YBCO[42–44] show a split of the zero-bias conductance peak, while others do not[45,46]. Other probes indicating time-reversal symmetry breaking include thermal conductivity[47], Coulomb blockade in nanoscale islands[5], and

STM tunneling at grain boundaries in FeSe[38]. As we argued in refs. [26,27] within the scenario with spontaneous loop currents, the split of the Andreev band might be difficult to resolve in a tunneling experiment because of the broken translational symmetry along the edge and associated variations in the superflow field. This leads to a smearing effect for tunnel contacts with an area larger than the coherence length and an expected wide, largely temperature-independent, peak centered at zero energy. In fact, this would be consistent with most tunneling experiments.

With an eye to inspire a new generation of experiments, we have presented results for the interplay between an external magnetic field, that induces screening supercurrents, and the phase transition at T^* into a state with the spontaneous loop currents at the edges. We have shown that the phase should be quantified in terms of its order parameter, the vector field $\mathbf{p}_s(\mathbf{R})$, which contains edge sources and sinks, as well as saddle points. At all these critical points, $\nabla\times\mathbf{p}_s\neq 0$. The $\mathbf{p}_s$ vector field drives the loop currents with opposite circulations in neighboring loops. The loop-current strength increases highly non-linearly, suppressing the paramagnetic response present for $T>T^*$. As the strength of the external magnetic field increases, the size of the Doppler shift due to the paramagnetic response grows linearly. Therefore, T^* decreases slightly as the magnitude of the external field increases. The influence of the external field, and in particular the sudden disappearance of the paramagnetic response, leads to observables which we argue should be visible in experiment. For example the "kink" in the total induced flux at T^*. The magnetic fluxes induced by the loop currents should be directly observable with recently developed scanning probes[36,37], and the sudden disappearance of the paramagnetic response should be observable with nano-SQUIDS and possibly in penetration-depth experiments. Furthermore, the large jump in heat capacity at the phase transition should be observable with nanocalorimetry[48].

The identification of the order parameter $\mathbf{p}_s(\mathbf{R})$, with its topological textures, leads to similarities with other systems, including general relativity[33], fluid dynamics[49], liquid crystals[50], and superfluid ^{3}He[51]. An interesting difference is that in those systems, there is typically a transition in a preexisting vector field to a state with topological textures. Here, instead, we have a singlet d-wave superconductor that spontaneously establishes $\mathbf{p}_s(\mathbf{R})$ with topological textures different than the traditional Abrikosov vortices.

Methods

Model and grain geometry. Our aim is to investigate the ground state of clean mesoscopic d-wave superconducting grains in an external magnetic field applied perpendicular to the crystal ab-plane, as shown in Fig. 8. As a typical geometry, we consider a square grain with side lengths $D=60\xi_0$, where $\xi_0=\hbar v_F/(2\pi k_B T_c)$ is the zero-temperature superconducting coherence length. Here, v_F is the normal state Fermi velocity, and k_B the Boltzmann constant. The sides of the system are assumed to be misaligned by a 45° rotation with respect to the crystal ab-axes, inducing maximal pair-breaking at the edges.

The external field is directed perpendicular to the xy-plane,

$$\mathbf{B}_{\rm ext} = -B_{\rm ext}\hat{\mathbf{z}}\|\hat{\mathbf{c}}. \quad (8)$$

We shall consider rather small external fields, and will use a field scale $B_{g1}=\Phi_0/\mathcal{A}$, corresponding to one flux quantum threading the grain of area $\mathcal{A}=D^2=60\xi_0\times 60\xi_0$. The flux quantum $\Phi_0=hc/(2|e|)$ is given in Gaussian CGS units. The field B_{g1} is larger than the lower critical field $B_{c1}\propto\Phi_0/\lambda_0^2$, where vortices can enter a macroscopically large superconductor, since the grain side length is smaller than the penetration depth. We assume that $\lambda_0=100\xi_0$, relevant for YBCO. The upper critical field $B_{c2}\propto\Phi_0/\xi_0^2$ is much larger than any field we include in this study. To be precise, we parameterize the field strength as

$$B_{\rm ext} = bB_{g1}, B_{g1}\equiv\frac{\Phi_0}{\mathcal{A}}, \quad (9)$$

and we will consider $b\in[0, 1]$.

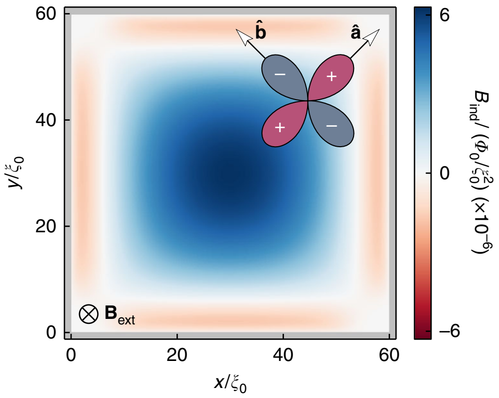

Fig. 8 Grain geometry. The system consists of a d-wave superconducting grain exposed to an external magnetic field $\mathbf{B}_{\rm ext}=-B_{\rm ext}\hat{\mathbf{z}}$. The crystal ab-axes are rotated 45° relative to the grain edges, inducing pair breaking at the edges of the system. The color scale shows the magnetic field $B_{\rm ind}$ induced in response to an external field of size $B_{\rm ext}=\Phi_0/2\mathcal{A}$ at a temperature $T=0.2T_c$. There is a diamagnetic response carried by the condensate in the interior, and a paramagnetic response carried by midgap surface Andreev states at the edges

Quasiclassical theory. We utilize the quasiclassical theory of superconductivity[52–54], which is a theory based on a separation of scales[55–58]. For instance, the atomic scale is assumed small compared with the superconducting coherence length, $\hbar/p_F\ll\xi_0$. This separation of scales makes it possible to systematically expand all quantities in small parameters such as $\hbar/p_F\xi_0$, Δ/ϵ_F, and $k_B T_c/\epsilon_F$, where Δ is the superconducting order parameter, p_F is the Fermi momentum, and ϵ_F is the Fermi energy. In equilibrium, the central object of the theory is the quasiclassical Green's function $\hat{g}(\mathbf{p}_F,\mathbf{R};z)$, which is a function of quasiparticle momentum on the Fermi surface $\mathbf{p}_F$, the quasiparticle center-of-mass coordinate $\mathbf{R}$, and the quasiparticle energy z. The latter is real $z=\epsilon+i0^+$ with an infinitesimal imaginary part $i0^+$ for the retarded Green's function, or an imaginary Matsubara energy $z=i\epsilon_n=i\pi k_B T(2n+1)$ in the Matsubara technique (n is an integer). To keep the notation compact, the dependence on the parameters $\mathbf{p}_F$, $\mathbf{R}$, and z will often not be written out. The hat on $\hat{g}$ denotes Nambu (electron-hole) space

$$\hat{g} = \begin{pmatrix} g & f \\ -\tilde{f} & \tilde{g} \end{pmatrix}, \quad (10)$$

where g and f are the quasiparticle and pair propagators, respectively. The tilde operation denotes particle-hole conjugation

$$\tilde{\alpha}(\mathbf{p}_F,\mathbf{R};z) = \alpha^*(-\mathbf{p}_F,\mathbf{R};-z^*). \quad (11)$$

The quasiclassical Green's function is parameterized in terms of two scalar coherence functions, $\gamma(\mathbf{p}_F, \mathbf{R}; z)$ and $\tilde{\gamma}(\mathbf{p}_F, \mathbf{R}; z)$, as[59–65]

$$\hat{g} = -\frac{i\pi}{1+\gamma\tilde{\gamma}}\begin{pmatrix} 1-\gamma\tilde{\gamma} & 2\gamma \\ 2\tilde{\gamma} & -1+\gamma\tilde{\gamma} \end{pmatrix}. \quad (12)$$

Note that with this parameterization, the Green's function is automatically normalized to $\hat{g}^2=-\pi^2\hat{1}$. The coherence functions obey two Riccati equations:

$$(i\hbar\mathbf{v}_F\cdot\nabla + 2z + 2\frac{e}{c}\mathbf{v}_F\cdot\mathbf{A})\gamma = -\tilde{\Delta}\gamma^2 - \Delta, \quad (13)$$

$$(i\hbar\mathbf{v}_F\cdot\nabla - 2z - 2\frac{e}{c}\mathbf{v}_F\cdot\mathbf{A})\tilde{\gamma} = -\Delta\tilde{\gamma}^2 - \tilde{\Delta}, \quad (14)$$

where $\mathbf{A}$ is the vector potential. These first-order non-linear differential equations are solved by integration along straight (ballistic) quasiparticle trajectories. Quantum coherence is retained along these trajectories, but not between neighboring trajectories. A clean superconducting grain in vacuum is assumed by imposing the boundary condition of perfect specular reflection of quasiparticles along the edges of the system.

The superconducting order parameter is assumed to have pure d-wave symmetry

$$\Delta(\mathbf{p}_F,\mathbf{R}) = \Delta_d(\mathbf{R})\eta_d(\theta), \quad (15)$$

where θ is the angle between the Fermi momentum $\mathbf{p}_F$ and the crystal $\hat{\mathbf{a}}$-axis, and $\eta_d(\theta)$ is the d-wave basis function:

$$\eta_d(\theta) = \sqrt{2}\cos(2\theta), \quad (16)$$

fulfilling the normalization condition

$$\int \frac{\mathrm{d}\theta}{2\pi} \left|\eta_\mathrm{d}(\theta)\right|^2 = 1. \tag{17}$$

The order parameter amplitude satisfies the gap equation

$$\Delta_\mathrm{d}(\mathbf{R}) = \lambda_\mathrm{d} N_\mathrm{F} k_\mathrm{B} T \sum_{|\epsilon_n| \le \Omega_\mathrm{c}} \int \frac{\mathrm{d}\theta}{2\pi} \eta^*_\mathrm{d}(\theta) f(\mathbf{p}_\mathrm{F}, \mathbf{R}; \epsilon_n), \tag{18}$$

where λ_d is the pairing interaction, N_F is the density of states at the Fermi level in the normal state, and Ω_c is a cutoff energy. The pairing interaction and the cutoff energy are eliminated in favor of the superconducting transition temperature T_c (see for example ref. [66]) as

$$\frac{1}{\lambda_\mathrm{d} N_\mathrm{F}} = \ln \frac{T}{T_\mathrm{c}} + \sum_{n \ge 0} \frac{1}{n + \frac{1}{2}}. \tag{19}$$

The above equations are solved self-consistently with respect to γ, $\tilde{\gamma}$, and Δ_d. As an initial guess, we assume a homogenous superconductor with a small modulation of the phase. The coherence functions on the boundaries have to be updated in each iteration, taking into account the specular boundary condition. The starting guess is the local homogeneous solution. After several iterations, the information of the initial guess for the coherence functions is lost[67].

We choose an electromagnetic gauge where the vector potential has the form

$$\mathbf{A}_\mathrm{ext}(\mathbf{R}) = \frac{1}{2} \mathbf{B}_\mathrm{ext} \times \mathbf{R}. \tag{20}$$

The total vector potential $\mathbf{A}(\mathbf{R})$, that enters Eqs. (13) and (14), is given by $\mathbf{A}_\mathrm{ext}(\mathbf{R})$ and the field $\mathbf{A}_\mathrm{ind}(\mathbf{R})$ induced by the currents $\mathbf{j}(\mathbf{R})$ in the superconductor (Eq. (27) below):

$$\mathbf{A}(\mathbf{R}) = \mathbf{A}_\mathrm{ext}(\mathbf{R}) + \mathbf{A}_\mathrm{ind}(\mathbf{R}). \tag{21}$$

The vector potential $\mathbf{A}_\mathrm{ind}(\mathbf{R})$ should be solved from Ampère's circuit law

$$\nabla \times \nabla \times \mathbf{A}_\mathrm{ind}(\mathbf{R}) = \frac{4\pi}{c} \mathbf{j}(\mathbf{R}), \tag{22}$$

with appropriate boundary conditions for the induced field inside and outside the sample. To take the full electrodynamics into account, $A_\mathrm{ind}(\mathbf{R})$ also needs to be computed self-consistently in each iteration. However, the strength of the electrodynamic back-coupling scales as κ^{-2}, where $\kappa \equiv \lambda_0/\xi_0$ is the dimensionless Ginzburg-Landau parameter. The electrodynamic back-coupling is therefore a very small effect for type II superconductors (typically $\kappa^{-1} \approx 10^{-2}$ for the cuprates). We have verified through fully self-consistent calculations that for grains with side lengths $D < \lambda$, as we limit ourselves to in this paper, it is always safe to neglect this back-coupling. For large system sizes, $D \gg \lambda$, back-coupling would ensure proper Meissner screening on the length scale λ in the interior for $b < 1$ and the establishment of a proper Abrikosov vortex lattice with inter-vortex distances of order λ for moderate fields $b > 1$, corresponding to field strengths of order $H_{\mathrm{c}1}$. Since the spontaneous fields appearing below T^* are located within a small distance of order $\xi_0 \ll \lambda$ from the boundary, the effect of back-coupling is small also in these cases. Only in very high fields, approaching $H_{\mathrm{c}2}$, where inter-vortex distances become of order ξ_0 may we expect a serious effect on T^*, but this is beyond the scope of this paper.

The induced magnetic flux density is computed as

$$\mathbf{B}_\mathrm{ind} = \nabla \times \mathbf{A}_\mathrm{ind}. \tag{23}$$

We consider a layered superconductor with many weakly, for our purposes negligibly, coupled layers stacked in the c-axis direction. This ensures translational invariance in that direction. Therefore, we neglect the problem of the field distribution around the superconductor and focus on the field induced at the ab-plane where we have simply $\mathbf{B}_\mathrm{ind} = B_\mathrm{ind}\hat{\mathbf{z}}$.

Gauge transformation. Once the Green's function and the order parameter have been determined self-consistently, we can perform a gauge transformation in order to make the order parameter a real quantity and in the process extract the superfluid momentum $\mathbf{p}_\mathrm{s}$. This can be illustrated by transforming the Riccati equation in Eq. (13). To begin with, the self-consistently obtained order parameter is complex, i.e.,

$$\Delta(\mathbf{p}_\mathrm{F}, \mathbf{R}) = |\Delta_\mathrm{d}(\mathbf{R})| \eta_\mathrm{d}(\theta) e^{i\chi(\mathbf{R})}. \tag{24}$$

We make the ansatz

$$\gamma(\mathbf{p}_\mathrm{F}, \mathbf{R}; z) = \gamma_0(\mathbf{p}_\mathrm{F}, \mathbf{R}; z) e^{i\chi(\mathbf{R})}, \tag{25}$$

and put that into the Riccati equation. We obtain

$$[i\hbar \mathbf{v}_\mathrm{F} \cdot \nabla + 2(z - \mathbf{v}_\mathrm{F} \cdot \mathbf{p}_\mathrm{s})]\gamma_0 = -|\Delta_\mathrm{d}| \eta_\mathrm{d}(\gamma_0^2 + 1), \tag{26}$$

where $\mathbf{p}_\mathrm{s}$ is defined in Eq. (1).

Observables. The current density is computed within the Matsubara technique through the formula

$$\mathbf{j}(\mathbf{R}) = 2\pi e N_\mathrm{F} k_\mathrm{B} T \sum_{\epsilon_n} \int \frac{\mathrm{d}\theta}{2\pi} \mathbf{v}_\mathrm{F} g(\mathbf{p}_\mathrm{F}, \mathbf{R}; \epsilon_n). \tag{27}$$

In the results section, we shall show this current density in units of the depairing current

$$j_\mathrm{d} \equiv 4\pi |e| k_\mathrm{B} T_\mathrm{c} N_\mathrm{F} v_\mathrm{F}. \tag{28}$$

The free-energy difference between the superconducting and the normal states is calculated with the Eilenberger free-energy functional[52]

$$\begin{aligned} \Omega_\mathrm{S}(B, T) - \Omega_\mathrm{N}(B, T) = \int \mathrm{d}\mathbf{R} \Big\{ & \tfrac{\mathbf{B}_\mathrm{ind}(\mathbf{R})^2}{8\pi} + |\Delta_\mathrm{d}(\mathbf{R})|^2 N_\mathrm{F} \ln \tfrac{T}{T_\mathrm{c}} \\ & + 2\pi N_\mathrm{F} k_\mathrm{B} T \sum_{\epsilon_n > 0} \Big[\tfrac{|\Delta_\mathrm{d}(\mathbf{R})|^2}{\epsilon_n} + i\mathcal{I}(\mathbf{R}; \epsilon_n) \Big] \Big\}, \end{aligned} \tag{29}$$

$$\mathcal{I}(\mathbf{R}, \epsilon_n) = \int \frac{\mathrm{d}\theta}{2\pi} \left[\tilde{\Delta}(\mathbf{p}_\mathrm{F}, \mathbf{R}) \gamma(\mathbf{p}_\mathrm{F}, \mathbf{R}; \epsilon_n) - \Delta(\mathbf{p}_\mathrm{F}, \mathbf{R}) \tilde{\gamma}(\mathbf{p}_\mathrm{F}, \mathbf{R}; \epsilon_n) \right]. \tag{30}$$

We have verified that this form of the free energy gives the same results as the Luttinger-Ward functional[26,55,64]. The entropy and specific heat capacity are obtained from the thermodynamic definitions

$$S = -\frac{\partial \Omega}{\partial T}, \tag{31}$$

$$C = T \frac{\partial S}{\partial T} = -T \frac{\partial^2 \Omega}{\partial T^2}. \tag{32}$$

Data availability. All relevant data are available from the authors.

Received: 13 December 2017 Accepted: 1 May 2018

References

1. Gol'tsman, G. N. et al. Picosecond superconducting single-photon optical detector. *Appl. Phys. Lett.* **79**, 705–707 (2001).
2. De Franceschi, S., Kouwenhoven, L., Schönenberger, C. & Wernsdorfer, W. Hybrid superconductor-quantum dot devices. *Nat. Nanotechnol.* **5**, 703–711 (2010).
3. Welp, U., Kadowaki, K. & Kleiner, R. Superconducting emitters of THz radiation. *Nat. Photonics* **7**, 702–710 (2013).
4. Fornieri, A. & Giazotto, F. Towards phase-coherent caloritronics in superconducting circuits. *Nat. Nanotechnol.* **12**, 944–952 (2017).
5. Gustafsson, D. et al. Fully gapped superconductivity in a nanometre-size $YBa_2Cu_3O_{7-\delta}$ island enhanced by a magnetic field. *Nat. Nanotechnol.* **8**, 25–30 (2012).
6. Kashiwaya, S. & Tanaka, Y. Tunnelling effects on surface bound states in unconventional superconductors. *Rep. Prog. Phys.* **63**, 1641–1724 (2000).
7. Löfwander, T., Shumeiko, V. S. & Wendin, G. Andreev bound states in high-T_c superconducting junctions. *Supercond. Sci. Technol.* **14**, R53–R77 (2001).
8. Baghdadi, R. et al. Fabricating nanogaps in $YBa_2Cu_3O_{7-\delta}$ for hybrid proximity-based Josephson junctions. *Phys. Rev. Appl.* **4**, 014022 (2015).
9. Xie, M. et al. Improved coupling of nanowire-based high-T_c SQUID magnetometers-simulations and experiments. *Supercond. Sci. Technol.* **30**, 115014 (2017).
10. Hu, C.-R. Midgap surface states as a novel signature for -wave superconductivity. *Phys. Rev. Lett.* **72**, 1526–1529 (1994).
11. Sato, M., Tanaka, Y., Yada, K. & Yokoyama, T. Topology of Andreev bound states with flat dispersion. *Phys. Rev. B* **83**, 224511 (2011).

12. Nagai, Y., Ota, Y. & Tanaka, K. Time-reversal symmetry breaking and gapped surface states due to spontaneous emergence of new order in *d*-wave nanoislands. *Phys. Rev. B* **96**, 060503 (2017).
13. Matsumoto, M. & Shiba, H. Coexistence of different symmetry order parameters near a surface in *d*-wave superconductors I. *J. Phys. Soc. Jpn.* **64**, 3384–3396 (1995).
14. Fogelström, M., Rainer, D. & Sauls, J. A. Tunneling into current-carrying surface states of high-T_c superconductors. *Phys. Rev. Lett.* **79**, 2754–2754 (1997).
15. Sigrist, M. Time-reversal symmetry breaking states in high-temperature superconductors. *Progr. Theor. Phys.* **99**, 899–929 (1998).
16. Honerkamp, C., Wakabayashi, K. & Sigrist, M. Instabilities at [110] surfaces of superconductors. *Europhys. Lett.* **50**, 368–374 (2007).
17. Potter, A. C. & Lee, P. A. Edge ferromagnetism from Majorana flat bands: application to split tunneling-conductance peaks in high-T_c cuprate superconductors. *Phys. Rev. Lett.* **112**, 117002 (2014).
18. Higashitani, S. Mechanism of paramagnetic Meissner effect in high-temperature superconductors. *J. Phys. Soc. Jpn.* **66**, 2556–2559 (1997).
19. Barash, Y. S., Kalenkov, M. S. & Kurkijarvi, J. Low-temperature magnetic penetration depth in d-wave superconductors: zero-energy bound state and impurity effects. *Phys. Rev. B* **62**, 6665–6673 (2000).
20. Löfwander, T., Shumeiko, V. S. & Wendin, G. Time-reversal symmetry breaking at Josephson tunnel junctions of purely *d*-wave superconductors. *Phys. Rev. B* **62**, R14653–R14656 (2000).
21. Vorontsov, A. B. Broken translational and time-reversal symmetry in unconventional superconducting films. *Phys. Rev. Lett.* **102**, 177001 (2009).
22. Hachiya, M., Aoyama, K. & Ikeda, R. Field-induced reentrant superconductivity in thin films of nodal superconductors. *Phys. Rev. B* **88**, 064519 (2013).
23. Higashitani, S. & Miyawaki, N. Phase transition to a time-reversal symmetry-breaking state in *d*-wave superconducting films with rough surfaces. *J. Phys. Soc. Jpn.* **84**, 033708 (2015).
24. Miyawaki, N. & Higashitani, S. Temperature dependence of the critical thickness of *d*-wave superconducting films. *Phys. Procedia* **65**, 25–28 (2015).
25. Miyawaki, N. & Higashitani, S. Fermi surface effect on spontaneous breaking of time-reversal symmetry in unconventional superconducting films. *Phys. Rev. B* **91**, 094511 (2015).
26. Håkansson, M., Löfwander, T. & Fogelström, M. Spontaneously broken time-reversal symmetry in high-temperature superconductors. *Nat. Phys.* **11**, 755–760 (2015).
27. Holmvall, P., Löfwander, T. & Fogelström, M. Spontaneous generation of fractional vortex-antivortex pairs at single edges of high-T_c superconductors. *J. Phys. Conf. Ser.* **969**, 012037 (2018).
28. Mermin, N. D. The topological theory of defects in ordered media. *Rev. Mod. Phys.* **51**, 591–648 (1979).
29. Effenberger, F. & Weiskopf, D. Finding and classifying critical points of 2D vector fields: a cell-oriented approach using group theory. *Comput. Vis. Sci.* **13**, 377–396 (2011).
30. Salomaa, M. M. & Volovik, G. E. Quantized vortices in superfluid ^{3}He. *Rev. Mod. Phys.* **59**, 533–613 (1987).
31. Walter, H. et al. Low-temperature anomaly in the penetration depth of $\mathrm{YBa_2Cu_3O_7}$ films: evidence for Andreev bound states at surfaces. *Phys. Rev. Lett.* **80**, 3598–3601 (1998).
32. Suzuki, S.-I. & Asano, Y. Paramagnetic instability of small topological superconductors. *Phys. Rev. B* **89**, 184508 (2014).
33. Gottlieb, D. H. & Samaranayake, G. The index of discontinuous vector fields. *New York J. Math.* **1**, 130–148 (1995).
34. Jubin, B. A generalized Poincaré-Hopf index theorem. Preprint at http://arxiv.org/abs/0903.0697v2 (2009).
35. Holmvall, P. *Modeling mesoscopic unconventional superconductors*. Licentiate thesis, Chalmers University of Technology https://research.chalmers.se/publication/253315 (2017).
36. Vasyukov, D. et al. A scanning superconducting quantum interference device with single electron spin sensitivity. *Nat. Nanotechnol.* **8**, 639–644 (2013).
37. Pelliccione, M. et al. Scanned probe imaging of nanoscale magnetism at cryogenic temperatures with a single-spin quantum sensor. *Nat. Nanotechnol.* **11**, 700–705 (2016).
38. Watashige, T. et al. Evidence for time-reversal symmetry breaking of the superconducting state near twin-boundary interfaces in FeSe revealed by scanning tunneling spectroscopy. *Phys. Rev. X* **5**, 031022 (2015).
39. Wang, J., Meir, Y. & Gefen, Y. Spontaneous breakdown of topological protection in two dimensions. *Phys. Rev. Lett.* **118**, 046801 (2017).
40. Kirtley, J. R. et al. Angle-resolved phase-sensitive determination of the in-plane gap symmetry in $\mathrm{YBa_2Cu_3O_{7-\delta}}$. *Nat. Phys.* **2**, 190–194 (2005).
41. Saadaoui, H. et al. Search for broken time-reversal symmetry near the surface of superconducting $\mathrm{YBa_2Cu_3O_{7-\delta}}$ films using β-detected nuclear magnetic resonance. *Phys. Rev. B* **83**, 054504 (2011).
42. Covington, M. et al. Observation of surface-induced broken time-reversal symmetry in $\mathrm{YBa_2Cu_3O_7}$ tunnel junctions. *Phys. Rev. Lett.* **79**, 277–280 (1997).
43. Dagan, Y. & Deutscher, G. Doping and magnetic field dependence of in-plane tunneling into $\mathrm{YBa_2Cu_3O_{7-x}}$: possible evidence for the existence of a quantum critical point. *Phys. Rev. Lett.* **87**, 177004 (2001).
44. Elhalel, G., Beck, R., Leibovitch, G. & Deutscher, G. Transition from a mixed to a pure *d*-wave symmetry in superconducting optimally doped $\mathrm{YBa_2Cu_3O_{7-x}}$ thin films under applied fields. *Phys. Rev. Lett.* **98**, 137002 (2007).
45. Neils, W. K. & Van Harlingen, D. J. Experimental test for subdominant superconducting phases with complex order parameters in cuprate grain boundary junctions. *Phys. Rev. Lett.* **88**, 047001 (2002).
46. Deutscher, G. Andreev–Saint-James reflections: a probe of cuprate superconductors. *Rev. Mod. Phys.* **77**, 109–135 (2005).
47. Krishana, K., Ong, N. P., Li, Q., Gu, G. D. & Koshizuka, N. Plateaus observed in the field profile of thermal conductivity in the superconductor $\mathrm{Bi_2Sr_2CaCu_2O_8}$. *Science* **277**, 83–85 (1997).
48. Diao, Z. et al. Microscopic parameters from high-resolution specific heat measurements on superoptimally substituted $\mathrm{BaFe_2(As_{1-x}P_x)_2}$ single crystals. *Phys. Rev. B* **93**, 014509 (2016).
49. Ma, T. & Wang, S. A generalized Poincaré-Hopf index formula and its applications to 2-D incompressible flows. *Nonlinear Anal. Real World Appl.* **2**, 467–482 (2001).
50. Kleman, M. & Lavrentovich, O. D. *Soft Matter Physics: An Introduction*. (Springer New York, New York, 2004).
51. Volovik, G. E. *The Universe In a Helium Droplet*. (Oxford University Press, Oxford, 2010).
52. Eilenberger, G. Transformation of Gorkov's equation for type II superconductors into transport-like equations. *Z. Phys.* **214**, 195–213 (2005).
53. Larkin, A. I. & Ovchinnikov, Y. N. Quasiclassical method in the theory of superconductivity. *Sov. Phys. JETP* **28**, 1200–1205 (1969).
54. Shelankov, A. L. On the derivation of quasiclassical equations for superconductors. *J. Low Temp. Phys.* **60**, 29–44 (1985).
55. Serene, J. W. & Rainer, D. The quasiclassical approach to superfluid ^{3}He. *Phys. Rep.* **101**, 221–311 (1983).
56. Eschrig, M., Heym, Jr & Rainer, D. Corrections to Fermi-liquid theory of correlated metals. *J. Low Temp. Phys.* **95**, 323–327 (1994).
57. Eschrig, M., Rainer, D. & Sauls, J. A. Effects of strong magnetic fields on pairing fluctuations in high-temperature superconductors. *Phys. Rev. B* **59**, 12095–12113 (1999).
58. Sauls, J. A. & Eschrig, M. Vortices in chiral, spin-triplet superconductors and superfluids. *New J. Phys.* **11**, 075008 (2009).
59. Nagato, Y., Nagai, K. & Hara, J. Theory of the Andreev reflection and the density of states in proximity contact normal-superconducting infinite double-layer. *J. Low Temp. Phys.* **93**, 33–56 (1993).
60. Schopohl, N. & Maki, K. Quasiparticle spectrum around a vortex line in a *d*-wave superconductor. *Phys. Rev. B* **52**, 490–493 (1995).
61. Schopohl, N. Transformation of the Eilenberger equations of superconductivity to a scalar Riccati equation. Preprint at http://arxiv.org/abs/cond-mat/9804064v1 (1998).
62. Eschrig, M., Sauls, J. A. & Rainer, D. Electromagnetic response of a vortex in layered superconductors. *Phys. Rev. B* **60**, 10447–10454 (1999).
63. Eschrig, M. Distribution functions in nonequilibrium theory of superconductivity and Andreev spectroscopy in unconventional superconductors. *Phys. Rev. B* **61**, 9061–9076 (2000).
64. Vorontsov, A. B. & Sauls, J. A. Thermodynamic properties of thin films of superfluid ^{3}He-A. *Phys. Rev. B* **68**, 064508 (2003).
65. Eschrig, M. Scattering problem in nonequilibrium quasiclassical theory of metals and superconductors: general boundary conditions and applications. *Phys. Rev. B* **80**, 134511 (2009).
66. Grein, R., Löfwander, T. & Eschrig, M. Inverse proximity effect and influence of disorder on triplet supercurrents in strongly spin-polarized ferromagnets. *Phys. Rev. B* **88**, 054502 (2013).
67. Nagai, Y., Tanaka, K. & Hayashi, N. Quasiclassical numerical method for mesoscopic superconductors: bound states in a circular d-wave island with a single vortex. *Phys. Rev. B* **86**, 094526 (2012).

Acknowledgements

We thank the Swedish Research Council for financial support. It is a pleasure to thank Mikael Håkansson, Niclas Wennerdal, and Per Rudquist for valuable discussions.

Author contributions

P.H. carried out the numerical calculations. P.H., A.B.V., M.F., and T.L. analyzed the results. P.H. and T.L. wrote the paper with contributions from A.B.V. and M.F.

Additional information

Supplementary Information accompanies this paper at https://doi.org/10.1038/s41467-018-04531-y.

Competing interests: The authors declare no competing interests.

Paper II: Supplementary Information

Broken translational symmetry at edges of high-temperature superconductors

Holmvall *et al.*

Supplementary Figures

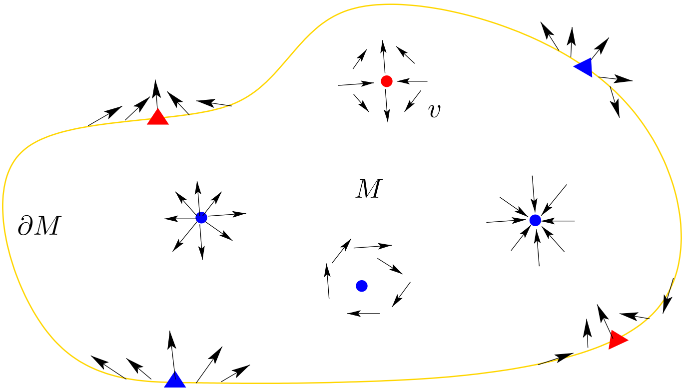

Supplementary Figure 1: **Schematic representations of typical critical points.** The critical points of the $\hat{\mathbf{p}}_{\mathrm{s}}(\mathbf{R})$ vector field inside the manifold are denoted by blue (+1) and red (−1) dots. For the critical points of the tangent field on the boundary of the manifold we use blue (+1) and red (−1) triangles. The triangle tip points inside or outside depending on the direction of the normal field at the critical point of the tangent field. The inside-pointing indices come with (+1/2) weight, whereas outside-pointing ones come with (−1/2) weight in the general expression Eq. (3) of the main text.

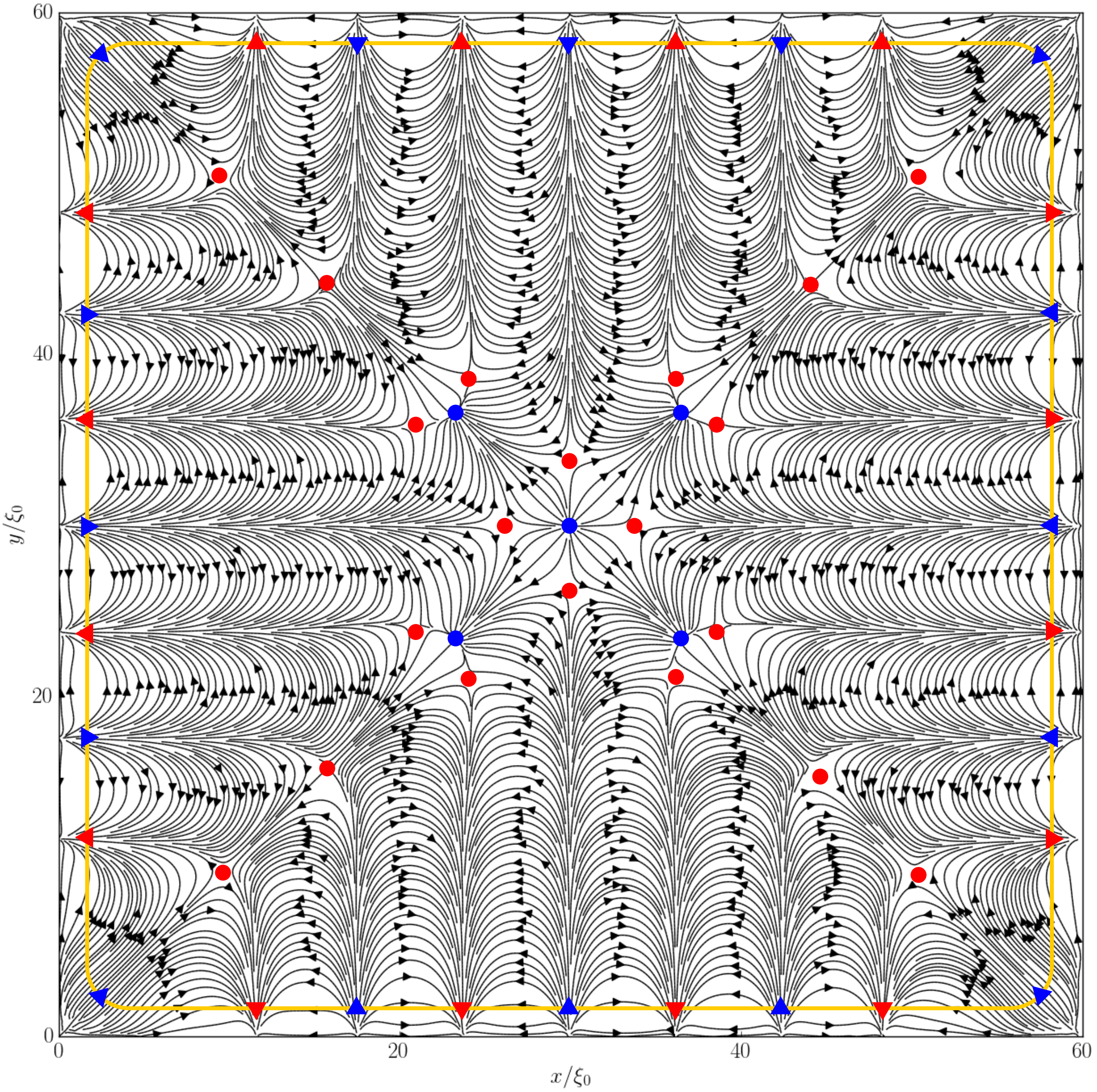

Supplementary Figure 2: **Critical points in the superflow vector field.** The indices of the critical points inside the volume are related to the critical points on the edge of the sample through the generalized Poincaré-Hopf theorem. We define a manifold boundary that circles the sample just inside the physical edge. It passes close enough to the sources and sinks of the superflow at the edge of the sample so that the critical points of the tangent field are determined by these. The 16 blue triangles indicate boundary critical points with index +1 and $\mathbf{p}_\mathrm{s}$ field pointing inwards, while the 16 red triangles mark boundary critical points with index −1 and field pointing outwards. The red dots in the interior mark 20 saddle points (index $I = -1$ each) while the 5 blue dots mark sources or sinks (index $I = +1$ each).

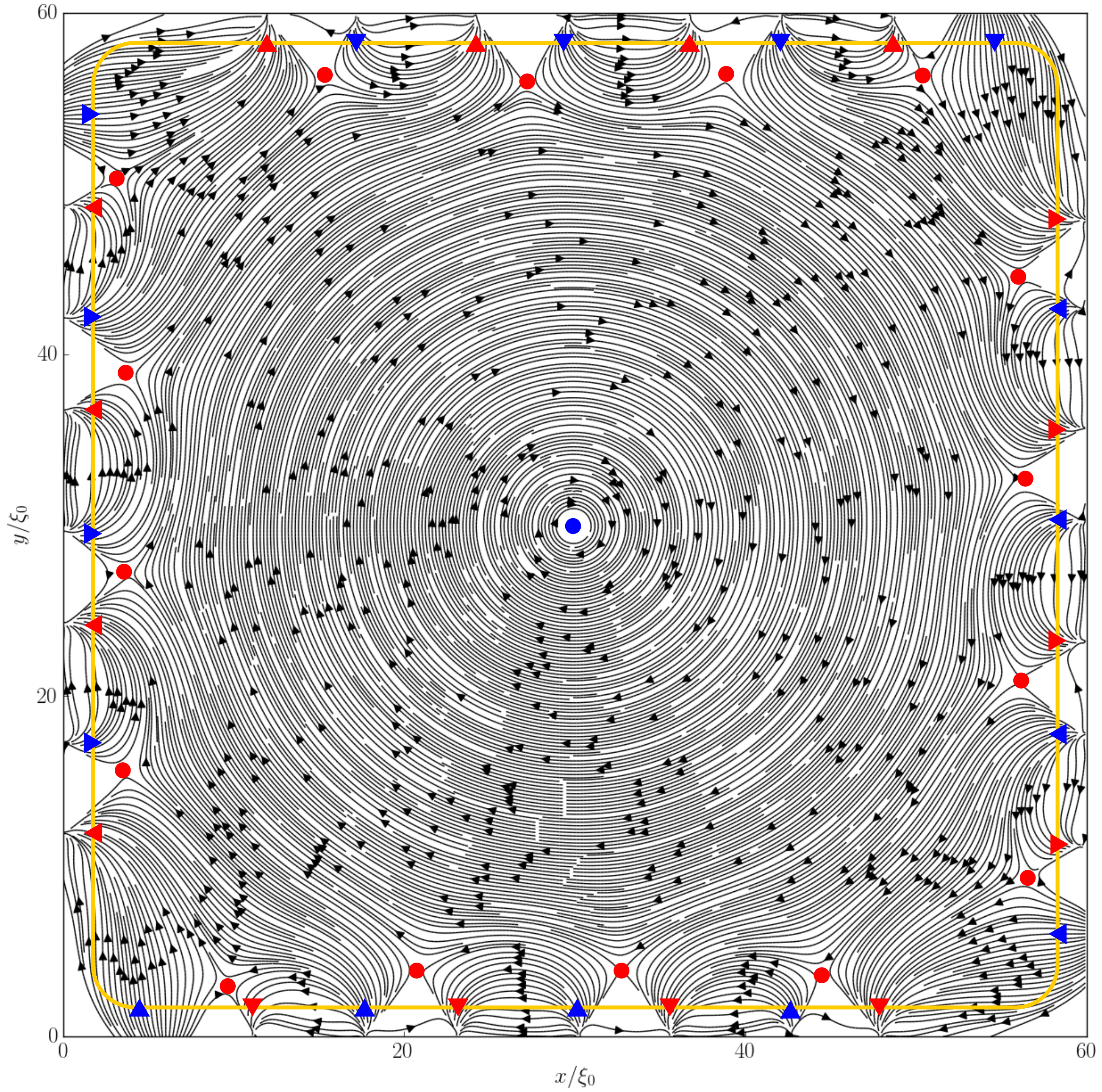

Supplementary Figure 3: **Critical points in uniform external magnetic field.** Critical points for a square grain with a uniform external magnetic field $B_{\mathrm{ext}} = 0.5B_{\mathrm{g1}}$, where $B_{\mathrm{g1}} = \Phi_0/\mathcal{A}$ with flux quantum Φ_0 over the grain area $\mathcal{A} = 60\xi_0 \times 60\xi_0$. The Poincaré indices inside the boundary sum to $1 - 16 = -15$ due to 1 center (blue dot) and the 16 saddle points (red dots), while it sums to $[16 \times (+1) - 16 \times (-1)]/2 = +16$ on the boundary. The total index thus sums to the expected Euler characteristics for a square $16 - 15 = 1 = \chi(\mathrm{square})$. Note that the absence of certain field lines is a technical shortcoming of the software used for plotting. See the corresponding quiver plot in Supplementary Figure **4** for greater detail.

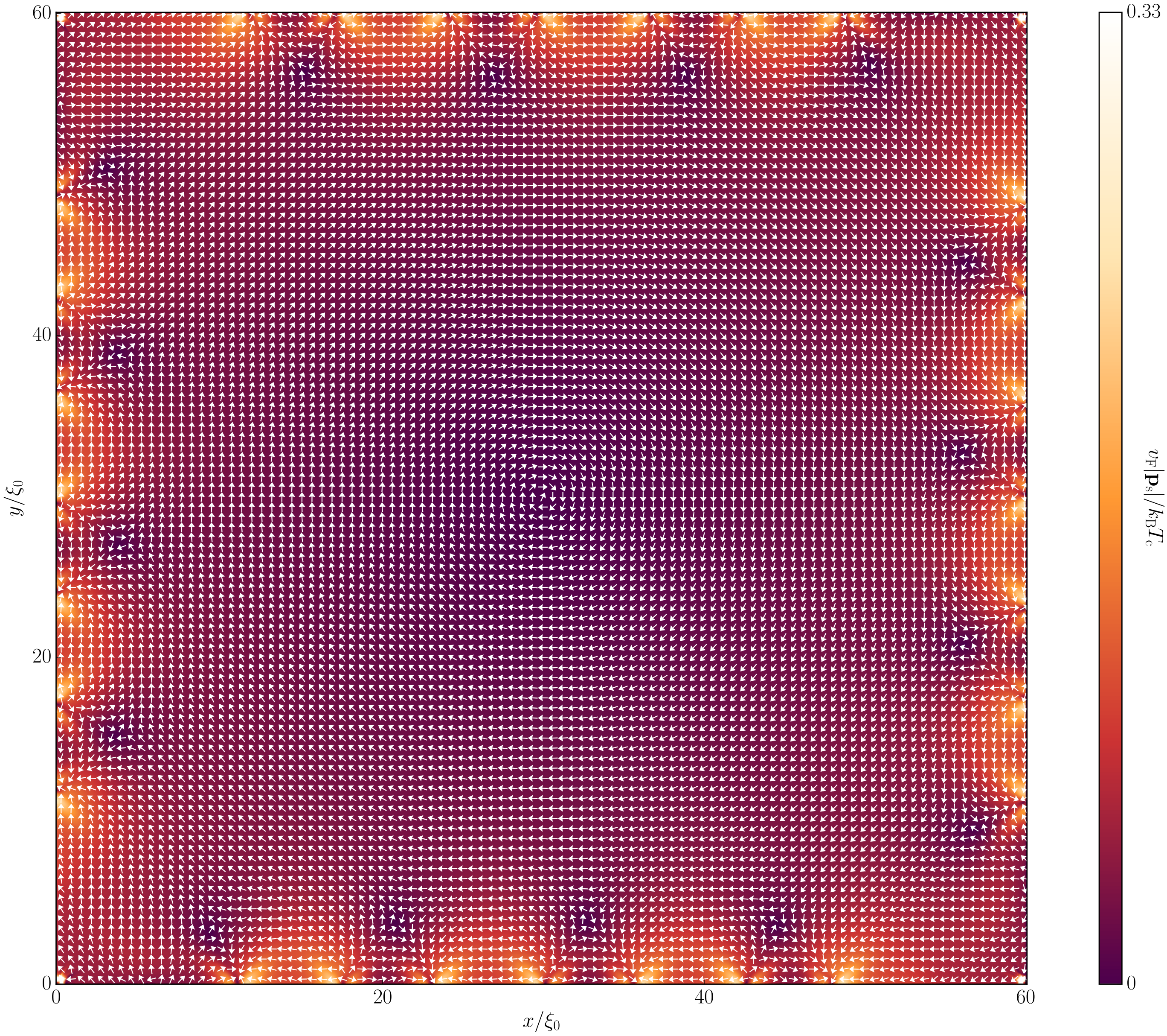

Supplementary Figure 4: **Superflow field in uniform external magnetic field.** The magnitude and direction of $\mathbf{p}_{\mathrm{s}}(\mathbf{R})$ from Supplementary Figure **3**.

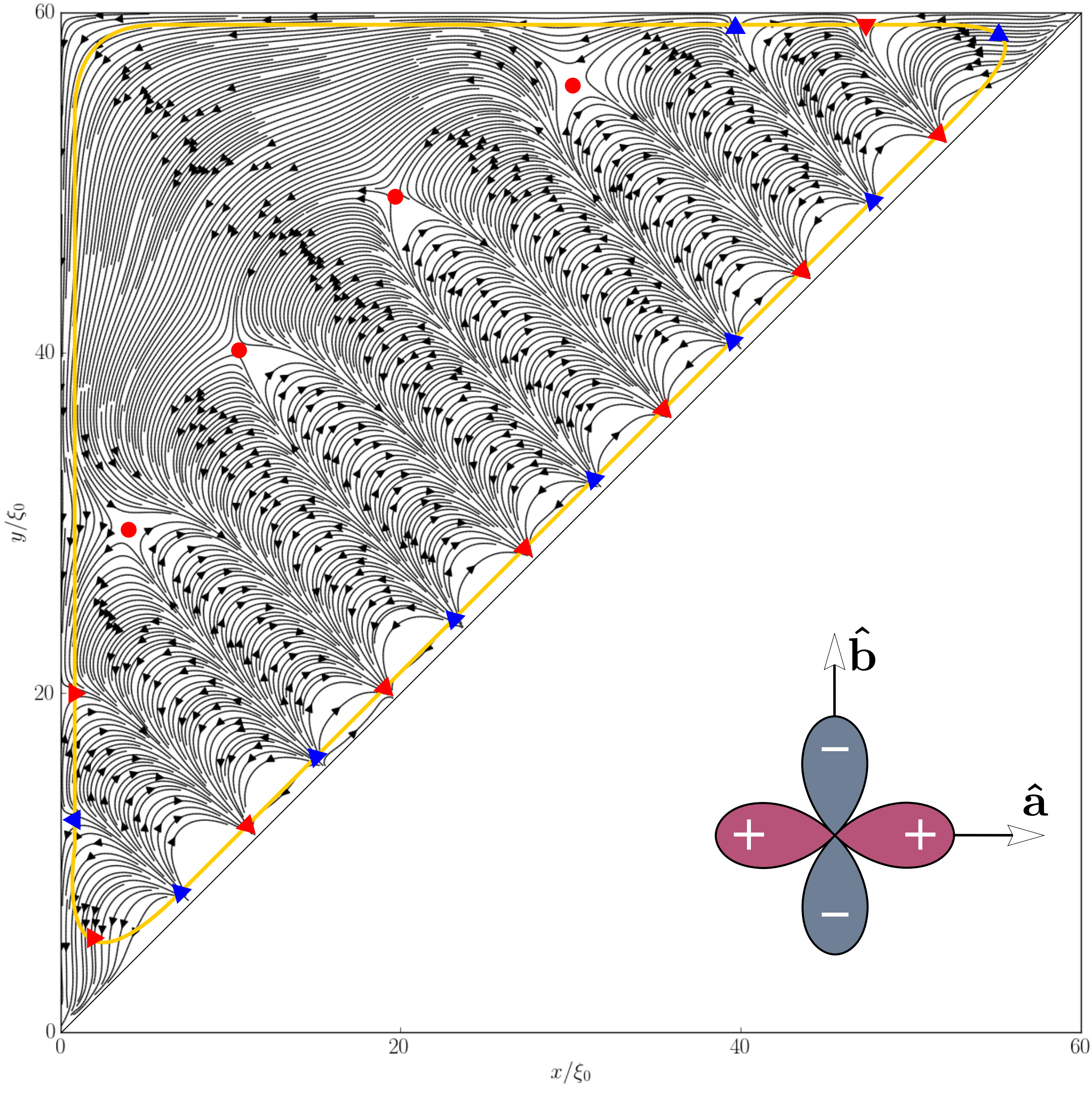

Supplementary Figure 5: **Critical points for a triangular grain.** For the triangle with the crystal *ab*-axes oriented as indicated in the drawing, we have a single pair breaking edge. The Poincaré indices inside the boundary sum to $4 \times (-1) = -4$ due to the 4 saddle points (red dots), while it sums to $[7 \times (+1) + 2 \times (-1) - 2 \times (+1) - 7 \times (-1)]/2 = 5$ on the boundary. The total index thus sums to the expected Euler characteristics for the triangle $5 - 4 = 1 = \chi(\text{triangle})$.

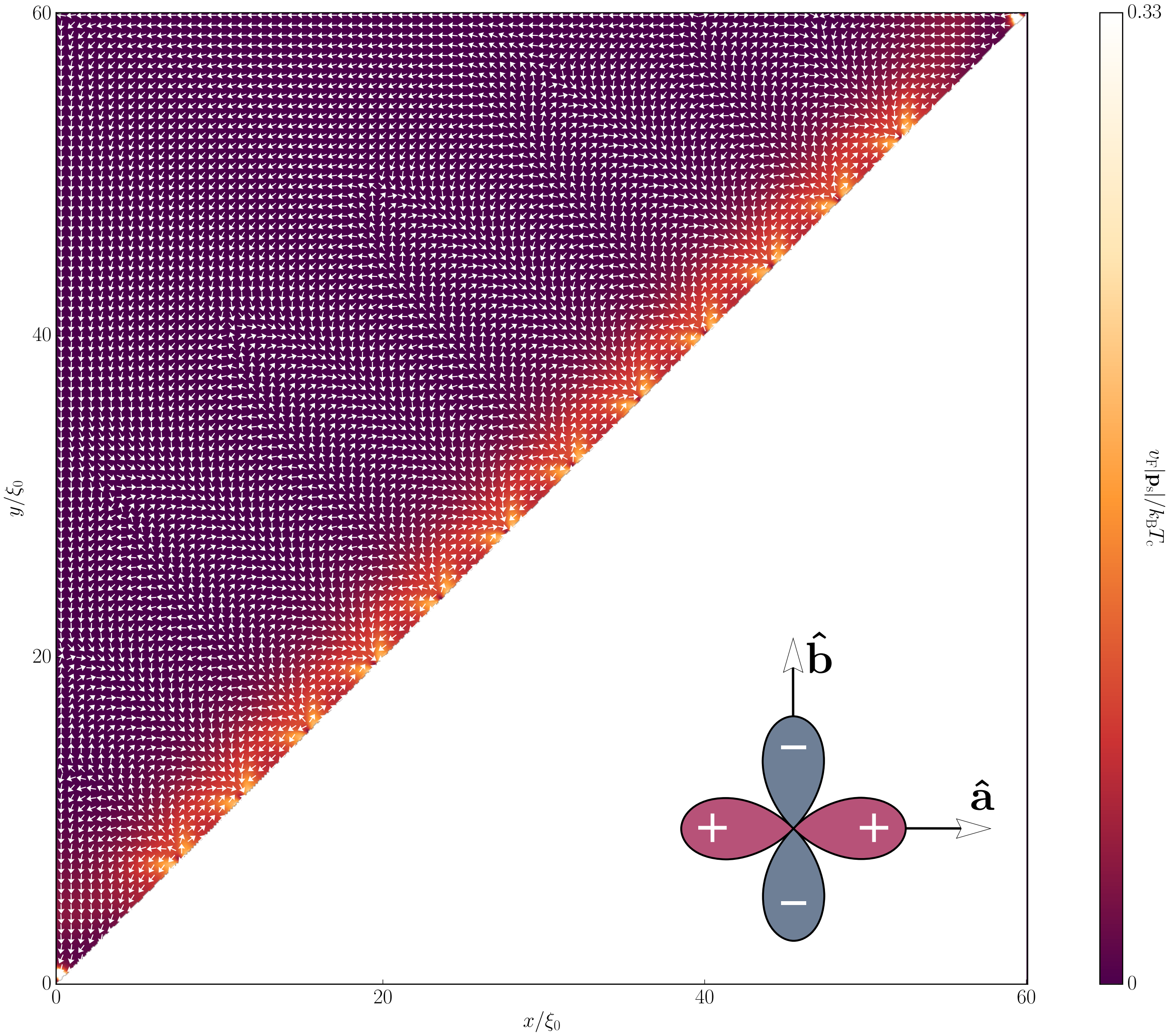

Supplementary Figure 6: **Superflow field for a triangular grain.** The magnitude and direction of $\mathbf{p}_\mathrm{s}(\mathbf{R})$ from Supplementary Figure **5**.

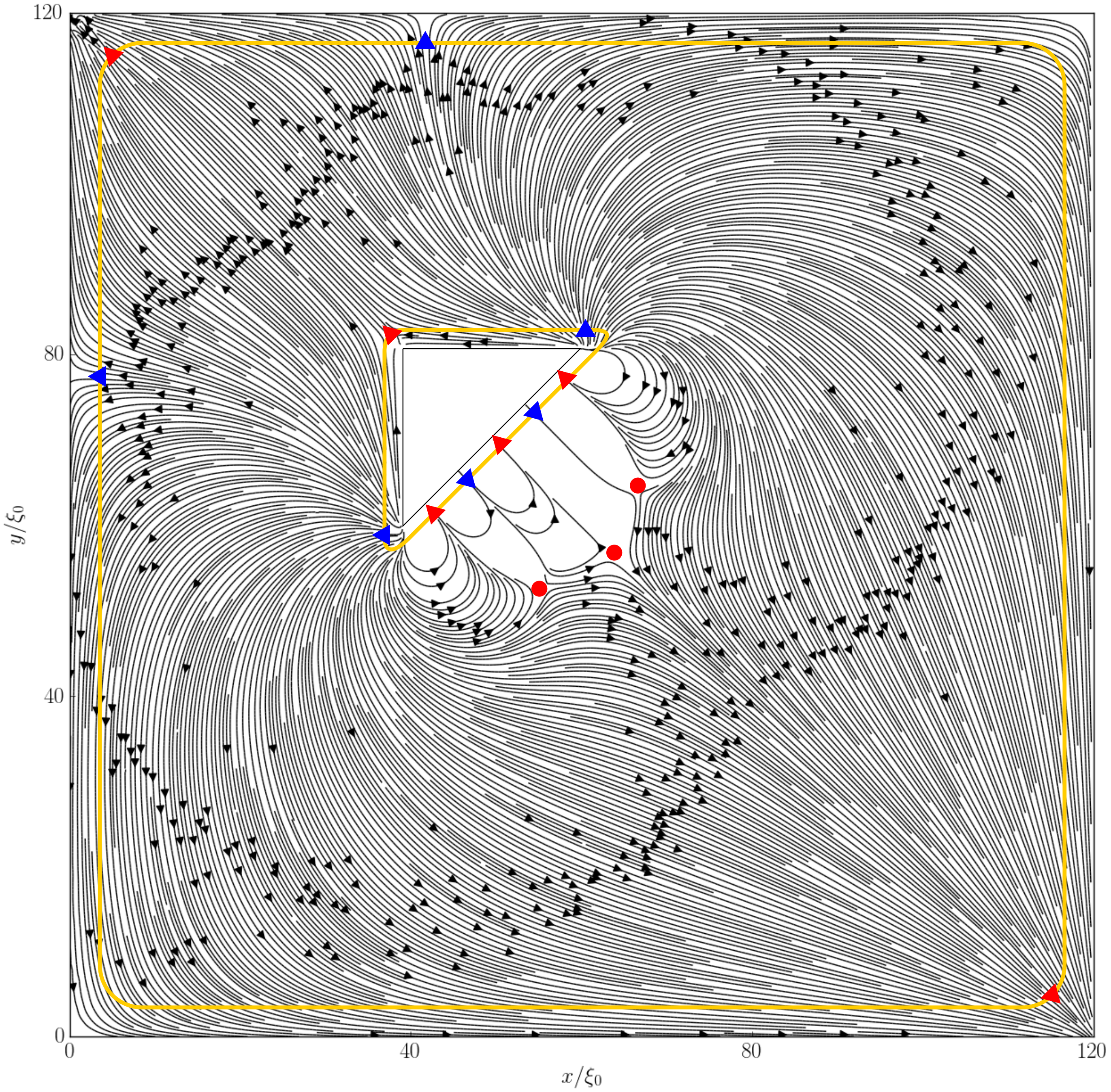

Supplementary Figure 7: **Critical points for a square grain with a hole.** The Poincaré indices between the outer and inner boundaries sum to $3 \times (-1) = -3$ due to the 3 saddle points (red dots), while it sums to $[-2 \times (+1) - 2 \times (-1)]/2 = 0$ on the outer boundary and $[4 \times (+1) + 1 \times (-1) - 3 \times (-1)]/2 = 3$ on the inner boundary. The total index thus sums to the expected Euler characteristics for a square with one hole $3 - 3 + 0 = 0 = \chi(\text{square} + 1\text{ hole})$.

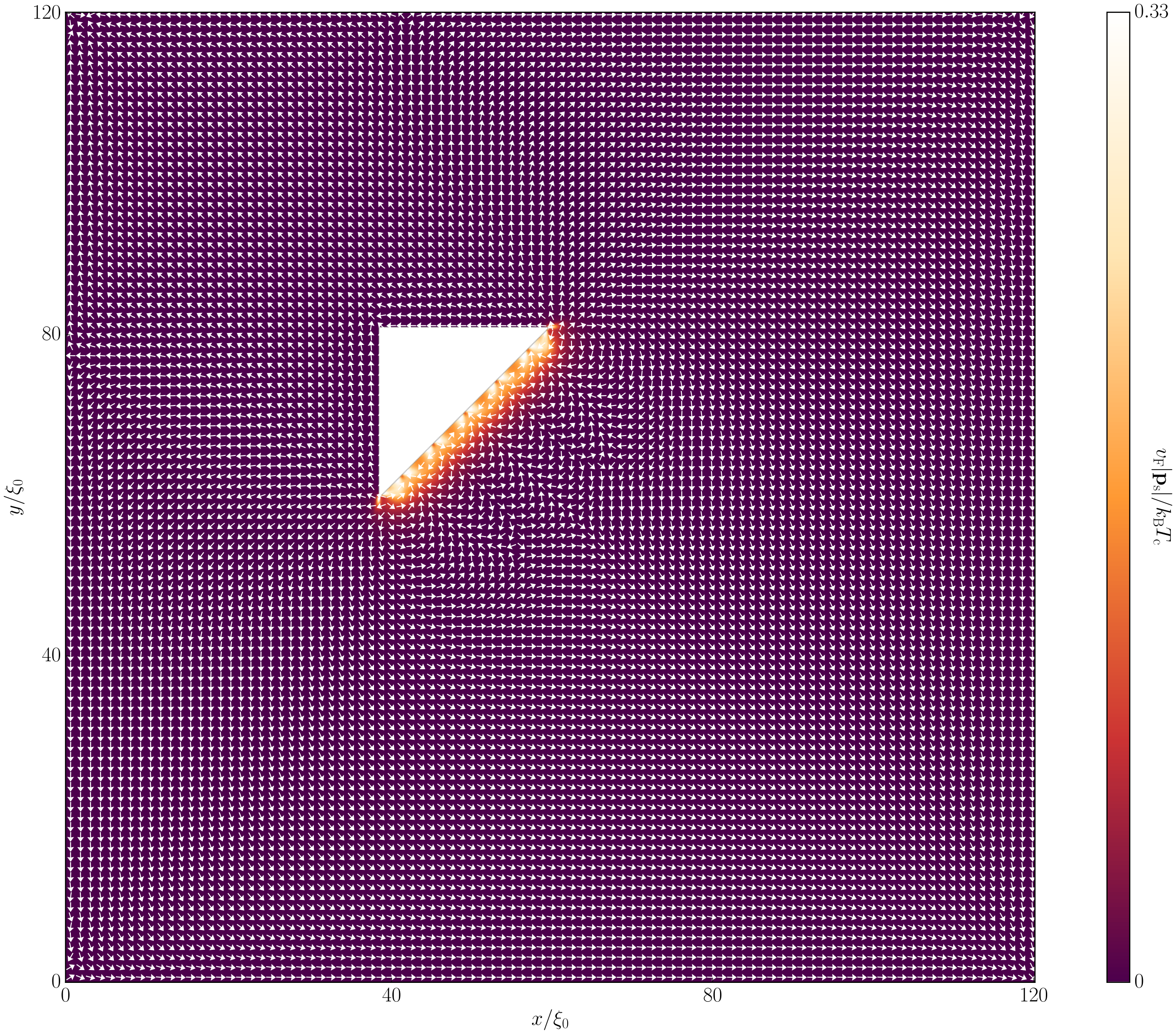

Supplementary Figure 8: **Superflow field for a square grain with a hole.** The magnitude and direction of $\mathbf{p}_s(\mathbf{R})$ from Supplementary Figure **7**.

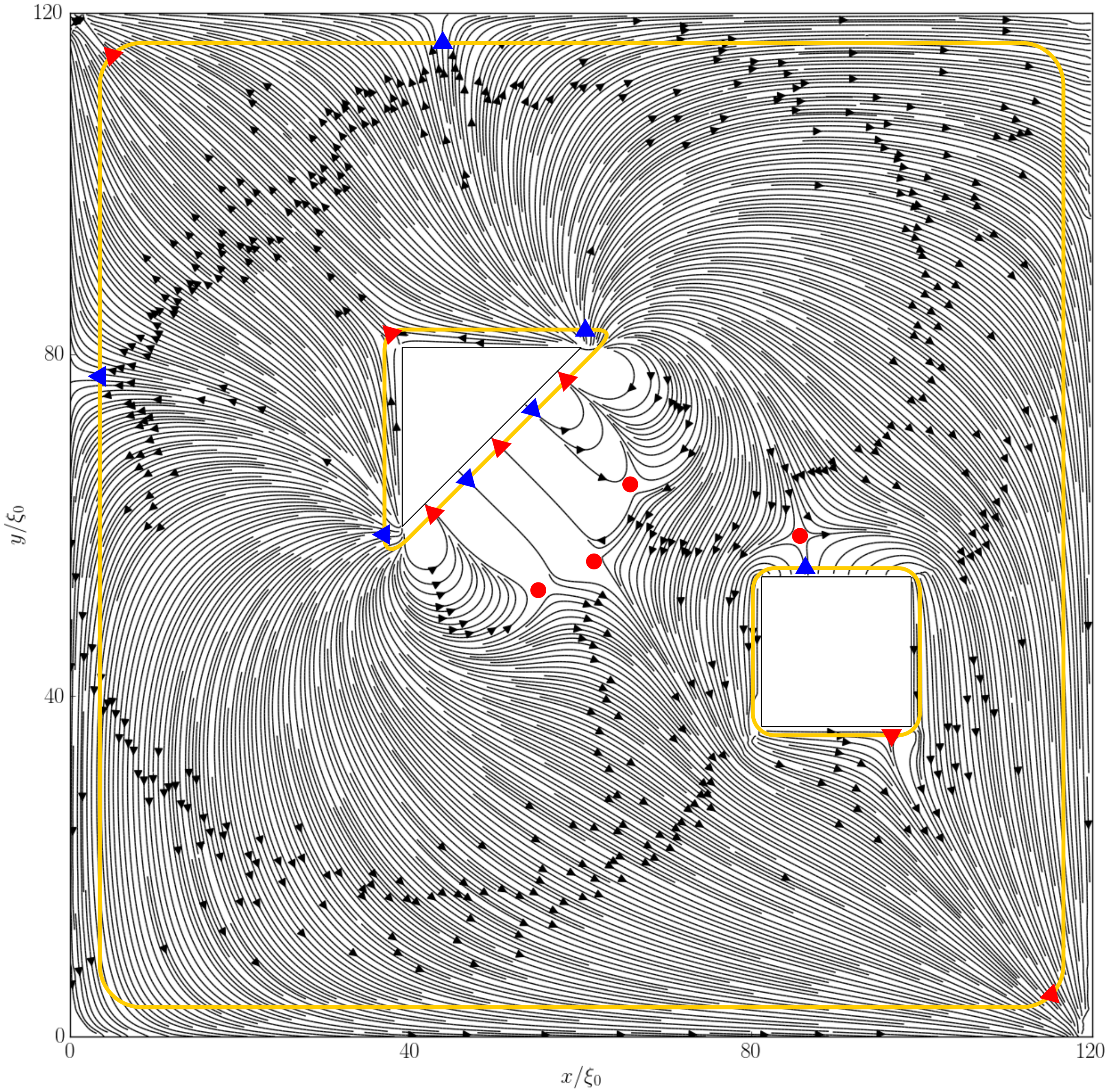

Supplementary Figure 9: **Critical points for a square grain with two holes.** The Poincaré indices between the outer and inner boundaries sum to $4 \times (-1) = -4$ due to the 4 saddle points (red dots), while it sums to $[-2 \times (+1) - 2 \times (-1)]/2 = 0$ on the outer boundary, $[4 \times (+1) + 1 \times (-1) - 3 \times (-1)]/2 = 3$ on the inner triangular boundary, and $(1 \times (+1) + 1 \times (-1))/2 = 0$ on the inner square boundary. The total index thus sums to the expected Euler characteristics for a square with two holes $3 - 4 + 0 + 0 = -1 = \chi(\text{square} + 2\text{ holes})$.

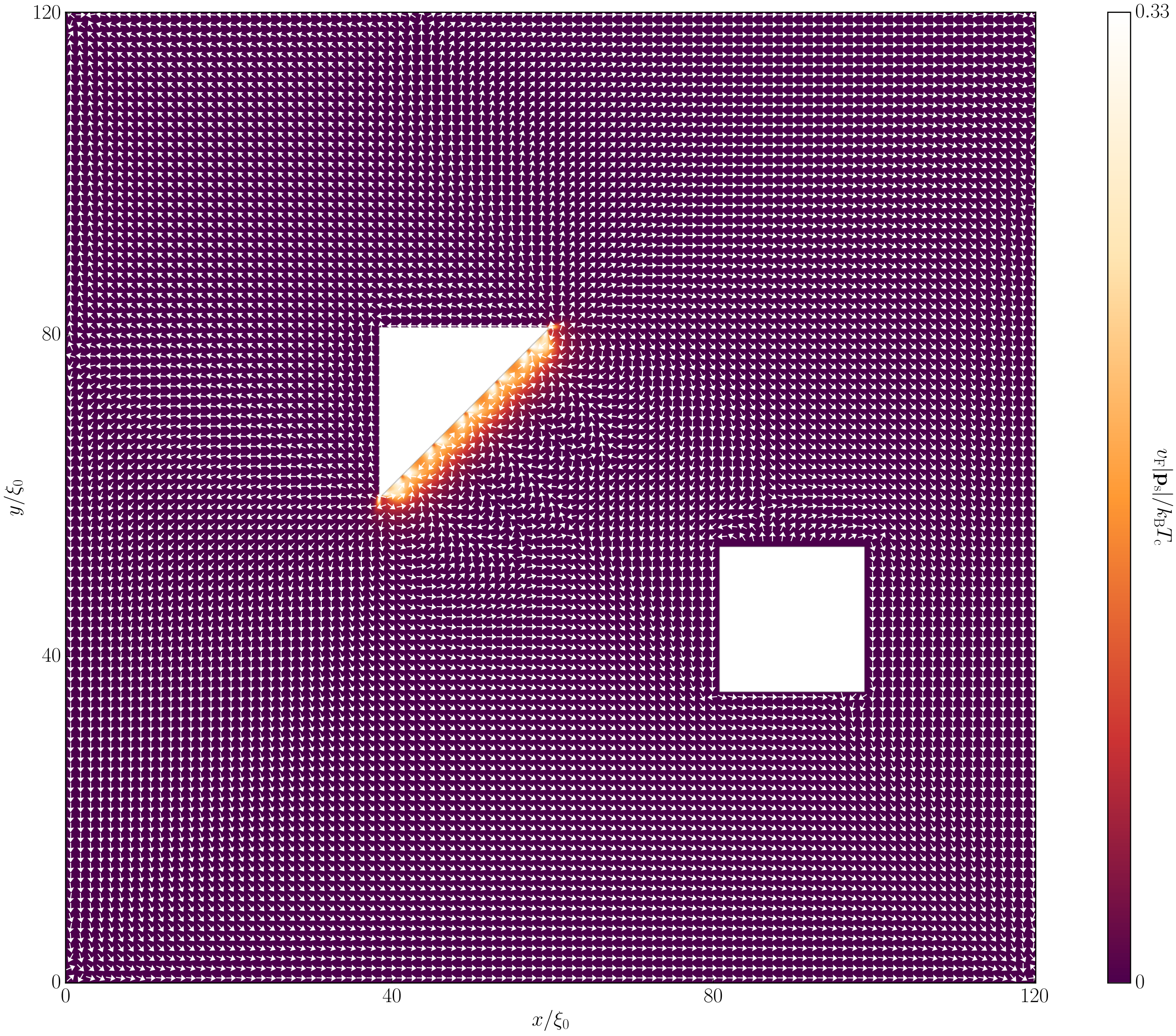

Supplementary Figure 10: **Superflow field for a square grain with two holes.** The magnitude and direction of $\mathbf{p}_s(\mathbf{R})$ from Supplementary Figure **9**.

Supplementary Notes

Supplementary Note 1. The Poincaré-Hopf theorem at work

We apply the generalized Poincaré-Hopf theorem to the vector field $\mathbf{p}_\mathrm{s}(\mathbf{R})$ of the new phase described in the main text, for various geometries and manifolds. In Supplementary Figure **2** we present the same vector field $\mathbf{p}_\mathrm{s}(\mathbf{R})$ as in Fig. 1 in the main text, but this time as a streamline plot. The locations of internal, two-dimensional, critical points are marked by colored dots, where the Poincaré index of saddle points is $I = -1$ (red dots), while the index for sinks, sources and centers is $I = +1$ (blue dots), see Supplementary Figure **1**. In Supplementary Figure **2**, these internal indices sum up to -15. In the formulation of the theorem, we are instructed to draw a boundary a small distance away from the sample edge, see the orange line. The one-dimensional critical points on this boundary, where the tangent vector of the field vanishes, are marked with colored triangles. These critical points are sinks (red triangles) and sources (blue triangles) with Poincaré indices $I = -1$ and $I = +1$, respectively. The direction of the triangle denotes the direction of the perpendicular vector, and hence if the index of the critical point is to be added ($\mathbf{p}_\mathrm{s}$ flowing in) or subtracted ($\mathbf{p}_\mathrm{s}$ flowing out). We count $16 \times (+1)$ critical points on the boundary with $\mathbf{p}_\mathrm{s}$ flowing in, and $16 \times (-1)$ points with $\mathbf{p}_\mathrm{s}$ flowing out. The theorem Eq. (3) in the main text gives

$$-15 + \frac{1}{2}\Big[16 - (-16)\Big] = 1 = \chi(\text{square}),$$

where the Euler characteristic of a square is $\chi(\text{square}) = 1$. Supplementary Figures **3** and **4** show that the theorem holds in the presence of an external magnetic field, while Supplementary Figures **5** and **6** show that it holds for other manifolds of the same kind, e.g. a triangle with a single pair-breaking edge, $\chi(\text{triangle}) = 1$.

To demonstrate that the theorem holds for other kinds of manifolds, superconducting grains with one and two holes are studied in a similar manner in Supplementary Figures **7**–**10**. For every hole that is added to the geometry, an additional boundary has to be drawn close around each additional hole, and the theorem states that the total Euler characteristic is reduced by one for each hole, i.e. $\chi(\text{square} + N \text{ holes}) = 1 - N$. Note that in contrast to the grains in the main paper and in Supplementary Figures **2**–**4**, where the crystal *ab*-axes are rotated 45° with respect to the outer edges of the system, the crystal *ab*-axes are aligned with the outer edges in Supplementary Figures **5**–**10**.

One of the consequences of the Poincaré-Hopf theorem is that the edges of a superconductor will host an even number of special points of the superflow field. This follows from the fact that all the indices are ± 1 and the Euler characteristic is an integer too. How these critical points of the superflow field distribute themselves on the edge, depends on the shape of the sample and geometrical symmetries.

Paper III

PHYSICAL REVIEW B **99**, 184511 (2019)

Spontaneous symmetry breaking at surfaces of *d*-wave superconductors: Influence of geometry and surface ruggedness

P. Holmvall,[1,*] A. B. Vorontsov,[2] M. Fogelström,[1] and T. Löfwander[1]
[1]*Department of Microtechnology and Nanoscience (MC2), Chalmers University of Technology, SE-41296 Göteborg, Sweden*
[2]*Department of Physics, Montana State University, Bozeman, Montana 59717, USA*

(Received 20 February 2019; revised manuscript received 2 May 2019; published 22 May 2019)

Surfaces of *d*-wave superconductors may host a substantial density of zero-energy Andreev states. The zero-energy flat band appears due to a topological constraint, but comes with a cost in free energy. We have recently found that an adjustment of the surface states can drive a phase transition into a phase with finite superflow that breaks time-reversal symmetry and translational symmetry along the surface. The associated Doppler shifts of Andreev states to finite energies lower the free energy. Direct experimental verification of such a phase is still technically difficult and controversial, however. To aid further experimental efforts, we use the quasiclassical theory of superconductivity to investigate how the realization and the observability of such a phase are influenced by sample geometry and surface ruggedness. Phase diagrams are produced for relevant geometric parameters. In particular, critical sizes and shapes are identified, providing quantitative guidelines for sample fabrication in the experimental hunt for symmetry-breaking phases.

DOI: 10.1103/PhysRevB.99.184511

I. INTRODUCTION

Quasiparticle scattering at interfaces and inhomogeneities of unconventional superconductors leads to pair breaking and the formation of Andreev states [1–3]. In a *d*-wave superconductor, these states form a spin-degenerate flat band at zero energy (midgap) that influences tunneling properties, leading to, e.g., zero-bias conductance peaks [4–7]. Furthermore, the Andreev states are bound within a few coherence lengths of the scattering centers, and might influence the superconducting state as a whole in mesoscopic systems [8]. The flat band of zero-energy states is enforced by topology [9], but costs free energy. There are several suggested mechanisms for shifting the states away from the Fermi energy, and thereby lowering the free energy in a phase transition where time-reversal ($\mathcal{T}$) and possibly more symmetries are broken. In one scenario, a subdominant attractive pairing channel is assumed to exist [5,10–12], for instance, *s* wave. At a temperature T_s^*, which depends on the interaction strength in the subdominant channel, it then becomes energetically favorable to form a composite order parameter $\Delta_d \pm i\Delta_s$, which breaks $\mathcal{T}$ symmetry and places the Andreev states at $\pm\Delta_s$. In a second scenario [13,14], the repulsive Coulomb interaction in the system may lead to a spin split of the Andreev states, thereby introducing a magnetic transition at a temperature T_{m}^*. In a third scenario there are no additional interaction terms in the Hamiltonian. Instead, the appearance of spontaneous superflow sustains Doppler shifts ($\epsilon \to \epsilon - \mathbf{v}_{\mathrm{F}} \cdot \mathbf{p}_{\mathrm{s}}$, where $\mathbf{v}_{\mathrm{F}}$ is the Fermi velocity and $\mathbf{p}_{\mathrm{s}}$ is the superfluid momentum) of the Andreev states to finite energies. This was first shown to be possible at translationally invariant surfaces [15–18]. In this case, the transition temperature $T^* \sim (\xi_0/\lambda)T_{\mathrm{c}} \ll T_{\mathrm{c}}$, where T_{c} is the superconducting transition temperature of the *d*-wave superconductor, is very low due to the unfavorable ratio between the superconducting coherence length ξ_0 and the penetration depth λ, which appears as a parameter when screening of the surface magnetic field is taken into account. In a ribbon geometry [19–23], Andreev states at the two opposite edges interact and hybridize, which provides additional energy shifts that enhance the transition temperature to $T^* \sim (\xi_0/D)T_{\mathrm{c}}$, where the ribbon width D satisfies $\xi_0 < D \ll \lambda$. Recently [24–26], we have shown that allowing also a breakdown of translational invariance, a single surface will sustain a superflow profile with a texture (see Fig. 1). The texture involves parts with counterdirected superflow that enables a restricted length scale of the order of the coherence length scale for the backflow in the bulk. The associated magnetic flux is then restricted to the coherence length scale, in contrast to the penetration depth scale in the translational invariant case. A high transition temperature, $T^* \sim 0.18T_{\mathrm{c}}$, can be achieved for the ideal case of a maximally pair-breaking specular surface of a clean *d*-wave superconductor. This T^* is relatively high, making this scenario very competitive, as long as $T^* > \{T_s^*, T_{\mathrm{m}}^*\}$, which depends on the interaction strengths in a particular superconducting material.

There are many experiments that support the claims of symmetry-broken phases [8,27–33]. However, there are several other experiments that report no signatures and, in particular, no direct imaging of the currents or magnetic fields that would arise in the different scenarios [34–38]. Within the scenario of spontaneous superflow with a texture, the breaking of translational invariance leads to inhomogeneous broadening of surface properties probed experimentally on a long length scale compared with the coherence length. The spontaneous currents arrange themselves as small loop currents, where neighboring loops have opposite circulation and magnetic field directions. Given the short length scale and the fact that

---

[*] holmvall@chalmers.se

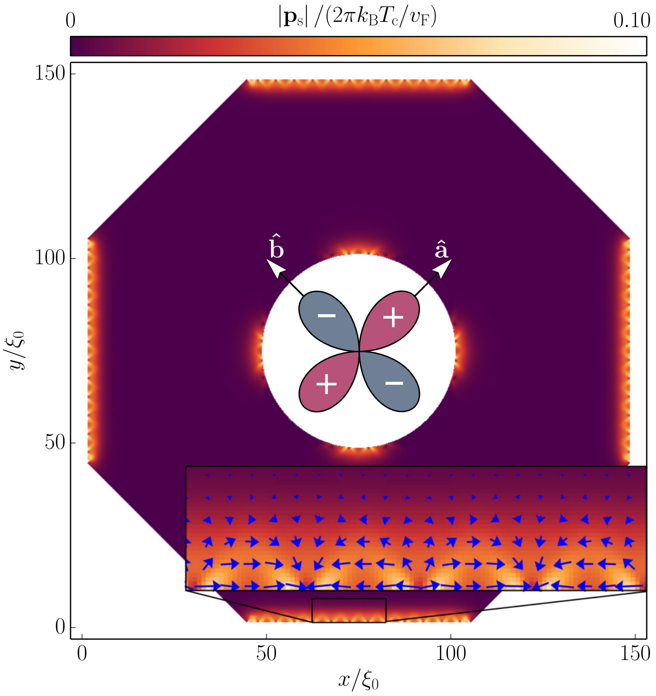

FIG. 1. A d-wave superconducting grain at temperature $T = 0.1T_c$ with spontaneous superflow (colors) that spontaneously breaks translational (along individual surface segments) and time-reversal symmetries. The Andreev states exist only at the pair-breaking edges, which for this sample the geometry occurs along the nodal directions. There is no superflow at surfaces along the lobe directions, since those surfaces have no Andreev states. The inset shows the vector field $\mathbf{p}_s$ (superfluid momentum) with a periodic structure of topological defects [25] in the form of edge sources and sinks.

there is no net current flow or flux, such a phase could easily have escaped observation. Such small fluxes and flows would be very difficult to detect unless using very local probes, e.g., single-spin detectors [39], scanning-tunneling spectroscopy [40,41], nano–superconducting quantum interference devices (SQUIDs) [42], magnetometry [43], and diamond cantilevers [44,45].

To aid such experimental verification, we study in this paper how the realization and observability of the translational symmetry-breaking phase is influenced by sample geometry and surface roughness. In addition, we suggest indirect observation by, e.g., penetration-depth measurements [46] and nanocalorimetry [47,48].

II. METHODS

We study two-dimensional superconducting grains of various geometries and sizes, with an anisotropic order parameter. In particular, we consider d-wave superconductivity with a cylindrically symmetric Fermi surface (see Fig. 1), but other order parameters that enable surface Andreev bound states are also of relevance (e.g., polar p-wave superconductors [49–53]). In the present system, the angle between the sample interface and the crystal *ab* axes (hence the d-wave order parameter lobes) directly influences the spectral weight of midgap Andreev states. The grains are assumed to be in vacuum and equilibrium, with spin degeneracy and negligible spin-orbit coupling. Furthermore, the grains are assumed to be clean with perfectly specular interfaces, but effects of disorder and diffuse scattering are discussed.

We utilize the quasiclassical theory of superconductivity [54–60], in which the Green's function $\hat{g}(\mathbf{p}_F, \mathbf{R}; z)$ governs quasiparticle and pair propagation through the Eilenberger equation

$$i\hbar \mathbf{v}_F \cdot \nabla_R \, \hat{g} + \left[\hat{\tau}_3\left(z + \mathbf{v}_F \cdot \frac{e}{c}\mathbf{A}\right) - \hat{h}, \hat{g}\right] = \hat{0}, \tag{1}$$

with the normalization condition

$$\hat{g}^2 = -\pi^2 \hat{1}. \tag{2}$$

Here, $\mathbf{p}_F$ is the quasiparticle momentum at the Fermi surface, $\mathbf{R}$ the center-of-mass coordinate, z the energy, $\hbar$ the reduced Planck constant, $\mathbf{v}_F$ the Fermi velocity, e the elementary charge, c the speed of light, $\mathbf{A}$ the electromagnetic gauge field, and $\hat{\tau}_3$ the third Pauli matrix, where the hat symbol denotes Nambu (electron-hole) space. The self-energies $\hat{h}$ are expressed in terms of the superconducting order parameter Δ,

$$\hat{h} = \begin{pmatrix} 0 & \Delta \\ \tilde{\Delta} & 0 \end{pmatrix}, \tag{3}$$

and the quasiclassical Green's function is described in terms of the quasiparticle and pair propagators g and f, respectively:

$$\hat{g} = \begin{pmatrix} g & f \\ -\tilde{f} & \tilde{g} \end{pmatrix}. \tag{4}$$

The tilde symbol denotes particle-hole conjugation:

$$\tilde{\alpha}(\mathbf{p}_F, \mathbf{R}; z) = \alpha^*(-\mathbf{p}_F, \mathbf{R}; -z^*). \tag{5}$$

To solve the Eilenberger equation, the Riccati formalism is used [61–67], in which the quasiclassical Green's function is parametrized in terms of two particle-hole coherence functions $\gamma(\mathbf{p}_F, \mathbf{R}; z)$ and $\tilde{\gamma}(\mathbf{p}_F, \mathbf{R}; z)$,

$$\hat{g} = -\frac{i\pi}{1 + \gamma\tilde{\gamma}} \begin{pmatrix} 1 - \gamma\tilde{\gamma} & 2\gamma \\ 2\tilde{\gamma} & -1 + \gamma\tilde{\gamma} \end{pmatrix}, \tag{6}$$

yielding two Riccati equations:

$$\left(i\hbar \mathbf{v}_F \cdot \nabla_R + 2z + 2\frac{e}{c}\mathbf{v}_F \cdot \mathbf{A}\right)\gamma = -\tilde{\Delta}\gamma^2 - \Delta, \tag{7}$$

$$\left(i\hbar \mathbf{v}_F \cdot \nabla_R - 2z - 2\frac{e}{c}\mathbf{v}_F \cdot \mathbf{A}\right)\tilde{\gamma} = -\Delta\tilde{\gamma}^2 - \tilde{\Delta}. \tag{8}$$

In this paper, a pure d-wave order parameter is assumed:

$$\Delta(\mathbf{p}_F, \mathbf{R}) = \Delta_d(\mathbf{R})\eta_d(\theta_F), \tag{9}$$

$$\eta_d(\theta_F) = \sqrt{2}\cos(2\theta_F), \tag{10}$$

where η_d is the d-wave basis function, and θ_F is the angle between the Fermi momentum and the crystal $\hat{\mathbf{a}}$ axis. The order parameter is solved self-consistently from the gap equation with the Matsubara technique:

$$\Delta_d(\mathbf{R}) = \lambda_d N_F k_B T \sum_{|\epsilon_m| \leqslant \Omega_c} \int \frac{d\theta_F}{2\pi} \eta_d^*(\theta_F) f(\mathbf{p}_F, \mathbf{R}; i\epsilon_m), \tag{11}$$

where λ_d is the pairing interaction, k_B the Boltzmann constant, ϵ_m the Matsubara energy, Ω_c a cutoff energy, and N_F the normal-state density of states at the Fermi surface (per spin).

We are using an electromagnetic gauge where the vector potential due to an external magnetic field directed perpendicular to the superconducting plane is given by

$$\mathbf{A}_{\rm ext}(\mathbf{R}) = \tfrac{1}{2}\mathbf{B}_{\rm ext} \times \mathbf{R}. \tag{12}$$

The total vector potential should also include the induced field $\mathbf{B}_{\rm ind}(\mathbf{R})$ generated by the currents in our grain, computable through the Maxwell equations. However, for the type-II superconductors that we are considering, the back-coupling can safely be neglected, as we have discussed in more detail in Refs. [24,25,68,69].

This theoretical formalism is implemented numerically to run on graphics processing units, where the above equations of motion are solved in parallel over different degrees of freedom, until self-consistency is achieved (see Refs. [24,25,68,69] for more details). Finally, various quantities are calculated, e.g., the gauge-invariant superfluid momentum $\mathbf{p}_s$ which we have identified [25] as the order parameter of the symmetry-broken phase

$$\mathbf{p}_s(\mathbf{R}) = \frac{\hbar}{2}\nabla\chi(\mathbf{R}) - \frac{e}{c}\mathbf{A}(\mathbf{R}), \tag{13}$$

where χ is the superconducting phase. The local density of states (DOS) at energy ϵ is calculated as a Fermi-surface average

$$N(\mathbf{R};\epsilon) = -\frac{N_F}{\pi}\int\frac{d\theta_F}{2\pi}\,{\rm Im}[g(\mathbf{p}_F,\mathbf{R};\epsilon+i\delta)], \tag{14}$$

where $\delta \to 0^+$ guarantees a retarded Green's function. The current density is calculated according to

$$\mathbf{j}(\mathbf{R}) = 2\pi e N_F k_B T\sum_{\epsilon_m}\int\frac{d\theta_F}{2\pi}\mathbf{v}_F g(\mathbf{p}_F,\mathbf{R};i\epsilon_m). \tag{15}$$

In the absence of impurity scattering, the free-energy difference between the superconducting and the normal state, at temperature T, may be calculated as [54]

$$\Omega(T) = \int d\mathbf{R}\left\{\frac{\mathbf{B}^2(\mathbf{R})}{8\pi} + |\Delta(\mathbf{R})|^2 N_F \ln\frac{T}{T_c} + 2\pi N_F k_B T\sum_{\epsilon_m>0}\left[\frac{|\Delta(\mathbf{R})|^2}{\epsilon_m} + i\mathcal{I}(\mathbf{R},\epsilon_m)\right]\right\}, \tag{16}$$

$$\mathcal{I}(\mathbf{R}) = \int\frac{d\theta_F}{2\pi}[\tilde{\Delta}(\mathbf{p}_F,\mathbf{R})\gamma(\mathbf{p}_F,\mathbf{R};i\epsilon_m) - \Delta(\mathbf{p}_F,\mathbf{R})\tilde{\gamma}(\mathbf{p}_F,\mathbf{R};i\epsilon_m)], \tag{17}$$

where $\mathbf{B}$ is the induced magnetic field and T_c the superconducting transition temperature. The heat capacity is obtained from the free energy according to

$$C(T) = -T\frac{\partial^2\Omega(T)}{\partial T^2}. \tag{18}$$

III. RESULTS AND DISCUSSION

We start by varying the angle between the interface and the crystal $\hat{\mathbf{a}}$ axis (Sec. III A), thus controlling the pair-breaking effect. We then vary the area of the grain to study finite-size effects (Sec. III B). Critical angles and areas are identified. These results are used to analyze superconducting grains of various shapes and different degrees of surface roughness (Sec. III C). We limit ourselves to mesoscopic roughness (see below), and we consider clean superconductors.

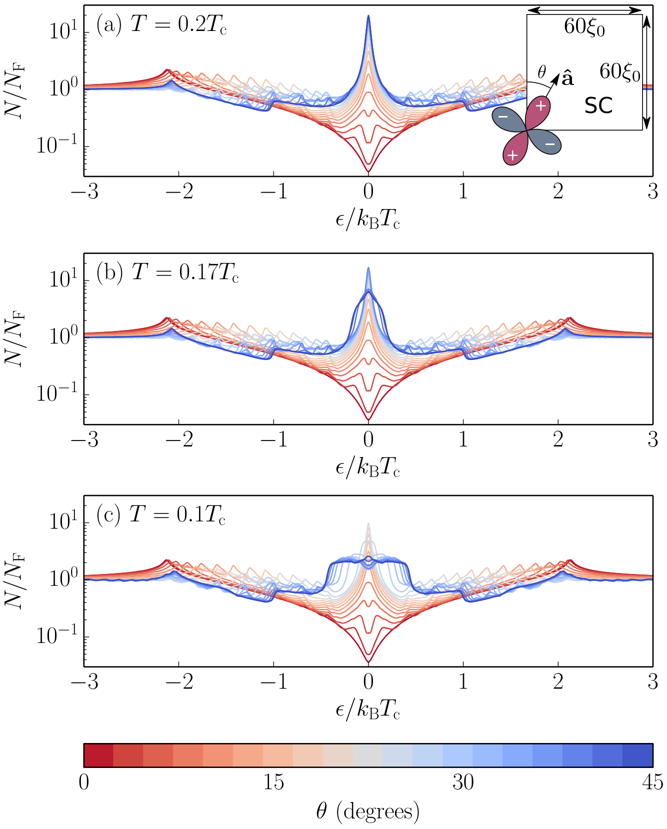

FIG. 2. The surface density of states averaged over one side of a $60\xi_0 \times 60\xi_0$ square grain with ${\rm Im}\,z = \delta = 0.02k_BT_c$. Different curves correspond to different values of θ, as indicated by colors. (a) Above the transition, the peak is narrow (note the logarithmic scale on the ordinate). The steps at $\epsilon \approx 1k_BT_c \approx \Delta_0/2$ come from the features in the DOS at the square corners, with $\Delta_0 \approx 2.14k_BT_c$ being the bulk gap. (b, c) As the temperature is lowered, the midgap states are broadened due to the presence of spontaneous superflow.

A. Critical interface angle

As the angle θ between a specular d-wave interface and the crystal $\hat{\mathbf{a}}$ axis is varied from perfectly aligned ($\theta = 0^\circ$) to perfectly misaligned ($\theta = 45^\circ$), the surface DOS changes from the typical gapless bulk DOS to one with a large zero-energy peak, as illustrated in Fig. 2(a). The states in the peak come from quasiparticles that scatter between directions with a sign change in the order parameter. These midgap states (MGSs) are thus enforced by the order parameter symmetry and associated with a significant increase in free energy and also a suppression of the order parameter at the interface. As the temperature is lowered, there is a phase transition at T^* where superflow appears spontaneously. The energy is lowered by Doppler shifting the zero-energy states to finite energies, as seen in Fig. 2(b). The magnitude of superflow, the

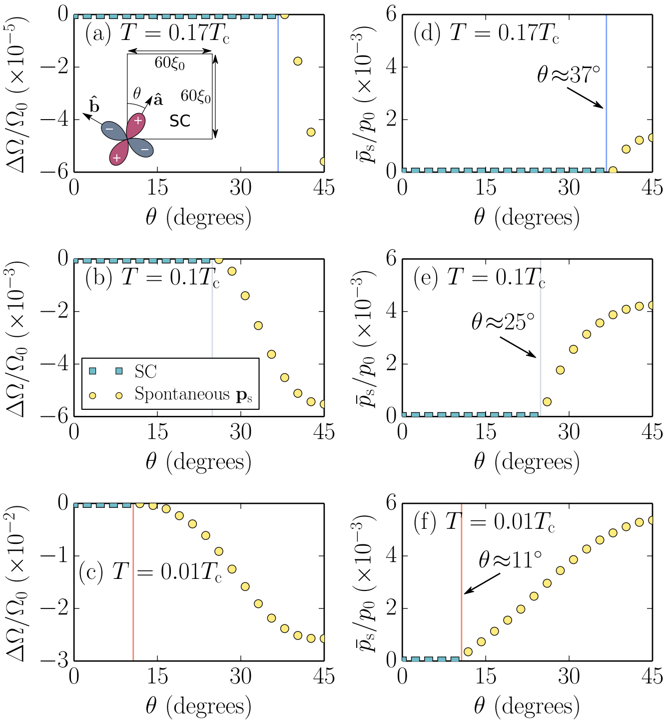

FIG. 3. (a)–(c) Free-energy difference between phases with and without spontaneous superflow, and (d)–(f) sample-averaged magnitude of the spontaneous superfluid momentum. These quantities are plotted versus the angle θ between the grain edges and the crystal $\hat{\mathbf{a}}$ axis in a square grain with area $\mathcal{A} = (60\xi_0)^2$, as illustrated in the inset in (a). Here, the units are $\Omega_0 \equiv \mathcal{A}N_F k_B^2 T_c^2$ and $p_0 \equiv 2\pi k_B T_c/v_F$. Note the varying scales in (a)–(c).

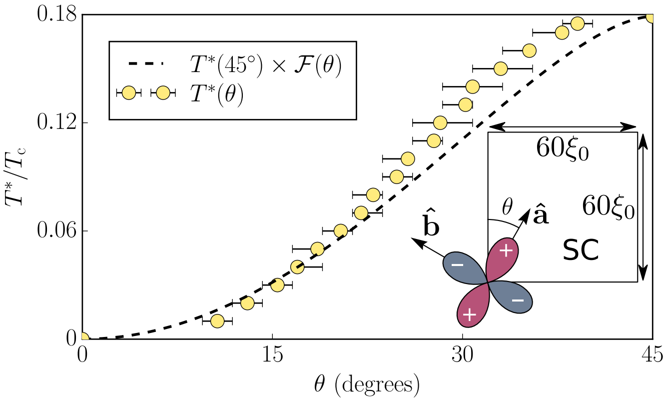

FIG. 4. Phase diagram showing the transition temperature T^* of the symmetry-broken phase, as a function of the angle θ between a vacuum-superconductor interface and the d-wave crystal $\hat{\mathbf{a}}$ -axis, in a grain of area $\mathcal{A} = (60\xi_0)^2$ (see inset). Error bars denote the uncertainty due to the discrete angular resolution. $T^*(\theta)$ is roughly described by the angular dependence of the MGS peak $N_{\rm MGS}$, denoted $\mathcal{F}(\theta)$ (dashed line), defined in Eq. (27).

$\mathbf{p}_s$ field seen in Fig. 1, increases as the temperature is lowered [25], as does then the Doppler shift and the energy gain as well, as seen by comparing Figs. 2(b) and 2(c). Figures 3(a)–3(c) show the free-energy gain $\Delta\Omega$ versus θ, defined as

$$\Delta\Omega = \Omega_S - \Omega_{\rm ms}, \tag{19}$$

where Ω_S and $\Omega_{\rm ms}$ are the free energies of the systems with and without spontaneous superflow, respectively. The latter might exhibit a higher free energy and is therefore referred to as a metastable state (ms). Figures 3(d)–3(f) show the sample-averaged magnitude of the superfluid momentum $\bar{p}_s$ versus θ, defined as

$$\bar{p}_s = \frac{1}{\mathcal{A}}\int d\mathbf{R}|\mathbf{p}_s(\mathbf{R})|, \tag{20}$$

where $\mathcal{A}$ is the sample area. From these figures, it is possible to identify a lowering of the free energy with $\mathbf{p}_s \neq 0$. A critical phase transition temperature $T^*(\theta)$, defined as the temperature where $\bar{p}_s$ becomes finite, is plotted in a phase diagram in Fig. 4. Error bars originate from the uncertainty due to the discrete angular resolution. The transition temperature T^* closely follows the spectral weight of the MGS peak, which can be controlled by various parameters such as surface roughness or, as in this case, by the interface orientation θ. This can be shown from a very general argument as follows. The gain in free energy due to a small shift of zero-energy states with narrow DOS $N_{\rm MGS}(\epsilon) = N_{\rm bs}\delta(\epsilon)$ by $\Delta\epsilon$ (e.g., $\propto \mathbf{v}_F\cdot\mathbf{p}_s$ Doppler shift) is [70]

$$\Delta F_b(T) = -\int_{-\infty}^{\infty} d\epsilon\, k_B T \ln\left(2\cosh\frac{\epsilon}{2k_BT}\right) \times [N_{\rm bs}\delta(\epsilon-\Delta\epsilon) - N_{\rm bs}\delta(\epsilon)], \tag{21}$$

which for $\Delta\epsilon \ll k_BT$ reduces to

$$\Delta F_b(T) \approx -N_{\rm bs}\frac{(\Delta\epsilon)^2}{8k_BT}. \tag{22}$$

The same spectral shift of the continuum states, however, increases energy, also $\propto (\Delta\epsilon)^2$ (e.g., superflow energy $\propto \mathbf{p}_s^2$) as $\Delta F_c(T) = A(T)(\Delta\epsilon)^2$, where the parameter $A(T)$ depends on the mechanism of the energy increase, and in principle should take into account the reduction of continuum states by $N_{\rm bs}$. The instability occurs when their sum is negative:

$$\Delta F_b(T^*) + \Delta F_c(T^*) \leqslant 0 \quad \Rightarrow \quad T^* \approx {\rm const}\,\frac{N_{\rm bs}}{A(T^*)}. \tag{23}$$

Assuming that $A(T)$ is relatively insensitive to temperature and to the transfer of spectral weight to bound states, the main effect on the transition temperature is from varying $N_{\rm bs}$:

$$T^* = {\rm const} \times N_{\rm bs}\,. \tag{24}$$

This argument can be further adjusted for broadening of the bound states by impurities, for example, and corrected for the continuum reduction $\delta T^* \propto O(N_{\rm bs}^2)$. For the θ rotation of the crystal axes we can estimate the height of the bound-state peak $N_{\rm bs}$ analytically. Neglecting the order parameter suppression, the low-energy Green's function at the surface is ($|z = \epsilon + i\delta| \ll |\Delta_{\rm in,out}|$)

$$g(z) = \frac{\pi}{z}\frac{2|\Delta_{\rm in}\Delta_{\rm out}|}{|\Delta_{\rm in}| + |\Delta_{\rm out}|}\Theta(-\Delta_{\rm in}\Delta_{\rm out}), \tag{25}$$

where Θ is the Heaviside function, and $\Delta_{\rm in/out} = \Delta(\theta_F)$, $\Delta(\pi - \theta_F)$ are the order parameters for incoming and outgoing trajectories, respectively. Averaging the DOS over the Fermi surface, as in Eq. (14), we get

$$N_{\mathrm{MGS}}(\epsilon,\theta) = -2N_{\mathrm{F}}\,\mathrm{Im}\,\frac{\Delta_0}{\epsilon+i\delta}\frac{2}{\pi}\mathcal{F}(\theta), \tag{26}$$

$$\Rightarrow N_{\mathrm{bs}} \propto \mathcal{F}(\theta) \equiv 1 - \frac{\cos^2 2\theta}{\sin 2\theta}\ln\left(\frac{1+\tan\theta}{1-\tan\theta}\right), \tag{27}$$

where Δ_0 is the bulk gap amplitude. Scaling of transition temperature by the zero-energy spectral weight $\mathcal{F}(\theta)$ is shown by the dashed line in Fig. 4. It shows a very close relation with the full numerical result, given the roughness of our estimate.

The phase diagram in Fig. 4 shows that there is robustness of the symmetry-broken phase against surface disorder at d-wave interfaces, and that even completely circular interfaces will host the phase as long as the radius of curvature is large enough, as seen in, e.g., Fig. 1.

B. Critical grain area

The spectral weight of zero-energy states is peaked at the interface, but extends almost $10\xi_0$ away from it. Square grains with side lengths smaller than $20\xi_0$ therefore exhibit pronounced finite-size effects, e.g., suppressed superconductivity and a reduced T_{c}, due to overlapping regions of MGS. In larger systems, the MGS from different interfaces will no longer overlap except in the corners. Quantities which are directly tied to the MGS, e.g., $|\mathbf{p}_{\mathrm{s}}(\mathbf{R})|$ and $\boldsymbol{j}$, are therefore expected to show a saturation for larger grain sizes.

We now quantify how the side length $\mathcal{L}$ of a square grain with maximally pair-breaking interfaces ($\theta = 45^\circ$) influences the transition temperature T^*, the heat capacity jump, as well as the average current magnitude of the symmetry-broken phase. Since the phase under investigation is a second-order phase transition, the transition temperature is appropriately extracted from where there is a discontinuity in the heat capacity [25]. Figure 5(a) shows $T^*(\mathcal{L})$ with and without an external magnetic field (circles and squares, respectively, left axis), and $T_{\mathrm{c}}(\mathcal{L})$ of the grain (thick dashed line, right axis). Here and in the following, the external magnetic field corresponds to half a flux quantum spread across the grain area, $B_{\mathrm{ext}} = \Phi_0/2\mathcal{L}^2$, where $\Phi_0 \equiv hc/2|e|$ is the unit of flux quantum. The deviation from $T_{\mathrm{c}}(\mathcal{L}) = T_{\mathrm{c}}^{\mathrm{bulk}}$ indicates finite-size effects. Hence, T^* decreases with $\mathcal{L}$ due to superconductivity being suppressed in the grain. The suppression is stronger with an external field as the resulting screening currents also suppress superconductivity. As the side length increases, the regions of MGSs no longer overlap and saturate to fixed sizes and shapes. The transition temperature therefore also saturates to a fixed value. Figure 5(b) shows how the sample-average heat-capacity jump changes with the side length (with and without external field), while Fig. 5(c) shows the sample-averaged magnitude of the current, defined as

$$\bar{j} = \frac{1}{\mathcal{A}}\int d\mathbf{R}|\mathbf{j}(\mathbf{R})|. \tag{28}$$

The heat-capacity jump in the bulk normal-superconducting phase transition is given by

$$\Delta C_d = \frac{2\alpha}{3}\mathcal{A}k_{\mathrm{B}}^2 T_{\mathrm{c}} N_{\mathrm{F}}, \tag{29}$$

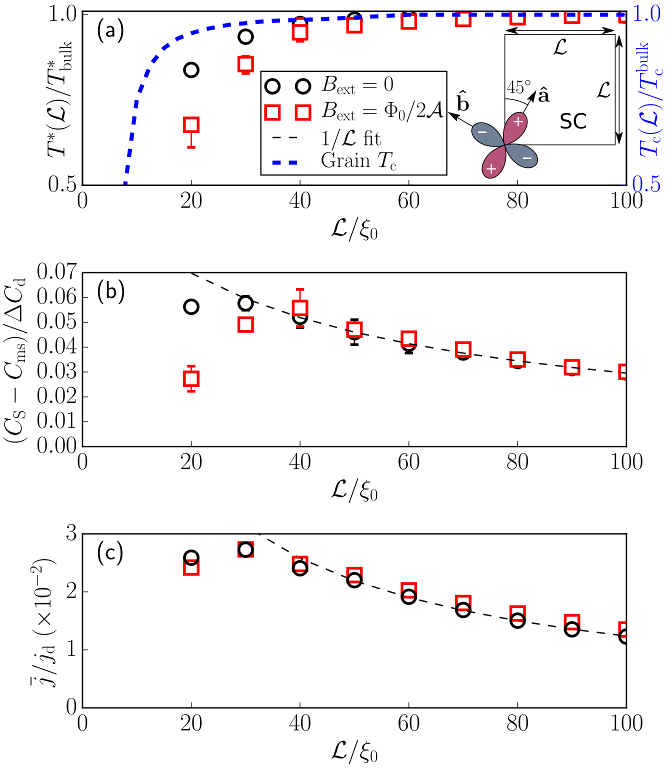

FIG. 5. Effect of sample size $\mathcal{L} \times \mathcal{L}$ with maximal pair-breaking edges (see inset) on (a) the transition temperature into the spontaneous superflow phase (circles and squares, left axis) and the superconducting transition temperature of the grain (dashed line, right axis), (b) the heat capacity jump of the spontaneous superflow phase transition, and (c) the sample-averaged current magnitude at $T = 0.1T_{\mathrm{c}}$. Error bars denote uncertainty due to (a) discrete resolution in temperature and (b) numerical uncertainty in the heat capacity.

where $\alpha = 8\pi^2/[7\zeta(3)]$ and ζ is the Riemann zeta function. Again, finite-size effects can be seen in Figs. 5(b) and 5(c) due to suppression of superconductivity at smaller $\mathcal{L}$. Furthermore, since the superfluid momentum is directly tied to the MGS, both $\mathbf{p}_{\mathrm{s}}$ and $\mathbf{j}$ saturate to fixed profiles at larger $\mathcal{L}$. Sample-averaged quantities, e.g., $\bar{j}$ and $(C_{\mathrm{S}} - C_{\mathrm{ms}})/\Delta C_{\mathrm{d}}$, thus scale as $\mathcal{L}^{-1}$, as evident by the fit. The fit breaks down at the onset of finite-size effects, resulting in a maximum at a finite $\mathcal{L} = \mathcal{L}_{\mathrm{c}} \approx 30\xi_0$.

These results imply that the observability of the phase through sample-averaged observables is maximized at a finite side length. This ratio will depend on the shape of the sample, and in particular the angles of the interfaces. Therefore, for, e.g., thermodynamic experiments aiming to verify the symmetry-broken phases, it might be advisable to fabricate thin rectangular grains or square grains of side lengths $\sim 30\xi_0$, for example, depending on the type of experiment. On the other hand, if the goal is instead to avoid this phase, very small grains with $\mathcal{L} < \mathcal{L}_{\mathrm{c}}$ are advisable.

C. Surface roughness

With the quantitative knowledge about how the size and the angle of the pair-breaking interfaces influence the symmetry-broken phase, we now qualitatively study the effect of surface

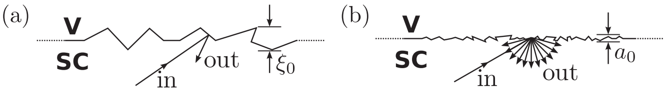

FIG. 6. (a) Mesoscopic surface roughness, where the disorder is on the coherence length scale or larger. The roughness is modeled as mesoscopic facets that scatter incoming quasiparticle states specularly. (b) In contrast, atomic surface roughness, where the disorder is on the atomic scale, i.e., generally much smaller than the superconducting coherence length, leads to diffuse scattering of any incoming quasiparticle state. This type of roughness is not considered in this work.

roughness. There are two well-defined regimes of surface roughness, here referred to as mesoscopic roughness (or ruggedness) and atomic surface roughness, as illustrated in Fig. 6.

Mesoscopic surface roughness refers to interfaces with a disorder that is on the order of the superconducting coherence length ξ_0 or larger, i.e., mesoscopic facets that scatter specularly. For high-temperature superconductors the coherence length is very short and this kind of ruggedness instead of atomic scale roughness can be a relevant regime. Figure 7 shows spontaneous magnetic fields caused by spontaneous superflow in square grains with side lengths of $150\xi_0$ [Figs. 7(a)–7(d)] and $60\xi_0$ [Figs. 7(e)–7(h)], with varying degrees of mesoscopic roughness. It is seen that, despite a rugged surface profile, the spontaneous superflow might appear. The two key prerequisites are that the facet angle with respect to the crystal $\hat{\mathbf{a}}$ axis must lie within the critical angle quantified in Fig. 4, and that the area around the facet is large enough to accommodate the superfluid momentum profile. These findings illustrate that the symmetry-broken phase is relatively robust against mesoscopic roughness.

Atomic surface roughness, on the other hand, refers to surfaces that have a disorder that is on the atomic length scale, e.g., the Bohr radius a_0 or the Fermi wavelength λ_F, which are both generally smaller than the superconducting coherence length. This disorder will lead to diffuse scattering of any incoming quasiparticle state, with a finite probability of backscattering. Hence, while a clean pair-breaking d-wave interface will induce a sign change for most quasiparticle scattering trajectories, diffusivity will severely reduce the number of such trajectories and thus also the spectral weight of midgap states. The inclusion of diffuse surface scattering is beyond the scope of this paper, but we note that it was previously shown that the symmetry-broken phase in ribbons persisted up to roughly 80% diffusivity [21]. For polar p-wave superconductors with the nodal direction along the interface, the order-parameter sign change accompanies all scattering trajectories independent of conservation of $p_\parallel$ (in contrast to d-wave superconductors). The zero-energy states in such a p-wave superconductor will thus be completely robust against surface diffusivity and backscattering, as was shown in Refs. [53,71]. However, since the sign change in the order parameter in that case comes from reflected trajectories, the robustness might be lost at interfaces with finite transmission into other systems, e.g., in junctions [3]. In summary, the crucial factor for the phase to appear is a significant spectral weight of midgap states caused by sign-changing quasiparticle scattering trajectories.

IV. SUMMARY AND CONCLUSIONS

The goal of this paper has been to provide a more complete picture of spontaneous symmetry breaking tied to zero-energy Andreev states, and to discuss experimental conditions where such phases can be observed. As an example, we have

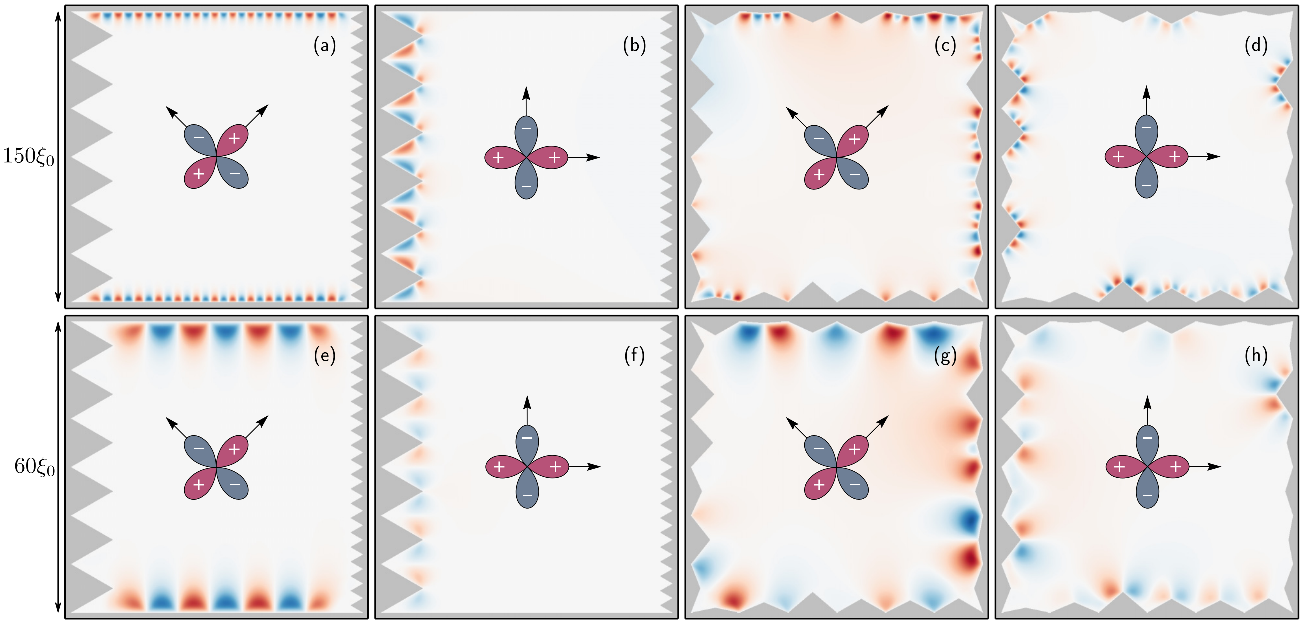

FIG. 7. *D*-wave grains with side lengths (a)–(d) $150\xi_0$ and (e)–(h) $60\xi_0$, and with different degrees of mesoscopic surface roughness (gray boundaries) of the type introduced in Fig. 6(a). Colors indicate the magnitude of magnetic fields induced by spontaneous currents, with a maximum and minimum flux density of roughly $\pm 10^{-5}\Phi_0/\xi_0^2$, where $\Phi_0 \equiv hc/2|e|$ is the magnetic flux quantum.

considered a particular phase with a spontaneous superfluid momentum due to pair-breaking interfaces in unconventional d-wave superconductors [24–26]. However, the results and the analysis presented in this paper can be extended to other phases and systems that host surface Andreev states, e.g., p-wave superconductors [49–53].

In particular, we have studied how the realization of such phases is influenced by suppressing the spectral weight of the midgap states (via changing the angle θ between the pair-breaking interface and the d-wave crystal $\hat{\mathbf{a}}$ axis), by the side length $\mathcal{L}$ of the grain, as well as by surface roughness.

It was found that the transition temperature $T^*(\theta)$ into the symmetry-broken phase follows the angular dependence of the zero-energy state peak $N_{\mathrm{MGS}}(\theta)$, showing robustness against variations in θ, even appearing at completely circular interfaces.

Furthermore, it was found that the sample-averaged observables (e.g., the heat-capacity jump in the phase transition) scale as $\mathcal{L}^{-1}$, down to a critical side length $\mathcal{L} = \mathcal{L}_c$. At this side length, superconductivity starts becoming suppressed. Hence, sample-averaged observables are generally maximized at $\mathcal{L}_c$. The critical side length depends on the shape of the sample; e.g., it was found that $\mathcal{L}_c \approx 30\xi_0$ for a square grain.

With the above quantitative knowledge about how the shape and the size of the grain influence the symmetry-broken phases, grains with different degrees of mesoscopic surface roughness were analyzed. The conclusion was that any pair-breaking interface can generate spontaneous superflow, as long as the interface is within the critical angle and there is enough area around the interface to form the associated spontaneous currents. Finally, we discussed atomic surface roughness, referring to interfaces with diffuse quasiparticle scattering. Due to the results of Refs. [21,53,71], the translational symmetry-breaking phase is expected to survive considerable atomic surface roughness, but more research is required.

We have seen that any effect that reduces the spectral weight of zero-energy states may impede the realization of the symmetry-broken phases and the formation of the spontaneous superfluid momentum with associated magnetic flux. In the same way, broadening of the Andreev state peak in the density of states can also be detrimental. Broadening can be due to impurity scattering [72], and will also be induced when the edge is contacted by, for instance, a metal probe with a finite transparency $\mathcal{T}$ at the interface. For impurities the broadening Γ is set by the impurity strength and density of impurities, while the interface to a metal contact gives a broadening of order $\Delta_d\mathcal{T}$ (see, e.g., the review in Ref. [3]). When the broadening becomes of the same order of magnitude as the Doppler shifts, i.e., when $\Gamma \sim k_B T^*$, the broken symmetry phase might not be energetically favorable anymore.

In conclusion, the advice to experimentalists aiming to study these phases is therefore to use systems with a maximized spectral weight of zero-energy Andreev states, with minimal interference from effects that broaden these states (e.g., atomic-scale surface roughness, impurities, and strong external fields). For measurements of sample-averaged (e.g., thermodynamic) quantities, it is desirable to maximize the pair-breaking surface-to-volume ratio, as long as the volume does not become so small that superconductivity is severely suppressed. Thus, a specific suggestion would be to use heavy ion bombardment to induce well-defined pair-breaking channels [46]. Another suggestion would be to deposit on a substrate a large array of rectangular or square-shaped thin-film d-wave grains with maximally pair-breaking edges, where the smallest side length is $\mathcal{L} = \mathcal{L}_c \approx 30\xi_0$, and then look for either a heat-capacity jump at $T = T^*$ with nanocalorimetry [47], or the mesoscopic currents and flux that we previously reported on [24–26] with local probes, e.g., single-spin detectors [39], scanning-tunneling spectroscopy [40,41], nano-SQUIDS [42], magnetometry [43], and diamond cantilevers [44,45].

There are still open questions regarding the survival of these symmetry-breaking phases at semitransparent or transparent interfaces, and how they are influenced by quantum-size effects using fully microscopic theories [73–80]. Furthermore, it would be interesting to see how the translational symmetry-breaking phase survives diffuse surface scattering [21,53], impurity effects [72], and in p-wave systems [49–53].

ACKNOWLEDGMENTS

The computations were performed on resources at Chalmers Centre for Computational Science and Engineering (C3SE) provided by the Swedish National Infrastructure for Computing (SNIC). We thank the Swedish Research Council for financial support. It is a pleasure to thank Mikael Håkansson for valuable discussions.

---

[1] L. J. Buchholtz and G. Zwicknagl, Phys. Rev. B **23**, 5788 (1981).
[2] C.-R. Hu, Phys. Rev. Lett. **72**, 1526 (1994).
[3] T. Löfwander, V. S. Shumeiko, and G. Wendin, Supercond. Sci. Technol. **14**, R53 (2001).
[4] Y. Tanaka and S. Kashiwaya, Phys. Rev. Lett. **74**, 3451 (1995).
[5] M. Fogelström, D. Rainer, and J. A. Sauls, Phys. Rev. Lett. **79**, 281 (1997).
[6] S. Kashiwaya and Y. Tanaka, Rep. Prog. Phys. **63**, 1641 (2000).
[7] J. A. Sauls, Philos. Trans. R. Soc. A **376**, 20180140 (2018).
[8] D. Gustafsson, D. Golubev, M. Fogelström, T. Claeson, S. Kubatkin, T. Bauch, and F. Lombardi, Nat. Nanotechnol. **8**, 25 (2013).
[9] M. Sato, Y. Tanaka, K. Yada, and T. Yokoyama, Phys. Rev. B **83**, 224511 (2011).
[10] M. Matsumoto and H. Shiba, J. Phys. Soc. Jpn. **64**, 3384 (1995).
[11] M. Matsumoto and H. Shiba, J. Phys. Soc. Jpn. **64**, 4867 (1995).
[12] M. Sigrist, Prog. Theor. Phys. **99**, 899 (1998).
[13] C. Honerkamp, K. Wakabayashi, and M. Sigrist, Europhys. Lett. **50**, 368 (2007).
[14] A. C. Potter and P. A. Lee, Phys. Rev. Lett. **112**, 117002 (2014).

[15] S. Higashitani, J. Soc. Phys. Jpn. **66**, 2556 (1997).
[16] A. L. Fauchère, W. Belzig, and G. Blatter, Phys. Rev. Lett. **82**, 3336 (1999).
[17] Y. S. Barash, M. S. Kalenkov, and J. Kurkijärvi, Phys. Rev. B **62**, 6665 (2000).
[18] T. Löfwander, V. S. Shumeiko, and G. Wendin, Phys. Rev. B **62**, R14653 (2000).
[19] A. B. Vorontsov, Phys. Rev. Lett. **102**, 177001 (2009).
[20] M. Hachiya, K. Aoyama, and R. Ikeda, Phys. Rev. B **88**, 064519 (2013).
[21] S. Higashitani and N. Miyawaki, J. Soc. Phys. Jpn. **84**, 033708 (2015).
[22] N. Miyawaki and S. Higashitani, Phys. Rev. B **91**, 094511 (2015).
[23] N. Miyawaki and S. Higashitani, Phys. Proc. **65**, 25 (2015).
[24] M. Håkansson, T. Löfwander, and M. Fogelström, Nat. Phys. **11**, 755 (2015).
[25] P. Holmvall, A. B. Vorontsov, M. Fogelström, and T. Löfwander, Nat. Commun. **9**, 2190 (2018).
[26] P. Holmvall, T. Löfwander, and M. Fogelström, J. Phys.: Conf. Ser. **969**, 012037 (2018).
[27] M. Covington, M. Aprili, E. Paraoanu, L. H. Greene, F. Xu, J. Zhu, and C. A. Mirkin, Phys. Rev. Lett. **79**, 277 (1997).
[28] K. Krishana, N. P. Ong, Q. Li, G. D. Gu, and N. Koshizuka, Science **277**, 83 (1997).
[29] Y. Dagan and G. Deutscher, Phys. Rev. Lett. **87**, 177004 (2001).
[30] R. Gonnelli, A. Calzolari, D. Daghero, L. Natale, G. Ummarino, V. Stepanov, and M. Ferretti, Eur. Phys. J. B **22**, 411 (2001).
[31] G. Elhalel, R. Beck, G. Leibovitch, and G. Deutscher, Phys. Rev. Lett. **98**, 137002 (2007).
[32] T. Watashige, Y. Tsutsumi, T. Hanaguri, Y. Kohsaka, S. Kasahara, A. Furusaki, M. Sigrist, C. Meingast, T. Wolf, H. v. Löhneysen, T. Shibauchi, and Y. Matsuda, Phys. Rev. X **5**, 031022 (2015).
[33] A. Bhattacharyya, D. T. Adroja, N. Kase, A. D. Hillier, A. M. Strydom, and J. Akimitsu, Phys. Rev. B **98**, 024511 (2018).
[34] D. F. He, X. H. Zeng, H.-J. Krause, H. Soltner, F. Rüders, and Y. Zhang, Appl. Phys. Lett. **72**, 969 (1998).
[35] R. Carmi, E. Polturak, G. Koren, and A. Auerbach, Nature (London) **404**, 853 (2000).
[36] J. Kirtley, C. Tsuei, A. Ariando, C. Verwijs, S. Harkema, and H. Hilgenkamp, Nat. Phys. **2**, 190 (2006).
[37] H. Saadaoui, G. D. Morris, Z. Salman, Q. Song, K. H. Chow, M. D. Hossain, C. D. P. Levy, T. J. Parolin, M. R. Pearson, M. Smadella, D. Wang, L. H. Greene, P. J. Hentges, R. F. Kiefl, and W. A. MacFarlane, Phys. Rev. B **83**, 054504 (2011).
[38] H. Saadaoui, Z. Salman, T. Prokscha, A. Suter, H. Huhtinen, P. Paturi, and E. Morenzoni, Phys. Rev. B **88**, 180501(R) (2013).
[39] D. Rugar, R. Budakian, H. Mamin, and B. Chui, Nature (London) **430**, 329 (2004).
[40] T. Nishio, T. An, A. Nomura, K. Miyachi, T. Eguchi, H. Sakata, S. Lin, N. Hayashi, N. Nakai, M. Machida, and Y. Hasegawa, Phys. Rev. Lett. **101**, 167001 (2008).
[41] T. Cren, L. Serrier-Garcia, F. Debontridder, and D. Roditchev, Phys. Rev. Lett. **107**, 097202 (2011).
[42] D. Vasyukov, Y. Anahory, L. Embon, D. Halbertal, J. Cuppens, L. Neeman, A. Finkler, Y. Segev, Y. Myasoedov, M. L. Rappaport, M. E. Huber, and E. Zeldov, Nat. Nanotechnol. **8**, 639 (2013).
[43] G. Széchenyi and A. Pályi, Phys. Rev. B **95**, 035431 (2017).
[44] M. Pelliccione, A. Jenkins, P. Ovartchaiyapong, C. Reetz, E. Emmanouilidou, N. Ni, and A. C. Bleszynski Jayich, Nat. Nanotechnol. **11**, 700 (2016).
[45] A. Ariyaratne, D. Bluvstein, B. A. Myers, and A. C. Jayich, Nat. Commun. **9**, 2406 (2018).
[46] H. Walter, W. Prusseit, R. Semerad, H. Kinder, W. Assmann, H. Huber, H. Burkhardt, D. Rainer, and J. A. Sauls, Phys. Rev. Lett. **80**, 3598 (1998).
[47] Z. Diao, D. Campanini, L. Fang, W.-K. Kwok, U. Welp, and A. Rydh, Phys. Rev. B **93**, 014509 (2016).
[48] K. Willa, Z. Diao, D. Campanini, U. Welp, R. Divan, M. Hudl, Z. Islam, W.-K. Kwok, and A. Rydh, Rev. Sci. Instrum. **88**, 125108 (2017).
[49] S.-I. Suzuki and Y. Asano, Phys. Rev. B **89**, 184508 (2014).
[50] V. V. Dmitriev, A. A. Senin, A. A. Soldatov, and A. N. Yudin, Phys. Rev. Lett. **115**, 165304 (2015).
[51] N. Zhelev, M. Reichl, T. S. Abhilash, E. N. Smith, K. X. Nguyen, E. J. Mueller, and J. M. Parpia, Nat. Commun. **7**, 12975 (2016).
[52] S. B. Etter, A. Bouhon, and M. Sigrist, Phys. Rev. B **97**, 064510 (2018).
[53] N. Miyawaki and S. Higashitani, Phys. Rev. B **98**, 134516 (2018).
[54] G. Eilenberger, Z. Phys. **214**, 195 (1968).
[55] A. I. Larkin and Yu. N. Ovchinnikov, Zh. Eksp. Teor. Fiz. **55**, 2262 (1968) [Sov. Phys. JETP **28**, 1200 (1969)].
[56] A. Shelankov, J. Low Temp. Phys. **60**, 29 (1985).
[57] J. Serene and D. Rainer, Phys. Rep. **101**, 221 (1983).
[58] M. Eschrig, J. Heym, and D. Rainer, J. Low Temp. Phys. **95**, 323 (1994).
[59] M. Eschrig, D. Rainer, and J. A. Sauls, Phys. Rev. B **59**, 12095 (1999).
[60] J. A. Sauls and M. Eschrig, New J. Phys. **11**, 075008 (2009).
[61] Y. Nagato, K. Nagai, and J. Hara, J. Low Temp. Phys. **93**, 33 (1993).
[62] N. Schopohl and K. Maki, Phys. Rev. B **52**, 490 (1995).
[63] N. Schopohl, arXiv:cond-mat/9804064.
[64] M. Eschrig, J. A. Sauls, and D. Rainer, Phys. Rev. B **60**, 10447 (1999).
[65] M. Eschrig, Phys. Rev. B **61**, 9061 (2000).
[66] A. B. Vorontsov and J. A. Sauls, Phys. Rev. B **68**, 064508 (2003).
[67] M. Eschrig, Phys. Rev. B **80**, 134511 (2009).
[68] M. Håkansson, Mesoscopic thin film superconductors: A computational framework, Chalmers University of Technology Technical Report No. MC2-300, 2015.
[69] P. Holmvall, Modeling mesoscopic unconventional superconductors, Chalmers University of Technology Technical Report No. MC2-375, 2017.
[70] A. B. Vorontsov, Philos. Trans. R. Soc. A **376**, 20150144 (2018).
[71] S.-I. Suzuki and Y. Asano, Phys. Rev. B **91**, 214510 (2015).
[72] A. Poenicke, Y. S. Barash, C. Bruder, and V. Istyukov, Phys. Rev. B **59**, 7102 (1999).
[73] J.-X. Zhu, B. Friedman, and C. S. Ting, Phys. Rev. B **59**, 3353 (1999).
[74] A. A. Shanenko, M. D. Croitoru, and F. M. Peeters, Europhys. Lett. **76**, 498 (2006).

[75] L.-F. Zhang, L. Covaci, M. V. Milošević, G. R. Berdiyorov, and F. M. Peeters, Phys. Rev. Lett. **109**, 107001 (2012).

[76] L.-F. Zhang, L. Covaci, M. V. Milošević, G. R. Berdiyorov, and F. M. Peeters, Phys. Rev. B **88**, 144501 (2013).

[77] H. Huang, Q. Liu, W. Zhang, and Y. Chen, Physica B **500**, 53 (2016).

[78] G.-Q. Zha, Z.-L. Yang, Y.-Y. Jin, and S.-P. Zhou, Phys. Rev. B **94**, 094510 (2016).

[79] Z.-L. Yang, G.-Q. Zha, and S.-P. Zhou, Physica C **544**, 6 (2018).

[80] Y. Nagai, Y. Ota, and K. Tanaka, Phys. Rev. B **96**, 060503(R) (2017).

Paper IV

28th International Conference on Low Temperature Physics (LT28) IOP Publishing
IOP Conf. Series: Journal of Physics: Conf. Series **969** (2018) 012037 doi:10.1088/1742-6596/969/1/012037

Spontaneous generation of fractional vortex-antivortex pairs at single edges of high-Tc superconductors

P Holmvall, T Löfwander and M Fogelström

Department of Microtechnology and Nanoscience – MC2, Chalmers University of Technology,
SE-41296 Göteborg, Sweden

E-mail: `holmvall@chalmers.se`, `tomas.lofwander@chalmers.se`,
`mikael.fogelstrom@chalmers.se`

Abstract. Unconventional d-wave superconductors with pair-breaking edges are predicted to have ground states with spontaneously broken time-reversal and translational symmetries. We use the quasiclassical theory of superconductivity to demonstrate that such phases can exist at any single pair-breaking facet. This implies that a greater variety of systems, not necessarily mesoscopic in size, should be unstable to such symmetry breaking. The density of states averaged over the facet displays a broad peak centered at zero energy, which is consistent with experimental findings of a broad zero-bias conductance peak with a temperature-independent width at low temperatures.

1. Introduction

It was established already in the 1990s that a number of high-temperature superconductors have an order parameter with $d_{x^2-y^2}$ symmetry [1]. In such materials, quasiparticle scattering at surfaces or off defects, where the sign of the d-wave order parameter changes for incoming and outgoing scattering trajectories, leads to the formation of Andreev bound states at zero energy [2–4]. For an ideal specular surface with [110]-orientation, all scattering trajectories include the sign change, and the spectral weight of these zero-energy Andreev bound states is very large: they form a flat band at zero energy as function of momentum parallel to the interface, $k_{\|}$. Shifting these mid-gap states to finite energies can lead to lowering of the free energy. Any mechanism providing such a shift can then lead to a phase transition into a new ground state with an associated broken symmetry [5, 6]. Several mechanisms have been proposed, all leading to spontaneous time-reversal symmetry breaking: development of a subdominant superconducting component of the order parameter in a time-reversal symmetry breaking combination with the dominant, e.g. $d_{x^2-y^2} + is$, [7–9]; magnetic ordering [10]; and, finally, spontaneous supercurrents [11–16]. The first two scenarios require an additional coupling constant leading to an associated mean-field order parameter, while the last does not. Which scenario that would be realized experimentally depends on material parameters, for instance the strength of the coupling constants. It was shown in Ref. [15] that the transition temperature within the third scenario is very large, of the order of 20% of the superconducting transition temperature T_c. As a consequence, the other scenarios can compete only if their corresponding coupling constants are very large, or if the phase with spontaneous supercurrents is suppressed for one reason or another.

So far, there are several transport experiments supporting spontaneous time-reversal symmetry breaking [17–23]. But direct measurements of the associated supercurrents and magnetic fields remain controversial [24, 25]. In our previous studies [15], we showed that this controversy could be related to the manner in which these currents and magnetic fields appear. We found a translational and time-reversal symmetry-breaking phase, in which a staggered pattern of fractional vortex-antivortex pairs forms like a necklace along the pair-breaking surface. The symmetric proportion of vortices to antivortices effectively eliminates any net current and magnetic flux, and the small size of the vortices of a few coherence lengths makes direct observation challenging.

Vorontsov found that a phase gradient can be generated through spontaneous time-reversal symmetry breaking in thin films [14, 26–29], caused by finite-size effects in the form of a proximity of two pair-breaking interfaces. In our previous work [15] we studied mesoscopic grains with only pair-breaking edges and found that the vortex-antivortex phase is more energetically favorable than the thin-film phase predicted by Vorontsov. In this study, we show that the vortex-antivortex phase can occur without finite-size effects. This is done by considering a system with a single pair-breaking edge.

2. Model and methods

We study a mesoscopic superconducting grain in vacuum and equilibrium, with a d-wave pairing symmetry. The sides of the system are perfectly aligned with the crystal ab-axes, except one facet which is misaligned by a 45° rotation (see Fig. 1). The facet gives rise to mid-gap states associated with surface pair-breaking, and has a side-length given in units of the superconducting coherence length $\xi_0 \equiv \hbar v_F / 2\pi k_B T_c$. Furthermore, a clean superconductor and a cylindrical Fermi surface is assumed.

To study this system, the quasiclassical theory of superconductivity [30, 31] is used. In this formulation, the superconducting d-wave order parameter $\Delta_d(\boldsymbol{R})$ depends on the anomalous Green's function (pair propagator) $f(\boldsymbol{p}_F, \boldsymbol{R}; \epsilon_n)$ through the gap equation

$$\Delta_d(\boldsymbol{R}) = V_d k_B T \int \frac{d\theta_{p_F}}{2\pi} \eta_d^*(\theta_{p_F}) \sum_{|\epsilon_n| \le \Omega_c} f(\boldsymbol{p}_F, \boldsymbol{R}; \epsilon_n), \tag{1}$$

at spatial coordinate $\boldsymbol{R}$, quasiparticle momentum $\boldsymbol{p}_F$ and Matsubara energy ϵ_n (these parameters will from now on be dropped for a compact notation). Here, θ_{p_F} is the angle between the Fermi momentum and the crystal ab-axes, $\eta_d(\theta_{p_F}) = \sqrt{2}\cos(2\theta_{p_F})$ the d-wave order parameter basis function, $V_d = -N_F \lambda_d$ the pair-potential, N_F the normal-state density of states at the Fermi surface, λ_d the pairing interaction, and Ω_c the cutoff energy. The anomalous Green's function is the off-diagonal component of the Matsubara Green's function

$$\hat{g} = \begin{pmatrix} g & f \\ -\tilde{f} & \tilde{g} \end{pmatrix}, \tag{2}$$

where *hat* denotes Nambu (electron-hole) space. The tilde operation denotes particle-hole conjugation, $\tilde{g}(\boldsymbol{p}_F, \boldsymbol{R}; \epsilon_n) = g^*(-\boldsymbol{p}_F, \boldsymbol{R}, \epsilon_n)$ [and the same for $\tilde{f}$]. The Green's function is obtained by solving the Eilenberger equation with the associated normalization condition

$$i\hbar \boldsymbol{v}_F \cdot \boldsymbol{\nabla}_R \hat{g} + \left[\hat{\tau}_3 z - \hat{\Delta}, \hat{g}\right] = \hat{0}, \tag{3}$$

$$\hat{g}^2 = -\pi^2 \hat{1}, \tag{4}$$

where $\hat{\Delta} = i(\hat{\tau}_2\Re\Delta_d + \hat{\tau}_1\Im\Delta_d)\eta_d(\theta_{p_F})$, and $\hat{\tau}_i$ $(i = 1, 2, 3)$ are the three Pauli matrices in Nambu space. The Eilenberger equation and the gap equation are solved self-consistently by the so-called Riccati technique (see for instance Ref. [32]). After self-consistency has been achieved, we compute observables such as the current density

$$\boldsymbol{j}(\boldsymbol{R}) = 4\pi e N_F k_B T \int \frac{d\theta_{p_F}}{2\pi} \boldsymbol{v}_F(\boldsymbol{p}_F) \sum_{\epsilon_n} g(\boldsymbol{p}_F, \boldsymbol{R}; \epsilon_n). \tag{5}$$

The magnetic flux density induced by the current density is calculated through Maxwells equations and Ampère's circuit law.

3. Results and discussion

Figure 1 shows the induced magnetic flux density for two different superconducting grains that both have a single pair-breaking facet. The flux is generated by the fractional vortex-antivortex phase, and the pair-breaking facet is formed by cutting away either a triangular corner or a triangular section in the middle of a square grain, as shown in Figs. 1 (a) and (b), respectively. Thus, in the latter case, the pair-breaking facet is completely surrounded by bulk superconductivity. The fact that the phase persists in these two systems clearly illustrates a contrast to the Vorontsov phase [14], which relies on the proximity of two pair-breaking edges. Figure 1 (c) shows a magnification of the pair-breaking facet in Figure 1 (a). As shown, there

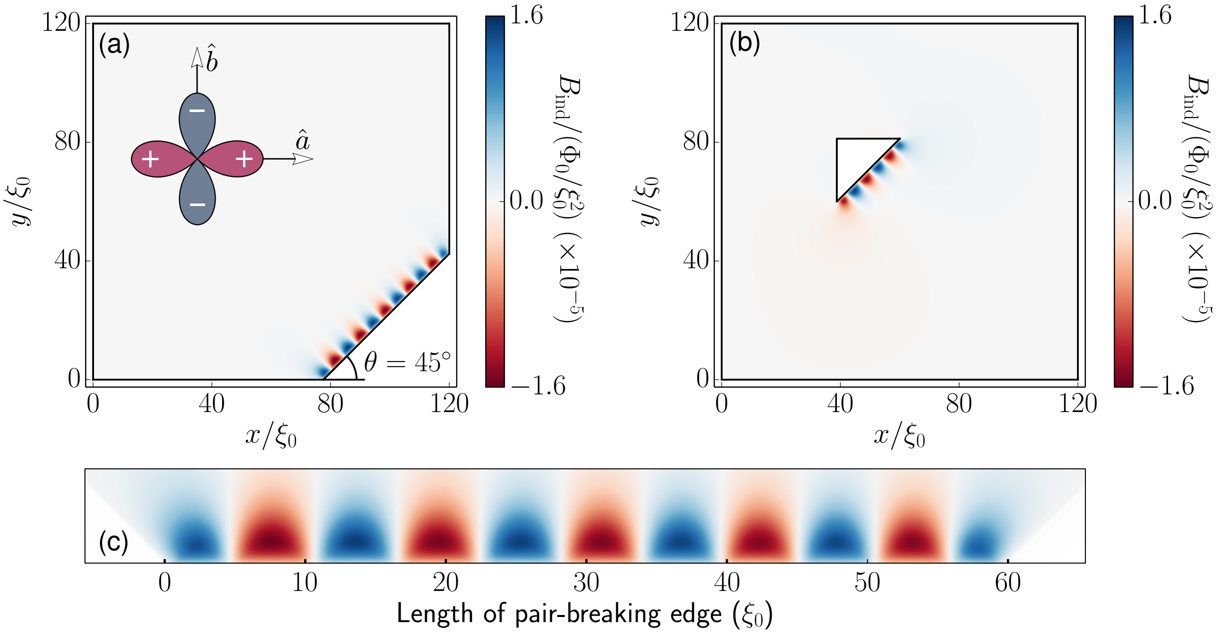

Figure 1. (Color online) (a) A d-wave superconducting grain at temperature $T = 0.1T_c$ with a spontaneously induced magnetic flux density, due to spontaneous generation of fractional vortices and antivortices. The latter breaks time-reversal and translational (along the facet) symmetries, and is linked to an energetically favorable Doppler shift of mid-gap states to finite energies. These mid-gap states are formed through pair-breaking along the diagonal grain facet, which is rotated 45° relative to the crystal ab-axes. All other grain edges are perfectly aligned with the crystal axes, as indicated by the graphics. In panel (b), a triangular portion of a square superconductor has been cut away, such that the pair-breaking facet is surrounded by bulk superconductivity. Panel (c) is a magnification of the pair-breaking facet in panel (a).

might be an unequal number of vortices and antivortices for certain sizes, although the flux density sums to zero. This is illustrated further in Fig. 2, where we vary the length of the pair-breaking facet in corner-cut systems. Each panel shows the induced flux along the pair-breaking facet in a square grain of side-length $120\xi_0$. The length of the facet varies from $2.5\xi_0$ in panel (a), to $66\xi_0$ in panel (f). There are two relevant regimes; one when the length of the facet is comparable to the fractional vortex size ($\sim 5\xi_0$), and another when it is much larger. In the latter case, the fractional vortices have a fairly constant diameter of $5\xi_0$, except the corner, or (outermost, vortices which are generally smaller. Lengthening the facet increases the size of the corner vortices, until they reach the same size as the central vortices, and new corner vortices are formed. Therefore, there might be an unequal number of vortices and antivortices for certain sizes. The flux density sums to zero, however, thanks to the corner vortices being much smaller. This again illustrates the fractionality of the vortices. The most striking feature, however, is that the phase survives even as the facet becomes smaller than $5\xi_0$, yielding a system with a single fractional vortex and a clear net flux. The system obviously finds it more favorable to shift the mid-gap states at the expense of having a net flux. Thus, the system with a single pair-breaking facet seems to lack a critical minimum size, in contrast to both the thin-film geometry [14], and the mesoscopic grain where all sides are pair-breaking [15].

Finally, Figs. 3 (a)–(b) show the density of states (DOS) along the facet for the systems in Figs. 2 (a)–(b), respectively. All other systems have an identical DOS as in panel (b). The solid

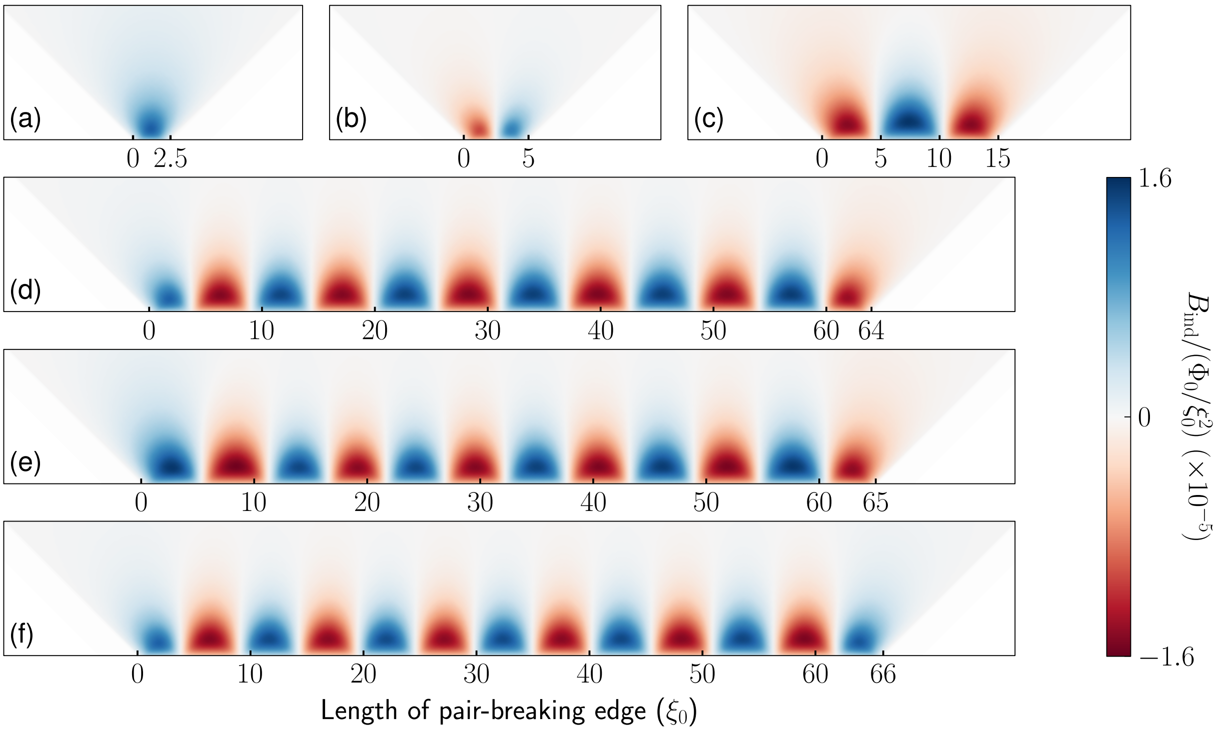

Figure 2. (Color online) Magnetic flux density due to spontaneous fractional vortices along a pair-breaking facet, where the length of the facet varies from panel (a) to (f). In each panel, the system is a square grain with a side-length of $120\xi_0$, with one of the corners cut off at a 45° angle to generate the pair-breaking facet, as illustrated in Fig. 1 (a). Due to finite-size effects, there might be an unequal amount of vortices and antivortices, although the total flux still adds to zero. The only exception is when the facet is smaller than the typical vortex size ($\sim 5\xi_0$) as in panel (a), at which point there is a single vortex and a net flux. The temperature is $T = 0.1T_c$.

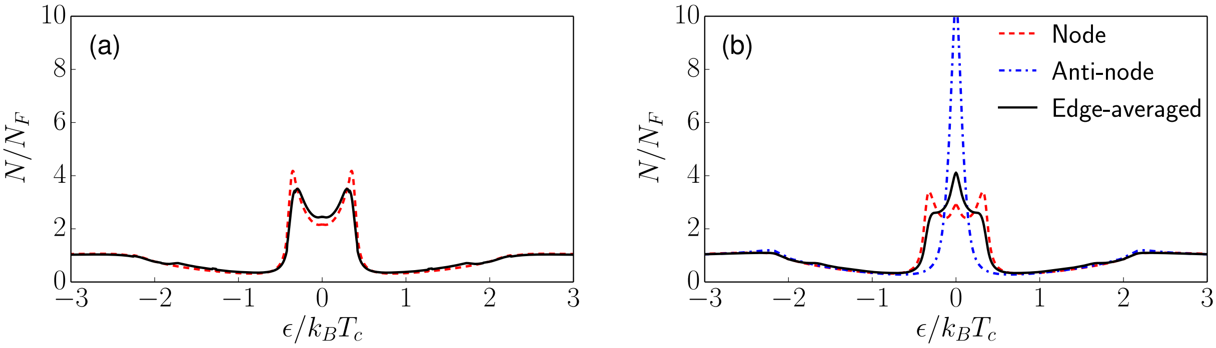

Figure 3. (Color online) Density of states as a function of energy at the pair-breaking facet, evaluated in the middle of a vortex current (dashed line) and between vortices (dot-dashed line). The solid line is the facet-averaged density of states. Panels (a)–(b) correspond to the systems in Figs. 2 (a)–(b), respectively. The rest of the systems have an identical DOS as in panel (b).

lines represent the facet-averaged DOS, the dashed lines the local DOS at a node (vortex) and the dot-dashed lines the local DOS at an anti-node (between vortices). System (a) has a single vortex, resulting in a fully split peak. All other systems show a wide peak in the facet-averaged DOS. This result would be observable in a tunneling experiment as a conductance peak centered at zero energy with a rather large width, that at low temperatures is temperature independent. Only for system (a), or with a very local probe (point contact with a diameter smaller than the superconducting coherence length) would a split conductance peak be observable.

4. Conclusions

We have used the quasiclassical theory of superconductivity to study a phase that spontaneously breaks translational and time-reversal symmetries at pair-breaking edges, in unconventional d-wave superconductors. Similar phases have been suggested by theory for quite some time, but up until now, have relied on finite-size effects and the proximity of two such pair-breaking edges. We have shown that such finite-size effects are not necessary for such a phase to exist, and that there is no clear critical size below which the phase disappears. This implies that any system with pair-breaking edges should be unstable to the formation of fractional vortices. Therefore, the phase should be present at a greater variety of systems than previously proposed, and lead to a broadening of zero-bias conductance peaks.

Acknowledgments

We thank the Swedish Research Council (VR) for financial support. It is a pleasure to thank Mikael Håkansson, Niclas Wennerdal and Anton Vorontsov for valuable discussions.

References

[1] Tsuei C C and Kirtley J R 2000 *Rev. Mod. Phys.* **72** 969
[2] Hu C R 1994 *Phys. Rev. Lett.* **72** 1526
[3] Kashiwaya S and Tanaka Y 2000 *Rep. Prog. Phys.* **63** 1641
[4] Löfwander T, Shumeiko V S and Wendin G 2001 *Supercond. Sci. Technol.* **14** R53
[5] Volovik G and Gor'kov L 1985 *Sov. Phys. JETP* **61** 843
[6] Sigrist M and Ueda K 1991 *Rev. Mod. Phys.* **63** 239
[7] Matsumoto M and Shiba H 1995 *J. Phys. Soc. Jpn.* **64** 3384
[8] Matsumoto M and Shiba H 1995 *J. Phys. Soc. Jpn.* **64** 4867

[9] Fogelström M, Rainer D and Sauls J A 1997 *Phys. Rev. Lett.* **79** 281
[10] Potter A C and Lee P A 2014 *Phys. Rev. Lett.* **112** 117002
[11] Higashitani S 1997 *J. Soc. Phys. Jpn.* **66** 2556
[12] Barash Y S, Kalenkov M S and Kurkijärvi J 2000 *Phys. Rev. B* **62** 6665
[13] Löfwander T, Shumeiko V S and Wendin G 2000 *Phys. Rev. B* **62** R14653
[14] Vorontsov A B 2009 *Phys. Rev. Lett.* **102** 177001
[15] Håkansson M, Löfwander T and Fogelström M 2015 *Nat. Phys.* **11** 755
[16] Nagai Y, Ota Y and Tanaka K 2017 *Phys. Rev. B* **96** 060503
[17] Covington M, Aprili M, Paraoanu E, Greene L H, Xu F, Zhu J and Mirkin C A 1997 *Phys. Rev. Lett.* **79** 277
[18] Krishana K, Ong N P, Li Q, Gu G D and Koshizuka N 1997 *Science* **277** 83
[19] Dagan Y and Deutscher G 2001 *Phys. Rev. Lett.* **87** 177004
[20] Gonnelli R, Calzolari A, Daghero D, Natale L, Ummarino G, Stepanov V and Ferretti M 2001 *Eur. Phys. J. B* **22** 411
[21] Elhalel G, Beck R, Leibovitch G and Deutscher G 2007 *Phys. Rev. Lett.* **98** 137002
[22] Gustafsson D, Golubev D, Fogelström M, Claeson T, Kubatkin S, Bauch T and Lombardi F 2013 *Nat. Nanotechnol.* **8** 25
[23] Watashige T, Tsutsumi Y, Hanaguri T, Kohsaka Y, Kasahara S, Furusaki A, Sigrist M, Meingast C, Wolf T, Löhneysen H v, Shibauchi T and Matsuda Y 2015 *Phys. Rev. X* **5** 031022
[24] Neils W K and Van Harlingen D J 2002 *Phys. Rev. Lett.* **88** 047001
[25] Kirtley J, Tsuei C, Ariando A, Verwijs C, Harkema S and Hilgenkamp H 2006 *Nat Phys* **2** 190
[26] Hachiya M, Aoyama K and Ikeda R 2013 *Phys. Rev. B* **88** 064519
[27] Higashitani S and Miyawaki N 2015 *J. Soc. Phys. Jpn.* **84** 033708
[28] Miyawaki N and Higashitani S 2015 *Phys. Proc.* **65** 25
[29] Miyawaki N and Higashitani S 2015 *Phys. Rev. B* **91** 094511
[30] Eilenberger G 1968 *Z. Phys.* **214** 195
[31] Larkin A I and Ovchinnikov Y N 1969 *Sov. Phys. JETP* **28** 1200
[32] Eschrig M 2009 *Phys. Rev. B* **80** 134511